

Lecture Notes in Civil Engineering

Zhishen Wu
Tomonori Nagayama
Ji Dang
Rodrigo Astroza *Editors*

Experimental Vibration Analysis for Civil Engineering Structures

Select Proceedings of the EVACES 2021

 Springer

Lecture Notes in Civil Engineering

Volume 224

Series Editors

Marco di Prisco, Politecnico di Milano, Milano, Italy

Sheng-Hong Chen, School of Water Resources and Hydropower Engineering,
Wuhan University, Wuhan, China

Ioannis Vayas, Institute of Steel Structures, National Technical University of
Athens, Athens, Greece

Sanjay Kumar Shukla, School of Engineering, Edith Cowan University, Joondalup,
WA, Australia

Anuj Sharma, Iowa State University, Ames, IA, USA

Nagesh Kumar, Department of Civil Engineering, Indian Institute of Science
Bangalore, Bengaluru, Karnataka, India

Chien Ming Wang, School of Civil Engineering, The University of Queensland,
Brisbane, QLD, Australia

Lecture Notes in Civil Engineering (LNCE) publishes the latest developments in Civil Engineering - quickly, informally and in top quality. Though original research reported in proceedings and post-proceedings represents the core of LNCE, edited volumes of exceptionally high quality and interest may also be considered for publication. Volumes published in LNCE embrace all aspects and subfields of, as well as new challenges in, Civil Engineering. Topics in the series include:

- Construction and Structural Mechanics
- Building Materials
- Concrete, Steel and Timber Structures
- Geotechnical Engineering
- Earthquake Engineering
- Coastal Engineering
- Ocean and Offshore Engineering; Ships and Floating Structures
- Hydraulics, Hydrology and Water Resources Engineering
- Environmental Engineering and Sustainability
- Structural Health and Monitoring
- Surveying and Geographical Information Systems
- Indoor Environments
- Transportation and Traffic
- Risk Analysis
- Safety and Security

To submit a proposal or request further information, please contact the appropriate Springer Editor:

- Pierpaolo Riva at pierpaolo.riva@springer.com (Europe and Americas);
- Swati Meherishi at swati.meherishi@springer.com (Asia - except China, and Australia, New Zealand);
- Wayne Hu at wayne.hu@springer.com (China).

All books in the series now indexed by Scopus and EI Compendex database!

More information about this series at <https://link.springer.com/bookseries/15087>

Zhishen Wu · Tomonori Nagayama · Ji Dang ·
Rodrigo Astroza
Editors

Experimental Vibration Analysis for Civil Engineering Structures

Select Proceedings of the EVACES 2021

 Springer

Editors

Zhishen Wu
Department of Urban and Civil, Faculty
of Engineering
Ibaraki University
Hitachi, Ibaraki, Japan

Tomonori Nagayama
Department of Civil Engineering
The University of Tokyo
Bunkyo, Tokyo, Japan

Ji Dang
Department of Civil and Environmental
Engineering
Saitama University
Saitama, Japan

Rodrigo Astroza
Faculty of Engineering and Applied
Sciences
Universidad de los Andes
Santiago, Chile

ISSN 2366-2557

ISSN 2366-2565 (electronic)

Lecture Notes in Civil Engineering

ISBN 978-3-030-93235-0

ISBN 978-3-030-93236-7 (eBook)

<https://doi.org/10.1007/978-3-030-93236-7>

© The Editor(s) (if applicable) and The Author(s), under exclusive license to Springer Nature Switzerland AG 2023

This work is subject to copyright. All rights are solely and exclusively licensed by the Publisher, whether the whole or part of the material is concerned, specifically the rights of translation, reprinting, reuse of illustrations, recitation, broadcasting, reproduction on microfilms or in any other physical way, and transmission or information storage and retrieval, electronic adaptation, computer software, or by similar or dissimilar methodology now known or hereafter developed.

The use of general descriptive names, registered names, trademarks, service marks, etc. in this publication does not imply, even in the absence of a specific statement, that such names are exempt from the relevant protective laws and regulations and therefore free for general use.

The publisher, the authors, and the editors are safe to assume that the advice and information in this book are believed to be true and accurate at the date of publication. Neither the publisher nor the authors or the editors give a warranty, expressed or implied, with respect to the material contained herein or for any errors or omissions that may have been made. The publisher remains neutral with regard to jurisdictional claims in published maps and institutional affiliations.

This Springer imprint is published by the registered company Springer Nature Switzerland AG
The registered company address is: Gewerbestrasse 11, 6330 Cham, Switzerland

Committees of EVACES 2021

International Scientific Committee

Ahmet E. Aktan, Drexel University, USA
Rodrigo Astroza, Universidad de los Andes, Chile
Flavio Barbosa, Federal University of Juiz de Fora, Brazil
Jan Bien, Wroclaw University of Science and Technology, Poland
Elsa Caetano, University of Porto, Portugal
Joel P. Conte, University of California San Diego, USA
Christian Cremona, Bouygues Construction, France
Alvaro Cunha, University of Porto, Portugal
Alexandre A. Cury, University of Juiz de Fora, Brazil
Guido De Roeck, KU Leuven, Belgium
Glauco Feltrin, EMPA, Switzerland
Alain Fournol, AVLS, France
Carmelo Gentile, Politecnico di Milano, Italy
Paweł Hawryszków, Wroclaw University of Science and Technology, Poland
Raid Karoumi, KTH Royal Institute of Technology, Sweden
Mieszko Kuźawa, Wroclaw University of Science and Technology, Poland
Maria P. Limongelli, Politecnico di Milano, Italy
Antonino Morassi, University of Udine, Italy
Patrick Paultre, University of Sherbrooke, Canada
Aleksandar Pavic, University of Exeter, United Kingdom
Luis F. Ramos, University of Minho, Portugal
Zhishen Wu, Ibaraki University, Japan
Jian Zhang, Southeast University, China

National Advisory Committee

Zhishen Wu, Ibaraki University
Akira Igarashi, Kyoto University
Kohju Ikago, Tohoku University
Chul-Woo Kim, Kyoto University
Takeshi Kitahara, Kanto Gakuin University
Kouichi Kusunoki, The University of Tokyo
Masayuki Nagano, Tokyo University of Science
Izuru Takewaki, Kyoto University

National Organizing Committee

Ji Dang, Saitama University
Chandra S. Goit, Saitama University
Jun Iyama, The University of Tokyo
Yasunao Matsumoto, Saitama University
Takashi Miyamoto, Yamanashi University
Takeshi Miyashita, Nagaoka University of Technology
Tomonori Nagayama, The University of Tokyo
Mayuko Nishio, Tsukuba University
Yoshihiro Nitta, Ashikaga University
Di Su, The University of Tokyo
Xin Wang, Ashikaga University

Preface

Research, development, and applications in experimental vibration analysis of civil engineering structures are being fed by the continuous progress in the fields of sensor and testing technologies, instrumentation, data acquisition systems, computer technology, data analysis techniques, and computational modeling and simulation of large and complex civil infrastructure systems. The objectives and challenges are to understand the behavior and state of health of structural, geo-structural, and soil-foundation-structural systems as well as predicting their remaining useful life using vibration data collected from these systems when subjected to operational and/or extreme loads. Advanced data analysis methods (e.g., system and damage identification, machine learning, and deep learning) are employed to extract information and knowledge from the data and to gain the insight required to support decision-making related to maintenance and inspection, retrofit, upgrade, rehabilitation, and emergency response of these systems.

EVACES, the International Conference on Experimental Vibration Analysis for Civil Engineering Structures, is a premier venue where recent progress in the field are presented and discussed by experts from all over the world. After the first eight successful editions of EVACES which took place in Bordeaux, France (2005), Porto, Portugal (2007), Wroclaw, Poland (2009), Varenna, Italy (2011), Ouro Preto, Brazil (2013), Dübendorf, Switzerland (2015), San Diego, United States of America (2017), and Nanjing, China (2019), EVACES 2021 was successfully held online from September 14–17th, 2021 and hosted by the University of Tokyo and Saitama University.

In the 2021 version of EVACES, a total of 201 participants were registered and 56 papers were presented. The topics of EVACES 2021 included but not limited to (1) damage identification and structural health monitoring, (2) testing, sensing and modeling, (3) vibration isolation and control, (4) system and model identification, (5) coupled dynamical systems (including human-structure, vehicle structure, and soil-structure interaction), (6) application of artificial intelligence techniques. Two special topics: (7) drive-by based technology, and (8) damage free and resilience for seismic disaster were also presented and discussed.

The conference was full of presentations of state-of-art studies, lively discussions, and friendly communications. Among many young participants and presenters, Chun-Man Liao, Elyas Bayat, Silvia Monchetti, Sal Saad Al Deen Taher, Haoqi Wang, and Fengming Yu were selected as the recipients of the Young Researcher Award of EVACES 2021.

Even though participants were physically away from each other, the online conference was a chance to meet old friends and make new friends. We hope these proceedings can be a collection of the excellent works presented at EVACES 2021, a proof of the progress in the research and a milestone of this area.

We would also like to thank the keynote speakers, Prof. Yozo Fujino, Prof. Yang Wang, Prof. Kazuhiko Kasai, and Prof. Eugene J. O'Brien for their splendid lectures. We believe their impressive research and their thought behind inspired all participants, in particular young researchers.

The International Scientific Committee and the National Advisory Committee, as listed in later pages, gave us tremendous support and guidance in our difficult time during the pandemic. Here, we would like to express our respect and appreciation for those help. The Organizing Committee members, as listed in the later pages, worked very hard the last two years to substantialize this conference. We appreciate for their great contributions very much. We would also like to express our gratitude to student assistants from the University of Tokyo and Saitama University for their help in the online conference management.

Hitachi, Japan
Saitama, Japan
Bunkyo, Japan
Santiago, Chile
September 2021

Zhishen Wu
Ji Dang
Tomonori Nagayama
Rodrigo Astroza

Contents

Damage Identification and Structural Health Monitoring	
Damage Assessment of Civil Structures Using Wave Propagation Analysis and Transmissibility Functions	3
Chun-Man Liao and Yuri Petryna	
SHM Campaign on 138 Spans of Railway Viaducts by Means of OMA and Wireless Sensors Network	15
Lorenzo Bernardini, Lorenzo Benedetti, Claudio Somaschini, Gabriele Cazzulani, and Marco Belloli	
Effect of Damage on Vibration Characteristics of Reinforced Concrete Deck Slabs in an Existing Steel Girder Bridge	27
Sania Gohar, Sonam Lhamo, Yasunao Matsumoto, and Satoru Sakuma	
Assessing Structural Health State by Monitoring Peridynamics Parameters in Operational Conditions	39
Gaetano Miraglia, Erica Lenticchia, Marco Civera, and Rosario Ceravolo	
Impact Damage Identification Using Chirped Ultrasonic Guided Waves for Health Monitoring of CFRP Vehicle Structures	51
Langxing Tan, Fengming Yu, Osamu Saito, Yoji Okabe, Taku Kondoh, Shota Tezuka, and Akihiro Chiba	
Bayesian Model Updating of a Simply-Supported Truss Bridge Based on Dynamic Responses	59
Xin Zhou, Chul-Woo Kim, Feng-Liang Zhang, Kai-Chun Chang, and Yoshinao Goi	
Vibration-Based Method for Structural Health Monitoring of a Bridge Pier Subjected to Environmental Loads	73
Mohamed Belmokhtar, Franziska Schmidt, Christophe Chevalier, and Alireza Ture Savadkoohi	

Damage Detection and Localization Using Autocorrelation Functions with Spatiotemporal Correlation	83
Jyrki Kullaa	
The Optimization Study of Apparent Damage Recognition Algorithm of Bridge Underwater Structure	97
Yeteng Wang, Haoyang Ding, Changlin Song, Yao Xiao, Ruiyang Yuan, and Zhishui Liang	
The Value of Different Monitoring Systems in the Management of Scoured Bridges	109
Pier Francesco Giordano, Luke J. Prendergast, and Maria Pina Limongelli	
Testing, Sensing, and Modeling	
Vibration Measurements on a Cable-Stayed Cyclist Arch Bridge for Assessment of the Dynamic Behaviour	125
Stefan Verdenius, Okke Bronkhorst, and Chris Geurts	
Experimental and Numerical Characterization of the Dynamic Behaviour of a Historic Suspension Footbridge	137
Elyas Bayat and Federica Tubino	
Vision-Based Vibration Measurement of Stay-Cables by Video Motion Magnification and Dynamic Mode Decomposition	149
Samten Wangchuk, Dionysius M. Siringoringo, and Yozo Fujino	
A Fiber-Optic Ultrasonic Visualization Technique for Damage Detection in a 1000 °C Environment	163
Fengming Yu, Osamu Saito, Yoji Okabe, and Zixuan Li	
Application of Regenerated Phase-Shifted Fiber Bragg Grating Sensors to Acoustic Emission Detection Under Elevated Temperature	173
Zixuan Li, Fengming Yu, Osamu Saito, and Yoji Okabe	
Experimental Investigation of Galloping Susceptibility of U Beams with Different Flange Porosity	183
Stanislav Hračov and Michael Macháček	
Development of Sensor Unit for Extraction/Transmission of Only Peak Acceleration Response	195
Yoshihiro Nitta and Akira Nishitani	
Indirect Estimation Method of Bridge Displacement Under Moving Vehicle Based on Measured Acceleration	207
Mingwei Wang, Yan Li, Guowei Lin, Baocheng Liu, and Changyun Ye	

In-Situ Measurements for the Structural Monitoring of Galleria dell’Accademia di Firenze (Italy): Preliminary Results of the Tribuna 223
 Silvia Monchetti, Gianni Bartoli, Michele Betti, Claudio Borri, Claudia Gerola, Andrea Giachetti, Cecilie Hollberg, Vladimir C. Kovacevic, Carlotta Matta, and Giacomo Zini

Structural Monitoring of an Aerial Tramway System During Operation: Modeling and Simulation Strategy with Experimental Data Validation 233
 Hugo Bécu, Claude-Henri Lamarque, Alireza Ture Savadkoohi, Michel Gillard, and Christophe Bottollier

Structural Modeling to Predict the Vibrations of a Footbridge Due to Pedestrian Movements 247
 Mehdi Setareh and Mohammad Bukhari

Vibration Serviceability of Two-Story Office Building: A Finite Element Modeling 257
 Fadi A. Al-Badour

Vibration Isolation and Control

An Economical Multiple-Tuned Mass Damper to Control Floor Vibrations 273
 Mehdi Setareh

Experimental Study of a Two-Degree-of Freedom Pendulum Controlled by a Non-smooth Nonlinear Energy Sink 283
 Gabriel Hurel, Alireza Ture Savadkoohi, and Claude-Henri Lamarque

Hybrid Simulation for Seismic Isolation Effectiveness Assessment of HDR Bearings at Low Temperature 295
 Yuqing Tan, Ji Dang, Akira Igarashi, Takehiko Himeno, Yuki Hamada, and Yoshifumi Uno

A Thermo-Mechanical Coupled Model of Hysteresis Behavior of HDR Bearings 307
 Yuqing Tan, Ji Dang, Akira Igarashi, Takehiko Himeno, and Yuki Hamada

Research on Seismic Response of Single-Tower Cable-Stayed Bridge Across Faults 321
 Feng Jiang, Li-Peng Liu, Feng-Chao Jiang, and Jia-Qi Li

Analysis on the Behavior of Seismic Retrofitting Steel Brace Based on Acceleration and Strain Response Measurements 335
 Tsuyoshi Koyama, Jun Iyama, Yoshihiro Fukushima, Shota Miyazaki, and Naoto Kato

System and Model Identification

Probabilistic Time-Variant Linear Finite Element Model Updating for Nonlinear Structural Systems 349

Felipe Mizon, Matías Birrell, José Abell, and Rodrigo Astroza

Ambient Vibration Based Modal Analysis and Cable Tension Estimation for a Cable-Stayed Bridge with Bayesian Approaches 365

W. J. Jiang, Chul-Woo Kim, Xin Zhou, and Yoshinao Goi

Tension Estimation Method for Cable with Damper and Its Application to Real Cable-Stayed Bridge 379

Aiko Furukawa, Katsuya Hirose, and Ryosuke Kobayashi

Evaluation of Damping Ratio of Buildings Using Seismic Interferometry Method 391

Zheng Zhang, Xin Wang, and Masayuki Nagano

Structural Parameter Identification of a Reinforced Concrete Frame Using Constrained Unscented Kalman Filter 401

Dan Li

Dynamic Response Evaluation of an Existing Bridge Structure Based on Finite Element Modeling 413

Muhammad Rashid and Mayuko Nishio

A New Attempt at Estimating Natural Vibration and Bending Deformation Characteristics of Super High-Rise Buildings Using Wave Interferometry 429

Xin Wang, Testushi Watanabe, and Masayuki Nagano

Structural Damage Identification Using Spectral Finite Element Modeling for Extended Timoshenko Beams 439

Krishna Modak, T. Jothi Saravanan, and Shanthanu Rajasekharan

Experimental Study on Identification of Structural Changes Using Wavelet Energy Features 453

Xiaobang Zhang, Yong Lu, Zachariah Wynne, and Thomas P. S. Reynolds

Identification of the Dynamic Properties of the Residential Tower New Orleans 469

A. J. Bronkhorst, D. Moretti, and C. P. W. Geurts

Coupled Dynamical Systems

Response Spectrum Method for Vehicle-Induced Bridge Vibration Serviceability Design 483

Haoqi Wang and Tomonori Nagayama

A Railway Vibration Simulation Considering Contact Conditions Between Structures and Ground 493
Toru Gondo, Hidefumi Yokoyama, and Yuta Mitsuhashi

Vortex Induced Vibration Analysis of a Triangle Prism at Different Velocities 503
Johny Shaida Shaik and Putti Srinivasa Rao

Effect of the Deterioration Degree of the Backside Weak Zone on the Seismic Response of the Tunnel and Surrounding Ground 517
Saddy Ahmed and Ying Cui

Application of Artificial Intelligence Techniques

Machine Learning Enhanced Nonlinear Model Parameter Selection from HDR-S Cyclic Loading Test 531
Katrina Montes, Ji Dang, Yuqing Tan, Akira Igarashi, and Takehiko Himeno

Autonomous Multiple Damage Detection and Segmentation in Structures Using Mask R-CNN 545
Sal Saad Al Deen Taher and Ji Dang

Nonlinear Model Classification of HDR-S Bearing Under Low Temperature Using Artificial Neural Network 557
Katrina Montes, Ji Dang, Yuqing Tan, Akira Igarashi, and Takehiko Himeno

Automatic Top-View Transformation and Image Stitching of In-Vehicle Smartphone Camera for Road Crack Evaluation 567
Jose Maria G. Geda, Kai Xue, and Tomonori Nagayama

Assessment of Damage in Composite Beams with Wavelet Packet Node Energy Features and Machine Learning 581
Yu Gu and Yong Lu

Scalable and Probabilistic Point-Cloud Generation for UAS-Based Structural Assessment 595
Qingli Zeng and ZhiQiang Chen

Drive-By Technology

Drive-By Detection of Midspan Cracking and Changing Boundary Conditions in Bridges 607
Robert Corbally and Abdollah Malekjafarian

Load Carrying Capacity and Vibration Characteristics of PC Box Girders with Damage 619
K. Takemura, Chul-Woo Kim, G. Hayashi, and E. Yoshida

The Validation of Sensor On-Vehicle for Evaluation of Actual Bridges with Signal Processing 631
Yuta Takahashi, Naoki Kaneko, Ryota Shin, and Kyosuke Yamamoto

Inverse Analysis for Road Roughness Profile Identification Utilizing Acceleration of a Moving Vehicle 643
Soichiro Hasegawa, Chul-Woo Kim, Naoya Toshi, and Kai-Chun Chang

Damage Free and Resilience for Seismic Disaster

Rheological Model and Parameter Identification of a Kinetic Sand Used as a Smart Damping Material 657
Jacek M. Bajkowski, Bartłomiej Dyniewicz, Czesław Bajer, and Jerzy Bajkowski

Numerical Investigation on Longitudinal Forces on Bridges of Indian Railways 665
Swapnil Chaurasia and Di Su

Monitoring-Based MBS-FEM Analysis Scheme for Wind-Vehicle-Bridge Interaction System and Experimental Validation 681
Qi Hu and Di Su

Damage Identification and Structural Health Monitoring

Damage Assessment of Civil Structures Using Wave Propagation Analysis and Transmissibility Functions



Chun-Man Liao and Yuri Petryna

Abstract A common damage detection method in civil engineering is to monitor dynamic characteristics such as natural frequencies and modal shapes, which are directly related to the structural stiffness. However, the discrepancy in measured natural frequencies may result from environmental changes, the soil-structure interaction or effects caused by earthquakes. This makes it difficult to decide whether the local change in structural properties is caused by damage or other factors. To address this challenge and thus improve the current damage detection method, the wave propagation analysis method and the transmissibility relationship were considered. In our study, the wave propagation field in structures was reconstructed by applying the Normalized-Input-Output-Minimization (NIOM) method to vibration recordings. Wave velocities and transmissibility functions were considered as reference values for the damage indicators. This paper demonstrates the evaluation of local property changes in two examples of large-scale structures: a 14-story RC building and a 64 m long pedestrian bridge. The proposed damage indicators show a clear correspondence to structural changes.

Keywords Damage detection · Damage indices · Normalized-Input-Output-Minimization · Transmissibility function · Wave propagation

1 Introduction

Structural health monitoring is an essential part in the prevention of structural failures that can threaten life safety. Many engineers prefer the vibration approach to obtain the dynamic response of structures. In civil engineering, the modal analysis is

C.-M. Liao (✉)
Bundesanstalt für Materialforschung und -prüfung (BAM), Berlin, Germany
e-mail: Chun-Man.Liao@bam.de

Y. Petryna
Institute for Civil Engineering, Technische Universität Berlin, Berlin, Germany

© The Author(s), under exclusive license to Springer Nature Switzerland AG 2023
Z. Wu et al. (eds.), *Experimental Vibration Analysis for Civil Engineering Structures*,
Lecture Notes in Civil Engineering 224,
https://doi.org/10.1007/978-3-030-93236-7_2

a useful tool for the vibration approach to identify the natural frequencies and mode shapes of structures. In terms of dynamic analysis, these characteristics are directly related to the structural stiffness and the system mass. Therefore, the change in vibration response is considered to be a direct influence of structural damage [1]. Since a decrease in frequency is expected as the damage progresses (causing a lower stiffness), some studies [2–4] aimed to determine the representative natural frequency of structures. However, vibration measurement is susceptible to change in temperature [5] or the sudden external excitation from earthquakes [6]. Accordingly, the change in measured dynamic properties is not reliable for damage detection.

To overcome this challenge, we applied wave propagation analysis, which is very commonly used in geophysics for characterizing soil properties [7]. The superiority of wave propagation lies in its continuum property, which can fulfil the wave screening in large-scale structures. Assuming that the wave features in the building structure are independent of the coupling of the building to the ground [8, 9] and the temperature, the detection of damage by the wave velocity change is more credible than by observing the global vibration response change. Thus, the wave velocity is more sensitive to the local structural properties change than to the natural frequency. Regarding this, wave propagation analysis has been proposed in this work for damage detection. We demonstrated how to determine the wave propagation in civil structures in practice. In this case, the dynamic response of the real structures was recorded first. Then the seismic interferometry technique was applied to the vibration recordings.

The seismic interferometry technique is based on the correlation of waves recorded at different receivers. The deconvolution of the motion recorded at several locations in a system results in an impulsive wave propagation in the system [9]. This impulse response is used to investigate earthquake records [10–14] and ambient vibrations [15] of building structures. However, the wave parameters estimated by the impulse response method are rather different from those during a strong earthquake motion, and thus bias the simplified wave propagation model. The Normalized-Input-Output-Minimization (NIOM) method [16] has been proposed for modeling wave propagation in multiple linear systems. This method has been used to study the strong motion records for buildings [17], but has not yet been applied to seismic noise vibration measurements.

This paper, according to the research work in [18], shows the application of NIOM to the ambient vibration measurement to retrieve the wave propagation in the real structure. The relationship between the wave velocities and the structural properties was revealed. To verify the wave propagation analysis for damage detection, the transmissibility function (TF) was introduced. The TF characterizes the structural properties, e.g. the mass, stiffness and damping ratio, in the frequency domain. The frequency amplitude of the TF reflects the critical frequency, which interprets the dominant modal frequency in the operational modal analysis [19]. The damage indicator is based on the shift of the frequency amplitude of the TF. For the definition of damage indices, the difference of the TF in two states (e.g. intact and damaged) was quantified.

2 Wave Propagation Analysis Method

2.1 Background

Generally, geophysicist use the wave propagation approach (seismic interferometry) to investigate the motions at the surface or along the depth of the soil. The deconvolution method is one of the interferometry techniques and can retrieve Green's function between two receivers. The feature of Green's function is the impulsive wave propagation, based on which the wave velocity can be estimated [9]. Since the wave propagation velocity depends only on the characteristics of the materials through which the wave propagates, the application of seismic interferometry in the subsoil has been extended to building structures [3, 10]. The assumption of the building structure is a layered continuum and can be considered as a multiple linear system.

2.2 Normalized-Input-Output-Minimization (NIOM)

In the following, a brief overview of the NIOM method for analyzing wave propagation in structures is given [16]. Taking the soil structure as an example, the statistical correlation of earthquake motions at different observation points is considered. When a time-invariant linear soil system is subjected to earthquake motion, the input and output of the system can be related in the frequency domain by means of transfer function $H(\omega_i)$.

$F(\omega_i)$ and $G(\omega_i)$ are the Fourier transforms of the actual ground motion input and output, respectively. The output at each frequency is given by:

$$G(\omega_i) = H(\omega_i)F(\omega_i), \quad (1)$$

where $i = 0, \dots, N - 1$ and $\omega_i = i \frac{2\pi}{N\Delta t}$. N is the number of samples, Δt is the sampling rate in the time domain.

This transfer function satisfies the relation of the new input model, $X(\omega_i)$, and the new output model, $Y(\omega_i)$, because the transfer function depends only on physical properties of the soil systems.

Assuming the amplitude of the new input is desired to be constant at an arbitrary point in time, the constraint holds:

$$\frac{1}{N\Delta t} \sum_{i=0}^{N-1} X(\omega_i) = 1. \quad (2)$$

Thus, the value of the new input is defined to be normalized to unity.

Using the method of Lagrange multipliers, squared Fourier amplitude spectra of the new input and the new output are minimized if they are subject to the constraint. Therefore,

$$L = \sum_{i=0}^{N-1} \{|X(\omega_i)|^2 + |Y(\omega_i)|^2\} - \lambda \left\{ \frac{1}{N \Delta t} \sum_{i=0}^{N-1} X(\omega_i) - 1 \right\}, \quad (3)$$

where λ is the Lagrange multiplier.

Consequently, the simplified new input model is determined by

$$X(\omega_i) = N \Delta t \frac{\frac{1}{1+|H(\omega_i)|^2}}{\sum_{n=0}^{N-1} \frac{1}{1+|H(\omega_n)|^2}} \quad (4)$$

and the response of the linear system by

$$Y(\omega_i) = N \Delta t \frac{\frac{H(\omega_i)}{1+|H(\omega_i)|^2}}{\sum_{n=0}^{N-1} \frac{1}{1+|H(\omega_n)|^2}}. \quad (5)$$

The impulsive wave propagation is obtained by the inverse Fourier transform of Eqs. (4) and (5).

3 Transmissibility Relationship

3.1 Transmissibility Function

A transmissibility function (according to the review [20]) is defined as the ratio of the Fourier transforms of two output responses in a stable linear dynamic system, i.e.

$$T_{lm}(\omega_i) = \frac{X_l(\omega_i)}{X_m(\omega_i)}, \quad (6)$$

where $X_l(\omega_i)$ and $X_m(\omega_i)$ denote the Fourier coefficients of the output response at the DOFs, l and m , respectively. The output at m is the reference.

This function of frequency ω_i gives the scalar product. Furthermore, the input information is not considered, which is an advantage in structural health monitoring during operation of structures.

3.2 Damage Index

To detect local damage in the large-scale structure, the transmissibility function (TF) based technique was adopted. Two output records at two sensor locations result in one TF. The sensitivity of a TF is reflected in the high value of the TF, corresponding to the critical frequency. If the structural properties in the partition between two receivers change, the critical frequency shifts. Thus, the difference of TF in two states (intact and damaged) is considered as the damage indicator. The damage index is defined as the total difference of the TF in the vicinity of the critical frequencies.

$$DI = \sum_{\omega_i} |T_{lm}^o(\omega_i) - T_{lm}^d(\omega_i)|, \quad (7)$$

where the superscripts “o” and “d” represent for the original state and the damaged state, respectively.

For the investigation of vertical vibrations of bridges, we propose the following equation:

$$DI = \sum_{\omega_i} \left| \frac{T_{lm}^o(\omega_i)}{\text{mean}(T_{lm}^o)} - \frac{T_{lm}^d(\omega_i)}{\text{mean}(T_{lm}^d)} \right|, \quad (8)$$

where $\text{mean}(T_{lm}^o)$ and $\text{mean}(T_{lm}^d)$ are the mean values of all amplitudes. They are used to normalize the TF.

The damage location will show a high damage index, which can potentially indicate the most weakened part due to damage in the structure.

4 Experimental Wave Propagation Analysis

4.1 14-Story Reinforced Concrete (RC) Building

We show a preliminary investigation of the NIOM method applied to reconstruct the wavefield in a 14-story reinforced concrete (RC) building (Fig. 1, left). The total height is 47 m. It is a twofold symmetric structure, except for the stiff shaft for stairwell (Fig. 1, right). There are three geophones on each floor (position reference to A, B and C). The measurement data are available in the TU Berlin research database.

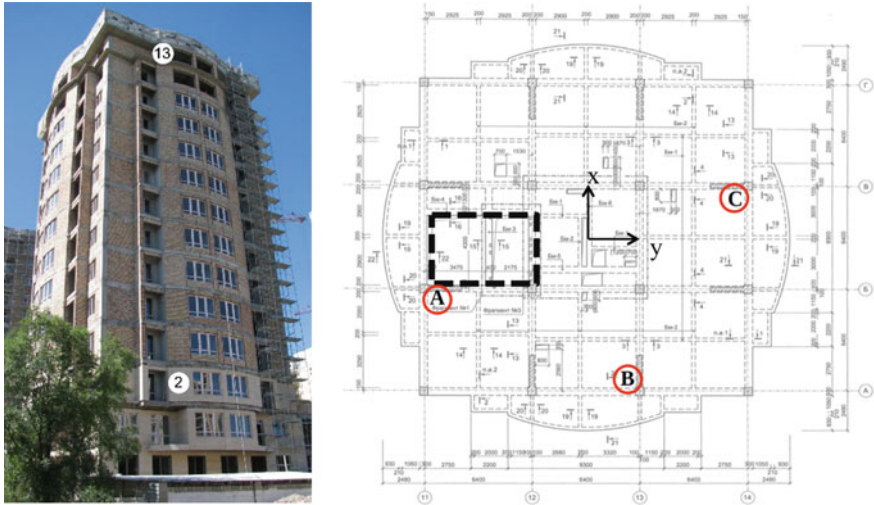


Fig. 1 Left: 14-story RC building in Bishkek, Kyrgyzstan. Right: Floor layout (image from project: Earthquake Model Central Asia)

4.2 Wave Propagation in the RC Building

Assuming the building structure as a multiple degree-of-freedom linear system, the NIOM method was applied to the ambient vibration recordings. This resulted in the wave propagation in two directions as shown in Fig. 2. The second floor is considered as the input position as the reference level.

4.3 Wave Velocity

We obtained the time lag of the wave peaks at position A, B and C in two directions. The wave velocities (Table 1) were estimated by the wave travel distance divided by the time lag.

The results reveal that the wave velocity is very sensitive to the local position. For instance, the wave velocities in two directions are not equal because the stiff shaft makes the overall structural stiffness higher in the y-direction than in the x-direction. In addition, the wave velocity in the x-direction is higher at position A than at the other positions because position A is close to the stiff shaft.

These results confirm the known fact: The higher the stiffness, the higher the wave velocity. This statement is considered to indicate the damage position causing the weak stiffness.

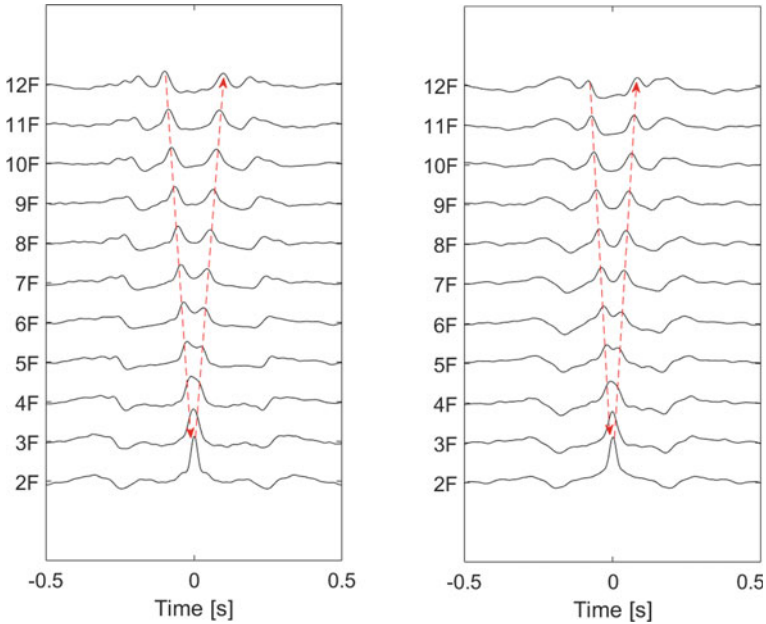


Fig. 2 Wavefield at position C in x direction (left) and in y direction (right)

Table 1 Wave velocities in the distance between 2 and 12 F [m/s]

Direction	Position A	Position B	Position C
<i>x</i>	371.8	342.9	334.2
<i>y</i>	400.0	394.0	400.0

5 Example of Damage Assessment

5.1 64 m Long Pedestrian Bridge

We carried out the ambient vibration measurement on a 64 m long pedestrian bridge in Berlin (Fig. 3, left). The geophones were placed on the bridge along the longitudinal direction (Fig. 3, right).

The first four mode shapes (Fig. 4) were identified from the vibration measurement.

It is noticeable that the first bending motion on the longer span (44 m) is shown in the first mode shape ($f = 2.15$ Hz). The first bending motion on the shorter span (20 m) is shown in the third mode shape ($f = 5.80$ Hz). These two mode shapes are considered as the dominant deformation on the longer and shorter span respectively.

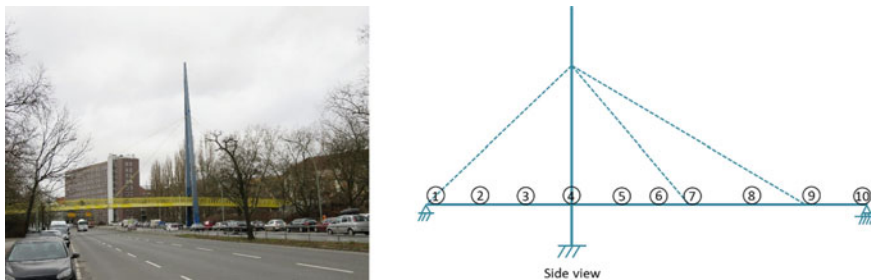


Fig. 3 Left: Pedestrian bridge “Volksparksteg” on Bundesallee in Berlin. Right: sensor position

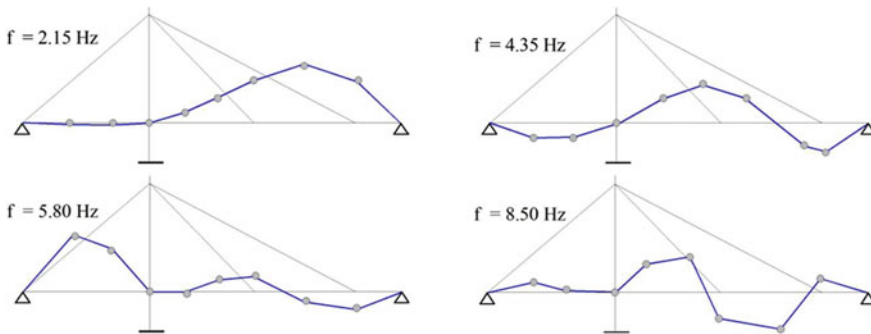


Fig. 4 Operational modal analysis results of the original bridge

5.2 Damage Scenarios

To investigate the proposed damage detection methods based on the wave velocity and damage index, the structural property change was intentionally induced by adding mass (approx. 150 kg) on the specific area (at sensor position 2, 7 and 8). The first mode shape of the bridge under three different conditions is shown in Fig. 5. The corresponding natural frequencies of the bridge are listed in Table 2.

The change in natural frequency indicated the different structural condition. However, the additional mass at position 2 cannot be identified by the natural frequency.

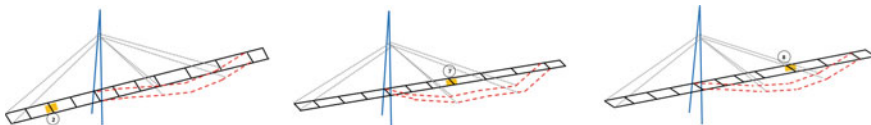


Fig. 5 The first bending mode shape in three different conditions

Table 2 Natural frequencies [Hz]

Original	Additional mass at (2)	Additional mass at (7)	Additional mass at (8)
2.15	2.15	2.00	2.02

Table 3 Wave velocities in the “cut-off” bridge [m/s]

Cut-off bridge	Original	Additional mass at (2)	Additional mass at (7)	Additional mass at (8)
Shorter span	588.0	622.5	588.0	588.0
Longer span	353.6	304.1	325.1	353.6

5.3 Wave Velocity

The application of NIOM was extended to the vertical vibration of the bridge. Since the wave field was disturbed on the pylon position separating the longer and shorter spans, we reconstructed the wave fields in two “cut-off” bridges. The wave velocities are listed in Table 3.

The wave velocity on the shorter span was increased by the additional mass at position 2, while no difference occurred due to the additional mass at positions 7 and 8. The local wave velocity change was more sensitive than global natural frequency.

On the other hand, the additional mass at position 2 and 7 caused the wave velocity to be low on the longer span. However, the additional mass at position 8 enhanced the cable strength. This ultimately made the damaged condition (mass and stiffness change simultaneously) too complicated to identify.

5.4 Damage Index by Use of Transmissibility Functions

We used Eq. (8) to compute the damage indices. The TF between successive sensors was taken into account. Therefore, comparing the damage indices in Fig. 6 helps to locate the damage position. Obviously, the high damage indices correlate well with the “damaged” part of the bridge.

6 Conclusion

This paper presents an exploratory study of the wave propagation analysis and the transmissibility function for damage detection in civil structures. The seismic interferometry technique based on deconvolution was applied to investigate the global vibration recordings. This is the first application of NIOM to ambient vibration response of a building structure and a pedestrian bridge. The wavefields in both structures were reconstructed. Discrepancies in wave velocity were revealed due to the

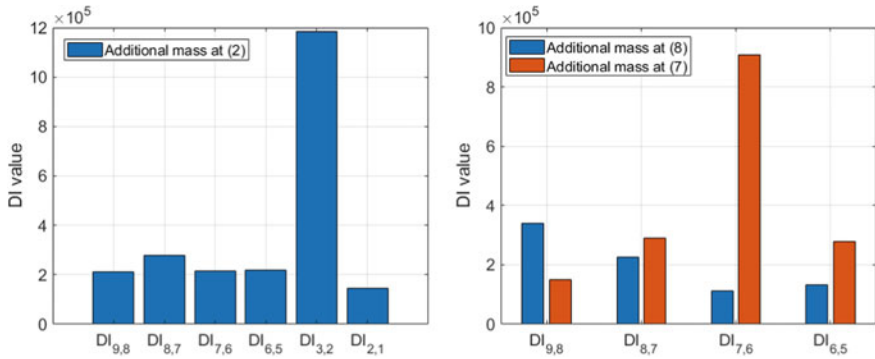


Fig. 6 The damage indices influenced by the additional mass at position 2 (left) and at position 7 and 8 (right)

difference in local structural stiffness. The similar phenomenon was also observed in the pedestrian bridge. The wavefields corresponding to the dominant bending modes indicated the individual wave velocity in the “cut-off” bridge. Moreover, the proposed damage index was used to verify the wave propagation result. This parameter is more beneficial than the natural frequencies to detect the local damage.

Acknowledgements The first author would like to thank the German Academic Exchange Service (DAAD) for their financial support and the colleagues at the Technische Universität Berlin for their contribution to the bridge vibration measurement.

References

1. Doebling SW, Farrar CR, Prime MB (1998) A summary review of vibration-based damage identification methods. *Shock Vib Dig* 30(2):91–105
2. Salawu OS (1997) Detection of structural damage through changes in frequency: a review. *Eng Struct* 19(9):718–723
3. Todorovska MI, Trifunac MD (2008) Earthquake damage detection in the Imperial County Services Building III: analysis of wave travel times via impulse response functions. *Soil Dyn Earthq Eng* 28(5):387–404
4. Trifunac MD, Ivanović SS, Todorovska MI (2001) Apparent periods of a building. I: Fourier analysis. *J Struct Eng* 127(5):517–526
5. Sohn H, Farrar CR, Hemez FM, Shunk DD, Stinemates DW, Nadler BR, Czarnecki JJ (2003) A review of structural health monitoring literature: 1996–2001. Los Alamos National Laboratory, USA, p 1
6. Todorovska MI (2009) Soil-structure system identification of Millikan Library North-South response during four earthquakes (1970–2002): what caused the observed wandering of the system frequencies? *Bull Seismol Soc Am* 99(2A):626–635
7. Yamada M, Mori J, Ohmi S (2010) Temporal changes of subsurface velocities during strong shaking as seen from seismic interferometry. *J Geophys Res: Solid Earth* 115(B3)
8. Şafak E (1999) Wave-propagation formulation of seismic response of multistory buildings. *J Struct Eng* 125(4):426–437

9. Snieder R, Sheiman J, Calvert R (2006) Equivalence of the virtual-source method and wave-field deconvolution in seismic interferometry. *Phys Rev E* 73(6):066620
10. Snieder R, Safak E (2006) Extracting the building response using seismic interferometry: theory and application to the Millikan Library in Pasadena, California. *Bull Seismol Soc Am* 96(2):586–598
11. Nakata N, Tanaka W, Oda Y (2015) Damage detection of a building caused by the 2011 Tohoku-Oki earthquake with seismic interferometry. *Bull Seismol Soc Am* 105(5):2411–2419
12. Rahmani M, Todorovska MI (2013) 1D system identification of buildings during earthquakes by seismic interferometry with waveform inversion of impulse responses-method and application to Millikan library. *Soil Dyn Earthq Eng* 47:157–174
13. Todorovska MI, Trifunac MD (2008) Impulse response analysis of the Van Nuys 7-storey hotel during 11 earthquakes and earthquake damage detection. *Struct Control Health Monit: Off J Int Assoc Struct Control Monit Eur Assoc Control Struct* 15(1):90–116
14. Nakata N, Snieder R, Kuroda S, Ito S, Aizawa T, Kunimi T (2013) Monitoring a building using deconvolution interferometry. I: earthquake-data analysis. *Bull Seismol Soc Am* 103(3):1662–1678
15. Nakata N, Snieder R (2014) Monitoring a building using deconvolution interferometry. II: ambient-vibration analysis. *Bull Seismol Soc Am* 104(1):204–213
16. Haddadi HR, Kawakami H (1998) Modeling wave propagation by using normalized input-output minimization (NIOM) method for multiple linear systems. *Doboku Gakkai Ronbunshu* 1998(584):29–39
17. Kawakami H, Oyunchimeg M (2003) Normalized input-output minimization analysis of wave propagation in buildings. *Eng Struct* 25(11):1429–1442
18. Liao CM (2021) Experimental and numerical damage assessment of structures by use of wave propagation analysis. Technische Universität Berlin, Germany. <https://doi.org/10.14279/depositonce-11297>
19. Devriendt C, De Sitter G, Guillaume P (2010) An operational modal analysis approach based on parametrically identified multivariable transmissibilities. *Mech Syst Signal Process* 24(5):1250–1259
20. Yan WJ, Zhao MY, Sun Q, Ren WX (2019) Transmissibility-based system identification for structural health monitoring: fundamentals, approaches, and applications. *Mech Syst Signal Process* 117:453–482

SHM Campaign on 138 Spans of Railway Viaducts by Means of OMA and Wireless Sensors Network



Lorenzo Bernardini, Lorenzo Benedetti, Claudio Somaschini,
Gabriele Cazzulani, and Marco Belloli

Abstract Condition-based monitoring applied to railway bridges represents a topic of major importance and interest among developed countries, such as Italy. In fact, bridges and viaducts represent key components of the transportation network, and therefore they increasingly draw infrastructure managers' attention. The present work is the result of a project carried out by Politecnico di Milano, consisting of a large experimental campaign conducted on a series of viaducts of the Italian railway network. The ensemble of structures under investigation is composed by 11 viaducts, for a total amount of spans equal to 138. According to a similarity criterion, the latter were subdivided into 8 groups, featured by different properties. Due to its transient nature, the experimental campaign was conducted by means of wireless accelerometers, and it consisted in the extraction of the main modal parameters of each analyzed viaduct span, as well as the characterization of the trains travelling on the line. Through the adoption of an operation modal analysis (OMA) technique, it was then possible to construct a large database of the dynamic features concerning the studied viaducts. This database may be exploited for future studies as an important baseline reference condition, by which potential outlier values may be captured, as a sign of damage occurrence among the monitored structures.

Keywords Operational modal analysis · Railway bridges · Wireless sensors network · Structural health monitoring · Condition-based monitoring

1 Introduction

High-speed railway lines play an important role in passengers and goods transportation within Italy. To ensure ride comfort and safety, infrastructure managers are continuously seeking improved condition-based monitoring systems, able to assess in real-time the health status of the structure and its time-trend [1]. As described in [2], the condition-based assessment of high-speed railway line usually focuses

L. Bernardini (✉) · L. Benedetti · C. Somaschini · G. Cazzulani · M. Belloli
Department of Mechanical Engineering, Politecnico di Milano, Milano, Italy
e-mail: lorenzo.bernardini@polimi.it

© The Author(s), under exclusive license to Springer Nature Switzerland AG 2023
Z. Wu et al. (eds.), *Experimental Vibration Analysis for Civil Engineering Structures*,
Lecture Notes in Civil Engineering 224,
https://doi.org/10.1007/978-3-030-93236-7_3

on two aspects, namely track irregularity and bridge natural frequencies [3, 4]. Since damage-sensitive, natural frequencies may be chosen as an index of the actual health status of a monitored structure: indeed, phenomena such as a crack generation/propagation, resistant section corrosion, deterioration and material ageing lead to a decreased bending stiffness of the bridge span and therefore lower natural frequencies [5]. Therefore, the idea of keeping track of the time evolution and trend of the natural frequencies regarding a certain structure (or a set of them) subject to observation can be useful from a monitoring point of view. In fact, a sudden change in terms of natural frequency may indicate the occurrence of a damage along the bridge/viaduct span, thus alarming the infrastructure manager, that can readily act in order to fix it, as soon as possible. In this context, detecting a damage at its earliest stage would mean an important achievement in terms of passenger safety and maintenance costs: it would allow to avoid sudden catastrophic failures and head to huge savings (i.e., optimized maintenance strategy). To do so, it is mandatory to get rid of any other environmental and operational aspects that influence the time evolution of the natural frequencies (i.e., temperature): this implies the use of processing algorithms such as the principal component analysis (PCA), as illustrated by the authors in [6]. Exploiting the natural frequency evolution as a structural health monitoring tool [7] requires the definition of a reference baseline to compare the new data with. An outlier value with respect to the reference condition may highlight the fact that a damage occurred on the structure subject to study [8]. Therefore, in the health monitoring working flow, the first step to accomplish consists of constructing a database that is representative of the (healthy) reference baseline to which new measures will be compared, to capture any sudden changes. As briefly mentioned above, the present work is the outcome of an experimental campaign conducted on 11 viaducts of a stretch of the Italian high-speed railway line; this resulted in a total amount of instrumented spans equal to 138. The purpose of this campaign is not just to build up a reference database for future studies, but also to investigate the possibility to infer the health status of a certain span directly from the statistic population regarding a group of spans that share the same material properties and geometrical dimensions (i.e., width and length).

Due to the transient nature of this campaign and the large number of spans under investigation, to enhance and ease the experimental operations, a set of wireless sensors was adopted, as described in detail in the following section.

The content of this paper is organized as follows: the first section aims at describing the experimental setup, providing a brief insight on the general framework concerning the campaign. Moreover, the set up and the equipment used are described in detail. The second section deals with the description of the signal processing techniques adopted for extracting modal parameters and moving loads properties respectively. Then, in the following part, the main outcomes of the experimental campaign are gathered and discussed. Final conclusions and main remarks, with a focus on possible future outlooks, are drawn in the last section.

2 Description of the Experimental Campaign

2.1 General Framework

Each span of the viaducts treated during the experimental campaign was instrumented by means of a couple of sensors placed at midspan (Fig. 1, left): moreover, for each viaduct, one single span was instrumented by a larger number of sensors (Fig. 1, right), namely ten, in order to capture higher order torsional and bending modes and pier contribution to the span motion. In addition to this, for each day of measurement a set of four sensors was used in order to get the number of train passages on the viaducts and to identify the speeds as well as the loading properties of the rail vehicles. The general framework depicted above was adopted to measure the first torsional and bending mode shapes and their associated frequencies, since these modes are the ones featured by the highest participant modal mass. The total amount of instrumented span, as briefly stated before, is equal to 138 units, that correspond to 11 different viaducts under experimental investigation during the campaign: eleven of them are featured by a simply supported beam section, while just one is featured by a closed deck section. Since the aim of this paper is to draw conclusions on the possibility of grouping spans having analogous dynamic properties, given that they share the same constructing material, same section and length, the single viaduct with a different cross-section typology was then discarded. This results in a final ensemble of spans that can be then divided, through geometrical similarity (span length), into eight groups, according to Table 1.

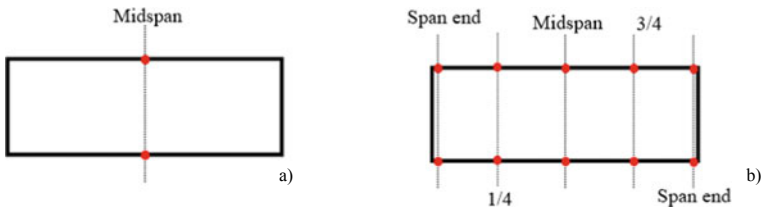


Fig. 1 Span top views: red circles represent sensors. **a:** span instrumented at midspan. **b:** finer mesh for the span

Table 1 Different span lengths

Span length (m)	23.6	24.7	31.2	33.6	34.5	34.7	35.6	36.5
Number of spans	4	15	3	14	7	40	8	38

2.2 Experimental Set up

Due to the large number of spans to be instrumented a wireless sensors network was adopted, to ease and speed up the whole experimental campaign. The adopted sensors consist of MEMS accelerometers, designed and produced by LORD microstrain, with a full scale of 10 g if mounted on the bridge side walkway (Fig. 2): instead, 40 g devices were mounted on the sleepers (Fig. 3) with the aim to classify the rail vehicles travelling on the viaduct. The latter were placed in the following way: each track is featured by a couple of accelerometers, positioned on two sleepers, spaced of a known distance (around 20 m). The sensors mesh was synchronized by means of their base station (Fig. 4). During the entire campaign, the sensors were left on the structure for at least 10/15 h, to acquire the largest number of transits as possible. To couple the sensors with the studied structure, each accelerometer was magnetically attached to a steel plate, which was then directly glued to the viaduct deck or sleeper.



Fig. 2 Wireless accelerometers mounted on the side walkway (10 g full-scale)

Fig. 3 Wireless accelerometers mounted on the sleepers (40 g full-scale)

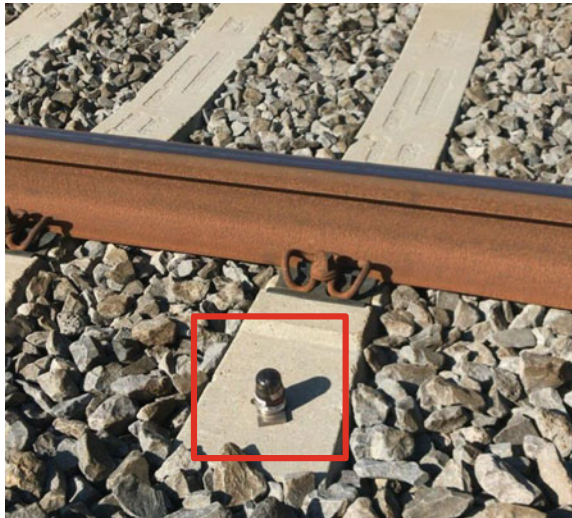


Fig. 4 Base station box and its antenna



Table 2 collects the acquisition properties of the sensors used during the experimental campaign: for each sensor, the record starts once the threshold value, in terms of acceleration, is exceeded and it stops after at least 40 s, in order to acquire the free decay of the span after the train transits. In fact, for modal properties identification the structure free decay is needed.

Table 2 Sensors acquisition properties

Sampling frequency of the deck accelerometers (Hz)	256
Sampling frequency of the sleepers accelerometers (Hz)	1024
Distance between consecutive sleepers accelerometers (m)	20
Trigger threshold for deck accelerometers (m/s ²)	0.05
Trigger threshold for sleepers accelerometer (m/s ²)	0.5
Pre-trigger (s)	5
Minimum observation length (s)	40

3 Signal Processing

3.1 Time Domain Analysis

The excited motion of the viaduct span response, measured through the sensors mounted on the sleepers, was exploited in order to determine the following properties of the travelling rail vehicles: the track, the train typology (number of wheelsets and their distance), the speed and the direction of motion. First of all, by computing and comparing the sums of the moving standard deviation of the acceleration signals sensed on the two tracks respectively, it is possible to determine on which track the train has actually travelled. Once the track has been determined, the direction of motion of the rail vehicle must be identified: knowing the sampling frequency and the spatial distance between adjacent sleepers accelerometers (see Table 2), through the cross-correlation algorithm, it is possible to obtain both the direction of motion of the vehicle and its speed (from the RMS of the vertical components of the signals measured on the track). Finally, again from the RMS of the vertical component of the signals measured on the sleepers, it is possible to recognize the vehicle typology travelling on the viaduct: as mentioned before, this identification was done by simply computing the number of travelling wheelsets and their relative distances. Therefore, from the number of axles and their spatial distance it is possible to find out which are the trains that travelled on the structure.

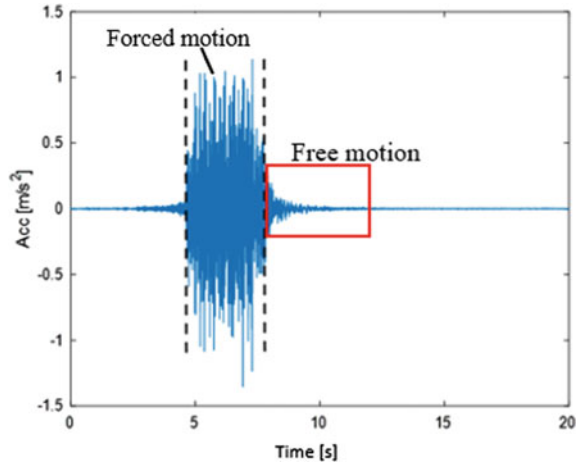
3.2 Modal Analysis

The main purpose of this work was the identification of the first natural frequencies of the viaducts under investigation. To do so the excited motion part was neglected in order to keep only the free decay of the response (see Fig. 5). Therefore, the first step consists of the removal of the forced motion from the global deck response, by means of a trigger logic. Once this operation is accomplished, it is possible to process the data for extracting the modal properties of the viaduct: this was done by means of the commercial software ARTEMIS, that exploits two different algorithms, namely Frequency Domain Decomposition (FDD) and Stochastic Subspace Identification (SSI-data) algorithms.

4 Results

It is now recalled that the spans were divided in different groups according to their length (i.e. eight, Table 1). Then, given the purpose of this work the results will be presented as follows: in order to be statistically consistent, only the outcomes (in terms of natural frequencies) concerning the span typologies featured by the highest

Fig. 5 Example of deck midspan response with the distinction of the forced and free motion



number of examples are provided to the reader. Therefore, the spans for which results are presented and discussed are the ones featured by one of the following lengths, namely 24.7 m, 33.6 m, 34.7 m and 36.5 m, while the others are neglected. In Fig. 6 the box plot of the frequencies associated to the first longitudinal mode shape grouped as a function of span length is shown. The same diagrams have been drawn also for the

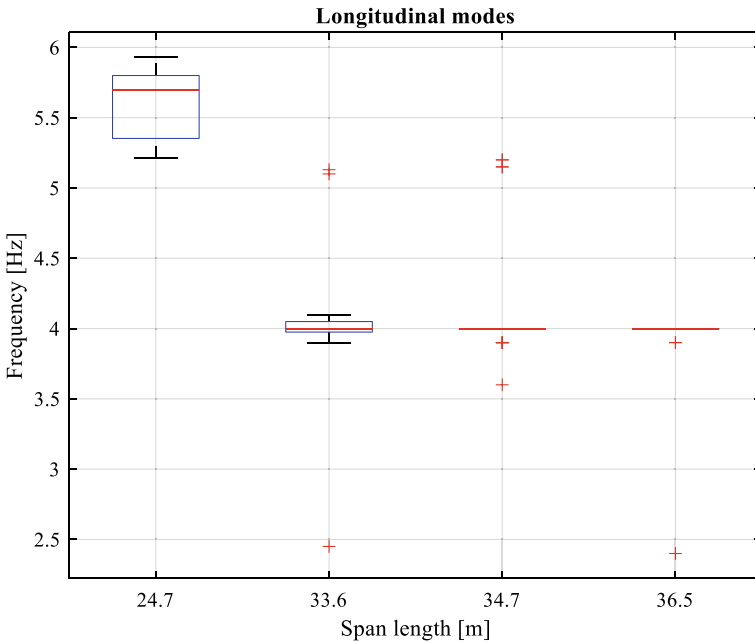


Fig. 6 Box plot for the frequencies associated to the 1st longitudinal mode

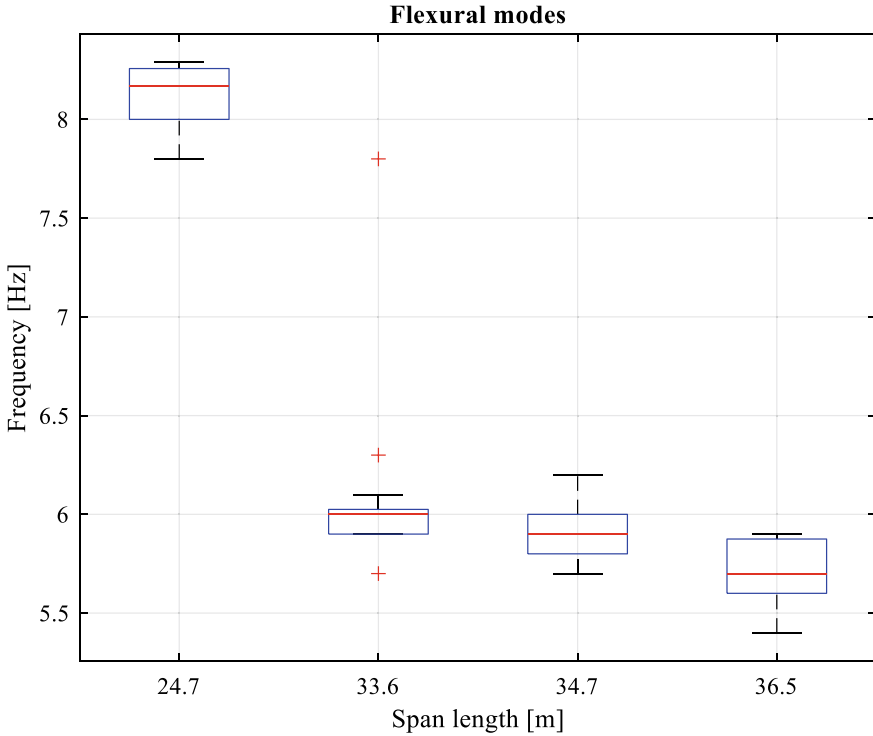


Fig. 7 Box plot for the frequencies associated to the 1st flexural mode

first bending and torsional mode shapes, again categorized as a function of the span length, as illustrated in Figs. 7 and 8 respectively. The longitudinal modes are featured by a larger presence of outlier frequency values than the other two mode typologies, as illustrated in Fig. 6 (see red crosses): referring to the span length of 34.7 m, it is worth mentioning that the outlier values are all due to one of the eleven investigated viaducts. This means that the longitudinal mode rather depends on constraints, such as pier height, bridge bearings and number of adjacent spans, than on the span length: that is why we observed such a large dispersion. In other words, given a certain span length, for the longitudinal mode shape associated frequency, we may find out a remarkable number of outliers depending on the bridge and its features (i.e. span boundary conditions).

As expected, in Fig. 7, it is possible to observe the progressive decrease of the first flexural natural frequency with the increase of the span length. Moreover, the number of outliers is lower than the one observed and described before: as a consequence, it is clear that spans sharing the same geometrical properties present closer values in terms of bending frequency, whatever is the bridge considered among the ones investigated during the experimental campaign. The same reasoning can be extended also to the first torsional frequency (see Fig. 8). In this specific case, it is worth also

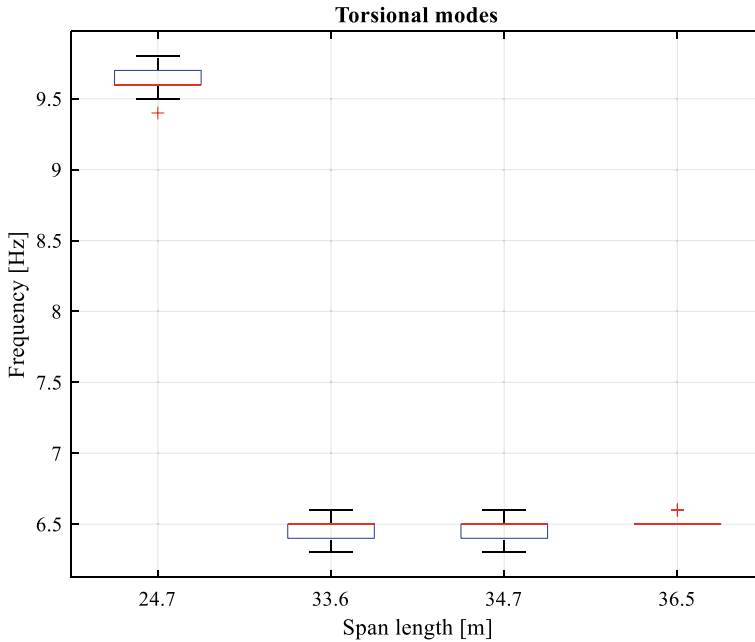


Fig. 8 Box plot for the frequencies associated to the 1st torsional mode

noticing that the span length seems to have a lower influence on the frequency than the previous case in the sense that if it does not change remarkably the resulting torsional frequency will not significantly differ.

According to authors opinion, the frequency dispersion concept presented above deserves to be further studied and deepened: in fact, the research is still ongoing in order to analyze and understand whether the dispersion at constant span length depends on the deck (i.e., its health status) or on span constraints.

5 Conclusions

The present paper is the result of an experimental investigation of the modal properties of a set of 11 railway viaducts. One purpose of this campaign was to identify the natural frequencies associated to the first longitudinal, flexural and torsional mode shapes: this was done with the idea to build up a reference baseline data set useful for future studies on the health status of those viaducts. In addition, this investigation represents a chance to evaluate the possibility of grouping, with a reasonable data dispersion, the natural frequencies of spans that share the same material and geometry but belong to different viaducts. In other words, this work aims to examine the impact played by different boundary conditions (f.i., pier height) on the aforementioned

frequencies values. The idea was to experimentally assess how remarkable are the frequency changes due to the viaduct under investigation, given that a certain span length is considered: therefore, we may hopefully be able to distinguish damage-associated outliers from the one depending instead on the bridge typology. The results concerning bending and torsional frequencies are promising since featured by a low number of outliers, thus meaning that these modes rather depend on the span geometry than on the considered viaduct (i.e., on boundary conditions). In other words, whatever is the viaduct, all the spans sharing the same length showed similar results in terms of flexural and torsional frequencies, with a small number of outliers. An extension of this result is that, if a span, that was never observed before belongs to a certain group featured by a specific length, and once investigated turns out that its first torsional and bending natural frequencies are far from the statistics of the corresponding population, it may mean that something wrong has occurred (i.e., a damage). As observed in the previous section, this reasoning is not valid for the longitudinal modes frequencies that present indeed a larger number of outliers: in this case it would be much more demanding to identify and associate a certain outlier to an actual damage occurrence. An aspect that deserves to be deepened in the next future studies is to investigate the effect of seasonal changes of temperature (and environmental conditions in general) on the modal properties of the studied spans: as already stated along the paper, environmental conditions changes may hide the damage, or cause false alarms. Therefore, as a first step, the reference data base must be constructed for each season of the year: in this way, frequency changes due to temperature seasonality may be somehow predicted and its influence (confounding effect) on the monitoring process is mitigated.

References

1. Islami K (2015) Vibration monitoring of long bridges and their expansion joints and seismic devices. In: MATEC web of conferences, vol 24, p 04004. <https://doi.org/10.1051/mateconf/20152404004>.
2. Xiao X, Xu X, Shen W (2021) Simultaneous identification of the frequencies and track irregularities of high-speed railway bridges from vehicle vibration data. *Mech Syst Signal Process* 152:107412. <https://doi.org/10.1016/j.ymssp.2020.107412>
3. Yang YB, Wang ZL, Shi K, Xu H, Wu YT (2020) State-of-the-art of the vehicle-based methods for detecting the various properties of highway bridges and railway tracks. *Int J Struct Stab Dyn*. <https://doi.org/10.1142/S0219455420410047>
4. Xiao X, Sun Z, Shen W (2020) A Kalman filter algorithm for identifying track irregularities of railway bridges using vehicle dynamic responses. *Mech Syst Signal Process* 138:1–20
5. Matsuoka K, Tokunaga M, Kaito K (2021) Bayesian estimation of instantaneous frequency reduction on cracked concrete railway bridges under high-speed train passage. *Mech Syst Signal Process* 161:107944. <https://doi.org/10.1016/j.ymssp.2021.107944>
6. Cunha Á, Caetano E, Moutinho C, Magalhães F (2013) Continuous dynamic monitoring of bridges: different perspectives of application. *Advanced materials research*, vol 745, pp 89–99. Trans Tech Publications, Switzerland. <https://doi.org/10.4028/www.scientific.net/AMR.745.89>

7. Salawu OS (1997) Detection of structural damage through changes in frequency: a review. *Eng Struct* 19(9):718–723. [https://doi.org/10.1016/S0141-0296\(96\)00149-6](https://doi.org/10.1016/S0141-0296(96)00149-6)
8. Chang K-C, Kim C-W (2016) Modal-parameter identification and vibration-based damage detection of a damaged steel truss bridge. *Eng Struct* 122:156–173. <https://doi.org/10.1016/j.engstruct.2016.04.057>

Effect of Damage on Vibration Characteristics of Reinforced Concrete Deck Slabs in an Existing Steel Girder Bridge



Sania Gohar, Sonam Lhamo, Yasunao Matsumoto, and Satoru Sakuma

Abstract This study focuses on applying vibration-based structural health monitoring on the rising issue of widespread deteriorations of reinforced concrete deck slabs. An investigation using ambient vibration measurement with eleven sensors in a deck panel was conducted to study the effect of damages on vibrational characteristics and dynamic parameters of the deck slabs of a real bridge. The investigation was carried out at three different deck panel locations, namely Panels 1, 2 and 3, with different levels of deterioration. To obtain the modal parameters, Eigenvalue Realization Algorithm (ERA) combined with Random Decrement (RD) technique was employed. The natural frequencies, damping ratios and mode shapes were used to describe the dynamic characteristic of deck panels. Of all modal characteristics, the sensitivity of damping ratio to damage has been proven to be highest with no requirement of numerous measurement locations for its identification (Cao et al. in *Smart Mater Struct* 26:043001, 2017). In this study, amplitude dependence of damping ratio was also investigated, since a change in the modal damping ratio can be used for damage identification but its dependence on amplitude remains a concern. The analytical study, through the method of Finite Element (FE), was also conducted, and the natural frequencies and mode shapes were extracted taking one deck panel as the focus of study. In addition, this study presents a closer look at the stabilization diagrams of all deck panels with different levels of deterioration.

Keywords Vibration-based structural health monitoring · Reinforced concrete deck slabs · Modal characteristics · Damage detection · Amplitude dependence

S. Gohar · S. Lhamo · Y. Matsumoto (✉)

Department of Civil and Environmental Engineering, Saitama University, Shimookubo, Saitama, Japan

e-mail: ymatsu@mail.saitama-u.ac.jp

S. Sakuma

Technology & Procurement Department, Kanto Regional Head Office, East Nippon Expressway Co., Ltd., Saitama, Japan

1 Introduction

In recent years, the structural degradation of the bridges has been a major issue in the bridge management system due to increased traffic loads, aging and challenging environmental conditions. The high intensity and frequency of loading generated by high traffic volume cause many problems. The most typical is fatigue damage in concrete slabs and steel welded girders. This may cause reduction in the integrity of the reinforced concrete (RC) deck slab and therefore shorten the life expectancy of the bridge superstructures. The deteriorating concrete deck has been one of the growing issues in the bridge maintenance system. It has been reported that in Japan more than 50% of the total maintenance cost is estimated to be spent for the repair and the renewal of RC bridge deck [2].

Several non-destructive techniques have been developed to inspect the safety and serviceability of deck slab. Vibration method of Structural Health Monitoring (SHM) has been receiving increasing attention from the engineering community as assistance to visual inspection to ascertain the health of a bridge, efficiently and effectively. The fundamental of vibration-based SHM is founded on the understanding that the structural damages lead to changes in mass, stiffness and damping properties of a structure, and hence induces changes in the dynamic characteristics e.g. natural frequency, mode shapes, and modal damping. Previous studies suggested that damping ratio is more sensitive to damage among all modal characteristics [1]. However, the amplitude dependence of damping ratio remains a concern while using it as a damage indicator in the field of SHM [3, 4].

The primary objective of this study is to understand and extend the possibility of vibration-based SHM technique on RC deck slabs through the investigation of the dynamic behavior of such deck slabs with different levels of deterioration. The investigation was carried out at three different deck panel locations, namely Panels 1, 2 and 3, with different levels of deterioration. For damage identification, natural frequencies, damping ratios and mode shapes along with Modal Assurance Criteria (MAC) and Coordinate Modal Assurance Criteria (COMAC) were evaluated. To obtain the modal parameters, ERA combined with the RD technique was employed. Finite element (FE) modeling was also performed in software-ANSYS Workbench 2019R2 Academic to provide a reference of comparison and discussion to the experimental study. In addition, stabilization diagrams and the amplitude dependence of damping ratio of different deck panels were investigated.

2 Experimental Method and Analysis

2.1 Bridge Description and Measurement Set up

The bridge adopted for the research purpose was built in 1975. It was a non-composite twin I-girder multi-span bridge with RC deck slab. This bridge operates three motor

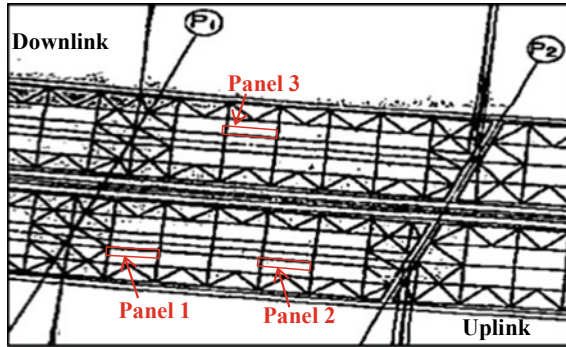


Fig. 1 Top view of the bridge’s span under investigation

lanes going each direction separated by a safe traffic shoulder. After years of operations, despite the equivalent share of traffic volumes on both sides and similar locations on the same highway, it was reported that the uplink side of the bridge has undergone earlier deterioration, particularly in the deck slab, as compared to its downlink side. For the purpose of investigation, two locations on the uplink side namely Panel 1 and Panel 2, and one location on the downlink side namely Panel 3 of deck slab were selected, as shown in Fig. 1. During visual inspection, Panel 1 was found to be in a better state than Panel 2 despite being located on the same lane side. Small cracks were observed near the stringer and girder of Panel 1, whereas the lower surface area of Panel 2 was damaged by large cracks in the longitudinal direction and noticeably near the main girders. The reason for more damage in Panel 2 could be its closer distance from the expansion joint located near the support P2. Amongst all inspected locations, Panel 3 appeared to be in a healthier state with no superficial cracks. To investigate the dynamic response of each deck panel with different levels of deterioration, measurements were taken with 11 number of piezoelectric accelerometers installed at locations shown in Fig. 2.

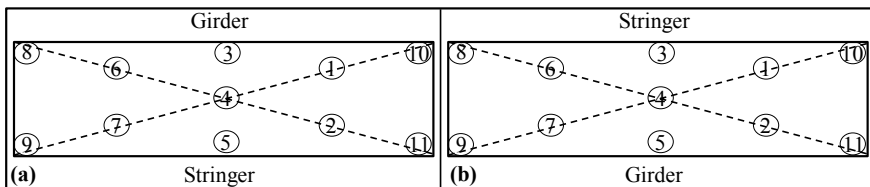


Fig. 2 Positions of accelerometers; a for Panel 1 and 2, b for Panel 3

2.2 Random Decrement Technique (RD)

Ambient data collected from 11 accelerometers installed at different locations (Fig. 2) were analyzed by RD technique to extract free responses [5]. Channel no. 2 was selected as the reference channel to obtain the triggering points. The choice of the channel was made based on the high amplitude response of the sensor. Data was recorded at a sampling frequency of 1652 Hz for 37.2 s time interval for each channel. With the initial triggering value of $a_o = 0.40 \text{ m/s}^2$ and overlapping time frame of $\tau = 0.5 \text{ s}$, free responses were extracted.

2.3 Eigenvalue Realization Algorithm (ERA)

The procedure of obtaining the free responses was followed by the identification of modal parameters using the conventional ERA method [6]. Maximum system order of 300 was considered sufficient for the identification of all physical modes, and the size of the Hankel matrix was 825×826 (r x s). Stabilization diagram was constructed to separate computational modes from physical modes fulfilling all the conditions with the corresponding value of modal amplitude coherence and modal assurance criteria >0.95 , modal damping difference <0.05 , and frequency difference $<0.005 \text{ Hz}$. In continuation to the analysis, correlation coefficients were calculated between the measured and ERA reconstructed time histories. The best correlation coefficient >0.95 and best system order containing all the physical modes were selected accordingly to identify the modal parameters.

2.4 Mode Shapes Based Criterion

Difference between the mode shapes identified from ERA for structural members with different levels of deterioration can be used as damage indicator. MAC and COMAC are the statistical tools for the comparison of mode shape vectors. From two sets of modal vectors such as $[\Psi_A]$ and $[\Psi_B]$ of m number of mode shapes with n number of coordinates, MAC and COMAC are calculated as follow: [7]

$$MAC_{(j)} = \frac{\sum_{i=1}^n (|[\Psi_A]_i [\Psi_B]_i|)^2}{\sum_{i=1}^n ([\Psi_A]_i)^2 \sum_{i=1}^n ([\Psi_B]_i)^2} \quad (1)$$

$$COMAC_{(i)} = \frac{\sum_{j=1}^m |[\Psi_A]_i^j [\Psi_B]_i^j|^2}{\sum_{j=1}^m ([\Psi_A]_i^j)^2 \sum_{j=1}^m ([\Psi_B]_i^j)^2} \quad (2)$$

where i (1,2,...,n) represents number of the coordinate or the measurement location, and j (1,2,...,m) represents number of the mode shape. MAC and COMAC values vary from 0 to 1. More is the difference between mode shapes of two sets, lower is the value of these indicators. MAC can be used as damage identification, whereas COMAC can be used for damage localization. If the modal vectors in a coordinate i from two sets of measurements are identical, the COMAC factor is close to 1 for that coordinate. A large deviation from unity can be interpreted as damage indication along that coordinate.

2.5 Finite Element Analysis

The analytical study using Finite Element (FE) Modelling was undertaken using software-ANSYS Workbench 2019R2 Academic. The model encompasses a concrete deck slab underlying pavement, longitudinal girders with vertical stiffener, stringer, cross beams and lateral bracing (Fig. 3). For the dimensions and material properties, design and construction documents of the bridge were referred.

In this study, the choice of boundary conditions was critical since the deck slab panels under investigation were at an intermediate location of bridge's span. The model was extended to both sides in the bridge axis direction by half the length of the deck panel, and free-free support was considered due to its simplicity since free-free support does not require special attention to exclude the influence of support rigidity. When the analytical results were compared with the experimental eigenvalue analysis results, the vibration mode characteristics were observed to be similar, especially in the high-frequency region. Therefore, this boundary condition was considered adequate for the FE analysis in this study.

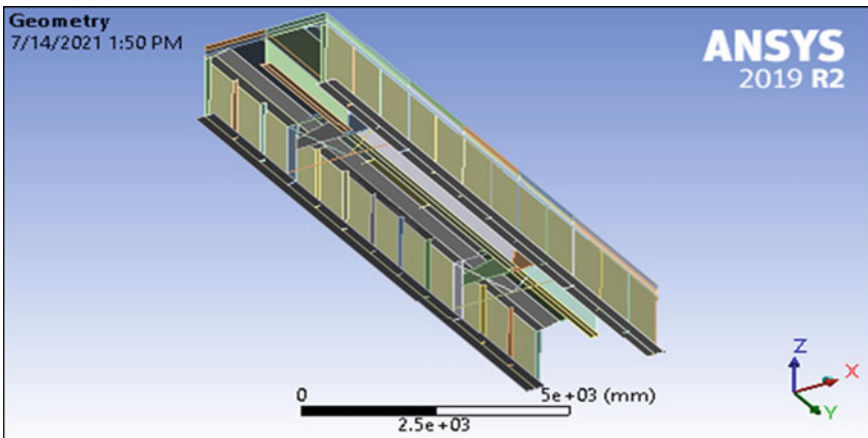


Fig. 3 Finite element model

3 Results and Discussions

Dynamic characteristics identified for all deck panels are presented in this section. The results of deck panels with different levels of deterioration are compared to observe the influence of damage on different parameters discussed below.

3.1 Modal Parameters

A comparison among modal natural frequencies, mode shapes and damping ratios of different deck panels was made. Panel 3 was considered as reference panel due to its relatively healthy state, and the MAC values obtained from similar mode shapes of Panels 1 and 2 were averaged for each panel. MAC for Panels 1 and 2 with respect to Panel 3 was 90% and 87%, respectively. The lower value of MAC for Panel 2 indicated more change in its mode shapes with respect to Panel 3, and that could be interpreted as more damage in Panel 2 than Panel 1. Figure 4 presents the results of modal natural frequencies and damping ratios of four similar modes identified in all deck panels, and the percentage change in the modal parameters of deck panels 1 and 2 with respect to Panel 3 is also presented. Natural frequency of Panel 3 was observed to be higher than the other panels, and the natural frequency of Panel 2, which was the most damaged panel, was observed to be the lowest. Since structural damages cause a reduction in the stiffness that in turn reduces the natural frequency of the member, these results interpret that Panel 2 was more damaged than the other two panels. Through the visual inspection of deck panels also, Panel 2 was observed to be more damaged. Since the damage in Panel 1 was not severe, insignificant difference was observed between the natural frequencies of Panel 1 and 3.

Comparison among the damping ratios of different deck panels is presented in Fig. 4b. The damping ratios of Panels 1 and 2 were observed to be lower than Panel 3. Generally, an increase in damping ratio has been observed after any structural damage [1], thus higher values of damping ratios for Panel 3 could indicate more damage in

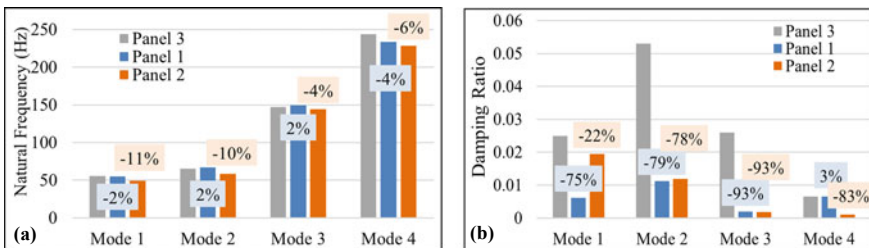


Fig. 4 Identified modal parameters for all deck panel; **a** Natural frequencies, **b** damping ratios (Note: The values in the percentage are the differences between the modal parameters of Panel 1 and 3, and Panel 2 and 3)

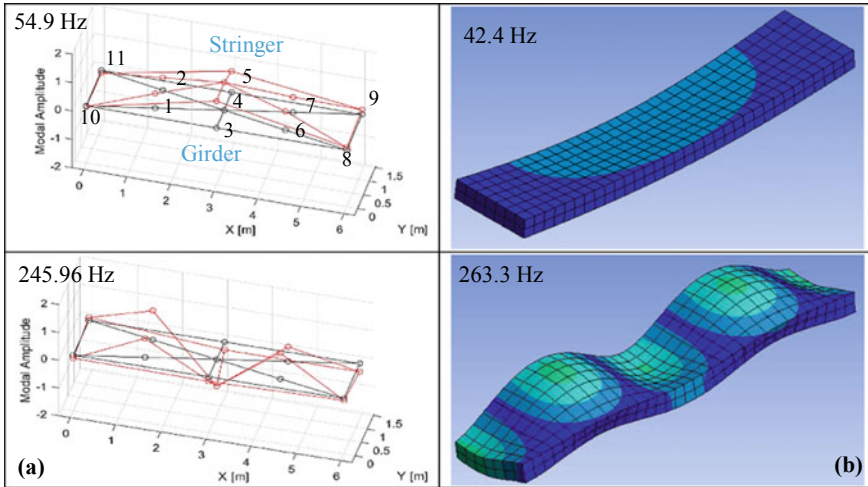


Fig. 5 Mode shapes of Panel 3 from: a ERA, b FE Analysis

it than deck panels 1 and 2. These results are contradictory to the results of visual inspection and interpretation of natural frequencies shown in Fig. 4a. Amplitude dependence of damping ratio could be a reason for such misleading results. Therefore, an investigation into the influence of amplitude of vibration on damping ratio was carried out and discussed in Sect. 3.4.

From FE analysis, local modes of deck slab were identified between a frequency range of 10–300 Hz. Some of the mode shapes are shown in Fig. 5. Natural frequencies of analytical modes were compared with similar experimental modes. A difference of 23% was noted between the natural frequencies of lower modes <60 Hz, however, the difference reduced to 7% in the higher frequency range from 60 to 300 Hz attributed to the insignificant effect of boundary conditions on higher modes. The analytically obtained mode shapes ascertain that the dynamic behavior of the deck panels exhibited dominant local deformation of the deck in around the same range of frequencies as investigated in the experimental analysis (Fig. 5). The analytical model was adequate to obtain the results under the scope of this study, however, when the analytical results are to be used solely for detailed investigation, the model needs to be revised by improving its boundary conditions to get the lower modes' results close to the experimental.

3.2 Mode Shape Based Criteria

In order to localize damage through the change in mode shapes of deck panels, COMAC was evaluated. Panel 3 was considered as reference, and the COMAC values were evaluated at each measurement location using the modal amplitudes of

Table 1 COMAC evaluated using modal amplitudes of experimental mode shapes of all deck panels

Deck panel	COMAC for different measurement locations										
	1	2	3	4	5	6	7	8	9	10	11
1–3	0.95	0.99	0.96	0.80	0.92	0.89	0.86	0.99	0.90	0.67	0.97
2–3	0.95	0.97	0.85	0.88	0.97	0.95	0.84	0.93	0.74	0.69	0.73

similar mode shapes of Panels 1 and 3, and Panels 2 and 3 in Eq. (2). The results are presented in Table 1. COMAC for Panel 2 was observed lower than Panel 1 for most of the locations, which could manifest damage in Panel 2 to be more than Panel 1. Furthermore, lower value of COMAC at location 9, 10 and 11 in Panel 2 could be an indication of damage at these locations. COMAC at location 10 of both panels was noticed to be the lowest among all locations, indicating the severity of damage along the girders that was evinced by the visual inspection of the bridge. Cracks were observed along the girder of Panel 1, and in Panel 2, corrosion was also noticed in some part of the girder during visual inspection.

3.3 Stabilization Diagrams

The stabilization diagrams obtained from ERA analysis were also utilized to study the differences in the dynamic characteristics among different deck panels. The number of vibration modes were found to differ for each deck panel as shown in Fig. 6. Overall, for Panel 3, the least number of modes were identified, whereas the deck panel with the most deterioration, such as Panel 2, had the largest number of modes. The distribution of natural frequencies was also noticed to differ for each deck panel (Fig. 6). For Panel 3, the least number of modes were identified in the frequency range up to 100 Hz compared to deck panels 1 and 2. For deck Panel 2, the number of modes in the frequency range of 100–200 Hz were more than Panel 1, whereas almost no mode was identified in the same frequency range for Panel 3. More number of modes were observed for deck Panel 3 in the higher frequency range of 200–300 Hz as compared to Panel 1 and 2. In the frequency range up to 200 Hz, the stabilization diagrams showed an increase in the number of modes with the increase in deterioration in different panels suggesting that stabilization diagrams might be used as damage indicator, however, above 200 Hz the results were contradicting, so further investigation is needed in this area.

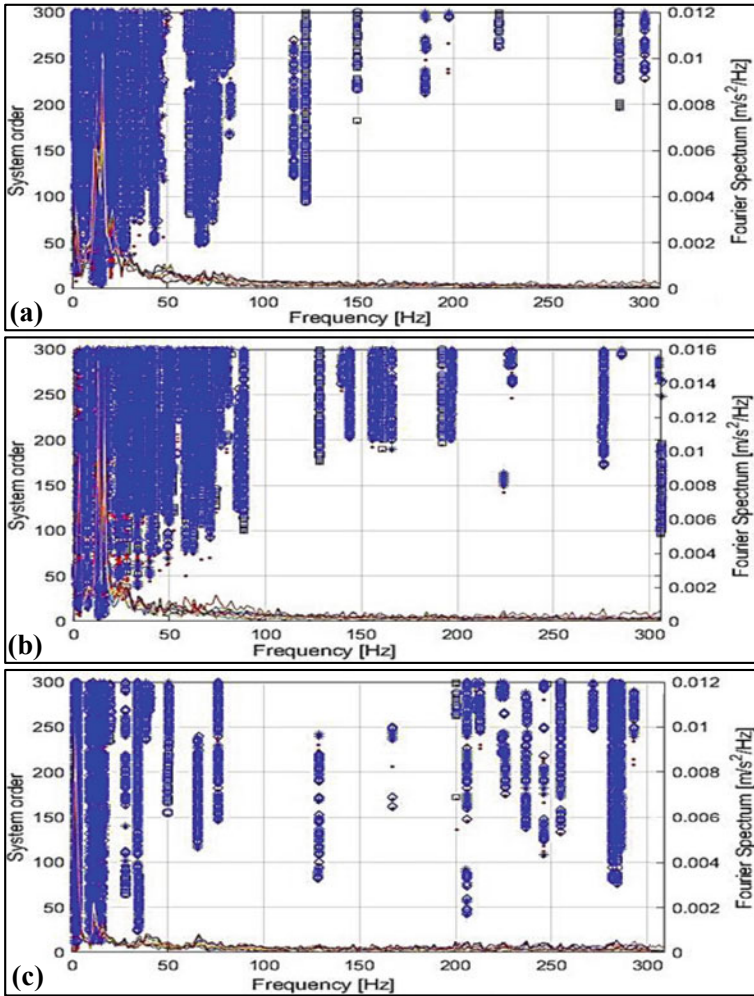


Fig. 6 Stabilization diagrams identified for; a Panel 1, b Panel 2, c Panel 3

3.4 Amplitude Dependence of Damping Ratio

Modal natural frequencies and damping ratios of different deck panels were compared in Sect. 3.1, and the maximum percentage difference between the natural frequencies of Panel 3 and other panels was observed to be 11%, whereas the percentage difference between the damping ratios was much higher, as shown in Fig. 4, indicating the sensitivity of damping ratio to damage. However, the identified damping ratios provided misleading predictions of damage, which could be attributed to the amplitude dependence of damping ratios. Thus, further investigation was carried out

on the amplitude dependence of damping ratio to improve the results of damping ratios to be associated with damage.

Figure 7a shows an example of free responses extracted using RD technique for Panel 2. Each of the peaks (P_1, P_2, \dots, P_n) up to 0.5 s in the RD signature was selected as the initial point, and ERA was performed keeping the length of data (D_1, D_2, \dots, D_n) same as 0.5 s for each analysis. All the modal parameters were identified from each set of data, and the damping ratios were plotted against initial amplitudes of four similar modes of all panels as shown in Fig. 8. Positive relationships were observed with different slopes and correlation coefficients ≥ 0.75 . To minimize the influence of amplitude on damping ratio, the damping ratios of all panels corresponding to similar initial amplitudes around 0.15 m/s^2 were compared (Fig. 7b). For Modes 3 and 4, the amplitudes and damping ratios were observed to be very small for Panels 1 and 2, therefore, the comparison was made between the results of first two modes. Damping ratios of Panel 1 and 2 were observed to be higher than Panel 3, however, the difference between Panel 1 and 3 was not significant (Fig. 7b), which could indicate Panel 2 as the most damaged panel. These results clearly indicated that it was not only the structural condition that caused variation in damping ratio, presented in Fig. 4, but amplitude dependence of damping ratio affected the results. Hence, in the case of damage identification using damping ratio, the amplitude of vibration must be taken into consideration for reliable results.

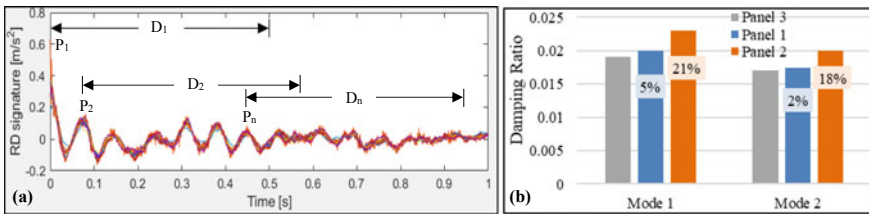


Fig. 7 a Free vibration response for Panel 2, b Damping ratio of Mode 1 and 2 with similar amplitudes for all panels

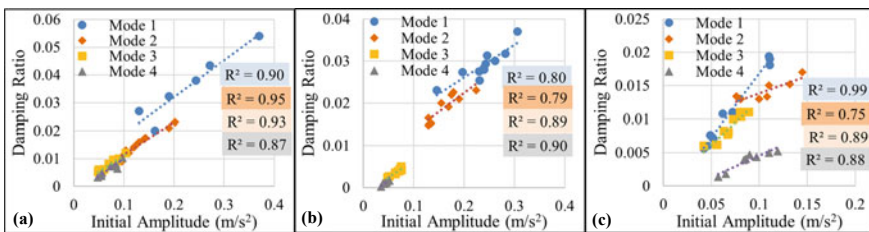


Fig. 8 Damping ratio and initial amplitude relationships for four similar modes for; a Panel 1, b Panel 2, c Panel 3

4 Conclusions

The influence of damage on dynamic parameters was studied in this paper by investigating the actual RC bridge deck panels with different levels of deterioration. This paper also presented a closer look into the stabilization diagram and amplitude dependence of damping ratio. In addition to the extraction of dynamic parameters from the vibration measurements, FE modeling was conducted to support the experimental observations. Based on the results discussed in this paper, the following conclusions were drawn:

- Damage induced reduction in the natural frequency of deck panels as the natural frequency of more damaged deck panel was observed to be lower than the relatively healthy panel (Fig. 4a). Whereas misleading results were observed for the damping ratio of different deck panels (Fig. 4b). To improve the results of damping ratio, amplitude dependence of damping ratio was investigated. Positive relationships were observed between the damping ratios and initial amplitudes of all studied modes. The comparison of damping ratios of all panels corresponding to similar amplitudes showed an increase in damping ratio with the increase in deterioration of panels (Fig. 7b). The results indicated the importance of consideration of vibration amplitude along with damping ratio, when associating it with damage, to avoid misleading predictions.
- Mode shape-based criterion, MAC and COMAC, were used to identify and localize damage. Mode shapes of Panel 3 were considered as reference due to the relatively healthy state of Panel 3. MAC for Panel 1 and 2 with respect to Panel 3 was 90% and 87%, respectively, and COMAC for Panel 2 was observed to be lower than Panel 1 for most of the locations (Table 1). The lower value of MAC and COMAC for Panel 2 indicated damage in it to be more than Panel 1. Moreover, COMAC was able to indicate severity of damage at location 10 along the girder where damage was evinced by the visual inspection of Panels 1 and 2.
- Stabilization diagrams were also utilized to study the differences in the dynamic characteristics between different deck panels. In the comparison of stabilization diagrams, number of modes identified for most damaged deck panel 2 were observed to be the highest of all three deck panels (Fig. 6). It could suggest that stabilization diagrams might be used as damage indicator, however, further investigation is needed in this area.

References

1. Cao MS, Sha GG, Gao FY, Ostachowicz W (2017) Structural damage identification using damping: a compendium of uses and features. *Smart Mater Struct* 26:043001. <https://doi.org/10.1088/1361-665X/aa550a>
2. NEXCO-Japan (2014) Regarding large-scale renewal and large-scale repair on the expressway. Managed by Eastern, Central and West Japan Expressway Co., Ltd. Available: <https://www.cnexco.co.jp/koushin/pdf/about.pdf>
3. Curadelli RO, Riera JD, Ambrosini D, Amani MG (2008) Damage detection by means of structural damping identification. *Eng Struct* 30(12):3497–3504
4. Mustafa S, Matsumoto Y, Yamaguchi K (2018) Vibration-based health monitoring of an existing truss bridge using energy-based damping evaluation. *J Bridg Eng* 23(1):04017114
5. Asmussen JC, Ibrahim R, Brincker, R (1998) Random decrement: identification of structures subjected to ambient excitation. In: *Proceedings of the 16th international modal analysis conference*, Santa Barbara, California, USA
6. Juang JN, Pappa RS (1985) An eigensystem realization algorithm for modal parameter identification and model reduction. *J Guid Control Dyn* 8(5):620–627
7. Silva JMM, Maia NMM (1998) *Modal analysis and testing*. Kluwer Academic Publishers, Dordrecht

Assessing Structural Health State by Monitoring Peridynamics Parameters in Operational Conditions



Gaetano Miraglia, Erica Lenticchia, Marco Civera, and Rosario Ceravolo

Abstract This paper aims to analyze the Peridynamics (PDs) theory and to exploit it for new possibilities in Civil Engineering by employing the theory for Structural Health Monitoring (SHM). In particular, the paper aims to exploit PDs for SHM and damage characterization of the built environment, at the structural scale, in operational conditions (i.e., without input sources). The reasons behind this study rely on the possibility to use PDs to emulate very complex structural behaviors effortlessly, using PDs as a paradigm to build low fidelity structural models of real systems. In the present paper, new features to characterize the damage (i.e., to detect, locate, and quantify it) are proposed thanks to a special definition of the peridynamic theory written in discrete form. These features are the Bond Extremity Acceleration (BEA) and Bond Extremity Velocity (BEV) conjectures, which are obtained by discretizing a system with the Bond Based PDs and using a micro-viscoelastic constitutive law at the bond level. Moreover, the authors show how the proposed peridynamic parameters are theoretically estimable with very robust techniques already used in SHM, such as the Stochastic Subspace Identification (SSI) algorithms. The considerations reported in the paper are verified with numerical (virtual) models. The paper concludes that PDs can be used to easily parametrize the built environment opening new research possibilities on the use of PDs for civil SHM. Additionally, the proposed BEA proves to be a very scalable and general parameter to be monitored in real systems (providing information on the presence, the location, and the amount of damage), this also due to its physical based meaning and the straightforward method of extraction in operational conditions.

Keywords Peridynamics · Structural health monitoring · Damage detection and localization · Low fidelity structural models · Structural simulator

G. Miraglia (✉) · E. Lenticchia · R. Ceravolo
Department of Structural, Geotechnical and Building Engineering, Polytechnic of Turin, Turin,
Italy
e-mail: gaetano.miraglia@polito.it

M. Civera
Department of Mechanical and Aerospace Engineering, Polytechnic of Turin, Turin, Italy

1 Introduction

Finding the right balance between accuracy and computational efficiency of structural simulators is essential to obtain valuable information on the health state of real structures in a feasible computational time. In reaching this balance, the parallel use of low fidelity and high fidelity structural models is helpful, being the first approach ideal to extract very fast information, while the second able to generate high quality knowledge on complex behaviors of real systems. However, if Structural Health Monitoring (SHM) techniques need to be applied to a large number of structures (e.g., urban area), very high-fidelity models result to be inadequate to obtain information in a feasible computational time.

Peridynamics (PDs) is a modern nonlocal theory of continuum established in early 2000 by Stewart Silling [1, 2] and Silling et al. [3]. The theory is recently attracting attention in the field of computational mechanics since it replaces the partial differential equations of the classical continuum theory with integral, spatial equations. This allows overcoming problems related to the representation of discontinuities in the matter, which can arise during damage (e.g., cracks), where the differential formulations are not defined. A comprehensive literature review of Peridynamic (from the Greek words *peri-* i.e., around, and *-dynami* i.e. force) applications and uses can be found in [4]. Basically, PD theory found its principle in the forces-interaction (*bonds*) of points. The matter is divided into infinitesimal portions characterized by their mass and volume. Each point k is then supposed to interact with its neighbours inside a region. The collection of all the points inside this region is called *family* of k . The family of k is, in turn, characterized by the *horizon*, i.e., the maximum distance for which the interactions between k and the other points of a body occur. The horizon defines the locality of the behavior of a system; the smaller the horizon, the more local the behavior will be. It has been demonstrated that the classical theory of elasticity can be considered as a limiting case of the PD theory as the horizon approaches zero [5–7]. When using PD in a modelling phase, the choice of the horizon represents a crucial aspect. It can be a constant or variable along the modelling space. Sometime, physics defines the value of horizon (e.g., when modelling particles, the interatomic potential defines the maximum interaction distance). In other cases the value of the horizon is not defined, and its definition should be based on calibration procedures [8]. When the standard local theory, instead, well describes the structural behavior, PD can still be used. In this case, the horizon should be as small as possible to fit the classical continuum theory, while when the nonlocal theory is used to model damage (e.g., crack growth and propagation), several works have related the value of the horizon with the value of the average distance between points used to discretize the continuum, [5, 8]. In this case, the horizon is commonly set to 3 times the spacing between points. PD is thus a candidate theory that can be used for modelling real systems. About the modelling of real systems, the work of Gosliga and Worden [9] is noteworthy. Here the authors propose the use of *Irreducible Element (IE) model*, which seeks to create a graphical representation of a system (using graph theory [10–12]) by breaking it down into its constituent parts, with the aim to assess the

similarity of structures. The system modelling plays an important role in the SHM of existing systems [13, 14]. In this field, important researches have been done by Farrar and Worden et al. [15–17], while the promising future of this discipline is also dictated by the technological advancement of the last years [18]. The importance of system identification in SHM is crucial and is due to the advantage of using the information extracted from identification techniques for defining damage [19]. Within this framework, damage can be defined as a change introduced in a system that negatively affects its current and future performance [17]. Thus, SHM techniques are precisely intended to provide some physical/non-physical based damage index with a broad range of validity, in the linear and nonlinear field.

In the present paper the authors propose PDs as a general method to build physical-based graph representations (i.e., with edges and nodes) of civil structural systems (i.e., low fidelity models) and built environment. Then, starting from this representation, two features are proposed for an efficient damage identification and SHM: the Bond Extremity Acceleration (BEA) and Bond Extremity Velocity (BEV). This is done presenting the basic theory of PDs and the proposed algorithm to estimate the BEA and BEV (Sect. 2). Then, some numerical verifications supporting the theory is reported (Sect. 3). Finally, the conclusions are drawn (Sect. 4).

2 Methods

In this section the methods are presented introducing the basic theory of Peridynamics and the procedure to identify the BEAs and BEVs using the Stochastic Subspace Identification (SSI) algorithms.

2.1 Basic Theory

The linearized micro-linear viscoelastic Bond Based PD (BBPD) equation of motion can be written in standard form as (bold is herein used for vectors, bold capital for matrices and italic for scalars):

$$\mathbf{M}\ddot{\mathbf{u}}(t) + \mathbf{C}\dot{\mathbf{u}}(t) + \mathbf{K}\mathbf{u}(t) = \mathbf{z}(t)$$

$$\mathbf{M} = \begin{bmatrix} \mathbf{M}_k & \mathbf{O}_3 & \dots \\ \mathbf{O}_3 & \ddots & \dots \\ \vdots & \vdots & \ddots \end{bmatrix}; \mathbf{C} = \begin{bmatrix} \sum_{j=1}^K \mathbf{C}_{kj} & -\mathbf{C}_{kj} & \dots \\ j \neq k & & \\ -\mathbf{C}_{kj} & \ddots & \dots \\ \vdots & \vdots & \ddots \end{bmatrix}; \mathbf{K} = \begin{bmatrix} \sum_{j=1}^K \mathbf{K}_{kj} & -\mathbf{K}_{kj} & \dots \\ j \neq k & & \\ -\mathbf{K}_{kj} & \ddots & \dots \\ \vdots & \vdots & \ddots \end{bmatrix} \quad (1)$$

where:

$$\begin{aligned}
\mathbf{M}_k &= m_k \mathbf{I}_3 \\
\mathbf{C}_{kj} &= v_{kj} \mathbf{K}_{kj} \\
\mathbf{K}_{kj} &= c_{kj} V_j V_k \boldsymbol{\Xi}_{kj} \\
\boldsymbol{\Xi}_{kj} &= \frac{\boldsymbol{\xi}_{kj} (\boldsymbol{\xi}_{kj}^T)}{\|\boldsymbol{\xi}_{kj}\|^3} \\
c_{kj} &= \begin{cases} c_{kj} & \text{if } \|\boldsymbol{\xi}_{kj}\| \leq h \\ 0 & \text{if } \|\boldsymbol{\xi}_{kj}\| > h \end{cases} \\
\boldsymbol{\xi}_{kj} &= \mathbf{x}_j - \mathbf{x}_k
\end{aligned} \tag{2}$$

In Eqs. (1) and (2) $\mathbf{x}_k = (x_{k,X}, x_{k,Y}, x_{k,Z})^T$ are the coordinates X, Y, Z of point k (similarly for j), $c_{kj} \geq 0$ is called bond elastic constant, and h is the horizon. V_j and V_k are the volumes, accounting for the volume corrections, associated to the points j and k respectively while $v_{kj} \geq 0$ is a bond damping constant; m_k is the mass associated to the point k , \mathbf{I}_3 is a 3×3 identity matrix and \mathbf{O}_3 is a 3×3 zero matrix. K is the number of points used to discretize the system. Then, $\mathbf{u}(t)$ and $\mathbf{z}(t)$ denote the displacement vector and the external force vector respectively, being t the time variable and $(\dot{})(t)$ the time derivate operator. Finally, \mathbf{M} , \mathbf{C} , and \mathbf{K} denote the mass, damping, and stiffness global matrices of the system.

2.2 Parameters Identification

From Eqs. (1) and (2) it is possible to derive two parameters that can be easily experimentally identified without input (operational conditions) sources; the Bond Extremity Acceleration (BEA) w'_{kj} , and the Bond Extremity Velocity (BEV) w''_{kj} , of the bond kj and the extremity k , which are here proposed as parameters to be monitored for SHM purpose:

$$\begin{aligned}
w'_{kj} &= \frac{c_{kj} V_j V_k}{m_k} \\
w''_{kj} &= w'_{kj} v_{kj}
\end{aligned} \tag{3}$$

It is worth noting that in Eq. (3), in general, $w'_{kj} \neq w'_{jk}$ and $w''_{kj} \neq w''_{jk}$ as $m_k \neq m_j$.

Starting from the acquired acceleration response $\ddot{\mathbf{u}}(t)$ it is possible to get an estimate of the system matrix $\hat{\mathbf{A}}$ (in the state space formulation) reduced to the number

of recorded Degree of Freedoms (DoFs), by using, for instance, SSI algorithms. The eigen-analysis performed on $\widehat{\mathbf{A}}$, after some manipulations, provides the real eigenvalues $\mathbf{\Lambda}$ of the reduced system (square values of the circular natural frequencies), the real eigenvectors $\mathbf{\Phi}$ (mode shapes), and the modal damping ratios \mathbf{Z} , where $\mathbf{\Lambda}$ is a diagonal matrix containing the sorted eigenvalues on the main diagonal, \mathbf{Z} is a diagonal matrix containing the corresponding damping ratios on the main diagonal, while $\mathbf{\Phi}$ is the eigenvectors matrix containing the corresponding eigenvectors in each column of the matrix. Performing the estimate of $\widehat{\mathbf{A}}$ on a dimension equal to the number of recorded DoFs, it is possible to get an estimate of the mass $\widehat{\mathbf{M}}$, damping $\widehat{\mathbf{C}}$, and stiffness $\widehat{\mathbf{K}}$ global matrices of the system reduced to these DoFs:

$$\begin{aligned}\widehat{\mathbf{K}} &= (\mathbf{\Phi}^T)^{-1}(\mathbf{\Lambda})(\mathbf{\Phi})^{-1} \\ \widehat{\mathbf{M}} &= (\mathbf{\Phi}^T)^{-1}(\mathbf{I})(\mathbf{\Phi})^{-1} \\ \widehat{\mathbf{C}} &= (\mathbf{\Phi}^T)^{-1}(2\mathbf{Z}\sqrt{\mathbf{\Lambda}})(\mathbf{\Phi})^{-1}\end{aligned}\quad (4)$$

where \mathbf{I} is an identity matrix with the same dimension of $\mathbf{\Lambda}$. Then, the BEAs and the BEVs can be estimated with:

$$\begin{aligned}\widehat{\mathbf{W}}' &= \left[-(\widehat{\mathbf{M}})^{-1}(\widehat{\mathbf{K}}) \right]^\circ (\mathbf{\Delta})^{\circ-1} \\ \widehat{\mathbf{W}}'' &= \left[-(\widehat{\mathbf{M}})^{-1}(\widehat{\mathbf{C}}) \right]^\circ (\mathbf{\Delta})^{\circ-1}\end{aligned}\quad (5)$$

$$\mathbf{\Delta} = \begin{bmatrix} \mathbf{I}_3 & \mathbf{\Xi}_{kj} & \dots \\ \mathbf{\Xi}_{kj} & \ddots & \dots \\ \vdots & \vdots & \ddots \end{bmatrix}$$

where $(\dots)^\circ(\dots)$ and $(\dots)^{\circ-1}$ denote the Hadamard product and inversion operator, respectively, while $\widehat{\mathbf{W}}'$ and $\widehat{\mathbf{W}}''$ contain the estimate of the BEAs w'_{kj} , and the BEVs w''_{kj} , respectively. The estimates of these features can be then refined by repeating the identification procedure on a second estimate of the of the system matrix $\widehat{\widehat{\mathbf{A}}}$:

$$\widehat{\widehat{\mathbf{A}}} = \begin{bmatrix} \mathbf{O} & \mathbf{I} \\ -(\widehat{\mathbf{M}})^{-1}(\widehat{\mathbf{K}}) & -(\widehat{\mathbf{M}})^{-1}(\widehat{\mathbf{C}}) \end{bmatrix}\quad (6)$$

obtaining the refined estimate of BEAs $\widehat{\mathbf{W}}'$, and BEVs $\widehat{\mathbf{W}}''$, where \mathbf{O} is a zero matrix with same dimension of \mathbf{I} .

3 Results and Discussion

In this section the previous described methods are applied to numerical benchmarks, and the verifications of the study are reported and discussed.

The numerical benchmarks are represented by 2 Multi Degree of Freedoms (MDOFs) systems. The first with 4 DoFs, while the second with 10 DoFs. For the sake of clarity, the systems are represented by a series of masses (spaced 1 m from each other) which vibrate in one direction. The systems are supposed to do not have a unique value of the masses or volumes, but these values are randomly extracted between 0.8 and 1 (for both mass [kg] and volume [m³] values). Thus, for the 4 DoFs system, 100 extractions of the model parameters (masses and volumes) have been performed. The same has been done for the 10 DoFs system. A dummy mass has been added to the systems in order to constrain the problem and avoid rigid body motions. Then, for each system, 4 cases of acquisitions have been assumed: 10 and 30 min of acquisitions with signals corrupted by a 5% and 20% of gaussian noise. The sampling frequency has been supposed equal to 100 Hz, while the vector of the external sources representing environmental noise has been approximated with samples extracted by a gaussian distribution with unitary variance. The horizon h , has been set to 3 m, while $c_{kj} = 2e3 \text{ N/m}^6$, and $v_{kj} = 1e - 3 \text{ sec}$ for all the bonds.

The methods described in Sect. 2 have been then applied and the discrepancy between *target* (theoretically correct) values and identified values of the BEAs and BEVs has been studied. Figure 1 reports the Probability Density Function (PDF) of the *average identification error* (mean values over the bonds of the absolute difference between target and identified values of BEAs and BEVs, normalized to the target value). Each PDF has been estimated with 100 samples. From the figure is possible to conclude that the error of BEV is higher and more dispersed than the error of BEA, and the error tend to decrease as the signal length increase.

Figure 2 depicts the *bond identification absolute error* (absolute difference between target and identified values of BEAs and BEVs, normalized to the target value, for each bond) for a case of the 4 DoFs system, with 10 min of records corrupted by 5% of gaussian noise. Also in this case it is possible to note as the errors on the bonds are higher for the estimates of the BEVs.

Then, a realization of the model parameters (masses and volumes) for the 4 DoFs and the 10 DoFs system has been used to study the *average identification error* at increasing damage. In this study, the first bond (bond between points 1 and 2) and the last bond (bond between points 3 and 4 for the 4 DoFs system, and between points 9 and 10 for the 10 DoFs system) have been damaged. It was supposed a damage multiplier (*bond damage*) between 0 and 1. This multiplier defines the new values of c_{12} and c_{21} as proportional to the initial value of $2e3 \text{ N/m}^6$. For the last bond

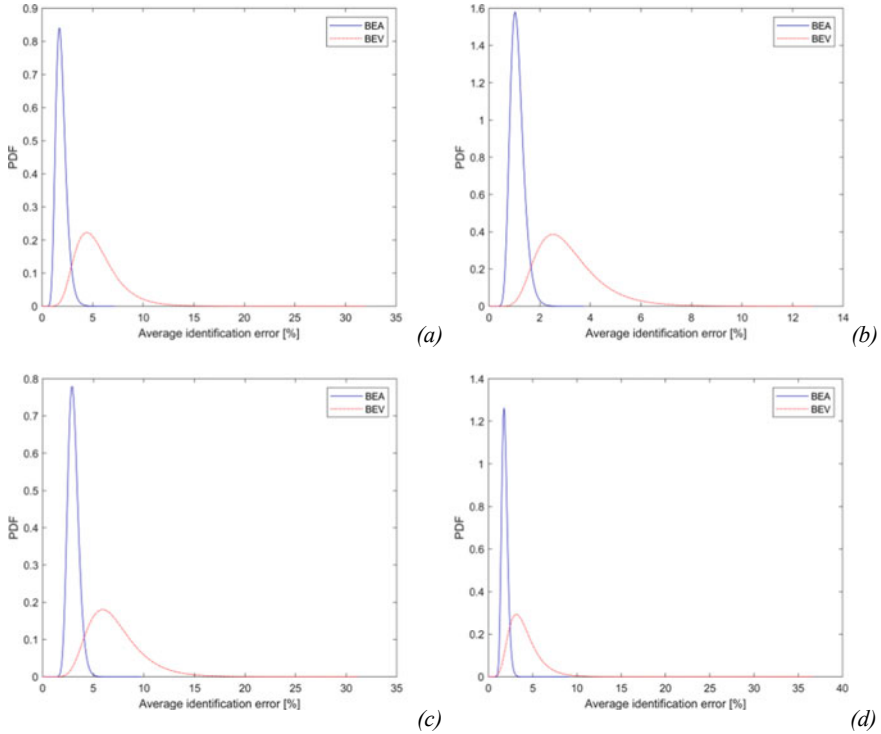


Fig. 1 Probability Density Function (PDF) of the average identification error [%] of BEAs and BEVs for a 4 DoFs system with 10 min (a), and 30 min (b) of records, and for a 10 DoFs system with 10 min (c) and 30 min (d) of records. All plots refer to 5% of gaussian noise in the records

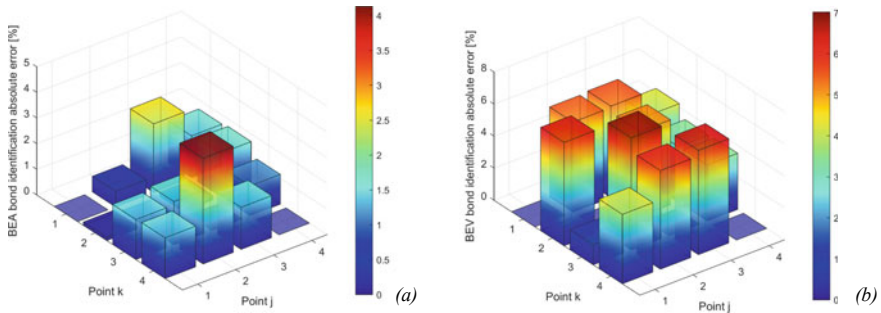


Fig. 2 Absolute identification errors [%] of BEAs (a) and BEVs (b) of the bonds k-j, for a generic 4 DoFs system with 10 min of records and 5% of gaussian noise in the records

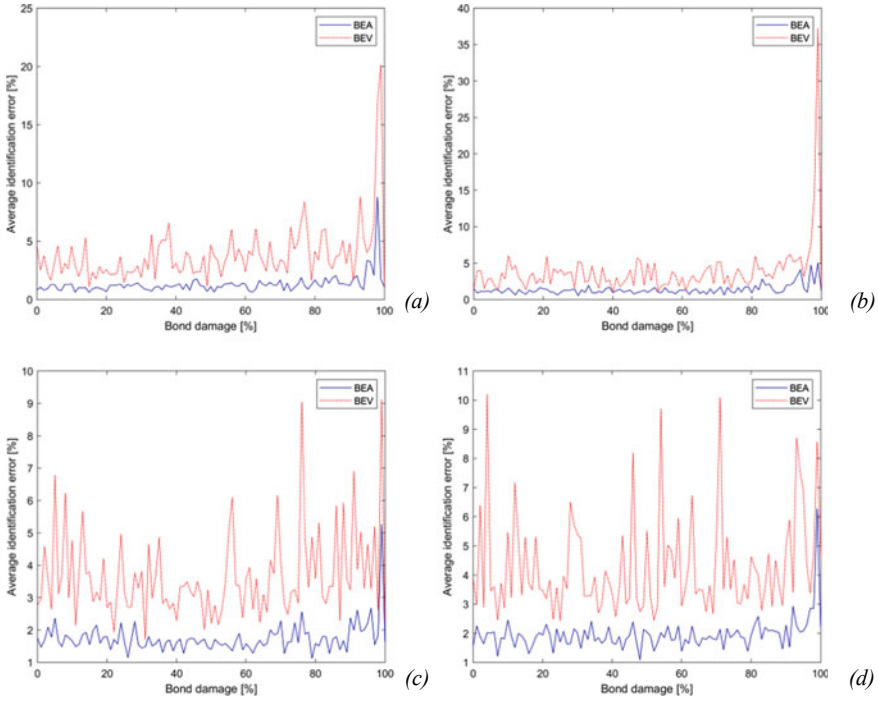


Fig. 3 Average identification error [%] of BEAs and BEVs as a function of the damage level [%] on the bond 1–2 for a 4 DoFs system with 5% (a), and 20% (b) of gaussian noise in the records, and for a 10 DoFs system with 5% (c), and 20% (d) of gaussian noise in the records. All plots refer to 30 min of records

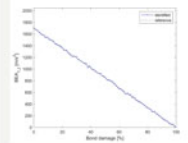
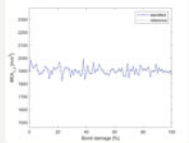
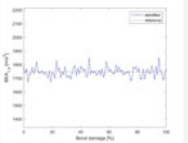
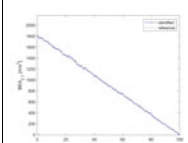
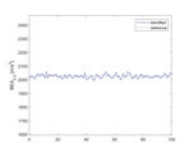
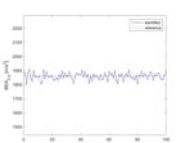
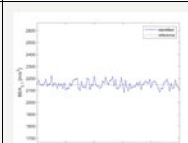
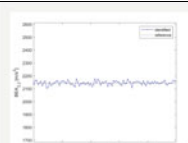
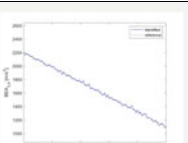
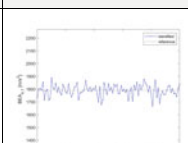
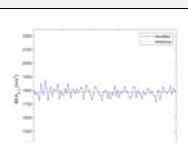
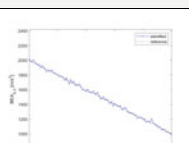
it was assumed a damage multiplier equal to the half of that one used for the first bond. Figure 3 reports the *average identification error* for some analyzed cases as a function of the *bond damage*.

From Fig. 3 it is possible to conclude that the error remains quite stable at increasing percentage of noise in data, and generally is higher and more unstable for the estimate of the BEVs. Then, Table 1 reports the comparison between target and identified values of BEAs as a function of the *bond damage* for the 4 DoFs system.

From the table is easy to observe that the only damaged bonds are those expected to be damaged, and the amount of damage is consistence with the expected values. In fact, the first bond reaches a value of BEA equal to 0, while the last bond reach half of its initial value for a bond damage on the first bond equal to 100%. Finally, the BEA values of the remaining bonds rightly remain unchanged as the damage increases.

Finally, as done for BEA, Table 2 reports the comparison between target and identified values of BEVs as a function of the *bond damage* for the 4 DoFs system.

Table 1 Discrepancy between target (dashed black line) and identified BEAs [m/s²] (blue line) as a function of the damage level [%] on the bond 1–2 for a 4 DoFs system with 30 min of records and 5% of gaussian noise in the records

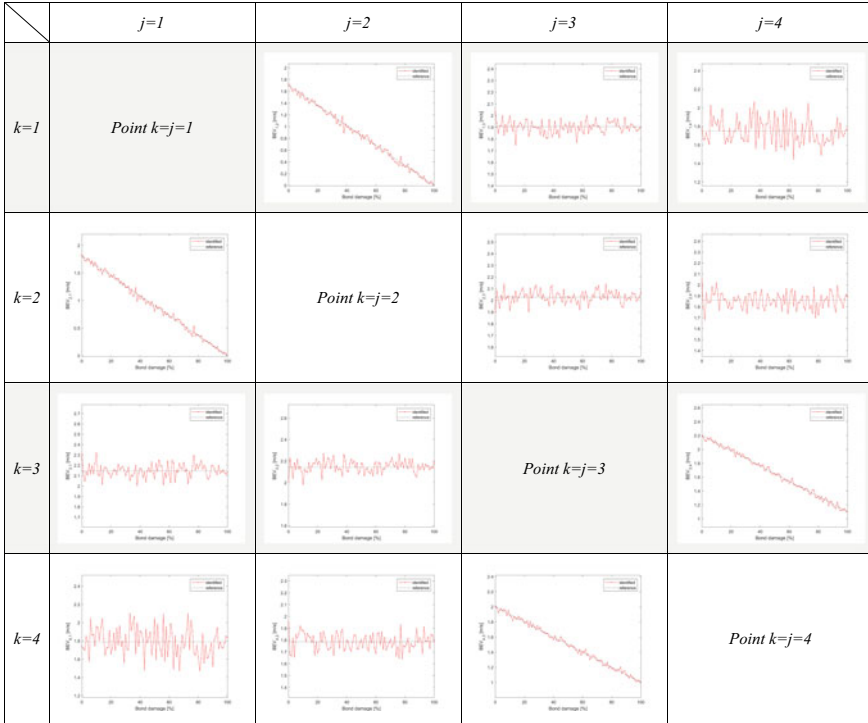
	$j=1$	$j=2$	$j=3$	$j=4$
$k=1$	<i>Point k=j=1</i>			
$k=2$		<i>Point k=j=2</i>		
$k=3$			<i>Point k=j=3</i>	
$k=4$				<i>Point k=j=4</i>

From the table is easy to observe that the only damaged bonds are those expected to change value, and the amount of changing is consistency with the expected values. In fact, the first bond reaches a value of BEV equal to 0, while the last bond reach half of its initial value for a bond damage on the first bond equal to 100%. Finally, the BEV values of the remaining bonds rightly remain unchanged as the damage increases, even if compared to the BEAs estimates, the BEVs values fluctuate more around the target values.

4 Conclusions

In the paper, the authors proposed Peridynamics as a generic method to generate low fidelity structural models and obtaining valuable and very fast information on the health state of a large number of structures. Then, the authors found that Peridynamics can be used to define physical-based graph representations (i.e., with edges and nodes) of civil structural systems. These findings, for now limited to numerical verifications, demonstrate that Peridynamics proves ideal for facing the SHM of vast

Table 2 Discrepancy between target (dashed black line) and identified BEVs [m/s] as a function of the damage level [%] on the bond 1–2 for a 4 DoFs system with 30 min of records and 5% of gaussian noise in the records



territories with computational effortless strategies, and physical-based (i.e., providing valuable information) representations of the built environment. In this regard, the proposed BEA proves to be a very scalable and general parameter to be monitored in real systems (providing information on the presence, the location, and the amount of damage), this also due to its physical based meaning and the straightforward method of extraction in operational conditions. About the results of the numerical verifications, it is possible to draw the following conclusions:

- The identification errors for BEV are generally larger and more dispersed (greater uncertainty) than those for BEA.
- The estimate of BEA and BEV remain quite stable to an increase of the percentage of noise in the records, while the errors little increase if the length of the acquisitions decrease.
- The BEA can be used for the damage identification, i.e., to detect, quantify, and localize the damage.
- The BEV, instead, is a dubious parameter, since its use strongly depends by the discrepancy between the model and the actual behavior of the system; therefore, its use for SHM purposes should be carefully evaluated.

The authors envisage low fidelity peridynamic models as a general method to allow physical-based SHM of systems over a territorial scale. For example, our results can be useful to generate network of built structures helping in the early warning of catastrophic events such as earthquakes, hurricanes, tornadoes, landslides, etc. In addition, structures built in the first half of the twentieth century are approaching or have surpassed their typical design life, meaning that there is a need to check the state of aging of structures over large areas. In this regard, low fidelity peridynamic models can be used to monitor very slow or sudden changes of structural states relying on very robust algorithms from established literature.

Although the results of the numerical verifications are promising, all considerations made must pass the experimental validation phase to be considered valid, which can represent the next step of this work.

References

1. Silling SA (2000) Reformulation of elasticity theory for discontinuities and long-range forces. *J Mech Phys Solids* 48(1):175–209
2. Silling SA (2001) Peridynamic modeling of the Kalthoff–Winkler experiment. In: Submission for 2001 Sandia prize computational science
3. Silling SA, Epton M, Weckner O, Xu J, Askari E (2007) Peridynamic states and constitutive modeling. *J Elast* 88(2):151–184
4. Javili A, Morasata R, Oterkus E, Oterkus S (2019) Peridynamics review. *Math Mech Solids* 24(11):3714–3739
5. Madenci E, Oterkus E (2014) Peridynamic theory and its applications, vol 17. Springer, Berlin
6. Silling SA, Zimmermann M, Abeyaratne R (2003) Deformation of a peridynamic bar. *J Elast* 73(1–3):173–190
7. Weckner O, Abeyaratne R (2005) The effect of long-range forces on the dynamics of a bar. *J Mech Phys Solids* 53(3):705–728
8. Bobaru F, Foster JT, Geubelle PH, Silling SA (2016) Handbook of peridynamic modeling. CRC Press, Boca Raton
9. Gosliga J, Worden K (2019) A general representation for assessing the similarity of structures. *Struct Heal Monit*
10. Bondy JA, Murty USR (1976) Graph theory with applications, vol 290. Macmillan, London
11. West DB (2001) Introduction to graph theory, vol 2. Prentice Hall, Upper Saddle River
12. Sanderson DJ, Peacock DCP, Nixon CW, Rotevatn A (2019) Graph theory and the analysis of fracture networks. *J Struct Geol* 125:155–165
13. Sohn H et al (2003) A review of structural health monitoring literature: 1996–2001. Los Alamos National Laboratory, USA, pp 1–7
14. Amezquita-Sanchez JP, Adeli H (2019) Nonlinear measurements for feature extraction in structural health monitoring. *Sci Iran* 26(6):3051–3059
15. Rogers TJ, Worden K, Fuentes R, Dervilis N, Tygesen UT, Cross EJ (2019) A Bayesian non-parametric clustering approach for semi-supervised Structural Health Monitoring. *Mech Syst Signal Process* 119:100–119
16. Farrar CR, Worden K (2007) An introduction to structural health monitoring. *Philos Trans R. Soc A Math Phys Eng Sci* 365(1851):303–315
17. Farrar CR, Worden K (2012) Structural health monitoring: a machine learning perspective. Wiley, Hoboken

18. Sony S, Laventure S, Sadhu A (2019) A literature review of next-generation smart sensing technology in structural health monitoring. *Struct Control Heal Monit* 26(3):e2321
19. Wang Z, Lin RM, Lim MK (1997) Structural damage detection using measured FRF data. *Comput Methods Appl Mech Eng* 147(1–2):187–197

Impact Damage Identification Using Chirped Ultrasonic Guided Waves for Health Monitoring of CFRP Vehicle Structures



Langxing Tan, Fengming Yu, Osamu Saito, Yoji Okabe, Taku Kondoh, Shota Tezuka, and Akihiro Chiba

Abstract Nowadays, carbon fiber reinforced plastic (CFRP) laminates are used as the structural components of mobilities in order to reduce their weight. However, the barely visible impact damages (BVIDs) in CFRP laminates may cause a significant degradation in the performance, seriously affecting the safety of daily use. Hence, structural health monitoring (SHM) systems that can detect the BVIDs in mobilities are urgently needed. In this research, we attempted to establish a method to identify impact damages in mobility structures made of CFRP based on ultrasonic guided waves transmitted and received by macro fiber composites (MFCs). From the response signals, some damage-sensitive features, such as the time of flight (ToF) delay and the amplitude of A_0 mode, can be extracted to evaluate the impact damage. The relation between the impact damage size and the maximum ToF delay was investigated for three kinds of CFRP plates: woven, non-woven and hybrid laminates. As a result, it was found that the maximum ToF delay increases linearly with an increase in the damage size for all the CFRP laminates. Moreover, the amplitude of A_0 mode was found to be largely affected by the damage length in the wave propagation direction. This attenuation can be used to identify the extension direction of the impact damage as a complement of the ToF delay distribution.

Keywords Carbon fiber reinforced plastic (CFRP) · structural health monitoring · Impact damage · Chirp signal · Lamb waves

L. Tan (✉) · F. Yu · O. Saito · Y. Okabe
Institute of Industrial Science, The University of Tokyo, Tokyo, Japan
e-mail: langxing@iis.u-tokyo.ac.jp

T. Kondoh · S. Tezuka · A. Chiba
Yamaha Motor Company Limited, Shizuoka, Japan

© The Author(s), under exclusive license to Springer Nature Switzerland AG 2023
Z. Wu et al. (eds.), *Experimental Vibration Analysis for Civil Engineering Structures*,
Lecture Notes in Civil Engineering 224,
https://doi.org/10.1007/978-3-030-93236-7_6

1 Introduction

Personal mobilities made of carbon fiber reinforced plastic (CFRP) laminates are likely to suffer from barely visible impact damages (BVIDs) while the owner is not aware. The BVIDs may cause a significant degradation in the performance, and seriously affect the safety of daily use. Hence, structural health monitoring (SHM) systems that can detect the BVIDs in mobilities are urgently needed.

Guided waves (e.g., Lamb waves in plates) are elastic perturbations that can propagate for long distances in thin-wall structures with small attenuation. Hence, they are suitable for SHM system monitoring a large area from a single point. In the previous research, burst waves were used as the input signals to excite Lamb waves, in order to detect an artificial delamination in a CFRP plate by measuring the Time of Flight (ToF) of Lamb waves [1]. However, burst signals with the limited frequency bandwidth are not effective to evaluate the actual impact damage in CFRPs. This is because the actual impact damages are much more complicated than the artificial delamination, and the interaction between ultrasonic wave and the actual damages may vary depending on the frequency. Hence, it is more efficient to detect and evaluate the actual impact damage comprehensively using one broadband signal.

In this research, we attempted to establish a method to evaluate impact damages in mobility structures made of CFRP based on broadband ultrasonic guided waves. From the received waves, we extract the response signals to tone burst excitation at certain frequencies, by using a transfer function. Then, by analyzing the extracted signals, we evaluate the magnitude of the impact damage.

This paper is organized as follows. We begin by observing the cross-section of impact damage area in three kinds of CFRP plates, in order to clarify the difference in the damage conditions of the laminates. In Sect. 3, the relationship between the impact damage size and the ToF delay in various CFRP plates was investigated experimentally, which was found to be linear. Moreover, the influence of the shape of an impact damage to the waveform was also investigated. Especially, we clarified the change in the amplitude of A_0 mode when the damage was enlarged in the direction of the wave propagation. The last section concludes the paper.

2 Cross-Sectional Observation of Impact Damage Area

Various CFRP plates with different layup configurations are used in manufacturing of the mobilities. Therefore, for practical application, the SHM system should be able to detect impact damages in various CFRP plates. Three kinds of CFRP plates were used in this research: woven CFRP plates ($[(0,90)/(45,-45)]_4$, 3.64 mm in thickness), non-woven-CFRP plates ($[0/90/45/-45/-45/45/90/0]_s$, 3.84 mm in thickness), and hybrid CFRP plates ($[(0,90)/(45,-45)/0/90/(0,90)/(45,-45)/(0,90)/(45,-45)]_s$, 3.7 mm in thickness). The impact damages in the plates were given by a drop weight impact test with the impact energy of 15.9 J.

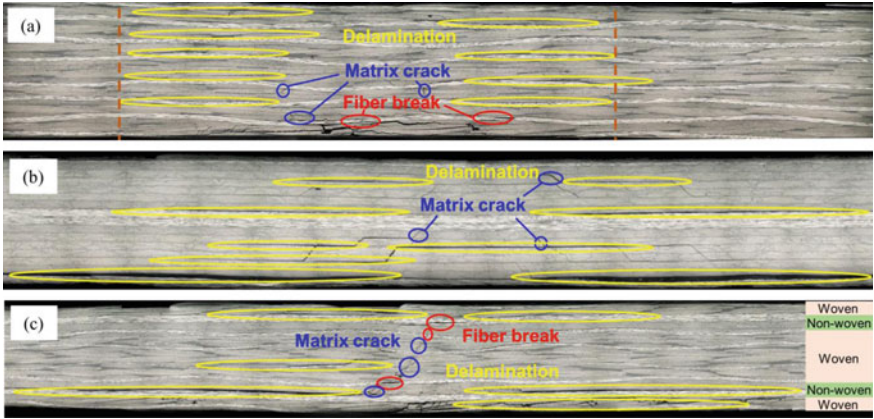


Fig. 1 Cross-section of the damaged area in **a** a woven CFRP plate, **b** a non-woven CFRP plate, and **c** a hybrid CFRP plate

The cross-sections of the impact-damaged area were observed with a digital microscope (VHX-950F, Keyence Corp.). In the woven CFRP plate (Fig. 1a), there are mainly three kinds of microscopic damages: delamination, matrix cracks, and fiber breaks. The delaminations distribute evenly over the whole damaged area, and the diameter of the damaged area is almost constant through the thickness. In the non-woven CFRP plate (Fig. 1b), the delaminations are the most dominant microscopic damage, and that at the nearest interface to the bottom surface is the largest. In the hybrid CFRP plate (Fig. 1c), there are mainly delamination at the interfaces between the non-woven plies and the woven plies and matrix cracks and fiber breaks in the woven plies. The microscopic damages in the hybrid CFRP plate are complicated, and can be regarded as the mixture of those in the woven and non-woven CFRP plates.

3 Damage Detection in Various CFRP Plates Using Chirp Ultrasonic Waves

3.1 Transfer Function Method

Chirp is a broadband signal in which the frequency increases in proportion to the time. Although the data acquisition is efficient in a case of chirp signal excitation, the direct analysis of the received signal is difficult because many propagation modes of Lamb waves can be excited and they are dispersive. Therefore, using a transfer function, we extract the response signals to tone bursts at certain frequencies from the response signal to the broadband chirp signal. The transfer function $H(\omega)$ relates the input signal $S(\omega)$ and response signal $R(\omega)$ in the frequency domain as follows

$$R(\omega) = H(\omega) \cdot S(\omega) \tag{1}$$

for a linear system of ultrasonic propagation [2]. We can obtain the transfer function experimentally by measuring the response to the chirp signal. Then, multiplying the transfer function by tone burst input signals made numerically, we can calculate the response signals to the tone burst signals in the frequency domain. The response signals in the time domain can be obtained by subsequent inverse Fourier transform. Using them, we can investigate the damage-sensitive features.

3.2 Experiment Setup

The experiment setup is shown in Fig. 2. Three kinds of CFRP plates ($300 \times 205 \text{ mm}^2$) as mentioned above were used in the experiments. A multifunction generator (NF, WF1973) was used to generate electrical signals. A macro fiber composite (MFC) (Smart Material, M-0714-P2) was the actuator to convert the electrical signal into the strain. The input signal to the MFC was a sinusoidal linear chirp sweeping from 10 kHz to 1 MHz. Meanwhile, another MFC was used as the receiver on the other side of the plate, and an oscilloscope (YOKOGAWA, DL850E) was used to

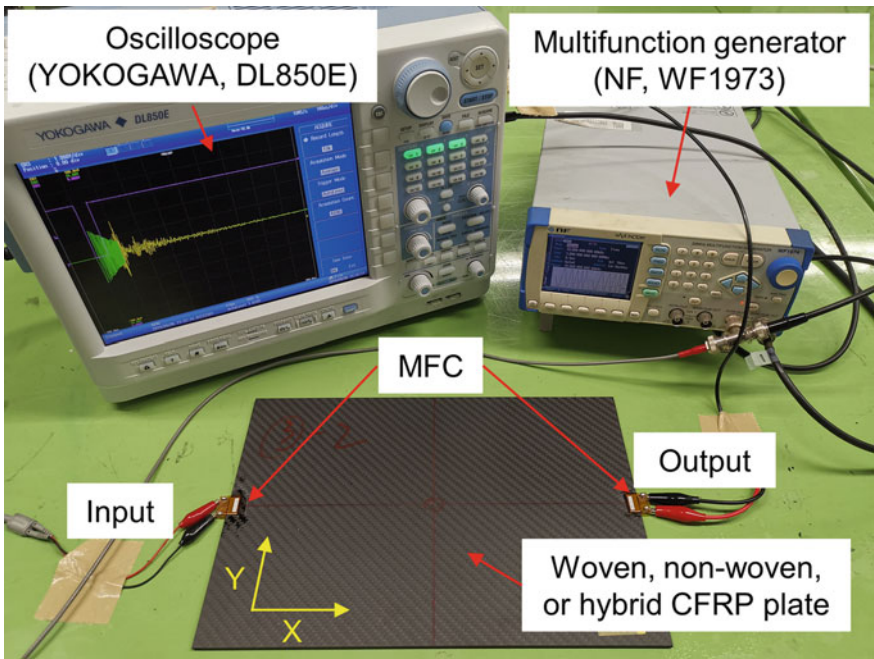


Fig. 2 Experiment setup

record the averaged input and output waveforms. As shown in Fig. 2, X direction is the propagation direction of Lamb waves, and Y direction is orthogonal to X direction on the plate.

3.3 Relation Between the Damaged Area and ToF Delay in Various CFRP Plates

The impact damages were given by the drop weight impact test with 15.9 J. They were first enlarged in the X direction by the second and third impacts, and were then enlarged in the Y direction by the fourth and fifth impacts. After each impact loading, the damaged area was observed using an ultrasonic C-scan (OLYMPUS, OMNISX-PA1664PR) as shown in Fig. 3.

The transfer function measurement by the chirp ultrasonic propagation was also conducted at each time. The response signals with various central frequencies were reconstructed numerically using the measured transfer function. Then, the ToF delay in damaged conditions from the intact condition of each plate over a broad bandwidth was calculated with a cross-correlation analysis. After that, the maximum ToF delay was obtained in each damaged condition. The relationship between the impact damage size and the maximum ToF delay is shown in Fig. 4. The result indicates that the ToF delay increases in proportion to the damage size. The result of the woven CFRP shows the best linearity among three kinds of CFRP plates. As for the hybrid

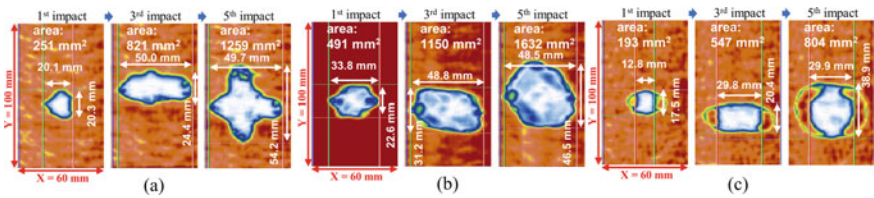


Fig. 3 C-scan observation results of impact damages in a a woven CFRP plate, b a non-woven CFRP plate, and c a hybrid CFRP plate

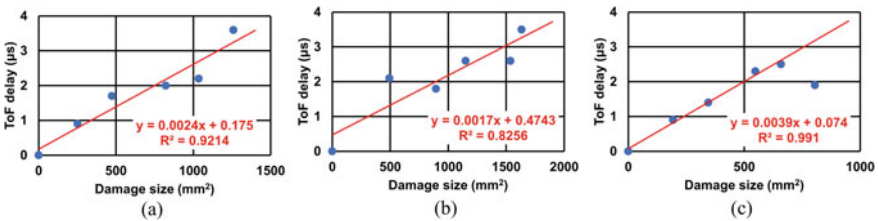


Fig. 4 Relationship between the impact damage size and the maximum ToF delay in a the woven CFRP plate, b the non-woven CFRP plate, and c the hybrid CFRP plate

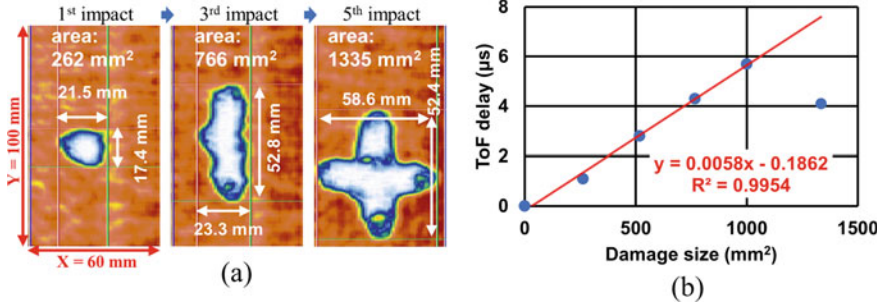


Fig. 5 Results for the woven CFRP plate No. 2: **a** C-scan observation and **b** the relationship between the impact damage size and the maximum ToF delay

CFRP plate, the ToF delay decreases after the fifth impact. This phenomenon may be attributed to the complex mixture of the impact damage in woven plies and that in non-woven plies.

3.4 Influence of Damage Shape to the ToF and the Amplitude of A_0 Mode

An experiment was conducted to investigate the influence of the impact damage shape. The experiment setup was the same as that in Fig. 2. Another woven CFRP plate with the same layup configuration was used. The specimen used in Sect. 3.3 was named the woven CFRP plate No. 1, and that used in this experiment was named the woven CFRP plate No. 2. In this experiment, in contrast to Sect. 3.3, the impact damage was first enlarged in the Y direction by the second and third impacts, and then in the X direction by the fourth and fifth impacts. Figure 5a shows the C-scan result, which is different from the result in Fig. 3a.

The experiment of the chirp ultrasonic propagation was conducted, and the relationship between the damage size and the maximum ToF delay was obtained as shown in Fig. 5b. A linear relationship between them can be observed from the intact condition to the fourth impact-damaged condition, which is in agreement with the result in Fig. 4a.

In order to find out other sensitive features in the waveforms to the impact damage shape, the reconstructed waveforms at 50 kHz were extracted, since the frequency of the maximum ToF delay in the woven CFRP plate appeared around 50 kHz. Then the amplitude of A_0 mode was obtained from the waveforms and plotted against the damage length in the X and Y directions in Fig. 6. In order to compare the amplitude of A_0 mode in each damaged condition between the two plates, the amplitude of A_0 mode was normalized by that in the intact condition. The amplitude of A_0 mode decreases significantly as the impact damage is enlarged in the X direction, while no obvious relation is found between the amplitude of A_0 mode and the damage

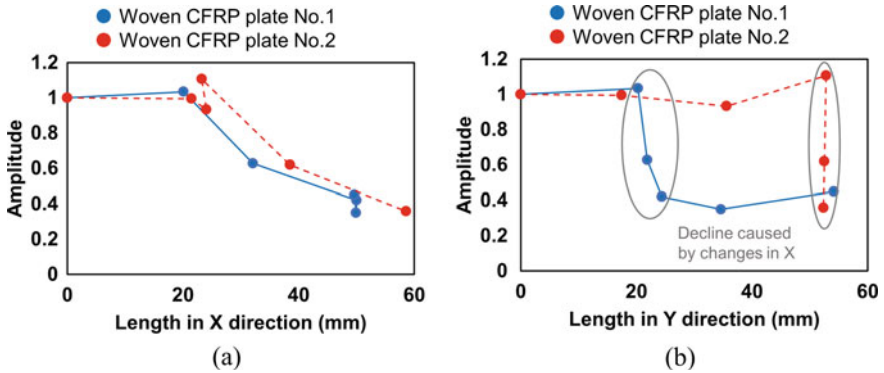


Fig. 6 Relation between the amplitude of A_0 mode and the damage lengths in **a** the X direction and **b** the Y direction

length in the Y direction. Hence, the amplitude of A_0 mode can be used to identify the extension direction of the impact damage as a complement of the ToF delay distribution.

4 Conclusions

In this research, an SHM system exciting and receiving broadband ultrasonic Lamb waves using MFC was proposed, in order to evaluate impact damages in mobility structures made of CFRP, comprehensively and reliably. First, the cross-section of the impact-damaged area in each kind of plate was observed, in order to clarify the difference in the damage conditions of three different CFRP laminates. Then, the relation between the impact damage size and the maximum ToF delay was investigated for the three kinds of plates. As a result, the relation was found to be approximately linear. It was also found that the attenuation of A_0 mode was largely affected by the damage length in the wave propagation direction, which can be used to identify the extension direction of the impact damage as a complement of the ToF delay distribution.

In summary, this SHM method using chirp ultrasonic waves is able to quantitatively evaluate the size and the extension of the impact damage shape in mobility structures made of CFRP laminates.

Acknowledgements This research was conducted as a part of the collaborative research with YAMAHA Motor Co., Ltd. "Health monitoring method for laminated composite members." since 2017 to 2020.

References

1. Okabe Y, Fujibayashi K, Shimazaki M, Soejima H, Ogisu T (2010) Delamination detection in composite laminates using dispersion change based on mode conversion of Lamb waves. *Smart Mater Struct* 19(11):115013
2. Michaels JE, Lee SJ, Croxford AJ, Wilcox PD (2013) Chirp excitation of ultrasonic guided waves. *Ultrasonics* 53(1):265–270

Bayesian Model Updating of a Simply-Supported Truss Bridge Based on Dynamic Responses



Xin Zhou, Chul-Woo Kim, Feng-Liang Zhang, Kai-Chun Chang,
and Yoshinao Goi

Abstract This study intends to investigate the application of model updating based on forced vibration data to a simply-supported truss bridge. A fast Bayesian FFT method was used to perform the modal identification obtained from field tests, and the Transitional Markov Chain Monte Carlo (TMCMC) algorithm is employed to generate samples. Although updating as many parameters as possible is the ideal model update process, it is not practical to identify all the parameters because of limitation of the experimental data. The bridge was thus divided into several clusters, and the values of the updated parameters of the members in the same cluster are assumed to be equal. Two model updating schemes were discussed as an example to investigate the effect of parameter selection, such as how to model the spring at each support, in model updating process. It was observed that although models with more parameters tend to fit better, the updated result often showed a different trend from the engineering prediction.

Keywords Bayesian model updating · Transitional Markov Chain Monte Carlo · Field vibration test · Damage detection · Simply-supported truss bridge

1 Introduction

In structural engineering, finite element (FE) models are widely used for structural analysis. Comparing to field experiments, FE analysis can save time and costs. However, due to the limited available information and simplification in modeling, uncertainties, such as material properties, geometric properties, boundary conditions,

X. Zhou · C.-W. Kim (✉) · K.-C. Chang · Y. Goi

Department of Civil and Earth Resources Engineering, Kyoto University, Kyoto 615-8540, Japan

K.-C. Chang

e-mail: kim.chulwoo.5u@kyoto-u.ac.jp

F.-L. Zhang

School of Civil and Environmental Engineering, Harbin Institute of Technology, Shenzhen 518055, China

and load conditions, invariably exist in the system. Model updating methods would calibrate these uncertain parameters in the FE model based on the measurement data, so called a data-driven model calibration.

One type of model updating method is based on Bayesian theory, which tries to find a probability distribution function (PDF) of the model parameters [1–11]. Au and Beck [3] and Beck and Au [4] applied the Bayesian-based method to reliability analysis. Beck and Yuen [5] and Muto and Beck [6] sought the most probable model from several model classes. Goller and Schueller [7] and Goller et al. [8] investigated uncertainties in the Bayesian model updating and weighting factors of each mode in the objective function. Yuen et al. [9] and Lam et al. [10, 11] extended the applicability and efficiency of the Bayesian-based method.

Although the Bayesian model updating method can provide a posterior distribution, the complexity of its PDF makes it difficult to generate samples directly from the posterior distribution. Therefore, an efficient sampler is necessary. A lot of sampling methods have been proposed, especially Metropolis–Hastings (MH) algorithm [12, 13], a special case of Markov chain Monte Carlo (MCMC) [14, 15]. Beck and Au [4] proposed Adaptive MH algorithm (AMH), using a sequence of intermediate distributions to converge on target distribution. Ching and Chen [16] used the importance sampling to replace the kernel density estimate (KDE) in AMH, called the transitional Markov chain Monte-Carlo (TMCMC) method. Goller et al. [17] proposed the parallelized MCMC.

The degree of freedom of the engineering structure is much higher than the laboratory model, and a typical engineering structure may consist of hundreds to thousands of members. Therefore, it is not practical for a member-level or element-level model updating of the actual engineering structure. Grouping multiple members into a cluster and assuming the members in the same cluster will share the same values of uncertain parameters can reduce the number of uncertain parameters to be updated if a suitable parameter selection scheme is available. Especially for the FE model update for damage detection, a proper design of the model update scheme will directly link to the accuracy of the damage detection by means of the FE model update. Moreover, with the growing interest in digital twins for civil infrastructures, the study of the applicability of FE model updating to various structural states is an extremely important topic. However, few studies investigate how to group structural members into a cluster considering the engineering significance of the updated model even in terms of damage detection, which is a driving force of this study.

This study intends to investigate the effect of updating structural parameters selection on the model updating of an actual simply-supported truss bridge even including the bridge with damage based on the Bayesian model updating method. The fast Bayesian FFT [18, 19] was used to identify the structural dynamic properties, and the TMCMC algorithm was used to generate samples. Two different model updating parameter schemes focusing on the spring at each support were examined and discussed the engineering significance of the updated results.

2 Methodology

2.1 Bayesian Model Updating Method

The formulation of the posterior PDF of uncertain parameter vector θ ($\theta \in \mathbf{R}^{N_\theta}$), under the condition system response D , is given as follows.

$$P(\theta|D, M) = \frac{P(D|\theta, M)P(\theta|M)}{P(D|M)} \quad (1)$$

where M is the assumed probabilistic model class for the structure; $P(D|M)$ is the evidence of model class M , and $P(D|M) = \int P(D|\theta, M)P(\theta|M)d\theta$; $P(\theta|M)$ is the prior PDF; $P(D|\theta, M)$ is the likelihood function, which donates the conditional probability of D given θ ; N_θ is the number of uncertain parameters.

Even if the experimental data available is insufficient to constraint all updated parameters, the Bayesian model updating methods also can provide a posterior distribution of the uncertain parameters.

Assuming the variances is same for each natural frequencies and mode shapes, the likelihood function becomes:

$$P(D|\theta, M) = c_l e^{-J(\theta)/2\sigma^2} \quad (2)$$

where $J(\theta) = \sum_{i=1}^{N_m} \left((1 - \langle \varphi_i(\theta), \hat{\varphi}_i \rangle)^2 + \left(1 - f_i(\theta)/\hat{f}_i \right)^2 \right)$; $f_i(\theta)$ and $\varphi_i(\theta)$ are the i th natural frequency and normalized mode shape vector under the given uncertain parameter vector θ obtained from the FE model while \hat{f}_i and $\hat{\varphi}_i$ are the measured values from the experiments; N_m is the total number of modes; c_l is the normalized constant which leads $\int P(D|\theta, M)dD = 1$.

2.2 Transitional Markov Chain Monte Carlo

In high-dimensional space, the MH algorithm also cannot keep a higher efficiency. Therefore, many researchers have proposed improved MCMC samplers. In this study, the TMCMC is used to generate samples efficiently. The TMCMC is based on the AMH method. The advantage of TMCMC is that it does not need kernel density estimation (KDE) which is difficult to calculate in high-dimension space. The essence of TMCMC is to use a series of asymptotic intermediate distributions, ($P(\theta|D)^{(j)}$ ($j = 1, 2, 3, \dots$)), to approach the final distribution. The importance sampling method is used to transfer between the intermediate distributions, ($P_j(\theta|D)$, $j = 0, 1, \dots, m$, $\theta \in \mathbf{R}^{N_\theta}$). With the value of j increasing, the $P(\theta|D)^{(j)}$ becomes more closed to the target distribution $P(\theta|D)$. MCMC approach is to solve

the problem that the number of distinct samples reduces due to the re-sampling progress.

For the asymptotic intermediate distribution $P_j(\theta|D, M)$, the values of their variances ($\sigma_j, j = 1 \dots m$) are different, and $P_j(\theta|D, M)$ is shown as:

$$P_j(D|\theta, M) = c_j e^{-J(\theta)/2\sigma_j^2} (\sigma_1 > \dots > \sigma_m = \sigma, j = 1, 2 \dots m) \quad (3)$$

Especially, assuming $P_0(D|\theta, M) = c_0$ follows a uniform distribution. The adjacent intermediate distributions are connected by importance sampling, and the weighting $w_j(\theta)$ is shown as:

$$w_j(\theta) = \frac{P_{j+1}(\theta|D, M)}{P_j(\theta|D, M)} \quad (4)$$

Then, with the normalized value weighting $w_{j,k}^n$, the sample sequence of $\theta_{j+1,k}$, which follows the distribution of $P_{j+1}(\theta|D, M)$, is generated from $\theta_{j,k}$.

$$\theta_{j+1,k} = \theta_{j,k}, \text{ with the probability } w_{j,k}^n = \frac{w_j(\theta_{j,k})}{\sum_{k=1}^{N_s} w_j(\theta_{j,k})} \quad (5)$$

3 Target Bridge and Vibration Test

This section would briefly introduce the target bridge, field tests, and modal identification. More details can be found in reference [20–22].

3.1 Target Bridge and FE Model

The target structure was a simply-supported steel truss bridge, as shown in Fig. 1. The length and width of the main span are 59.2 m and 3.6 m. It was built in 1959 and removed in 2012. The ambient and vehicle-induced vibration experiments were conducted before the bridge removal. The bridge was closed prior to the experiment.

The FE model in ABAQUS is created based on shell elements for concrete slabs and beam and truss elements for steel members. The boundary conditions were treated as perfect roller and pin. However, the boundary conditions are a significant source of uncertainties in the model, and three types of springs were considered and added to the supports at P1 and P2.



Fig. 1 Mode shapes of the building

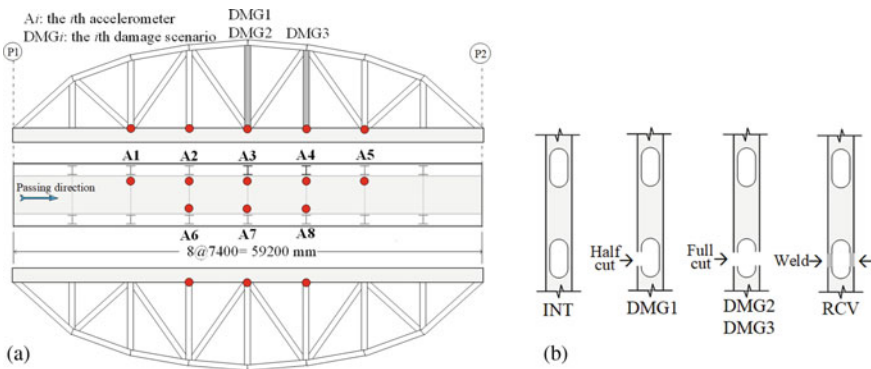


Fig. 2 a Sensor layout and b damage scenario

3.2 Field Test and Damage Scenario

Eight uniaxial accelerometers were installed on the deck of the bridge to measure the vibration data as shown in Fig. 2a. Five damage scenarios (INT, DMG1, DMG2, RCV, and DMG3) were considered consecutively in this bridge as shown in Fig. 2b. As a damage, two tension members were severed as shown in Fig. 2b. A 21 kN vehicle was used to excite the bridge with an average speed of about 20 km/h under each damage scenario.

3.3 Modal Identification

Prior to the model updating process, modal identification based on experimental data is necessary. This section would take the INT state as an example to illustrate the modal identification process.

The PSD and singular value spectrum of acceleration data measured by all eight sensors under the INT state are shown in Fig. 3. Vibration modes of six peaks indicate well-excited modes, and are taken as the candidate modes to be updated. The natural frequencies of these six modes were close to 3 Hz, 5 Hz, 7 Hz, 9.5 Hz, 10.5 Hz, and 13 Hz, respectively. To reduce random errors, the same experimental procedure was repeated about 10 times. The last mode, which is close to 13 Hz, is not stable because it cannot be found in most runs, therefore, this mode is not considered. Their histograms with the normal distribution fit are shown in Fig. 4 with those from damage cases (DMG1, DMG2, RCV, and DMG3). The MPV value and coefficient of variation of the frequency are summarized in Table 1. The corresponding mode shapes of INT state are presented in Fig. 5a. It includes first bending mode, first torsional mode, second bending mode, second torsional mode, and third bending mode from the top to the bottom. Those mode shapes for the DMG2 and DMG3 states are shown in Fig. 5b, c respectively. It is noted that modes shapes under DMG3 states differed from those under INT and DMG2 states.

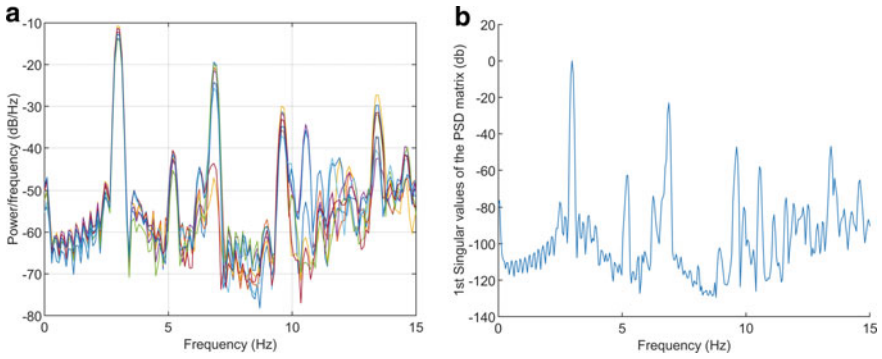


Fig. 3 a PSD and b singular value spectrum estimate for all channels

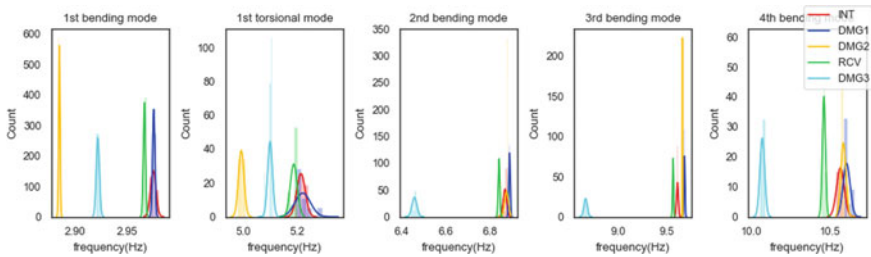


Fig. 4 Histograms with the normal distribution fit of the identified frequencies

Table 1 Identified natural frequencies (MPV: most probable value; CV: coefficient of variance)

Mode	1st bending frequency		1st torsional frequency		2nd bending frequency		3rd bending frequency		4th bending frequency	
	MPV (Hz)	CV (%)	MPV (Hz)	CV (%)	MPV (Hz)	CV (%)	MPV (Hz)	CV (%)	MPV (Hz)	CV (%)
INT	2.98	0.0932	5.21	0.3181	6.87	0.0088	9.61	0.1087	10.57	0.2472
DMG1	2.98	0.0397	5.22	0.5803	6.89	0.0508	9.69	0.0571	10.61	0.2229
DMG2	2.89	0.0259	4.99	0.2232	6.88	0.1308	9.67	0.0195	10.59	0.1623
RCV	2.97	0.0378	5.19	0.2603	6.84	0.0571	9.57	0.0603	10.46	0.1015
DMG3	2.92	0.0555	5.10	0.1870	6.46	0.1800	9.66	0.3200	10.07	0.1686

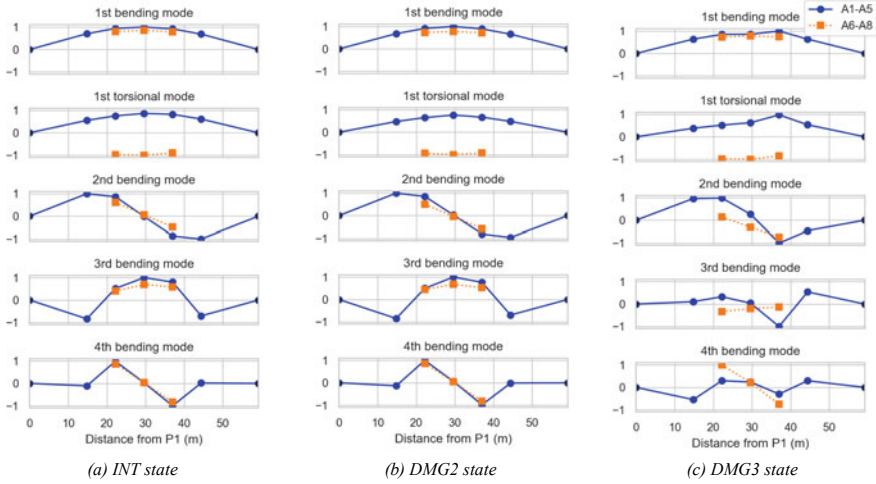


Fig. 5 Identified mode shape **a** INT state **b** DMG2 state **c** DMG3 state

4 Model Update

4.1 Model Updating Scheme

The FE model consists of more than one hundred members and contains approximately three thousand elements. As a result of the limited experimental information, no matter member-level or element-level the model updating is impossible. To reduce the number of the updating parameters, several substructure blocks, each of which consists of multiple members, were imported into the system. In the same block, the material properties of members are set to be the same value. Indeed, the types of defined uncertain parameters have a significant impact on the Bayesian FE model updating process.

To discuss the effect of different model updating schemes, two types of schemes were investigated, as presented in Fig. 6a, b, in which Case 1 model indicates the FE model considering two horizontal springs, four vertical springs, and four rotation springs at supports while Case 2 model indicates the FE model considering springs in the longitudinal direction at P1. The main part of the bridge model was divided into eight blocks, and three types of model parameters, such as spring constants, steel stiffnesses, and concrete stiffnesses, are considered in both two cases. The parameters starting with ‘SS400’ and ‘spring’ indicate the stiffness of steel members and spring constants, respectively. ‘RC’ means the stiffness of the reinforced concrete. Three types of springs, two horizontal springs, four vertical springs, and four rotation springs, are taken as candidate parameters to present the uncertainties in the boundary conditions. The difference between Case 1 and Case 2 is the number of considered springs. In Case 1, all three types of springs were taken into account; in Case 2, only

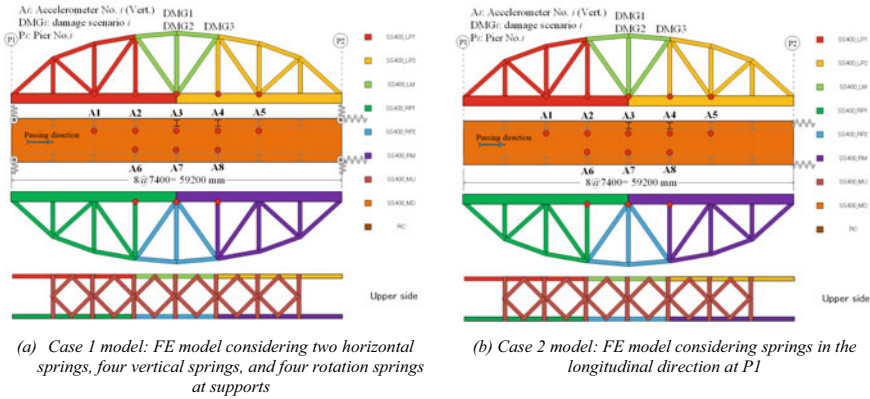


Fig. 6 Model updating scheme **a** Case 1 model: FE model considering two horizontal springs, four vertical springs, and four rotation springs at supports **b** Case 2 model: FE model considering springs in the longitudinal direction at P1

the two horizontal springs were considered, constants of vertical springs = ∞ , and constants of rotation springs = 0.

4.2 Case 1 Model: FE Model Considering Two Horizontal Springs, Four Vertical Springs, and Four Rotation Springs at Supports

Table 2 presents the MPV of the updated natural frequencies and MACs for Case 1. From INT state to DMG2 state, a full cut was applied to the tension member on the sensor A3. Therefore, the decreasing of SS400_LM was the expected phenomenon. However, as shown in Fig. 7 the updated distribution SS400_LM is increased while the updated spring constants are decreased.

4.3 Case 2 Model: FE Model Considering Springs in the Longitudinal Direction at P1

MPV of the updated natural frequencies and MACs for Case 2 are summarized in Table 3. Figure 8 shows the distributions of some updated parameters. A decrease of SS400_LM can be observed as expected. Due to the DMG2 damage, SS400_LP1 and SS400_LP2 were almost unchanged, but SS400_RM was decreased despite an increase of SS400_RP1 and SS400_RP2.

Table 2 Updated natural frequencies of Case 1 model: FE model considering two horizontal springs, four vertical springs, and four rotation springs at supports

Mode	1st bending mode		1st torsional mode		2nd bending mode		3rd bending mode		4th bending mode	
	MPV (Hz)	MAC	MPV (Hz)	MAC	MPV (Hz)	MAC	MPV (Hz)	MAC	MPV (Hz)	MAC
INT	3.04	0.9967	4.69	0.9968	6.70	0.9947	9.59	0.9982	10.54	0.9978
DMG2	2.99	0.9986	4.84	0.9848	6.99	0.9912	9.78	0.9907	10.85	0.9909

MPV: most probable value of the frequency; MAC: modal assurance criteria

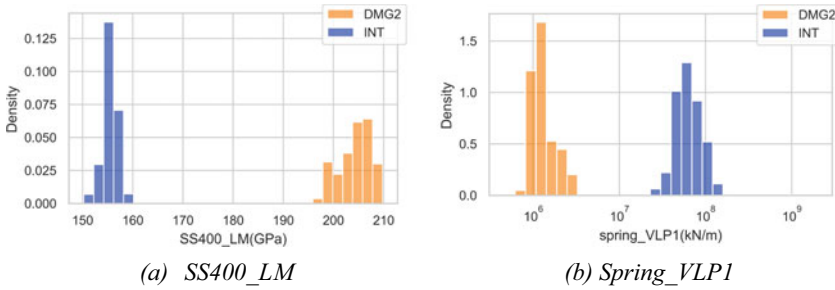


Fig. 7 Updated parameters of Case 1 model: FE model considering two horizontal springs, four vertical springs, and four rotation springs at supports **a** SS400_LM **b** Spring_VLP1

4.4 Discussion

It was not reasonable to consider many springs at supports like Case 1 model. For Case 2 model, after removing vertical and torsional springs, the updated result as expected was observed even though the updated stiffness for some members in the opposite sides of the damage was increased. Different amounts of sensor information of the members on two sides might affect the model updating results. It indicates the importance of the parameter selection based on the number of sensors, the location of sensors, the type of sensor, and the design of the bridge model for FE model update considering engineering goals.

5 Conclusions

This study indicates that the deployment of sensors, how many sensors are installed, or where is the location of the sensors, affects the selection of parameters. How to choose the updated parameters is a significant problem in model updating especially for damage detection. On the one hand, the limited data cannot constrain too many parameters, which leads to an unreasonable solution; on the other hand, decreasing the number of parameters means less identified information from the updated model.

Model updating problem is essentially an optimization problem, and the criterion of the optimal model is the objective function. The model update process finds the mathematically optimal solution based on the objective function. However, the purpose of model updating is not to obtain a model that can fit the objective function well but to find parameter values that can correctly reflect the real situation of the bridge. In other words, the goal of the FE model update is to identify the parameter distributions with physical meanings. The real challenge in the application of the model updating to damage detection is narrowing the gap between the engineering meaning and mathematical optimal model.

Table 3 Updated natural frequencies of Case 2 model: FE model considering springs in the longitudinal direction at P1

Mode	1st bending mode		1st torsional mode		2nd bending mode		3rd bending mode		4th bending mode	
	MPV (Hz)	MAC	MPV (Hz)	MAC	MPV (Hz)	MAC	MPV (Hz)	MAC	MPV (Hz)	MAC
INT	3.09	0.9997	5.06	0.9939	6.68	0.9808	10.12	0.9961	10.63	0.9668
DMG2	3.09	0.9992	4.79	0.9852	6.56	0.9921	9.83	0.9907	10.28	0.9986

MPV: most probable value of the frequency; MAC: modal assurance criteria

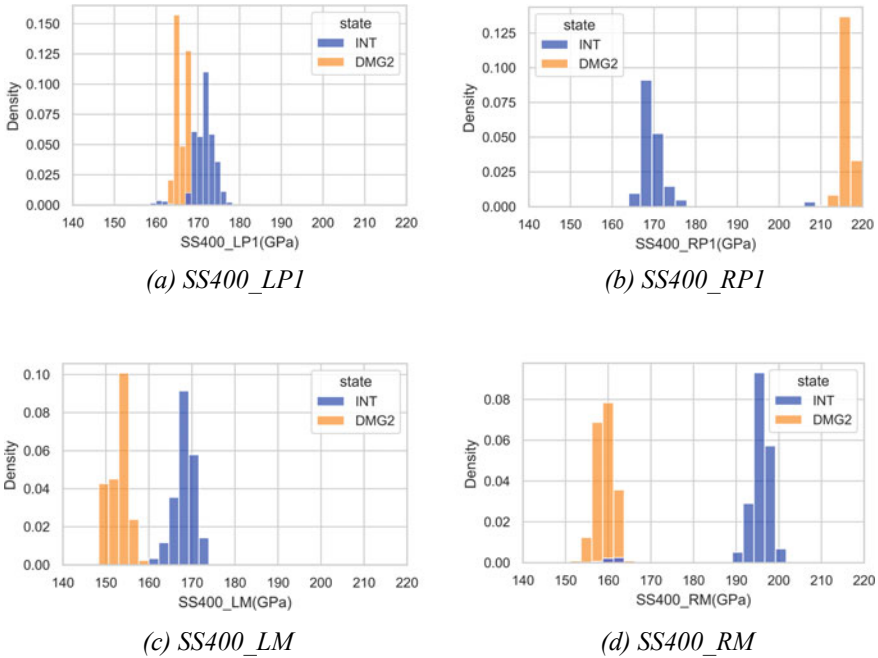


Fig. 8 Updated parameters of Case 2 model: FE model considering springs in the longitudinal direction at P1 **a** SS400_LP1 **b** SS400_RP1 **c** SS400_LM **d** SS400_RM

Existing studies on the FE model update have not fully investigated the feasibility of the FE model update for damaged structures and damage detection. Therefore, considering the FE model update for damage simulation and damage detection, further comprehensive investigations, such as proper parameter selection, proper deployment of sensors, are needed.

Acknowledgements This study is partly sponsored by a Japanese Society for the Promotion of Science (JSPS) Grant-in-Aid for Scientific Research (B) under project No.19H02225. That financial support is gratefully acknowledged.

References

1. Beck JL, Katafygiotis LS (1998) Updating models and their uncertainties. I: Bayesian statistical framework. *J Eng Mech* 124(4):455–461
2. Katafygiotis LS, Beck JL (1998) Updating models and their uncertainties. II: model identifiability. *J Eng Mech* 124(4):463–467
3. Au S-K, Beck JL (1999) A new adaptive importance sampling scheme for reliability calculations. *Struct Saf* 21(2):135–158
4. Beck JL, Au S-K (2002) Bayesian updating of structural models and reliability using Markov chain Monte Carlo simulation. *J Eng Mech* 128(4):380–391

5. Beck JL, Yuen K-V (2004) Model selection using response measurements: Bayesian probabilistic approach. *J Eng Mech* 130(2):192–203
6. Muto M, Beck JL (2008) Bayesian updating and model class selection for hysteretic structural models using stochastic simulation. *J Vib Control* 14(1–2):7–34
7. Goller B, Schueller GI (2011) Investigation of model uncertainties in Bayesian structural model updating. *J Sound Vib* 330(25):6122–6136
8. Goller B, Beck JL, Schueller GI (2012) Evidence-based identification of weighting factors in Bayesian model updating using modal data. *J Eng Mech* 138(5):430–440
9. Yuen KV (2010) Bayesian methods for structural dynamics and civil engineering. John Wiley & Sons
10. Lam H-F, Yang J, Au S-K (2015) Bayesian model updating of a coupled-slab system using field test data utilizing an enhanced Markov chain Monte Carlo simulation algorithm. *Eng Struct* 102:144–155
11. Lam H-F, Yang JH, Au S-K (2018) Markov chain Monte Carlo-based Bayesian method for structural model updating and damage detection. *Struct Control Heal Monit* 25(4):e2140
12. Metropolis N, Rosenbluth AW, Rosenbluth MN, Teller AH, Teller E (1953) Equation of state calculations by fast computing machines. *J Chem Phys* 21(6):1087–1092
13. Hastings WK (1970) Monte Carlo sampling methods using Markov chains and their applications. *Biometrika* 57(1):97–109
14. Tierney L (1994) Markov chains for exploring posterior distributions. *Ann Stat* 1701–1728
15. Mosegaard K, Tarantola A (1995) Monte Carlo sampling of solutions to inverse problems. *J Geophys Res Solid Earth* 100(B7):12431–12447
16. Ching J, Chen Y-C (2007) Transitional Markov chain Monte Carlo method for Bayesian model updating, model class selection, and model averaging. *J Eng Mech* 133(7):816–832
17. Van Overschee P, De Moor BL (2012) Subspace identification for linear systems: Theory–Implementation–Applications. Springer Science & Business Media
18. Au S-K (2011) Fast Bayesian FFT method for ambient modal identification with separated modes. *J Eng Mech* 137(3):214–226
19. Au S-K, Zhang F-L, Ni Y-C (2013) Bayesian operational modal analysis: theory, computation, practice. *Comput Struct* 126:3–14
20. Chang KC, Kim CW (2016) Modal-parameter identification and vibration-based damage detection of a damaged steel truss bridge. *Eng Struct* 122:156–173
21. Kim CW, Zhang FL, Chang KC, McGetrick PJ, Goi Y (2021) Ambient and vehicle-induced vibration data of a steel truss bridge subject to artificial damage. *J Bridge Eng* 26(7):04721002
22. Zhang FL, Kim CW, Goi Y (2021) Efficient bayesian fft method for damage detection using ambient vibration data with consideration of uncertainty. *Struct Control Health Monit* 28(2):e2659

Vibration-Based Method for Structural Health Monitoring of a Bridge Pier Subjected to Environmental Loads



Mohamed Belmokhtar, Franziska Schmidt, Christophe Chevalier,
and Alireza Ture Savadkoohi

Abstract This paper proposes a method for structural monitoring using operational modal analysis (OMA). Frequency domain decomposition (FDD) of the output-only system is developed to define new modal parameters to be monitored. Parameters from OMA make it possible to characterize the structure using experimental modal analysis (EMA). The method is applied to a bridge pier subjected to scour. Indeed, a prestressed concrete, motorway bridge on A71 in France has been equipped with sensors to follow in real time the vibrational behavior and external events such as temperature, hydraulic flow velocity and scour depth. This measuring chain is connected to a central acquisition system. Collected data are post-processed in the frequency domain combining a standard method for modal parameter estimation and statistic methods using averaging and Principal Component Analysis (PCA). A fully automated method is developed by correlating operational modal parameters with data of external event. Finally, an assessment of the evolution of the structural health condition of the bridge in real time is carried out.

Keywords Modal analysis · Output only · Frequency domain decomposition · Principal component analysis

1 Introduction

Many researchers and engineers focus on structural health monitoring (SHM) by analyzing the response of the bridge itself under external loadings, which are controlled or not by humans. One of the most practical ways for health monitoring

M. Belmokhtar (✉) · F. Schmidt
MAST/EMGCU, Gustave Eiffel University, Champs-sur-Marne, France
e-mail: mohamed.belmokhtar@univ-eiffel.fr

C. Chevalier
GERS/SRO, Gustave Eiffel University, Champs-sur-Marne, France

A. Ture Savadkoohi
LTDS/ENTPE, UMR CNRS 551, University of Lyon, Vaulx-en-Velin, France

© The Author(s), under exclusive license to Springer Nature Switzerland AG 2023
Z. Wu et al. (eds.), *Experimental Vibration Analysis for Civil Engineering Structures*,
Lecture Notes in Civil Engineering 224,
https://doi.org/10.1007/978-3-030-93236-7_8

of structures is the vibration-based monitoring [1] using modal analysis theory. The principle is to identify the mathematical link between input (induced excitations by environment, human, etc.) and output (response), which is named transfer function. This function is defined with parameters such as the natural frequencies and the mode shapes. Because of their sensibility to any changes, these parameters indicate the health of the structure [2, 3]. In this work, we study a real case study, a prestressed concrete, motorway bridge in France. Data are extracted from an acquisition chain with a pre-processing set up to acquire realistic responses of the structure by avoiding undesirable phenomena such as leakage or aliasing [4]. Then, identification of modal parameters is carried out. There are several methods of post processing, for example directly by analyzing the time response [5]. On the other side, [6] applied moving average method in order to detect scour. Data can also be analyzed in frequency domain [7, 8] and/or time-domain [9–11]. We focus on frequency analysis of the Bridge response under environmental loads.

2 Theoretical Background of Modal Analysis

2.1 Transfer Function and Modal Parameters

For a mechanical system with n degrees of freedom (n DOF) characterized by its transfer matrix $[h(t)] = (h_{ij}(t))_{i,j \in [1,n]}$ we have the following relationship:

$$\{y(t)\} = [h(t)] * \{x(t)\} \quad (1)$$

where $\{x(t)\}$ and $\{y(t)\}$ are respectively the input and output vectors and $\cdot * \cdot$ denotes the convolutional product. In the Laplace domain “ p ” we can rewrite Eq. (1) as:

$$\{Y(p)\} = [H(p)] * \{X(p)\}. \quad (2)$$

By introducing $\omega_r, \{\phi_r\}$ and ζ_r which are respectively the natural frequency, the mode shape and the damping ratio of the r -th mode, projection on the modal base [12] gives:

$$[H(p)] = \sum_{r=1}^n \frac{Q_r \{\phi_r\} \{\phi_r\}^T}{p - \lambda_r} - \frac{Q_r \overline{\{\phi_r\}} \{\phi_r\}^H}{p - \lambda_r^*}, \quad (3)$$

where Q_r is a scaling factor, and by considering ω_{0r} the frequency associated to the undamped mode r , $\lambda_r = -\zeta_r \omega_{0r} + j\omega_r$, $\{\phi_r\}$ the shape vector of the mode r and ζ_r the damped coefficient. $\bar{\cdot}$, \cdot^T and \cdot^H are respectively the complex conjugate, the transpose and conjugate of the transpose. In Eq. (3), the transfer function is an easy way to identify modal parameters by directly observing frequency responses of

input and output. Unfortunately, in real time and conditions, because of the unknown input, this analysis becomes impossible and needs output-only analysis [12, 13].

2.2 Output-Only System and Operational Modal Analysis

Despite the lack of information on the input, we assume that the external load can be assumed as a white noise in the frequency range in which we want to analyze the signals. For a civil engineering structure such as a bridge, the most important loads may be traffic loads and wind. In [14], this assumption (of white noise) was proven for traffic loads while in [15], authors encourage engineers and scientists to consider wind as a white noise excitation for low frequencies (1–20 Hz).

As shown in [12], correlation between signals is a first step for analysis for output-only systems. By introducing $R_{xy}(p)$ the Laplace transform of $r_{xy}(\tau)$, the correlation between signals $\{y(t)\}$ and $\{x(t)\}$ at the time τ , the following relationship can be written:

$$[G_{yy}(p)] = [H(p)][G_{xx}(p)][H(p)]^H, \quad (4)$$

where $([G_{yy}(p)])_{ij} = R_{y_i y_j}(p)$, $\forall i, j \in [1, n]$ is the power spectral density matrix of output signals or the Laplace transform of $([g_{yy}(\tau)])_{ij}$ the correlation matrix of outputs. It is a Hermitian matrix. For white noise inputs, as in [12, 13], we can write $[G_{xx}(p)] = [C]$ as a constant which leads for very low damping and near the natural frequencies ω_k to:

$$[G_{yy}(j\omega)] = [\bar{\phi}] \left[\text{diag} \left(\frac{2d_k \zeta_k \omega_{0k}}{(\zeta_k \omega_{0k})^2 + (\omega - \omega_k)^2} \right) \right] [\phi]^T, \quad (5)$$

with $p = j2\pi f(j^2 = -1)$ and,

$$d_k = \frac{Q_k^2 \{\phi_k\}^H [C] \{\phi_k\}}{2\zeta_k \omega_{0k}}. \quad (6)$$

So, in Eq. (5), under hypothesis of white noise and low damping, a simple eigenvalue decomposition (EVD) of the power spectral matrix leads us to extract natural frequencies ω_k and mode shapes $\{\phi_k\}$.

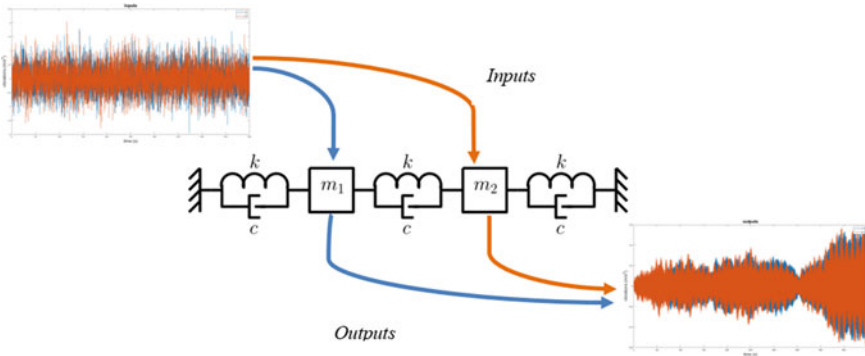


Fig. 1 System of 2 DOF under white noise solicitations during $\Delta T = 30$ secondes at the sampling frequency $F_s = 10\text{Hz}$ with $m_1 = 1$, $m_2 = 0.5$, $k = 50$ and $c = 0.001$

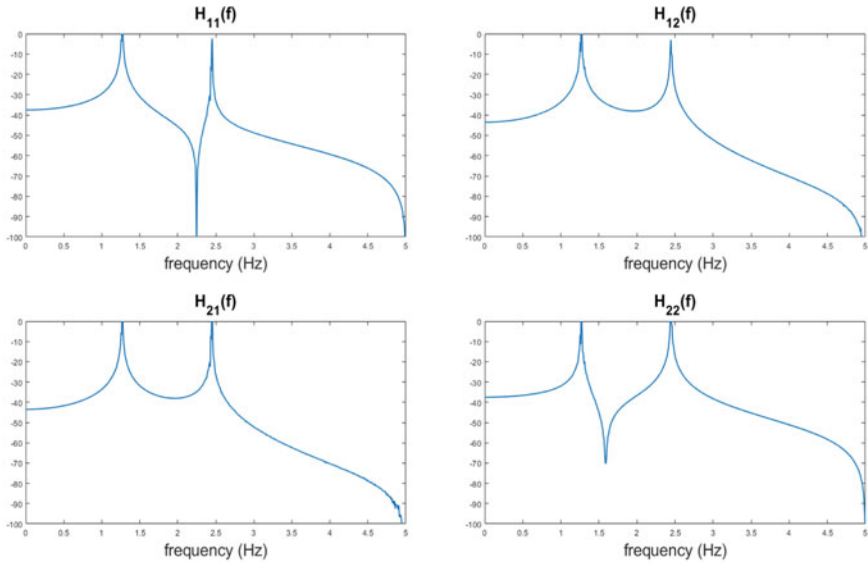
2.3 Examples for Eigenfrequencies Identification

Now, let us move on an example of 2 DOF system as showed in Fig. 1. Inputs $\{x(t)\} = \{x_1(t), x_2(t)\}$ are considered as a white noise with the same power on each point. In Fig. 1, $m_1 = 1$, $m_2 = 0.5$, $k = 50$ and $c = 0.001$ and an acquisition is simulated during $\Delta T = 5$ min with a sampling frequency $F_s = 10\text{Hz}$. Outputs $\{y(t)\} = \{y_1(t), y_2(t)\}$ are generated using zero-order hold method of the state space model [4]. For undamped modes, the obtained eigenfrequencies from an eigenvalue decomposition are $f_{1_0} = 1.267\text{Hz}$ and $f_{2_0} = 2.448\text{Hz}$. In Fig. 2, by “pick picking” method of the frequency response transfer function, we assume that the eigenfrequencies of the damped system showed in Fig. 1 are $f_1 = 1.269\text{Hz}$ and $f_2 = 2.450\text{Hz}$. In Fig. 2a, transfer function is calculated with perfect conditions, i.e., assuming that we know all inputs and outputs and $\{Y(f)\} = [H(f)]\{X(f)\}$. In Fig. 2b, assuming an output-only system, power spectral density matrix of Eq. (5) is calculated and diagonalized. Figure 2 shows that, from the point of view of eigenfrequencies identification, this is a good method for light damping and distant modes.

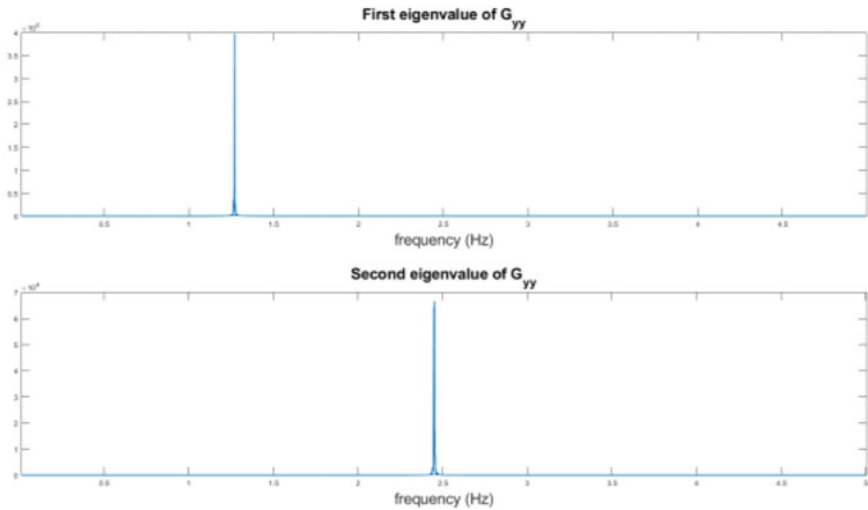
3 Vibration-Based Monitoring of a Highway Bridge

3.1 Presentation of the Monitoring

Monitoring has been installed on a French motorway bridge, on highway A71 crossing the Loire river. It’s a prestressed bridge with a total length of 400 m (5 spans: one of 50 m, two of 75 m and two of 100 m). The speed limit for vehicles on the bridge is 110 km/hours. Engineers have been conducting bathymetric measurements for several years and they observed an important variation in the soil



a Transfer function response on frequency domain.



b Eigenvalues decomposing of power spectral density matrix in frequency domain.

Fig. 2 Comparison between both methods (Eqs. 3 and 5)

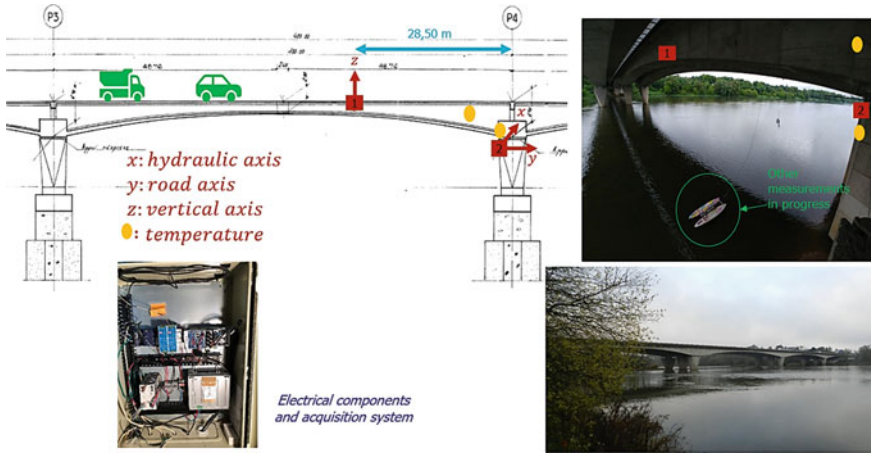


Fig. 3 Presentation of the monitored bridge

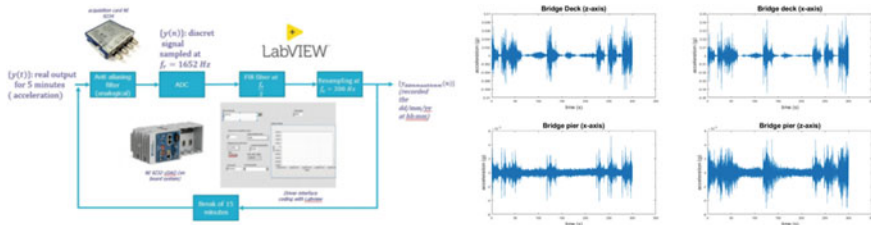


Fig. 4 Pre-processing and processing of one acquisition

level around pier P4 due to erosion. That’s why we decided to monitor this pier using accelerometers and thermometers. Other instrumentation methods around this pier are in progress (Bathymetry, water level and flow velocity) in collaboration with SSHEAR Project (<https://sshear.ifsttar.fr/>). Figure 3 presents the bridge and the installed sensor devices.

We continuously monitor the vibration response of the bridge by recording an acquisition every 20 min. In the study which is presented here, we focus on vibration measurements only. The diagram in Fig. 4 shows the acquisition chain that has been set up, in order to avoid some phenomena such as aliasing for these measures.

3.2 Eigenvalue Decomposition of Signals for a Revisited Principal Component Analysis

Principal component analysis (PCA) is a geometric method which aims at projecting orthogonally information through uncorrelated dimensions. In this respect, our

method has the same goal but data should be centered. Now for all the next results, we will process centered reduced data.

We should pay attention to the assumptions of Eq. 5, particularly that it is available near the natural frequencies and for n DOF system with n modes. In practice, mechanical systems have an infinite number of modes and DOF, but it can be supposed finite for a discrete and finite frequency range. In fact, by definition of a Hermitian matrix, $\forall \omega$,

$$[G_{yy}(j\omega)] = [P(\omega)][D(\omega)][P(\omega)]^H, \quad (7)$$

with $[P(\omega)]$ is a unitary matrix and $[D(\omega)]$ a diagonal matrix. Each matrix is continuous with respect to ω .

An important assumption for our study is to suppose that $\{[P(\omega)]\}_r$ contains a subset of m mode shapes ($\{\phi_{sub_1}\}, \dots, \{\phi_{sub_m}\}$), and that in the vicinity of the frequency of the mode sub_m ,

$$\{[P(\omega)]\}_r \approx \overline{\{\phi_{sub_m}\}}, \text{ and } ([D(\omega)])_r \approx \frac{2d_{sub_m} \zeta_{sub_m} \omega_{osub_m}}{(\zeta_{sub_m} \omega_{osub_m})^2 + (\omega - \omega_{sub_m})^2}. \quad (8)$$

In other words, each eigenspace of data can be interpreted as a combination of physical modes which are correlated. And near a frequency resonance, only one mode is activated.

Then, to ensure the continuity during diagonalization-frequency step process, our algorithm of eigenvalue decomposition (EVD) researches similarity with the previous step using MAC value [4]:

$$\text{MAC}(\{[P(\omega)]\}_i, \{[P(\omega)]\}_j) = \frac{|([P(\omega)]\}_i^H \{[P(\omega)]\}_j)|^2}{(\{[P(\omega)]\}_i^H \{[P(\omega)]\}_i)(\{[P(\omega)]\}_j^H \{[P(\omega)]\}_j)}. \quad (9)$$

In literature, the most common method for operational modal analysis is the singular value decomposition (SVD). Brincker et al. [12] introduced this method for modal analysis. Figure 5 compares SVD method and EVD using MAC values (EVD-MAC) of the bridge and at the date of the 11st November 2020. SVD always sorts in descending order the singular values. Figure 5 shows the interest of our method: the first singular values have physical sense for SVD but the last ones can be assumed to be noise. In our methods all dimensions have potentially a physical sense. For example, the fourth eigenvalue in Fig. 5 contains a lot of information in very low frequency (0–20 Hz).

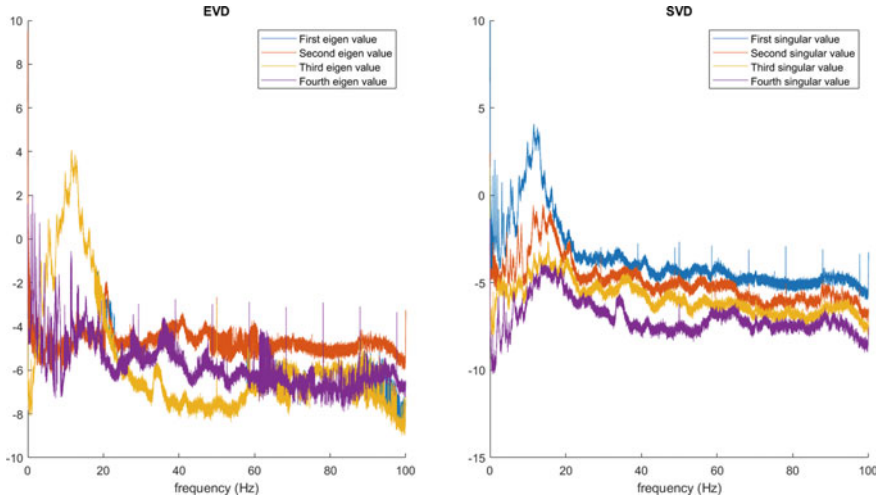


Fig. 5 EVD-MAC versus SVD of the bridge (11st November 20, 220, logarithmic scale)

3.3 Results and Discussions About the Method

First, in order to monitor daily frequency response, we made the choice to average correlation during one day noticed by $\left[\widehat{G}_{yy}(j\omega)\right]$ in order to monitor daily natural frequencies. In fact, temperature has a daily periodicity, especially inside the bridge where concrete has an inertial temperature [16]. Then averaging is a good method to reduce noise [4]:

$$\left[\widehat{G}_{yy}(j\omega)\right] = \frac{1}{N_a} \sum_{a=1}^{N_a} \left([G_{yy}(j\omega)]\right)_a, \tag{10}$$

where N_a is the number of acquisitions for one day and $\left([G_{yy}(j\omega)]\right)_a$ the acquisition at the date “a”.

Figure 6 shows how the method of post processing works by considering averaging of Eq. 9 and continuity with MAC value defined in Eq. 10.

If we zoom EVD-MAC result in Fig. 5, we can see some discontinuity of the response. This discontinuity appears when two modes are close or away the frequency resonance. In fact, our hypothesis is not respected. As showed Fig. 7, we must emphasize that a lot of modes are present for this bridge: we have a lack of sensors.

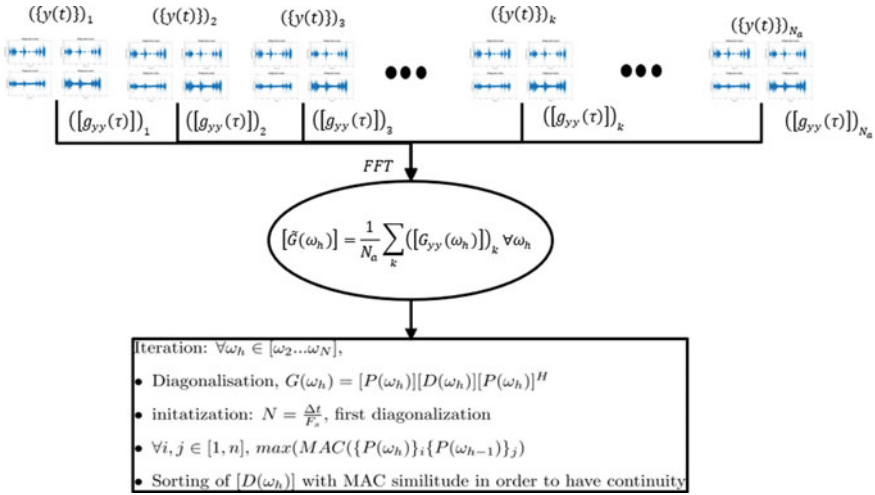


Fig. 6 Principle of EVD-MAC

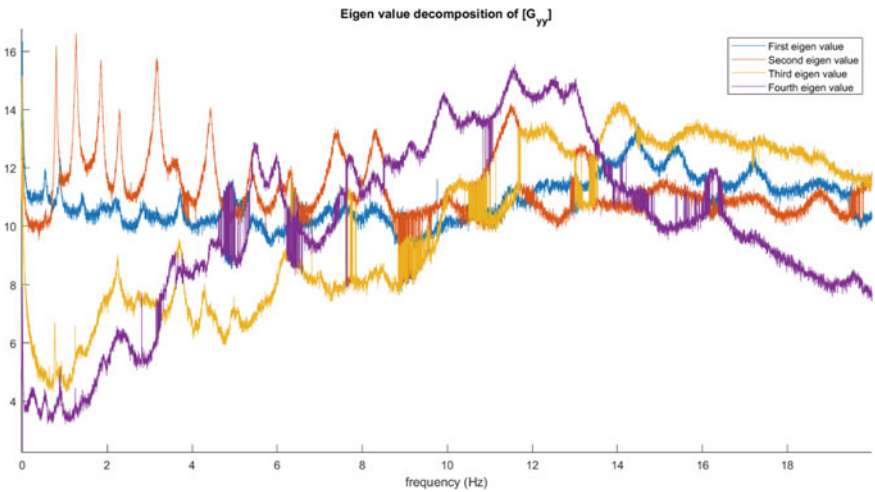


Fig. 7 EVD-MAC in frequency range of [0–20 Hz]

4 Conclusions

To conclude, in this work we started by developed analytical formulas for operational modal analysis. These formulas were for an ideal case where we have n modes and n sensors of outputs. Then by applying this method for the real bridge, we did some assumptions, especially the continuity of eigenspaces through frequencies. In order to respect it in post-processing method we introduce MAC value and name this new

method EVD-MAC. However, by observing the responses, there are some discontinuity which are not present for SVD method. We think that more post-processing and smooth method can correct these problems. But we should pay attention to not lost information because our signals are already averaged and have already been treated a lot. This paper cannot be considered as a validation of the model but it encourages us to continue: the best way to validate method is to use more sensors.

Acknowledgements The authors would like to thank The Ministère de la transition écologique et solidaire for supporting this research.

References

1. Doebling SW, Farrar CR, Prime MB, Shevitz DW (1996) Damage identification and health monitoring of structural and mechanical systems from changes in their vibration characteristics: a literature review. 5 . Friswell, M.I., and Mottershead, J.E. (1995) Finite element model updating in structural dynamics. Kluwer Academic Publishers, Boston, USA
2. Salawu OS (1997) Detection of structural damage through changes in frequency: a review. *Eng Struct* 19(9):718–723
3. Carden EP, Fanning P (2004) Vibration based condition monitoring: a review. *Struct Health Monit* 3(4):355–377. Publisher: SAGE Publications
4. Heylen W, Lammens S, Sas P (2013) Modal analysis, theory and testing. KU Leuven, Belgium
5. Box GE, Jenkins GM, Reinsel GC, Ljung GM (2015) Time series analysis: forecasting and control, 5th Edition. Wiley
6. Foti S, Sabia D (2011) Influence of foundation scour on the dynamic response of an existing bridge. *J Bridge Eng* 16(2):295–304
7. Herlufsen H, Gade S, Moller N, Konstantin-Hansen H (2003) Frequency domain techniques for operational modal analysis. In: Proceedings of the 21st International Modal Analysis Conference (IMAC-21), 17–26
8. Zhang L, Wang T, Tamura Y (2010) A frequency–spatial domain decomposition (FSDD) method for operational modal analysis. *Mech Syst Sig Proc* 24(5):1227–1239
9. Rajasekaran S, Varghese SP (2005) Computers and concrete 2(6):481–498
10. Yan YJ, Cheng L, Wu ZY, Yam LH (2007) Development in vibration-based structural damage detection technique. 21:2198–2211
11. Law SS, Li XY, Zhu XQ, Chan SL (2005) Structural damage detection from wavelet packet sensitivity. *Eng Struct* 27(9):1339–1348
12. Brincker R, Zhang L, Andersen P (2001) Modal identification of output only systems using frequency domain decomposition. *Smart Mater Struct* 10(3):441–445
13. Pioldi F, Ferrari R, Rizzi E (2016) Output-only modal dynamic identification of frames by a refined FDD algorithm at seismic input and high damping. *Mech Syst Signal Process* 68–69:265–291
14. Ditlevsen O (1994) Traffic loads on large bridges modeled as white noise fields. *J Eng Mech* 120(4):681–694
15. Cremona C (2009) Investigations et évaluations dynamiques des ponts. Laboratoire Central des Ponts et Chaussées
16. Peeters B, De Roeck G (2001) One-year monitoring of the z24-bridge: environmental effects versus damage events. *Earthquake Eng Struct Dynam* 30(2):149–171

Damage Detection and Localization Using Autocorrelation Functions with Spatiotemporal Correlation



Jyrki Kullaa

Abstract In vibration-based structural health monitoring, data analysis for damage detection can be done in the time domain or in the feature domain. Time-domain methods have certain advantages compared to feature-domain methods. For example, statistical analysis may be more reliable, because the data dimensionality is often low and the number of data points large. In addition, the algorithm can be fully automated, because system identification is not necessary. In this paper, autocorrelation functions (ACF) replace the direct response measurements in the time-domain data analysis. ACFs have many advantages compared to the actual time history records. Their accuracy can be controlled by choosing a proper measurement period. Spatiotemporal correlation between the ACFs can be utilized, because they have the same form as a free decay of the system for stationary random processes. This makes it possible to manage with a smaller number of sensors. In the proposed method, a spatiotemporal covariance matrix is estimated using the ACFs of the training data from the undamaged structure under different environmental or operational conditions. Using novelty detection techniques, an extreme value statistics control chart is designed to detect damage. The direction of the largest discrepancy between the training and test data is used to localize damage. A numerical experiment was performed by simulating vibration measurements of a bridge deck under stationary random excitation and variable environmental conditions. The excitation or environmental variables were not measured. Damage was a crack in a steel girder. ACFs outperformed both direct measurement data and virtual sensor data in damage detection. Damage localization was successful in all cases.

Keywords Structural health monitoring · Damage detection · Autocorrelation function · Spatiotemporal correlation · Environmental or operational effects

J. Kullaa (✉)

Department of Automotive and Mechanical Engineering, Metropolia University of Applied Sciences, Helsinki, Finland

e-mail: jyrki.kullaa@metropolia.fi

1 Introduction

Structural health monitoring (SHM) of large civil engineering structures has many challenges. First, the excitation is unknown and the vibration response is only measured. The objective is to track changes in the vibration characteristics of the structure. If the excitation is stationary, the modal parameters (natural frequencies, mode shape vectors, and damping) can be extracted using system identification techniques particularly developed for output-only data [1–3].

Second, damage detection depends heavily on the signal-to-noise ratio (SNR) of the data [4]. Therefore, noise reduction is important. System identification can be also considered a means to reduce noise, because it includes a lot of averaging. Another approach that is applied less frequently is data analysis directly in the time domain using the raw measurement data or the corresponding virtual sensor data [5]. The method works also for nonstationary processes provided the number of sensors is greater than the number of active modes. Then the sensor network is redundant and it is possible to predict a sensor's reading using the remaining sensors' data at the same time instant (spatial correlation). Virtual sensing results in reduction of measurement noise, which can significantly enhance detection performance [6].

Third, influences of environmental or operational variability on the dynamic characteristics of the structure often mask the effects of damage [7]. The normal variability must be included in the training data in order to distinguish between the environmental or operational effects and damage [8].

Time-domain and feature domain methods for damage detection were compared [9], and it was found that the features were more sensitive to damage than the actual or virtual sensor data. This was probably due to the fact that the features had a higher SNR than the sensor data. However, damage detection in the time domain has certain advantages compared to that in the feature domain. For example, the data dimensionality is often lower and the number of data points larger, which is advantageous in statistical analysis. Also, the algorithm can be fully automated, as system identification is not necessary.

In this paper, time-domain damage detection is applied to autocorrelation functions (ACF) instead of measured time records. For stationary random excitation, the ACFs have the same form as the free decay. The free decays can then be treated as time-domain data. The ACFs can be estimated automatically and their accuracy can be controlled with the measurement period T [10]. In addition, the free decay has a special mathematical expression for each mode allowing temporal correlation. More specifically, one can predict the ACF at any time lag from two data points of the ACF. The ACFs between sensors are also correlated making it possible to utilize spatiotemporal correlation. The number of time lags in the ACFs can be selected to control the amount of data. Training data under different environmental or operational conditions are nevertheless needed.

The paper is organized as follows. Autocorrelation functions are introduced in Sect. 2. Damage detection and localization in the time domain under varying environmental or operational conditions is outlined in Sect. 3. Detection and localization

of an open crack in a bridge girder are studied in Sect. 4, in which a finite element model is used to generate vibration measurements under different environmental and operational conditions. Concluding remarks are given in Sect. 5.

2 Autocorrelation Functions

Damage detection in the time domain is investigated by replacing the actual response measurements with corresponding autocorrelation estimates. This can be justified for stationary random processes [10]. Correlation functions are also primary data in output-only modal identification, because they include all the necessary information about the dynamic characteristics of a linear structure [2]. Auto- and cross-correlation have also been utilized in damage detection by applying singular value decomposition to the empirical Hankel matrix [11].

The autocorrelation function (ACF) of a zero-mean sample time history record $x(t)$ is [10]:

$$R_{xx}(\tau) = E[x(t)x(t + \tau)] \quad (1)$$

where $E[\cdot]$ is the expectation operator. The ACF can be estimated with a direct method or by using FFT computations [10]. An FFT-based method with a single FFT-spectrum is used this study, because it is much faster when the measurement period is very long.

For a viscously damped SDOF system under white noise excitation with a constant power spectral density S_0 , the displacement autocorrelation function at lag τ can be expressed as [12]:

$$R_{xx}(\tau) = \frac{\pi \omega_n S_0}{2k^2 \zeta} \left(\cos \omega_d |\tau| + \frac{\zeta}{\sqrt{1 - \zeta^2}} \sin \omega_d |\tau| \right) \exp(-\omega_n \zeta |\tau|) \quad (2)$$

where ω_n is the natural angular frequency, k is the spring constant, ζ is the damping ratio, and $\omega_d = \omega_n \sqrt{1 - \zeta^2}$ is the damped natural angular frequency. It can be seen that the ACF is symmetric about $\tau = 0$. Therefore, only positive lags τ will be considered. Then, Eq. (2) has the following form.

$$R_{xx}(\tau) = (A \cos \omega_d \tau + B \sin \omega_d \tau) e^{-a\tau} \quad (3)$$

where A , B , a , and ω_d are constants. Notice that Eq. (3) has the same form as the free vibration of a viscously damped SDOF system. This particular form is now studied. The same form applies also to velocity and acceleration ACFs.

Consider three different time lags, for which R_{xx} are available: τ , $\tau + p\Delta t$, and $\tau + q\Delta t$. where p and q are positive integers. It is now proved that any three data

points from the ACF are linearly correlated, or redundant.

$$\begin{aligned}
 R_{xx}(\tau + p\Delta t) &= [A \cos \omega_d(\tau + p\Delta t) + B \sin \omega_d(\tau + p\Delta t)]e^{-a(\tau + p\Delta t)} \\
 &= [\cos \omega_d \tau (A \cos p\Delta t + B \sin p\Delta t)e^{-ap\Delta t} \\
 &\quad + \sin \omega_d \tau (-A \sin p\Delta t + B \cos p\Delta t)e^{-ap\Delta t}]e^{-a\tau} \\
 &= [C \cos \omega_d \tau + D \sin \omega_d \tau]e^{-a\tau}
 \end{aligned} \tag{4}$$

where

$$\begin{aligned}
 C &= (A \cos p\Delta t + B \sin p\Delta t)e^{-ap\Delta t} \\
 D &= (-A \sin p\Delta t + B \cos p\Delta t)e^{-ap\Delta t}
 \end{aligned} \tag{5}$$

are constants. Similarly,

$$R_{xx}(\tau + q\Delta t) = [E \cos \omega_d \tau + F \sin \omega_d \tau]e^{-a\tau} \tag{6}$$

where

$$\begin{aligned}
 E &= (A \cos q\Delta t + B \sin q\Delta t)e^{-aq\Delta t} \\
 F &= (-A \sin q\Delta t + B \cos q\Delta t)e^{-aq\Delta t}
 \end{aligned} \tag{7}$$

are constants. Next, if the three data points are linearly dependent, the following relationship applies.

$$R_{xx}(\tau) = bR_{xx}(\tau + p\Delta t) + cR_{xx}(\tau + q\Delta t) \tag{8}$$

Now it is shown that b and c are constants independent of τ . Substituting Eqs. (3), (4), and (6) into Eq. (8), yields

$$\begin{aligned}
 (A \cos \omega_d \tau + B \sin \omega_d \tau)e^{-a\tau} &= b[C \cos \omega_d \tau + D \sin \omega_d \tau]e^{-a\tau} \\
 &\quad + c[E \cos \omega_d \tau + F \sin \omega_d \tau]e^{-a\tau}
 \end{aligned} \tag{9}$$

or

$$(-A + bC + cE) \cos \omega_d \tau + (-B + bD + cF) \sin \omega_d \tau = 0 \tag{10}$$

Because the equation must be valid for any τ , the terms in the parentheses must be zero. They are written in the matrix form

$$\begin{bmatrix} C & E \\ D & F \end{bmatrix} \begin{Bmatrix} b \\ c \end{Bmatrix} = \begin{Bmatrix} A \\ B \end{Bmatrix} \quad (11)$$

Because the coefficient matrix and the right-hand side vector are constants, the regression coefficients are fixed for the given time lags. This means that for any τ , $R_{xx}(\tau)$ can be computed if the values at time lags $\tau + p\Delta t$, and $\tau + q\Delta t$ are available. This is the basis for temporal correlation in damage detection. Mathematically, if matrix \mathbf{H} is constructed by adding time-shifted ACFs as rows, then $\text{rank}(\mathbf{H}) = 2$.

Spatial correlation is considered next. Let us assume that in a MDOF system only one mode is active with a mode shape vector ϕ . Then the modal coordinate for the whole system is $q(t)$. The response vector is then $\mathbf{x}(t) = \phi q(t)$. The autocorrelation function at DOF i is

$$\begin{aligned} R_{x_i x_i}(\tau) &= E[x_i(t)x_i(t + \tau)] = E[\phi_i q(t)\phi_i q(t + \tau)] \\ &= \phi_i^2 E[q(t)q(t + \tau)] = \phi_i^2 R_{qq}(\tau), \quad 0 \leq \tau \leq T \end{aligned} \quad (12)$$

The ACFs at different DOFs are all of the same except for the scaling factor ϕ_i^2 . Therefore, there is also spatial correlation between the ACFs of each mode, which can be utilized in damage detection if the response is measured with a sensor network. If the number of active modes n is greater than one, the modal matrix is $\Phi = [\phi_1 \ \phi_2 \ \dots \ \phi_n]$ and the ACF of DOF i is

$$\begin{aligned} R_{x_i x_i}(\tau) &= E[x_i(t)x_i(t + \tau)] = E \left[\sum_r \Phi_{ir} q_r(t) \sum_s \Phi_{is} q_s(t + \tau) \right] \\ &= E \left[\sum_r \sum_s \Phi_{ir} \Phi_{is} q_r(t) q_s(t + \tau) \right] \end{aligned} \quad (13)$$

For lightly damped modes and well-separated modal frequencies, the modal amplitudes $q_r(t)$ and $q_s(t)$ are almost statistically independent for $r \neq s$ [12]. In that case, Eq. (13) is approximately

$$R_{x_i x_i}(\tau) \approx E \left[\sum_r \Phi_{ir}^2 q_r(t) q_r(t + \tau) \right] = \sum_r \Phi_{ir}^2 R_{q_r q_r}(\tau) \quad (14)$$

For closely-spaced modes, the cross-terms in Eq. (13) cannot be neglected. How this affects damage detection would require further investigation.

Data accuracy, or more specifically, the signal-to-noise ratio (SNR), is an important factor in detection. Therefore, high accuracy of the ACF estimates should be pursued for in the design of an SHM system. The error variance of the ACF is inversely proportional to the record length T [10]. Therefore, T should be as large as possible. The error also depends on the frequency-damping product $\omega_n \zeta$, with a larger product resulting in a smaller error [13]. It was also shown that the ACF estimate has a considerable noise tail, which is independent of the actual system, and

should be removed [13]. In this study, the number of lags in the ACFs was chosen to be 300. It was also shown that white noise increases the error of ACF at zero lag [10], but band-limited white noise would affect also the first few time lags [14]. In this paper, however, all lags from τ equal to 0 to 300 were retained.

3 Damage Detection and Localization in the Time Domain

Damage detection is applied to the ACFs in the time domain treating the ACFs as if they were measured time histories. Comparison is also made using the actual response measurements or the corresponding virtual sensor data. First, the covariance matrix with a selected model order are estimated using training data from the undamaged structure under different environmental or operational conditions. Whitening transformation is applied to the covariance matrix [15]. This transformation is then fixed and applied to the test data resulting in the residual vector between the model and the new data. All residuals are subjected to principal component analysis (PCA). Retaining the first principal component scores of the residuals, the data dimensionality is decreased to one. An extreme value statistics [16] control chart [17] is then designed for the first PC scores of the residuals with appropriate control limits and subgroup size [5]. In this paper, the probability of false alarms equal to 0.001 is used.

Damage location is assumed to correspond to the direction of the first principal component of the residuals. The largest projection of the first PC on the sensor DOFs is assumed to reveal the sensor closest to damage.

4 Numerical Example

Numerical simulations were performed using a finite element model of a stiffened bridge deck (Fig. 1). The structure was 30 m long and 11 m wide. It had four longitudinal and three lateral stiffeners. The modelling was done using four-node

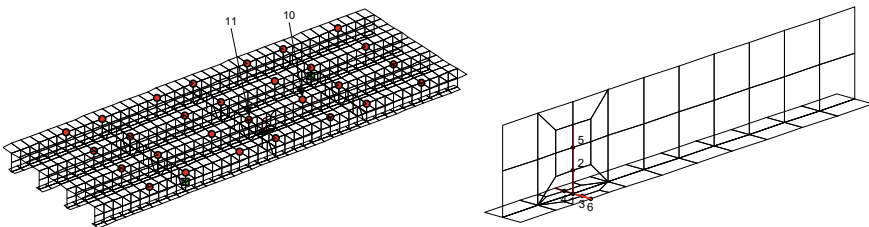


Fig. 1 Left: Finite element model of a bridge deck. The 28 sensor positions are shown as red circles and the two excitation points as green squares. Damage is shown with red lines. Sensor 11 was located nearest to the crack. Right: A detail of the steel girder with damage. The crack is shown with red lines and the numbers indicate the order in which the connecting nodes separated resulting in an increasing crack size

discrete Kirchhoff quadrilateral shell elements with a diagonal mass matrix. The deck was made of concrete with a Young’s modulus of $E = 40$ GPa (at temperature $T = 0$ °C), Poisson ratio of $\nu = 0.15$, density of $\rho = 2500$ kg/m³, and thickness of 250 mm. The stiffeners were made of steel ($E = 207$ GPa, $\nu = 0.30$, $\rho = 7850$ kg/m³). The longitudinal stiffeners had a web with a thickness of $t = 16$ mm and a height of $h = 1.4$ m. The bottom flange had a thickness of $t = 50$ mm and a width of $b = 700$ mm. The lateral stiffeners were 1.4 m high and 30 mm thick plates.

The nodes of the bottom flanges were simply supported at both ends of the bridge. Longitudinal displacements were fixed only at one end of the bridge. The corners of the concrete deck were supported in the lateral and vertical directions.

Temperature had an effect on the stiffness of the concrete deck. It was assumed that temperature along the width was constant, but along the length it was linearly varying including a zero-mean Gaussian noise with a standard deviation of $\sigma_T = 0.2$ °C in each row of elements. The ends of the bridge were at random temperatures between -20 °C and $+40$ °C. The relationship between the temperature and the Young’s modulus was stepwise linear as shown in Fig. 2 left. There were thus an infinite number of possible distributions of the Young’s modulus in the bridge deck. Different realizations of the distributions of the Young’s modulus along the bridge are plotted in Fig. 2 right. The Young’s modulus of each element was constant, determined using the temperature at the midpoint. Notice that the temperature or the Young’s modulus were not measured, but they were considered latent variables.

Two independent random loads were applied at two nodes in the vertical direction, shown as green squares in Fig. 1. Because ambient excitation was assumed, steady state response was measured. For the steady state analysis, periodic pseudorandom excitations in the frequency range between 0 and 20 Hz with random amplitudes and phases were generated [18], and the analysis was performed in the frequency domain [12]. The excitation was not measured.

The response was computed with a modal superposition algorithm using the first 30 modes. The analysis period was over 43 min, or more precisely 2621.44 s, with a

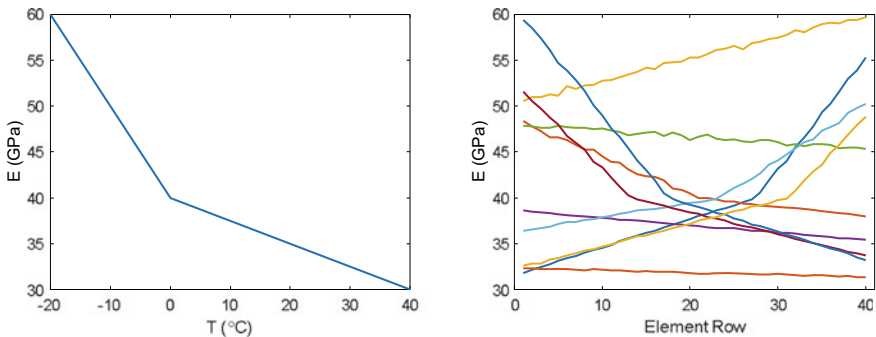
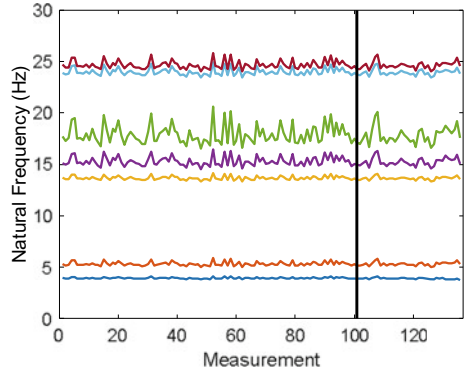


Fig. 2 Left: The effect of temperature on the Young’s modulus of the concrete. Right: Ten realizations of the longitudinal distributions of the Young’s modulus of the concrete

Fig. 3 The first seven natural frequencies indicating the influences of the environmental variables and damage. The data on the left side of the vertical line were from the undamaged structure



sampling frequency of 100 Hz. One measurement period then included $2^{18} = 262,144$ samples from each sensor.

Vertical accelerations were measured at 28 points shown in Fig. 1. An equal amount of noise was added to the signals, so that the average signal-to-noise ratio was $SNR = 30$ dB.

The number of measurements was 136. The first 100 measurements were acquired from the undamaged structure under random environmental conditions. Damage was a crack in a steel girder, which was simulated by removing the contact between elements at selected nodes. The crack was located between sensors 10 and 11, but slightly closer to sensor 11. The damage location is plotted in red in Fig. 1. Six different crack configurations were modelled with an increasing severity by removing the contact at 1–6 nodes. They are shown in the detailed plot in Fig. 1 indicating the order in which the nodes were separated. Only the last damage scenario reached to the edge of the flange. Each damage scenario was monitored with six measurements under random environmental and operational conditions. As a result, the last 36 measurements were from a damaged structure.

Figure 3 shows the first seven natural frequencies in all 136 measurements. The variability due to environmental variation is clearly seen. The vertical line separates the data from the undamaged and damaged structure. It is difficult to visually observe damage from the variability of the natural frequencies.

The training data were the first 70 measurements. They were also used to design the control charts. The test data were the last 66 measurements, from which the last 36 were from the damaged structure.

4.1 Time History Analysis

For a reference, damage detection was performed analyzing both the physical and the virtual sensor data. Virtual sensors were estimated using the full time histories,

but the first 1000 samples from each measurement were only selected for damage detection.

EVS control charts for damage detection are plotted in Fig. 4 with model order 0 for the physical sensor data (left) and virtual sensor data (right). The largest damage level was only detected from the physical sensor data, whereas the two largest damage levels were detected using the virtual sensor data. The same EVS control charts with model order 30 are shown in Fig. 5 for the physical sensor data (left) and virtual sensor data (right). The two largest damage levels were detected from the physical sensor data, whereas the three or four largest damage levels were detected using the virtual sensor data. Logarithmic scaling was applied to the vertical axes for clarity.

The advantageous effect of noise reduction of the virtual sensors on damage detection can be clearly seen. In addition, spatiotemporal correlation increased the

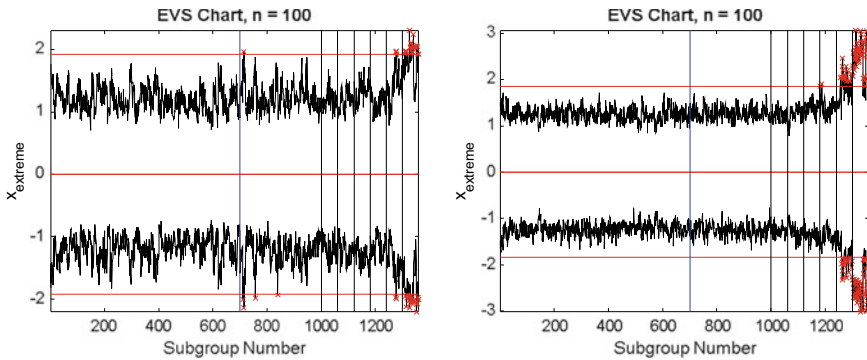


Fig. 4 Damage detection using control charts with model order = 0. Left: physical sensor data. Right: virtual sensor data. The data on the left side of the leftmost vertical line were used as the training data, and the other vertical lines indicate the six damage levels with an increasing severity

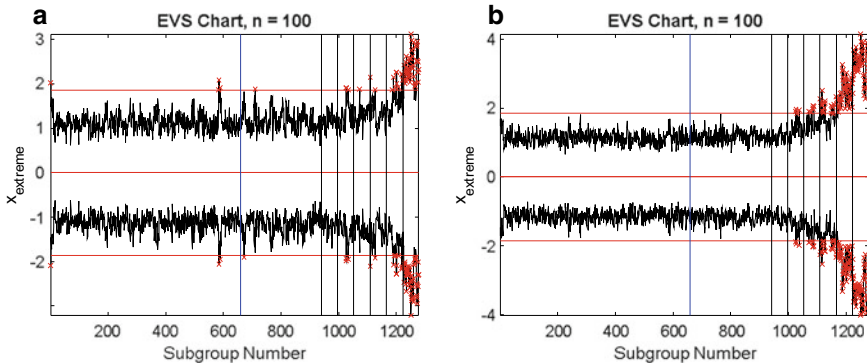


Fig. 5 Damage detection using control charts with model order = 30. **a** Physical sensor data, **b** virtual sensor data

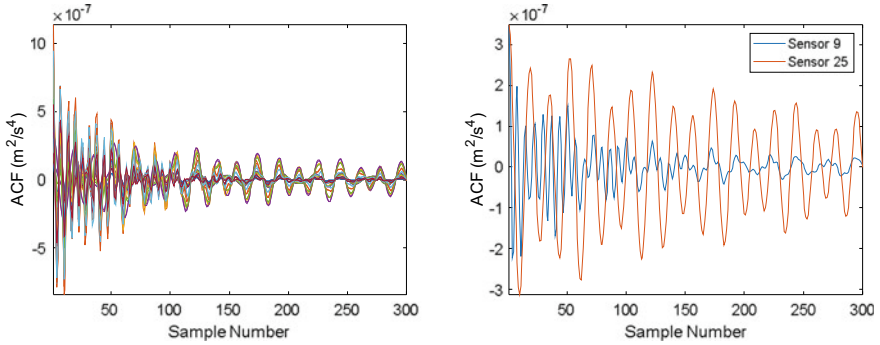


Fig. 6 Estimated autocorrelation functions from measurement 31 with $T = 44$ min. Left: all 28 sensors. Right: sensors 9 and 25

detection performance with either data compared to spatial correlation only. In all cases, damage was localized to sensor 10.

4.2 Autocorrelation Function Analysis

The accuracy of the autocorrelation function depends on the measurement period T . Therefore, it is crucial to select a proper T . In this study, the number of samples was $N = 2^{18} = 262,144$ corresponding to $T = 44$ min. The autocorrelation functions at the first 300 lags were computed from a single FFT-spectrum. Model orders 0 and 30 were studied (spatial correlation and spatiotemporal correlation, respectively).

Sample autocorrelation functions from measurement 31 are shown in Fig. 6 left for all 28 sensors and on the right for sensors 9 and 25. Because the response included participation of several modes, the AFCs do not look like free decays of a single degree-of-freedom system.

The EVS control charts for the ACFs are plotted in Fig. 7 using spatial correlation only (left) or spatiotemporal correlation with a model order of 30 (right). With spatial correlation, damage level 1 remained undetected, while using spatiotemporal correlation, all damage levels were detected. Logarithmic scaling was applied to the vertical axis for clarity. With spatial correlation, damage was localized to sensor 10 (Fig. 8 left), whereas using spatiotemporal correlation, damage was localized to sensor 11 (Fig. 8 right).

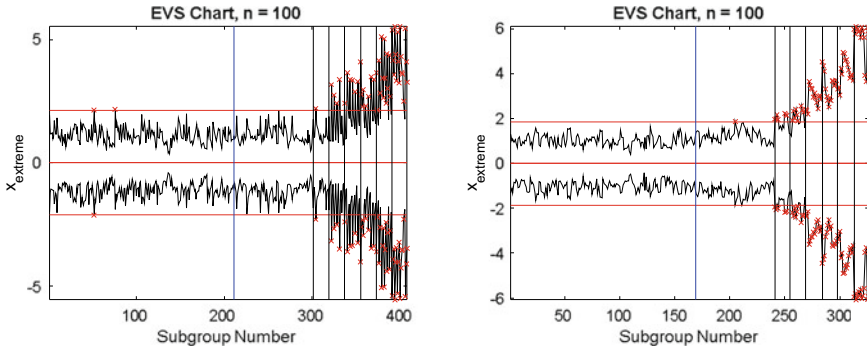


Fig. 7 EVS control charts for ACFs with $T = 44$ min. Left: model order = 0. Right: model order = 30. The data on the left side of the leftmost vertical line were used as the training data, and the other vertical lines indicate the six damage levels with an increasing severity

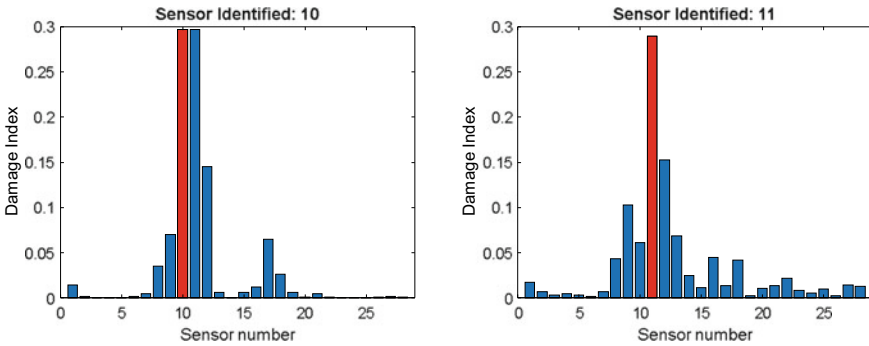


Fig. 8 Damage localization using autocorrelation functions. $T = 44$ min. Left: model order = 0. Right: model order = 30

5 Conclusions

Correlation functions play a key role in operational modal analysis. However, to the author’s knowledge, this was the first time when autocorrelation functions were applied directly to damage detection in the time domain.

A comparison of damage detection performance was made using response time records or virtual sensor data. Because the measurement data and the detection algorithm were the same in all cases, differences in the results were due to the selected features only (physical sensor data, virtual sensor data, or ACFs). ACFs of a random process have a mathematical expression allowing spatiotemporal correlation to enhance detection. Moreover, the accuracy of the ACFs can be controlled by selecting a proper measurement period. In the simulated case, ACFs outperformed response data in damage detection provided a long measurement period was

used. Spatiotemporal correlation produced better results than spatial correlation only. Damage localization was successful in all cases.

ACFs have also some limitations: the excitation is assumed stationary and the measurement period must be long. Fortunately, it is possible to use also shorter time records and estimate the spectral functions by averaging [10]. For nonstationary records, direct response data with model order equal to zero (spatial correlation) is an alternative.

Another issue are structures with damping depending on the vibration amplitude [3]. Then the temporal correlation is more complicated. A possible solution is to treat variable damping as an environmental influence, which must be present in the training data. This issue is left for a further study.

Another open question remains for structures with closely-spaced modes discussed in Sect. 2. The modal coordinates may be correlated, which has an influence on the ACFs and consequently on damage detection.

Other possibilities and limitations of ACFs in damage detection will be studied in the future. Experimental validation is also necessary.

Acknowledgements This research has been supported by Metropolia University of Applied Sciences.

References

1. Brincker R, Ventura C (2015) Introduction to operational modal analysis. Wiley, Chichester, West Sussex
2. Rainieri C, Fabbrocio G (2014) Operational modal analysis of civil engineering: an introduction and guide for applications. Springer Science+Business, New York, USA
3. Au S-K (2017) Operational modal analysis. Modeling, Bayesian inference, uncertainty laws. Springer, Singapore
4. Kay SM (1998) Fundamentals of statistical signal processing. Detection theory. Prentice-Hall, Upper Saddle River, N.J., USA
5. Kullaa J (2020) Robust damage detection in the time domain using Bayesian virtual sensing with noise reduction and environmental effect elimination capabilities. *J Sound Vib* 473: 115232
6. Kullaa J (2018) Bayesian virtual sensing in structural dynamics. *Mech Syst Signal Process* 115:497–513
7. Sohn H (2007) Effects of environmental and operational variability on structural health monitoring. *Philos Trans R Soc A: Math Phys Eng Sci* 365:539–560
8. Kullaa J (2011) Distinguishing between sensor fault, structural damage, and environmental or operational effects in structural health monitoring. *Mech Syst Signal Process* 25(8):2976–2989
9. Kullaa J (2019) Comparison of time domain and feature domain damage detection. In: Proceedings of the 8th international operational modal analysis conference (IOMAC 2019), Copenhagen May 12–14, 2019, pp 115–126
10. Bendat JS, Piersol AG (2010) Random data: analysis and measurement procedures, 4th edn. Wiley, Blackwell, Hoboken, N.J., USA
11. Basseville M (2009) Model-based statistical signal processing for change and damage detection. In: Boller C, Chang F-K, Fujino Y (eds) Encyclopedia of structural health monitoring. Wiley, pp 677–695
12. Clough RW, Penzien J (1993) Dynamics of structures. 2nd edn. McGraw-Hill, New York

13. Tarpø M, Friis T, Georgakis C, Brincker R (2020) The statistical errors in the estimated correlation function matrix for operational modal analysis. *J Sound Vib* 466:115013
14. Orlowitz E, Brandt A (2019) Influence of noise in correlation function estimates for operational modal analysis. In Mains M, Dilworth BJ (eds) *Topics in modal analysis & testing*, vol 9, Conference proceedings of the society for experimental mechanics series, pp 55–64
15. Kullaa J (2012) Whitening transformation in damage detection. In: Del Grosso AE, Basso P (eds) *Smart structures: Proceedings of the 5th European Conference on Structural Control — EACS 2012*, Genoa, Italy, June 18–20, 2012
16. Worden K, Allen D, Sohn H, Farrar CR (2002) Damage detection in mechanical structures using extreme value statistics. In: *SPIE Proceedings*, Vol. 4693, 9th annual international symposium on smart structures and materials, San Diego, CA, pp 289–299
17. Montgomery DC (1997) *Introduction to statistical quality control*, 3rd edn. Wiley, New York
18. Brandt A (2011) *Noise and vibration analysis: signal analysis and experimental procedures*. Wiley, Chichester, Hoboken, N.J., USA

The Optimization Study of Apparent Damage Recognition Algorithm of Bridge Underwater Structure



Yeteng Wang, Haoyang Ding, Changlin Song, Yao Xiao, Ruiyang Yuan, and Zhishui Liang

Abstract Due to the characteristics of the underwater environment and the influence of imaging equipment, the quality of apparent structural damage images is difficult to guarantee and the accuracy of damage recognition is relatively low. Deep learning algorithm is increasingly widely used in the field of image identification. Especially, when it is used in damage identification, the labor costs can be saved and the identification accuracy of damage categories and specific information are improved. A FCN-based full convolutional neural network is designed in the template of VGG16. Firstly, the underwater structure damage picture is preprocessed, and the picture data used is optimized. Then, the fuzzy mechanism is used to deal with the noise interference of the underwater picture and the data set of the damage pictures can be observed and expanded through cropping method. Therefore, the iterative simulation and parameter optimization can be done on the FCN full convolutional neural network model on a larger scale, and the image recognition algorithm will be improved. The data set simulation research results show that the crack damage identification accuracy obtained by the deep learning method can reach more than 90%, which improves the accuracy of underwater structure damage identification. The results will provide a certain theoretical foundation for underwater structural damage and assessment.

Keywords Underwater structure · Damage identification · FCN full convolutional neural network · Data set · Simulation iteration

1 Introduction

During the operation of the bridge, the structure will inevitably occur diseases and damage, if not timely detection and maintenance, it will seriously threaten the safety of the bridge structure. Due to the worse external environment (such as wind, wave

Y. Wang · C. Song · Y. Xiao · R. Yuan · Z. Liang (✉)
School of Civil Engineering, Southeast University, Nanjing 210089, China
e-mail: zs_liang@seu.edu.cn

H. Ding
Nanjing Foreign Language School, Nanjing 210000, China

© The Author(s), under exclusive license to Springer Nature Switzerland AG 2023
Z. Wu et al. (eds.), *Experimental Vibration Analysis for Civil Engineering Structures*,
Lecture Notes in Civil Engineering 224,
https://doi.org/10.1007/978-3-030-93236-7_10

and sea water), the underwater structure is more likely to be damaged, and the damage is more serious. Most of the damage of bridge underwater structure starts or appears on the surface of the structure, which is mainly manifested as cracks, corrosion of reinforcement, concrete defects, necking, exposed reinforcement, etc., thus affecting the overall structural safety. Therefore, it is necessary and significant to detect the apparent damage of underwater structures.

At present, in the underwater damage detection methods, the recognition method based on vision has been widely studied and applied because it is more intuitive and accurate. However, the processing of the acquired image is a major difficulty in the process of recognition. The existing method is manual judgment and evaluation, which is mainly based on personal subjective evaluation, so it is difficult to scientifically quantify the evaluation basis. The algorithm based on image processing is also a hot direction in the field of structural damage image recognition. In the research of [1–3], histogram, threshold, morphological operation and other means are used to identify the damage in the image. The threshold segmentation method, edge detection method, region growth method and other algorithms proposed in this paper have the advantages of high contrast and low cost. The damage images with clear background have good performance, but they have their own shortcomings in image quality requirements, difficulty of algorithm implementation, anti-interference and so on.

In recent years, deep learning algorithm has great advantages in object detection and semantic segmentation, and has good model robustness, so it has been widely studied and applied in structural apparent damage recognition, among which convolution neural network (CNN) [4] and full convolution neural network (FCN) [5–7] are widely used. CNN structure is suitable for image level classification and regression tasks. After the structural damage (such as cracks) image is input, it goes through a series of convolution layer, nonlinear layer, pooling layer and fully connected layer, and is mapped into a fixed length feature vector. Finally, a probability numerical description of the whole damage image is obtained; FCN transforms the full connection layer of traditional CNN into convolution layers, which can accept the input of structural damage image of any size. The deconvolution layer is used to sample the feature image of the last convolution layer, so that it can recover to the same size of the input image, so that a prediction can be made for each pixel, and the spatial information in the original input image is retained. Finally, pixel by pixel classification is carried out on the up sampled feature map, and the pixel range of the target object is directly output. In addition, in view of the quality problems of underwater apparent structure damage image, the influence of image quality problems on recognition accuracy can be reduced through pre-processing and post-processing.

In this paper, aiming at the influence of the image quality of underwater environment on the recognition of bridge underwater structure disease, an intelligent underwater structure apparent damage disease recognition algorithm based on FCN full convolution neural network is proposed. A new algorithm flow is proposed.

The image preprocessing and conditional random field terminal processing are introduced to reduce the uneven brightness and the noise caused by underwater environment. In order to solve the problem of low definition, the accuracy of pixel recognition is further improved.

2 Underwater Damage Identification

2.1 Background

Due to the characteristics of underwater bridge diseases, the acquired underwater images are often doped with specific noise, which will cause great interference to the further identification and processing of bridge damage. Therefore, it is necessary to preprocess the acquired underwater images. The purpose of pretreatment is to eliminate the interference of underwater noise, such as bubbles, overexposure and other non-destructive factors. In view of the single processing is difficult to achieve the best standard, this project uses different preprocessing schemes to obtain the local optimal processing, and then collates into a complete image information. Threshold segmentation is a low-cost image information extraction method at the present stage. However, for the information singleness and clarity requirements of the image, according to the process architecture shown in (Fig. 1), we will carry out two kinds of processing on the underwater image. Here, we specify that preprocessing channel 1 and preprocessing channel 2 should be distinguished. Since our goal is to achieve both the underwater damage classification task and the underwater damage segmentation task, the establishment of different preprocessing channels will bring great convenience to solve different problems.

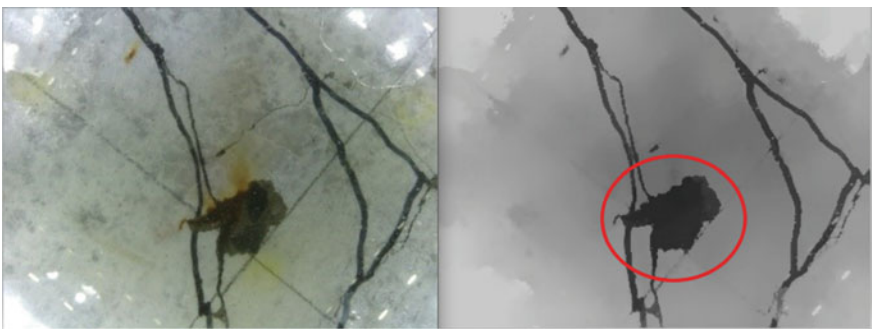


Fig. 1 The gray image after preprocessing channel one

2.2 Pretreatment Channel 1

Mean shift blur is one of the image edge preserving filtering algorithms. It is often used to remove noise before watershed segmentation, which can greatly improve the effect of watershed segmentation. The basic principle is as follows: in n -dimensional space, there are a certain number of samples, we select one of them, draw a circle with the sample as the center and the given length as the radius, find the centroid of the sample in the circular region, that is, the point with the highest density, and then continue the above iterative process with the point as the center until the final convergence. Taking any point P_0 of SRC on the input image as the center, a spherical space with the radius of SP in the physical space and Sr in the color space is established. The coordinates in the physical space are x, y , and the coordinates in the color space are R, G, B (or HSV), forming a 5-Dimensional vector space.

The ranges of physical space X and y are the length and width of the image, and the ranges of color space R, G and B are $0\sim 255$ respectively. Compared with the default value of 3×3 convolution window is $[-1, 0, 1]$, we can calculate the mean value of the space window and color value window of the image, and get DX and Dy , as well as the new RGB color value. In the image space window and color value window, DX and Dy , as well as the new RGB color value are calculated.

It is found that the mean shift fuzzy is suitable for dealing with large underwater damage. On the basis of eliminating bubbles and impurity noise, the edge information of erosion part is greatly retained, which is conducive to the further learning of neural network.

2.3 Pretreatment Channel 2

For the digital image with intensity levels in the range of $[0, L - 1]$, the histogram can be expressed as a discrete function $H(rk) = nk$, where rk is the intensity value of the k -th level, and nk is the number of pixels in the image with the gray value of rk . In other words, the gray histogram of the image represents the gray distribution of the image. In practical application, histogram is usually normalized and then processed. It is assumed that the dimension of gray image is $M \times N$. MN is the total number of pixels in the image, then the normalized histogram can be expressed as

$$p(rk) = \frac{nk}{MN}, k = 0, 1, \dots, L - 1 \quad (1)$$

In other words, $p(rk)$ represents the estimation of the probability of occurrence of the gray level rk in the image, and the sum of all components of the normalized histogram is equal to 1.

The following is to understand histogram equalization from a mathematical point of view. Suppose that the image to be processed is a gray image, r represents the gray level of the image to be processed, and the value range is $[0, L - 1]$, then r

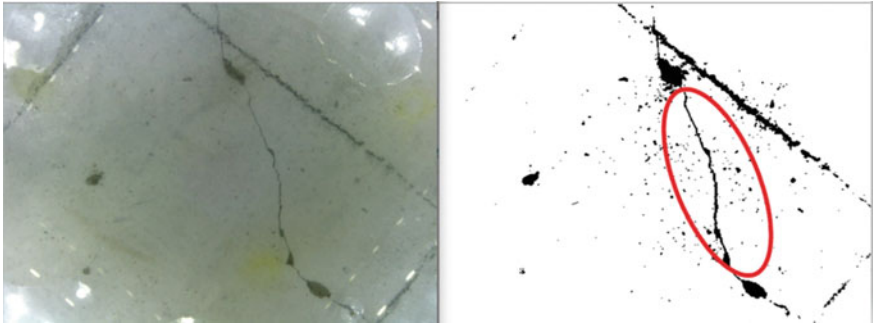


Fig. 2 The gray image after preprocessing channel two

$= 0$ represents black, $r = L - 1$ represents white, and the process of histogram equalization corresponds to a transformation T :

$$s = T(r), 0 \leq r \leq L - 1 \tag{2}$$

That is to say, for a certain gray value r of the input image, the gray value s of the corresponding position of the balanced image can be obtained by transforming t . The transformation t satisfies the following conditions.

- (a) $T(r)$ increases strictly monotonically on $[0, L - 1]$;
- (b) When $0 \leq r \leq L - 1$, $0 \leq T(r) \leq L - 1$.

In condition (a), $t(R)$ is required to be strictly monotonically increased to ensure that the output gray value corresponds to the input gray value one by one, and the relative size relationship between the gray values of the pixels remains unchanged, so as to avoid problems in inverse transformation; Condition (b) ensures that the gray range of the output image is the same as that of the input image. In practice, the processed image is usually an integer gray value, and all results must be rounded to the nearest integer value. Therefore, when the strict monotone condition is not satisfied, the method of finding the closest integer matching is used to solve the problem that the inverse transform is not unique.

Experimental results show that equalization is helpful to the extension of image histogram, and the gray level range of the image is wider after equalization, which effectively enhances the contrast of the image. Then, the information of crack damage can be extracted (Fig. 2).

2.4 Effect Comparison

Compared with Otsu, the commonly used image binary search method, it can be seen that the pretreatment proposed in this paper can effectively avoid the disadvantages

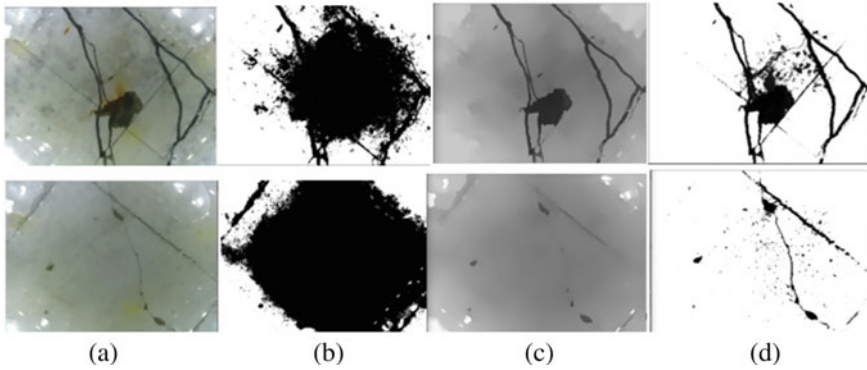


Fig. 3 Effect comparison. **a** Original picture; **b** OTSU; **c** Preprocessing channel one; **d** Preprocessing channel two

of threshold method, and the crack information and erosion information can be integrated to obtain the complete image information (Fig. 3) (Tables 1, 2, 3, and 4).

2.5 Image Recognition Based on CNN Network

Step 1: BATCH_SIZE

Step 2: LEARNING_RATE_BASE

Step 3: *LEARNING_RATE_DECAY* = 0.99

Step 4: Regularization parameter

REGULARIZER = 0.0001

Table 1 BATCH_SIZE
(STEP = 10,000)

BATCH_SIZE	Accuracy	Study time
100	0.992	16 min
150	0.9921	23 min 27 s
200	0.9922	31 min 21 s

Table 2
LEARNING_RATE_BASE

LEARNING_RATE_BASE	Accuracy	Study time
0.001	0.9855	16 min 13 s
0.005	0.992	16 min
0.01	0.9937	16 min 7 s

Table 3 STEP (BATCH = 100)

STEP	Accuracy	Study time
10,000	0.992	16 min 13 s
25,000	0.9938	32 min 24 s
50,000	0.9931	1 h 12 min 7 s

Table 4 stddev

STEP	Accuracy	Study time
stddev	Accuracy	Study time
0.1	0.992	16 min
0.05	0.9926	15 min 19 s

If the regulator is too small, it is easy to over fit and too large to under fit.

Step 5: Iterations Times

Step 6: *MOVING_AVERAGE_DECAY* = 0.99.

Step 7: Standard deviation of truncated normal distribution *stddev*.

When *stddev* = 0.05, the single batch error is significantly reduced, the average error is about 0.15, hundreds of learning converges to a higher accuracy (about 0.9), which may be a good parameter to reduce the number of learning.

When *stddev* = 0.01, the accuracy is low in the first few hundred times of learning.

2.6 Semantic Segmentation Based on FCN Network

In this section, the preprocessed image is segmented semantically, and the commonly used TensorFlow deep learning open source framework is adopted. The neural network model based on vgg16 can more accurately identify the categories of the image and realize the accurate classification of the underwater structure apparent damage categories. Taking the maxpool as the boundary, vgg16 has six hierarchical structures, and a total of 16 deep networks. Among them, 13 layers convolution and 5 layers pooling are mainly responsible for feature extraction, and the last three layers complete semantic segmentation. All activation functions are activated using Relu [8]. The FCN method is used to classify the rocks. Using this idea, we adjusted vgg16 (Fig. 4).

In order to realize the damage visualization, it is necessary to carry out pixel level semantic segmentation for the detected images with damage, and do intensive segmentation task for the image, judge the category of each pixel, and assign the specified label for each pixel. In the future, we will do the corresponding geometric parameter statistics for these tags.

ConvNet Configuration					
A	A-LRN	B	C	D	E
11 weight layers	11 weight layers	13 weight layers	16 weight layers	16 weight layers	19 weight layers
input (224×224 RGB image)					
conv3-64	conv3-64 LRN	conv3-64 conv3-64	conv3-64 conv3-64	conv3-64 conv3-64	conv3-64 conv3-64
maxpool					
conv3-128	conv3-128	conv3-128 conv3-128	conv3-128 conv3-128	conv3-128 conv3-128	conv3-128 conv3-128
maxpool					
conv3-256 conv3-256	conv3-256 conv3-256	conv3-256 conv3-256	conv3-256 conv3-256 conv1-256	conv3-256 conv3-256 conv3-256	conv3-256 conv3-256 conv3-256 conv3-256
maxpool					
conv3-512 conv3-512	conv3-512 conv3-512	conv3-512 conv3-512	conv3-512 conv3-512 conv1-512	conv3-512 conv3-512 conv3-512	conv3-512 conv3-512 conv3-512 conv3-512
maxpool					
conv3-512 conv3-512	conv3-512 conv3-512	conv3-512 conv3-512	conv3-512 conv3-512 conv1-512	conv3-512 conv3-512 conv3-512	conv3-512 conv3-512 conv3-512 conv3-512
maxpool					
FC-4096					
FC-4096					
FC-1000					
soft-max					

Fig. 4 Hierarchy of VGG16

The deeplab series of deep neural networks based on vgg16 mainly do intensive semantic segmentation tasks for images. In order to avoid the decrease of receptive field and spatial resolution caused by continuous pooling layer or down sampling layer, deep lab uses up sampling and deconvolution. At the same time, parallel multi-scale network hierarchical sampling is used to reduce the amount of computation and optimize the size of the output feature map. Deeplab also innovatively uses whole convolution to ensure that the receptive field does not change during the sampling process, while reducing the parameters and optimizing the training rate (Figs. 5 and 6).

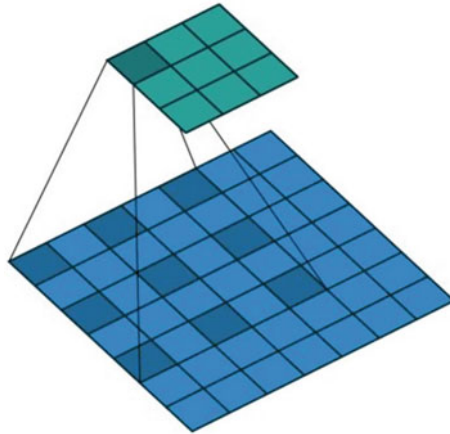


Fig. 5 Void convolution

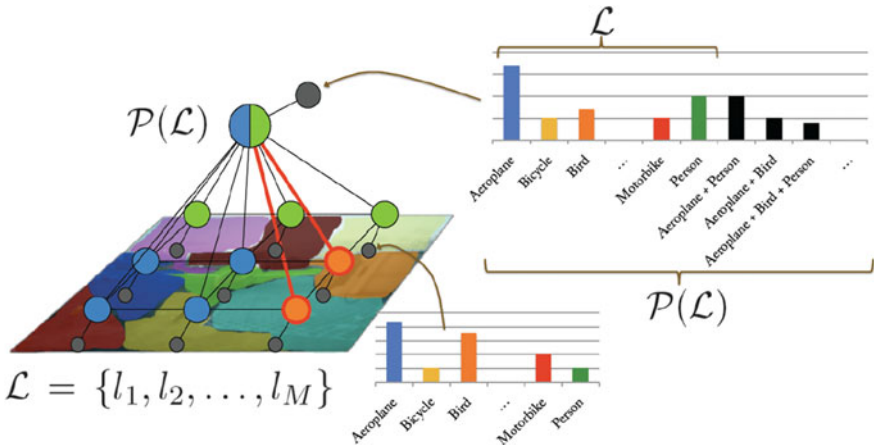


Fig. 6 Schematic diagram of CRF

2.7 Conditional Random Field Terminal Processing

Finally, we use fully connected conditional random fields (FCRFS) to optimize the segmentation boundary in the back end of deep lab. Yan Z. et al. used the conditional random field method to optimize the road pixel level segmentation [9], which is a good help for image segmentation.

Make random variable $x; I$ is the label of pixel i , $X; I \in I = 1, 2, \dots, l_L$, the variable X is a random vector composed of $X_1, X_2 \dots X_{n_V}$, n is the number of pixels in the image.

Suppose figure $g = (V, E)$, where $V = X_1, X_2 \dots X_n$, global observation is I . The conditions are in accordance with Gibbs distribution.

$$P(X = x|I) = \frac{1}{z(I)} \exp(-E(x|I)) \quad (3)$$

In the fully connected CRF model, the energy of tag x can be expressed as:

$$E(x) = \sum_i \theta(x_i) + \sum_{ij} \vartheta_{ij}(x_i, x_j) \quad (4)$$

Among them, $\theta_i(x_i)$ is a unitary energy term, which means dividing pixel i into label a ; The binary energy term $\vartheta_{ij}(x_i, x_j)$ is to segment pixel i and j simultaneously the energy of Z . The binary energy term describes the relationship between pixels, and encourages similar pixels to assign the same labels, while pixels with large differences to assign different labels. The definition of “distance” is related to the color value and the actual relative distance. So this CRF can make the image segmentation at the boundary as much as possible. Minimize the energy above to find the most likely segmentation. The difference of fully connected conditional random fields is that the binary potential function describes the relationship between each pixel and all other pixels, so it is called “fully connected”.

In deep lab, the unitary energy comes directly from the output of FCN

$$\theta_i(x_i) = -\log P(x_i) \quad (5)$$

In general, deep lab still uses the Encoder–Decoder structure of FCN, which simplifies the training process and reduces the training parameters by reusing the parameters in the down sampling layer. The high-level features of the encoder are easy to capture longer distance information. In the decoder stage, the information of the encoder stage is used to help recover the details and spatial dimensions of the target. Experiments show that adding the final processing can enhance the pixel level segmentation, so as to achieve better accuracy of underwater damage segmentation.

2.8 Recognition Results

The following shows some results of image recognition (Fig. 7).

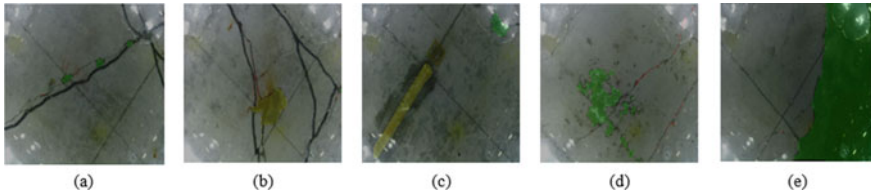


Fig. 7 Recognition results **a** exposed reinforcement-green; **b** exposed reinforcement-yellow, crack-red; **c** exposed reinforcement-yellow; **d** exposed reinforcement-green, crack-red; **e** exposed reinforcement-green

3 Conclusions

In this study, we design a full convolution neural network based on FCN, optimize the data set through the appropriate preprocessing method of underwater images, use the fuzzy mechanism to deal with the noise interference of underwater images, and expand the data set by using the cutting method, and innovatively propose the damage identification algorithm framework of preprocessing, neural network and post-processing. At present, there are not enough data sets in this study. In the future, we can obtain the suitable data sets for the algorithm through experiments, and further train the neural network to improve the recognition accuracy.

Acknowledgements This work is funded by the State Key Research Development Program of China (Grant No. 2019YFC1511100), and Natural Science Foundation (52079031).

References

1. Sinha SK, Fieguth PW (2006) Automated detection of cracks in buried concrete pipe images. *Autom Constr* 15(1):58–72
2. Yu SN, Jang JH, Han CS (2007) Auto inspection system using a mobile robot for detecting concrete cracks in a tunnel. *Autom Constr* 16(3):255–261
3. Adhikari RS, Moselhi O, Bagchi A (2014) Image-based retrieval of concrete crack properties for bridge inspection. *Autom Constr* 39:180–194
4. Cha YJ, Choi W, Büyüköztürk O (2017) Deep learning-based crack damage detection using convolutional neural networks. *Comput-Aided Civ Infrast Eng* 32(5):361–378
5. Yang X, Li H, Yu Y, Luo X, Huang T, Yang X (2018) Automatic pixel-level crack detection and measurement using fully convolutional network. *Comput-Aided Civ Infrastruct Eng* 33(12):1090–1109
6. Bang S, Park S, Kim H, Kim H (2019) Encoder-decoder network for pixel-level road crack detection in black-box images. *Comput Aided Civ Infrastruct Eng* 34(8):713–727
7. Xue D, Tang Q, Wang A, Zhang L, Zhou H (2019) FCN-based intelligent identification of crack geometry in rock or concrete. *Chin J Rock Mech Eng* 38(S2):3393–3403
8. Shelhamer E, Long J, Darrell T (2017) Fully convolutional networks for semantic segmentation. *IEEE Trans Pattern Anal Mach Intell* 39(4):640–651
9. Yan Z, Li Y, Yan G (2020) Road segmentation method based on multi-feature fusion and conditional random field. *Comput Syst Appl* 29(03):240–245

The Value of Different Monitoring Systems in the Management of Scoured Bridges



Pier Francesco Giordano, Luke J. Prendergast, and Maria Pina Limongelli

Abstract Bridge scour is a leading cause of failure for bridges over waterways and is very difficult to detect accurately. Due to the large number of bridges on typical networks and the limited availability of financial resources within asset agencies, decision-makers must prioritize certain structures when it comes to management in the event of flooding. In response to the notable challenges associated with scour detection, methods that can monitor the actual performance of a scoured bridge have become popular in recent years, especially dynamic Structural Health Monitoring (SHM). One such approach relies on monitoring changes in the natural frequency of a bridge structure due to the occurrence of scour, which represents a change in the structural boundary conditions and therefore results in a change in modal behavior. A further reduction of the uncertainty involved in the problem can be obtained by monitoring the scour depth. The decision to install a monitoring system on a bridge must be balanced by the financial benefit of doing so, as limited resources often need to be carefully rationed. The Value of Information (VoI) from Bayesian decision analysis can be used to compute the benefit of installing a permanent monitoring system (scour or structural monitoring system). The VoI can be defined as the expected reduction in management cost related to informed decision-making, that is when the decision is aided by the newly acquired information. A case study is presented whereby different monitoring systems are considered to be installed on a typical bridge to support emergency management during a flood. A comparison of the relevant benefits, accounting for multiple flood events and scenarios, is carried out to identify the optimal monitoring strategy.

Keywords Scour · Bridge · Emergency management · Vibration-based SHM · Scour depth monitoring

P. F. Giordano (✉) · M. P. Limongelli
Department of Architecture, Built Environment and Construction Engineering, Politecnico Di Milano, Milan, Italy
e-mail: pierfrancesco.giordano@polimi.it

L. J. Prendergast
Department of Civil Engineering, Faculty of Engineering, University of Nottingham, Nottingham, UK

1 Introduction

The occurrence of scour erosion is one of the main reasons for the early failure of bridges with foundations in water [1]. It is highly challenging to detect as it tends to occur around bridge foundations under benign water flows as a result of changing channel properties and natural river evolution, in addition to under the action of aggressive water flows during floods [2]. Scour results in a reduction of the strength and stiffness of foundations and can lead to structural instability [3], typically manifesting as excess settlements or even partial and complete collapse [4].

Due to the severity of the problem and its widespread nature, a significant amount of research has been dedicated in recent years to developing reliable monitoring systems for scour. These include the installation of physical sensors to detect scour hole development, e.g. [1], as well as online damage detection systems using vibration-based health monitoring techniques [5]. The main issue with the deployment of schemes of this nature lies with their cost, ongoing maintenance, and associated measurement uncertainty arising from differences in the nature of their operation. For this reason, it is becoming very important for asset managers to be equipped with the tools required to facilitate decisions being made about which assets should be targeted for monitoring on given infrastructure networks.

A general framework to estimate the benefit of installing a permanent SHM system to support the emergency management operation of bridges at risk of scour during flood events was proposed by the authors of this paper [6]. This framework is based on the Value of Information (VoI) from Bayesian decision analysis [7]. The VoI is a metric to quantify the impact of new information in a decision scenario. It can be interpreted as the money saved by the decision-maker each time she or he uses the new information [8, 9]. The interest in the VoI of the SHM community has grown increasingly in the last few years [10]. In this paper, a case study is presented considering different monitoring systems being installed on a typical bridge and a comparison of their performance, in terms of the provided benefit in supporting flood emergency management, is undertaken.

2 VOI Framework

2.1 Bayesian Decision Theory

The Bayesian decision theory deals with decision-making in uncertain environments, that is when the state of the system, i.e., the bridge in our case, is not known with certainty. Specifically, the decision-maker must select the optimal action among a set of N actions $A_n, n = 1, \dots, N$ with limited knowledge on the system that can be in one of L damage states $DS_l, l = 1, \dots, L$. The optimal action is the one corresponding to minimum expected costs (i.e., the action which maximizes the expected

utility [11]). The decision-maker assigns a probability to each damage state based on the available knowledge she or he has on the system. A monitoring system, which can provide J possible outcomes $O_j, j = 1, \dots, J$, might give insight into the actual condition of the bridge. According to the amount of information available, different decision analyses can be carried out. The decision analysis performed without additional information from monitoring is referred to as Prior decision analysis. When new information is available, the decision-maker can carry out a Posterior decision analysis. Before collecting new information, the decision-maker can carry out a Pre-Posterior decision analysis. The VoI is one of the most relevant outcomes of the Pre-Posterior analysis. The three types of decision analysis and the VoI are detailed in the following sections.

2.2 Prior Decision Analysis

During the prior analysis, the decision-maker must select the optimal action \hat{A} using the available information on the state of the bridge, i.e., she or he uses the prior probabilities of the damage states to compute the expected cost of each action A_n , as follows:

$$E[c(A_n)|Q] = \sum_{l=1}^L E[c(A_n)|DS_l]P(DS_l|Q) \quad (1)$$

where $E[c(A_n)|DS_l]$ is the expected cost of the action A_n when the state of the bridge is DS_l ; and $P(DS_l|Q)$ is the prior probability of DS_l , which in the case of scour emergency management can be conditional on the flow rate Q . The term $E[c(A_n)|DS_l]$ can be computed as:

$$E[c(A_n)|DS_l] = c_F(A_n)P(F|A_n, DS_l) + c_{\bar{F}}(A_n)[1 - P(F|A_n, DS_l)] \quad (2)$$

where $P(F|A_n, DS_l)$ is the probability of failure conditional on the action A_n and the damage state DS_l ; and $c_F(A_n)$ and $c_{\bar{F}}(A_n)$ are the costs of bridge failure and survival, respectively, which depend on the action A_n . The optimal action \hat{A} is chosen as the one which minimizes the expected costs according to Eq. 3. In general, the optimal action is conditional on the flow rate Q . The cost corresponding to the optimal action is called c_1 , see Eq. 4.

$$\hat{A} = \hat{A}(Q) = \underset{n}{\operatorname{argmin}} E[c(A_n)|Q] \quad (3)$$

$$c_1(Q) = E[c(\hat{A})|Q] = \sum_{l=1}^L E[c(\hat{A})|DS_l]P(DS_l|Q) \quad (4)$$

2.3 Posterior and Pre-posterior Decision Analysis

When new information is available, it can be used to update the prior probabilities of the damage states and thus to carry out a Posterior decision analysis. This is done through the well know Bayes' Theorem, which reads:

$$P(DS_l|O_j, Q) = \frac{P(O_j|DS_l)P(DS_l|Q)}{P(O_j|Q)} \quad (5)$$

where $P(DS_l|O_j, Q)$ is the posterior, i.e., updated, probabilities of the damage state DS_l ; $P(O_j|DS_l)$ is the probability of observing the monitoring outcome O_j conditional on the damage state DS_l , which is commonly named the likelihood function; and the denominator $P(O_j|Q)$ is the total probability of the monitoring outcome O_j , which is obtained as:

$$P(O_j|Q) = \sum_{l=1}^L P(O_j|DS_l)P(DS_l|Q) \quad (6)$$

The expected cost of an action A_n , $E[c(A_n)|O_j, Q]$, is computed similarly to Eq. 1, but considering the posterior probabilities of the damage states:

$$E[c(A_n)|O_j, Q] = \sum_{l=1}^L E[c(A_n)|DS_l]P(DS_l|O_j, Q) \quad (7)$$

The optimal action \tilde{A}_{O_j} and its expected cost $E[c(\tilde{A}_{O_j})|O_j, Q]$ depend on the observed outcome O_j , see Eqs. 8 and 9.

$$\tilde{A}_{O_j} = \tilde{A}(O_j, Q) = \underset{n}{\operatorname{argmin}} E[c(A_n)|O_j, Q] \quad (8)$$

$$E[c(\tilde{A}_{O_j})|O_j, Q] = \sum_{l=1}^L E[c(\tilde{A}_{O_j})|DS_l]P(DS_l|O_j, Q) \quad (9)$$

Before collecting the new information, the decision-maker can carry out a Pre-Posterior decision analysis, in which she or he "pretends" that the new information from the monitoring system is available. Specifically, a Posterior decision analysis is made for each possible outcome O_j . After that, the resulting expected costs of the optimal actions are weighted over the corresponding probability of the outcome O_j , as follows:

$$c_0(Q) = \sum_{j=1}^J E \left[c(\tilde{A}_{O_j}) | O_j, Q \right] P(O_j | Q) \quad (10)$$

The resulting expected cost $c_0(Q)$ can be understood as the expected cost of the informed decision-making and can be used to quantify the benefit associated with the new information. This is discussed in the following section.

2.4 Value of Information

Before installing a monitoring system, the decision-maker can quantify its benefit by means of the VoI which is computed as the difference between the expected cost of the optimal action from Prior analysis, see Eq. 4, and the expected cost of the informed decision making from Pre-Posterior analysis, see Eq. 10, as follows:

$$\text{VoI}(Q) = c_1(Q) - c_0(Q) \quad (11)$$

In the case of emergency management of scoured bridges, the VoI generally depends on the flow rate Q (due to the dependency of the prior probabilities on this parameter). The expected VoI can be obtained considering the Probability Density Function (PDF) of Q , as follows:

$$\text{VoI} = \int_Q \text{VoI}(Q) f(Q) dQ \quad (12)$$

The VoI computed according to Eq. 12 relates to a single flood event. Instead, the decision-maker might be interested in computing the VoI related to multiple events, over a reference period, e.g., the life cycle of the structure or the monitoring system. To address this issue, the Life-Cycle VoI, VoI_{LC} , is introduced [12], as follows:

$$\text{VoI}_{LC} = \sum_{i=1}^{T_{LC}} \lambda \frac{\text{VoI}}{(r+1)^i} \quad (13)$$

where T_{LC} is the reference period (in years) considered in the analysis, λ is the expected number of floods in one year, and r is the discount rate. The VoI_{LC} should be compared to the expected life-cycle cost of the monitoring system over the reference period, C_{SHM} , to obtain the Net Life-Cycle VoI [13], NVoI_{LC} as follows:

$$\text{NVoI}_{LC} = \text{VoI}_{LC} - C_{SHM} \quad (14)$$

If the NVoI_{LC} is negative, the monitoring system should not be installed. Besides, the NVoI_{LC} can be used to compare different monitoring systems.

2.5 Value of Perfect Information

The framework of the VoI presented so far relates to a monitoring system that provides an “imperfect” outcome, which is commonly the case in real applications due to the effect of several sources of uncertainty (e.g., those due to environmental and operational factors or data processing errors). In the ideal case of a monitoring system that provides “perfect” information, the so-called Value of Perfect Information (VoPI) can be computed [9]. It reads:

$$\text{VoPI}(Q) = c_1(Q) - \sum_{l=1}^L E[c(A^*)|DS_l]P(DS_l|Q) \quad (15)$$

where the term $E[c(A^*)|DS_l]$ represents the expected cost of the optimal action A^* when the state of the bridge is DS_l . The VoPI constitutes the upper bound for the VoI thereby representing the maximum benefit that can be obtained by installing a monitoring system.

2.6 Implementation Aspects

The application of the VoI framework in practice requires the definition of several elements, specifically: (i) damage states, (ii) prior probabilities; (iii) probabilities of failure, (iv) cost of failure and survival associated with different management actions, (v) likelihood functions for Bayesian updating, and (vi) modeling of scour hazard. In this study, these elements are defined as follows.

Damage states. The L damage states are determined based on scour depth intervals defined by fixed scour thresholds th_l , $l = 1, \dots, L$, where $th_1 = 0$. For $l \neq L$, the bridge will be in DS_l for scour depths y_s in the interval $[th_l, th_{l+1})$. The bridge will be in damage state L for scour depths higher than th_L .

Prior probabilities. The prior probabilities of the different damage states are computed as:

$$\begin{aligned} P(DS_l|Q) &= P\left[\{y_s \geq th_l\} \cap \{y_s < th_{l+1}\}\right] \text{ for } l \neq L \\ P(DS_l|Q) &= P(y_s \geq th_l) \text{ for } l = L \end{aligned} \quad (16)$$

The scour depth distribution can be computed using equations available in the literature incorporating the uncertainty in the relevant geometric and hydraulic variables. In this study, the Hydraulic Engineering Circular (HEC-18) design formula [14] is used, which reads

$$\frac{y_s}{y_1} = 2.0\lambda_{y_s} K_1 K_2 K_3 K_4 \left(\frac{a}{y_1} \right)^{0.65} Fr_1^{0.43} \quad (17)$$

where y_1 is the flow depth upstream of the pier; K_1 , K_2 , K_3 , and K_4 are the correction factors for pier nose shape, angle of attack of flow, bed conditions, and armoring by bed material, respectively; a is pier width; Fr_1 is the Froude Number, and λ is the model correction factor. The Froude Number is computed as $Fr_1 = V_1/\sqrt{gy_1}$, where V_1 is the mean velocity of flow upstream of the pier; g is the acceleration due to gravity. In this study, for demonstration purposes, the variable y_1 and V_1 are computed using the following equations valid for a channel with a rectangular cross-section:

$$y_1 = \left(\frac{Qn}{Bs^{0.5}} \right)^{3/5} \quad (18)$$

$$V_1 = \frac{Q}{By_1} \quad (19)$$

where Q is the flow rate; B is the average width of the channel; n is the Manning's coefficient, and s is the slope of the channel.

Probabilities of failure. The probability of failure in each damage state is generally evaluated by comparing the capacity of the bridge with the demand imposed by external actions. Several failure modes might be considered, such as vertical failure, overturning, pile buckling, and bending failure. The presence of scour is expected to reduce the capacity of the bridge. Several reliability methods are available to compute the probability of failure [15].

Costs. As for the cost of failure and survival for different management actions, both direct and indirect costs should be considered. For instance, the closure of the bridge to traffic will generate indirect costs for users related, for instance, to increased travel distance [16]. The failure of the bridge generally implies direct costs, such as rebuilding costs and costs related to human life loss [17]. The computation of direct and indirect costs in emergency management is discussed in [6, 13].

Likelihood functions. The likelihood functions link the monitoring outcome to the damage state of the bridge. Several methods are available to estimate these quantities, see for instance [13]. In this work, it is supposed the vibration-based SHM system provides the first natural frequency of the structure. The presence of scour modifies the boundary conditions of the bridge and as a consequence its dynamic properties, including the modal frequencies. Nevertheless, the values of the natural frequencies of structures are generally affected by several sources of uncertainty including environmental and operational factors and vibration data acquisition and processing. The distribution of this modal parameter in the different damage states must account for the different sources of uncertainty. As for the scour depth monitoring system,

it directly provides the scour depth at piers which can be directly associated with a damage state. In this work, as a first approximation, it is supposed that the scour depth monitoring system is not affected by uncertainty.

Flood hazard. The VoI is computed before the actual estimation of a monitoring system thereby future flood events must be “forecasted” through a suitable probabilistic model. In this study, we exploit the properties of the Peaks over Threshold (POT) series model [18] which is particularly appropriate to represent multiple flood events. Specifically, a flood event is defined in this context as a river discharge event exceeding a flow threshold, Q_0 . The POT model is composed of two probabilistic models: (1) a model for the annual number of flood events and (2) a model for the flood magnitude. Herein, we assume that the number of events in one year follows a Poisson distribution. Instead, the flood magnitude is assumed to be exponentially distributed.

3 Demonstration Case Study

The VoI framework described in the previous sections is applied to a demonstration case study of a bridge with one pier in water. The decision problem involves a decision-maker that must decide if the installation of a monitoring system to support traffic management operations during a flood is financially worthwhile. In addition to choosing whether or not to install a monitoring system, the decision-maker must choose which monitoring system to install, between a vibration-based SHM system that provides the first natural frequency of the structure and a scour depth monitoring system. The results obtained are not general but are useful to illustrate the VoI procedure in case the decision-maker has to choose between multiple monitoring strategies.

The possible management actions during a flood are to keep the bridge open or close it to traffic. During the flood, the bridge can be in three damage states. For scour depths in the interval $0 \leq y_s < 2\text{m}$ the structure is in the damage state DS_1 , in interval $2 \leq y_s < 4\text{m}$ the structure is in DS_2 ; for $y_s \geq 4\text{m}$ the structure is in DS_3 (in this case study example). Without the information from a monitoring system, the decision-maker uses the HEC-18 design equation to estimate the scour depth and thus the damage state of the bridge. The probabilities of the damage states are conditional on the value assumed by the flow rate. The input variables used in the computation of the prior probabilities of the different damage states are displayed in Table 1.

The probabilities of failure for different damage states and actions used in the calculations are displayed in Table 2. The probabilities of failure increase with the increasing severity of the damage state due to the reduced capacity of the bridge. It is assumed that, for the same damage state, the probabilities of failure are higher when the bridge is open due to the effect of traffic.

Table 1 Input variables for scour depth calculation

Variable	Unit	Distribution	Mean	CoV
K_1	–	Det	1	–
K_2	–	Det	1	–
K_3	–	Uniform	1.2	0.048
K_4	–	Det	1	–
a	m	Det	1.2	–
B	m	Lognormal	50	0.05
s	–	Lognormal	0.003	0.05
λ_{ys}	–	Normal	0.55	0.52
n	–	Lognormal	0.025	0.28

Table 2 Probabilities of failure for different damage states and actions

Damage state	$A_n = Open$	$A_n = Close$
DS_1	$1 \cdot 10^{-5}$	$1 \cdot 10^{-6}$
DS_2	$1 \cdot 10^{-2}$	$1 \cdot 10^{-3}$
DS_3	$1 \cdot 10^{-1}$	$1 \cdot 10^{-2}$

The cost of bridge failure and survival depending on the selected action are shown in Table 3. The cost of failure when the bridge is open includes direct costs (the cost of rebuilding the bridge and the costs of human losses) and indirect costs (increasing travel distance). If the bridge is open and it does not collapse, there are no costs. The cost of failure when the bridge is closed includes direct costs (the cost of rebuilding the bridge but not the costs of human losses) and indirect costs (increasing travel distance). In case the bridge is closed, and it does not collapse, the costs relate to indirect losses limited to the duration of the emergency phase.

Regarding the likelihood functions modeling the outcome of the vibration-based SHM system, it is highlighted that a range of frequency values corresponds to each damage state and the observations are affected by several sources of uncertainties, as discussed in the previous sections. Assuming that K values of the first natural frequency F_k ($k = 1, 2, \dots K$) correspond to each damage state DS_i , the probability that the vibration-based SHM provides an outcome O_j , when the structure is in a damage state DS_i , $P(O_j|DS_i)$, can be formulated as follows:

Table 3 Cost of bridge failure and survival depending on the selected action

Cost	$A_n = Open$	$A_n = Close$
$c_F(A_n)$	10, 000, 000\$	1, 000, 000\$
$c_{\bar{F}}(A_n)$	0\$	100, 000\$

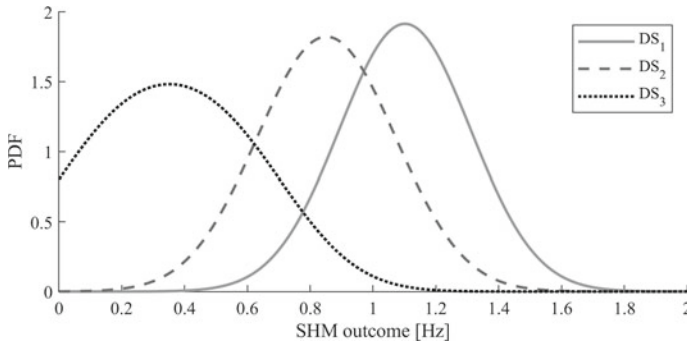


Fig. 1 Likelihood functions

$$P(O_j|DS_l) = \sum_{k=1}^K P(O_j|F_k)P(F_k|DS_l) \quad (20)$$

where $P(O_j|F_k)$ is the probability of observing O_j when the frequency is F_k and $P(F_k|DS_l)$ is the probability that F_k occurs when the structure is in a damage state DS_l . In this case, both the frequency and the observation are continuous variables, thus the integral version of Eq. 20 should be employed. To obtain the likelihood functions, it is assumed that in each damage state the frequency values are uniformly distributed in this case study. The assumed frequency range relevant to DS_1 is 1.0–1.2 Hz, the range relevant to DS_2 is 0.7–1.0 Hz, and the range relevant to DS_3 is 0.0–0.7 Hz. The distribution of the observation of each frequency value is modeled as a Normal distribution centered in correspondence of the frequency value with a standard deviation equal to 0.2 Hz. The resulting likelihood functions are truncated in order to have positive frequency value only, see Fig. 1. Regarding the scour depth monitoring system, the framework of the VoPI is exploited, thereby the modeling of the likelihood functions is not required in this case.

In this application, it is supposed that the reference time for the computation of the VoI is 20 years, the expected number of floods per year λ is 1, $Q_0 = 500\text{m}^3/\text{s}$, the scale parameter of the exponential distribution of flood magnitude is $\nu = 0.0033(\text{m}^3/\text{s})^{-1}$, and the discount rate is $r = 0.01$.

4 Results

The results of the VoI analysis are presented and discussed in this section. Specifically, Fig. 2a displays the expected costs of the two management actions from Prior analysis, i.e., using the prior probabilities of damage states. Both costs increase with increasing flow rate since the probability of being in more severe damage states

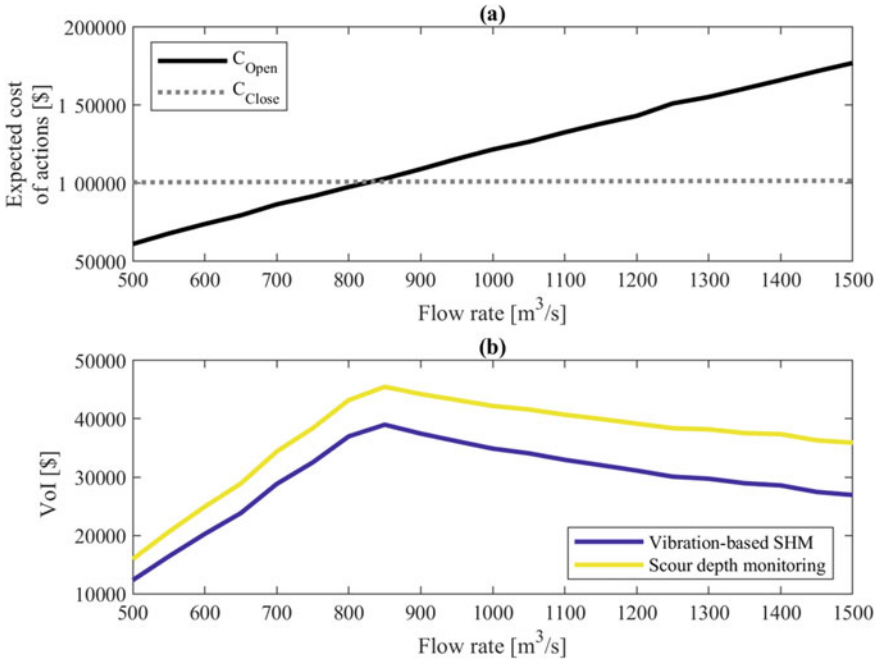


Fig. 2 **a** Expected costs of management actions from Prior analysis; **b** VoI related to different monitoring systems

increases (even if the slope of the line relating to the action “close the bridge” is almost zero). For flow rate values lower than about 800 m^3/s , the optimal action is to leave the bridge open to traffic whereas for higher values of the flow rate the bridge should be closed. Figure 2b shows the VoI as a function of Q for the two monitoring strategies. For the same value of Q , the VoI is higher for scour depth monitoring thanks to the hypothesis of perfect information. The VoI of the two monitoring systems presents a peak in the proximity of the intersection points between the expected management costs in Prior analysis, see Fig. 2a.

Figure 3 indicates which monitoring system should be installed as a function of their Life-Cycle costs. The white dashed lines indicate the maximum Life-Cycle costs for the two monitoring systems. In the yellow area, the scour depth monitoring system should be installed. In the blue area, the vibration-based SHM system should be installed. In the cyan region, no monitoring system should be installed. It is highlighted that in the case where the cost of the two monitoring systems is zero, the scour depth monitoring system should be installed since it provides higher VoI (which in this specific case is equal to the NVoI).

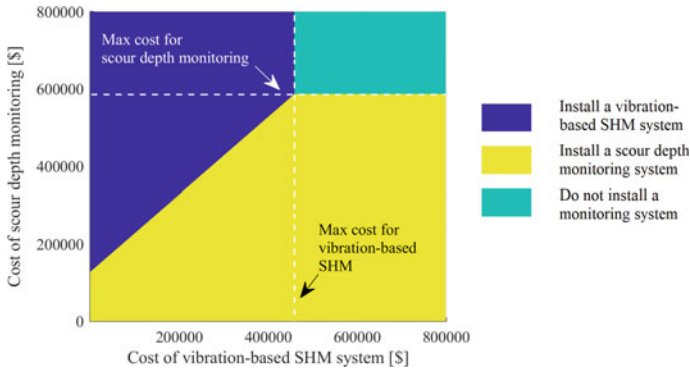


Fig. 3 Selection of the optimal monitoring strategy

5 Conclusions

In this paper, the framework of the VoI from Bayesian decision analysis is described and applied in the context of traffic emergency management of bridges with scoured foundations occurring during flood events. The framework of the VoI accounts for the uncertainty affecting the decision problem (such as the uncertainty in the damage state of the bridge during a flood, the uncertainty in the monitoring outcome, and the uncertainty in the intensity of future flood events) and the Life-Cycle costs of the monitoring systems. The VoI is used to select the best data collection strategy among three possible options, namely: (1) installing a vibration-based SHM system, (2) installing a scour depth monitoring system, and (3) not installing any monitoring system. A sensitivity analysis is carried out showing which is the optimal monitoring strategy as a function of the Life-Cycle costs of the two monitoring systems. It is demonstrated that the VoI can be used to quantify the benefit of a given data acquisition strategy (including the strategy “do not collect additional data”) thereby supporting decision-makers in the optimal allocation of limited financial resources.

Acknowledgements This study was partially funded by the Italian Civil Protection Department within the project WP6-2019-21 ReLUI Project “Structural Health Monitoring and Satellite Data”. The second author wishes to acknowledge the Faculty of Engineering at the University of Nottingham for travel funding to facilitate this collaboration.

References

1. Prendergast LJ, Gavin K (2014) A review of bridge scour monitoring techniques. *J Rock Mech Geotech Eng* 6:138–149. <https://doi.org/10.1016/j.jrmge.2014.01.007>
2. Forde MC, McCann DM, Clark MR, Broughton KJ, Fenning PJ, Brown A (1999) Radar measurement of bridge scour. *NDT E Int.* [https://doi.org/10.1016/S0963-8695\(99\)00026-2](https://doi.org/10.1016/S0963-8695(99)00026-2)

3. Malekjafarian A, Kim C, Obrien EJ, Prendergast LJ, Fitzgerald PC, Nakajima S (2020) Experimental demonstration of a mode shape-based scour monitoring method for multi-span bridges with shallow foundations. *J Bridge Eng* (In Press). [https://doi.org/10.1061/\(ASCE\)BE.1943-5592.0001586](https://doi.org/10.1061/(ASCE)BE.1943-5592.0001586)
4. Foti S, Sabia D (2011) Influence of foundation scour on the dynamic response of an existing bridge. *J Bridge Eng*. [https://doi.org/10.1061/\(ASCE\)BE.1943-5592.0000146](https://doi.org/10.1061/(ASCE)BE.1943-5592.0000146)
5. OBrien EJ, McCrum DP, Khan MA, Prendergast LJ (2021) Wavelet-based operating deflection shapes for locating scour-related stiffness losses in multi-span bridges. *Struct Infrastruct Eng*:1–16. <https://doi.org/10.1080/15732479.2021.1937235>
6. Giordano PF, Prendergast LJ, Limongelli MP (2020) A framework for assessing the value of information for health monitoring of scoured bridges. *J Civil Struct Health Monit* 10:485–496. <https://doi.org/10.1007/s13349-020-00398-0>
7. Raiffa H, Schlaifer R (1961) *Applied statistical decision theory*. John Wiley & Sons, New York (N.Y.)
8. Zonta D, Glisic B, Adriaenssens S (2014) Value of information: impact of monitoring on decision-making. *Struct Control Health Monit* 21:1043–1056. <https://doi.org/10.1002/stc.1631>
9. Straub D (2014) Value of information analysis with structural reliability methods. *Struct Saf* 49:75–85. <https://doi.org/10.1016/j.strusafe.2013.08.006>
10. Zhang W-H, Lu D-G, Qin J, Thöns S, Faber MH (2021) Value of information analysis in civil and infrastructure engineering: a review. *J Infrastruct Preserv Resil* 2:16. <https://doi.org/10.1186/s43065-021-00027-0>
11. Verzobio A, Bolognani D, Quigley J, Zonta D (2021) Quantifying the benefit of structural health monitoring: can the value of information be negative? *Struct Infrastruct Eng* 1:1–22. <https://doi.org/10.1080/15732479.2021.1890139>
12. Giordano PF, Prendergast LJ, Limongelli MP (2020) Impact of climate change on the value of information for bridges at risk of scour. *IALCCE 2020*, 2020
13. Giordano PF, Limongelli MP (2020) The value of structural health monitoring in seismic emergency management of bridges. *Struct Infrastruct Eng* 1–17. <https://doi.org/10.1080/15732479.2020.1862251>
14. Richardson EV, Harrison LJ, Richardson JR, Davis SR (1993) *Evaluating scour at bridges*. Publ. FHWA-IP-90-017, Federal Highway Administration, US Department of Transportation, Washington, DC
15. Ditlevsen O, Madsen H (1996) *Structural reliability methods*. Wiley, Chichester
16. Imam BM, Chryssanthopoulos MK (2012) Causes and consequences of metallic bridge failures. *Struct Eng Int* 22:93–98. <https://doi.org/10.2749/1016866612X13216060213437>
17. NASEM (2007) *Risk-based management guidelines for scour at bridges with unknown foundations*. <https://doi.org/10.17226/23243>
18. Kottegoda NT, Rosso R (2009) *Applied statistics for civil and environmental engineers*. Wiley-Blackwell

Testing, Sensing, and Modeling

Vibration Measurements on a Cable-Stayed Cyclist Arch Bridge for Assessment of the Dynamic Behaviour



Stefan Verdenius, Okke Bronkhorst, and Chris Geurts

Abstract The new cable-stayed arch bridge *Tegenbosch* (Eindhoven, the Netherlands) needed an assessment of its dynamic behaviour under wind loading due to its slender design. Because of wind-induced vibration issues on a number of bridges in the Netherlands with similar designs, it was decided to examine if vortex excitation, wind-rain induced vibration, galloping or parametric excitation might occur. Measurements were performed to determine the natural frequencies and damping ratios of the 32 cables and the deck. All cables were individually assessed, by measuring the vibrations of the cables induced with a step relaxation excitation by pre-tensioning and releasing a lashing strap. The natural frequencies of the cables were determined by evaluating the transfer functions of the measured excitation force and acceleration; damping ratios were obtained with the half-power bandwidth method. To determine the natural frequencies of the deck, 12 accelerometers were placed at different locations on the deck, after which the deck was excited using a 250 kg impact hammer at five locations. The first natural frequency of the cables varied between 2.11 Hz for the longest cable and 8.51 Hz for the shortest cable. The lowest value of the logarithmic decrement for damping found was 0.0059. Based on the damping values, a lowest Scruton number of 58 was determined using NEN-EN 1991-1-4, meaning that vortex excitation will not lead to any problems. Using the measured natural frequencies it is shown that the critical wind velocity for galloping is larger than the occurring wind speed. The same conclusion holds for wind-rain induced vibrations, where the critical velocity is calculated using the natural frequency and the damping value. The lowest horizontal natural frequency of the deck was found to be 0.41 Hz; the lowest vertical natural frequency is 2.05 Hz. Since the natural frequencies of some of the cables coincide with the natural frequencies of the deck, parametric excitation might occur. In case parametric excitation is indeed a problem in practice, it is advised to add extra damping to the system.

Keywords Cable-stayed bridge · Wind-induced vibrations · Natural frequency · Damping · Parametric excitation

S. Verdenius (✉) · O. Bronkhorst · C. Geurts
Unit Building, Infrastructure and Maritime, TNO, Delft, The Netherlands
e-mail: stefan.verdenius@tno.nl

© The Author(s), under exclusive license to Springer Nature Switzerland AG 2023
Z. Wu et al. (eds.), *Experimental Vibration Analysis for Civil Engineering Structures*,
Lecture Notes in Civil Engineering 224,
https://doi.org/10.1007/978-3-030-93236-7_12

1 Introduction

The city of Eindhoven in The Netherlands has developed a new cable-stayed bridge for bicycles, named *Tegenbosch*. This bridge has a span of 132 m and a width of only 6 m, resulting in a slenderness of 22. Due to its slender design, an assessment of the dynamic behaviour of the bridge was needed to verify that vibrations of the hangers would not occur, as was the case for the *Erasmusbridge* (Rotterdam) and the *Hovenring* (Eindhoven) where vibrations possibly led to fatigue damage [1, 2]. In the case of the *Erasmusbridge*, a number of cables started to vibrate a few months after the opening of the bridge due to a combination of wind and rain. A number of possible measures was examined, such as coupling of the cables (leading to a shorter vibrating length and thus resulting in higher natural frequencies and more damping) and adaptation of the cable surface (to prevent water streams along the length of the cable). After careful consideration it was decided to add two dampers to each cable, which removed the vibration problem. At the *Hovenring*, a ‘floating’ circle-shaped bicycle bridge, vibrations due to wind occurred shortly after opening. Due to its circular shape wind is always unfavourable for one or more cables. As a temporary measure, cables were coupled. Also for the *Hovenring* the permanent solution was found in adding dampers.

Based on these experiences, it was decided to perform an experimental campaign before the opening of the cyclist bridge *Tegenbosch*. These measurements had as goal to assess whether vibrations might occur due to vortex excitation, galloping, the combination of rain and wind, and parametric excitation, thereby allowing the asset owner to take measures if needed.

2 Assessment of Wind-Induced Bridge Vibrations

Wind-induced vibrations in bridges can be caused by different phenomena:

- Vortex excitation
- Galloping
- Wind-rain induced vibrations
- Parametric excitation

This section describes these phenomena and discusses guidelines which can be used for their assessment. Vortex excitation can lead to vibrations when, due to wind blowing across a structural member such as a cable, vortices are shed alternately from one side to the other, whereby alternating low-pressure zones are generated on the downwind side of the structure giving rise to a fluctuating force acting at right angles to the wind direction [3]. To prevent vortex excitation, NEN-EN 1991-1-4 [4] specifies that the critical wind speed needs to be larger than 1.25 times the 10 min average wind speed v_m for the area of interest:

$$\frac{bn}{S_t} > 1.25v_m \quad (1)$$

In Eq. (1) b is the cable diameter, n is the natural frequency of the cable and S_t is the Strouhal number. In case the critical wind speed is lower than 1.25 times the average wind speed v_m , which is for instance the case when natural frequencies are low, a second equation is given in NEN-EN 1991-1-4 to determine to what extent vortex excitation can occur. Hereto the Scruton number S_c is determined:

$$S_c = \frac{2\delta m_{i,e}}{\rho b^2} \quad (2)$$

In Eq. (2) $m_{i,e}$ is the equivalent mass of the cable per length, ρ the density of the air and δ the logarithmic decrement of damping. The equivalent mass can be determined according to Appendix F.4 from NEN-EN 1991-1-4. Since the cables from bridge *Tegenbosch* have a constant mass over the complete length of the cable, $m_{i,e}$ can be taken equal to the mass per length. While no minimum value for the Scruton number is given in NEN-EN 1991-1-4, research from Hansen [5] and Grala et al. [6] shows that excitation is limited if the Scruton number is larger than 20.

Galloping is the vibration of a flexible construction perpendicular to the wind direction. For galloping to occur, the cross section of the construction must be asymmetric. In general galloping will not occur for hangers, because they have symmetric cross sections. However, when ice is attached to the surface of the cable the cross section can be asymmetric and galloping can occur. Galloping has been observed on in-service bridges and has been reproduced in several wind tunnel experiments, e.g. [7, 8]. For galloping to occur, NEN-EN 1991-1-4 specifies that the critical wind speed must be larger than 1.25 times the average wind speed v_m :

$$2S_c nb/a_G > 1.25v_m \quad (3)$$

The starting wind speed as formulated in Eq. (3) is dependent on the Scruton number S_c (and thus on the damping δ and equivalent mass per length $m_{i,e}$ of the cable), the natural frequency of the cable and the diameter of the cable. The parameter a_G is an instability factor, given in table E.7 from NEN-EN 1991-1-4.

A third phenomena is related to the combination of wind and rain, leading to vibrations of the cables. No guidelines for these vibrations are given in NEN-EN 1991-1-4, but a model is given in the research of Berkel [9]. In this research it is stated that for these vibrations to occur it must be raining, and the occurrence depends on the critical wind speed:

$$v_{crit} = \frac{4n\delta m}{-\rho b C_{y,1}} \quad (4)$$

The critical wind speed is again dependent on the natural frequency of the cable n and the damping of the cable δ . The cable diameter b and mass per length m also

play an important role. The coefficient $C_{y,1}$ in Eq. (4) is the first derivative of the lift coefficient, taken equal to 0.86. The critical wind speed must be between 10 m/s and 18 m/s for these vibrations to occur. Lower wind speeds do not excite the cable, and higher wind speeds blow the rain of the cable. Wind-rain induced vibrations only occur if the cable is placed under an angle of 20 to 60 degrees and if the surface is smooth, so that the rain water can flow along the cable. This flow of water can then, due to the wind, create two streams of water that influence the air flow around the cable.

Parametric excitation is the phenomena that the cables resonate with the deck, see e.g. [10, 11]. This occurs if the natural frequency of a cable is equal or close to the natural frequency of the deck. NEN-EN 1993-1-11 [12] states that the natural frequency of the cables should be more than 20% higher or lower than the natural frequency of the deck to prevent parametric excitation. This can either be achieved by changing the natural frequencies by adapting the construction, or the excitation can be suppressed by adding dampers to either deck or cables.

Concluding, it can be stated that to assess these four phenomena the natural frequencies of cables and deck must be known, as well as the damping of the cables. To determine these dynamic characteristics of the bridge *Tegenbosch* a measurement campaign was performed which is described in the next section.

3 Measurement Setup

3.1 Bridge *Tegenbosch*

The bridge *Tegenbosch*, shown in Fig. 1, consists of a 21 m high arch which supports the deck with 32 cables. The cables are M64 S460 Macalloy bars, with a mass of 22.2 kg/m, varying in length from 8.76 m to 24.77 m. Due to the length of the cables in combination with the limited length of the bars, all cables consisted of two or three rigidly coupled bars. The planned force in the cables ranges from 295 to 400 kN.

3.2 Cables

Vibration measurements were performed on all 32 cables to determine the natural frequencies and damping ratios. All cables were assessed one by one; Fig. 2a and b show pictures of the measurement setup for one cable. For each measurement, four Sundstrand QA700 accelerometers (range of 30 g) were used, placed at two locations along the length of the cable to prevent loss of data in case one of the measurement locations is in a node of the cable. At each location, one accelerometer measured vibrations parallel to the bridge (x-direction); the other accelerometer measured perpendicular to the bridge (z-direction). Once the accelerometers were



Fig. 1 Bicycle bridge Tegenbosch [13]

attached to the hanger, a lashing strap was used to pretension the cable in a direction of 45 degrees with respect to the x - and z -direction, see Fig. 2c. An HBM U9C load cell (range of 5000 N) was used to determine the tension in the lashing strap. After pre-tensioning the strap to 1000 N, the strap was released and the cable was left to vibrate for almost one minute. This process was repeated five times per cable, while continuously monitoring the accelerations of the cable.

3.3 Deck

To measure the natural frequencies of the deck, 12 Sundstrand QA700 accelerometers were placed on the deck at multiple positions, as depicted by the numbers in Fig. 3. The red dots indicate accelerometers measuring in vertical direction only; the green dots indicate locations where accelerometers measure in both vertical and horizontal (z -) direction. The letters A to E in Fig. 3 indicate the excitation positions. The exact locations of the accelerometers and excitations are listed in Table 1. The excitation locations were chosen such that the fundamental modes of the deck are excited appropriately. Note that the accelerometers were positioned such that they are not exactly in a node ($1/2L$, $1/3L$ or $1/4L$ with L being the length of the bridge). At each excitation location listed in Table 1 the deck was excited five times, while continuously measuring the accelerations at all locations. The deck was excited using a movable 250 kg impact hammer as shown in Fig. 2d. To introduce enough

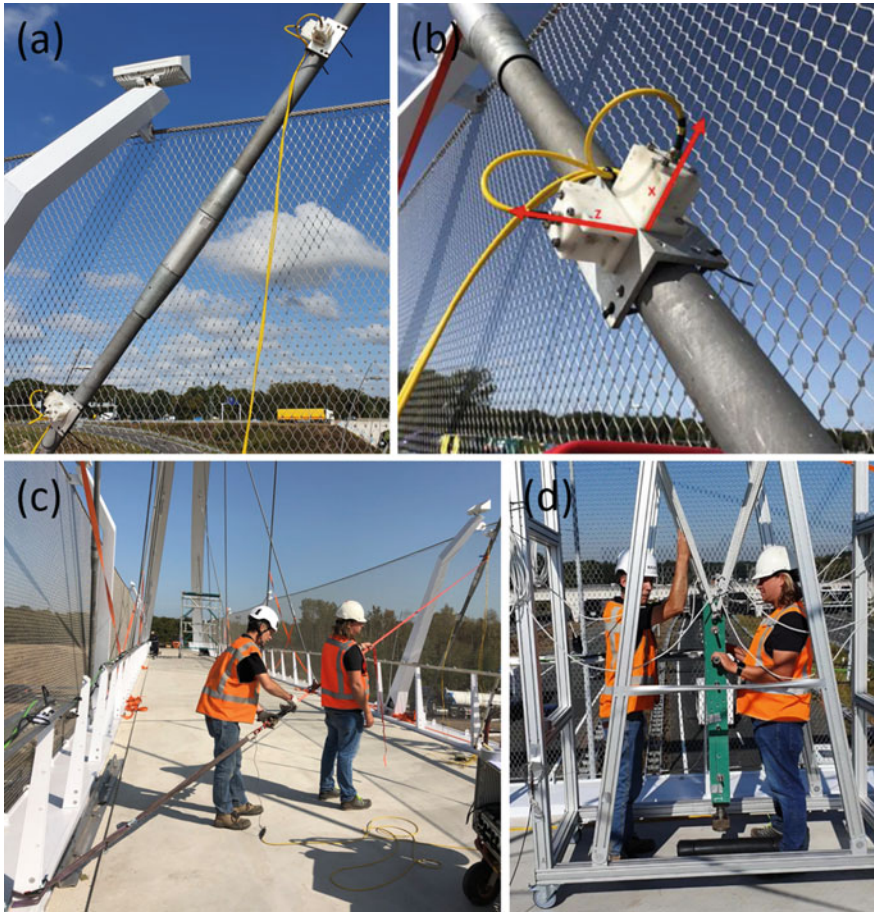


Fig. 2 Pictures of the setup of the measurements: **a** Two measurement positions along the length of the cable, **b** at each location two accelerometers were placed, measuring in two directions. **c** The step-relaxation excitation of the cables was realised with a lashing strap. **d** The deck was excited with a 250 kg impact hammer

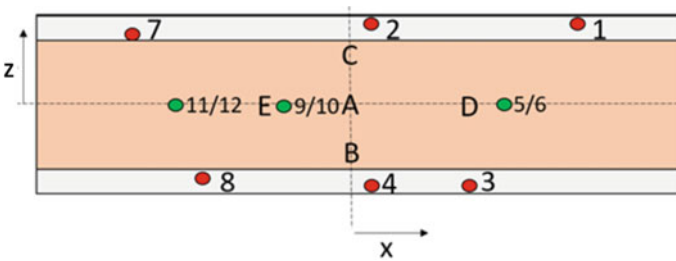


Fig. 3 Numbered locations of the accelerometers on the bridge deck measuring in two directions (green) and vertical direction only (red). The letters A to E indicate the excitation locations

Table 1 Positions of the accelerometers and excitation locations

Accelerometer	X [m]	Z [m]		Excitation	X [m]	Z [m]
1	42	2.8		A	0	0
2	5	2.8		B	0	-1.2
3	25	-2.8		C	0	1.2
4	5	-2.8		D	25	0
5/6	30	0		E	-10	0
7	-45	2.4				
8	-30	-2.4				
9/10	-10	0				
11/12	-35	0				

energy in the low frequency range, rubber slabs were placed on top of the deck. The impact of the hammer on the deck was measured using a piezoelectric Kistler load cell with a range of 60 kN. After the deck was excited five times with the hammer at all five locations, an additional measurement was done by measuring the natural vibration of the deck for 10 min (without excitation).

4 Data Evaluation

To determine natural frequencies and damping of the cables, the measured accelerations of the cable and the force in the lashing strap were evaluated. As an example both signals are shown synchronous in time in Fig. 4 for one accelerometer at one cable for all five consecutive excitations. Data was sampled with a rate of 500 Hz and filtered with an 8th order Butterworth-filter with a cut-off frequency of 30 Hz. In Fig. 4 the different stages of the step-relaxation excitation (tightening the strap, releasing the strap and free vibration of the cable) can clearly be distinguished. The upper figure shows the force in the lashing strap, the lower figure shows the acceleration of the cable.

The individual excitations are indicated in Fig. 4 using red lines as the start of the excitation (releasing the lashing strap) and black lines as the end of the cable vibration and the start of a new excitation by tensioning the lashing strap. Only the time segments between the red and black lines were used for data evaluation; the period of tightening the lash is thus not evaluated. Each accelerometer of each cable was assessed individually.

All five segments from Fig. 4 were combined into one continuous signal, and the transfer function of the applied force in the lashing strap and the measured acceleration was determined. The transfer function was determined using the built-in Matlab Fourier Transform function 'tfestimate' in combination with a Hanning window. The resulting spectral image of one accelerometer of one cable is shown in Fig. 5a, in

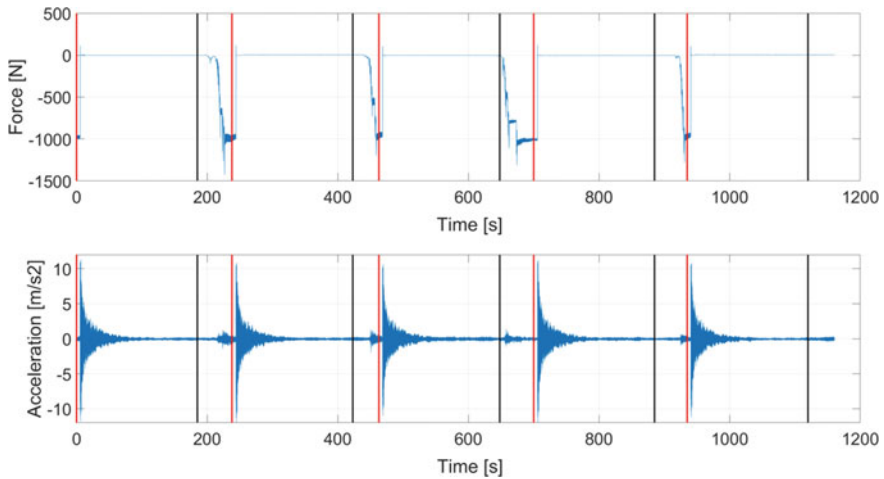


Fig. 4 Example of the registered excitation force (top) and acceleration (bottom) at one cable as an effect of five consecutive excitations

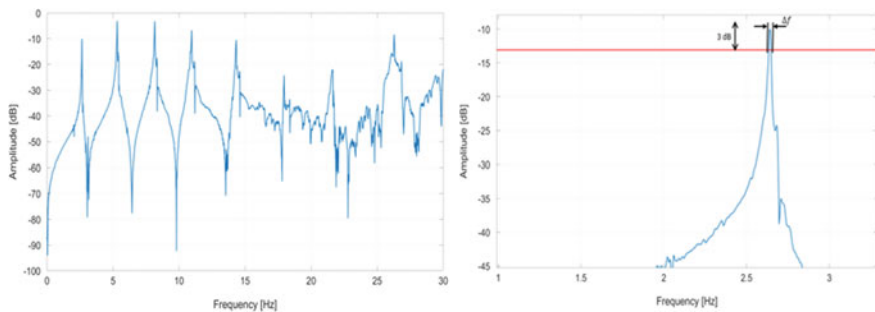


Fig. 5 Example of a transfer function for one accelerometer of one cable: **a** Visualization of the first natural frequencies. **b** Detailed depiction of determining Δf , the width of the transfer function at a magnitude of 3 dB below the peak of the transfer function

which the individual natural frequencies can clearly be distinguished as peaks in the amplitude. Transfer functions were determined for all four accelerometers individually. For some hangers slightly differing natural frequencies were found for the x- and z-direction. Although these differences were very small (on average around 1%), assessment took place on the results of both the x- and z-direction.

A similar procedure was followed to determine the natural frequencies of the deck. For each excitation position (A to E) individual transfer functions were determined for each accelerometer. On top of this, the natural frequencies of the deck in case of no excitation (the ‘freerun’) were determined by taking the Fourier Transform of the measured accelerations only.

Damping of the cables was determined by applying the half-power bandwidth method to the spectral representation of the transfer function [14]. Since the amount of damping might differ per mode, the logarithmic decrement of damping δ was determined for each of the lowest three frequencies by using Eq. (5):

$$\delta = \frac{2\pi}{\sqrt{\frac{Q^2}{0.25} - 1}} \quad (5)$$

The parameter Q in Eq. (5) is determined by dividing the natural frequency f_e by the width of the transfer function Δf at a magnitude of 3 dB below the magnitude of the natural frequency, as schematically depicted in Fig. 5b.

5 Results

5.1 Natural Frequencies and Damping Values

Natural frequencies and logarithmic damping decrements of all cables were determined to assess if vibrations would take place. The first natural frequency ranged from 2.11 Hz for the longest cable to 8.51 Hz for one of the shortest cables. The lowest value of the logarithmic decrement of damping δ was found to be 0.0059; the highest value was 0.1292. In the design of the bridge, a logarithmic decrement of a minimum of 0.0063 was assumed based on the experience from previous projects (*Hovenring*). For the 192 natural frequencies that are examined, only one value (0.0059) was marginally below this minimum.

Regarding the results of the deck, it was found that the freerun lead to the lowest horizontal natural frequency (0.41 Hz) which was not found when using the impact hammer (0.80 Hz). The first vertical natural frequency was 2.05 Hz, found at all excitation positions (including freerun).

5.2 Dynamic Phenomena

Using Eq. (1) in combination with a cable diameter b of 60 mm, a Strouhal number S_r of 0.18 and an averaged wind speed v_m of 25.7 m/s (wind area III, open surrounding and a reference height of 30 m), the first natural frequency of the cables should be larger than 90 Hz for vortex excitation not to occur. Since this condition is not met, it was examined to what extent vortex excitation could occur. Hereto the Scruton number S_c is determined through Eq. (2). When using the lowest value of the logarithmic decrement found (0.0059), a Scruton number of 58 was calculated. It is thus shown that the criterium $S_c > 20$ by Hansen [5] regarding vortex excitation is met.

The starting wind speed for galloping is calculated using Eq. (3), with a value of 1.0 for a_G as listed in table E.7 of NEN-EN 1991-1-4. When solving Eq. (3) for each cable individually with its corresponding Scruton number and lowest natural frequency, a minimum starting wind speed of 37 m/s is found. Since this wind speed is more than 1.25 times the average wind speed v_m (25.7 m/s) no galloping will occur.

For rain-wind vibrations to occur, the wind speed as defined in Eq. (4) must be between 10 and 18 m/s. When determining the critical wind speed v_{crit} for the situation of bridge *Tegenbosch*, a minimum wind speed of 43 m/s is found, which is more than twice the wind speed at which vibrations due to rain and wind are found to occur.

The condition regarding parametric excitation cannot be met, since multiple natural frequencies of the deck coincide with one or more cables. For example, the natural frequency of 2.05 Hz of the deck is very close to the lowest natural frequency of the cables (2.11 Hz), meaning that parametric excitation might occur. Since all cables have different natural frequencies, it is unlikely that parametric excitation of the full deck will occur. However, in case parametric excitation does turn out to be a problem in practice, additional damping could be added to the system as was for example done for the *Erasmusbridge*.

6 Conclusions

All 32 cables of the cable-stayed bridge *Tegenbosch* were assessed to determine if vortex excitation, wind-rain induced vibrations or galloping would take place. To this end, each cable was individually excited using a lashing strap, whilst measuring the acceleration in two directions. Evaluating the transfer function of the applied force and the measured acceleration in the frequency domain led to the natural frequencies and logarithmic decrement of damping per cable. For all cables it was found that theoretically neither vortex excitation, nor wind-rain induced vibrations or galloping would occur. In a similar way the vibration of the deck was measured using an impact hammer, from which the natural frequencies of the deck were determined. Since these natural frequencies coincide with the natural frequencies of some of the cables, parametric excitation might occur. However, since all cables have different natural frequencies, it is unlikely that parametric excitation of the full deck will occur. In case parametric excitation turns out to be a problem in practice, additional damping could be added to the system to temper the vibration.

Acknowledgements The authors would like to thank the experimental team of TNO that performed the measurements on the bridge, being Erik Slijs, Peter van der Meer and Ron Lautz. Special thanks goes to Henri Steenberghe for helping in the evaluation of the data. Finally the authors would like to thank the city of Eindhoven for their help and assistance in the measurements.

References

1. Reusink JH, Zwarte dempers houden tuien definitief in bedwang, Bouwen met staal 137, July 1997
2. Fietsrotonde Hovenring Eindhoven afgesloten: kabels op knappen – foto's en video, Omroep Brabant, January 2012
3. Fu F (2018) Design and analysis of tall and complex structures. Butterworth-Heinemann
4. NEN-EN 1991-1-4+A1+C2, Eurocode 1: Belastingen op constructies – Deel 1-4: Algemene belastingen – Windbelastingen, December 2011
5. Hansen SO, Vortex-induced vibrations of structures, Structural Engineers World Congress 2007, November 2007
6. Grala P, Loredó-Souza AM, Rocha MM, A comparison study between seven procedures to predict vortex-induced vibrations on industrial chimneys, Revista Sul-Americana de Engenharia Estrutural, August 2018
7. Yamauchi K, Uejima H, McTavish S, Larose G (2016) Effects of a helical fillet on the wind-induced response of bridge cables in dry conditions. In: Proceedings of the 8th international colloquium on bluff body aerodynamics and applications
8. Cheng S, Larose G, Savage M, Tanaka H, Irwin P (2008) Experimental study on the wind-induced vibration of a dry inclined cable – part I: Phenomena. J Wind Eng Ind Aerodyn 96
9. van Berkel P, van der Veen C, Noorlander K (2000) Trillingen in tuibruggen door regen en wind, Cement
10. Sun BN, Wang ZG, Ko JM, Ni YQ (2003) Parametrically excited oscillation of stay cable and its control in cable-stayed bridges. J Zhejiang Univ
11. Pinto da Costa A, Lilien J (1994) Parametric excitation of cables of cable-stayed bridges. In: International conference A.I.P.C.-F.I.P
12. NEN-EN 1993-1-11+C1, Eurocode 3: Ontwerp en berekening van staalconstructies – Deel 1-11: Ontwerp en berekening van op trek belaste componenten, December 2011
13. www.meerhoven.nl
14. Papagiannopoulos GA, Hatzigeorgiou GD, On the use of the half-power bandwidth method to estimate damping in building structures, Soil Dynamics and Earthquake Engineering 31, March 2011

Experimental and Numerical Characterization of the Dynamic Behaviour of a Historic Suspension Footbridge



Elyas Bayat and Federica Tubino

Abstract This paper investigates the dynamic characteristics and behavior of a historic suspension footbridge through experimental and numerical studies. Ambient vibration tests were performed on the footbridge to extract the modal parameters of the structure such as natural frequencies, damping ratios, and mode shapes. The modal properties were identified from ambient vibration tests adopting the Stochastic Subspace Identification (SSI) technique. The availability of a numerical model reproducing accurately the dynamic characteristics of the footbridge is essential to carry out numerical studies on the footbridge under different dynamic loading scenarios. Due to the lack of the original technical drawings of the footbridge, a geometrical survey was carried out in order to determine the geometric characteristics of the structural elements. Furthermore, the deformed configuration of the main cable under dead load was experimentally measured during the field survey. The results of field vibration tests were used to calibrate and validate the numerical model of the footbridge, e.g., boundary conditions, and initial cable tension. The present study reports the results of the geometrical survey, of the operational modal analysis, and of the numerical modeling of the footbridge. Moreover, the 3-D Finite Element Model of the footbridge and its calibration with respect to ambient vibration tests are reported. After calibration of the finite element model, a good agreement was observed between computed and measured natural frequencies and mode shapes.

Keywords Ambient vibration tests · Finite element modeling · Modal identification · Suspension footbridges · Geometrical nonlinearity

1 Introduction

Suspension bridges have been widely utilized from ancient times until now due to their advantages to build long, light, and slender bridges. There are many suspension bridges in the world built in the 19th Century that are still in use (see, e.g. [1–4]).

E. Bayat (✉) · F. Tubino

Department of Civil, Chemical and Environmental Engineering, University of Genoa, Genoa, Italy
e-mail: elyas.bayat@edu.unige.it

© The Author(s), under exclusive license to Springer Nature Switzerland AG 2023
Z. Wu et al. (eds.), *Experimental Vibration Analysis for Civil Engineering Structures*,
Lecture Notes in Civil Engineering 224,
https://doi.org/10.1007/978-3-030-93236-7_13

137



Fig. 1 Different views of the footbridge

These bridges as historical structures have usually uncertain conditions regarding their current structural properties and serviceability for the loading scenarios. This is due to the fact that these bridges were designed based on loads and methods that might be different from the current service loads and approaches that are used to design new suspension footbridges. For instance, the Ramello footbridge (Fig. 1) that was completed in 1954 and located in the countryside of La Spezia in Italy, has been still employed for crossing pedestrian and light vehicular traffic until 2019. To continue using this historic footbridge, it is essential to investigate its current structural properties to ensure current serviceability condition of the footbridge against dynamic loadings. The dynamic characteristics of the footbridge such as natural frequencies, mode shapes, and damping ratios can be estimated experimentally by using modal identification techniques [3]. These dynamic properties serve as a basis to build a reliable Finite Element Model (FEM) of the footbridge for further analytical studies such as vibration serviceability assessment of the footbridge under human and wind loadings [5]. Ambient vibration testing is a very common technique to identify modal parameters, particularly for historic structures since it does not require excitation equipment. However, in the case of ambient vibration testing, only the response of the structure is measured and the loading condition is unknown [4]. Therefore, a modal parameter identification technique such as Peak Picking (PP), Frequency Domain Decomposition (FDD), Stochastic Subspace Identification (SSI), should be used to perform an operational modal analysis on the output measurement data to extract modal parameters of the structure [6]. The present paper aims to describe the dynamic characterization of the Ramello footbridge in several tasks. Firstly, field surveys that have been conducted on the footbridge to estimate geometric properties of the footbridge are described. Secondly, the details of four ambient vibration tests

with different measurement setups performed on the footbridge are reported. Then, the identified modal parameters of the footbridge from operational modal analysis using the SSI technique are presented. Finally, a 3D FE model for the footbridge is developed and the numerically-obtained dynamic properties are compared with those derived from operational modal analysis.

2 Description of Footbridge

The Ramello suspension footbridge, shown in Fig. 1, that was built in 1954, is located in the countryside of La Spezia in Italy and crosses over the Vara River. As the design information concerning the geometry and material properties of structural elements was not available, some field inspections were performed on the footbridge to obtain the geometrical properties of the structure using station theodolite and vernier caliper. According to conducted field surveys, the geometric properties of the footbridge and its elements can be described as shown in Fig. 2. The suspension footbridge has a single span with a length of 90 m and a width of 2.28 m. The footbridge comprises two main suspended cables which connect two reinforced concrete pylons from one side of the river to the opposite side. The pylons have a height of 8.2 m with respect to the bridge deck that provide a cable sag of 7.05 m at the middle of the footbridge span. The ends of main cables are anchored into the ground at distances of 7.9 m and 7.2 m from the left and right pylons, respectively, as shown in Fig. 2. Each main cable is composed of three individual spiral strands with a nominal diameter of 4 cm and 61 galvanized steel wires per strand in each cable plane. There are 89 hangers made of rolled steel with a C-shaped cross-section to connect the main cables to the steel floor beams with a step of one meter. The bridge deck as shown in Fig. 3, includes a grid of steel floor beams and stringers, and timber planks. The transverse and longitudinal timber planks which have a square cross-section with dimensions around 80 mm, are used to provide more connection surfaces with steel floor beams to convey pedestrian loads as well as providing a walking surface for the pedestrians. The bridge deck consists of two rolled steel stringers with I-shaped cross-sections that have a center-to-center distance of 1.78 m from each other. In addition, 89 rolled steel floor beams with an I-shaped cross-section with lengths of 2.4 m are used in the bridge deck to transmit the loads from the deck to the hangers. Concerning the connection between stringers and floor beams, a welded connection is used to link the bottom flanges of stringers to the top flanges of floor beams. The ends of floor beams are directly joined to the bottom ends of hangers by using bolted connections;

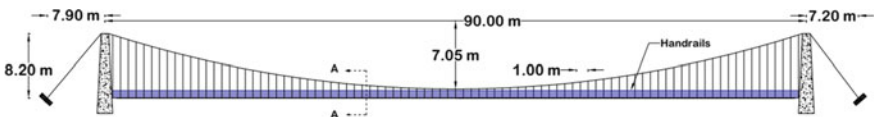


Fig. 2 Elevation of the footbridge

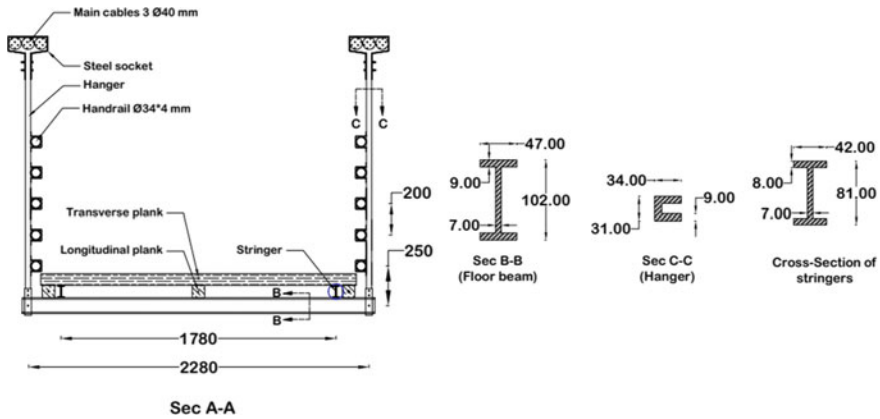


Fig. 3 Cross section and dimensions of the footbridge structural elements (in mm)

while the other ends of hangers are connected to the main cables by using bolted connections and steel sockets which keep the cables in contact with each other and avoid any relative displacements of cables. Handrails of the footbridge are made of circular hollow steel sections and connected to the hangers with joints that are able to restrain the relative translational movement between the handrails and the hangers in the vertical direction. More details regarding the dimensions of the footbridge elements which were obtained through the field survey are shown in Figs. 2 and 3. It should be noted that the tension force of main cables was not measured during the field tests and it is considered as an unknown parameter in the present study that will be estimated in the next sections using Finite Element (FE) modeling of the footbridge.

3 Ambient Vibration Testing

Field dynamic testing of structures such as ambient vibration tests can provide accurate and reliable data regarding current dynamic characteristics of structures. As shown in Fig. 4, four ambient vibration tests with different measurement setup arrangements were carried out on the footbridge to identify its dynamic characteristics. The first measurement setup arrangement for ambient vibration test was implemented for the footbridge in January 2019; while the other measurement setups were carried out in January 2021 to identify more in detail the mode shapes of the footbridge. Since the footbridge is a symmetric structure and also the first two ambient test setups have shown symmetric dynamic behaviour of the structure, the accelerometers in the third and fourth ambient tests were mounted only on one-half the footbridge deck to extract more precisely the vertical mode shapes of the bridge

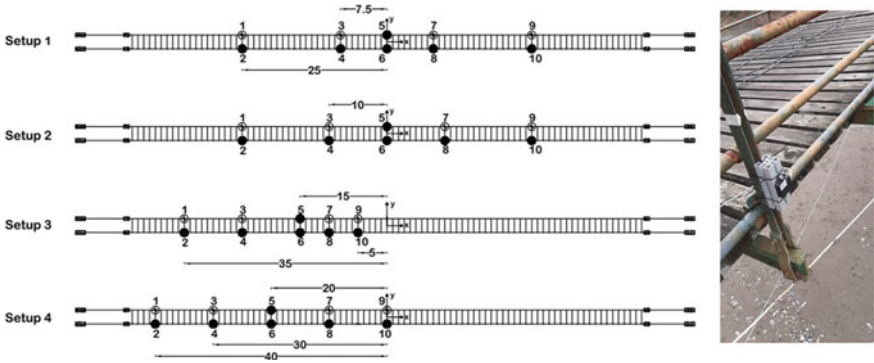


Fig. 4 Layout and location of accelerometers along the bridge deck for different measurement setups

deck. Ambient vibration tests were performed on the footbridge deck using a 14-channel data acquisition system with 10 low-cost MEMS triaxial accelerometers that are able to measure accelerations in $\pm 6g$ range with a sensitivity of $333mV/g$ and a nominal 0–200 Hz bandwidth. The dynamic response of the footbridge was measured at 10 different locations in each measurement setup including measurement of only vertical acceleration of all the locations and transverse accelerations of four locations (locations 1, 3, 7, and 9). In each measurement setup, the ambient vibrations were simultaneously recorded for one hour. Furthermore, the acceleration response was recorded with a sampling frequency of 500 Hz. As shown in Fig. 4, all the accelerometers were mounted on the hangers, close to the joint between floor beams and hangers.

4 Modal Identification of the Footbridge

The modal identification was carried out on the obtained raw data from ambient vibration tests using the Stochastic Subspace Identification (SSI) technique [7]. The data processing and modal identification were performed by using MACEC that is a MATLAB-based toolbox [8]. The order N of a structure’s model is usually selected in a wide range to construct a reliable stabilization diagram that allows recognizing the real structural modes (from noise modes) whose properties do not vary considerably for different model’s order. In the present study, stochastic state-space models are identified for different orders of the footbridge’s model, ranging from 2 to 200 for the data set of the first setup and 2 to 100 for the data set of the other setups, with an increment of 2. Figure 5 plots the extracted stabilization diagrams by applying the SSI technique to the obtained dataset from each measurement setup to identify stable modes. Furthermore, the power spectral density functions of the measured

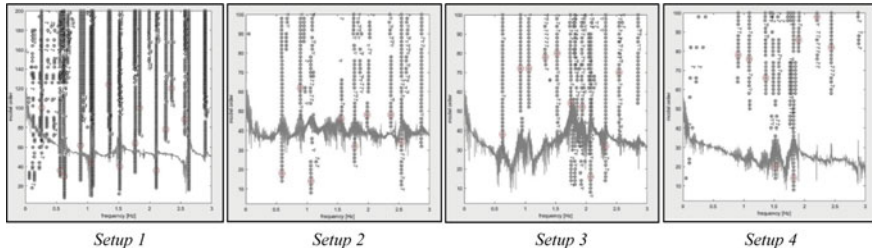


Fig. 5 Stabilization diagrams produced by using SSI method for 1–4 test setups

accelerations are superimposed on the stabilization diagrams, confirming that the identified poles correspond to peaks in the acceleration spectra.

Table 1 and Fig. 6 report, respectively, the natural frequencies and damping ratios and mode shapes of 11 natural vibration modes, that were identified by combining and averaging the obtained results from the implemented modal identification technique for different setups. The natural frequencies of identified mode shapes in the frequency range of 0.25–2.6 Hz are reported, that are of interest for possible vibration serviceability assessment of the footbridge in the vertical direction under walking load. Indeed different researches [9] have shown that the normal walking frequency of pedestrians is in the range of 1.6–2.4 Hz. The detected natural mode shapes of the footbridge include one Lateral mode (L), two Torsional modes (T), and eight Bending (B) modes that have Symmetric (S) or Asymmetric (A) shapes. According to Table 1, it can be seen that the identified frequencies greater than 1 Hz are quite stable and reliable since these frequencies were found in most of the vibration measurements. On the contrary, some modes were not consistently identified from all the measurement setups: this circumstance can be due to the fact that these modes were not significantly excited in some ambient tests. For instance, the first two modes were identified only from test setup 1 that was carried out on a different day with respect to setups 2–4. In addition, most identified modal parameters are related to bending modes in the vertical plane, showing that the lateral and torsional modes were not considerably excited in ambient vibration tests.

5 Finite Element Modeling of the Footbridge

In the present study, a 3D finite element model of the footbridge has been developed using ANSYS software [10] to conduct the numerical modal analysis of the footbridge. The model was built based on the geometry and structural properties measured from the field surveys and then updated according to obtained results from ambient vibration tests. Within the ANSYS code, the cables were modelled using the 3D spar element “LINK180” that is a uniaxial tension–compression element with three degrees of freedom at each node. According to technical data [11], the effective steel area, density, modulus of elasticity and Poisson’s ratio of each spiral strand was

Table 1 Identified modal parameters using SSI-DATA

Mode	Mode shape	Setup/test	Frequency (Hz)	Damping ratio (%)	Mode	Mode shape	Setup/test	Frequency (Hz)	Damping ratio (%)
1	L-S	1	0.259	2.051	7	B-S	1,2,3,4	1.531	1.730
2	B-A	1	0.560	2.462	8	B-A	1,2,3,4	1.803	1.946
3	B-S	1,2,3	0.612	3.040	9	B-S	1,2,3,4	1.980	1.050
4	T-A	3	0.922	3.600	10	B-A	1,2,3,4	2.310	0.766
5	T-S	1,2,3	1.062	2.500	11	B-S	1,2,3,4	2.520	0.177
6	B-A	1,3,4	1.344	2.160					

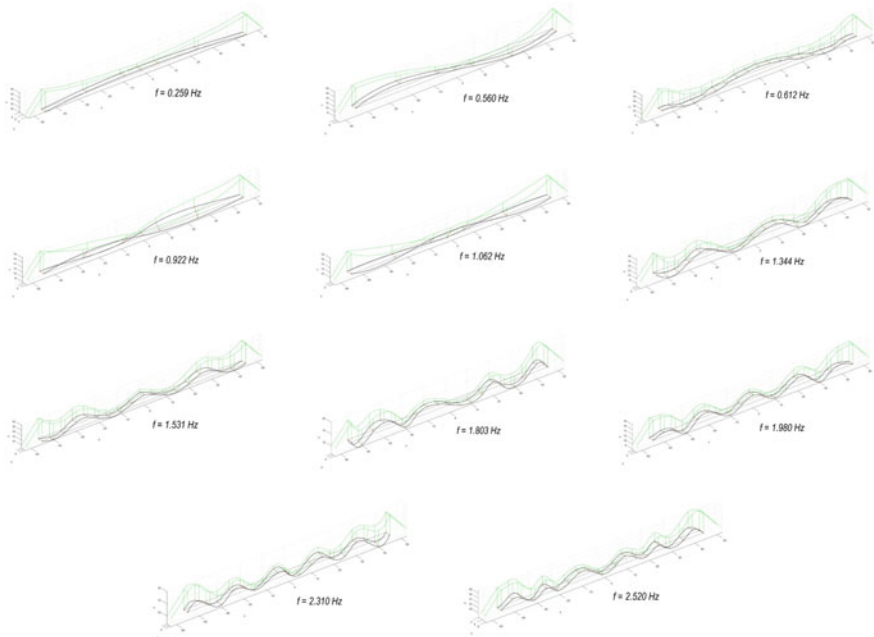


Fig. 6. 3D representation of identified mode shapes using SSI technique

taken as 940mm^2 , 8300kg/m^3 , 135GPa and 0.3 , respectively. Furthermore, the floor beams, stringers, and hangers were modelled using the 3D elastic beam element “BEAM 4” with six degrees of freedom per node that can be subjected to tension, compression, torsion, and bending. The modulus of elasticity and density for these structural elements were assumed as 210GPa and 7850kg/m^3 , respectively. The timber boards and handrails were assumed as nonstructural elements with considering their weights in the dead loads and their effects on the dynamic properties as lumped masses applied on the steel grid and hangers, modelled with the concentrated mass element “MASS 21”. The values of density for timber boards and handrails were taken as 700kg/m^3 and 7850kg/m^3 , respectively. Modeling of pylons was ignored with assuming high stiffness at the pylon saddles and the pylons were considered as a boundary condition for the cables; therefore, the cables were allowed to have only longitudinal sliding over the pylons. The anchor blocks have not been modelled and it was assumed that the ends of cables were restrained to the ground by pinned supports. According to Fig. 7, in the finite element modeling, it was assumed that the main cables were hinged to the hangers and floor beams. The bottom flanges of stringers were connected to the top flanges of floor beams with fixed joints and also the ends of stringers were fixed to the ground. A nonlinear static analysis (considering P-delta effect along with large deformation effect) was performed to estimate initial tension of main cables which has a significant effect on initial configuration and total stiffness of the footbridge [1, 12]. According to the finite element model, the



Fig. 7 Representation of boundary conditions of structural elements

initial tension in the main cables was obtained about 189 KN based on trial-and-error procedure to reach a convergence of the possible minimum vertical deflection for different points of the bridge deck. Following the completion of footbridge modeling in ANSYS, including geometry, materials, elements, cross sections, boundary conditions and applied loadings, modal analyses was performed on the footbridge model to extract dynamic properties of the structure. It should be mentioned that the modal analysis was conducted after the nonlinear static analysis of the footbridge, subjected to the dead loads and pretension of the cables, in order to determine the geometric tangent stiffness matrix which is used in the modal analysis. The general view of FE model of the footbridge is shown in the Fig. 8 and the natural frequencies of the first twenty modes obtained from FE modeling are summarized in Table 2.

Fig. 8 General view of finite element model of the footbridge

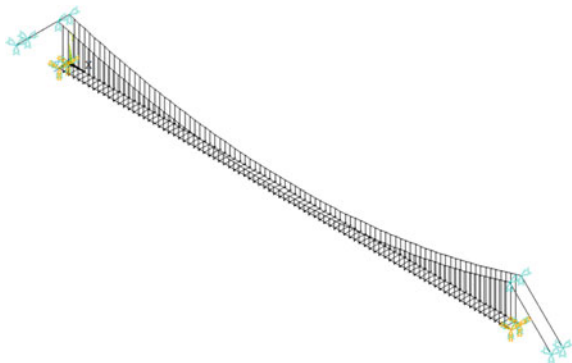


Table 2 Dynamic properties of the footbridge obtained through FE modeling

Mode	Mode shape	Frequency (Hz)	Mode	Mode shape	Frequency (Hz)	Mode	Mode shape	Frequency (Hz)
1	L-S	0.242	8	T-A	0.885	15	L-S	1.576
2	L-A	0.403	9	L-S	0.905	16	L-A	1.743
3	B-A	0.497	10	B-S	1.077	17	B-A	1.815
4	L-S	0.573	11	L-A	1.121	18	B-S	2.101
5	B-S	0.619	12	L-S	1.252	19	B-A	2.317
6	L-A	0.733	13	B-A	1.338	20	B-S	2.594
7	B-A	0.881	14	B-S	1.530			

The validation of the finite element model can be performed by comparing the natural frequencies and corresponding mode shapes obtained numerically and experimentally. In the present study, the bending vibration modes which were identified consistently from all ambient tests and also are important in terms of vibration serviceability assessment of the footbridge under human-induced excitation, are shown in Fig. 9 and compared with their equivalent mode shapes extracted from the ambient vibration tests in Table 3. The Modal Assurance Criterion (MAC) parameter is used to investigate the correlation of these calculated and identified mode shapes which is defined as [13]:

$$MAC(\phi_{F,i}, \phi_{N,j}) = \frac{(\phi_{F,i}^T \phi_{N,j})^2}{(\phi_{F,i}^T \phi_{F,i})(\phi_{N,j}^T \phi_{N,j})} \tag{1}$$

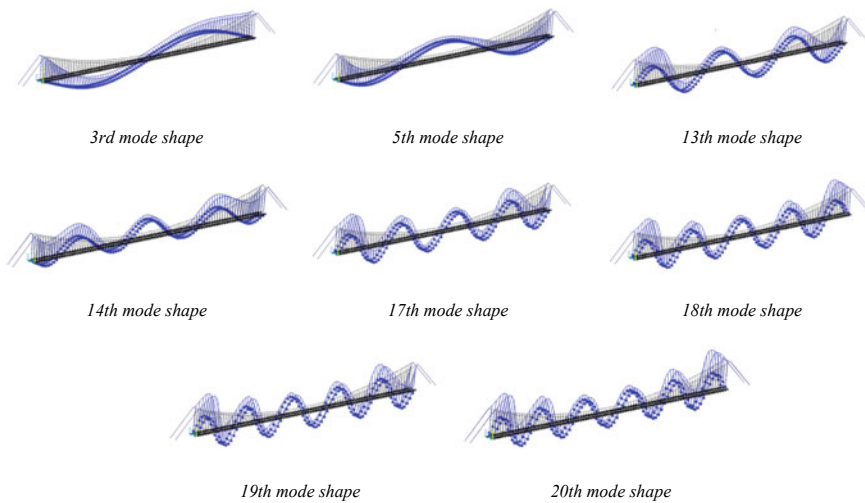


Fig. 9 Bending mode shapes obtained through FE modeling

Table 3 Comparison of numerical and experimental modal parameters for eight bending vibration modes

FE results		Experimental results		MAC values
Mode	Frequency (Hz)	Mode	Frequency (Hz)	
3	0.497	2	0.560	0.984
5	0.619	3	0.612	0.995
13	1.338	6	1.344	0.986
14	1.530	7	1.531	0.989
17	1.815	8	1.803	0.986
18	2.101	9	1.980	0.952
19	2.317	10	2.310	0.992
20	2.594	11	2.520	0.736

where $\phi_{F,i}$ is a vector which represents the i th mode shape extracted from field vibration tests, $\phi_{N,j}$ is a vector that represents the j th mode shape obtained numerically, and T stands for transpose. The MAC value equal to 1 shows a perfect correlation between the numerical and experimental vibration mode shapes; while the MAC value equal to 0 indicates that the mode shapes are completely uncorrelated. Generally, the MAC value greater than 0.8 shows a very good match between two mode shapes. According to Table 3, the MAC values for seven modes are very close to one which shows a very good match between numerical and experimental results; while the MAC value 0.736 for the 20th mode shape of numerical results, indicates that this mode does not completely match with its counterpart mode shape identified through ambient vibration tests. However, the obtained mode shapes and frequencies from FE modeling generally show a good agreement with the obtained results from conducted ambient tests on the footbridge.

6 Conclusion

In this paper, an experimental and numerical study on a historic suspension footbridge located in Italy was presented. A FE model was provided based on geometric field surveys and ambient vibration tests. Four ambient vibrations testing with different measurement setup arrangements were used to accurately identify modal parameters of the footbridge. Within the frequency range 0–2.6 Hz, eleven vibration modes including one lateral, two torsional, and eight bending mode shapes, were identified from different ambient tests using the SSI technique. However, some modes (specifically lateral and torsional modes) were not consistently detected from all ambient vibration tests, indicating that those modes were not significantly excited during ambient vibration testing. Results obtained from ambient tests were used to build a reliable FE model to reflect the dynamic behaviour of the footbridge with reasonable accuracy. The tension force of main cables was estimated numerically based on the

initial equilibrium configuration of the footbridge under dead loads obtained through the field surveys. This parameter has a significant effect on the dynamic characteristics of the footbridge during building and calibrating the FE model. Generally, a good agreement of natural frequencies and of mode shapes was found between the FE modeling and ambient vibration testing. The validated FE model of this historic footbridge can be used as a baseline model to investigate the structural performance and vibration serviceability assessment of the footbridge under different loading scenarios such as crossing pedestrians and wind loading.

References

1. Ren WX, Blandford GE, Harik IE (2004) Roebling suspension bridge. I: finite-element model and free vibration response. *J Bridg Eng* 9(2):110–118
2. Ren WX, Harik IE, Blandford GE, Lenett M, Baseheart AT (2004) Roebling suspension bridge. II: ambient testing and live-load response. *J Bridg Eng* 9(2):119–126
3. Gentile C, Gallino N (2008) Ambient vibration testing and structural evaluation of an historic suspension footbridge. *Adv Eng Softw* 39(4):356–366
4. O'Donnell D, Wright R, O'Byrne M, Sadhu A, Edwards Murphy F, Cahill P, Kelliher D, Ghosh B, Schoefs F, Mathewson A (2017) Modelling and testing of a historic steel suspension footbridge in Ireland. *Proc Instit Civ Eng Bridg Eng* 170(2):116–132
5. Tubino F, Piccardo G (2016) Serviceability assessment of footbridges in unrestricted pedestrian traffic conditions. *Struct Infrastruct Eng* 12(12):1650–1660
6. Giraldo DF, Song W, Dyke SJ, Caicedo JM (2009) Modal identification through ambient vibration: comparative study. *J Eng Mech* 135(8):759–770
7. Peeters B, De Roeck G (2001) Stochastic system identification for operational modal analysis: a review. *J Dyn Syst Meas Control* 123(4):659–667
8. De Roeck G, Peeters B (1999) MACEC2. 0—Modal analysis on civil engineering constructions. Department of Civil Engineering, Catholic University of Leuven, Belgium
9. Živanović S, Pavić A, Reynolds P (2005) Vibration serviceability of footbridges under human-induced excitation: a literature review. *J Sound Vib* 279(1–2):1–74
10. ANSYS, User's Manual, Version 5.6 (1999) Swanson Analysis Systems, Inc., Houston, Pennsylvania, USA
11. EN1993, BS (2006) 1–11. Eurocode 3: design of steel structures-Part 1–11: design of structures with tension components. British Standards Institution
12. Bruno L, Venuti F, Nascé V (2012) Pedestrian-induced torsional vibrations of suspended footbridges: Proposal and evaluation of vibration countermeasures. *Eng Struct* 36:228–238
13. Maia NMM, e Silva JMM (1997) Theoretical and experimental modal analysis. Research Studies Press

Vision-Based Vibration Measurement of Stay-Cables by Video Motion Magnification and Dynamic Mode Decomposition



Samten Wangchuk, Dionysius M. Siringoringo, and Yozo Fujino

Abstract Routine inspection of stay cable of cable-stayed bridges is essential to ensure structural performance and integrity. Currently, there are three types of inspection or measurement systems: static-direct inspection using loadcell, magnetic-based permeability measurement, and vibration measurement. The vibration measurement is widely employed because of its efficacy and practicality. The current vibration measurements of stay cables include contact type such as accelerometers and non-contact type such as laser Doppler vibrometer. However, they have numerous limitations such as: requirement for physical access and limited spatial information in the case of contact accelerometers, and expensive and laborious choice in using laser vibrometer. The recent advancement in computer vision has benefited researchers in exploring a middle path of using video measurements to extract meaningful displacement information. A single video data can be used to obtain displacement at any desired location of the target structure which in the other methods would either require to mount at multiple locations or conducting repetitive tests. In this paper the cable vibration is captured by video camera and the Phase-based Video Motion Magnification method is implemented to magnify the cable micro-vibration. The modal parameters of the cable such as natural frequencies, mode shapes and damping ratios are extracted from the time-history data which are obtained by analyzing the video data and Discrete Centroid Searching Method by applying Dynamic Mode Decomposition. At first, the method is experimentally verified on cable specimen and then extended to a full-scale cable-stayed bridge application, a pedestrian cable-stayed bridge in Tokyo. The results from video data are compared with Laser Doppler Vibrometer which was simultaneously used to record the cable vibration. The close agreement in the results of experiments and full-scale test demonstrate the efficacy of the proposed method in extracting modal parameters useful for condition assessment of the cables in a cable-stayed bridge.

S. Wangchuk (✉)

Department of Infrastructure and Urban Society, Yokohama National University, Kanagawa, Japan

D. M. Siringoringo · Y. Fujino

Yokohama National University, Kanagawa, Japan

Keywords Vibration measurement · Vision-based · Motion magnification · Image processing technique · Modal analysis

1 Introduction

The know-how on inherent dynamic characteristics of a structural system entails information on natural frequencies, damping ratios, and mode shapes. Structural Health Monitoring (SHM) offers this information which are then used to update the existing structural model and record as a reference for new design control. The fluctuation in these modal parameters imply some changes in the structural component owing to constant loading and exposure to forces of nature. Therefore, it is of prime importance to adopt effective modal identification technique in view of not just quality but also quantity of vibrational data. In this way, the goal of SHM to provide reliable time-varying structural condition of civil structures can be achieved.

1.1 Conventional Vibration Measurement Techniques

In estimating modal properties of large infrastructures like bridges and buildings in their operational condition the usual practice is to use Operational Modal Analysis (OMA). The common approach is to use vibration response of the structures such as acceleration, velocity or displacement obtained under unknown input condition. The structure responses are obtained by various types of vibration sensors which can be broadly categorized as contact and non-contact sensors. Contact sensors like accelerometers are attached to the structural members for vibration measurement. However, the use of contact sensors has numerous limitations, such as mass loading effect and low spatial and temporal resolution due to single point measurement. A non-contact vibration measurement system can provide higher spatial resolution measurements and added consistent information. Many non-contact measurement methods like speckle pattern interferometry and holographic interferometry multi-object tracking algorithm and GPS with wavelet filtering techniques are utilized in the past. Laser Doppler vibrometer and radar measurement system with their distant measurement and scanning capability have been utilized in the past to measure structural vibration. These measurement systems, however, are relatively expensive for mass usage.

1.2 Vision-Based Vibration Measurement

To achieve high measurement resolution a promising alternative non-contact measurement method through the use of digital video cameras; which are relatively

less expensive and easy to set up is gaining its superiority. With available image processing algorithms, full-field modal information can be obtained successfully from video camera-based measurements.

One of the challenges in applying vision-based measurement system to civil structures is the inability to capture small amplitude structural motion during ambient vibration. However, recent advancements in computer vision have made a breakthrough via motion magnification techniques. By employing the motion magnification algorithm, one can extract detailed structural motion even under very small amplitude of excitation. The phase-based video motion magnification (PVMM) technique [1], has been successfully implemented to obtain the amplified vibration of an object for various purposes ranging from heart rate detection in the medical science to machinery vibration in the mechanical engineering. Various computer vision-based signal processing and machine learning techniques have been developed to extract vibration response of the structure from image analysis. Notable methods use principles centroid detection [2], edge detection [3], template matching [4], principal component analysis and blind source separation [5], etc.. However, most of these studies concentrate on single point tracking which is insufficient to make any conclusion on overall dynamics of a structure.

1.3 Application to Full-Scale Monitoring of Stay-Cables

In this research, a description on implementation of phase-based motion magnification technique for non-contact modal analysis of cable is described. These cables which are primary load carrying component of cable-stayed bridge undergo ambient vibration amplification under the forces of nature. Although these cables are protected with weather effective coatings like the PE (Polyethylene coating) they can undergo corrosion and result to reduction in tension of cables. Therefore, to ensure the overall safety of the bridge system periodic monitoring and assessment of these cables are of utmost importance.

The micro-vibrations of stay-cables are recorded by video camera and amplified by PVMM technique. Based on the amplified vibration the spatial displacements along the structure are extracted using Discretized Centroid Searching Method (DCSM). Finally, the displacement responses are utilized to obtain modal parameters of the cables using the Dynamic Mode Decomposition (DMD) method. The content in this paper is organized such that the basics on the methodologies (i.e. PVMM, DCSM and DMD) are explained first. Then experimental verification is provided to demonstrate feasibility of the method for displacement extraction and estimation of modal parameters. Finally, implementation of the method to practical field measurements on existing cables is described.

2 Methodology

The three main methodologies employed in this study to obtain multimode modal parameters are: (1) Phase-based Video Motion Magnification (PVMM) to amplify small-scale motion of the structure, (2) Discretized Centroid Searching Method (DCSM) to extract spatial displacement response of the structure from video frames; and (3) Natural Excitation Technique-Dynamic Mode Decomposition (NExT-DMD) to estimate modal parameters of the structure. Figure 1 illustrates flowchart of all steps and detail processes required. In this section, theoretical background on the methodologies are explained concisely, while detailed explanation on each method are available from the main references.

2.1 Phase-Based Video Motion Magnification

Video measurement of a vibrating object consists of temporally displaced frames with image intensity, $I(x + \delta(x, t))$ where x is the pixel coordinate, and $\delta(x, t)$ is the spatially and temporally varying local motion. The magnitude and local phase determine the characteristics of captured video motion, and they can be obtained from two-dimensional Fast Fourier Transform (2D-FFT) by multi-scale and localized filters. The phase information gives a better estimate of the motion than the magnitude (amplitude) as it is unaffected by illumination effects and surface conditions. The

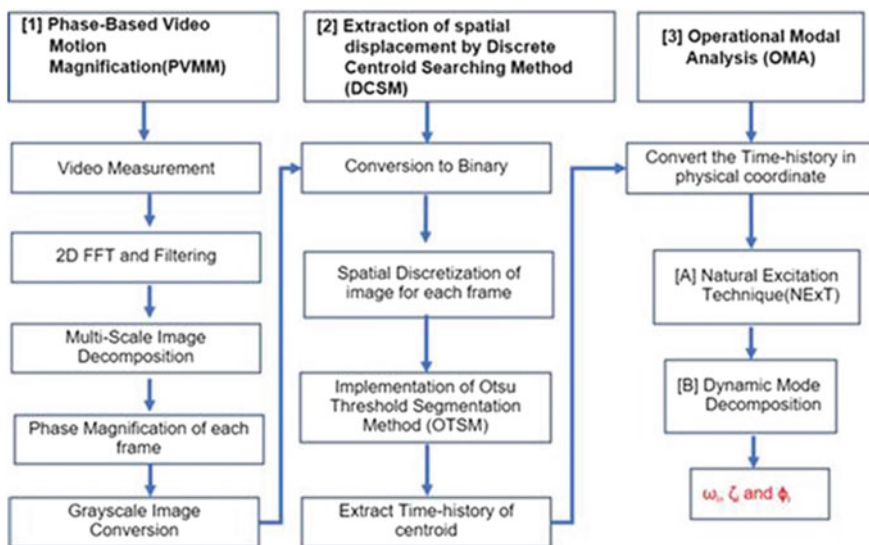


Fig. 1 A flowchart of the procedure for Operational Modal Analysis using phase-based video motion magnification

PVMM algorithm decomposes the signal of a video into local spatial amplitude and phase using a complex-valued steerable pyramid filter bank.

$$I(x + \delta(x, t)) = \sum_{\omega=-\infty}^{\infty} B_{\omega}(x, t) = \sum_{\omega=-\infty}^{\infty} P_{\omega} e^{i2\pi\omega(x+\delta(x,t))} \quad (1)$$

where $B_{\omega}(x, t)$ represents the sinusoid sub-band $\omega(x + \delta(x, t))$ denotes the phase that contains motion information. The motion can be manipulated by altering the phase as in the Fourier shift theorem. The phase $\omega(x + \delta(x, t))$ is temporally filtered to isolate motion in a specific temporal frequency range, and then multiplied by magnification factor α as $I(x + (1 + \alpha)\delta(x, t))$. This will magnify the phase of particular sub-band $B_{\omega}(x, t)$ and result in

$$\tilde{B}_{\omega}(x, t) = B_{\omega}(x, t) e^{i\alpha 2\pi\omega\delta(x,t)} = P_{\omega} e^{i2\pi\omega(x+(1+\alpha)\delta(x,t))} \quad (2)$$

$\tilde{B}_{\omega}(x, t)$ is a complex sinusoid that has $(1 + \alpha)$ times magnified input motion. Consequently, the phases of each coefficient are magnified for each frame by this factor. The motion magnified video can be reconstructed by collapsing the pyramid of the complex steerable pyramid filters, which is a half octave bandwidth. The local spatial phase signals are decomposed temporally using Fourier transform into a series of sinusoids representing harmonic motion. The phase signals are then bandpass filtered, amplified, and recombined back to form a video of magnified motion.

2.2 Extraction of Spatial Displacement by Discretized Centroid Searching Method

The phase magnified video provides a four-dimensional (4D) array as, a -by- b -by-3-by- k and it is divided into k separate frames of still image. The real color images are converted to grayscale by eliminating the hue and saturation information while retaining the luminance. The idea of discretized centroid searching method is to obtain the spatial displacement time history of a vibrating object by dividing the object into numerous discretized cropped regions. Figure 2 illustrates schematically the process of tracing displacement of vibrating object by DCSM. At first, the grayscale-converted still image sampled at time t is divided into certain number of grids (xy) containing the vibrating object and the background. In each area, centroid of the discretized object $C_{xy}(t)$ is computed by employing the Otsu Threshold Segmentation method (OTSM). Centroids of the discretized cropped regions associated with the vibrating object are retained for the consecutive frame $t, t + 1$, until the last frame. They are then combined to trace the centroids movement over the length of video. The centroid locations represent the movement of the discretized object,

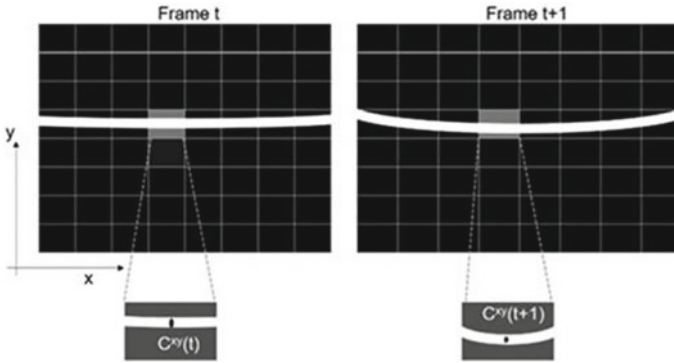


Fig. 2 Schematic figure of tracing the centroid movement of vibrating object

and they can be independently extracted to obtain the object's spatial displacement time history.

After converting the temporal frame of magnified motion from grayscale to binary image, the image is divided into several grids for implementation of DCSM. As illustrated by Fig. 2 by dividing the original frame or R rows and C columns into n rows and m of columns of grids, the binary image number corresponding to i th row and j th column can be defined as:

$$S(i, j) = \mathbf{bin}((i - 1)R/n + 1 : iR/n, (j - 1)C/m + 1 : jC/m) \quad (3)$$

where \mathbf{bin} defines the binary image matrix. The centroid information of each grid in the pixel resolution is estimated by OTSM and then transformed from pixel resolution to physical coordinate by some scaling factor. This procedure is repeated for all frames of temporal image to obtain spatial displacement of the structure over the length of video.

2.3 Dynamic Mode Decomposition

In this study the Dynamic Mode Decomposition (DMD) [6] is adopted for modal extraction from spatial displacement time history of a vibrating object obtained by the DCSM. These responses are the magnified responses obtained by DCSM at a specific frequency range ω_i . They are expressed as $z_{\omega_i}(\chi, t)$; where χ denotes the spatial coordinate of the object $\chi = 1, 2, \dots, m$; and t is the time. Assuming that the sequence of images can be discretized in time by equal time interval Δt , the continuous time variable can be represented as a discrete variable k where $k = 0, 1, 2, \dots, (p + q)$. The time-history of magnified spatial deformation can be rewritten in a matrix form as:

$$\mathbf{Z}_{\omega_i}(k) = [z_{\omega_i}(1, k) \ z_{\omega_i}(2, k) \ \dots \ z_{\omega_i}(m, k)]^T \quad (6)$$

One can construct an input matrix \mathbf{X} that consists of consecutive time-sampled data of the size p and q , where p and q are number selected such that matrix \mathbf{X} is full rank and enough number of data is included.

$$\mathbf{X} \triangleq \begin{bmatrix} \mathbf{Z}_{\omega_i}(0) & \mathbf{Z}_{\omega_i}(1) & \dots & \mathbf{Z}_{\omega_i}(q-1) \\ \mathbf{Z}_{\omega_i}(1) & \mathbf{Z}_{\omega_i}(2) & \dots & \mathbf{Z}_{\omega_i}(q) \\ \vdots & \vdots & \ddots & \vdots \\ \mathbf{Z}_{\omega_i}(p-1) & \mathbf{Z}_{\omega_i}(p) & \dots & \mathbf{Z}_{\omega_i}(p+q-2) \end{bmatrix} \quad (7)$$

Next, a new input matrix \mathbf{Y} is constructed using shifted time displacement data. Similarly, size of the matrix is determined by integer p and q as follows.

$$\mathbf{Y} \triangleq \begin{bmatrix} \mathbf{Z}_{\omega_i}(1) & \mathbf{Z}_{\omega_i}(2) & \dots & \mathbf{Z}_{\omega_i}(q) \\ \mathbf{Z}_{\omega_i}(2) & \mathbf{Z}_{\omega_i}(3) & \dots & \mathbf{Z}_{\omega_i}(q+1) \\ \vdots & \vdots & \ddots & \vdots \\ \mathbf{Z}_{\omega_i}(p) & \mathbf{Z}_{\omega_i}(p+1) & \dots & \mathbf{Z}_{\omega_i}(p+q) \end{bmatrix} \quad (8)$$

The singular value decomposition (SVD) of input matrix \mathbf{X}

$$\mathbf{X} = \mathbf{U} \mathbf{\Sigma} \mathbf{V}^* \quad (9)$$

where \mathbf{U} is $pm \times n$, $\mathbf{\Sigma}$ is diagonal matrix with the size $n \times n$, \mathbf{V} is $q \times n$ and $*$ denotes the conjugate transpose. Here, n is the rank of the reduced SVD approximation of \mathbf{X} . Next, the matrix $\tilde{\mathbf{A}}$ which is the low-order dimensional linear model is defined as:

$$\tilde{\mathbf{A}} \triangleq \mathbf{U}^* \mathbf{Y} \mathbf{V} \mathbf{\Sigma}^{-1} \quad (10)$$

Then, we compute the eigenvalues and eigenvectors of matrix $\tilde{\mathbf{A}}$,

$$\tilde{\mathbf{A}} \mathbf{W} = \mathbf{W} \mathbf{\Lambda} \quad (11)$$

where columns of matrix \mathbf{W} denote the eigenvectors and $\mathbf{\Lambda}$ is a diagonal matrix containing the corresponding eigenvalues λ_i . Finally, the eigen-decomposition of matrix \mathbf{A} is reconstructed from matrix \mathbf{W} and $\mathbf{\Lambda}$ by the following equation:

$$\mathbf{\Phi} = \mathbf{Y} \mathbf{V} \mathbf{\Sigma}^{-1} \mathbf{W} \quad (12)$$

The eigenvectors of matrix \mathbf{A} that is the dynamic decomposition mode are given by columns of $\mathbf{\Phi}$; (ϕ_i) . The eigenvalues λ_i are expressed in z-domain. They are

related to modal characteristics using the following transformation: $\lambda_i = \ln(\tilde{\lambda}_i)/\Delta t$. Finally, the natural frequency (ω_i) and damping ratio (ξ_i) are obtained as:

$$\omega_{0i} = \sqrt{Re(\lambda_i)^2 + Im(\lambda_i)^2}, \xi_i = \frac{-Re(\lambda_i)}{\omega_{0i}} \quad (13)$$

3 Experimental Verification

To validate the technique of Phase-based Video Motion Magnification (PVMM), displacement extraction using Discrete Centroid Searching Method and system identification by Natural Excitation Technique-Dynamic Mode Decomposition (NExT-DMD) experimental verification was conducted on a cable specimen. The specimen is selected to model the stay cables used in the cable-stayed bridges. The cable specimen is made of rubber with dimensions: effective length 1530 mm with diameter of 40 mm and thickness 2 mm. The cable is held in place within a steel frame with one end fixed and at the other end loaded by some weight. The cable is excited vertically with an impact and the in-plane cable vibration is measured. The cable vibration is recorded in a natural lighting condition using Sony 4K NXCAM with a pixel resolution of 3840×2160 at a frame rate of 30fps. Laser doppler vibrometer (LDV) Polytec's RSV-150 with a sampling rate of 4000 samples/sec is also placed on perpendicular direction to the cable vibration to measure the displacement for validation of video processed results. The experimental setup is shown in Fig. 3.

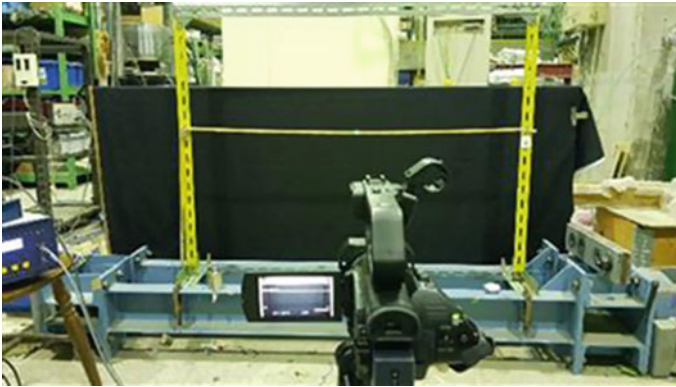


Fig. 3 Experimental setup

3.1 Implementation of PVMM and DCSM

The video measurement capturing the cable vibration is post-processed by applying the Phase-based Video Motion Magnification (PVMM) in the selected frequency band. The pixel resolution of the recorded video for further processing is down sampled at $1200 \times 420 \times 3600$ cropping only the pixels containing cable, where 1200×420 represents resolution and 3600 represents the number of frames in the video, sampled at the frequency 30 Hz. The magnified frames are kept separated for implementing the proposed displacement extraction technique, as shown in Fig. 4. The true-color (RGB) image is converted to a grayscale image and binary image, which is utilized to compute the center of mass of the region (centroid).

The first set of PVMM is done for wide frequency range of 0.5 Hz–14.5 Hz to identify the frequencies present in the cable vibration and the amplification factor, α is kept as 1. The displacement amplitude is in the range of ± 0.5 mm, which is a small invisible motion. FFT is performed on the displacement time history obtained and the identified natural frequencies are 4.028, 8.071 and 12.06 Hz. Figure 5 shows the free vibration response of cable by Laser Doppler Vibrometer which was simultaneously used to measure the cable vibration.

The first three cable modes identified as 4.053, 8.057 and 12.06 Hz are in good agreement with the results from video measurement by Discrete Centroid Searching

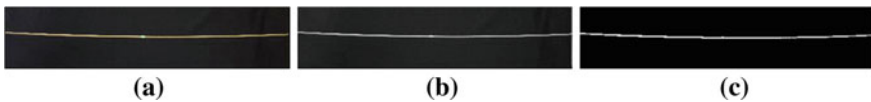


Fig. 4 Temporal frame of magnified motion of cable vibration; **a** 20th RGB frame of magnified motion; **b** converted grayscale image; **c** converted binary image and centroid

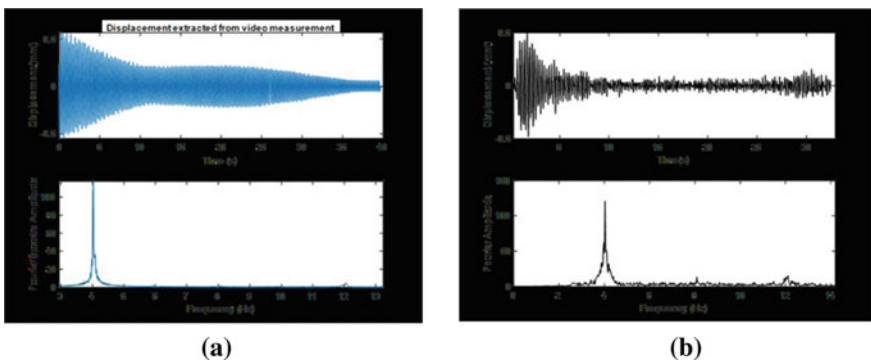


Fig. 5 Experimental Verification: Procedure for video analysis and displacement extraction; **a** Displacement extracted by tracking the centroid from video measurement and Fourier spectra; **b** displacement measured by LDV and corresponding Fourier spectra

Table 1 Results of comparison of lab verification; Vision and LDV

Measurement type	Frequency (Hz)		
	Mode 1	Mode 2	Mode 3
Vision	4.028	8.071	12.06
Laser	4.028	8.081	12.08
% Discrepancy	0	0.12	0.16

Method. The maximum discrepancy in the experimental data is 0.16% which is within the acceptable range of approximation as tabulated in Table 1.

Using PVMM the cable modes are isolated by magnifying the video in their respective frequency band of interest, such as for 1st mode (3.9–4.1 Hz) and (7.9–8.1 Hz) for 2nd mode. This ensures that the reconstructed video shows cable vibration only in their 1st mode and 2nd mode respectively. The next step is to apply DCSM to obtain full-field dense displacement information along the length of the specimen.

Figure 6a shows the black and white image of some ‘xth’ frame of the first mode and the corresponding segmentation into 30 equal parts is shown in Fig. 6b. Number of rows and columns are extracted from the magnified binary image, in the first case (Mode 1) binary image size is $214 \times 1260 \times 2100$ meaning number of rows(R) is 214, column(C) is 1260 and whereas 2100 represents number of frames in the video. The first modal frequency identified though classical FFT is 4.021 Hz which is same for all the segmented images. However, its displacement amplitude differs which is as expected because while considering the first mode deflection in the center would be maximum (P15) and will be minimal as it is tracked towards both the ends (P15-P1 and P15-P30).

This displacement information shown in Fig. 7a is used as input for Dynamic Mode Decomposition from which system identification is carried out. Figure 7b and c shows the mode shape plot obtained by Dynamic Mode Decomposition and identified modal frequency of 4.02 Hz and estimated damping ratio of 0.188% for 1st Mode and 8.14 Hz and 0.116% for the 2nd Mode.



Fig. 6 Image segmentation; **a** still frame of cable specimen; **b** segmented image into 30 equal parts

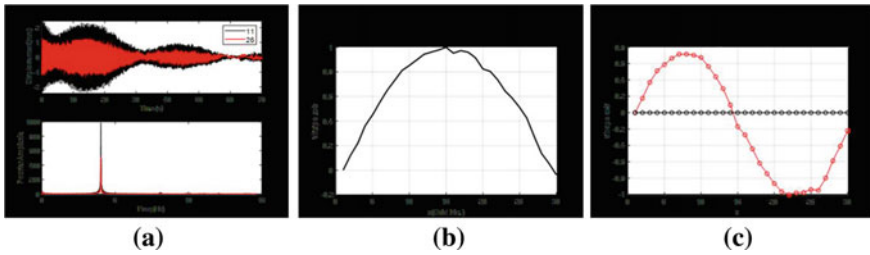


Fig. 7 Image segmentation; **a** centroid time history (P11 and P26); **b** mode 1 **c** mode 2

4 Full-Scale Implementation

The proposed method of frequency identification using Discrete Centroid Searching Method (DCSM) by displacement extraction from a video measurement is extended to a full-scale cable-stayed pedestrian bridge at Shinagawa, Japan.. This cable-stayed bridge is a single tower double cable plane with five pairs of cables on each cable plane. The Pylon is ‘A’ shaped 40 m high which divides the bridge into asymmetric spans of main span over 90 m and side span of 49.4 m. The cable is made of PC high strength wires composed of 37 strands of each having 7 mm diameter. The longest cable length which is on the main span is 75.468 m and shortest is 29.630 m on the side span. These cables welded at both ends; on the tower and at the girder, supports the steel box girder bridge deck over which pedestrians ply.

The cable vibration is captured by Sony NXCAM camera with pixel resolution 3840×2160 at frame rate of 30fps. Simultaneously, the cable vibration is recorded using Laser Doppler Vibrometer (Polytec’s RSV-150) of 4000samples/s for validation of video processed results. Both devices measured the target cable from the same location as shown in Fig. 8. The measurement is made in an outdoor setting

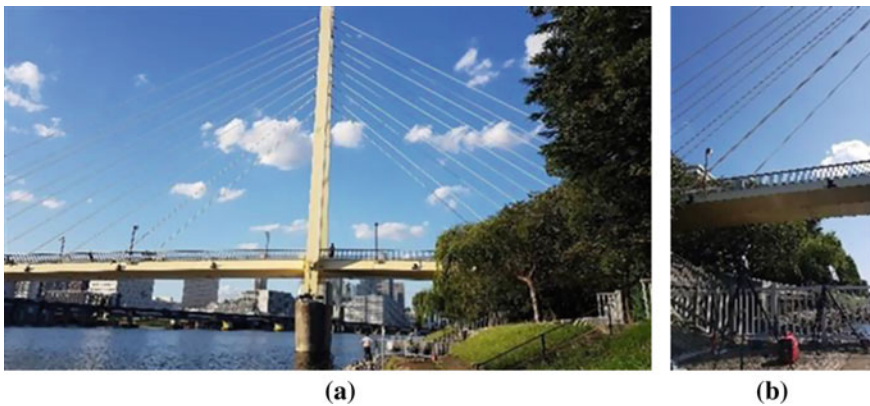


Fig. 8 **a** Kamome cable-stayed pedestrian bridge (cable S); **b** measurement set up

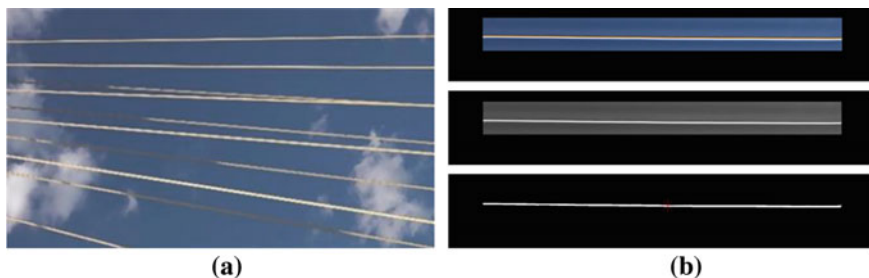


Fig. 9 Procedure for video analysis and displacement extraction; **a** RGB frame of the original recorded video; **b** down sampled (246×230) RGB frame for analysis; converted grayscale image; converted binary image and centroid

by initially exciting the cable with pull and release mechanism to vibrate the cable in in-plane mode.

4.1 Result of Measurement by LDV and Video Processing

The process of displacement extraction is adopted taking the magnified frame after Phase-based Video Motion Magnification (PVMM), converting the RGB frame to grayscale image, then to black and white image and finding the centroid for each segmented image series. The frequencies identified using Centroid Method is used as reference to isolate the embedded modes and then motion magnified in a narrow band of frequency. The spatial displacement extraction using DCSM and modal parameter identification using NExT-DMD is tested on cable S of Kamome Bridge. It is the second longest cable on the side span downstream side of the cable plane measuring 49.75 m. Figure 9 shows the video pre-processing procedure requiring down sampling of original video measurement of 3840×2160 to 2130×190 containing only the cable under analysis (S) with clear background.

Fig. 10a shows the free vibration responses obtained by processing the video and corresponding Fourier spectra. Whereas Fig. 10b shows the result from Laser measurement of the same cable which was taken simultaneously. The result shows that there is no discrepancy in frequencies obtained using vision for both mode frequency of the cable. Table 2. shows a comparative result through LDV and Vision.

The magnified video is now segmented into various columns to obtain dense displacement information along full length of the cable by applying Discrete Centroid Method. These displacement information from the discretized images are used as input for Dynamic Mode Decomposition from which system identification is carried out. Figure 11b shows the mode shape plot for First cable mode obtained by Dynamic Mode Decomposition with identified modal frequency as 1.465 Hz. The estimated damping ratio of 0.72% is obtained by applying NExT to the displacement time history response of the discretized images. Note that the full length of cable S was

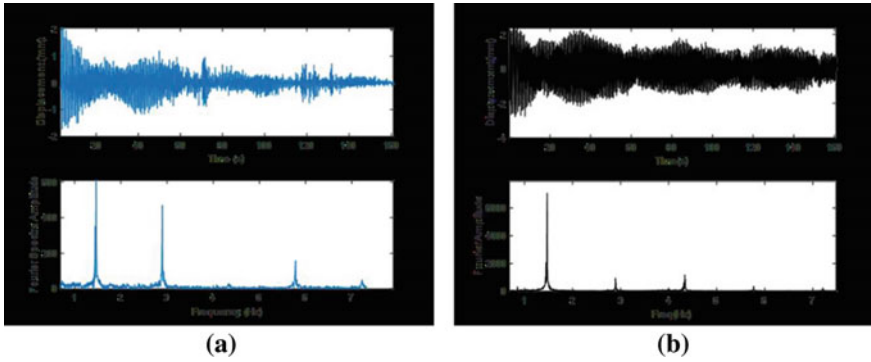


Fig. 10 Full-scale Implementation: Procedure for video analysis and displacement extraction; **a** Displacement extracted by tracking the centroid from video measurement and Fourier spectra; **b** displacement measured by LDV and corresponding Fourier spectra

Table 2 Results comparison of Full-scale implementation; Vision and LDV

Measurement type	Frequency (Hz)				
	Mode 1	Mode 2	Mode 3	Mode 4	Mode 5
Vision	1.465	2.897	4.336	5.782	7.222
Laser	1.468	2.89	4.337	5.768	7.211
% Discrepancy	0.20	0.24	0.02	0.24	0.15

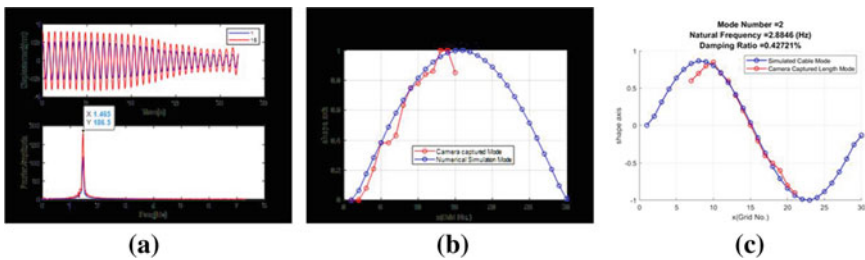


Fig. 11 Image segmentation; **a** centroid time history (P1 and P15); **b** mode 1 **c** mode 2

not captured, and the mode shape obtained is just for half length. Better results can be obtained by taking video measurement of full length of the cable for clearer mode shapes. The similar process of PVMM and DCM is applied to other modes to quantify the mode shapes and estimate damping by the Natural Excitation Technique-Dynamic Mode Decomposition (NEX-T-DMD). The results for Second Mode is as shown in Fig. 11c.

5 Conclusions

Non-contact experimental modal analysis of stay-cables by vision measurement is demonstrated in this research. The vision-based modal analysis is performed by implementing three significant methods, viz. (1) phase-based video motion magnification (PVMM) method to magnify small amplitude of ambient vibration, (2) the discretized centroid searching method (DCSM) to extract spatial displacement of the cable, and (3) dynamic mode decomposition (DMD) for identification of modal parameters. The proposed method was first numerically and experimentally tested in laboratory to check its efficacy. Comparison of the results with measurement using laser doppler vibrometer have demonstrated that displacement can be extracted from vision measurement with reasonable accuracy with maximum discrepancy of 0.16%.

The practical importance of the proposed method is that it allows for modal identification of an object in a non-contact manner using a simple video measurement from a distance under small amplitude of ambient excitation. Since, the natural frequencies identified using this method is in good agreement with most sensitive laser data, it can further be used to estimate cable tension which is one of the parameters requiring routine inspection in structural health monitoring (SHM) of stay-cables.

Although full-scale implementations on cables have shown promising results, the accuracy can be increased if further issues related to environmental effects during measurement can be avoided or otherwise corrected. Further, to better assess the target structure, study on out-of-plane information with the use of stereo camera to obtain motion of structure in 3D can be explored in future.

Acknowledgements The first author is grateful to MEXT scholarship for the Master's program in Japan during this research work. The team is also thankful to Bridge and Structure Laboratory, The University of Tokyo for supporting with measurement devices.

References

1. Wadhwa N, Rubinstein M, Durand F, Freeman WT (2013) Phase-based video motion processing. *ACM Trans Graph* 32(4):1–10
2. Otsu N (1979) A threshold selection method from gray-level histograms. *IEEE Trans Syst Man Cyber* 9(1):62–66
3. Bhowmick S, Nagarajaiah S (2020) Identification of full-field dynamic modes using continuous displacement response estimated from vibrating edge video. *J Sound Vib* 115657
4. Feng D, Scarangllo T, Feng MQ, Ye Q (2017) Cable Tension force estimate using novel noncontact vision-based sensor. *Measurement* 99: 44–52
5. Chen JG, Wadhwa N, Cha YJ, Durand F, Freeman WT, Buyukozturk O (2015) Modal identification of simple structures with high-speed video using motion magnification. *J Sound Vib* 345:58–71
6. Kutz JN, Brunton SL, Brunton BW, Proctor JL (2016) *Dynamic mode decomposition: data-driven modeling of complex systems*. Society for Industrial and Applied Mathematics

A Fiber-Optic Ultrasonic Visualization Technique for Damage Detection in a 1000 °C Environment



Fengming Yu, Osamu Saito, Yoji Okabe, and Zixuan Li

Abstract Heat-resistant structures constitute important civil infrastructure, such as thermal and nuclear power plants. Structural health monitoring (SHM) techniques based on the measurement of ultrasonic guided waves are expected to evaluate the reliability of the aging heat-resistant structures at high temperatures. However, since commercial piezoelectric acousto-ultrasonic actuators and sensors have a limited heat resistance up to 200 °C, they are inapplicable to establishing the high-temperature SHM. Optical fiber acoustic sensors (OFAS) are potential candidates for high-temperature acoustic sensing because they are made from silica glass that withstands temperatures exceeding 1000 °C. As one type of OFAS, fiber-optic Bragg grating (FBG) sensing systems have been developed to detect ultrasonic waves with a high sensitivity comparable to the PZT sensors. The purpose of this research is to build a high-temperature in-situ damage diagnosis using a laser ultrasonic visualization system combined with a remote FBG-based sensing configuration. In this method, an ultrasonic wave is excited by the laser irradiation on the surface of a material and then received by the remotely installed FBG sensor. Because both wave excitation and wave sensing parts have excellent heat resistance, the proposed system enables a stable ultrasonic measurement at elevated temperatures. In this article, the ultrasonic visualization was demonstrated in a specimen of heat-resistant material at a temperature of 1000 °C. A wavenumber-frequency analysis based on a three-dimensional Fourier transform was also conducted to extract the wave components corresponding to the reflection caused by an artificial defect in the specimen. As a result, the filtered visualization results enabled precise damage detection in the high-temperature environment.

Keywords Structural health monitoring · High-temperature environment · Optical fiber ultrasonic sensor · Ultrasonic visualization · Laser ultrasonics · Damage diagnostics

F. Yu (✉) · O. Saito · Y. Okabe
Institute of Industrial Science, The University of Tokyo, Tokyo, Japan
e-mail: houmei@iis.u-tokyo.ac.jp

Z. Li
School of Engineering, The University of Tokyo, Tokyo, Japan

© The Author(s), under exclusive license to Springer Nature Switzerland AG 2023
Z. Wu et al. (eds.), *Experimental Vibration Analysis for Civil Engineering Structures*,
Lecture Notes in Civil Engineering 224,
https://doi.org/10.1007/978-3-030-93236-7_15

1 Introduction

High-temperature structural health monitoring (SHM) techniques are expected to ensure the reliability of aging heat-resistant structures constituting thermal and nuclear power plants. As an SHM method, the inspection with guided ultrasonic waves is sensitive to microscopic damages over a large area. Hence, the method can effectively evaluate the global integrity of large-scale structures by monitoring the damage occurrence [1]. Piezoelectric acousto-ultrasonic actuators and sensors are widely used to establish the SHM methods at room temperatures [2]. However, it is difficult to apply those devices at high temperatures due to their limited heat resistance up to 200 °C.

In contrast, optical fiber sensors are attractive for establishing high-temperature sensing technologies because they are inscribed in silica-glass fibers with good resistance to high temperatures exceeding 1000 °C [3]. As a type of optical fiber sensor, fiber-optic Bragg grating (FBG) sensors have been widely used for ultrasonic measurement [4]. The FBG is a periodic perturbation of the refractive index along the core of a single-mode optical fiber [5]. When an input light propagates through the FBG in the optical fiber, reflections occur along the grating due to the refractive index's variation. The reflected wavelength is known as the Bragg wavelength. A dynamic strain in the FBG mainly leads to the change in the grating pitch, thus shifting the Bragg wavelength of FBGs. Hence, the ultrasonic strain wave can be detected by demodulating the wavelength shift with high-speed interrogation systems.

However, compared with PZT sensors, the conversational FBG sensors have a relatively low ultrasonic sensitivity. To enhance the sensitivity, a phase-shifted FBG (PSFBG) has been widely introduced in the development of fiber-optic ultrasonic sensing systems [6]. The PSFBG is manufactured by inserting a phase shift into the periodic perturbation of the refractive index. The inserted phase shift point induces an additional narrow dip with a steep linear slope in the middle of the reflectivity spectrum. Taking advantage of the spectral characteristic, Wu and Okabe [7] developed a PSFBG balanced ultrasonic sensing system with a high sensitivity comparable to the PZT sensors. Another major advantage of the PSFBG is the short effective gauge length concentrated around the phase-shifted point. This characteristic enables a response to the ultrasonic wave with an extremely short wavelength, thus broadening the sensing frequency bandwidth.

Unfortunately, the FBG-type sensing systems are unapplicable at high temperatures because the optical gratings inscribed in the core of optical fibers become unstable at temperatures exceeding 400 °C and vanish at 900 °C. To overcome the problem, the authors constructed a PSFBG-based remote ultrasonic sensing configuration [8]. In the configuration, a point of the optical fiber is bonded on the structure at high temperature, and the PSFBG is placed away from the high-temperature environment. Then the optical fiber is used as an ultrasonic waveguide to transmit ultrasonic waves from the bonding point on the structure to the PSFBG in the room temperature environment. Since the ultrasonic waveguide formed by the optical fiber has great

heat resistance, this remote adhesion configuration can receive ultrasonic waves at a temperature of up to 1000 °C with high sensitivity and excellent stability.

With the help of the remote sensing configuration, we established a passive method with the PSFBG sensor by the measurement of damage-induced acoustic emission (AE) signals in heat-resistant materials at a temperature as high as 1000 °C [9]. The AE measurement is effective in real-time damage monitoring but is unable to detect existing damages. In practice, an active method is also required for the evaluation after the damages appear in the structures.

In the traditional active methods based on FBG sensing, the PZT-made actuators are widely used to excite the ultrasonic wave. However, it is difficult to use the PZT devices at high temperatures due to their low heat resistance, as previously mentioned. To resolve the problem, we combined the remote sensing method with a laser ultrasonic excitation. A non-contact manner makes the laser ultrasonic excitation attractive for the application in a harsh environment. Moreover, many papers [10–14] have expanded the use of laser ultrasonics to visualize the propagation of ultrasonic guided waves in structures. Since the inspection with ultrasonic visualization can realize reliable and intuitive damage identification, many related methods are researched and developed to diagnose aircraft structures and civil structures.

Details about the configuration of our proposed laser ultrasonic sensing system and the principle of wave visualization are described in the next chapter. Then, in Chap. 3, an experiment will demonstrate that the system effectively visualizes the propagation of ultrasonic waves in a ceramic specimen at elevated temperatures. Furthermore, a signal processing for extracting the damage-induced reflection wave from the visualization results enables precise detection of an artificial defect in the specimen at a temperature as high as 1000 °C.

2 Ultrasonic Visualization System

2.1 System Configuration

In the laser ultrasonic excitation, a pulsed laser beam is irradiated onto the surface of a material, as depicted on the left side of Fig. 1. An elastic wave is induced by the thermal expansion around the point of laser illumination [15]. This non-contact way protects the laser oscillator from thermal exposure to achieve a stable wave excitation at elevated temperatures. Also, the position of the laser illumination point can be specified by controlling the direction of the laser beam.

In this research, a system of laser ultrasonic visualizing inspector (LUVI-CP2, Tsukuba Technology Co., Ltd) was used to excite the ultrasonic wave with a 0.65 μJ YAG laser (pulse width: 2 ns, a beam diameter: 0.5 mm). In the system, the laser was input into a galvanometer mirror. The precise rotation of the mirror can control the direction of the laser beam. With the help of the system, the waveform data set

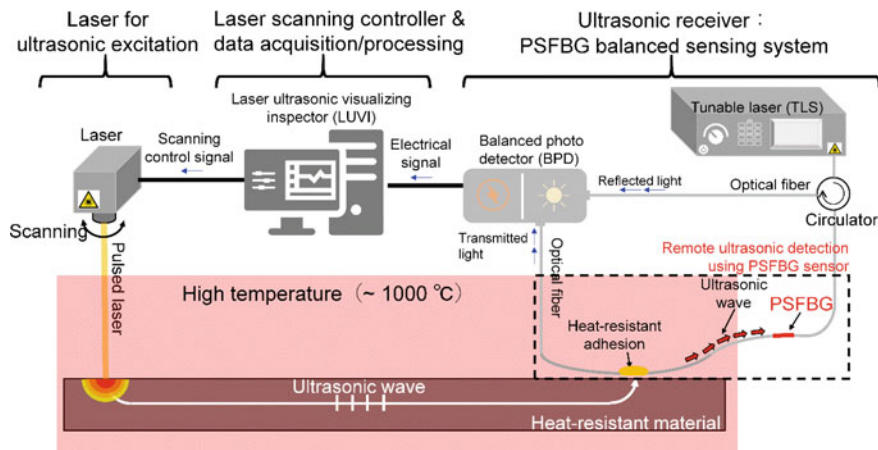


Fig. 1 Architecture of a laser ultrasonic measurement by the remotely installed PSFBG ultrasonic sensing system

used for visualizing the propagation of ultrasonic waves in a specific area can be generated by an automatic laser scan.

The remotely installed PSFBG was used as a sensor to receive ultrasonic waves during the laser scan, as illustrated on the right side of Fig. 1. In the remote ultrasonic measurement, the laser ultrasonic wave propagates from the irradiation point to the adhesion point as a guided wave in the structure. At the adhesion point, the wave transforms into a basic longitudinal wave, with an axial strain component in the core of the optical fiber, and a basic flexural wave, which primarily consists of the shear strain component in the core. Reference [8] has clarified that the PSFBG inscribed in the core (ϕ 10 μm) of the glass fiber (ϕ 125 μm , without polymer coating) is only sensitive to the axial strain. In addition, since the longitudinal mode exhibits no dispersion in the optical fiber, the waves propagate along the optical fiber retaining their original waveform information at the adhesion point until arriving at the sensing point. Hence, the ultrasonic waveguide formed with the optical fiber enables accurate ultrasonic measurement with the PSFBG sensor. Moreover, the ultrasonic damping in the optical fiber is so small that the remote measurement is feasible with the length of the waveguide exceeding 500 mm. In addition, since the ultrasonic waveguide formed by the silica-made optical fiber has the inherent characteristic of heat resistance, the remotely installed PSFBG sensor can perform appropriate ultrasonic measurements with excellent stability even at a temperature of 1000 $^{\circ}\text{C}$.

In this research, the PSFBG was connected to a balanced sensing system [7] to demodulate the Bragg wavelength shift caused by the strain perturbation of the ultrasonic wave. In the system, a tunable laser (TLS, Agilent 81682A) was used as a light source to input a very narrow-band light into the PSFBG through a circulator.

Then, both the transmitted light and the reflected light from the PSFBG were guided into a balanced photodetector (BPD, New focus 2117). In the BPD, the two light components are subjected to differential processing to remove the laser intensity noise in the system and double the AC components corresponding to the dynamic strain in the PSFBG.

The optical power is then converted into an electrical signal at the BPD. After being gained via an amplifier, the waveform signals are acquired by the abovementioned LUVI system. Images of the wave propagating in the objective region are synthesized from the recorded waveform data in the system. The details of the data processing and the principle of ultrasonic visualization are explained in the next section.

2.2 Principle of Ultrasonic Visualization

Reference [10] suggested that ultrasonic waves are reversible in a measurement system of laser ultrasonics. It means that a waveform excited by laser illumination at one point and received by a sensor at another point is equivalent to the waveform that is excited at the position of the sensor and acquired around the illumination point inversely.

In this research, we assume that the reversibility is also applicable to our PSFBG sensing system. In Fig. 2 (a), ①, ②, and ③ denote three examples of laser illumination points; **A** and **B** depict the adhesion point of the optical fiber and the position of the PSFBG sensor, respectively. In real ultrasonic detection, one waveform detected by the PSFBG sensor corresponds to a one-time wave excitation at each laser illumination point. Figure 2b shows the examples of the detected burst waveforms corresponding to the three pulsed laser illumination points. A waveform group is acquired to evaluate a two-dimensional (2-D) wavefield by the automatic laser scan within the defined area. All waveform data are labeled by the positions of illumination points. Hence, the acquired data set can be treated as a three-dimensional (3-D) data matrix. Since an ultrasonic wave guided by the optical fiber is nondispersive, the 3-D data matrix acquired at point **B** (PSFBG sensor) is also able to accurately reflect the propagation behavior of an ultrasonic wave at point **A** (adhesion point).

Moreover, based on the reversibility of wave propagation, the above-collected data can inversely represent the propagation of ultrasonic waves that are excited at the fixed-point **A** and received at each illumination point, as illustrated in Fig. 2c. Hence, the amplitudes at a specific time of all recorded ultrasonic waves are plotted at the corresponding illumination locations in a contour map as brightness to synthesize one frame. The frame displays the magnitude distribution of the ultrasonic wave propagating from the **A** into the defined area at the time. Finally, the ultrasonic wave can be visualized by the continuous showing of the time-series frames. Some examples obtained in a practical demonstration of laser ultrasonic visualization with the PSFBG sensor are provided in Fig. 2d.

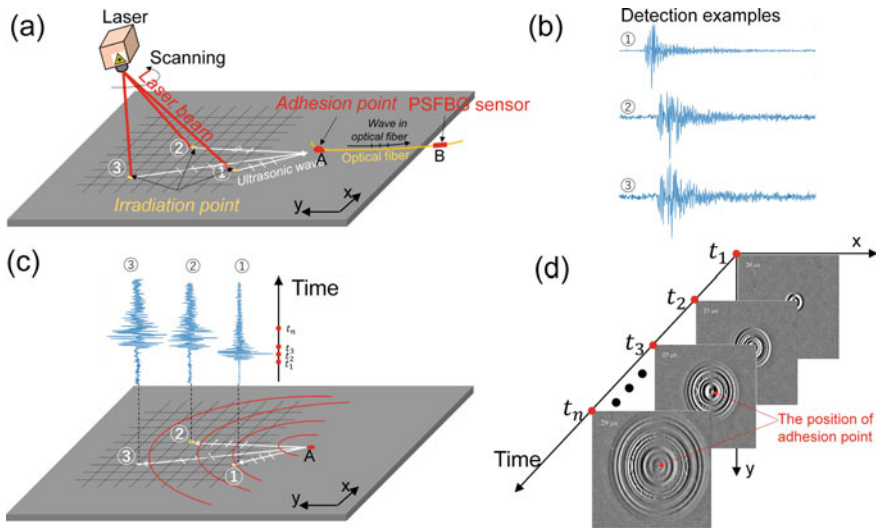


Fig. 2 Principle of laser-ultrasonic visualization technology using the remotely installed PSFBG sensor. **a** The schematic diagram of an experiment for collecting the waveform data set. **b** The examples of the detected ultrasonic signals. **c** An illustration for the process of visualizing ultrasonic waves based on the detected waveform data. **d** The examples of visualized results for the propagation of the ultrasonic wave

3 Experiments of High-Temperature Laser Ultrasonic Visualization

An experiment was conducted to verify the ability of the proposed system to visualize ultrasonic waves propagating in a SiC ceramic plate heated at a temperature of 1000 °C. Figure 3a illustrates the experimental setup. A heater capable of heating up to 1000 °C was produced by winding a Kanthal wire around a ceramic rod and then installed in an open furnace made of ceramic fiberboard. A heat-resistant glass plate transmissive for laser lights was placed over the sample as the cover of the open furnace. The laser was irradiated from the laser oscillator placed above the furnace. The laser beam penetrates through the glass plate and illuminates the surface of the specimen in the furnace for wave excitation. A scanning area of 145 mm in length and 20 mm in width was defined to match the size of the ceramic specimen. We allocated 101 grid points of laser illumination along the X-axis (the longitudinal direction) and 21 along the Y-axis (the transverse direction) in the specified area. To reduce noise in the detected ultrasonic signals, 32 waveforms were excited and averaged at each point. The optical fiber was bonded to the back surface of the ceramic plate by heat-resistant carbon paste (G7716, Ted Pella, Inc.) to transmit the laser ultrasonic waves from the ceramic plate to the PSFBG sensor placed outside of the furnace.

In order to demonstrate that the proposed method is effective for the damage diagnosis at high temperatures, a notch with a length of 4 mm was formed on the

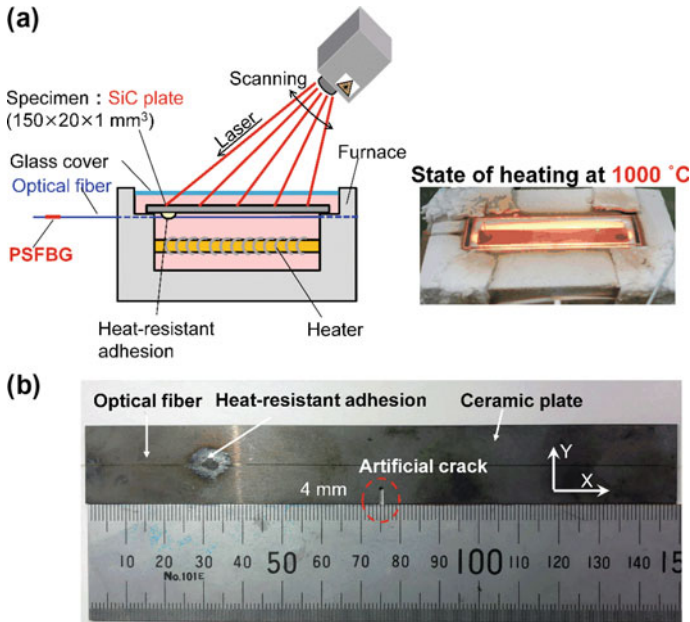


Fig. 3 Setup for the verification experiments of high-temperature laser ultrasonic visualization. **a** The configuration of the furnace and **b** The specimen with an artificial defect

lower side at a distance of 75 mm away from the left end of the plate, as shown in Fig. 3b. The width of the crack was approximately 1.5 mm, the same as the width of the cutter.

Figure 4 shows the visualization result for the ultrasonic wave propagation in the notched ceramic plate at a temperature of 1000 °C. Figure 4a represents that the wave is excited at the position of the adhesion point. The following graphs show that the wave propagates in the ceramic plate along the positive x-axis direction. This experiment verified that the laser ultrasonic measurement with the remotely installed PSFBG sensor was able to visualize the wave propagation at the temperature.

A white line denoted the position of the artificial crack in those visualization results. However, it is still difficult to identify the damage-induced change from the results because of the complicated propagation behavior of the ultrasonic wave in the SiC plate. To clarify the presence of the damage from the visualized results, we extracted the wave components corresponding to the reflection caused by an artificial defect based on a wavenumber-frequency analysis. The procedure of the analysis is described as follows.

As previously mentioned in Sect. 2.2, the visualization results for wave propagation are synthesized from a 3-D matrix of time–space data. After the 3-D Fourier transform (FT) was applied to the matrix, a spectral representation is obtained with three orthogonal variables, k_x , k_y , and f , which correspond to the ultrasonic wavenumbers along the X-axis direction and Y-axis direction and the frequency,

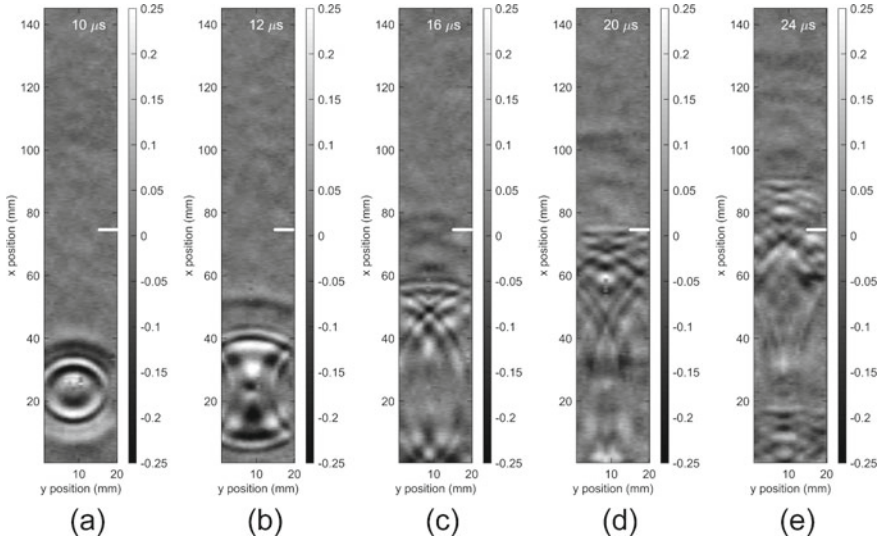


Fig. 4 Visualization of an ultrasonic wave in a specimen with an artificial defect at 1000 °C

respectively. In the wavenumber-frequency domain, the visualized ultrasonic wave is decomposed into infinite numbers of harmonic plane waves. If f is assumed to be a positive real number, then the propagation direction of the harmonic wave is determined by the signs of the wavenumbers k_x and k_y . In the FT results for the ultrasonic wave visualized in Fig. 4, the wave components propagating in the upward and downward directions had positive and negative k_x , respectively. Since the incident wave propagates in the upward direction, the crack-caused reflection wave can be extracted by filtering the wave component with negative k_x from the 3-D FT results. The direction can be further specified by determining the sign of k_y . For instance, when selecting the harmonic wave with negative k_y from the backward-direction wave, we can extract the wave components propagating in the lower-left direction in Fig. 4. Lastly, the extracted harmonic plane waves are composed together by an inverse 3D FT to restructure the filtered visualization results in the time-space domain again.

The above process was employed to separate the backward waves from Fig. 4c. In Fig. 5a, a spatial window was applied to the original image to highlight the wave components propagating from 30 to 85 mm in the longitudinal direction. Figure 5b represents the wave components propagating in the lower-left directions. A comparison between Fig. 5a and b reveals that the reflection wave is generated after the incident wave passes through the artificial defect. Moreover, a comparison among Fig. 4a, b, and c indicates that the reflection at 16 μs is caused by the fastest mode arriving at the notch earlier than the other wave modes. In accordance with the dispersive characteristics of Lamb waves in a planar structure, the firstest mode was identified as the basic symmetric (S_0) mode, which has the highest group velocity in the isotropic solid media. Figure 6 gives another example at 24 μs when the basic

Fig. 5 Wave decomposition result based on wavenumber-frequency filtering at $16 \mu\text{s}$. **a** The original result. **b** The lower-left backward wave

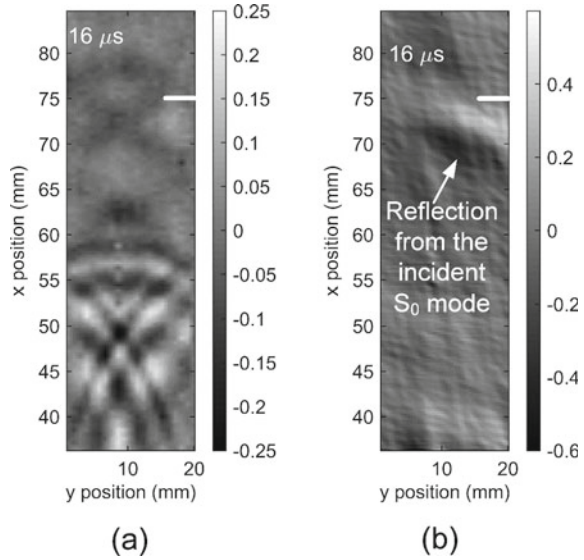
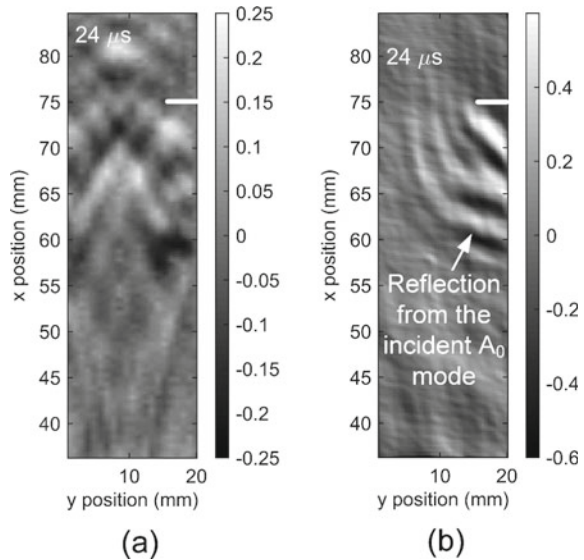


Fig. 6 Wave decomposition result based on wavenumber-frequency filtering at $24 \mu\text{s}$. **a** The original result. **b** The lower-left backward wave



asymmetric (A_0) mode is reflected by the notch. This result indicates that the wave components corresponding to the A_0 mode have a wavelength shorter than S_0 . It is also able to predict the position of the damage from the source of the backward wave of A_0 .

4 Conclusions

In this research, the combination of the remote PSFBG ultrasonic sensing configuration and the LUVI system enabled a successful laser ultrasonic visualization for a heat-resistant specimen at a temperature of 1000 °C. In addition, a clear damage diagnosis was achieved by observing the image of the crack-reflected wave components filtered from the visualization result. Because of the enhanced performance, the PSFBG-based laser ultrasonic visualization system potentially contributes to establishing a comprehensive and efficient high-temperature SHM approach for heat-resistant structures.

Acknowledgements This work was supported by JST A-STEP (JPMJTR20R3) and JSPS KAKENHI Grant Number JP18H01332. This work was also supported by Japan Boiler Association Grants in Aid for Research on Boilers and Pressure Vessels.

References

1. Mitra M, Gopalakrishnan S (2016) Guided wave based structural health monitoring: a review. *Smart Mater Struct* 25:053001
2. Giurgiutiu V (2014) Chapter 12 - Wave propagation SHM with PWAS transducers, structural health monitoring with piezoelectric wafer active sensors, 2nd edn, pp 639–706
3. Mihailov SJ (2012) Fiber Bragg grating sensors for harsh environments. *Sensors* 12
4. Wu Q, Okabe Y, Yu F (2018) Ultrasonic structural health monitoring using fiber Bragg grating. *Sensors* 18
5. Hill KO, Meltz G (1997) Fiber Bragg grating technology fundamentals and overview. *J Lightwave Technol* 15:1263–1276
6. Deepa S, Das B (2020) Interrogation techniques for pi-phase-shifted fiber Bragg grating sensor: a review. *Sens Actuator A-Phys* 315:112215
7. Wu Q, Okabe Y (2012) High-sensitivity ultrasonic phase-shifted fiber Bragg grating balanced sensing system. *Opt Express* 20:28353–28362
8. Yu F, Okabe Y, Wu Q, Shigeta N (2016) Fiber-optic sensor-based remote acoustic emission measurement of composites. *Smart Mater Struct* 25:105033.
9. Yu F, Okabe Y (2017) Fiber-optic sensor-based remote acoustic emission measurement in a 1000 °C environment. *Sensors* 17
10. Takatsubo J, Yashiro S, Tsuda H, Toyama N, Lee JR, Ogisu T (2007) Nondestructive detection of delamination and debonding of CFRP by a laser-based ultrasonic visualization method. *Proc SPIE Int Soc Opt Eng* 6531
11. Ruzzene M (2007) Frequency–wavenumber domain filtering for improved damage visualization. *Smart Mater Struct* 16:2116–2129
12. Toyama N, Ye J, Kokuyama W, Yashiro S (2018) Non-contact ultrasonic inspection of impact damage in composite laminates by visualization of lamb wave propagation. *Appl Sci* 9
13. Lee J, Shin H, Chia CC, Dhital D, Yoon D, Huh Y (2011) Long distance laser ultrasonic propagation imaging system for damage visualization. *Opt Lasers Eng* 49:1361–1371
14. Park B, An Y, Sohn H (2014) Visualization of hidden delamination and debonding in composites through non-contact laser ultrasonic scanning. *Compos Sci Technol* 100:10–18
15. Saito O, Higuchi N, Sen E, Okabe Y (2019) Analysis of ultrasonic waves generated by oblique incidence of a laser. *Insight - Non-Destr Test Cond Monit* 61:714–719

Application of Regenerated Phase-Shifted Fiber Bragg Grating Sensors to Acoustic Emission Detection Under Elevated Temperature



Zixuan Li, Fengming Yu, Osamu Saito, and Yoji Okabe

Abstract Structural health monitoring (SHM) techniques applicable in high-temperature environments are necessary for monitoring the integrity of heat-resistant civil structures, such as thermal and nuclear power plants. Acoustic emission (AE) detection can be potentially used to establish the real-time passive SHM method. Conventional AE sensors are made from piezoelectric materials, whose operational temperature is limited up to 200 °C. Hence, it is difficult to use those AE sensors at elevated temperatures. As an alternative, optical fiber sensors are potential for developing high-temperature sensing technologies because they are fabricated from silica glass with excellent heat resistance over 1000 °C. As a kind of optical fiber sensors, highly sensitive fiber Bragg grating (FBG) sensors have been widely used in AE detection. However, the diffraction grating of the FBG disappears at temperatures over 600 °C. To solve the issue, we proposed a new FBG-based AE sensing system with a regenerated fiber Bragg grating (RFBG). The RFBG is fabricated by annealing the conventional FBG at a high temperature of 920 °C. During the annealing process, the seed FBG once disappears completely, and then a new grating is regenerated again, which has an excellent heat-resistance property. The RFBG was then applied to detect simulated AE waves that were excited by a laser irradiation on the surface of a ceramic plate in a high-temperature furnace heated up to 1000 °C. As a result, our proposed RFBG sensing system succeeded in the detection of the simulated AE waves at elevated temperatures. Based on the experimental results, we believe that the use of RFBG sensors contributes to establishing an RFBG-based high-temperature SHM technique.

Keywords Structural health monitoring · High-temperature environment · Acoustic emission · Optical fiber sensor · Regenerated fiber Bragg grating

Z. Li (✉)

School of Engineering, The University of Tokyo, Tokyo, Japan

F. Yu · O. Saito · Y. Okabe

Institute of Industrial Science, The University of Tokyo, Tokyo, Japan

1 Introduction

Aging problems of heat-resistant structures in civil infrastructure, such as thermal and nuclear power plants, have received considerable attention. The non-destructive testing (NDT) techniques, such as visual testing, eddy current testing, and ultrasonic testing, are applied to evaluate the reliability and integrity of the structures. However, the NDT techniques require the structures to be shut down and cooled to room temperature, thus causing a long-term downtime to finish the testing. Therefore, structural health monitoring (SHM) techniques are desirable to monitor the heat-resistant structures in high-temperature environments in order to reduce the downtime and the maintenance cost.

Acoustic emission (AE) detection can be potentially used to establish the SHM method. AE is an elastic stress wave generated by a rapid release of energy from a localized source related to crack formation or plastic deformation [1]. A passive real-time SHM can be achieved by the detection of AE signals.

Conventional AE sensors are made from piezoelectric materials, whose sensing temperature are limited up to 200 °C. Hence, it is difficult to use those AE sensors at elevated temperatures. As an alternative, optical fiber sensors are potential for developing high-temperature sensing technologies because they are fabricated from silica glass with excellent heat resistance over 1000 °C.

The fiber Bragg grating (FBG) sensor is a type of optical fiber sensors. The FBG is a periodic perturbation of the refractive index along the core of an optical fiber, which is produced by exposing an optical fiber to a spatially varying pattern of ultraviolet intensity [2]. When a light passes through the FBG in the optical fiber, the FBG reflects a narrow-band light with a central wavelength called the Bragg wavelength, resulting in a reflection spectrum with a peak at the Bragg wavelength. A dynamic strain in the FBG mainly leads to the change in the grating pitch, thus shifting the Bragg wavelength of FBGs. The strain waveform of AE is detected accordingly by a high-speed interrogation of the shift in the Bragg wavelength.

However, FBGs have low sensitivity to acoustic signals. Recently, a phase-shifted FBG (PSFBG) has been introduced to address the issue. The PSFBG is manufactured by inserting a phase shift into the middle of the uniform FBG. The phase shift induces an additional narrow dip with a steep linear slope in the reflection spectrum, thus increasing the sensitivity drastically. Meanwhile, the effective grating length is very short around the phase-shifted point, which largely broadens the bandwidth of the frequency response of the PSFBG. Taking advantage of the PSFBG, Wu and Okabe [3] have developed a novel balanced sensing system, which is able to respond to the AE signals with high sensitivity over a broad bandwidth.

Although the silica-glass optical fibers have excellent heat resistance in themselves, the index gratings become unstable with the rising temperature at 400 °C and vanish completely at 900 °C. To overcome the problem, we constructed a PSFBG-based remote ultrasonic sensing configuration [4]. In the configuration, the heat-resistant optical fiber guides the AE signals from the sample in a high-temperature furnace to a PSFBG sensor located at room temperature. The AE signal simulated by

a pencil lead break (PLB) was detected successfully by the method at a temperature as high as 1000 °C. However, the remote installation may limit its application to SHM, which requires a sensor directly installed in a high-temperature environment.

Thus, the development of heat-resistant FBGs is important. Recently, an annealing process is found to be able to regenerate a new heat-resistant grating after the disappearance of the seed FBG [5]. The regenerated FBG is known as RFBG. Several studies [6–8] have demonstrated that the regenerated FBG (RFBG) can survive at temperatures higher than 1000 °C. At present, RFBGs are used as temperature and strain sensors [9, 10]. However, AE detection based on RFBGs has not been investigated yet.

The purpose of this research is to verify the ability of the RFBG sensor to detect AE in a high-temperature environment. Furthermore, to enhance the performance of the RFBG-based AE sensor, we also annealed the PSFBG to fabricate a regenerated PSFBG (RPSFBG). Section 2 describes the regeneration process of a uniform FBG and PSFBG and validates the heat resistance of the RFBG and RPSFBG. In Sect. 3, we test the frequency response of the RFBG and RPSFBG at elevated temperatures by detecting a broadband ultrasonic wave. In Sect. 4, we apply the RPSFBG to detect simulated AE waves that are excited by a laser irradiation on the surface of a ceramic plate at a temperature of up to 800 °C.

2 Regeneration of Fiber Bragg Grating and Phase-Shifted Fiber Bragg Grating

In our research, we used a UV-induced uniform FBG (Fujikura, Ltd., Tokyo, Japan) with a grating length of 5 mm as the seed grating for regeneration. The reflectivity spectrum of the FBG were monitored using a spectrum analyzer (MS9710C; Anritsu, Atsugi city, Japan) during the annealing process. The peak value in the spectrum was measured to evaluate the process of grating regeneration during the annealing. The result is shown in Fig. 1a, along with the thermal history.

Figure 1a shows that reflectivity of the FBG decreases as the temperature increases in the range from 400 °C to 700 °C. At a temperature of 700 °C, the FBG was pre-annealed for one hour in order to regenerate the FBG with stronger heat-resistant stability [11]. When the temperature was raised to 920 °C, the peak reflectivity exhibited a drastic decrease, and eventually dropped to zero. This phenomenon indicated that the seed grating vanished completely. However, the grating was regenerated via isothermal annealing at 920 °C. After approximately 30 min, the peak reflectivity returned to a level of -33dBm and retained a constant value, indicating the formation of the RFBG.

We conducted the same annealing process on a seed PSFBG with a gauge length of 5 mm, which was fabricated into the same type of optical fiber as the FBG. The change in peak reflectivity on the spectrum is shown in Fig. 1b. The regeneration process was similar to that of FBG.

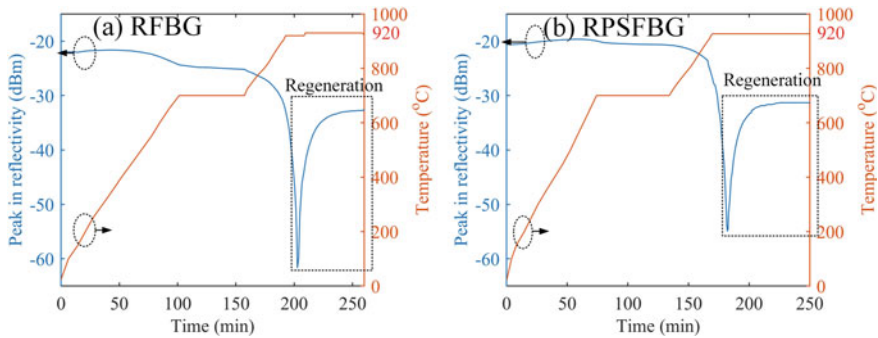


Fig. 1 Peak reflectivities and thermal history during the regeneration process of **a** RFBG and **b** RPSFBG

Then, we validated the heat resistance of the regenerated gratings by measuring the spectra of the RFBG and RPSFBG while reheating the RFBG and RPSFBG from room temperature to 900 °C. Figure 2 shows the spectra of RFBG and RPSFBG at individual temperatures. From the results, it is found that the Bragg wavelength of both the RPSFBG and the RFBG becomes longer linearly as the temperature increases. On the other hand, the shapes of spectra and the peak reflectivity remained the same as the temperature rose to 900 °C. These experimental results verify the stability of the RFBG and RPSFBG at elevated temperatures.

Because the sensitivity of FBGs is determined by the edge condition in the reflection spectra, we compared the precise spectra of regenerated gratings with their corresponding seed gratings. Figure 3a shows the overlap between the reflectivity spectrum of FBG and that of the RFBG. It indicates that the reflectivity of the RFBG decreases after annealing process. The same phenomenon also can be observed from the results corresponding to the RPSFBG, as shown in Fig. 3b. A comparison between the two spectra indicates that the narrow sharp dip in the spectrum of the seed PSFBG

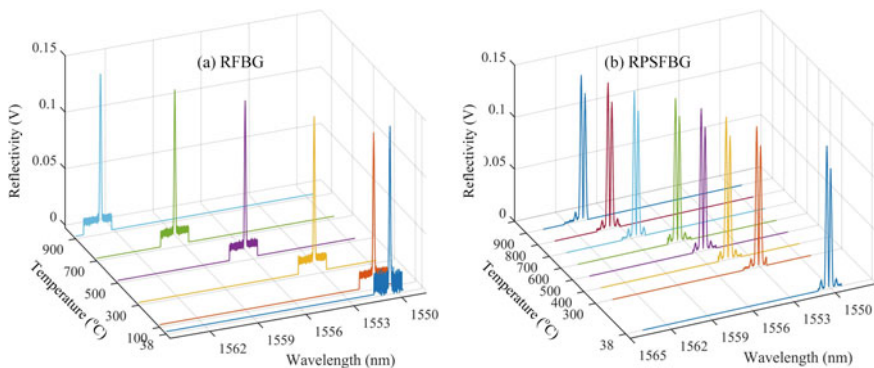


Fig. 2 Spectra of **a** RFBG and **b** RPSFBG, measured at temperatures from room temperature to 1000 °C

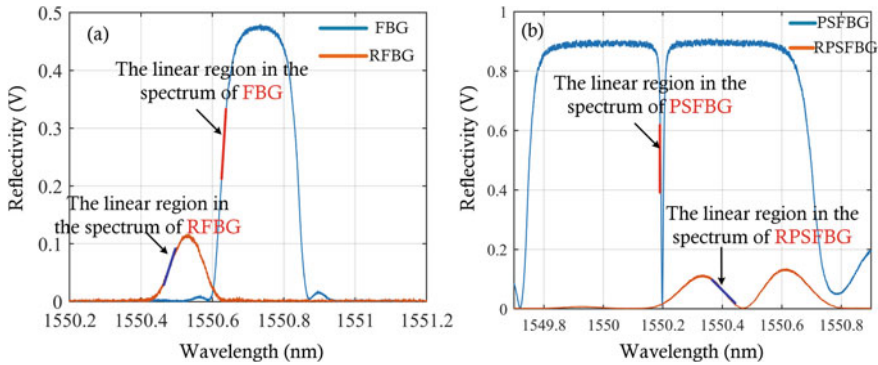


Fig. 3 Comparison of the spectra of **a** FBG and RFBG, **b** PSFBG and RPSFBG

transformed into a broad dip with a gentle slope. Since the slope of the edge is degraded, the ultrasonic sensitivity of the RPSFBG is lower than that of the PSFBG.

Although the sensitivity of the RPSFBG decreased drastically, the following experiments in Sect. 3 will show that the RPSFBG maintained its broadband frequency response in acoustic detection at elevated temperatures.

3 Acoustic Sensing System with the RFBG and RPSFBG

In this research, a demodulation system was proposed on the basis of edge filtering method [3] to measure the AE wave in the regenerated gratings. As shown in Fig. 4, the sensing system consists of a tunable laser source (TLS, 81681A; Agilent, Carpinteria, CA) with a 100-kHz linewidth and a 0.1-pm tunable resolution, an RFBG, a circulator, a photodetector (2117, New Focus, CA) and data acquisition. The laser used to illuminate the RFBG also performs the filtering function. Therefore, the wavelength

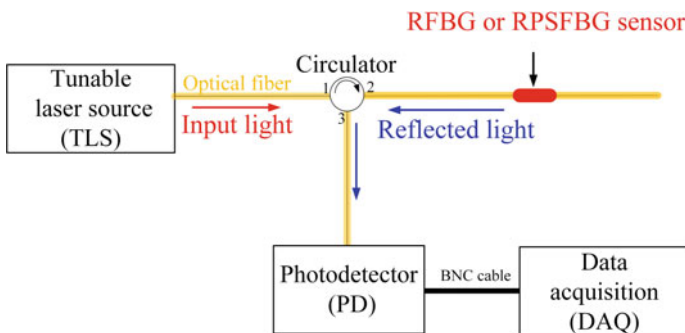


Fig. 4 Schematic of the RFBG (RPSFBG) sensing system

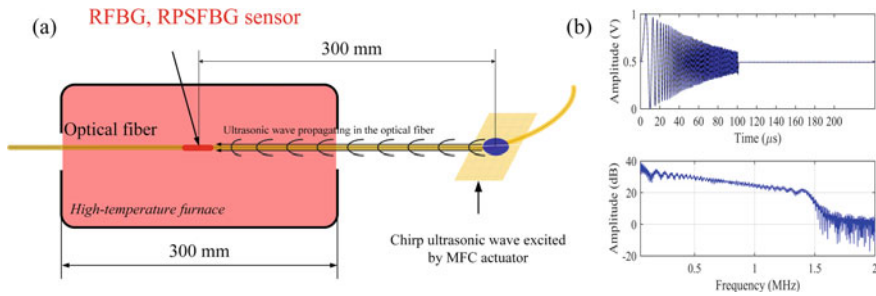


Fig. 5 Experiment to evaluate the sensor performance at high temperature: **a** schematic of the experimental setup, **b** input signal of ultrasonic chirp wave

of the TLS is adjusted at the edge of the spectrum of the RFBG sensor. Based on this edge filter, the strain-induced Bragg wavelength shift can be demodulated from the reflected light intensity changes. The reflected light from the RPSFBG is then directed toward the photodetector by the circulator. The ultrasonic signal can be acquired after the PD converts the optical power into electric voltage.

Before applying the RPSFBG sensor to AE detection, we deployed an active acousto-ultrasonic measurement to testify the performance of the sensor in a high-temperature environment. Figure 5a illustrates that the regenerated gratings were placed in a furnace to receive the ultrasonic wave propagating in the optical fiber at high temperatures. Our previous research [12] has already proven that the optical fiber can be used as a stable ultrasonic waveguide due to its high heat-resistant temperature as high as 1000 °C. Hence, the shape of ultrasonic waveform will not be distorted by the rising temperatures. Furthermore, the optical fiber was directly glued on a PZT-type actuator at room temperature. This setup protects the ultrasonic measurement from the influence caused by the thermal exposure to the ultrasonic source and the adhesive. Hence, the quality of ultrasonic measurement is only determined by the performance of the regenerated grating sensor. Moreover, a broadband ultrasonic chirp wave was excited by the actuator to evaluate the bandwidth of the sensor response over a broad frequency range from 50 kHz to 1.5 MHz. The waveform and frequency spectrum are shown in Fig. 5b.

We used two heat-resistant regenerated gratings to detect the same chirp ultrasonic wave at elevated temperatures from 100 to 900 °C in steps of 200 °C. Figure 2 shows that the Bragg wavelength of RPSFBG and RFBG becomes longer with the temperature increase. To eliminate the influence caused by temperature changes, we used the TLS to adjust the light wavelength to keep the laser indexing the linear edge area of the reflection spectra. In the experiment, 4096 measured waves were averaged to remove white noise. The signals received by the RPSFBG and FBG sensors at different temperatures are overlapped in Fig. 6a and c.

Because both sensors exhibited excellent heat resistance, they successfully performed stable detection at high temperatures. Figure 6a shows that the RPSFBG sensor responds to the chirped ultrasonic signal with almost the same waveform and

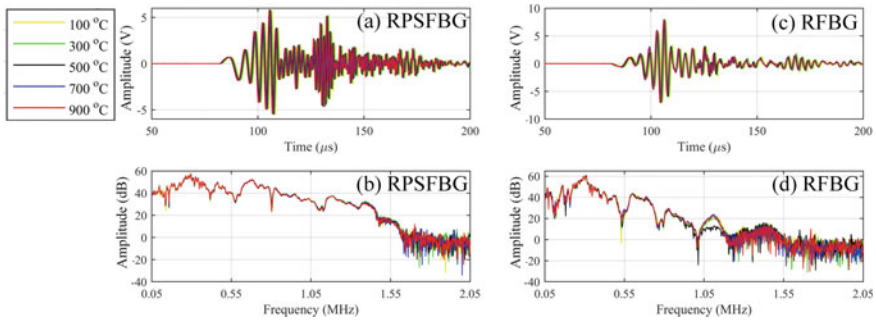


Fig. 6 Received signals of **a** RPSFBG and **c** RFBG and Fourier transform results of **b** RPSFBG and **d** RFBG

amplitude at different temperatures. Furthermore, the Fourier transform results in Fig. 6b show that the RPSFBG sensor has a broad response to the chirp ultrasonic wave in the frequency range from 50 kHz to 1.5 MHz, even in high-temperature environments. Figure 6c indicates that the RFBG sensor also achieves high-temperature ultrasonic detection as stable as RPSFBG sensor. However, a comparison between Fig. 6a and c indicates a difference between the two groups of waveforms received by the two sensors. Both the RPSFBG and RFBG responded to the wave components arriving first at 80 μs . However, only the RPSFBG responds to the wave components with the higher frequency after 120 μs . Figure 6d indicates that this phenomenon is ascribed to the narrower frequency response of RFBG sensor that is limited lower than 0.6 MHz.

The seed PSFBG has been proven to have a much broader frequency response than the seed FBG [3] due to its extremely short effective sensing length around the phase-shifted point. The above results demonstrated that the annealing process hardly affected the effective sensing length of the grating sensors.

4 Simulated ae Detection Using rpsfbg at Elevated Temperatures

In this section, we conducted an experiment to verify the ability of the above system to detect AE. Figure 7 shows the schematic of the experiment. We used a SiC ceramic plate of 150 mm length and 20 mm width. Different from the experiment in Sect. 3, the RPSFBG was placed near the adhesive point with a heat-resistant carbon paste (G7716, Ted Pella, Inc.) on the SiC ceramic plate to detect the acoustic signals, instead of using the optical fiber as the waveguide. The SiC ceramic plate was placed inside a high-temperature furnace and connected to the sensing system.

Since a real damage-induced AE source was difficult to be excited in the furnace, we used a laser-ultrasonic excitation to simulate the AE source. After a laser beam

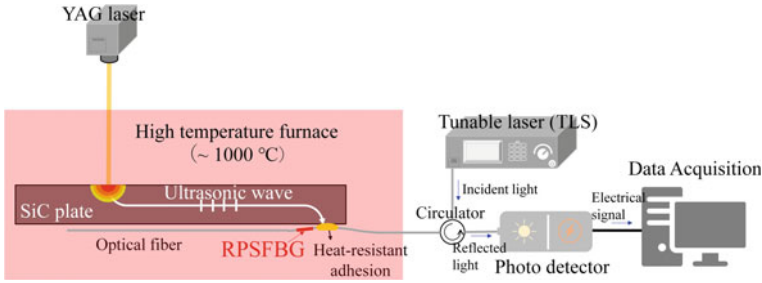


Fig. 7 Schematic of the simulated AE detection system

is irradiated onto the surface of the plate, an elastic wave is induced by the thermal expansion around the irradiation point. The laser ultrasonic excitation is a non-contact method and can be used in a high-temperature environment. In this experiment, a 0.65 mJ YAG laser (pulse width: 2 ns, a beam diameter: 0.5 mm) was used for emitting a pulsed laser beam as the source of a simulated AE signal. The YAG laser oscillator was placed above the furnace, and a pulsed laser beam emitted from the YAG laser illuminated the surface of the ceramic plate. The illumination point was adjusted to the center of the plate.

Then, we heated the furnace from room temperature to 150 °C, 300 °C, 450 °C, 600 °C, and 800 °C. At each temperature, one simulated AE signal was acquired with the RPSFBG sensing system after one pulsed laser beam was emitted. The received signals are shown in Fig. 8.

Figure 8a shows the received temporal signals. The RPSFBG responded to the signals from room temperature to 800 °C successfully. This result indicates that the RPSFBG is able to detect the simulated AE signals at a temperature as high as 800 °C. Moreover, the amplitude of the signals remained at the same level independent of the temperature, due to the stability of the spectrum of the RPSFBG at temperatures up to 900 °C, which was verified in Sect. 2.

Figure 8b demonstrates that the RPSFBG responds to the simulated AE signals over a broadband frequency range from 0 to 2.0 MHz at elevated temperatures. It was noticeable that the high-frequency component increased at temperature of 800 °C. As described in Sect. 3, the RPSFBG was proven to respond to ultrasounds steadily even though the temperature increases. Therefore, the change in frequency response probably resulted from the changes in properties of the ceramic plate or the adhesive caused by the elevated temperatures. This issue should be further investigated in future research.

5 Conclusions

In this research, we annealed a PSFBG to fabricate an RPSFBG with excellent heat resistance. Similarly to the seed PSFBG, the RPSFBG also exhibited broadband frequency response. Then, we achieved simulated AE detection at high temperatures

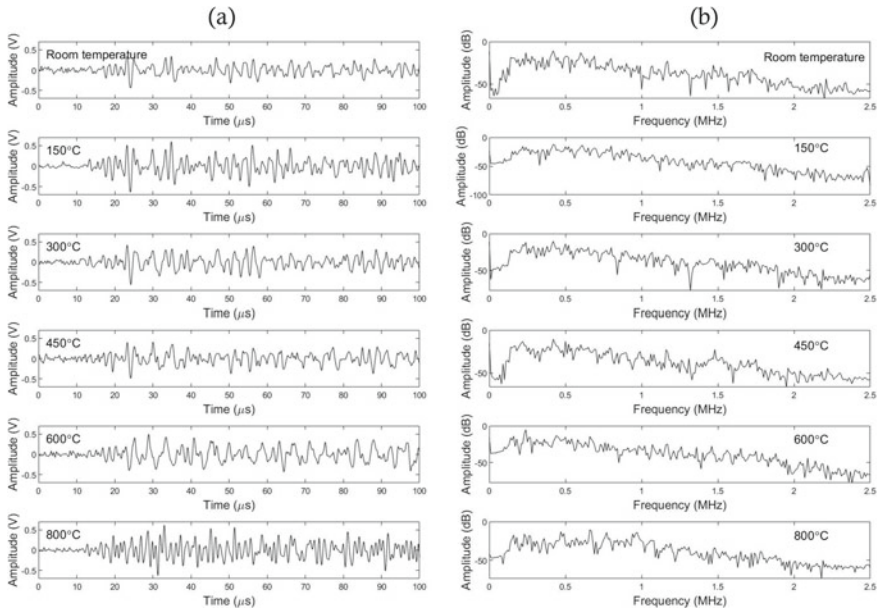


Fig. 8 Responses of RPSFBG to the simulated AE signal: **a** temporal signals, **b** fast Fourier transformation of the temporal signals

of up to 800 °C by the RPSFBG. Based on the experimental results, we believe that the use of RPSFBG sensors contributes to establishing an RPSFBG-based high-temperature SHM technique.

Acknowledgements This work was supported by JST A-STEP (JPMJTR20R3) and JSPS KAKENHI Grant Number JP18H01332. This work was also supported by Japan Boiler Association Grants in Aid for Research on Boilers and Pressure Vessels.

References

1. Roberts TM, Talebzadeh M (2003) Acoustic emission monitoring of fatigue crack propagation. *J Constr Steel Res* 59(2003):695–712
2. Erdogan T (1997) Fiber Grating spectra. *J Lightwave Technol* 15(8)
3. Wu Q, Okabe Y (2012) High-sensitivity ultrasonic phase-shifted fiber Bragg grating balanced sensing system. *Opt Express* 20(27):28353–28362
4. Yu F, Okabe Y, Wu Q, Shigeta N (2016) Fiber-optic sensor-based remote acoustic emission measurement of composites. *Smart Mater Struct* 25:105033 (8pp)
5. Polz L, Dutz F, Maier R, Bartelt H, Roths J (2021) Regenerated fibre Bragg gratings: a critical assessment of more than 20 years of investigations. *Opt Laser Technol* 134:106650
6. Barrera D, Finazzi V, Villatoro J, Sales S, Pruneri V (2012) Packaged optical sensors based on regenerated fiber Bragg gratings for high temperature applications. *IEEE Sens J* 12(1):107–112

7. Cook K, Shao L, Canning J (2012) Regeneration and helium: regenerating bragg gratings in helium-loaded germanosilicate optical fibre. *Optic Mater Express* 2(12):1733
8. Shao L, Canning J, Wang T, Cook K, Tam H (2013) Viscosity of silica optical fibres characterized using regenerated gratings. *Acta Mater* 61(16):6071–6081
9. Laffont G, Cotillard R, Ferdinand P (2013) Multiplexed regenerated fiber Bragg gratings for high-temperature measurement. *Meas Sci Technol* 24(9):094010
10. Wang T, Shao L-Y, Canning J, Cook K (2013) Temperature and strain characterization of regenerated gratings. *Opt Lett* 38(3):247–249
11. Laffont G, Cotillard R, Ferdinand P (2013) Multiplexed regenerated fiber Bragg gratings for high-temperature measurement. *Meas Sci Technol* 24(9):94010
12. Yu F, Okabe Y (2017) Fiber-optic sensor-based remote acoustic emission measurement in a 1000 °C environment. *Sensors* 17(12):2908

Experimental Investigation of Galloping Susceptibility of U Beams with Different Flange Porosity



Stanislav Hračov and Michael Macháček

Abstract The paper presents the outcomes from the experimental investigation of the proneness of the set of slender U-beams to the transversal galloping. All analysed beams are geometrically identical with the U-shaped cross section given by the side ratio equal to 2 (having the short side perpendicular to the flow) and the depth equal to 1/3rd of its breadth, but they differ in the porosity of their flanges. The prisms with six different levels of flange porosity were subjected to wind tunnel testing in the smooth flow in order to determine their aerodynamic drag and lift coefficients for various angles of wind attack. The susceptibility of each individual case was assessed based on the classical quasi-steady theory. Den Hartog criterion expressed in the form of the slope of transversal force coefficient incorporating obtained drag and lift coefficients was applied. The significant positive slope indicating the proneness to transversal galloping was determined for U-beams with porosity up to fifty percent. The prism with flange porosity of seventy five percent revealed as a practically stable due to low positive value of slope within only narrow angular interval around zero angle of wind attack. Finally, the beams with higher flange porosities can be considered according their negative slope of transverse force coefficient as stable in terms of galloping. The comparison with the results from the aerodynamic tests of the prisms with rectangular cross-sections having side ratios equal to two and six, which represent limiting cases for analysed U-profiles, is also given and discussed in detail.

Keywords Galloping instability · U-beams · Aerodynamic coefficients · Wind tunnel testing · Porosity

S. Hračov (✉) · M. Macháček

Department of Dynamics and Aerodynamics, Institute of Theoretical and Applied Mechanics, Czech Academy of Sciences, Prague, Czech Republic
e-mail: hracov@itam.cas.cz

1 Introduction

The action of wind on structures can lead to the self-excited motions of various types such as flutter, galloping or static divergence [1]. The structural geometry and mainly its typical cross-section play an important role in the proneness to each of these phenomena. In this paper, the susceptibility of the selected beams with U-shaped cross-section, which is typical, e.g., for footbridge decks with railing or bridge decks with wind barriers, to the transverse galloping is analysed. The galloping is self-excited motion represented by a harmonic oscillation normal to the wind direction usually with high amplitudes and low frequency after reaching the critical wind velocity. With the further increase in the wind speed above the critical value, the amplitudes of the oscillation grow due to negative damping. The assessment of the proneness to the galloping is usually based on the quasi-steady theory utilizing the results of the static force measurements of the analysed body in the wind tunnel. According to this approach, a positive slope of the transverse force coefficient conditions the possible occurrence of the galloping [2]. The galloping onset wind velocity estimated on basis of the quasi-steady approach is inversely proportional to this slope and proportional to mass-damping parameter called Scruton number [3].

From about the 1960s to the present days, many authors have focused on the study of the galloping of the sharp-edged bodies, predominantly the prismatic ones with the square or rectangular cross sections. Numerous wind tunnel tests identified the rectangular cylinders with side ratio, SR , between 0.75 and 3 being prone to galloping [4–6]. Paper [6] presents a detailed literature survey of the wind tunnel measurements carried out on the rectangular prisms with side ratios between one and two. The results of these tests indicates a significant variability of galloping proneness determined for both profiles, which is caused probably by the different flow and test conditions, i.e., an oncoming turbulence, a blockage or an edge sharpness of the aerodynamic and aero-elastic models. Nevertheless, the majority of the measurements determined higher susceptibility than indicates the galloping stability parameter presented in Eurocode [7]. Thus, the use of this normative coefficient does not seem to be conservative at all.

The previous wind tunnel tests performed by the authors on non-porous U-beams associated with side ratio equal to 2 revealed a similar galloping susceptibility as rectangular cylinders with the same side ratio [8]. The effect of U-profile depth proved to be minimal. On the other hand, the influence of the 75% flange porosity was observed to be more significant and increasing with the increase in the depth of the profile. In this paper, the effect of flange porosity of U-profile onto the proneness based on quasi-steady approach is studied in more detail. The six levels of porosity covering the cases from non-porous to almost fully porous flanges were analysed for the highest depth of the profile used in the previous measurements [8]. For each porosity, the results of static wind tunnel test in the form of aerodynamic lift, drag and transversal force coefficients are presented and discussed. The comparison with the outputs of the test of rectangular cylinder with side ratios equal to two and six are given.

2 Aerodynamic Models and Wind Tunnel Tests Description

Six geometrically identical U-shaped aerodynamic models different only in their flange porosity were built and tested in the climatic boundary-layer wind tunnel of the Institute of Theoretical and Applied Mechanics, Czech Republic. All models were 160 cm long and had the U-shaped cross section with along and across wind dimensions $B = 30$ cm and $D = 15$ cm, respectively, see Fig. 1.

Each specimen was assembled from a wooden rectangular prism and a pair of plastic flanges with certain degree of porosity. The wooden prism had rectangular cross section with dimensions 30×5 cm. The flanges were built from two plastic nets that were glued onto the frontal and rear sides of a tiny plastic frame in order to secure a sufficient stiffness of the flanges, see Fig. 2a. The nets had an axial 7 mm square grid and a specific degree of fill for each individual case. In total five degrees of fill of the nets, i.e., five porosities of the flanges, p , were tested ranging from 0% up to 90%, see Fig. 2b. The total height and thickness of both flanges were 10 cm

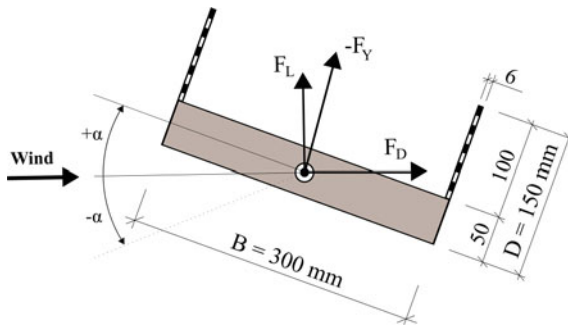


Fig. 1 Geometry of U-shaped cross-section

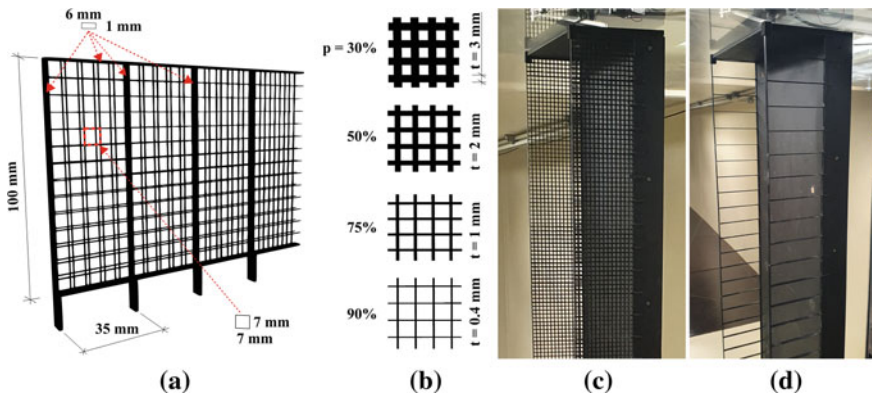


Fig. 2 a Flanges layout, b degree of the fill of the nets for various porosity, c photo of specimen with flange porosity $p = 75\%$, d photo of specimen with the plastic frame only

and 6 mm, respectively. Moreover, the specimen only with this plastic frame, i.e., without nets was tested in order to define its influence onto the results, see Fig. 2d. Finally, the prisms with rectangular cross-sections given by the side ratios equal to two and six were tested for comparison purposes with each individual U-profile.

The specimens were placed vertically into the measuring part of the aerodynamic test section of the wind tunnel, which is 1.9 m wide and 1.8 m high. The models were enclosed between wooden and plastic end-plates to enforce bidimensional flow conditions, see Fig. 3. Two load cells ATI Industrial Automation sensors Mini 40 were used for measuring the aerodynamic forces caused on the bodies of the specimens by the wind load for the angles of wind attack, α , in the range from -15° to $+15^\circ$. These sensors were fixed to the upper and lower ends of the specimens and to the specially designed synchronized rotation mechanisms, see Fig. 3. These mechanisms, that were attached to the floor and the ceiling of the aerodynamic section, enabled rotation of the specimens with the very small angle step, $\Delta\alpha = 0.2^\circ$. Thus, the alternation of aerodynamic coefficients, which are determined from the measured forces, with the changing angle, α , can be detected very precisely. This small step was used for α in the range from -2.5° to 2.5° , while a larger step $\Delta\alpha = 0.5^\circ$ was used for α up to $\pm 5^\circ$

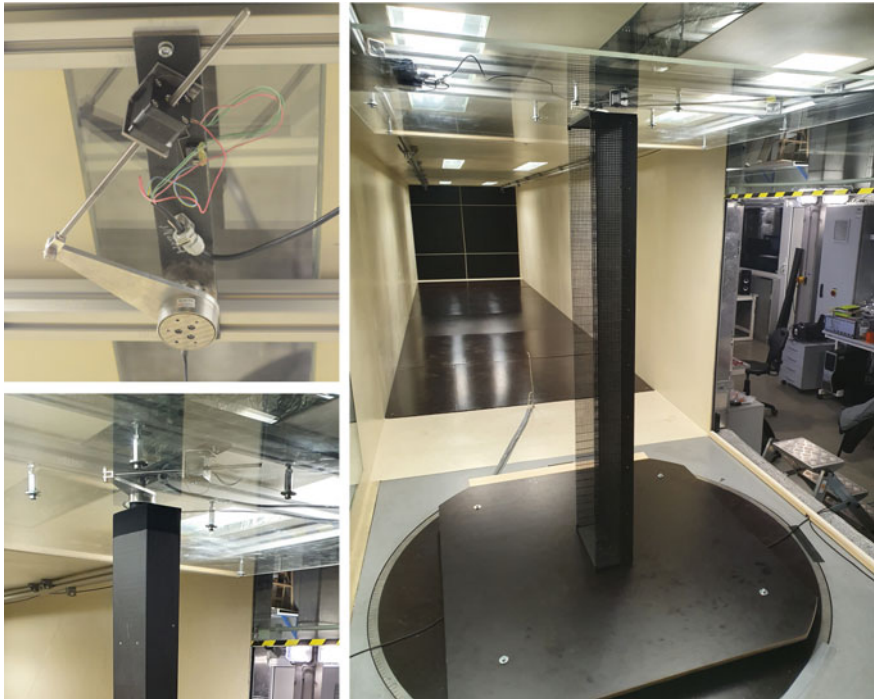


Fig. 3 Photo of the load cell with the rotation mechanism fixed to the frame of the ceiling of the tunnel (upper left), snapshot of the connection of the rectangular prism with the sensor at the ceiling (bottom left); U-shaped specimen installed in the aerodynamic section of the wind tunnel (right)

and finally for even higher $\alpha > 5^\circ$ the step $\Delta\alpha = 1^\circ$ was adopted. The data from the sensors were recorded for 60 s, which was sufficient with respect of the ergodicity and stationarity of the process, with a sampling frequency $fs = 1000$ Hz.

All wind tunnel tests were conducted in a nominal smooth flow with a turbulence intensity around 1%. Wind velocity was measured at 40 cm above the floor using the Pitot tube. The Pitot tube was located in an undisturbed flow approx. 180 cm in front of the model see the photo in Fig. 2. The independence of the aerodynamic force coefficients on the Reynolds number, Re , was successfully verified for wind velocity ranging from 4 ms^{-1} to 19 ms^{-1} . The tests were finally performed at a wind speed of about 14 m/s, i.e., corresponding to $Re = 2.8e^5$ normalized using along-wind dimension B .

3 Methodology Used for Assessing Susceptibility to Galloping

The static wind tunnel tests were carried out to determine the drag and lift coefficients needed to predict the susceptibility of the individual profiles to transverse galloping according to the quasi-steady theory. The drag and lift coefficients, C_D and C_L , respectively, were calculated for each angle of wind attack, α , from the measured aerodynamic forces according to their definitions:

$$C_D(\alpha) = \frac{2 \cdot F_D(\alpha)}{\rho \cdot U^2 \cdot D \cdot L}, \quad (1)$$

where F_D and F_L are mean values of measured drag and lift forces, respectively, ρ is air density, U is the mean wind velocity, D is the across-wind dimension and L represents the length of the model. The aerodynamic forces were determined as a sum of the forces measured by both sensors in the corresponding directions. The modelling of the flanges in different porosity, the effect of which can be mutually compared, required a production of larger models. This led to a higher blockage of the wind tunnel in the range of 7.9–11.7% depending on simulated angle of the wind attack. Thus, the corrections of the measured wind speeds based on a comparison of the results of CFD simulations carried out in the software COMSOL for the profiles placed in almost unbounded 2D space and in the confined 2D space simulating the actual cross-section of the wind tunnel were incorporated.

The proneness to galloping were assessed using Glauert-den Hartog instability criterion:

$$\frac{dC_L}{d\alpha} + C_D < 0, \quad (2)$$

which is verified for zero angle of wind attack, i.e., for $\alpha = 0^\circ$. This criterion was derived from a solution of one DOF system loaded by transverse force, F_Y , see e.g. [2] and Fig. 1:

$$F_Y(\alpha) = -F_D(\alpha) \cdot \sin(\alpha) - F_L(\alpha) \cdot \cos(\alpha) = \frac{1}{2} \cdot \rho \cdot U^2 \cdot D \cdot L \cdot C_{FY}(\alpha), \quad (3)$$

where

$$C_{FY}(\alpha) = -C_D(\alpha) \cdot \sin(\alpha) - C_L(\alpha) \cdot \cos(\alpha) \quad (4)$$

The positive slope of C_{FY} around $\alpha = 0^\circ$ represents a necessary condition for galloping proneness of the analysed bodies and an equivalent version of the instability galloping criterion (2). The value of the slope of the transverse force coefficient, C_{FY} , is also equal to the value of the galloping stability parameter a_g given in Eurocode [7] and used for calculation of the critical wind velocity of the unstable profiles:

$$a_g = \left. \frac{dC_{FY}}{d\alpha} \right|_{(\alpha=0^\circ)} = - \left(\left. \frac{dC_L}{d\alpha} + C_D \right) \right|_{(\alpha=0^\circ)}. \quad (5)$$

4 Wind Tunnel Tests Results

The drag and lift coefficients related to all tested U-beams as well as to the rectangular prisms with $SR = 2$ and $SR = 6$, which represent the reference cases for all measurements, are presented in Fig. 4f for various angles of wind attack. In order to be comparable, all coefficients are in this figure normalized to the same height $D = 150$ mm.

The curve of the drag coefficient, C_D , with three inflection points in the analysed angular interval, which is typical for the rectangular prism with $SR = 2$, was observed only for the non-porous U-profile. Other U-profiles with non-zero degree of flange porosity have only one inflection point, i.e. minimum of C_D , similarly to the case of rectangular prism with $SR = 6$. While this rectangular cylinder has the minimum of C_D at zero angle, the minima of the porous U-profiles are shifted towards the positive angles of the wind attack. Not only the similar courses, but also a proximity of the curves, i.e., closely spaced values of C_D related to the rectangle with $SR = 2$ and to the non-porous U-profile was determined. The proximity of the curves and values was also found between the U-shaped profiles with the porosities $p = 30\%$ and $p = 50\%$ as well as between the U-shaped profiles with the porosities $p = 75\%$ and $p = 90\%$. An assumption of the decreasing drag with the increase in flange porosity is valid only for majority of positive angles of attack. For negative angles,

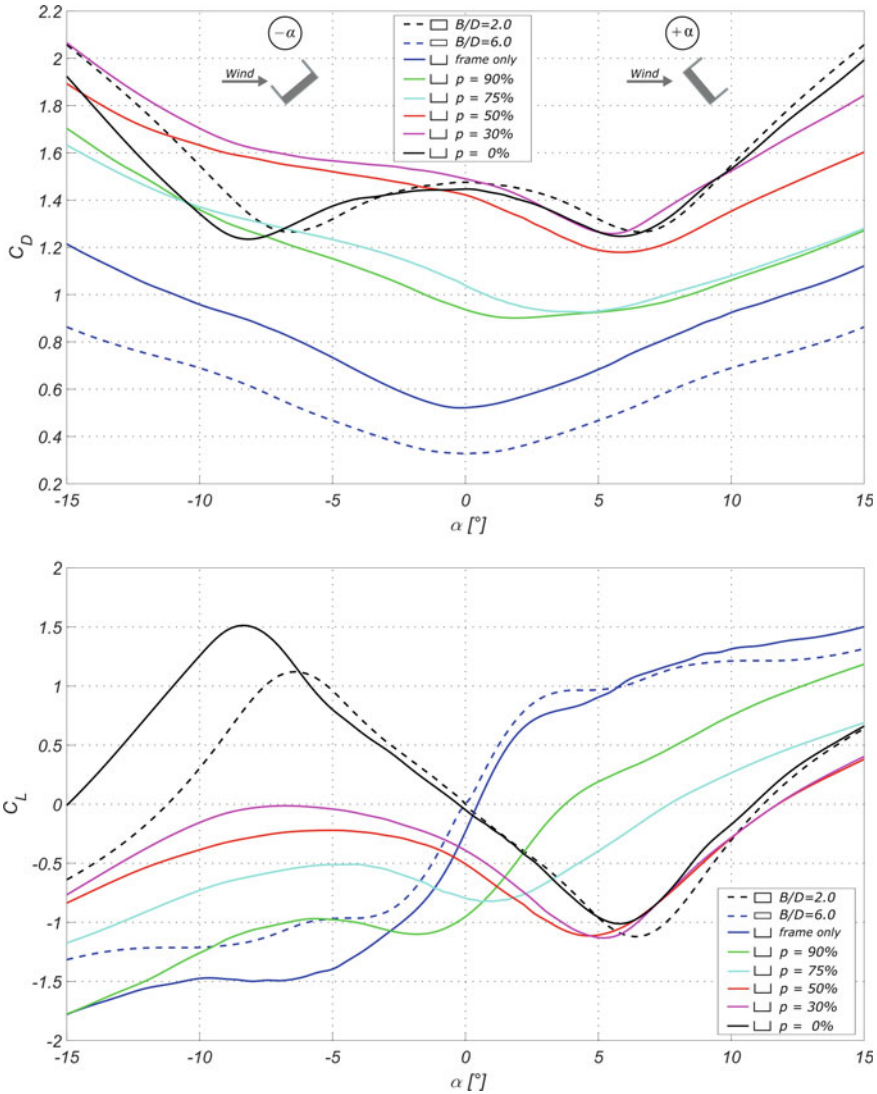










Fig. 4 The drag coefficient, C_D , and lift coefficient, C_L , of the cylinders with rectangular and U-shaped cross-sections for various angles of wind attack

the U-shaped cross-section with $p = 30\%$ revealed to have the highest aerodynamic drag. The expected slight increase in the drag of rectangular prism with $SR = 6$ due to fixing of the flanges consisting only from the plastic frame without the nets was confirmed. The values of C_D corresponding to the zero angle of wind attack are presented for all tested bodies in Table 1. A significant decrease in this value in the case of U-beams was determined for porosity above 75%

Table 1 The aerodynamic parameters of the tested profiles

Cross section	B/D [l]	Porosity [%]	$C_D (\alpha = 0^\circ)$ [l]	$dC_L/d\alpha$ [l]	a_g [l]	$\Delta\alpha_{IP} [^\circ]$	$(\alpha_{IP^-}; \alpha_{IP^+}) [^\circ]$
	2	0	1.48	-11.29	9.81	12.4	$\langle -6.2; 6.2 \rangle$
	2	0	1.45	-9.60	8.15	13.8	$\langle -8.2; 5.6 \rangle$
	2	30	1.49	-7.35	5.86	9.8	$\langle -4.8; 5.0 \rangle$
	2	50	1.42	-8.15	6.73	8.0	$\langle -3.6; 4.4 \rangle$
	2	75	1.04	-3.35	2.31	4.6	$\langle -4.0; 0.6 \rangle$
	2	90	0.94	9.42	-	-	-
	2	frame	0.52	26.92	-	-	-
	6	0	0.33	22.36	-	-	-

A necessary condition for possibility of the galloping proneness is the negative slope of the lift coefficient, C_L , around zero angle of the wind attack. Analysis of the curves related to C_L for all analysed beams determined the negative slope for the rectangular prism with $SR = 2$ and for the U-beams with flange porosity up to 75%, see Table 1. The slope of C_L was calculated as a linear regression of values related to angles α from -1° to $+1^\circ$. The only the exception represented the case with the flange porosity $p = 75\%$, where only angular range from -0.5° to $+0.5^\circ$ due to inflection point at $\alpha = 0.6^\circ$ was used.

The range of angles corresponding to negative slope of C_L , i.e. the angular distance between the inflection points of the curves in Fig. 4, is decreasing with the increase in the porosity. The U-beams with the flange porosity higher than 75% and the prism with rectangular cross-section with $SR = 6$ can be due to the positive slope of C_L around zero angle considered as stable with respect to the transversal galloping. In the case of U-beam with zero flange porosity, the curve of C_L is very close to the curve of the rectangular prism with $SR = 2$. Only the extremes of C_L corresponding to the inflection points are higher, especially maximum for negative stall angle, and these extremes are shifted in the direction of negative angular axis. The curves of C_L for porosities $p = 30\%$ and $p = 50\%$ have in the analysed angular interval similar trend and lie very close to each other. In the range of the positive angles, these curves follow the curve corresponding to the non-porous U-profile. On the other hand, in the interval of negative angles, the change of the slope of C_L for both porosities is with the decreasing angle towards the angle related to the inflection point more gradual. The influence of the plastic frame on C_L revealed as minimal. Only small differences in comparison with the rectangular prism with $SR = 6$ can be found for angles lower than -3° .

In Fig. 5 the transverse force coefficient, C_{Fy} , is reported against the angle of attack for all analysed profiles. Moreover, the intervals of angles of attack around zero angle, $\Delta\alpha_{IP}$, for which C_{Fy} has the positive slope, are presented in Table 1. In this table, also the boundaries α_{IP^-} and α_{IP^+} of the interval, $\Delta\alpha_{IP}$, which define the inflection points of the curves, are stated. The performed tests indicate that the interval, $\Delta\alpha_{IP}$, is decreasing with the increase in the flange porosity. In the case of

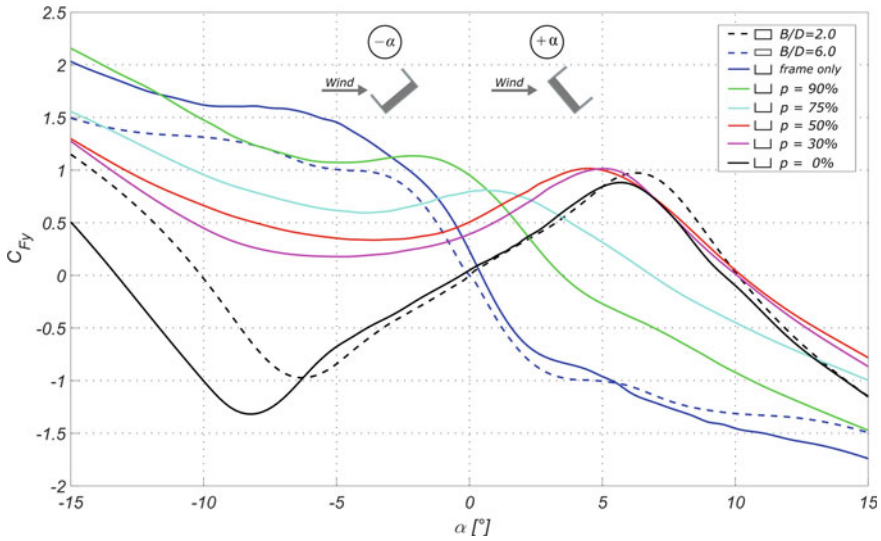


Fig. 5 The transverse coefficient, C_{Fy} , of the cylinders with rectangular and U-shaped cross-sections for various angles of wind attack

zero porosity, this angular interval is even slightly wider than for rectangular prism with $SR = 2$.

The galloping stability parameter, a_g , calculated from the slopes of C_L and drag coefficient, C_D , for zero angle of attack is also listed in Table 1. Significantly higher stability parameter $a_g = 9.81$ for rectangular prism with $SR = 2$ than the value $a_g = 2$ provided by Eurocode [7] was observed. Nevertheless, it was confirmed by many authors, that this standardized value is not conservative [6]. The similar values to our result can be found in [5] or [9], where $a_g = 8.8$ and $a_g = 8.6$, respectively, are given. Only a little less value of the parameter $a_g = 8.15$ was determined for the non-porous U-shaped beam. Thus, a similar strong susceptibility to galloping as for the rectangular prism with $SR = 2$ can be expected. According to the determined values of a_g and the ranges of $\Delta\alpha_{IP}$, the U-profiles with porosities $p = 30\%$ and $p = 50\%$ represent also the unstable cross-sections. However, due to lower a_g , narrower $\Delta\alpha_{IP}$ and also significant reduction of positive slope C_{Fy} with the decreasing negative angles, their galloping susceptibility is expected to be lower. The results for both porosities indicate the higher critical wind velocities and the lower responses than for zero porosity, when assuming the identical structural parameters. The U-beam with the flange porosity $p = 75\%$ can be considered as a practically stable, although the positive slope of C_{Fy} around zero angle exists. The angular range of this positive slope is very narrow, which limits the maximum level of the response. Due to the negative slope of C_{Fy} around zero angle of the wind attack the U-beams with the flange porosity higher than 75% as well as the rectangular prisms with $SR = 6$ with or without fixed plastic frames are expected to be stable in terms of transversal galloping.

5 Conclusions

The proposed paper presents the outcomes from the experimental aerodynamic testing of the slender beams with U-shaped cross section carried out in the closed-circuit wind tunnel of ITAM AS CR. The set of six U-beams having identical ratio of the along-wind to the across-wind dimension equal to 2:1 was tested in the smooth flow conditions in order to determine their galloping susceptibility. The individual U-beams differ in the level of the flange porosity, which ranges from 0% to almost 100%. For comparison purposes, also the rectangular cylinders with side ratios 2:1 and 6:1 were tested.

The assessment of the proneness to transverse galloping was based on quasi-steady approach, i.e., on the analysis of the sign of the slope of the transverse force coefficient around the zero angle of the wind attack. The determination of this slope requires performing the aerodynamic measurement of the forces induced by the wind flow on the analysed bodies for various angles of the wind attack. In the present case, the forces were measured and recorded for the angle of attack in the range from -15° to $+15^\circ$. From the mean values of the drag and lift forces the corresponding drag and lift coefficients were evaluated and utilized for the calculation of the transverse force coefficient.

The analysis of the results determined the U-beams with porosity lower than 75% and the rectangular prism with side ratio 2:1 as potentially unstable from the point of view of transversal galloping. The U-profile with the non-porous flanges can be considered as a strongly susceptible to galloping almost similarly as rectangular cross-section with side ratio 2:1. The galloping susceptibility of other U-profiles was in general decreasing with the increase in the level of porosity up to the value of 75%. The negative slope of transverse force coefficient was observed for the U-beams with porosity higher than 75% and for the rectangular prism with side ratio equal to 6:1. These profiles can be assumed as stable in terms of transverse galloping. In the near future, the obtained results and conclusions are expected to be verified by aero-elastic wind tunnel tests.

Acknowledgements The research was supported by the project No. 19-21817S of the Czech Science Foundation (GAČR).

References

1. Blevins RD (2001) Flow-induced vibration. Krieger Pub Co, Malabar, Florida, USA
2. Paidoussis MP, Price SJ, de Langre E (2014) Fluid-structure interactions: cross-flow induced instabilities. Cambridge University Press, New York, NY, USA
3. Holmes JD (2015) Wind loading of structures. CRC Press, Taylor & Francis Ltd, London, UK
4. Parkinson GV (1963) Aeroelastic galloping in one degree of freedom. In: 1st Symposium on wind effects on buildings and structures, Teddington, UK
5. Washizu K, Ohya A, Ostuki Y, Fujii K (1978) Aeroelastic instability of rectangular cylinders in heaving mode. *J Sound Vib* 59(2):195–210. Elsevier

6. Ruscheweyh H, Hortmanns M, Schnakenberg C (1996) Vortex-excited vibrations and galloping of slender elements. *J Wind Eng Ind Aerodyn* 65(1–3):347–352
7. Mannini C, Marra AM, Bartoli G (2014) VIV–galloping instability of rectangular cylinders: review and new experiments. *J Wind Eng Ind Aerodyn* 132:109–124
8. EN 1991-1-4 (2010) Eurocode 1—Actions on structures—Part 1–4: General actions—Wind actions. CEN/TC 250, Brussels, Belgium
9. Hračov S, Macháček M (2020) Susceptibility of U-profiles with different geometry and porosity to galloping. *EASD Proc EUROLYN* 621–630
10. Hansen SO (2013) Wind loading design codes. fifty years of wind engineering—prestige lectures from the sixth European and African conference on wind engineering. University of Birmingham, UK, pp 35–68

Development of Sensor Unit for Extraction/Transmission of Only Peak Acceleration Response



Yoshihiro Nitta and Akira Nishitani

Abstract This paper presents the sensor units which are developed to store autonomously only the acceleration peak value data and the basic scheme of sending those data to the web server. The developed sensor unit consists of Raspberry Pi 3B, digital MEMS accelerometer and Low Power Wide Area (LPWA) network device. Having the transmitted data volume limitation, LPWA network device advantageously enables long-distance communication with such a low power as can be operated on the battery. The proposed algorithm associated with the developed sensor unit would be able to extract the peak absolute acceleration response of a structure to every single earthquake. The sensor unit implemented into each building would transmit the peak absolute acceleration response as well as the basic structural information (such as structure type and fundamental frequency) to the web server utilizing LPWA network device. The developed sensor unit would provide the useful information for estimating the damage situation in the area in which the building is located. The proposed sensor unit has been tested utilizing the opportunity of full-scale steel hospital building shake table experiments at the E-Defense.

Keywords Sensor unit · LPWA · Maximum absolute acceleration

1 Introduction

The recent progress of computer and data-communication technologies has brought a variety of engineering innovations and paradigm shifts, then with many engineering fields stepping into new stages. The civil engineering field is certainly one of such cases. For the last couple of decades, civil engineers have been attempting to integrate various advanced-technology-based systems into civil structures to enhance the

Y. Nitta (✉)

Division of Architecture and Civil Engineering, Ashikaga University, Ashikaga, Japan
e-mail: nitta.yoshihiro@g.ashikaga.ac.jp

A. Nishitani

Research Institute for Science and Engineering, Waseda University, Tokyo, Japan

structural safety and improve the functionality. A typical example of those systems is the cyber-based sensing system [1, 2] covering a broad area such as an entire city area, for instance. Such a cyber-based sensing system would contribute to the rapid judgement of the area damage state and prompt decision making on the required action strategy soon after an earthquake. The system consists of two processes: one collects the necessary information; and the other evaluates the collected information and estimates the damage situation of the target area.

For the purpose of developing the above-mentioned cyber-based sensing system leading to prompt decision-making on required activities in case of disastrous seismic event, this paper presents the basic scheme of autonomous storing and sending only the peak value data of absolute acceleration response to the web server with such a developed sensor unit. In the typical advanced cyber-based sensing system, the several wireless sensor units are usually installed into a building [3–6]. For estimating the damage index from the data sent by each sensor unit, the time-synchronization of the data from each sensor unit is important. For time-synchronization, however, the complex algorithm would be required and many protocols should be sent and received between multiple sensor units by using wireless network. For avoiding that effort-consuming work, the developed sensing unit installed into the building only sends the peak values of absolute acceleration response of the top floor, then without any time-synchronization needed. And the web server receiving the peak value information of several sensor buildings would provide the “pseudo” absolute acceleration response spectrum in the framework of the cyber-based sensing system.

The developed sensor unit consists of Raspberry Pi 3B, MEMS digital accelerometer and Low Power Wide Area (LPWA) network device. Having the transmitted data volume limitation, the LPWA network device advantageously enables long-distance communication with such a low power as can be operated on the battery. The proposed algorithm associated with the developed sensor unit would be able to extract the peak absolute acceleration response of a structure to every single earthquake, even if multiple earthquake continuously occurs. With the LPWA network device, the sensor unit implemented into each building would transmit to the web server the peak absolute acceleration response as well as the basic structural information, such as structure type and fundamental frequency. The sensor unit would provide the useful information for estimating the damage situation in the area. The proposed sensor unit has been tested at the opportunity of full-scale steel hospital building shake table experiments at the E-Defense. The experiments have been conducted by applying several levels of seismic input excitations to this real scale model building so as to induce various structural damage situations.

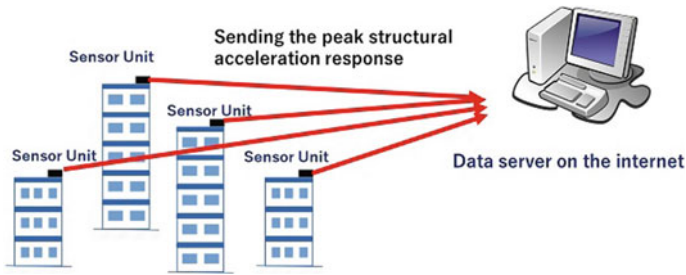


Fig. 1 Concept of the proposed cyber-based sensing system

2 Developing the Sensor Unit for Extraction/Transmission of Peak Acceleration

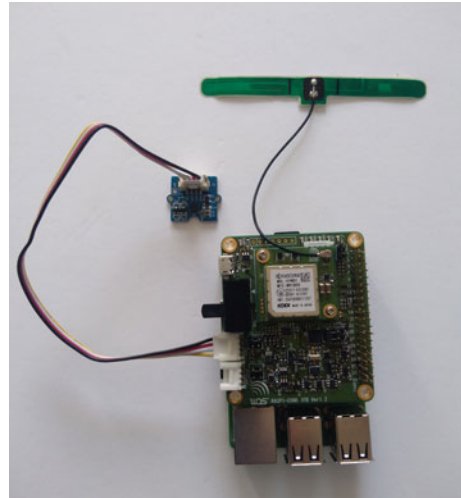
2.1 Concept of the Cyber-Based Sensing System

After the occurrence of an earthquake, it is strongly demanded to make the prompt decision toward the disaster recovery associated with the rapid judgement or predicting of the area damage. For estimating the area damage, the response spectrum provides very useful information about which frequency range of structures would be severely affected by the earthquake. And also SI value [7] calculated from the response spectrum supplies one of damage indices for area. For calculating the response spectrum, measuring the earthquake ground acceleration data on each site is needed. In addition, a lot of response computation with those earthquake data would be required to obtain the response spectrum for several site on real time. Thus, in this research, the concept of the pseudo absolute response spectrum based on the actual response data is proposed by using the cyber-based sensing system. With the measured structural response and the fundamental frequency information of each building, the pseudo absolute response spectrum could be available on real time. Figure 1 shows the schematic model of the proposed concept. The web server makes the pseudo absolute acceleration response spectrum from the stored data file. Such a pseudo response spectrum would be of great help for the decision making toward the disaster recovery.

2.2 Details of the Sensor Unit

Considering the concept of the cyber-based sensing system, the proto-type sensor unit for extraction and transmission of the peak absolute acceleration response of a structure has been manufactured. The basic components of the sensor unit are Raspberry Pi 3B; a digital 3-axis MEMS accelerometer; a real-time clock (RTC); and Low Power Wide Area (LPWA) network device, IoT-Pi. The Raspberry Pi 3B

Fig. 2 Developed sensor unit



employs the Cortex-A53 quad-core 1.4 GHz of ARM processor as CPU and utilizes the Raspbian OS, which is one of the Linux OS. So, Raspberry Pi 3B can accept various program languages and use the various calculation tools on the internet. And Raspberry Pi 3B is able to directly connect to the digital accelerometer using I2C interface. MMA7660FCT [8] as 3-axis digital accelerometer is employed. Maximum acceleration range of MMA7660FCT is 1.5G, and maximum sampling rate is 120 Hz. The sensitivity of MMA7660FCT is 21.33 LSB/g. MMA7660FCT can send 3-axis acceleration data to Raspberry Pi 3B utilizing I2C. IoT-Pi has RTC module, GPS module and LPWA communication module utilizing LTE-M. IoT-Pi can transmit and store the measuring data on the Excel file of Google drive. RTC and GPS module on IoT-Pi provide the useful information for time synchronization of several sensor unit. One unit of developed sensor unit costs about US\$650 including one year LPWA communication contract fee. Figure 2 shows the developed sensor unit.

For the purpose of extracting the peak absolute acceleration response to an earthquake, the measuring algorithm is developed. The developed measuring algorithm consist of two modules; one identifies the end of structural response and the other distinguishes the earthquake response from such pulse-like response as those to door closing or human walking, for example. To identify the end time of the structural response, the information on the duration of the structural response is utilized. In this research, the algorithm recognizes that it is the end of the structural response when the duration is over 30 s. The main frequency components of the pulse-like vibration due to door closing or walking are usually in the range of high frequencies, which are typically different from the fundamental frequencies of the structure. Such a pulse-like response does not exceed the duration of several sec. To appropriately extract the earthquake response, the pulse-like response is distinguished with the magnitude of the measurement duration. Based on several experimental results, the time of 35 s is employed as the threshold value for recognizing the earthquake response. The

developed algorithm sends the peak absolute acceleration response to Excel file on Google drive and stores the time history data measured during earthquake as backup data in Raspberry Pi3.

3 Experimental Verification with Full-Scale Model Building at d-Defense

To investigate the capabilities of the sensor unit and algorithm for extraction and transmission of the peak absolute acceleration response, the developed sensor units have been implemented into the full scale hospital building specimen at the E-Defense. The specimen of the full scale steel-structured building model consists of a four-story quake-resistant building and a three-story base-isolated building [9]. These two buildings are connected to each other with a crossing corridor. Figure 3 shows the overview of this hospital building specimen. During December 4 and 8, 2020, two kinds of seismic input motion were applied to the building model on the shaking table; one is JMA Kobe 1995 and the other OS2, a long period artificial ground motion expected in Osaka. Table 1 shows the schedule list of shaking table tests on December 4 and 8. As shown in this table, white-noise excitations were applied to the model hospital in addition to the two main quakes. Two of the sensor units shown in Fig. 4 were installed on the first and roof floors of the four story building. Only the sensor unit on the roof floor sent the peak.



(a) Whole picture of the hospital building model

(b) Four-stories building model

Fig. 3 Hospital building model. **a** Whole picture of the hospital building model. **b** Four-stories building model

Table 1 Schedule of the shaking test

Date	Input ground motion	Level
1:00 p.m. on 4th December	White noise	–
1:30 p.m. on 4th December	OS2	50%
1:50 p.m. on 4th December	White noise	–
0:30 p.m. on 8th December	White noise	–
1:00 p.m. on 8th December	JMA Kobe	50%



(a) Sensor unit on first floor



(b) Sensor unit on Roof floor

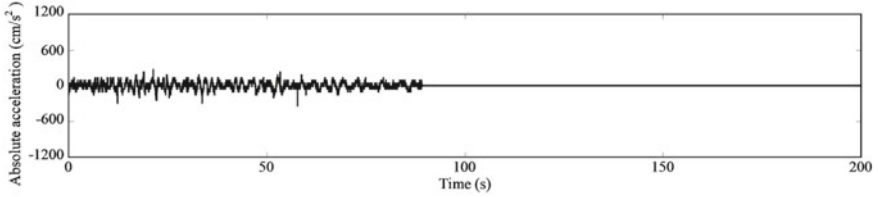
Fig. 4 Sensor units installed on first and roof floor. **a** Sensor unit on first floor. **b** Sensor unit on roof floor

absolute acceleration values to the Excel file in the Google drive. The threshold acceleration amplitude value for the measurement start was set 150 cm/s^2 . For warranty, all the detected peak absolute acceleration responses including electric noise and shock waves during the E-defense shaking table tests were stored and sent to Google drive.

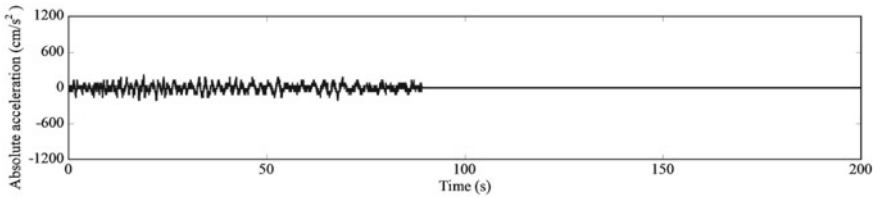
Responding to OS2, the two sensor units were succeeded to store both the time history and peak values of absolute acceleration response inside the Raspberry Pi 3B. But, as a result, the sensor unit on the roof floor could not send the peak values to Google drive. The reason was that the poor radio wave condition of LTE-M caused the interrupted transmission to Google drive. The extracted peak values and stored time histories by the two sensor units are shown, respectively, in Table 2 and Fig. 5. With respect to the white noise waves, the sensor unit on the roof floor did measure

Table 2 Measured peak absolute acceleration response for OS2 on 4th December

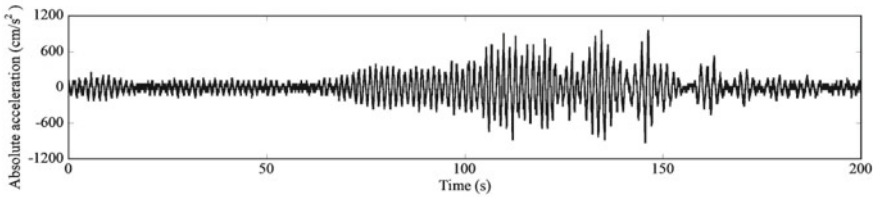
Time of date	Floor	Direction	Peak value (cm/s ²)
1:30:26 p.m	1st floor	X	335
1:30:10 p.m	1st floor	Y	220
1:30:26 p.m	Roof floor	X	945
1:30:26 p.m	Roof floor	Y	990



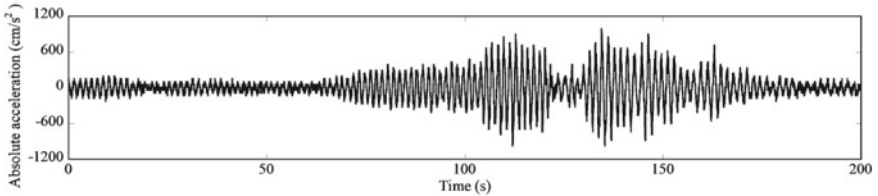
(a) X-direction time history of first floor



(b) Y-direction time history of first floor



(c) X-direction time history of roof floor



(d) Y-direction time history of roof floor

Fig. 5 Stored time histories for OS2. **a** X-direction time history of first floor. **b** Y-direction time history of first floor. **c** X-direction time history of roof floor. **d** Y-direction time history of roof floor

Table 3 Measured peak absolute acceleration response at the roof floor for white noise on 4th December

Time of date	Direction	Peak value (cm/s ²)
1:02:28 p.m	X	78
1:02:28 p.m	Y	151
1:54:38 p.m	X	155
1:54:41 p.m	Y	103

those data but the unit on the first floor could not do because the amplitudes of the first floor accelerations were too small. The peak values extracted by the sensor unit are shown in Table 3.

Regarding JMA Kobe, only the sensor unit on the roof floor could store the time history of absolute acceleration response and send its peak values to Google drive, while the sensor unit on first floor was not successful due to the OS system error of Raspberry Pi 3B. The list of extracted values in Excel file on Google drive are shown in Table 4. Table 4 includes the peak values for the shock wave and electric noises. Figure 6 shows the time histories of JMA Kobe, and Fig. 7 shows the typical time histories of the shock wave. These figures tell how important the algorithm distinguishing the difference between the earthquake response and the pulse-like response is.

The above results indicate that the proposed sensor unit could extract the peak values of absolute acceleration responses and transmit them to the Excel file in Google drive.

4 Implementation for Actual Buildings

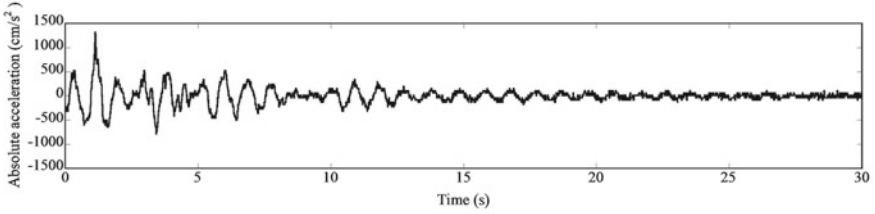
To demonstrate the capabilities of the developed sensor unit and algorithm in a real structure, two sensor units are installed on the top floors of two RC buildings in Ashikaga University in Tochigi, Japan; they are seven- and four-story buildings. For this actual building application, the 3 axis digital MEMS accelerometer, MMA7660FCT does not have enough sensitivity for small and moderate earthquake. Then, new 3 axis digital MEMS accelerometer, BMA400 [10], is employed. BMA400 has the same I2C interface as MMA7660FCT and is able to select the measuring range of acceleration, 2G, 4G, 8G and 16G. In this application, 2G has been selected, with the sensitivity for 2G range being 1024 LSB/g. Compared with MMA7660FCT, BMA400 has higher sensitivity with a sampling rate of 100 Hz. Figures 8 and 9 show the buildings and the installed sensor units.

In the real building application, the threshold acceleration amplitude value for measurement start and peak value storage is set 15 cm/s² with the threshold value of duration equal to 25 s. If the duration does not exceed 30 s, the peak response value would not be stored. For warranty, however, the time history of acceleration response is recorded. As of the end of June, 2021, the two sensor units have not measured any

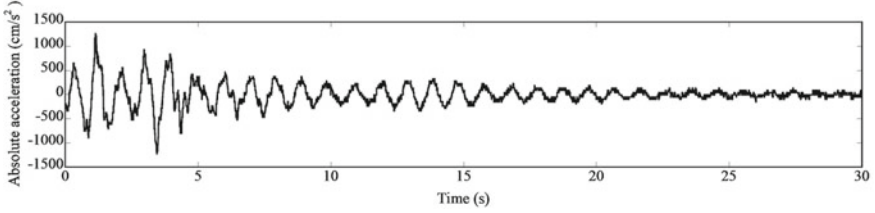
Table 4 Measured peak absolute acceleration response at the roof floor

Time of date	Input motion	Direction	Peak value (cm/s ²)
9:21:06 a.m	Electric noise	Y	116
9:21:13 a.m	Electric noise	X	102
9:21:42 a.m	Shock wave	Y	118
9:22:03 a.m	Shock wave	X	382
9:23:10 a.m	Electric noise	X	102
9:22:10 a.m	Electric noise	Y	164
9:54:58 a.m	Electric noise	X	151
9:55:01 a.m	Electric noise	Y	96
10:17:40 a.m	Electric noise	X	152
10:17:58 a.m	Electric noise	Y	137
10:32:11 a.m	Electric noise	X	151
10:32:11 a.m	Electric noise	Y	97
10:48:43 a.m	Electric noise	X	150
10:48:46 a.m	Electric noise	Y	98
10:59:49 a.m	Electric noise	X	151
10:59:56 a.m	Electric noise	Y	98
11:22:54 a.m	Electric noise	X	150
11:22:54 a.m	Electric noise	Y	98
11:32:39 a.m	Electric noise	X	151
11:32:48 a.m	Electric noise	Y	144
11:34:32 a.m	Electric noise	X	151
11:34:32 a.m	Electric noise	Y	98
11:42:13 a.m	Electric noise	X	150
11:42:17 a.m	Electric noise	Y	135
11:43:53 a.m	Electric noise	X	150
11:43:53 a.m	Electric noise	Y	98
12:29:50 a.m	Electric noise	X	150
12:29:50 a.m	Electric noise	Y	98
12:33:31 a.m	White noise	X	150
12:33:31 a.m	White noise	Y	98
13:02:49 a.m	JMA Kobe	X	1317
13:02:49 a.m	JMA Kobe	Y	1255

acceleration data yet since such an earthquake as to trigger the measurement has not occurred since the sensor unit setting.

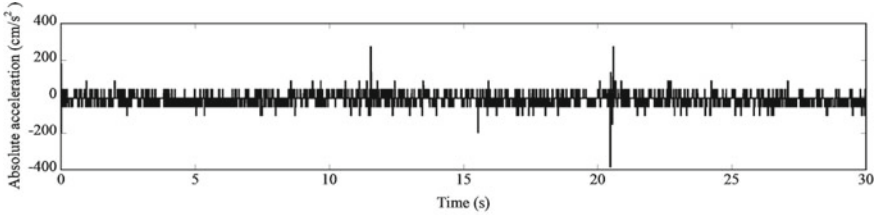


(a) Time history of X direction

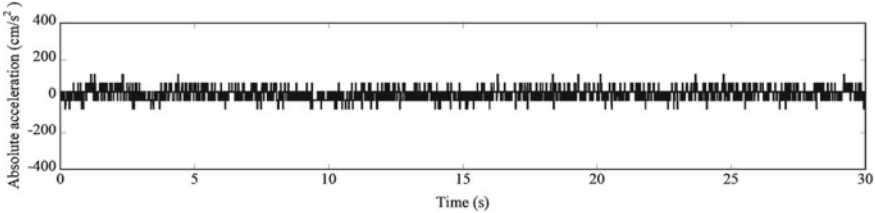


(b) Time history of Y direction

Fig. 6 Stored time histories of the roof floor for JAM Kobe. **a** Time history of X direction. **b** Time history of Y direction



(a) Time history of X direction

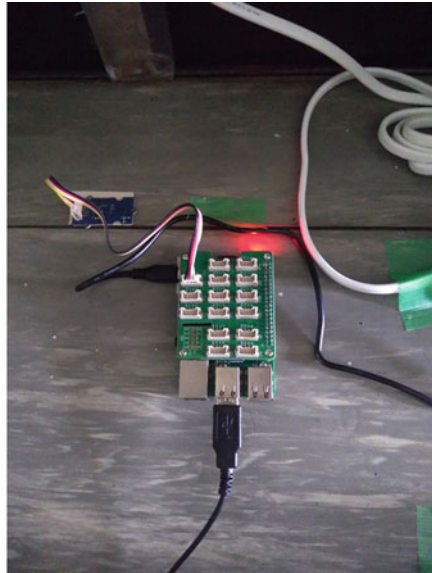


(b) Time history of Y direction

Fig. 7 Stored time histories of the roof floor for Shock wave. **a** Time history of X direction. **b** Time history of Y direction



(a) Seven story RC building

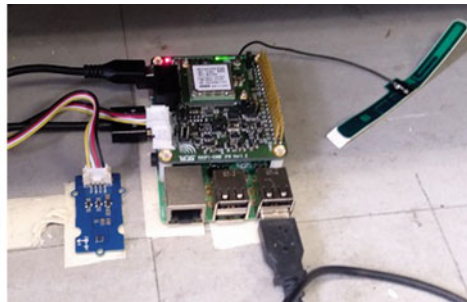


(b) Sensor unit on seventh floor

Fig. 8 Sensor units installed on seven-story building. **a** Seven story RC building. **b** Sensor unit on seventh floor



(a) Four story RC building



(b) Sensor unit on fourth floor

Fig. 9 Sensor units installed on four-story building. **a** Four story RC building. **b** Sensor unit on fourth floor

5 Conclusions

This paper presents the basic scheme of autonomous storing only the peak values of absolute acceleration responses and sending those data to the web server with a developed sensor unit. The developed sensor unit is composed of: (1) Raspberry Pi 3B; (2) 3-axis digital MEMS accelerometer; and (3) Low Power Wide Area (LPWA)

network device. The algorithm is also developed for extracting the peak absolute acceleration response to an earthquake. It consists of two modules: one is to identify the end of structural response; and the other is to distinguish the difference between the seismic and pulse-like responses (such as response to door closing or human walking). The effectiveness of the proposed system has been demonstrated by the full-scale hospital building model experiments conducted at E-defense. The results of E-defense shaking table test indicate that the proposed sensor unit and algorithm can extract the peak absolute acceleration response data and transmit them to the Excel file in Google Drive. The developed sensor unit and algorithm would provide the useful information for estimating the damage situation in the area.

Acknowledgements The research presented in this paper has been supported by Tokyo Metropolitan Resilience Project of National Research Institute for Earth Science and Disaster Resilience (NIED). The presented E-defense shake table experiment was prepared, planned and conducted by the leadership of Dr. M. Kurata (Kyoto University) and Dr. Y. Kawamata (NIED).

References

1. Ozer E, Feng MQ (2019) Structural reliability estimation with participatory sensing and mobile cyber-physical structural health monitoring systems. *Appl Sci* 9
2. Pal PS, Khuntia S (2020) Structural health monitoring using neural networks in IoT and cps paradigm—a review. *Int J Sci Res Eng Dev* 3(5):871–892
3. Nagayama T (2007) Structural health monitoring using smart sensors. PhD thesis, University of Illinois at Urbana-Champaign, Department of Civil and Environmental Engineering
4. Cho S, Yun C-B, Lynch JP, Zimmerman AT, Spencer BF Jr, Nagayama T (2008) Smart wireless technology for structural health monitoring of civil structures. *Steel Struct* 8:267–275
5. Ishikawa K, Mita A (2008) Time synchronization of a wired sensor network for structural health monitoring. *Smart Mater Struct* 17:1–6
6. Fu Y, Mechitov K, Hoang T, Kim J, Memon SA, Spencer Jr BF (2020) Efficient and high-precision time synchronization for wireless monitoring of civil infrastructure subjected to sudden events. *Struct Control Health Monit* 28(3)
7. Housner GW (1952) Spectrum intensity of strong motion earthquake. In: *Proceedings of the symposium on earthquake and blast effects on structures*, pp 20–36
8. NXP Semiconductors (2012) MMA7660FC Data Sheet, NXP Semiconductors
9. Akazawa M, Saburi K, Kurata M, Matsuo S, Kawamata Y (2019) Structural design and ultimate state behavior of low-rise critical buildings. In: *Summaries of technical papers of annual meeting, AIJ, BIII*, pp 1233–1234
10. Bosh Sensortec GmbH (2021) BMA400 Data Sheet, Bosh Sensortec GmbH

Indirect Estimation Method of Bridge Displacement Under Moving Vehicle Based on Measured Acceleration



Mingwei Wang, Yan Li, Guowei Lin, Baocheng Liu, and Changyun Ye

Abstract Direct measurement of dynamic displacement during bridges load testing usually is time-consuming, expensive and sometimes is difficult to perform. This paper proposes an indirect measurement method of bridge dynamic displacement by acceleration integration. The dynamic-static separation processing and a multi-round baseline correction technique based on least squares method are used in the proposed approach. After the baseline of measured acceleration data is corrected totally, the filter is used to eliminate high frequency noise and separate quasi-static and free vibration response before integrating. Considering the natural difference between dynamic and static response an innovative effective baseline correction method is established during acceleration integration process. The accuracy and feasibility of proposed displacement estimated method is verified based on a real bridge in-situ dynamic load test. The results indicate that the proposed method has a satisfied accuracy and can be applied in engineering practice.

Keywords Moving vehicle · Acceleration integration · Dynamic-static separation · Least squares method · Baseline correction

1 Introduction

Displacement measurement plays an important role during loading tests and health monitoring for bridges, which can be used to evaluate structural actual stiffness and service state of bridges. Methods of displacement measurement can generally be divided into two types: contact and non-contact. Though contact displacement sensor

M. Wang (✉) · Y. Li

School of Transportation Science and Engineering, Harbin Institute of Technology, Harbin, China
e-mail: 1429769448@qq.com

G. Lin · C. Ye

Jinan Urban Construction Group Co., Ltd, Jinan, Shandong, China

B. Liu

Tianjin Transportation Committee, Tianjin, China

commonly has good accuracy, usually it is difficult to find a relatively fixed reference point due to the restriction of site condition and structural forms during field test. Typical non-contact methods such as GPS are only suitable to long-span flexible bridges with large deformation, but are inapplicable to small and medium span bridges. In recent years, the displacement measurement method based on machine vision has become a research hotspot, but there is still a certain distance from practicality. At the same time, its sensitivity to light and weather conditions also limits the wide application of this method in transportation infrastructure maintenance [1]. Relatively speaking, the accelerometer does not need a fixed reference point, and can be used in testing easily with low cost. Moreover, the bridge displacement response can be obtained through acceleration signal integration in theory. Therefore, indirect estimation based on the measured acceleration has been proposed as an effective method of bridge displacement measurement [2–4].

The literature review indicates that time-domain and frequency-domain integration are two main integration methods for obtaining displacement through acceleration signal. For the frequency-domain integration, the quasi-static response of bridge is determined by the low frequency part of acceleration spectrum signal, therefore the low frequency noise has significant influence on the accuracy of frequency domain integration result [5]. For the time domain integration, small errors of vibration signal will accumulate and finally deviate from actual value and baseline. Recent years some research have been performed in this field. Chen et al. [6] proposed a polynomial fitting method of extreme value to eliminate the trend of error, and the displacement curve with good accuracy is obtained. However, this method only works on the linear trend term and constant error term, cannot eliminate the error induced by random noise. Hidehiko Sekiya et al. [7] got displacement response by integrating forced and free vibration acceleration respectively, and found that the method works only by high resolution acceleration sensors under low noise environment. The proposed method cannot completely eliminate the error caused by inherent characteristic of sensor. Umekawa et al. [8] proposed a baseline correction method of fitting error trend term by spline curve after direct double integration of acceleration, but it is only suitable for the slight baseline drift. Effective error elimination methods are necessary for the recorded response signals with not so satisfactory accuracy. Zheng et al. [9] proposed an online real-time acceleration integration scheme based on the recursive least squares method, high-pass filter and integrator. The results show that the baseline correction through least squares method can effectively reduce the acceleration integral error. However, since the target baseline in velocity and displacement baseline correction is set to zero horizontal line, it cannot be directly applied to the cases when the bridge does not vibrate around zero horizontal line, such as vehicle-induced vibration.

Hence, the present study proposes a method of bridge displacement response measurement which can be used for typical operation condition and dynamic load testing. An acceleration time domain integration approach based on dynamic-static separation and least squares method is established by combining with a more effective baseline correction strategy. This article mainly includes two parts: in Sect. 2, the

basic principle, process and key points of the proposed method for indirect displacement measurement are deduced and introduced. In Sect. 3, the real bridge field test verification and related parameters study for the proposed method is introduced.

2 Estimation Method of Bridge Dynamic Displacement Under Moving Vehicle Based on Measured Acceleration

2.1 Framework and Implementation Process of the Proposed Method

The acceleration signal usually may deviate from the actual value due to environmental and equipment noises, and that will lead to obvious baseline drift. However, this deviation exists in the entire frequency domain, so the errors cannot be completely separated by filtering [8]. The dynamic response of bridge under moving vehicle can be considered as a superposition of free vibration and the quasi-static response with different baselines respectively. Considering the characteristics of dynamic response and measured acceleration signals for bridge under moving vehicle, a new displacement response estimation algorithm is proposed in this paper. A multi-strategy combined with low-pass, band-pass filtering and multi-round baseline correction of acceleration signals are performed in the proposed method based on acceleration time domain integration. The framework and process of the displacement estimation method can be described as Fig. 1.

The detailed steps of the proposed method can be summarized as follows.

- Step 1 Intercept the time period from the front axle on the bridge to the rear axle off the bridge from the measured acceleration signal.
- Step 2 Perform the first baseline correction with the least squares method.
- Step 3 Obtain quasi-static acceleration and free vibration acceleration with filter based on FFT.
- Step 4 Integrate the accelerations relatively to obtain the velocities.
- Step 5 For the free vibration velocity, perform the baseline correction with least squares method; for the quasi-static velocity, perform the baseline correction by subtracting the mean value.
- Step 6 Integrate the velocities relatively to obtain the displacements.
- Step 7 For the free vibration displacement, perform the baseline correction with least squares method, and the quasi-static displacement is no longer corrected.
- Step 8 Superimpose the two to obtain final estimated displacement.

The specific principle and application of the above method will be discussed in the following parts.

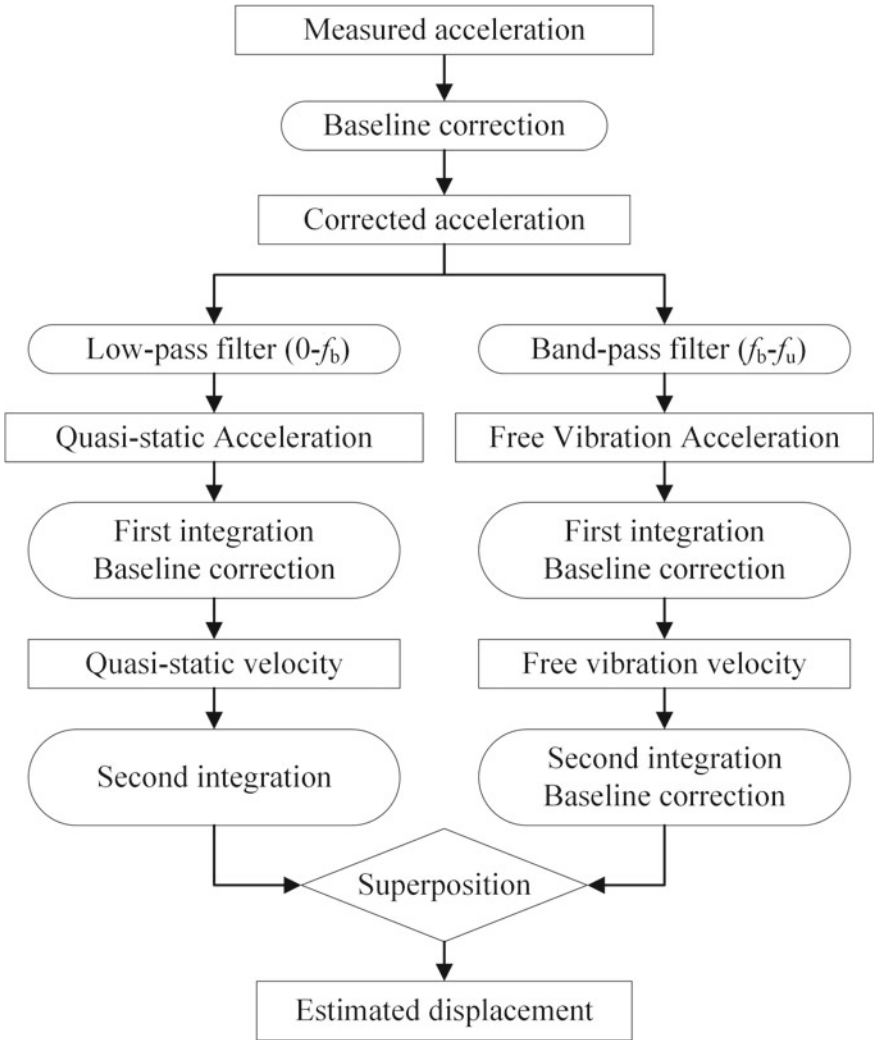


Fig. 1 Process of acceleration integration method based on dynamic-static separation and least squares method

2.2 Principle of Acceleration Integration Based on Dynamic-Static Separation

Cut-off frequency filter is used to process the acceleration signal before the integration in the proposed method. The structure quasi-static response is obtained with low-pass filter. Band-pass filter is applied to obtain the free vibration response and filter out the high frequency components to reduce the estimation error. The filtering expression is defined as:

$$y(\omega) = \sum_{k=0}^{N-1} H(k) X(k) e^{j2\pi k\omega/N} \quad (1)$$

where N is the amount of measured acceleration sampling points; $X(k)$ is the acceleration signal after Fourier transform; $H(k)$ is the frequency response function of the filter, when low-pass filter is selected the function is defined as:

$$H(k) = \begin{cases} 1 & (k\Delta f \leq f_b) \\ 0 & (k\Delta f > f_b) \end{cases} \quad (2)$$

When the band-pass filter is selected, the function expression can be given as:

$$H(k) = \begin{cases} 1 & (f_b \leq k\Delta f \leq f_u) \\ 0 & (k\Delta f < f_b \text{ or } k\Delta f > f_u) \end{cases} \quad (3)$$

where f_b is the boundary frequency between free vibration and quasi-static response; f_u is the upper cut-off frequency; $\Delta f = f/N$ is the frequency resolution; f is the sampling frequency.

If the whole process of bridge displacement response caused by the passing vehicle is regarded as one vibration period, the boundary frequency between free vibration and quasi-static response can be calculated according to the vehicle passing time. The upper cut-off frequency can be determined by estimating the natural frequency range which dominates the structure dynamic response through numerical simulation or dynamic test.

In time domain, the dynamic displacement of the bridge can be obtained by double integration of the acceleration:

$$u(T) = \int_0^T v(t)dt + u_0 = \int_0^T \left[\int_0^T a(t)dt + v_0 \right] dt + u_0 \quad (4)$$

where u is displacement; v is velocity; a is acceleration; v_0 is initial velocity; u_0 is initial displacement.

Assuming that the initial velocity and displacement are equal to 0, the displacement calculation expression can be written as follow based on the trapezoidal formula:

$$\begin{aligned}
 u(T) &= \frac{\Delta t}{2} \sum_{i=1}^{T/\Delta t-1} [v(t_i) + v(t_{i+1})] \\
 &= \frac{\Delta t}{2} \sum_{i=1}^{T/\Delta t-1} \left\{ \sum_{i=1}^{T/\Delta t-1} [a(t_i) + a(t_{i+1})] + \sum_{i=2}^{T/\Delta t} [a(t_i) + a(t_{i+1})] \right\} \quad (5)
 \end{aligned}$$

where Δt is the sampling interval; t_i is the sampling time point.

2.3 Principle of Multi-Round Baseline Correction

In order to solve the baseline drift problem of the displacement curve obtained by acceleration integration and to improve the accuracy of displacement estimation, a multi-round baseline correction strategy is proposed in this paper. The baseline correction based on least squares method is performed on the measured acceleration signal, the integral velocity and displacement data, respectively. Meanwhile, for the uncertainty of the quasi-static response baseline, an error correction method of mean value subtraction is proposed for the quasi-static velocity response obtained by integration.

2.3.1 Baseline Correction Based on Least Squares Method

The least squares method is used to fit the baseline of unprocessed data. The result is called the fitted baseline. The essence of the method is to construct a function as follow:

$$\phi(t) = \sum_{k=0}^m c_k \varphi_k(t) \quad (6)$$

According to $x_u(t_i)$, find a approximate function $\phi(t)$ to meet:

$$\sum_{i=1}^N [\phi(t_i) - x_u(t_i)]^2 = \min \quad (7)$$

where $\varphi_k(t) = t^k$ ($k = 0, 1, \dots, m$) is the best square approximation function, its coefficient is c_k , and the highest order is m ; $x_u(t_i)$ is the uncorrected data values.

The purpose of obtaining the fitted baseline is to determine the actual case of the uncorrected data baseline drift so that the correction can be performed. It has been shown that fitting the uncorrected data with a linear polynomial can achieve better results [9]. The degree and coefficients of the polynomial can be determined by fitting and trial calculations based on the bridge measured data.

The corrected curve can be obtained by subtracting the difference between the fitted baseline and the target baseline from the uncorrected data:

$$x(t) = x'(t) - [\phi(t) - f(t)] \tag{8}$$

where $x(t)$ is the baseline corrected acceleration or displacement; $f(t)$ is the target baseline, for free vibration signals, it is the zero horizontal line.

2.3.2 Baseline Correction Based on Mean Value Substraction

Since only the free vibration term remains in the bridge response after the car goes off the bridge, the static displacement of the bridge is restored to 0. Therefore, the quasi-static displacement at the moment the car goes off the bridge can be expressed by the quasi-static velocity according to Eq. (5) as:

$$\bar{u}(t_N) = \frac{\Delta t}{2} \sum_{i=1}^{N-1} [\bar{v}(t_i) + \bar{v}(t_{i+1})] = 0 \tag{9}$$

Divide both sides of the equation by $\Delta t/2$ to get:

$$\begin{aligned} \sum_{i=1}^{N-1} [\bar{v}(t_i) + \bar{v}(t_{i+1})] &= \bar{v}(t_1) + 2 \sum_{i=2}^{N-1} \bar{v}(t_i) + \bar{v}(t_N) \\ &= 2 \sum_{i=1}^N \bar{v}(t_i) - \bar{v}(t_1) - \bar{v}(t_N) = 0 \end{aligned} \tag{10}$$

Considering that the bridge static velocity response at the time of the front axle on the bridge $\bar{v}(t_1)$ and the rear axle off the bridge $\bar{v}(t_N)$ are 0, it can be deduced that the mean value of the quasi-static velocity response for the whole process of the vehicle passing through is 0, that is:

$$\frac{1}{N} \sum_{j=1}^N \bar{v}(t_j) = 0 \tag{11}$$

Therefore, a correction formula for quasi-static velocity response curve obtained by first integration is proposed:

$$\bar{v}(t_i) = \bar{v}_u(t_i) - \frac{1}{N} \sum_{j=1}^N \bar{v}_u(t_j) \quad (12)$$

where $\bar{v}_u(t_i)$ is uncorrected quasi-static velocity response.

3 Engineering Application and Experiment Verification

3.1 Test Bridge and Dynamic Load Test Scheme

The test bridge is a pre-stressed concrete fabricated simply supported hollow slab bridge. Its total length is 147 m and the span arrangement is $2 \times 13 \text{ m} + 5 \times 20 \text{ m}$. The 20 m span of the bridge is chosen for the dynamic vehicle load test to provide data support for the application and validation of the proposed method. The bridge appearance is shown in Fig. 2a, the half cross section and vehicle loading position are shown in Fig. 3.

A three-axle truck which is commonly used in China highway bridge test is selected (shown in Fig. 4). The parameters are $P1 = 6.88\text{t}$, $P2 = P3 = 19.61\text{t}$, $D1 = 3.85 \text{ m}$, $D2 = 1.80 \text{ m}$, $D3 = 1.35 \text{ m}$. Restricted by the field test conditions, the vehicle was set to cross the bridge at a constant speed of 20–40 km/h. The speed case of the vehicle passing the bridge shall be subject to the actual vehicle speed.

In order to gather the dynamic response of the bridge under moving vehicle, acceleration measurement points were arranged at the middle of 5# beam, and displacement measurement points were arranged at the middle of 5#, 7#, 9# and 11# beams. The dynamic signal test system DH5922 of Donghua Company was used to record the dynamic response at each measurement point with a sampling frequency of 200 Hz. The layout of acceleration and displacement sensors and the field test process are shown in Fig. 2b, c. Taking the speed of 30.4 km/h as an example, the measured acceleration and displacement response at the middle of 5# beam are shown in Fig. 5.

3.2 Acquisition Implementation of Displacement Response Based on Acceleration

The acceleration time history signal of 5# beam is selected as an example when the vehicle average speed is 30.4 km/h, and the method proposed in this paper is applied to estimate the dynamic displacement. According to the observation records of the vehicle position at the field, the time period from the front axle on the bridge to the rear axle off the bridge is accurately intercepted. This acceleration data baseline is fitted by least squares method with a linear function with the method proposed in



Fig. 2 Field test: **a** appearance of the bridge; **b** displacement sensors layout; **c** acceleration sensors layout

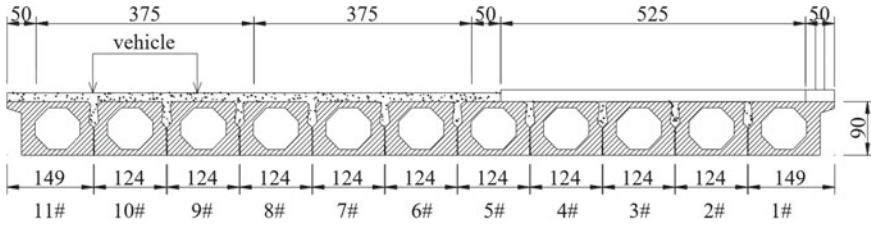


Fig. 3 Half cross section and vehicle loading position (cm)

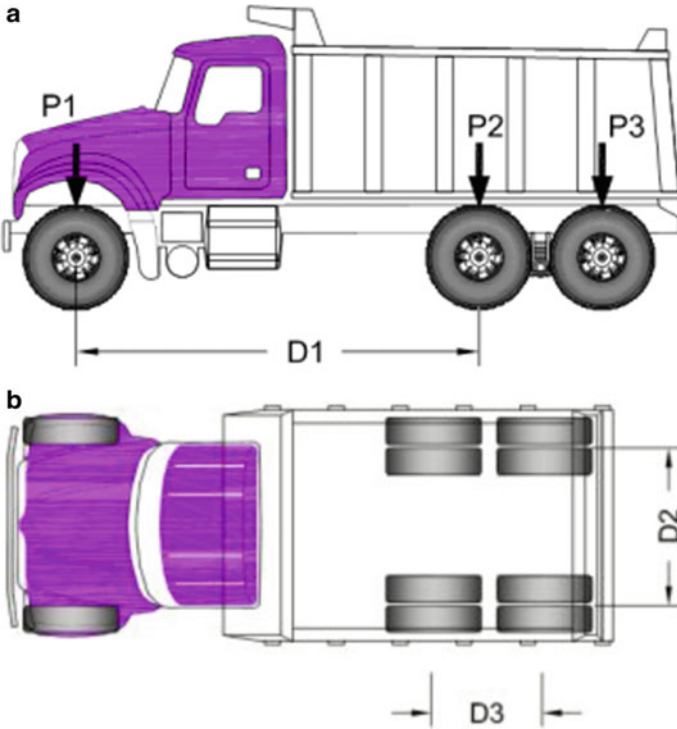


Fig. 4 The truck used in field test

Sect. 2, then the first baseline correction is carried out. The original and modified data are shown in Fig. 6a, b.

This study found that the natural frequency range which plays a dominant role in the dynamic response of the bridge is contained within ten orders. A spatial finite element model of the bridge is established with Midas civil, and the structural modal analysis is performed. The tenth order natural frequency of the bridge is 23.96 Hz, so the upper cut-off frequency is selected as 24 Hz. The passing time of the vehicle is 2.985 s, and the quasi-static response frequency of the bridge excited by this is

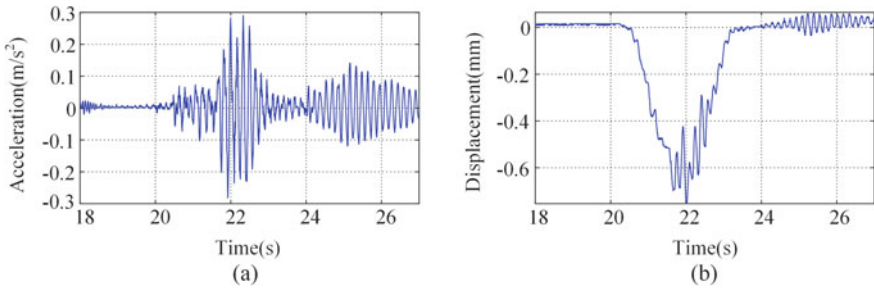


Fig. 5 Measured dynamic response of the middle of 5# beam when vehicle passes the bridge at 30 km/h: **a** time history acceleration response; **b** time history displacement response

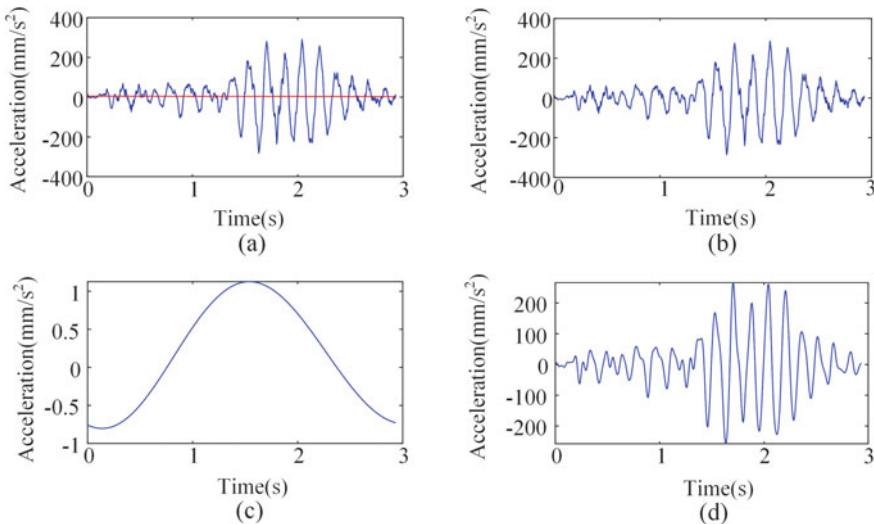


Fig. 6 First baseline correction and dynamic-static separation: **a** acceleration measurement and baseline; **b** corrected acceleration; **c** quasi-static Acceleration; **d** free Vibration Acceleration

about 0.35 Hz. In this case, the boundary frequency can be confirmed as 0.4 Hz. Then, the signal is analyzed in frequency domain through fast Fourier transform, so as to obtain the free vibration and quasi-static acceleration response by filter (shown as Fig. 6c, d).

From the comparison of the curves before and after processing, it can be seen that the baseline drift in the original acceleration data is corrected with least squares method. The filtered free vibration acceleration curve is more continuous and smooth. It shows that the band-pass filter can effectively remove the high frequency noise interference, and the follow-up integration error trend term can be reduced.

After integrating the quasi-static acceleration signal obtained in the above steps, the mean value of velocity data is calculated and the baseline correction is performed

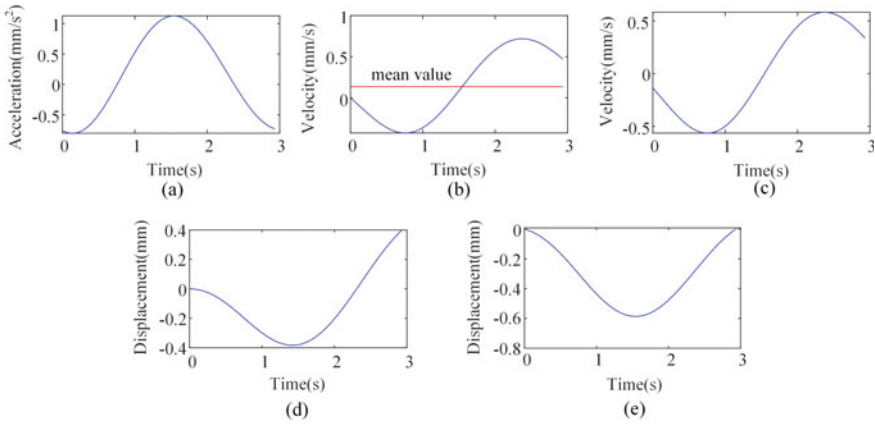


Fig. 7 Quasi-static acceleration integration and correction: **a** quasi-static acceleration; **b** quasi-static velocity and mean value calculation; **c** corrected quasi-static velocity; **d** displacement obtained by uncorrected velocity; **e** displacement obtained by corrected velocity

according to the method proposed in Sect. 2. The integration and correction process is shown in Fig. 7. It can be observed that the quasi-static displacement obtained by direct integration of the velocity has error trend terms, resulting in baseline drift. The baseline correction by subtracting the mean value can better solve the problem.

The free vibration acceleration response is integrated, then the correction method is applied to fit the baseline of velocity and displacement response curves by least squares method with a linear function. The integration process and final superimposed displacement are shown in Fig. 8.

3.3 Results Analysis

The bridge displacements at different test vehicle speeds are estimated based on the measured accelerations. The comparison between the estimated and the corresponding measured dynamic displacement curves of other vehicle speed conditions is shown Fig. 9.

In order to evaluate the accuracy of this indirect measurement method, the relative peak error is introduced to assess the agreement between the estimated and measured displacement time history curves (as shown in Eq. 13).

$$\zeta_P = \frac{|\max|d_M| - \max|d_E||}{\max|d_M|} \tag{13}$$

where d_E represents the bridge integral displacement at any moment; d_M represents the measured displacement at any moment.

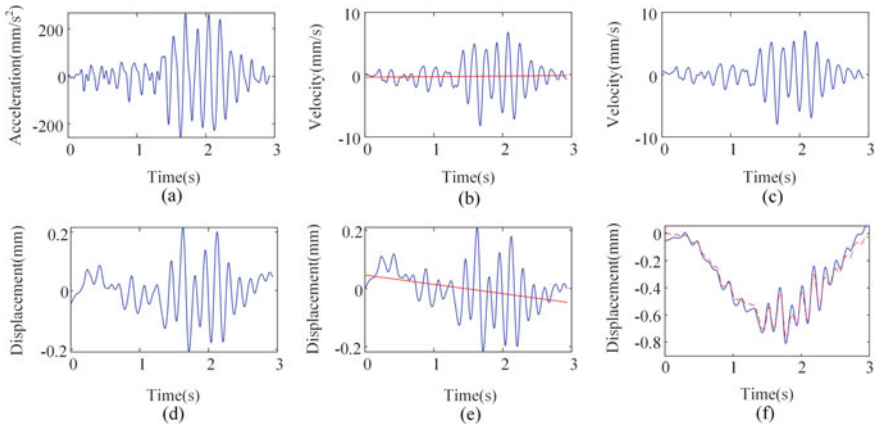


Fig. 8 Free vibration acceleration integration and correction: **a** free vibration acceleration; **b** free vibration velocity and baseline drift; **c** corrected free vibration velocity; **d** free vibration displacement and baseline fit; **e** corrected free vibration displacement; **f** comparison of estimated and measured displacement

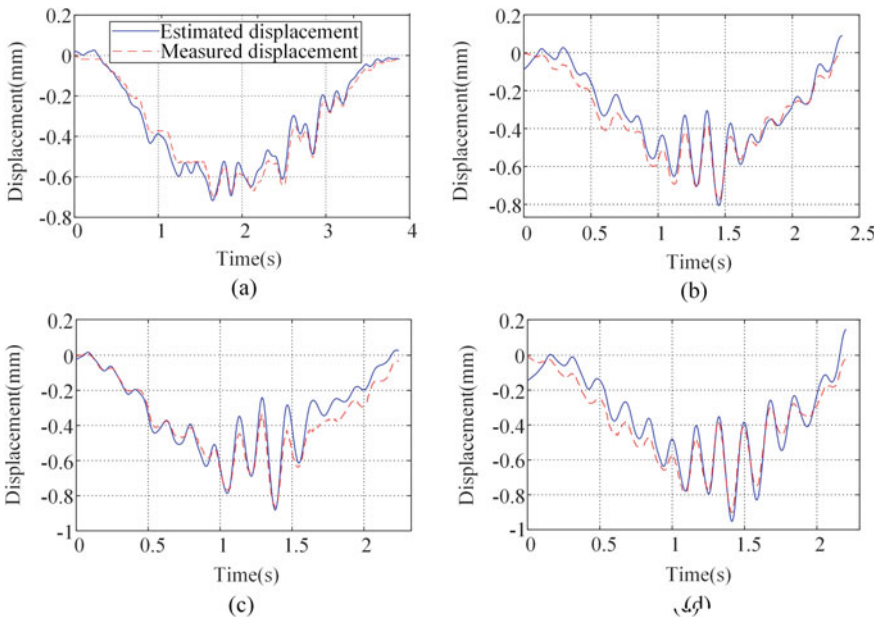


Fig. 9 Comparison of estimated displacement and measured displacement at different speeds: **a** 23.4 km/h; **b** 36.7 km/h; **c** 40.5 km/h; **d** 41.2 km/h

Table 1 Error analysis of estimated displacement at different vehicle speeds

Vehicle speed (km/h)	23.4	30.4	36.7	40.5	41.2
Peak difference (mm)	0.021	0.041	0.069	0.015	0.049
Relative peak error ζ_P (%)	3.04	5.29	8.70	1.68	5.41

The calculated assessment indexes are listed in Table 1.

The error analysis indicates that the peak differences between the indirect estimated and the measured value are in the range of 0.015–0.049 mm, and the average value of the five speed conditions is 0.039 mm. The relative peak errors are ranged from 1.68 to 8.7% and the average value is 4.82%. It shows that the displacement obtained by integration has a good accuracy.

4 Conclusions

Based on the current theories of indirect displacement estimation by acceleration, this paper studies and analyzes the time-domain integration fundamental and the baseline correction method. An indirect measurement approach of bridge dynamic displacement is proposed. It is combined with the dynamic-static separation of measured acceleration and the baseline correction based on least squares method. The proposed method is applied to actual indirect displacement measurement through a bridge dynamic load test and the feasibility is verified. The following conclusions are drawn:

- (1) The displacements obtained by this method match well with the measured displacements. It indicates that the method has a good engineering applicability.
- (2) The approach is simple to operate in practical application. In addition to the arrangement of acceleration sensors, it only needs to record the time of the vehicle on and off the bridge. Moreover, it has certain generality for bridges of different structural forms.
- (3) In this study, the span of test bridge is small, so the amplitude of displacement response under vehicle load is low, which is a factor leading to the increase of the relative error. In addition, because of the short passing time, the bridge quasi-static displacement would not completely restore due to damping effect when the vehicle went off the bridge. Therefore, this is also one of the reasons of estimation error for the basic assumption of Eq. (9) cannot be totally met.

In future research, more comparative test studies will be conducted on bridges of different types. The influence of various factors on the applicability of the method will be further investigated, and the development of engineering applications will be promoted.

References

1. Ma ZX, Chung JY, Liu PP, Sohn H (2021) Bridge displacement estimation by fusing accelerometer and strain gauge measurements. *Struct Control Health Monit* 28(6)
2. Park KT, Kim SH, Park HS, Lee KW (2004) The determination of bridge displacement using measured acceleration. *Eng Struct* 27(3):371–378
3. Hong YH, Kim HK, Lee HS (2010) Reconstruction of dynamic displacement and velocity from measured accelerations using the variational statement of an inverse problem. *J Sound Vib* 329(23):4980–5003
4. Zhu H, Zhou YJ, Hu YM (2020) Displacement reconstruction from measured accelerations and accuracy control of integration based on a low-frequency attenuation algorithm. *Soil Dyn Earthq Eng* 133
5. Hester D, Brownjohn J, Bocian M, Xu Y (2017) Low cost bridge load test: calculating bridge displacement from acceleration for load assessment calculations. *Eng Struct* 143
6. Chen WZ, Wang BW, Hu XY (2010) Acceleration signal processing by numerical integration. *J Huazhong Univ Sci Tech (Natural Science Edition)* 38(1):1–4
7. Sekiya H, Kimura K, Miki C (2016) Technique for determining bridge displacement response using MEMS accelerometers. *Sensors* 16(2)
8. Umekawa Y, Suganuma H (2018) Bridge displacement monitoring using acceleration measurement for efficient bridge management. *Maintenance, safety, risk, management and life-cycle performance of bridges*, pp 11–14
9. Zheng WH, Dan DH, Cheng W, Xia Y (2019) Real-time dynamic displacement monitoring with double integration of acceleration based on recursive least squares method. *Measurement* 141

In-Situ Measurements for the Structural Monitoring of Galleria dell'Accademia di Firenze (Italy): Preliminary Results of the Tribuna



Silvia Monchetti, Gianni Bartoli, Michele Betti, Claudio Borri, Claudia Gerola, Andrea Giachetti, Cecilie Hollberg, Vladimir C. Kovacevic, Carlotta Matta, and Giacomo Zini

Abstract The paper introduces recent results of experimental activities carried out on the Tribuna of the Galleria dell'Accademia di Firenze (Italy) where the Michelangelo's David is exhibited to the public. The work aims to investigate the dynamic behaviour of the Tribuna through the analysis of the accelerations measured by two triaxial stations roving in different positions. The experimental layout, in terms of instruments choice and its position, was carefully designed by considering both the architectonic features of the structure and the masterpieces collected in the Tribuna, such as paintings and sculptures which could not be moved during the measurements. The investigation activity was performed in the framework of a wider research project co-founded by Tuscany Region and Galleria dell'Accademia di Firenze with the aim to preserve the museum complex and the works of art inside. A computational model is herein proposed to illustrate the process of calibration, and its advantages in terms of model reliability, through the comparison between the experimental results and the model output itself. More in detail, the research deal with the issue related to the analyses of a portion of the structure, extracted from the whole complex, and the boundary conditions which need to be assigned in order to represent the actual interaction with the surrounding buildings. The workflow discussed in this paper, and applied to the case study of Galleria dell'Accademia di Firenze, represents a meaningful test bench from drawing general remarks on the topic of historical museum complex conservation.

Keywords Historical museum complex · Dynamic identification · Model calibration · In-situ measurements

S. Monchetti (✉) · G. Bartoli · M. Betti · C. Borri · A. Giachetti · G. Zini
Department of Civil and Environmental Engineering, University of Florence, Florence, Italy
e-mail: silvia.monchetti@unifi.it

V. C. Kovacevic
CEO Kobe Innovation Engineering, Florence, Italy

C. Gerola · C. Hollberg · C. Matta
Galleria dell'Accademia di Firenze, Florence, Italy

1 Introduction

The Galleria dell'Accademia di Firenze is famous all over the world due to the extensive collection of Michelangelo's sculptures, one of all: the Michelangelo's David. The Galleria dell'Accademia di Firenze was founded by Grand Duca Pietro Leopoldo between 1784 and 1787 as art museum for academics. The new institution was born as an aggregate of preexisting structures occupying the premises of the Hospital of San Matteo and the convent of San Niccolò in Cafaggio. Further modification underwent in 1872 when, under the design of the Arch. E. De Fabris, started the construction of the Tribuna to host the Michelangelo's David. The construction of the Tribuna has continued down to 1882 and, even if the structural configuration of the museum has not been substantially changed since the end of Tribuna construction, the building has been continued to undergo maintenance and restoration works until now. Indeed, the Galleria dell'Accademia di Firenze appears as an intricate museum complex: various structural units, marked their different era and different construction techniques, testify to the evolution in the project over the time. And it is in this context that the DAVID project was conceived. Acronym of Defense of cultural heritage and Assessment of Vulnerability through Innovative technologies and Devices, the DAVID project aims to preserve the museum complex and the works of art inside. One of the objective of the project is the joint evaluation of the risk between the structure and the contained works of art. This places the focus, on the one hand, the importance of achieving a high level of knowledge of the structure (material properties, restraint conditions, structural configuration, dynamic behaviour, ...) and, on the other hand, the need to define proper computational structural models. With the aim of collecting all available information on the Galleria dell'Accademia di Firenze, this paper takes advantage of the results introduced by De Stefano and Cristofaro [1] which reported the main outcomes of an extensive diagnostic campaign which allowed to assess the material properties and the constructive details of the whole museum complex. The matter of the definition of a reliable and robust computational model for the museum complex was initially discussed by Kovacevic et al. [2] through proposing a methodology for an automated processing of the geometrical information obtained from point clouds data, through BIM (Building Information Model) implementation and finite element modelling, for structural analysis. In this context, this paper summarizes the results of new structural dynamic identification on the Tribuna, one of the structural units of the Galleria dell'Accademia di Firenze with the aim of providing additional knowledge on its dynamic behaviour and to enhance the level of knowledge so far reached.

2 In-Situ Measurements

2.1 The Tribuna

The design of the Arch. E. De Fabris places the Tribuna at the end of a path, the Galleria dei Prigioni, which supports the visitors to discover the Michelangelo's works. The central area of the Tribuna is dominated by Michelangelo's David, it has a square plan with 8.70 m long sides, and it ends in an exedra. This central space is covered with a circular skylight which ensures natural lighting. The Tribuna is integrated to the other halls of the museum through side wings which exhibit paintings of the sixteenth Century (Fig. 1). The historic documentation of the Galleria dell'Accademia di Firenze [3] reports which the construction works of the Tribuna, started in 1872, were almost entirely realized as a new structure. The walls, as highlighted by the available in situ inspections [1], show a good quality of the masonry texture that alternates bands of squared stone elements and bricks, Fig. 2.

The mechanical parameters of these masonries can be gained from the double flat-jack tests performed on some masonry panels, as indicated in Fig. 2 and Table 1. All the qualitative and quantitative information about the characteristics of the Tribuna masonry panels allow to gain a good level of knowledge on the materials but



Fig. 1 Accademia Gallery (red dotted line) and the Tribuna (orange area)

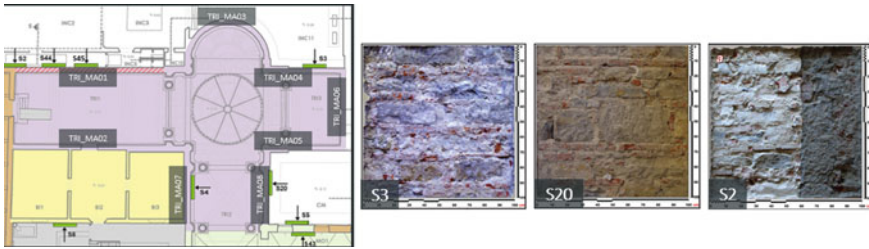


Fig. 2 Mechanical characterization of the masonry

Table 1 Properties of the masonry

ID		Era	Masonrytypology	Mechanical parameters [MPa] = (μ , σ)
TRI_MA01	S2	1873–1880	Category III (MIT 2019) [4]: Roughly cut stone with good texture Masonry with alternating stone and brickwork string courses, built with the inclusion of pre-existing masonry	Double flat-jacks: $E = (1370, 292)$, $f_m = (1,04, 0,29)$
TRI_MA04	S3	1873–1880	Category V (MIT 2019) [4]: Stone blocks squared Masonry with alternating stone blocks squared and brickwork string courses	Double flat-jacks: $E = (2490, 397)$, $f_m = (1,54, 0,99)$
TRI_MA08	S20	1873–1880	Category V(MIT 2019) [4]: Stone blocks squared Masonry with alternating stone blocks squared and brickwork string courses	Double flat-jacks not available

no information about the connection between the Tribuna and the other structural units of the museum complex are available. This latter aspect introduces a relevant source of uncertainty in the definition of the numerical model. In order to obtain information on the dynamic behavior of the Tribuna and its connection level with the other structural units with minimal invasiveness techniques, an experimental campaign based on ambient vibration test is performed.

2.2 Ambient Vibrations Set-Up

The experimental campaign was based on the measure of accelerations under ambient vibrations. In particular, PCB sensors 393-B31 and 393-B12 were used, by means of two triaxial stations roving in different positions. The peculiar location, especially

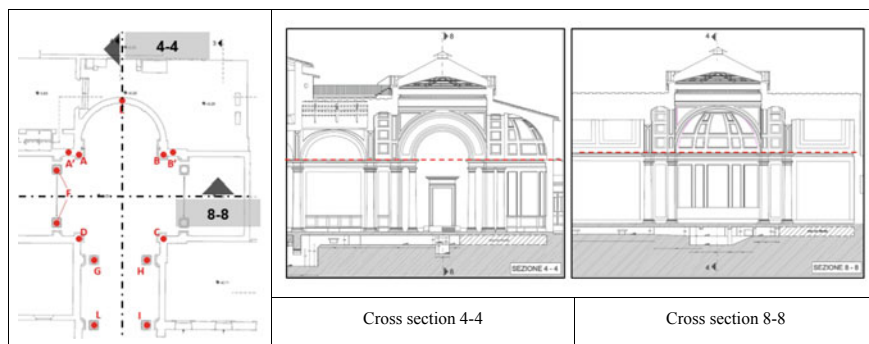


Fig. 3 Sensor layout during the Ambient Vibration Tests; the red line in the cross-sections represent the sensor height during the tests

the paintings and sculptures which could not be moved during the measurements, limited the current preliminary experimental campaign. Therefore, by referring to the plan (Fig. 3), eleven locations (were selected to record simultaneously the two triaxial stations placing one of them on the ground, and the other above it, on the cornices already used for other systems (Fig. 4). Only in one case, it was possible to record simultaneously the two triaxial stations at the same height on the cornices.

Generally, each test was performed recording the six acceleration signals for about 900 s, at a sampling frequency equal to 4800 Hz. All the signals were firstly filtered by means of a third-order IIR Butterworth filter between 0.5 and 100 Hz. The frequency band was set in order to avoid noise at very low and very high frequencies, also taking into account for the preliminary results given by the numerical model.

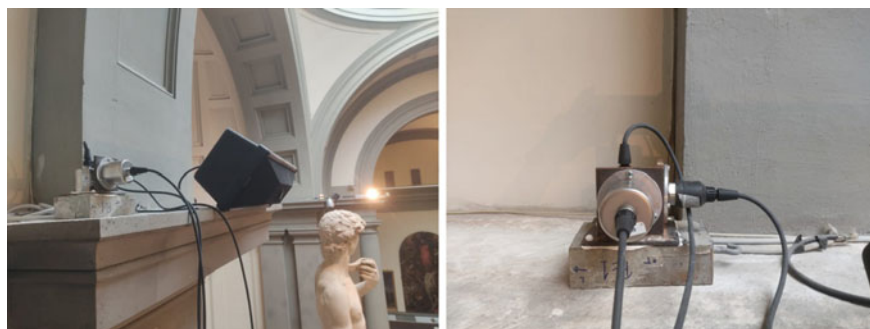


Fig. 4 Triaxial station during the AVTs

2.3 Results of the Preliminary Experimental Campaign

In the current work, the aim of the preliminary experimental campaign was to obtain modal parameters useful to tune the numerical model [5], dealing with inherent practical problems of such a peculiar environment. The main results referred to a frequency domain analysis, firstly by considering the Average Normalized Power Spectral Density (ANPSD) [6], then each acceleration spectrum was analyzed to have an insight on the local-dynamic behavior of the structure.

The main issue was represented by the many air-conditioning units in the room, necessary to keep opportune environmental conditions for the David's sculpture: each one of them was source of interferences to the measures, visible as spikes in the frequency band of interest. Moreover, given that it was not possible to record simultaneously the accelerations on different locations, a proper dynamic identification cannot be performed. Even if, the results of the ANPSD (Figs. 5 and 6) cannot allow to identify a clear set of resonant frequencies, some indications about the dominant frequency band can be attained. Therefore, an empirical approach was used to properly interpret the results by looking at the peaks obtained in the spectra of the accelerations collected in each station (A-L). The spectra were evaluated by averaging the one-sided results of the discrete Fourier transform obtained on all the samples of windows composed by 2^{16} points, with an overlapping of 50%. In this way it was possible to obtain a frequency resolution of about 0.07 Hz. By ordering the peaks on tables, it was possible to identify the non-structural peaks as those observed

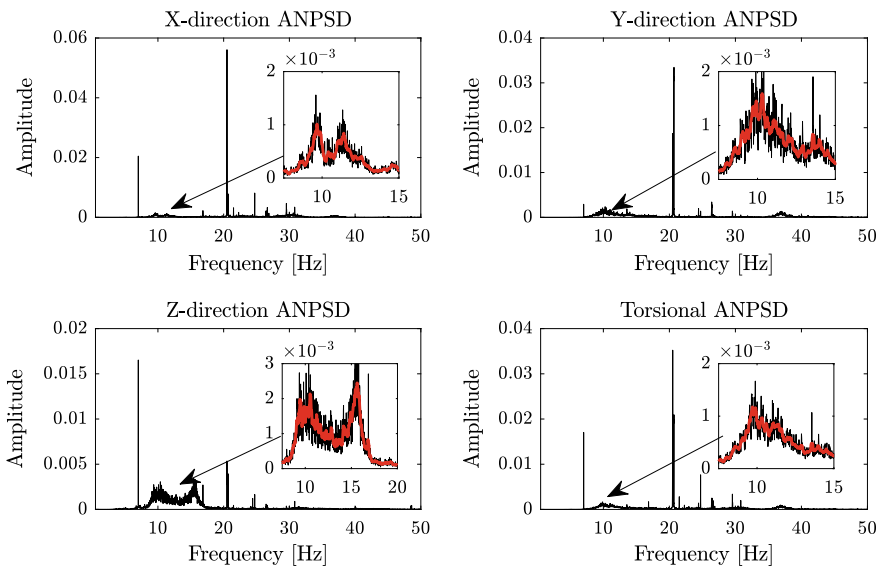


Fig. 5 The ANPSD of the central nave of the Galleria dell'Accademia di Firenze; the red line is the moving mean of the spectral densities

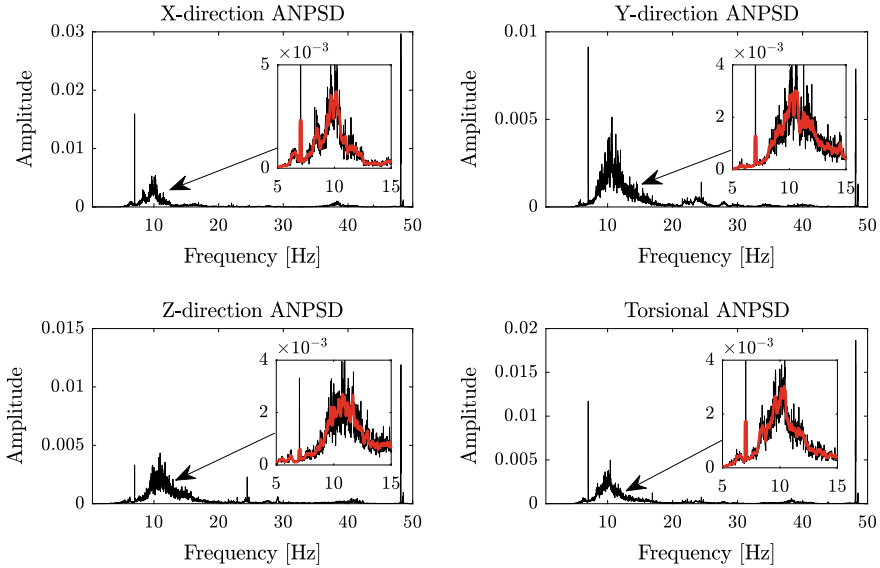


Fig. 6 The ANPSD of the transversal nave of the Galleria dell'Accademia di Firenze

for each spectrum with the same frequency down to the second decimal place (in some cases, the same spike was observed for sensors oriented on perpendicular directions). After a double check on the spectra, the non-structural peaks were deleted and a further distinction was carried out trying to distinguish peaks related to local or global effects. Thanks to this simple approach, it was found a first mode at about 4.2 Hz and a second mode at about 5.2 Hz, respectively consistent with a torsional and a translational (along the direction parallel to Cross section 4-4, Fig. 3) mode shapes. The first mode was identified through the sensors placed on the corridor far away from the David's sculpture (stations D-G-H-I-L), while the second mode was identified on all the location analyzed.

3 Numerical Modelling

The Finite Element (FE) software CODE ASTER [7] was used to reproduce the numerical model of the Tribuna, with different level of detail (Fig. 7). The geometry model was created on the base of the laser scanner survey, performed by Geomatics and Communication for Cultural Heritage Laboratory (GeCo Laboratory, University of Florence). The FE model was built with 2D elements to represent the masonry panels and the slabs, and 1D elements to represent the columns around the central area of the Tribuna and the beams of the glass roof over the Michelangelo's David. The CODE ASTER model was employed to perform linear modal analyses with the aim to

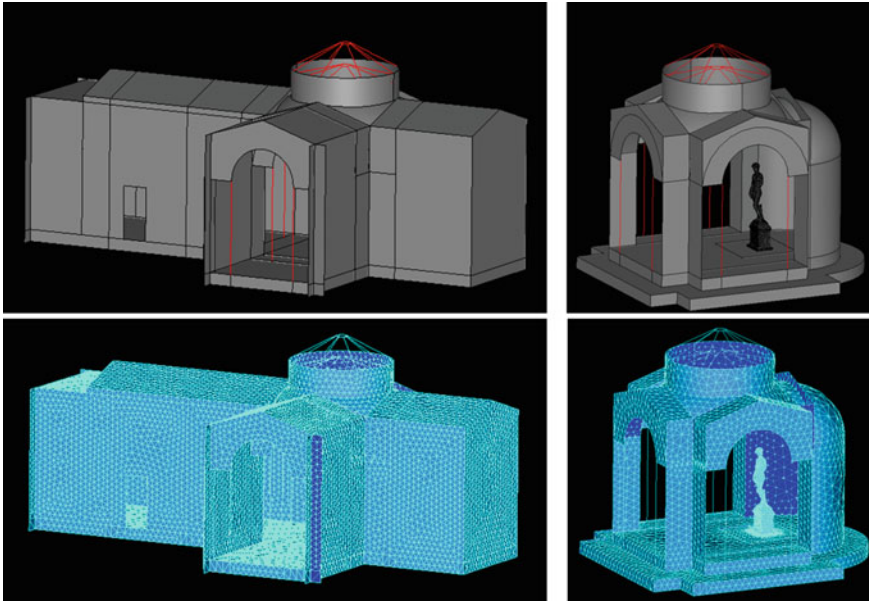
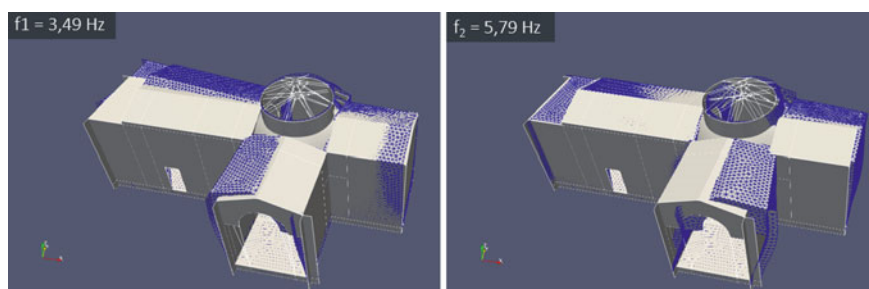


Fig. 7 Numerical models of the Tribuna

compare the experimental results with different configurations of the restraint conditions provided by the adjacent structural units. With respect to the various (unknown) input parameters which characterize this museum complex, the mechanical properties of the masonry was assumed on the base of the results by the double flat-jack (Table 1) and the restraint condition provided by the soil was assumed as fixed support. The main source of uncertainty was thus considered related to the restraint condition provided by the adjacent structural units: the Sala dei Gessi and the Galleria dei Prigioni. In order to reproduce this contribution, parametric modal analyses can be performed in order to assess the stiffness effect of the non-modelled adjacent structural units. Ideal restraints, to represent the walls intersecting between the Tribuna and the other structural units, were designed through 2D elements (extended for the masonry panel height with 100 mm of thickness) by applying a full horizontal constraint on the free vertical edge. These panels were adequately arranged according to the effective orientation of the adjacent structural units. The panels stiffness was parametrically tuned to compare the results of dynamic simulation of the Tribuna with those of the experimental campaign in terms of both natural frequencies and modal displacements on the control points defined in the experimental set-up. A preliminary set of analyses was carried out by considering different stiffness of the restraint panels (E^*) in order to simulate various scenario: from no interaction between the Tribuna and the adjacent structural units to full restrained (Table 2). Additional set of analyses will be carried out for the follow-up of the DAVID project, which will

Table 2 First two natural frequencies as function of the lateral restrained provided by adjacent structural units

Elastic modulus of adjacent buildings (MPa)	f_1 (Hz)	f_2 (Hz)
$E^* = 0$ (no restrained)	3.49	5.79
$E^* = 500$	4.23	6.01
$E^* = 10^6$ (full restrained)	4.71	6.23

**Fig. 8** First two natural frequencies of the Tribuna

be useful to evaluate the sensitivity of the computational output as function of the input variability (Fig. 8).

4 Conclusions

The paper has presented development and results of the experimental activity carried out on the Tribuna: one of the structural unit of the Galleria dell'Accademia di Firenze. This experimental activity was developed as part of the DAVID project which, in the first part of its activity, was aimed to increase the level of knowledge on the structural properties of the museum complex (e.g. mechanical characterization of the masonry, restraint conditions, ...) through new set of experimental data. The preliminary results, herein introduce, confirm as a comprehensive identification of the dynamic behaviour of the Tribuna requires a careful evaluation of the restraint conditions provided by the adjacent buildings and the study of the effect of the other sources of uncertainty, such as the material properties of the masonry and the restraint condition provided by the soil interaction. This work represents an ongoing research: in the following more detailed analyses and results will be presented.

References

1. De Stefano M, Cristofaro MT (2020) The complex of the Galleria dell'Accademia di Firenze: keeping in safety. *Proc Struct Integr* 29:71–78
2. Kovacevic VC et al (2019) An integrated computational approach for heritage monumental museums. In: 7th International conference on computational methods in structural dynamics and earthquake engineering (COMPDYN), Crete, Greece, pp 2878–2892. <https://doi.org/10.7712/120119.7117.19725>
3. Mignani D (2010) Applicazione della Direttiva della Presidenza del Consiglio dei Ministri del 12/10/2007 per la valutazione e riduzione del rischio sismico del Patrimonio Culturale— Approfondimento della ricerca storica delle fasi costruttive e dei lavori eseguiti nella Galleria dell'Accademia di Firenze. Ministero per i beni e le attività culturali, pp 1–46
4. MIT 2019 (2009) Circolare n. 7 del 21 gennaio 2019. Istruzioni per l'applicazione dell'«Aggiornamento delle “Norme tecniche per le costruzioni”» di cui al decreto ministeriale 17 gennaio 2018
5. D'Altri AM, Sarhosis V, Milani G, Rots J, Cattari S, Lagomarsino S, Sacco E, Tralli A, Castellazzi G, de M (2020) Modeling Strategies for the Computational Analysis of Unreinforced Masonry Structures: Review and Classification. *Archives of Computational Methods in Engineering* 27(4):1153–1185. <https://doi.org/10.1007/s11831-019-09351-x>
6. Ventura CE, Felber AJ, Stierner SF (1995) Experimental Investigations of Dynamics of Queensborough Bridge. *J Perform Constructed Facil* 9(2):146–155. [https://doi.org/10.1061/\(ASCE\)0887-3828](https://doi.org/10.1061/(ASCE)0887-3828)
7. Pieraccini M, Betti M, Forcellini D, Dei D, Papi F, Bartoli G, Facchini L, Corazzi R, Kovacevic VC (2017) Radar detection of pedestrian-induced vibrations on Michelangelo's David. *PLOS ONE* 12(4):e0174480. <https://doi.org/10.1371/journal.pone.0174480>

Structural Monitoring of an Aerial Tramway System During Operation: Modeling and Simulation Strategy with Experimental Data Validation



Hugo Bécu, Claude-Henri Lamarque, Alireza Ture Savadkoohi, Michel Gillard, and Christophe Bottollier

Abstract The present study aims at building and calculating a global static model of a long-distance single span aerial tramway with non-symmetric tracks and anchored cables at extremities. From a design engineering point of view, aerial cable transport system is a complex structure involving several theoretical and practical issues due to diversity of phenomena at stake. Hence, appropriate framework is required to have relevant results according to the aim of the study. Influence of structural parameters modification occurring during system operation is analyzed by a static and quasistatic calculations. It provides information on parametric evolution through cable length unwound at drive bull-wheel as a previous step of dynamics study with a cable velocity. Hypotheses are discussed and modelling choices are confirmed by a comparison with experimental data measured on a real system.

Keywords Aerial cable transport systems · Flexible structures · Nonlinear statics · Catenary curve · Test/model

1 Introduction

Aerial tramway is a well-established means of aerial cable transport system in mountainous regions where high vertical elevations must be ranged while having a growth potential of use in urban areas. Design studies dedicated to standard cable transport system engineering applications are based on statics assumptions with the cable at rest [1–3]. On the other hand, their dynamics is widely studied in scientific literature in a simplified way without considering the entire system but only one cable portion, excluding cable translation movement [4], or several spans coupled by supports [5], with a cable translation velocity [6].

H. Bécu (✉) · C.-H. Lamarque · A. Ture Savadkoohi
University of Lyon, ENTPE, LTDS UMR CNRS 5513, Vaulx-en-Velin, France
e-mail: hugo.becu@entpe.fr

M. Gillard · C. Bottollier
DCSA Ingénieur Conseil, Meylan, France

© The Author(s), under exclusive license to Springer Nature Switzerland AG 2023
Z. Wu et al. (eds.), *Experimental Vibration Analysis for Civil Engineering Structures*,
Lecture Notes in Civil Engineering 224,
https://doi.org/10.1007/978-3-030-93236-7_21

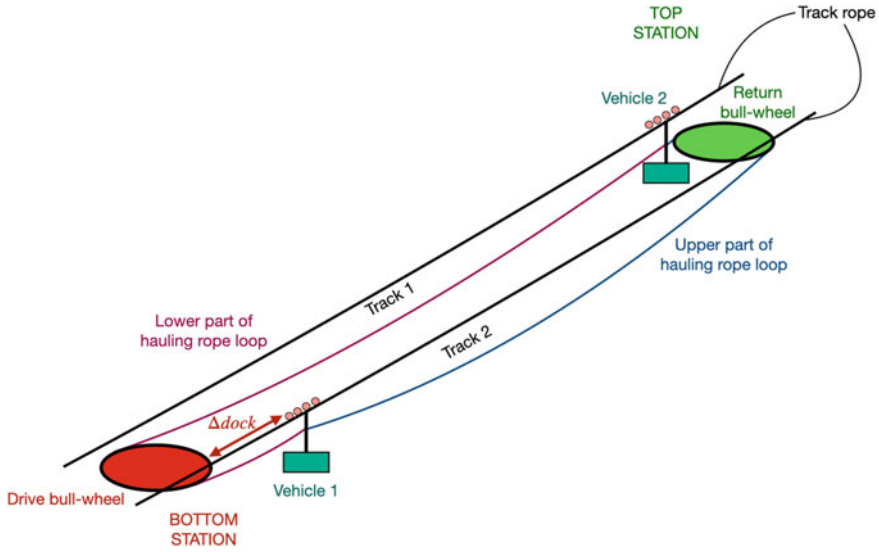


Fig. 1 Aerial tramway diagram

In this work, the statics cable model is based on catenary equations with elasticity correction considering cable elongation due to loading. The system under consideration is illustrated in Fig. 1. Vehicles are represented by punctual masses carried by track ropes and pulled by a haul rope. At the bottom station, haul rope loop is coupled between the two tracks by a drive bull-wheel connected to a driving system which controls cable position. A return bull-wheel closes the loop at the top station. Due to asymmetry of cable characteristics along the haul rope loop and carrier loading, some practical consequences appear as a shift of vehicles docking at stations.

An engineering challenge is the monitoring of the haul rope loop length during aerial tramway operation. The haul cable length changes due to permanent strain mainly during the first years after installation. Also, temperature and loading variations are the cause of cable length and sag modifications. To prevent cable damage or its contact with obstacles along the track, monitoring of cable length evolution provides important information for the operator to plan maintenance operation like cable shortening or replacement.

In this study, vehicles are clamped on haul rope loop with grips by a friction mechanism. Vehicles are often uncoupled from the cable to prevent any slip along the haul rope due to clamping force decrease or cable damage at the contact surface. Vehicles are moved to a new position along the haul loop. So upper and lower haul rope length separating the two carriers can change during these maintenance tasks.

In absence of dedicated sensors to measure haul cable length evolution with enough precision, a common practice of skilled person is to go through intermediate quantity measures. Thus, cable angles at stations without vehicles along the cable loop or shift length of vehicles docking at stations are directly measured on

the system for specific known configuration. Then, these experimental data are put in a suitable model of the system which allows to access haul cable length value.

2 Modeling

2.1 Cable

A cable element model is chosen to represent each steel cable length located between two singular points of the system as station or vehicle. Cable model hypotheses are:

- force per unit length is supposed to be a uniform and planar distribution in (O, e_x, e_y) basis: the cable is hanging under gravity action as $-\mu g \mathbf{e}_y$;
- the cable mechanical and geometric properties are uniform along the cable represented by a line;
- the cable is inextensible;
- the cable flexural rigidity is negligible: the contact force in the cable is only tension $T > 0$.

Catenary element is an algebraic equation describing cable statics equilibrium position $y(x)$, $x \in [x_A, x_B]$ under previous assumptions [3] given in the form:

$$y(x) = \tau \cosh\left(\frac{x}{\tau} + K_1\right) + K_2, \quad (1)$$

with catenary parameters $\tau = \frac{\mathcal{F}_x}{\mu g}$, $K_1 = \operatorname{argsh}\left(\frac{\mathcal{F}_y}{\mathcal{F}_x}\right) - \frac{\mu g x_A}{\mathcal{F}_x}$, $K_2 = -\frac{\mathcal{F}_x}{\mu g} \sqrt{1 + \left(\frac{\mathcal{F}_y}{\mathcal{F}_x}\right)^2} + y_A$ depending on boundary conditions such as (x_A, y_A) position of left catenary extremity, x_B abscissa of right catenary extremity and $\mathbf{F} = \mathcal{F}_s \mathbf{e}_x + \mathcal{F}_t \mathbf{e}_y$ the load at the left extremity (see Fig. 2).

An elastic correction of catenary Eq. (1) allows to consider cable stretching according to an elastic constitutive law

$$T = EA\varepsilon, \quad (2)$$

with E the Young's modulus (Pa), A the cable section area (m^2) and ε the linear strain measure such as current cable length

$$l = \int_0^{L_R} (1 + \varepsilon) dS, \quad (3)$$

with L_R the unstretched reference cable length.

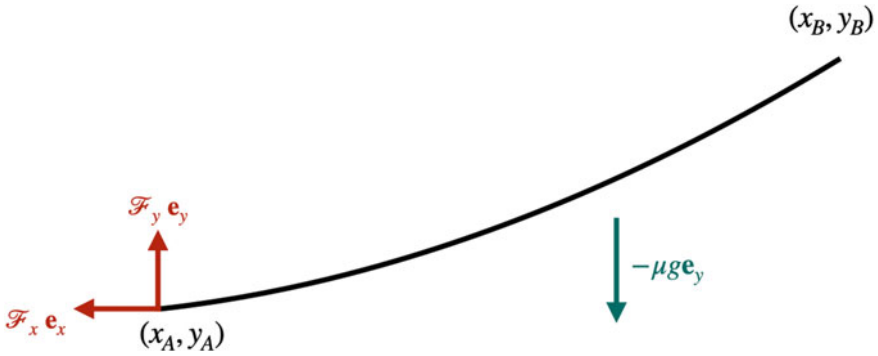


Fig. 2 Cable element

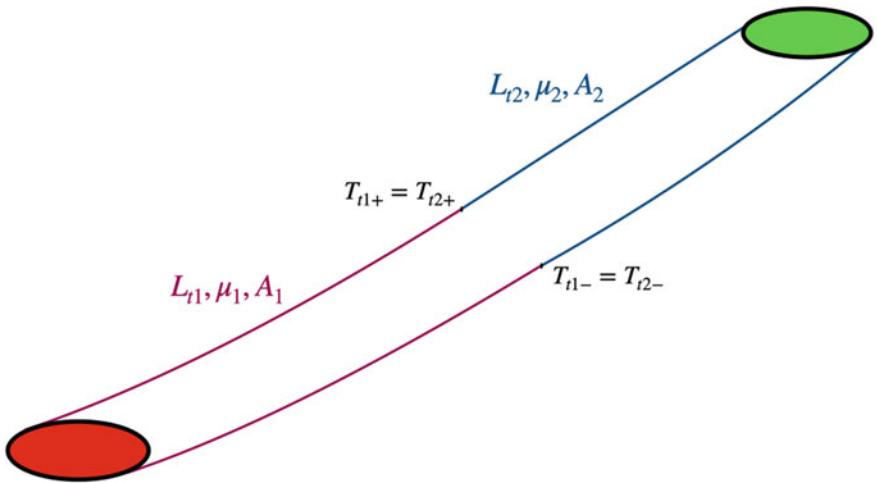


Fig. 3 Haul rope loop diagram

It's usual to install a heavier cable on the upper part of the haul rope loop acting as counterweight on the system. So, the haul rope characteristics (weight per unit length, section, length) are not uniform along the loop. A modeling strategy is to consider two different cable elements respectively of L_{l1} and L_{l2} unstretched length, coupled with tension continuity equations at each element extremities (see Fig. 3).

2.2 Vehicles

Vehicles are represented by point masses (M_{v1}, M_{v2}) (see Fig. 4) carried by one track rope for each side and pulled by a haul rope loop. Vehicles are coupled with

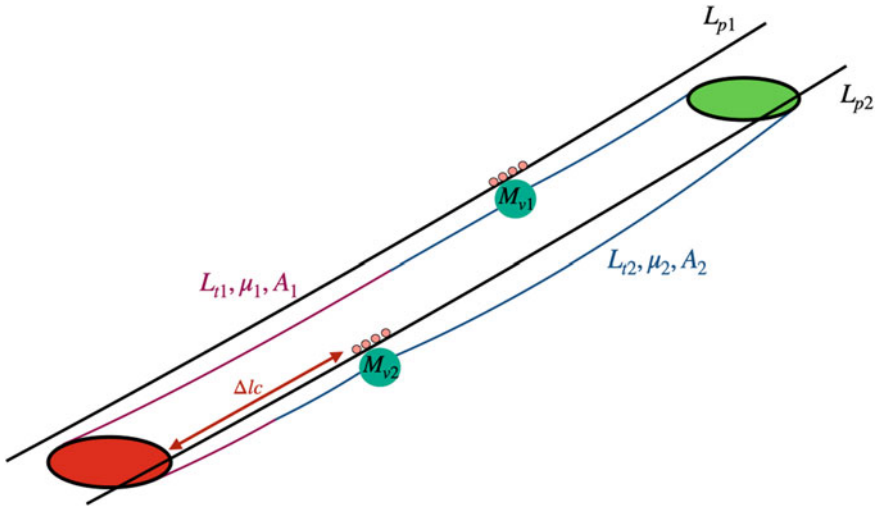


Fig. 4 Haul and track ropes with vehicles diagram

cables by a cart rolling without friction on the track rope and clamped on the haul loop. Suspended vehicle equilibrium equation is provided in [4] and is coupled with cables by the catenary tension given in the following form, for $x \in [x_A, x_B]$

$$T(x) = \mu g \tau \cosh\left(\frac{x}{\tau} + K_1\right). \tag{4}$$

2.3 Tracks Coupling

In the aerial tramway model, tracks 1 and 2 are coupled by the haul rope loop by intermediary of anchored pulleys located at bottom and top stations. A drive bull-wheel connected to a driving system controls the cable length Δl_c unwound at the bottom station. The quantity Δl_c is a model input given by the designer. At the top station, the return bull-wheel is free to rotate according to a friction contact law involving cable tension values in entrance T^+ and exit T^- such as

$$T^+ = T^- \exp(\pm c_f \phi), \tag{5}$$

with c_f rolling resistance coefficient at return bull-wheel and ϕ cable winding angle around the pulley. The two track ropes on each side of the system are independent, embedded at extremities and respectively of L_{p1} and L_{p2} unstretched lengths (see Fig. 4).

3 Static Calculation

The problem of full system equilibrium is written applying statics equations to vehicles and boundary conditions at each catenary extremity. It yields to a set of nonlinear equations with catenary parameters (τ_k , K_{1k} , K_{2k}) of each cable portion and vehicle positions as unknown. Model inputs are system geometry (top and bottom stations positions), cable properties (length, Young's modulus, section area), vehicle masses (M_{v1} , M_{v2}) and cable unwinding control value Δl_c at driving station. In the next subsections, the system behavior without and with inclusions of vehicles will be discussed.

3.1 Without Vehicles

The first model is investigated without vehicles along cables. This model is equivalent to the practical situation where vehicles are removed from haul rope for cable angles measure on each track at top and bottom stations. Thus, tracks are only coupled by the haul rope loop and track ropes are not involved in the haul rope loop statics equilibrium.

β parameter is introduced as a correction parameter of haul rope unstretched length input considering for uncertainty on the current cable length of the aerial tramway system. The total unstretched length of haul rope loop model input L_t becomes

$$L_t = \beta(L_{t1} + L_{t2}) \quad (6)$$

According to Fig. 5, angle sensitivity is higher at the bottom station: for $\beta \in [0.983, 1.06]$, angle $\alpha_b \in [-1.3, 1]$ rad at the bottom station and $\alpha_t \in [0.64, 1]$ rad at the top station on track 1.

3.2 With Vehicles

The full model of the system includes vehicles and track ropes. It is supposed that the heaviest haul rope cable is located between vehicles on the upper part of the loop with a L_{tt} length and the lightest one on the lower part with a L_{tb} length.

γ parameter is introduced as a correction considering for uncertainty on vehicles position along haul rope loop due to maintenance vehicle removing. The lengths of lower part L_{tb} and upper part L_{tt} of haul rope loop separating the two vehicles become

$$L_{tb}^{cor} = \beta \times L_{tb} + \gamma \quad (7)$$

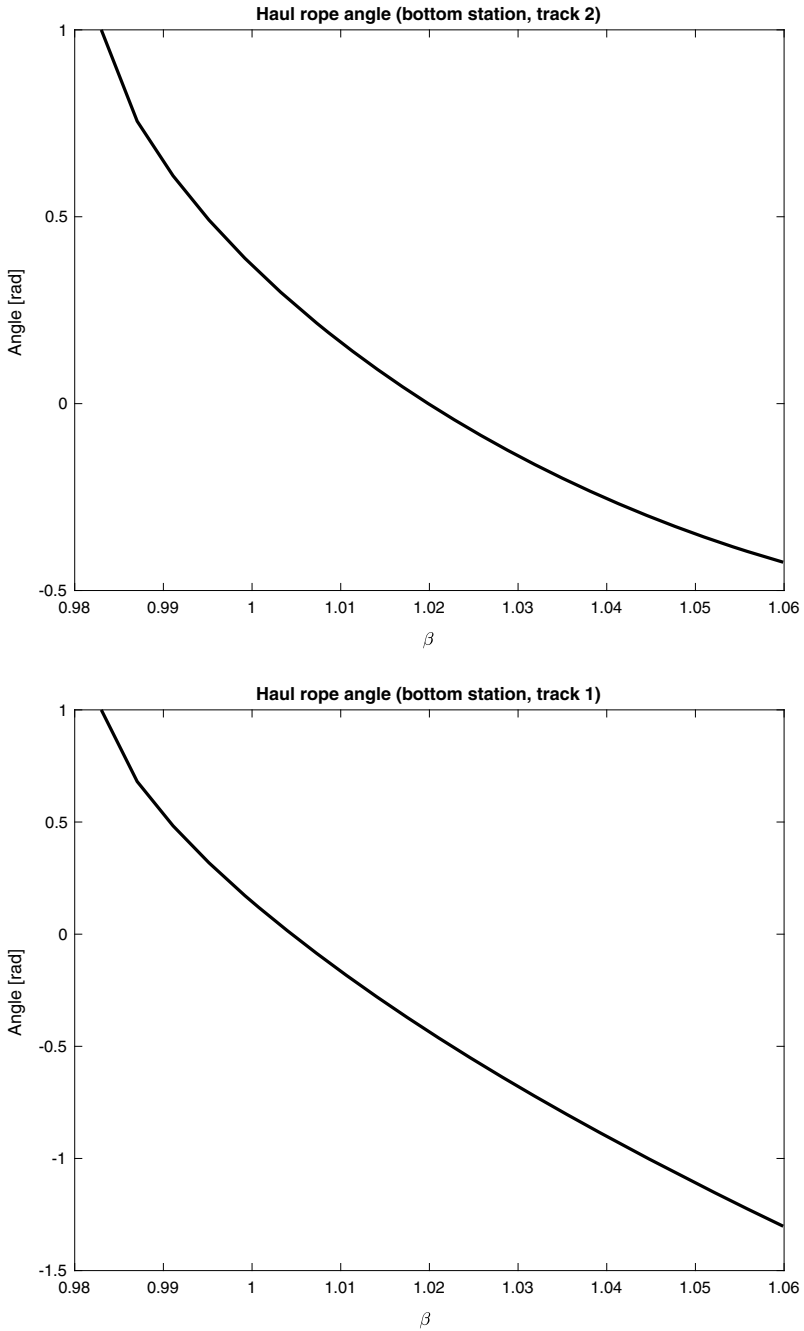


Fig. 5 Haul rope angles at stations without vehicles on the cable loop, as a function of β parameter

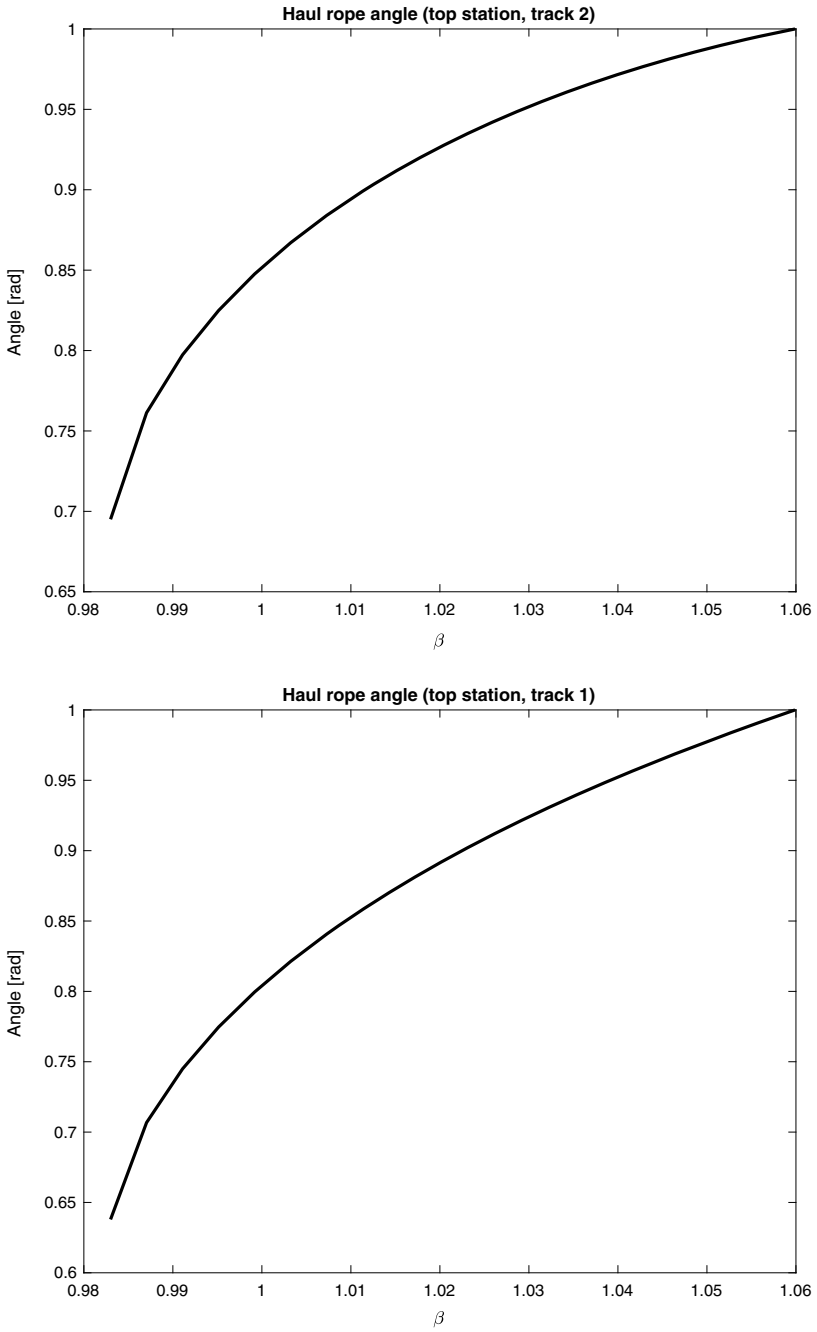


Fig. 5 (continued)

$$L_{t2}^{cor} = \beta \times L_{tt} - \gamma \tag{8}$$

Shift docking length $\Delta dock$ characterizes the non-simultaneity of vehicles arrivals at top and bottom station due to track asymmetry (see Fig. 1). Indeed, cable geometry and mechanical characteristics are not the same on the top part and on the bottom part of the haul rope loop: $L_{tb}^{cor} \neq L_{tt}^{cor}$, $\mu_1 \neq \mu_2$, $A_1 \neq A_2$. For practical reasons, the vehicle located at the driving bull-wheel (bottom station) enters the last one while the top vehicle is already at the top station in mechanical stop: shift docking length is the remaining cable length to unwind by driving pulley while the top vehicle is already stopped. This quantity $\Delta dock$ can be easily measured on the real system. In Fig. 6, shift docking length is calculated for different values of β parameter while in Fig. 7 shift docking length is calculated for different γ parameter values with β fixed. A linear variation of $\Delta dock$ can be observed with respect to β .

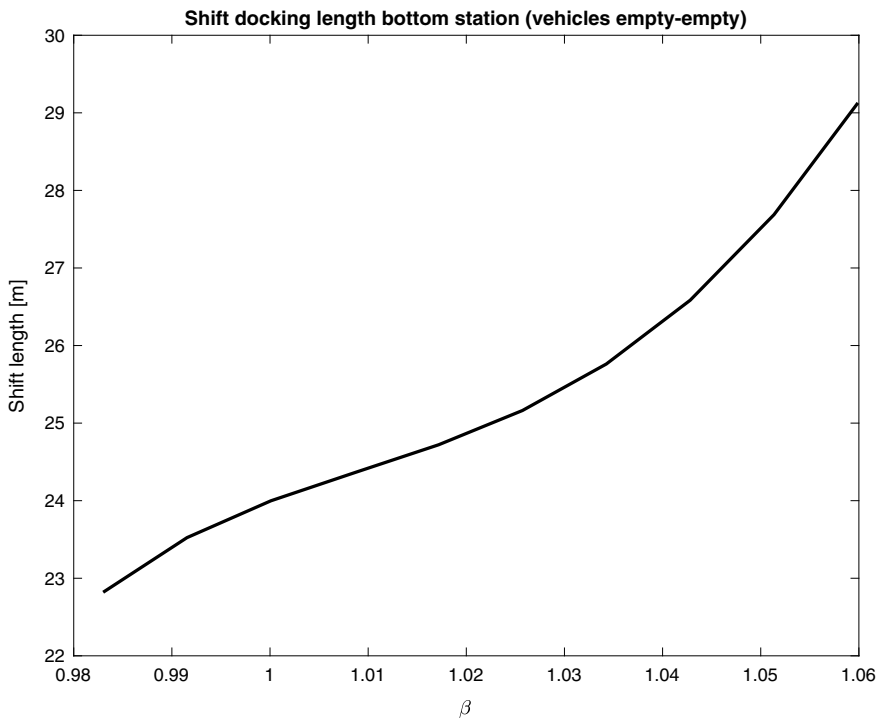


Fig. 6 Shift docking length at bottom station as a function of β parameter ($\gamma = 0$)

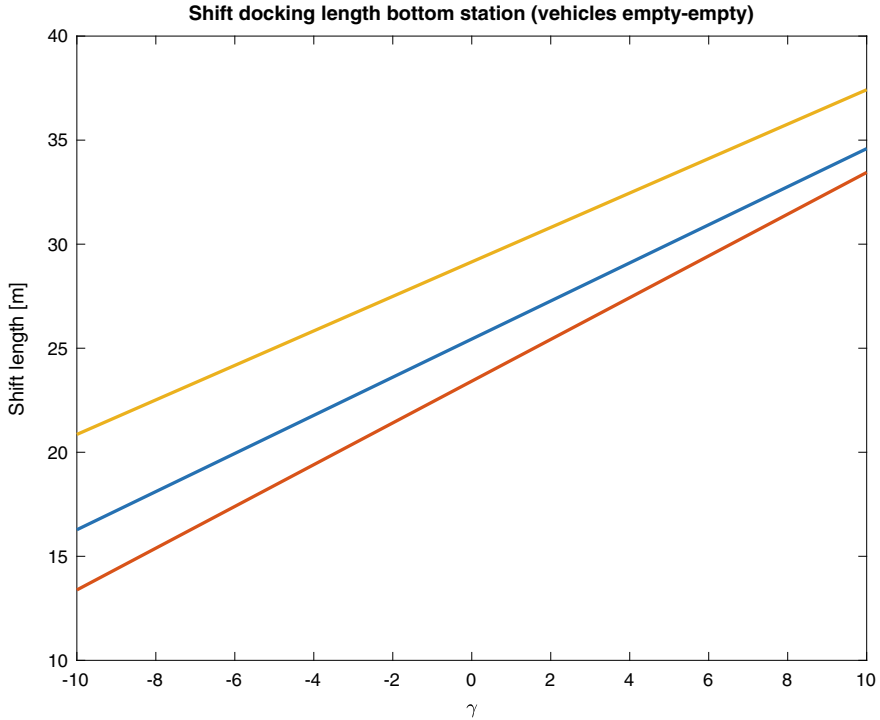


Fig. 7 Shift docking length at bottom station as a function of γ parameter ($\beta = 0.99$ [red], $\beta = 1.03$ [blue], $\beta = 1.06$ [yellow])

4 Experimental Validation

A set of experimental data collected on a real aerial tramway allows to address the inverse problem of identification. It consists in estimating model parameters from experimental data. The schematize of a direct and inverse process is depicted in Fig. 8.

First, haul rope angles were measured at rest on each track in stations without vehicles on the line and for a given control length Δl_c at the driving station (see Table 1). Then, once empty vehicles were clamped on the haul loop, a shift docking length $\Delta dock = 25.2$ m was observed during an operating cycle.

In the direct problem, unknown \mathbf{Y} is catenary parameter vector for each $n_{portion}$ cable portion and vehicle positions depending on model input \mathbf{X} and model intern parameter \mathbf{p} . Unknown vector is calculated solving a set of nonlinear equations of the model, such as $\mathbf{H}(\mathbf{X}, \mathbf{Y}, \mathbf{p}) = 0$.

The inverse problem comes from a partial lack of knowledge about the model internal parameters \mathbf{p} . Adding information on the model exit \mathbf{Y}_{obs} (measures) allows to rebuild missing information. Inverse problem consists in finding \mathbf{p} such as $\mathbf{H}(\mathbf{X}, \mathbf{Y}_{obs}, \mathbf{p}) = 0$. For the system application, $\mathbf{p} = (\beta, \gamma)^T$, \mathbf{Y}_{obs} is the set of 4

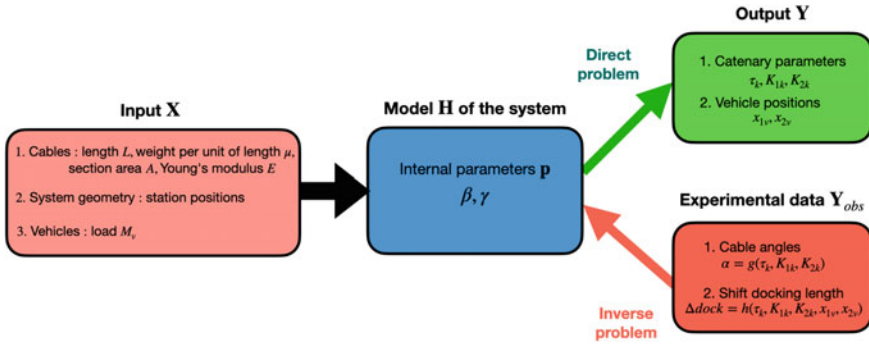


Fig. 8 Direct problem and identification process of the aerial tramway model

Table 1 Cable angle measurement at stations

Measurement position	Cable slope (°)
Bottom station—track 1	0.9
Bottom station—track 2	6.25
Top station—track 1	52.0
Top station—track 2	48.9

cable slope measures $\alpha_i = g_i(\tau_k, K_{1k}, K_{2k}), i \in [1, 4], k \in [1, n_{portion}]$ and $\Delta dock$ value. Inverse problem can be reformulated as a minimization problem such as

$$\mathbf{p}^* = argmin J(\mathbf{p}) = argmin \| \mathbf{g}(\mathbf{Y}(\mathbf{X}, \mathbf{p})) - \mathbf{Y}_{obs} \| \tag{9}$$

$$H(\mathbf{X}, \mathbf{Y}, \mathbf{p}^*) = 0 \tag{10}$$

4.1 Identification of β

The inverse problem defined by Eqs. (9) and (10) is applied for identification of β parameter using the model without vehicles and the cable slope experimental measures collected on the system. It provides $\beta = 0.9972$.

4.2 Identification of γ

Identification of γ parameter consists in using the full model of the system with vehicles and plotting shift docking length as a function of γ parameter for $\beta = 0.9972$

(result of previous identification). Then, the γ value associated with the experimental $\Delta dock = 25.2\text{m}$ is read by interpolation. $\gamma = 4.34\text{m}$ is obtained.

5 Conclusions

A statics model of an aerial tramway system based on analytical catenary equation is proposed to follow cable length modification from experimental values collected on a real system. The experimental validation of the numerical statics model opens perspectives to use this tool in optimal research, for instance to optimize cycle duration anticipating shift docking length and by adjusting cable control law according to vehicle loading (see Fig. 9). Quasistatic calculation using control length Δl_c at driving pulley as evolution parameter gives information about the system when haul loop cable is moving. As perspectives of this work, a modal analysis around statics equilibrium will give information about mode shapes and frequencies evolution with a parametrization by Δl_c to account for time varying system modification when vehicles are moving. From an applied perspective, modal information is useful to predict dynamic response content during transient dynamics, to design acceleration

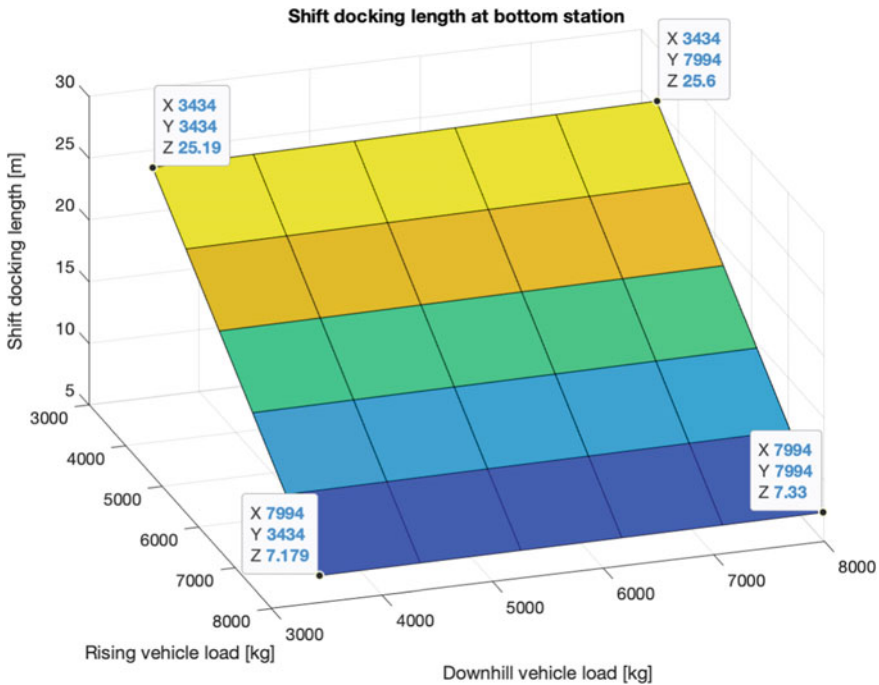


Fig. 9 Shift docking length at bottom station as a function of vehicle load for $\beta = 0.9972$ and $\gamma = 4.34\text{ m}$

and braking control curves of the cable reducing cable oscillation amplitudes, to detect eventual instabilities of the system by a stability analysis, etc.

Acknowledgements The authors thank DCSA company and ANRT (CIFRE n°2019/1376) for supporting this work.

References

1. Lehanneur L (1962) Conférences sur les téléphériques à voyageurs, Lecture notes, École nationale des Ponts et Chaussées, Paris, France
2. Goirand P (1983) Calcul des câbles de transporteurs aériens, in Techniques de l'Ingénieur (A973)
3. Hurel G, Laborde J, Jézéquel L (2017) Calcul du comportement dynamique d'une portée de téléphérique bicâble à l'aide de bases modales. In: 13th national structural mechanics seminar (CSMA), Giens, France
4. Hurel G, Laborde J, Jézéquel L (2019) Simulation of the dynamic behavior of a bi-cable ropeway with modal bases, Topics in modal analysis & testing, vol 9. Conference Proceedings of the Society for Experimental Mechanics Series, https://doi.org/10.1007/978-3-319-74700-2_5
5. Knawa-Hawryszko M (2017) Influence of motion parameters on incidence of resonant track rope vibrations in a bi-cable ropeway system. In: X International conference on structural dynamics, Eurodyn
6. Renezeder HC, Steindl A, Troger H (2005) On the dynamics of circulating monocable aerial ropeways. PAMM · Proc Appl Math Mech 5: 123–124. <https://doi.org/10.1002/pamm.200510042>

Structural Modeling to Predict the Vibrations of a Footbridge Due to Pedestrian Movements



Mehdi Setareh and Mohammad Bukhari

Abstract Two major footbridge failures were reported during the nineteenth century when soldiers marched over them in unison. They resulted in large number of casualties. Even though modern footbridges are not generally in danger of failure due to such activities, they can be susceptible to vibrations when pedestrians move across them. These can become excessively large if people walk or march in unison at the footbridge resonance frequency or its subharmonics. The vibration serviceability issue of the Millennium Bridge over the Thames River in London is a well-known example of such problems. Therefore, it is essential for the structural designer to be able to predict the vibration response of the footbridge due to pedestrian movements with an acceptable accuracy. This paper details the vibration testing and computer modeling of a footbridge. The computer model has been updated to accurately represent the structure. The footbridge vibrations due to the movements of various groups of people at the subharmonics of its resonance frequency were measured. The computer model was then subjected to human footfall forces and the predicted responses were compared with those from the measurements. It is known that the human-structure interactions (HSI) can affect the predicted response of footbridges. However, the incorporation of HSI into a computer model is generally a complex process. By equating the computed and measured Vibration Dose Value (VDV), equivalent damping ratios of the structure due to the HSI effects were found which showed an almost linear increase with the number of the pedestrians.

Keywords Footbridge dynamic response · Human-structure interaction (HSI) · Structural modeling · Ground reaction force (GRF) · Vibration dose value (VDV)

M. Setareh (✉)
School of Architecture and Design, Virginia Tech, Blacksburg, VA, USA
e-mail: setareh@vt.edu

M. Bukhari
Department of Mechanical Engineering, Virginia Tech, Blacksburg, VA, USA

1 Introduction

High strength of modern construction materials such as steel has allowed architects and engineers to design long span and slender footbridges. Even though such structures can resist the applied static loads, they might be susceptible to excessive vibrations when people cross them. This may result in the failure of the structure in extreme cases. Failures of bridges due to marching soldiers in the nineteenth century have been reported [1]. Fortunately, modern footbridges are not prone to structural failure but can be susceptible to large vibrations due to human movements. The most publicized case of excessive footbridge vibrations was the London Millennium Bridge over the Thames River in 2000 [2].

To prevent excessive footbridge vibrations, engineers need to be able to predict their behavior accurately. This requires the development of an accurate computer model of the structure and also realistic forcing functions of the pedestrians. Vibration testing of footbridges to update the computer models, and measurement of the footfall forces can provide helpful guidance to obtain more accurate structural response. However, the interaction between the moving footbridge and pedestrians can affect the structural response. The problem of human structure interactions (HSI) has been studied by various researchers over the past two decades [3].

Zivanovic et al. [4] studied the dynamic response due to an individual crossing a footbridge. They used a single-degree-of-freedom system to represent a pedestrian crossing a footbridge. They found that the HSI can result in a damping increase of ten-folds of that for an empty footbridge.

Van Nimmen et al. [5] investigated the impact of vertical HSI on the dynamic behavior of footbridges due to pedestrian movements. They decomposed the pedestrians' contact force into the force exerted by the pedestrians on a perfectly rigid surface and an interaction term determined by the mechanical interaction between the person and the structure (HSI). Wei [6] considered the human-human interactions on the resulting crowd-induced loading and structural response using a numerical study. Mohammed and Pavic [7] considered the effects of HSI on the floor frequency response function in terms of changes in the natural frequency and damping ratio. The available literature has mainly tried to investigate the effects of the HSI on floor vibrations by conducting detailed structural analysis. However, most of the analytical studies cannot be easily adopted by the practicing engineers due to their complexity and time required to conduct the analysis.

This paper provides information on the vibration testing and computer modeling of a footbridge. The computer model was updated to accurately represent the structure. Ground reaction forces of a number of human subjects were measured and the footbridge vibration due to the crossing of various groups of pedestrians at the subharmonic of the footbridge resonance frequency were measured. The computer model was then subjected to human footfall forces and the predicted responses were compared with those found from the measurements. The effects of the HSI on the footbridge equivalent damping ratio were found by equating the measured

and computed Vibration Dose Values (VDV). The results show that the footbridge equivalent damping ratio increased with an increase in the number of pedestrians.

2 Description of the Footbridge

The footbridge, which connects a multi-story building to a parking structure, is located in Blacksburg, Virginia, see Fig. 1. It consists of two steel Pratt trusses at 2.44 m apart. The total length of the footbridge is 35.6 m and has a clear depth of 2.29 m. All the truss members are made of Hollow Structural Shapes (HSS) which are welded together. The top chord, bottom chord, verticals, and diagonals are made of HSS152.4 × 152.4 × 9.5, HSS203.2 × 152.4 × 9.5, HSS152.4 × 152.4 × 9.5 and HSS101.6 × 76.2 × 6.4, respectively. The truss panel points are 2.74 m apart. The footbridge floor deck consists of a 20-gauge, 51 mm-thick form metal deck with 101 mm of concrete topping (total thickness = 152 mm). The concrete has a compression strength of 24 MPa. Figure 2 shows the elevation of the footbridge truss.



Fig. 1 Side view of the footbridge

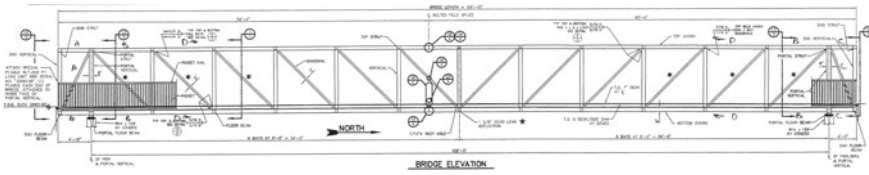


Fig. 2 Elevation of the footbridge truss

Table 1 Measured versus computed dynamic properties of the footbridge

Mode	Type	f_n (measured) (Hz)	f_n (computed) (Hz)	ζ_n
1	Lateral	3.83	3.8	0.0097
2	Vertical	4.09	4.08	0.0104
3	Longitudinal	4.73	4.86	0.0544

3 Vibration Tests

Three different sets of tests were conducted: (1) Field modal tests to estimate the dynamic properties of the footbridge for computer model updating purposes; (2) Field walk tests to evaluate the response of the structure; and (3) Laboratory footfall force measurements to estimate the ground reaction force to be used for the computer modeling and prediction of the footbridge dynamic response.

3.1 Modal Tests

Modal tests were conducted to estimate the dynamic properties of the footbridge. An APS 400 and APS 113 electrodynamic shakers oriented vertically and horizontally, respectively, were used to excite the various lower modes of the footbridge. To excite the vertical modes, a burst chirp of 3.5–18.5 Hz with 40 s measurement block and 5 averages were used. To excite the horizontal modes, a 3–18.5 Hz burst chirp with 40 s measurement block and 5 averages were used. MEScope software [8] was used to curve fit the collected data. Table 1 shows the measured natural frequencies (f_n) and their corresponding damping ratios (ζ_n).

3.2 Walk Tests

The walk tests were conducted by up to 30 volunteers. They walked at four different speeds: 123 spm (steps per minute) which represents the half-harmonic of the measured first vertical mode natural frequency; 115 and 130 spm (frequencies below



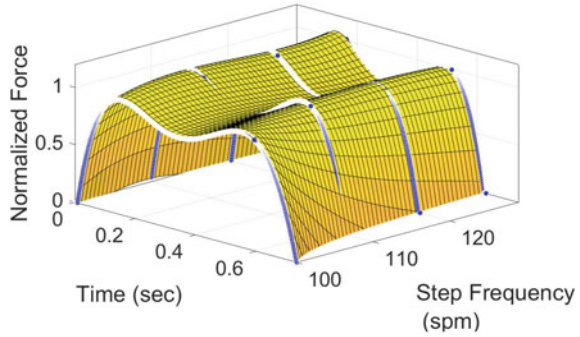
Fig. 3 Volunteers walking across the footbridge

and above the half harmonic of the first vertical mode natural frequency), and random. Vibrations due to the random walks were not used in this study. PCB393C accelerometers were placed at the center of the footbridge on both sides to record the vibrations along the three orthogonal directions. However, since the largest vibrations occurred in the vertical direction, only those measurements are used in this study. Using a metronome to synchronize their movements, different groups of volunteers (1, 2, 6, 8, 16, 20, 28, and 30 people) crossed the footbridge from one end to the other and stopped while the measurements were completed. Figure 3 shows a group of volunteers crossing the footbridge during one of the tests.

3.3 Ground Reaction Force Tests

To estimate the forcing function for computer simulations, the ground reaction forces (GRF) of a group of volunteers were measured using a force platform located at the Virginia Tech Vibration Testing Laboratory. Each individual walked over the force platform at different step frequencies to measure the GRF of the right and left feet. Male and female volunteers participated in these tests. The measured GRFs were first curve fitted for each step frequency and then used a surface fit to obtain a closed form equation for the GRF as a function of time and step frequency. Figure 4 shows the surface fit used in this study.

Fig. 4 Surface-fit of the measured GRFs



4 Computer Model Updating

A computer model of the footbridge was created using the SAP2000 software [9]. The modeling was first conducted using the footbridge design drawings and then updated to have close dynamic properties to the measurements. Table 1 shows the measured natural frequencies (f_n) and damping ratios (ζ_n) along with the computed natural frequencies using this model. Since the higher modes could not significantly contribute to the response of the footbridge when excited by the pedestrians, they were not included in the table.

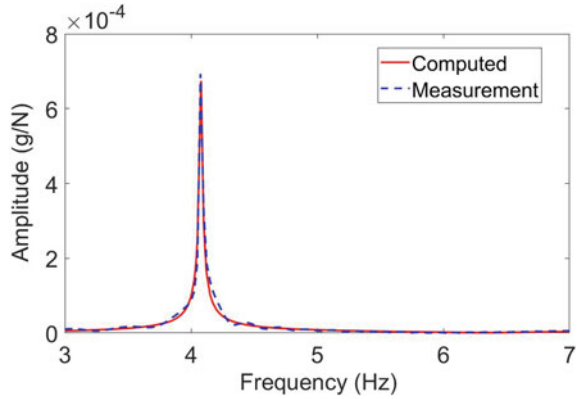
To check the correlation between the measured and computed mode shapes and evaluate the accuracy of the computer model, the modal assurance criterion (MAC) [10] for the first three measured and computed modes was obtained:

$$\begin{bmatrix} 0.976 & 0.086 & 0.000 \\ 0.005 & 0.986 & 0.000 \\ 0.134 & 0.264 & 0.962 \end{bmatrix}$$

The result shows a very good correlation between the measured and computed mode shapes as the diagonal elements of the MAC matrix are close to unity and off-diagonal elements are close to zero.

The measured and computed frequency response functions (FRF) of the footbridge midspan were compared as shown in Fig. 5. From this figure it can be noted that the computed FRF closely follows the measurement. From these results, it can be concluded that the computer model can provide a very good representation of the dynamic behavior of the footbridge.

Fig. 5 Measured and computed FRFs



5 Equivalent Damping Ratio for the HSI Effects

From the comparison of the footbridge response due to the excitation by the pedestrians when walking at the above, below, and at the resonance, it was found that the largest amplitude of vibration was when the walks were conducted at the structure’s resonance frequency without people. Therefore, it was concluded that the pedestrian’s masses did not greatly affect the natural frequency of the footbridge and acted mainly as applied force only.

However, the HSI impacted the dynamic response of the footbridge and resulted in a decrease in the structural vibrations. To provide a practical and simplified method of incorporating HSI in the footbridge structural analysis, the effects of the HSI were considered to result in an increase in the structural damping. It has been shown that the Vibration Dose Value (VDV) can provide a reliable evaluation of vibration by humans [11–14]:

$$VDV = \left[\int_{t=0}^{t=T} a_w^4(t) dt \right]^{1/4} \tag{1}$$

In the above equation, T is the period during which a person is exposed to vibration. In this study each measurement included a forced vibration response (while the pedestrians were walking on the footbridge) and a free vibration response during which they were standing still for the measurement to get completed. The forced vibration duration was used for T as the main focus of this study was the effects of active HSI phenomenon on the footbridge dynamic response. $a_w(t)$ is the frequency-weighted acceleration. Here, the weighting function, W_k , as recommended by ISO 2631-1 [15] has been used. Considering T in seconds and $a_w(t)$ in m/s^2 , the unit of VDV is $m/s^{1.75}$. As Eq. (1) demonstrates, VDV accumulates the vibration effects rather than averaging them and increases with duration. The VDV is robust and insensitive to the variations of starting or ending of the measurement time. It is sensitive to the maximum vibration as humans are sensitive to peak accelerations

[16]. Therefore, it was concluded that VDV is the best criterion to evaluate the footbridge vibrations.

The VDV from the measurements (VDV_m) for different number of pedestrians were computed. The same was done using the computer model subjected to the GRF found using curve fitting of the measured responses as discussed before (VDV_c). It is interesting to note that the measured VDV_s were relatively unchanged when different groups of pedestrians crossed the footbridge. This can mainly be attributed to an increase in HSI effects with larger numbers of pedestrians.

The damping ratios used in the computer model to obtain the footbridge response were those found from the modal tests (without the human subjects). Figure 6 shows the measured and computed VDV_s (VDV_m and VDV_c) for different number of pedestrians, which demonstrates large discrepancies between them. The damping ratios (ζ_a) in the computer model was increased in an attempt to have the same computed VDV_s (VDV_a) as from the measurements (VDV_m). Figure 6 shows the adjusted VDV_s (VDV_a) have almost perfect match with those from the measurement (VDV_m).

Figure 7 shows the variation of damping ratios (ζ_a) due to the HSI effects versus the number of pedestrians (N) crossing the footbridge. It shows that there is an almost linear relationship between these two parameters and larger damping ratios

Fig. 6 Variation of the measured VDV (VDV_m), computed VDV without damping adjustment (VDV_c) and VDV with adjusted damping (VDV_a) versus the number of pedestrians (N)

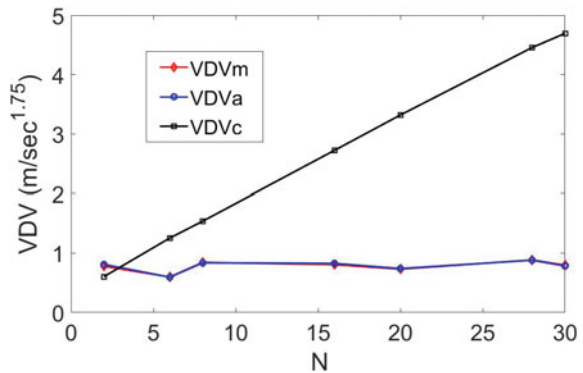
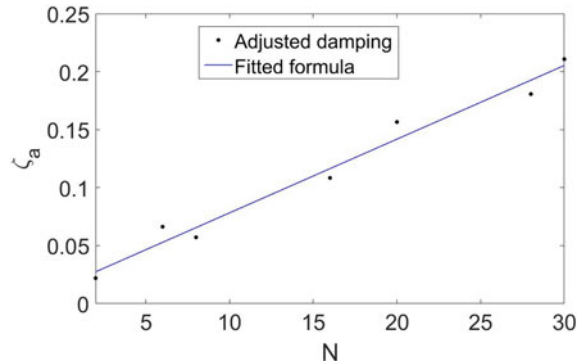


Fig. 7 Variation of the adjusted damping (ζ_a) versus the number of pedestrians (N)



are expected when more people cross the footbridge. It is noted that the large damping increases can also be attributed to the variation in the footfall forces, the fact that the GRFs were measured on a rigid platform, and the variations in the pedestrians' step frequencies.

6 Summary and Conclusion

This paper presented a detailed study of the dynamic properties and responses of a footbridge subjected to the excitations by a number of pedestrians. It consisted of the modal testing of the footbridge and computer model updating based on the results of these tests. It also studied the ground reaction forces exerted by individual human subjects to develop the forcing functions required for the computer analysis of the footbridge. The results of the study showed that the pedestrians did not greatly affect the footbridge natural frequency. However, the HSI resulted in an increase in the equivalent modal damping ratio of the structure based on the comparison of the measured with computed VDV's. The increase in the damping ratio was almost proportional to the number of pedestrians crossing the footbridge.

Acknowledgements The research presented here was supported by the National Science Foundation of the USA under grant number CMMI-1335004. This support is gratefully acknowledged. Any opinions, findings, and conclusions expressed in this paper are those of the writer and do not necessarily reflect the views of the National Science Foundation.

References

1. Dupuit MM (1850) Commission inquiry report on the circumstances and causes of the failure of the lower channel suspension bridge. *Ann Roads Bridges Tech Sect* 394–411
2. Dallard P, Fitzpatrick AJ, Flint A, Le Bourva S, Low A, Ridsdill-Smith RM, Willford M (2001) The London millennium footbridge. *Struct Eng* 79(22):17–33
3. Shahabpoor E, Pavic A, Racic V (2016) Interaction between walking humans and structures in vertical direction: a literature review. *Shock Vib* 2016:1–22
4. Zivanovic S, Pavic A, Reynolds P (2005) Human-structure dynamic interaction in footbridges. *Bridge Eng* 158(BE 4):165–177
5. Van Nimmen K, Lombaert G, De Roeck G, Van den Broeck P (2017) The impact of vertical human-structure interaction on the response of footbridges to pedestrian excitation. *J Sound Vib* 402(2017):104–121
6. Wei X (2020) A simplified method to account for human-human interaction in the prediction of pedestrian-induced vibrations. *Struct Control Health Monit* 1–20
7. Mohammed A, Pavic A (2021) Human-structure dynamic interaction between building floors and walking occupants in vertical direction. *Mech Syst Signal Process* 147(2021):1–23
8. Vibrant Technology, Inc (2016) ME'scope VES 6.0. Scotts Valley, California
9. Computers and Structures, Inc. (2021) SAP 2000—static and dynamic finite element analysis of structures. California, Berkeley
10. Allemang RJ (2003) The modal assurance criterion—twenty years of used and abuse. *Sound Vib* 37(8):14–23

11. Griffin MJ, Whitham EM (1980) Discomfort produced by impulsive whole-body vibration. *J Acoust Soc Am* 68(5):1277–1284
12. Griffin MJ, Whitham EM (1980) Time dependency of whole-body vibration discomfort. *J Acoust Soc Am* 68(5):1522–1523
13. Howarth HVC, Griffin MJ (1988) Human response to simulated intermittent railway-induced building vibration. *J Sound Vib* 120(2):413–420
14. Howarth HVC, Griffin MJ (1990) The relative importance of noise and vibration from railways. *Appl Ergon* 21(2):129–134
15. ISO 2631-1, (1997) Mechanical vibration and shock—evaluation of human exposure to whole-body vibration—Part 1: General requirements—ISO 2631-1, 2nd edn. International Organization for Standardization, Geneva, Switzerland
16. Griffin MJ (2007) Predicting the feeling of vibration in buildings. *Proc Inst Acoust* 29(2):1–15

Vibration Serviceability of Two-Story Office Building: A Finite Element Modeling



Fadi A. Al-Badour

Abstract In this work, a finite element model (FEM); built and solved in Abaqus environment, was developed to study the structural vibration levels and frequencies induced by human activity; i.e. walking, in two-level steel structure office units. The three-dimensional model considers two units assembled side by side. The developed geometrical model consists of beams and trusses elements generated using structure proposed dimensions. The structure is composed of multiple materials i.e. hot rolled rectangular bars, C steel channels, and floors\slabs made from cement. Elastic properties were only considered in the material model, while material damping was idealized as viscous damping using Rayleigh model. The model treated all joints; bolts or welds, to be rigid, therefore tie constraints were applied at all connections and joints. Fixed-free boundary conditions were considered for structure columns while other points presenting foundation support were constrained in the vertical direction only. Walking-induced forces were described based on multiple parameters; mainly human body mass, and pacing frequency, which are directly related to walking characteristics; specifically, step size and walking speed. Two load models were considered, first, a simple force model considering the walking induced force as a concentrated harmonic force applied at a fixed point. The second, a moving concentrated load applied along a predefined path. The structure natural frequencies and mode shapes were extracted first, and then dynamic explicit analysis to determine the vibration levels (acceleration) was performed. The finite element results are compared to simplified model described in design guide 11 by AISC. The estimated vibration levels using finite element analysis were found to be exceeding the comfort zone (ISO 2631-2), while calculations based on design guide 11 found to be at the boundary of the described limits.

F. A. Al-Badour (✉)

Mechanical Engineering Department, King Fahd University of Petroleum and Minerals, Dhahran 31261, Saudi Arabia

e-mail: fbadour@kfupm.edu.sa

Interdisciplinary Research Center—Advanced Materials, King Fahd University of Petroleum and Minerals, Dhahran 31261, Saudi Arabia

Keywords Humane induced vibration · Finite element modeling · Comfort zone · ISO 2631-2 · Design guide 11

1 Introduction

Steel engineering structures are widely utilized in commercial buildings offices and in some residential houses. With the increase in demand for open spaces in commercial offices as well as giving the freedom in controlling /adjusting the office layout, large span floors with minimum number of columns are favorable and can be achieved using light weight and thin structures, without the compromise of strength. Such flexible material are expected to vibrate at higher amplitudes than acceptable levels set by standards and codes. During the design phase, structure dynamic behavior must be investigated by performing vibration serviceability assessments to ensure structural integrity and comfort of residents. When various loads i.e. harmonic forces generated from machines like pumps, air conditioning systems, etc., or induced by human activities; such as walking, running, or physical exercising, excite the structure and the induced vibrations can cause discomfort to occupancies. Vibrations induced by human activities are expected to resonate long span floors fundamental frequency as they falls within the range of 5–8 Hz. Building codes require the investigation of structural dynamic behavior if the building fundamental frequency is less than 6 Hz; according to ISO 10137-2007 [1]. Determining the exact response of the system presents several challenges, especially the walking induced forces, which is affected by many parameters including pacing frequency, speed, contact time, step length and width. Moreover, the number of walking persons and their moving path [2] would also affect the induced forces as well the system damping [2, 3]. Generally, a vibration problem consists of three major elements namely the source of vibration, the transmission path through which the energy propagates and the receiver. For the transmission path, the structure design, materials, assembly, and welded joints play a major role in the analysis, and sometimes are difficult to simulate. A recent review paper by Zandy et al. [4] summarized the majority of recent force models. Also, other walking force models are available in the literature and presented in a number of standards and codes, such as the one presented by American Institute of Steel Construction Design Guide 11 (AISC/CISC DG 11), Steel Construction Institute (SCI P354), The Concrete Center (CCIP-016) and the human induced vibrations of steel structures (HIVOSS). Out of the different models listed above, the first two models/codes (AISC/CISC DG 11, SCI P354) are based on approximating the waking forces by using Fourier series with different Fourier coefficients. CCIP-016 code depends on Finite Element Analysis (FEA) in predicting the walking force from the modal mass, modal stiffness and the natural frequency. Whereas a polynomial expression is used to estimate a single foot fall in HIVOSS modle and in developing a continued footfallforces. for Combination of different single footfall at an interval of time was considered [5] and found to be dependent on the step size. For buildings with fundamental frequency greater than 10 Hz, codes recommend the use of FEA.

In this work, dynamic analysis through frequency, harmonic, and dynamic implicit analysis were performed to study the dynamic response and evaluate it against occupant comfort criteria, considering single point load as well as moving load. The finite element analysis (FEA) results were also compared to AISC DG11.

2 Problem Idealization and Modeling

2.1 Structure Concept

The office's concept is based on portable cabins with repetitive modules. Four single modules are used to create one unit as shown in Fig. 1. The ground floor is designed considering the hot-rolled (HR) IPE 200 AA; standard section, resting on foundation blocks. While the first floor consists of a cross truss system 9.5×3.75 m made from rectangular tubes $80 \times 80 \times 4$ mm, which will support IPE 200 AA skid. The floors

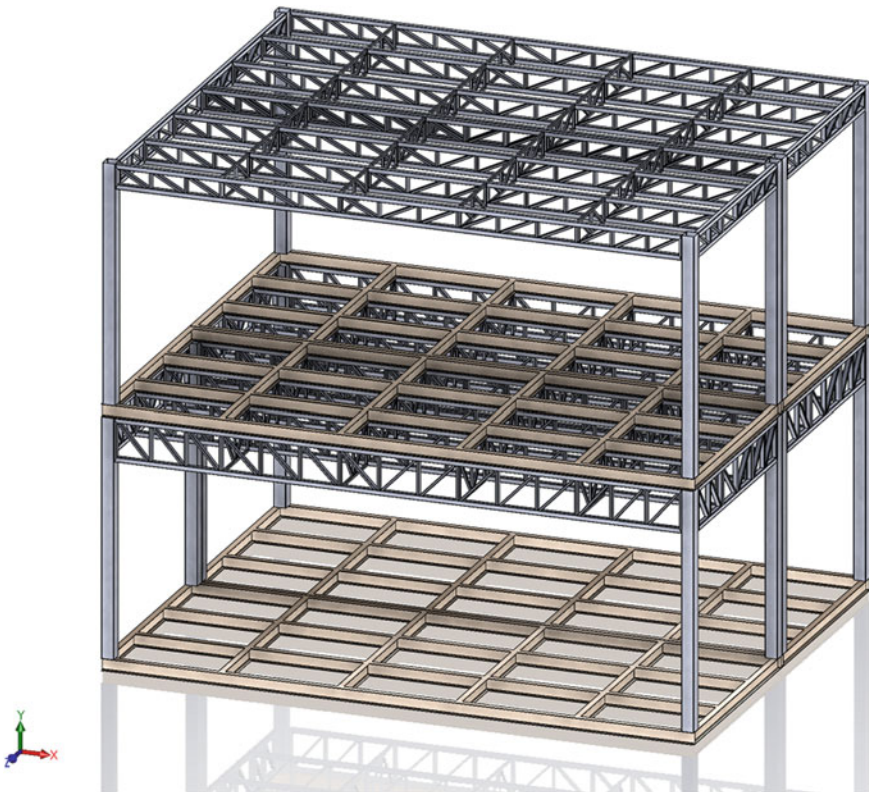


Fig. 1 3D model of two-story structure

are considered to be cement boards placed on top of a light gauge steel skid made from C section; not presented in Fig. 1. Between the cement boards, a thin layer of rubber 5 mm is sandwiched to provide additional damping.

2.2 Estimating Waking Induced Vibrations Using AISC Design Guide 11 [6]

In this work, combined panel mode was considered for determining the fundamental frequency. The design adopted the joist and grader configurations as illustrated in Fig. 2. The following analysis is considered for low fundamental frequency structures, where the induced walking forces may cause the floor to resonate. Following AISC DG 11, the floor vibration (acceleration) maximum amplitude can be calculated using Eq. (1)

$$\frac{a_p}{g} = \frac{P_o e^{-0.35 f_n}}{\xi W} \tag{1}$$

where P_o is the modified person weight, $\approx 290N(65lb)$, W is the effective panel weight (N), f_n is the fundamental frequency in Hz, g is gravity acceleration; 9.81 m/s^2 , and ζ is the damping ratio. In this analysis, a combined panel mode was considered, where joist and grader midspan deflections Δ_j and Δ_g , respectively were determined using Eq. (2) assuming simply supported beam with uniformly distributed load. The Fundamental frequency can be then evaluated using Eq. (3).

$$\Delta = \frac{5wL^4}{384E_s I_t} \tag{2}$$

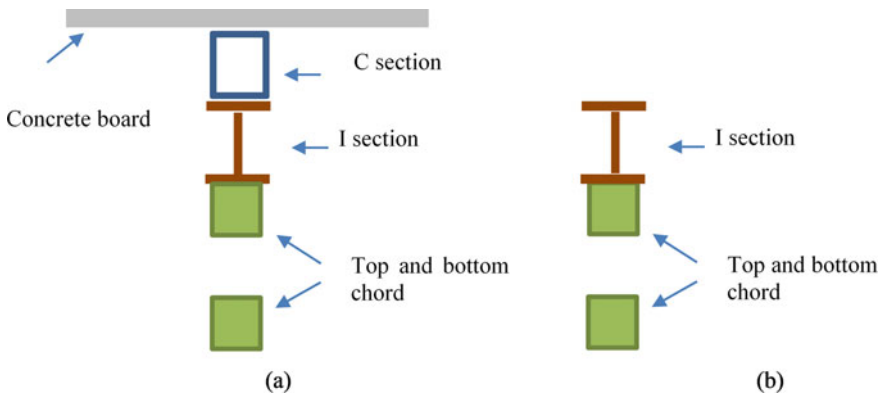


Fig. 2 a Truss joist model 9500 mm long, b truss girder model 3750 mm long

Table 1 Estimated parameters according to AISC DG 11

Parameter	Description	Value
Δ_j	Joist mid span deflection	1.441 mm
Δ_g	Grader mid span deflection	0.149 mm
f_n	Natural frequency	14.14 Hz
ξ	Combined damping	0.03
W	Total equivalent weight	15,992 N
a/g	Acceleration ratio	4.14×10^{-3}

where E_s is modulus of elasticity of steel = 200 GPa, I_t is transformed moment of inertia [m⁴], w is uniformly distributed weight per unit length (actual, not design, dead and live loads) supported by the member [N/m], and L is member span in [m]. Details on calculating the transformed moment of inertia can be found in [6].

$$f_n = 0.18 \sqrt{\frac{g}{\Delta_j + \Delta_g}} \tag{3}$$

Damping ratio was estimated using recommended component damping by AISC DG 11 [6]. For the structure overall damping ration was calculated by algebraically adding the components damping ratios. The damping ratio depends on the office fit out. In this paper, a paper office fit-out with ceiling and ducts was considered. Following the calculations described in AISC DG 11, the values of parameters needed to estimate the acceleration peak value are listed in Table 1 along with evaluated acceleration using Eq. (1). It can be noticed that the acceleration ratio is below the recommended tolerance limits for offices $\frac{a_p}{g} \leq 5 \times 10^{-3}$.

2.3 Finite Element Modeling

The developed finite element model (FME) was generated and solved in abaqus environment. The geometrical model presented one complete unit which was constructed using 1D lines to present the beams, columns, and bars with proper section of each part. This was adopted to minimize the complexity during mesh generation and reduce the computational time. The cement boards (floors), were constructed using shell elements. The columns and trusses were meshed using 25,558 quadratic line elements of type B32, with an approximate size of 0.05 m long, and 13,996 linear quadrilateral shell elements of type S4R were used to model the concrete board. Displacement boundary conditions were applied at the outside corners of the ground floor to present the foundation fixtures while other points were constrained only in the vertical direction. All trusses skid and columns at mating points were tie constrained assuming rigid connection. Figure 3 presents the meshed geometry and applied boundary conditions.

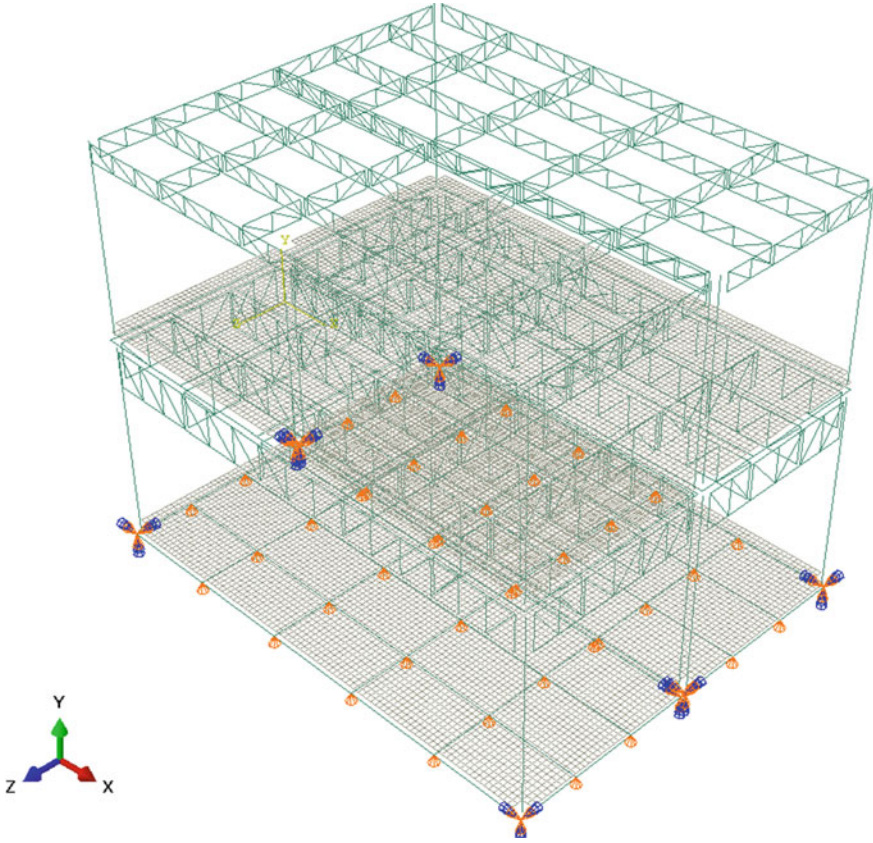


Fig. 3 Mesh and boundary conditions FEM

In this work, a simple force model (SFM) of footfall force using Fourier series was adopted. The model was used by many researchers; for example [3, 4]. The SFM presents the forces induced by walking in three directions, i.e. vertical, lateral (across the walking path), and longitudinal (along walking path) as shown in Eq. (4) [2].

$$\begin{aligned}
 F_v(t) &= G + \sum_{i=1}^n G\alpha_i \sin(2\pi i f_p t - \varphi_i) \\
 F_{lat}(t) &= \sum_{i=1/2}^n G\alpha_i \sin(2\pi i f_p t - \varphi_i) \\
 F_{log}(t) &= \sum_{i=1}^n G\alpha_i \sin(2\pi i f_p t - \varphi_i)
 \end{aligned} \tag{4}$$

where $F(t)$ is the foot-fall force as function of time, subscripts *v*, *lat*, *log* are vertical, lateral and longitudinal, respectively. G is the walking person weight, which ranges from 700 to 800 N [4], α_i is the Fourier coefficient for the *i*th harmonic, and defined as dynamic load factor, f_p is the pacing frequency (Hz), t is time in seconds, φ_i is the phase shift in radians of the *i*th harmonics with respect to first one, n is the number of contributing harmonics. $\alpha_1 = 0.5$, $\alpha_2 = 0.2$, $\alpha_3 = 0.1$, while $\varphi_{2,3} = \pi/2$ were considered in this model following [2]. For the lateral forces the Fourier series is assessed at frequencies ($f_p/2$, f_p , and $3f_p/2$), while longitudinal at the same frequencies of vertical force (f_p , $2f_p$, and $3f_p$). The values used to calculate the dynamic force were $G = 700$ N for walking person weight, and pacing frequencies of $f_p = 1.4$ and 2 Hz, assuming normal descents.

Three materials were used to construct the building, i.e. steel, concrete and rubber sheets sandwiched between the concrete floors. As the dynamic response of the system is of this work interest, only elastic properties were considered in addition to other physical parameters including density and damping ratios; assuming viscus damping. Table 1 lists the adopted material properties [6–8]. Rayleigh damping model was considered in the material level, damping can be also introduced in the solver. Rayleigh damping coefficients α and β represent the mass and stiffness proportional damping coefficients respectively. α and β can be calculated using Eq. (5), assuming the damping ratio is equal for all modes [9].

$$\begin{Bmatrix} \alpha \\ \beta \end{Bmatrix} = \frac{2\zeta}{\omega_i + \omega_j} \begin{Bmatrix} \omega_i \omega_j \\ 1 \end{Bmatrix} \tag{5}$$

where ζ is the damping ratio; see Table 2, ω_i is the fundamental natural frequency and ω_j is an upper natural frequency of interest which were evaluated in the initial step assuming un-damped system.

The FEM was solved over three steps; initially a static analysis was conducted to introduce the effect of structure weight on initial stresses in the structure, this step results were not included in this paper. Then, frequency analysis was preformed to identify the natural frequencies and mode shapes. Lastly, harmonic analysis was performed to determine the system frequency response. Rayleigh damping coefficients were initially calculated based on the results of frequency analysis, then harmonic analysis was followed after implementing material damping properties.

Table 2 Materials physical properties

Material	Density (kg/m ³)	Modulus of elasticity (GPa)	Poison ratio	Damping ratio
Steel	7800	200	0.3	0.01
Concrete	1350	7.66	0.2	0.05
Rubber	920	0.5×10^{-3}	0.49	0.05

3 Results and Discussion

3.1 Frequency Analysis

Frequency analysis was performed to identify the fundamental frequency of the structure without and with nonstructural elements i.e. cement slab. By solving the developed model, the first 20 modes were extracted. Modes that are below 9 Hz are shown in Fig. 4. Based on frequency analysis results, the first fundamental frequency is around 4 Hz, moreover two more modes are below 10 Hz. Accordingly, it is expected that the walking induced loads would result in resonance rather than transient response [10]. Therefore, serviceability can be assessed by analyzing steady-state response. The frequency analysis, was repeated after including the cement slab. It was noticed that the natural frequencies have shifted slightly to the left, resulting in reducing the fundamental frequency by 0.1 Hz only.

3.2 Modal Analysis

As explained above, having the structure fundamental frequency below 10 Hz, a simple force model described earlier in Sect. 2.3 can be considered. Moreover, the walking induced forces could be applied at a single (stationary) node and the response of the same node can be used to estimate steady-state response. Figure 5 presents the system frequency response at the point of load.

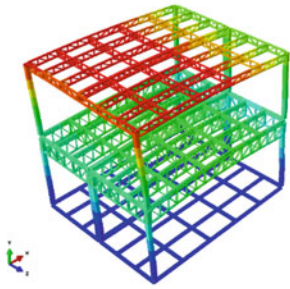
Harmonic analysis results indicates that the first vertical resonance is above 20 Hz, while longitudinal and lateral modes are below 10 Hz. The acceleration peak could be estimated using equation (Eq. 6) [6].

$$a_p = FRF_{Max} \alpha Q \rho \quad (6)$$

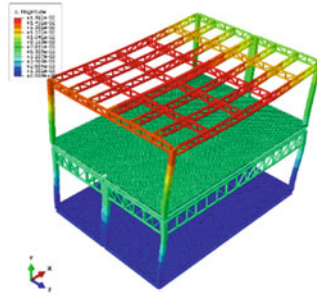
where FRF_{Max} is the maximum frequency response function magnitude at frequencies below 9 Hz, [%g/N], Q is bodyweight 750 N, ρ is resonant build-up factor, and α is dynamic coefficient that can be approximated using equation (Eq. 7).

$$\alpha = 0.09e^{-0.075f_n} \quad (7)$$

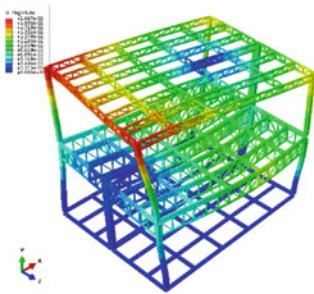
Using the above equations; Eqs. (6) and (7), the calculated peak acceleration was found equal to 0.615%g, which is above the accepted tolerance according to ISO 2631-2 [new reference]. Further analysis was performed to estimate the acceleration at the point of load in three directions; vertical, longitudinal, and lateral, presented in Fig. 6. The estimated peak acceleration was found to be around 0.07 m/s²; considering a fundamental pacing frequency of 1.4 Hz (slow walking). For an intermediate walking speed a pacing frequency of 2 Hz was applied, and results can be found in



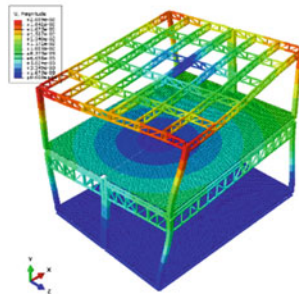
Lateral mode (1) $F=4.2167$ Hz



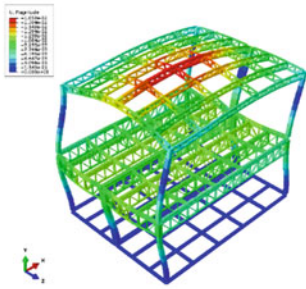
Lateral mode (1) $F=4.11408$ Hz



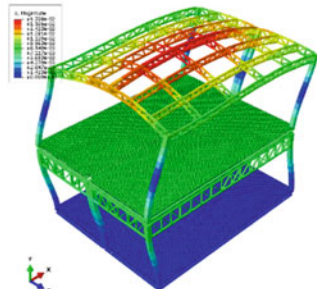
Twisting mode (3) $F=6.119$ Hz



Twisting mode (2) $F=5.994$ Hz



Coupled vertical and longitudinal (6)
 $F=8.7823$ Hz



Coupled vertical and longitudinal (5)
 $F=8.1383$ Hz

Fig. 4 Natural frequencies and modes shape

Fig. 5 Frequency response

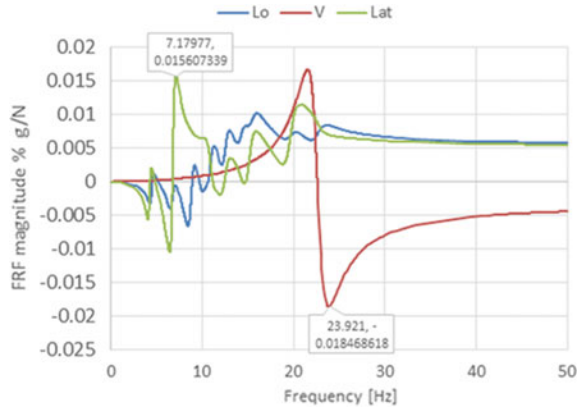


Fig. 6 Acceleration in three direction during steady state harmonic excitation at pacing frequency 1.4 Hz

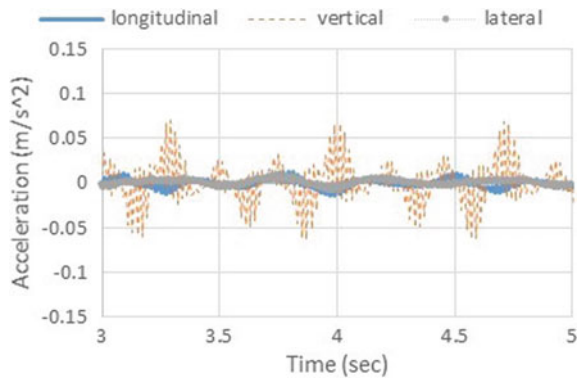
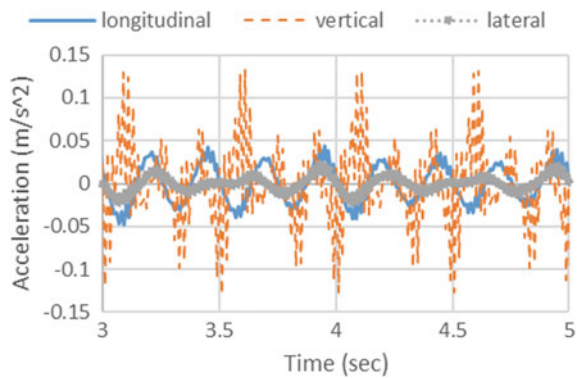


Fig. 7 By comparing peak amplitude in both analysis, at faster walking speed (2 Hz) the peak amplitude was almost doubled for all deflection modes i.e. vertical, longitudinal and lateral. Although the simple force model harmonics are up to 3 times the

Fig. 7 Acceleration in three direction during steady state harmonic excitation at pacing frequency 2 Hz



spacing frequency, but still the time response indicate high frequency content which represent a transient phenomenon.

Based on the estimated acceleration peaks; above, The vibration levels were found to be exceeding the recommended level of vibration in offices and residential buildings (0.005 m/s^2) [6, 11]. In this analysis, the structure was considered empty. According to Shahabpoor et al. and Brad et al. [3, 12], damping of occupied buildings is larger than empty one. For example, Shahabpoor et al. [3] reported that 50% of FRF magnitude dropped when 3 people were occupying the floor, which is returned due to human structure interaction (HSI), where the human body dissipates part of vibration energy.

The walking induced force was also simulated by considering a moving concentrated load over a predefined path. The dynamic analysis of structure with a moving load was performed on the structure including the cement slabs. The loads and their distribution for single person walking over a surface were extracted from the experimental work reported by Bard et al. [12] to identify the span between the right and left foot as well as walking speed. Figure 8 presents the estimated acceleration

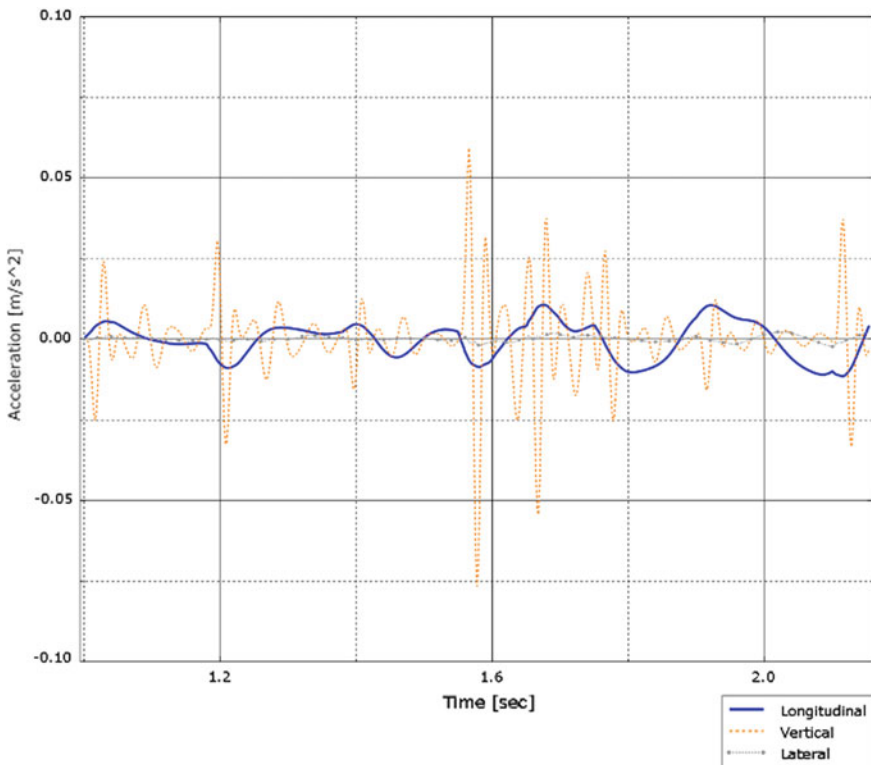


Fig. 8 Acceleration in three direction during implicit dynamic analysis at pacing frequency 2 Hz (moving load)

Table 3 Comparison between FEA and manual calculation

Method	Estimated (a/g)%
Harmonic analysis (FEA)	0.62
FEA (stationary)	1.27
FEA (moving load)	0.61
Design guide 11	0.43
Tolerance limit	0.5

at a midpoint (away from point of load). It can be noticed that vertical response is the highest. Moreover, the decaying envelop is showing a transient response for this mode of vibration. It was reported by Tosa and Gomes [2] that structural response considering a moving force is 30% lower as compared to simple force model (stationary).

By comparing estimated acceleration, using the developed FEM and calculation following AISC DG 11 [6], it can be noticed that vibration levels estimated using AISC DG 11 are lower a compared to ones estimated using the developed FEM. Moreover, the fundamental vertical vibration mode was under estimated as compared to FEA results. Table 3 presents a comparison between four different evaluation methods considered in this paper. Also the acceleration amplitudes (peak) are compared to maximum recommended amplitude per ISO 2631-2, 1989 [11].

4 Conclusions

In this work, serviceability of two-story office building was investigated through finite element modeling as well as standard design calculation following AISC DG 11. Two force induced walking models were consider in this paper, the first model considered foot fall loads as concentrated harmonic force (not moving), which closely represent harmonic analysis. The second model was presenting the induced force as moving concentrated time varying load acting as a drop force. Based on estimated vibration levels the following conclusions could be drawn.

1. The finite element analysis revealed that the fundamental frequency is around 4 Hz in lateral and longitudinal directions while the first vertical mode was around 23 Hz, the later was found higher than the estimated fundamental frequency calculated based on the combined panel model following AISC DG 11 (14 Hz).
2. The acceleration peaks in the vertical direction were found higher in FEA as compared to one estimated by the design guide.
3. Based on estimated acceleration in the three axes with respect to walking path i.e. longitudinal, vertical and lateral, the acceleration levels where found to be slightly above ISO recommended value of 0.005 m/s^2 for the frequency range

from 4–8 Hz. Keeping in mind that this analysis is following the guidelines where nonstructural materials are not included.

4. Transient mode was found in the vertical vibration due to footfall load due to higher fundamental vertical mode frequency, above 10 Hz.
5. Low fundamental frequencies in longitudinal and lateral direction can easily match with pacing frequency and its harmonics, therefore resonance is expected.

Acknowledgements The author would like to acknowledge the support provided by King Fahd University of Petroleum and Minerals (KFUPM).

References

1. International Organization for Standardization (2007) Bases for design of structures–serviceability of buildings and walkways against vibrations. ISO 10137:2007
2. Toso MA, Gomes HM (2018) A coupled biodynamic model for crowd-footbridge interaction. *Eng Struct* 177:47–60
3. Shahabpoor E, Pavic A, Racic V, Zivanovic S (2017) Effect of group walking traffic on dynamic properties of pedestrian structures. *J Sound Vib* 387:207–225
4. Muhammad Z, Reynolds P, Avci O, Hussein M (2019) Review of pedestrian load models for vibration serviceability assessment of floor structures. *Vibration* 2(1):1–24
5. Feldmann M, Heinemeyer C, Butz C, Caetano E, Cunha A, Galanti F, Waarts P (2009) Design of floor structures for human induced vibrations. JRC–ECCS joint report
6. Murray TM, Allen DE, Ungar EE, Davis DB (2016) Vibrations of steel-framed structural systems due to human activity. Design Guide 11 American Institute of Steel Construction
7. Adams V, Askenazi A (1999) Building better products with finite element analysis. Cengage Learning
8. Van Nimmen K, Lombaert G, De Roeck G, Van den Broeck P (2014) Vibration serviceability of footbridges: evaluation of the current codes of practice. *Eng Struct* 59:448–461
9. Song Z, Su C (2017) Computation of Rayleigh damping coefficients for the seismic analysis of a hydro-powerhouse. *Shock Vib*
10. Mohammed AS, Pavic A, Racic V (2018) Improved model for human induced vibrations of high-frequency floors. *Eng Struct* 168:950–966
11. Evaluation of human exposure to whole-body vibration—Part 2: Continuous and shock-induced vibration in buildings (1 to 80 Hz). International Organization for Standardization, 1989 ISO 2631–2 (1989)
12. Bard D, Sonnerup J, Sandberg G (2008) Human footsteps induced floor vibration. *J Acoust Soc Am* 123(5):3356
13. Evaluation of human exposure to whole-body vibration—Part 2: Continuous and shock-induced vibration in buildings (1 to 80 Hz), International Organization for Standardization, 1989 ISO 2631–2, 1989
14. Evaluation of human exposure to whole-body vibration—Part 2: Continuous and shock-induced vibration in buildings (1 to 80 Hz), International Organization for Standardization, 1989 ISO 2631–2, 1989

Vibration Isolation and Control

An Economical Multiple-Tuned Mass Damper to Control Floor Vibrations



Mehdi Setareh

Abstract Excessive vibrations of architectural structures have become a prevalent design issue in recent years. The high strength of construction materials, optimized design of structures, and the desire of architects for large open space building layouts have resulted in a number of serviceability issues in existing building structures. In an attempt to search for an economical method of resolving this issue, a new multiple-tuned mass damper (MTMD) has been designed and tested. The device consists of four steel plates cantilevered from a central hub. Each plate (wing) has a central slot that can be used for the movement of steel weights to modify the natural frequencies of the MTMD during the tuning phase. In addition, air dampers connected to each wing provide the required damping for the optimal tuning of the MTMD. This paper details the design of this novel MTMD and provides the analytical equations developed for the tuning of the device. It also provides information on the field tuning of the device to a laboratory floor susceptible to large vibrations due to human movements. In addition, results of the walking and bouncing tests conducted at the Virginia Tech Vibration Testing Laboratory to evaluate the effectiveness of the device are discussed. It is concluded that the proposed device can provide an economical and effective method of floor vibration mitigation.

Keywords Multiple tuned mass damper · Floor vibration · Vibration serviceability · MTMD tuning · Walk and bounce excitations

1 Introduction

Excessive floor vibrations have become an important serviceability issue in recent years. In fact, the number of building floors having such problems in the past twenty years is more than the reported cases during the entire twentieth century. The main reasons for such increase in the number of problem floors are: (1) reduction in floor mass resulting from the use of higher strength construction materials; (2) reduction

M. Setareh (✉)

School of Architecture and Design, Virginia Tech, Blacksburg, VA, USA

e-mail: setareh@vt.edu

© The Author(s), under exclusive license to Springer Nature Switzerland AG 2023
Z. Wu et al. (eds.), *Experimental Vibration Analysis for Civil Engineering Structures*,
Lecture Notes in Civil Engineering 224,
https://doi.org/10.1007/978-3-030-93236-7_24

273

in damping due to less office furniture, and fewer partitions; (3) reduction in stiffness due to the use of optimized design approaches, which generally result in less stiff supporting members; (4) reduction in the natural frequency of floor systems caused by larger floor span lengths; and (5) increase in the number of rhythmic activities such as rock concerts, aerobics, indoor jogging, etc.

When an excessive floor vibration occurs, there are generally few options available to the structural engineer. Tuned Mass Dampers (TMDs) have been used to control these vibrations and correct the problem. TMDs which are generally tuned to a specific mode of vibration, consists of elements to provide mass, stiffness, and damping. The first application of TMDs was proposed by Frahm [1] in 1911 to control the rolling motions and vibrations of the hull of ships. Later Ormondroyd and Den Hartog [2], Brock [3] and Den Hartog [4] contributed to the theory of vibration reduction of undamped systems using TMDs.

Many attempts have been made to increase the effectiveness of TMDs when used for floor vibration control, among them are the works by Setareh et al. [5, 6] using pendulum and semi-active TMDs, and Varela and Battista [7] where they used steel plates directly hung from the supporting floor beams. Two main issues exist when using TMDs to control floor vibrations. First, it is possible that several modes of a floor can be susceptible to large vibrations due to human movements. The second issue is the high costs of fabrication, installation and tuning of those devices. A number of attempts by researchers have been made to address the first issue. Snowdon et al. [8] proposed the use of a cruciform TMD made of two free-free beams with a lumped mass at the end to control several modes of a general distributed mechanical system.

This paper introduces a multiple-tuned mass damper (MTMD) made of simple components to fabricate and easy to install and tune. The device is designed such that its natural frequencies can be adjusted by changing its stiffness and mass. In addition, adjustable dampers are used to provide more versatility in its application. The design of the MTMD is discussed and its optimum dynamic properties are computed. The installation of the device on a laboratory floor to control three modes of vibration are discussed and the results obtained from the measurements are compared with those from the analytical predictions. In addition, the results of various walk and bounce tests by a group of volunteers to demonstrate the effectiveness of the device to control the vibrations due to human movements are presented.

2 Description of the MTMD and the Test Floor

The MTMD consists of two steel plates cantilevered from a central hub at the center of the plates. The steel plates provide the MTMD stiffness. Each cantilever (or wing) has a slot at its center which allows the weight plates which provide MTMD mass to move along each wing and be secured. This allows both the stiffness and mass of the MTMD to be adjusted. To provide damping adjustable air dampers are used.

The device components are easy to fabricate and assemble. Therefore, unlike the existing TMD design, the developed MTMD is very affordable and can be easily mass

Fig. 1 The test structure at the Virginia Tech Vibration Testing Laboratory



produced. Also, the device dimensions are such that the MTMD can be housed within the typical floor plenums. The assembly of the device is very easy as all components are bolted to each other and does not require skilled personnel. In addition, the tuning of the device can be accomplished by using a vibration application on a smartphone.

All the tests presented in this study were conducted at the Virginia Tech Vibration Testing Laboratory (VTVTL). The facility houses a two-story full-scale test structure that was used for studies conducted here. Figure 1 shows the test structure at the VTVTL. Figure 2 shows the MTMD placed at the quarter point of the test floor used for this study, which consists of a 9.14 m by 9.14 m concrete floor with steel beams supported by columns at its corners. Table 1 shows the measured natural frequencies and damping ratios of the test floor.

3 MTMD Design Parameters

To design the MTMD, its optimum dynamic parameters need to be computed [9]. These are the optimum MTMD frequency ratio (f) and damping ratio (ζ_M) for given mass ratio (μ) and floor damping ratio (ζ). Since the MTMD is made of four wings, it can be tuned to a maximum of four different floor vibration modes.

Only three wings of the MTMD were used in this study to tune them to the first three modes of vibration of the floor. To compute the optimum non-dimensional design parameters of the MTMD, the effective mass (weight) of the floor for its first three modes had to be computed. A computer model of the test structure including both floor levels was created using SAP 2000 computer software [10] and was updated



Fig. 2 The MTMD placed at the quarter point of the test floor

Table 1 Measured natural frequencies and damping ratios of the test floor

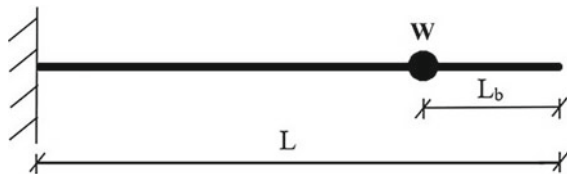
Mode number	Natural frequency (Hz)	Damping ratio (%)
1	5.225	0.51
2	9.225	0.36
3	10.650	0.42

to closely represent the measured dynamic properties of the floor using the measured floor modal damping ratios. The effective weights (masses) of each mode were found using the frequency response function (FRF) at the corresponding resonance frequencies [11]: $W_{ef1} = 61\text{KN}$; $W_{ef2} = 54.5\text{KN}$; and $W_{ef3} = 42.6\text{KN}$

The MTMD effective masses were also needed to be found in order to compute the non-dimensional design parameters. For this purpose, each wing of the MTMD was considered as a cantilever beam with a movable mass (weight) as shown in Fig. 3.

The cantilever length, L , for each wing was computed by setting the analytical natural frequency shown in Eq. (1) equal to its measured counterpart [11]:

Fig. 3 Cantilever beam model representing each MTMD wing



$$f_n = \frac{1}{2\pi} \sqrt{\frac{3EIg}{(L - L_b)^3 W_e}} \tag{1}$$

$$W_e' = \frac{0.22 W_p L^3}{(L - L_b)^3} \tag{2}$$

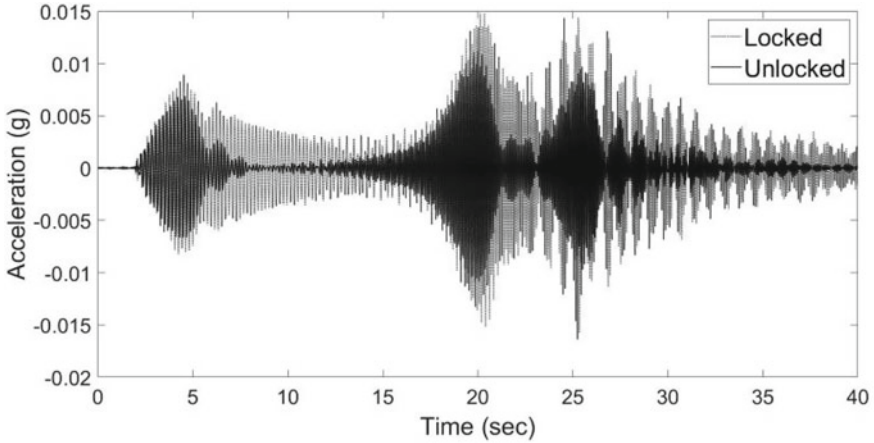
$$W_e = W + W_e' \tag{3}$$

where E is the modulus of elasticity of the wings (steel), I is the moment of inertia of the wing cross-section, g is the gravitational acceleration. W_p is the total weight of the wing plate, W_e is the effective weight of each wing of the MTMD, and W is the total weight of movable plates. The MTMD effective weights (masses) were adjusted based on the modal amplitude at the location of the MTMD placement on the floor (the quarter point for this study) which were found to be: $\mu_1 = 0.0018$, $\mu_2 = 0.00325$, and $\mu_3 = 0.00167$ for the first three modes, respectively. Using the measured floor damping ratios as shown in Table 1, the predicted non-dimensional frequency ratios (f) and MTMD damping ratios (ζ_M) for the three modes of vibration were computed. The predicted reduction in the floor response for the first three modes were equal to 74%, 85%, and 78%, respectively [11].

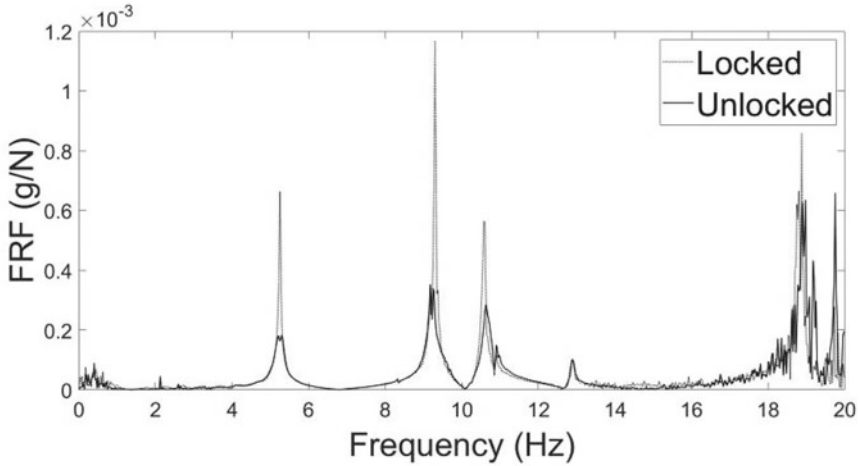
Figure 4 shows the time responses and the frequency response functions (FRF) of the floor with the MTMD inactive (locked wings) and active (unlocked wings). A burst chirp excitation was used for the tests. The measured average reduction in the responses of the first three vibration modes of the floor were 67%, 50%, and 48%, respectively.

4 Walk and Bounce Tests

The MTMD performance was evaluated by conducting a series of tests on the laboratory floor. Thirty volunteers participated in the walking and bouncing tests. For the walk tests, the human subjects were asked to walk individually on the floor at the corresponding sub-harmonics of the first and second mode natural frequencies of the floor. The third mode natural frequency was above 10 Hz, which cannot result in a floor resonant behavior due to human activity. Therefore, the tests were not planned to excite this mode of the vibration of the floor. Each person walked from one end of the floor along the centerline to the opposite end and waited until the measurement was complete. The selected step frequencies for walking at the first mode sub-harmonic was 158 spm (steps per minute) and for the second mode was 139 spm. Figure 5 shows a sample of the measured floor response in the time and frequency domains when the subject walked at the first mode sub-harmonic (158 spm). The average reduction in the vibration due to the use of MTMD for the first mode was 59% and for the second mode was about 42%. It was noted that even though the mass ratio for the second mode was higher, due to the lower participation



(a) Time domain

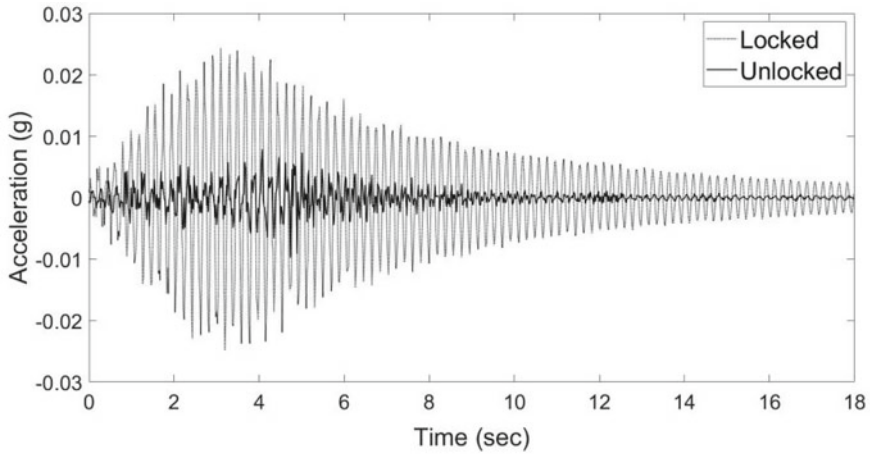


(b) Frequency domain

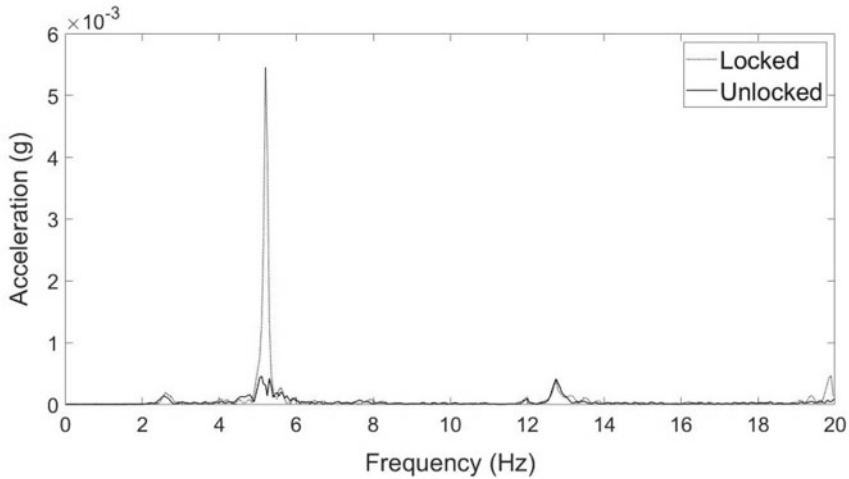
Fig. 4 Floor response in time domain and frequency domain (FRF)

of the second mode in the floor response and smaller walk dynamic load factor, the second mode vibration reduction level was smaller.

The floor responses were also measured when the MTMD was active (unlocked) and inactive (locked) while the individual human subject bounced on the floor. A bounce excitation occurs when the person moves up and down by bending his/her knees without leaving the floor. This typically represents movements of people while engaging in a dance like activity. To excite the first mode each individual bounced at



(a) Time history

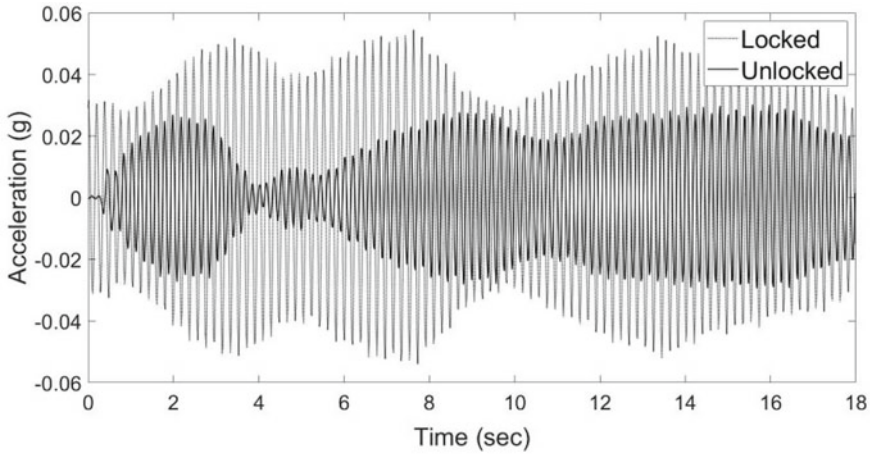


(b) Frequency spectrum

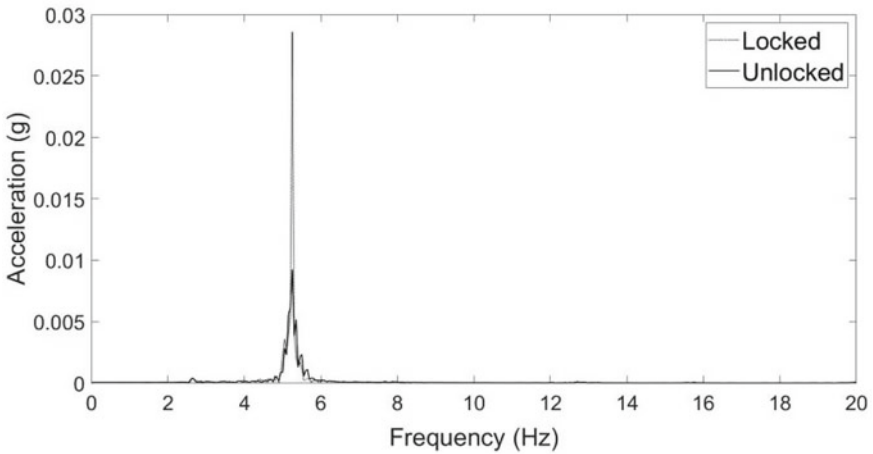
Fig. 5 Comparison of the floor responses in the time and frequency domains when the MTMD was locked and unlocked as the subject walked at the first mode subharmonic (158 bpm)

158 bpm (bounce per minute) while standing at the center of the floor. Figure 6 illustrates the comparison of the floor center responses in the time and frequency domains when the MTMD was in the locked and unlocked positions while an individual bounced.

To excite the second mode, the same tests were repeated when the individuals stood at the quarter point of the floor and conducted bounces at 139 bpm. Figure 7 shows the comparison between the response of the quarter point of the floor in the time



(a) Time history

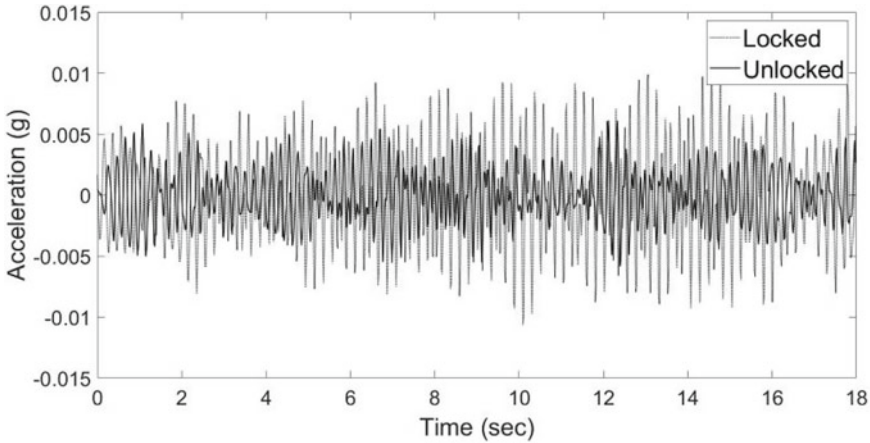


(b) Frequency spectrum

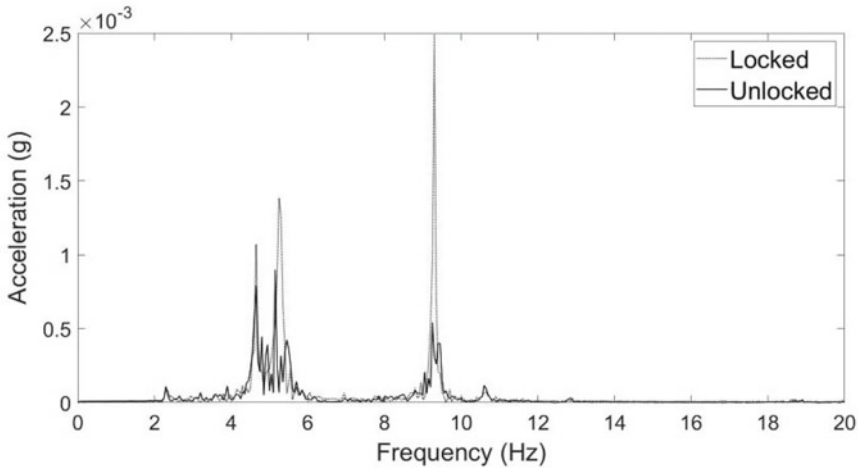
Fig. 6 Comparison of the floor responses in time and frequency domains when the MTMD was locked and unlocked as the subject bounced at the first mode subharmonic (158 bpm) standing at the floor center

and frequency domains when the MTMD was in the locked and unlocked positions while an individual bounced.

The average reduction in the floor vibration by using the MTMD when excited by the human subjects bounce excitation was about 45%.



(a) Time history



(b) Frequency spectrum

Fig. 7 Comparison of the floor responses in the time and frequency domains when the MTMD was locked and unlocked as the subject bounced at the second mode subharmonic (139 bpm) standing at the floor one-quarter point

5 Summary and Conclusion

At times reducing floor vibrations due to human movements through making structural modification such as changing stiffness and/or mass can be cost prohibitive. An economical method of alleviating excessive floor vibrations was introduced which

consists of the application of a multiple tuned mass damper (MTMD). The MTMD introduced in this study, is made of simple components that are easy to fabricate and assemble. It can be used for controlling vibration at the design stage of the structure or as a method to correct existing problem floors.

This paper presented the equations to compute the MTMD dynamic parameters in order to predict its effectiveness in controlling vibrations. A number of laboratory tests were conducted. The results of the tests showed the effectiveness of the device in controlling different modes of floor vibrations while having very small mass ratios within 0.16–0.18% range. The results of the conducted walk and bounce tests by a group of individuals also demonstrated the effectiveness of the MTMD in controlling two modes of vibrations of a laboratory test floor.

Acknowledgements The research presented here was supported by the National Science Foundation under grant number CMMI-1335004. This support is gratefully acknowledged. Any opinions, findings, and conclusions expressed in this paper are those of the writer and do not necessarily reflect the views of the National Science Foundation. Ms. Stephanie Renard provided technical assistance on this paper.

References

1. Frahm H (1911) Device for damping of bodies. U.S. Patent No. 989,958
2. Ormondroyd J, Den Hartog JP (1928) The theory of the dynamic vibration absorber. *Trans Am Soc Mech Eng* 50:9–22
3. Brock JE (1946) A note on the damped vibration absorber. *J Appl Mech Am Soc Mech Eng* 13, A-284
4. Den Hartog JP (1947) *Mechanical vibrations*, 3rd edn. McGraw-Hill Book Co., Inc, New York, New York
5. Setareh M, Ritchey JK, Murray TM, Baxter A (2006) Application of a pendulum tuned mass damper for floor vibration control. *J Perform Constr Facil Am Soc Civ Eng* 20(1):64–73
6. Setareh M, Ritchey JK, Murray TM, Koo JH, Ahmadian M (2007) A semi-active tuned mass damper for floor vibration control. *J Struct Eng Am Soc Civ Eng* 133(2):242–250
7. Varela WD, Battista RC (2011) Control of vibrations induced by people walking on large span composite floor decks. *Eng Struct* 33:2485–2494
8. Snowdon JC, Wolfe AA, Kerlin RL (1984) The cruciform dynamic vibration absorber. *J Acoust Soc Am* 75(6):1792–1799
9. Setareh M, Renard S (2019) Study of a multiple-tuned mass damper for excessive floor vibrations mitigation. Interdependence between Structural Engineering and Construction Management in Structural Engineering and Construction STR-112-1–STR-112-6
10. Computers and Structures, Inc. (2017) SAP2000-static and dynamic finite element analysis of structures. California, Berkeley
11. Renard S, Setareh M (2017) Study of the multiple-tuned mass damper to reduce vibration serviceability issues. Unpublished report, Virginia Tech, Blacksburg, Virginia

Experimental Study of a Two-Degree-of-Freedom Pendulum Controlled by a Non-smooth Nonlinear Energy Sink



Gabriel Hurel, Alireza Ture Savadkoohi, and Claude-Henri Lamarque

Abstract We seek to control the oscillations of a two degree-of-freedom pendulum under base excitation with a non-smooth nonlinear energy sink (NES) since the main structure is nonlinear. Thanks to the multiple time scales method, an analytic model is built. At fast time scale, a slow invariant manifold with stable and unstable zones describes the behavior of the system. Some singular point correspond to bifurcations responsible to the control of the main structure. At the next slow time scale, the equilibrium points of the system are calculated. A pseudo-periodic regime can exist and create a thresholding of the energy of the main structure. In order to validate the theoretical model, we built a reduced model in our laboratory. The pendulum made with a threaded rod and a steel mass, is hung from a jib crane, which is excited horizontally or vertically by an electrodynamic shaker. Increasing and decreasing sine sweeps allows to exhibit show the response for a wide range of frequency. The NES is made with a steel cylinder oscillating freely between two elastic boundaries creating a piece-wise linear law. Different configurations of excitation and orientation of the NES are tested. The first results highlight the nonlinear behavior of the pendulum. Then, the results show a good qualitative agreement with the theory and a good efficiency of the desired control on a wide range of frequency.

Keywords Passive control · Pendulum · Nonlinear energy sink · Reduced model · Shake table

1 Introduction

Due to wind, acceleration or emergency braking, the ropeway vehicles can oscillate around two horizontal axes. This is uncomfortable for passengers and dangerous for the structure. Many solutions have been designed to control the dynamics of structures, which can be sorted in two categories: active systems with a control loop and passive systems that do not need energy supply. The first passive system is the

G. Hurel · A. Ture Savadkoohi (✉) · C.-H. Lamarque
Univ Lyon, ENTPE, LTDS UMR CNRS, 5513, 69518 Vaulx-en-Velin Cedex, France
e-mail: alireza.turesavadkoohi@entpe.fr

© The Author(s), under exclusive license to Springer Nature Switzerland AG 2023
Z. Wu et al. (eds.), *Experimental Vibration Analysis for Civil Engineering Structures*,
Lecture Notes in Civil Engineering 224,
https://doi.org/10.1007/978-3-030-93236-7_25

tuned mass damper (TMD) [1] which can absorb the energy at the frequency on one mode. For a non-linear system where the natural frequencies as a function of the amplitude of vibration are not constant, the TMD cannot be used. It has been showed that to introduce non-linear terms in the restoring force function of the damper can improve its efficiency [2]. For the nonlinear energy sink (NES) [3, 4], no linear term exists in the restoring force function, so that no frequency is targeted. Hurel et. Al studied how a NES can control both modes of a two degrees-of-freedom pendulum [5, 6]. They verified the efficiency of the NES in case of vertical parametric excitation [7] and provided tools to determine the design parameters of the NES [8].

In Sect. 2 of this article, we describe the studied system, and in Sect. 3 we give the main results of an analytical analysis with the multiple time scales method. We present the experimental set-up in Sect. 4 and the obtained results in Sect. 5. Finally, we conclude in Sect. 6.

2 System

The two-degree-of-freedom pendulum of mass M is hung at its top O with a hinge linkage in a gravitational field g . It can rotate around \vec{y} and \vec{x} axes with angles φ and ψ respectively. Its center of mass G is located at a distance L from O . Its matrix of inertia \mathbf{I} is diagonal in the main reference of frame.

A NES is coupled to the pendulum at the distance a from O with an orientation α as seen on Fig. 1. The NES is made of a mass $m \ll M$, moving with a viscous damping c_u on a length $2d$ between two elastic barriers of stiffness k . The piece-wise linear restoring force function F as a function of the displacement of the mass u is represented on Fig. 2.

$$F(u) = \begin{cases} k(u + d) & \text{if } u < -d \\ 0 & \text{if } -d < u < d \\ k(u - d) & \text{if } u > d \end{cases}$$

The system is excited with the displacement of the base of the pendulum $x_O(t)$, $y_O(t)$ and $z_O(t)$.

3 Theoretical analysis

3.1 Governing Equations of the System

The kinetic energy (E_k) and the potential energy (E_p) of the system read:

$$E_k = \frac{1}{2}M(\dot{x}_G^2 + \dot{y}_G^2 + \dot{z}_G^2) + \frac{1}{2}\mathbf{I}_{xx}\varphi^2 + \frac{1}{2}\mathbf{I}_{yy}\psi^2 + \frac{1}{2}M(\dot{x}_m^2 + \dot{y}_m^2 + \dot{z}_m^2) \quad (1)$$

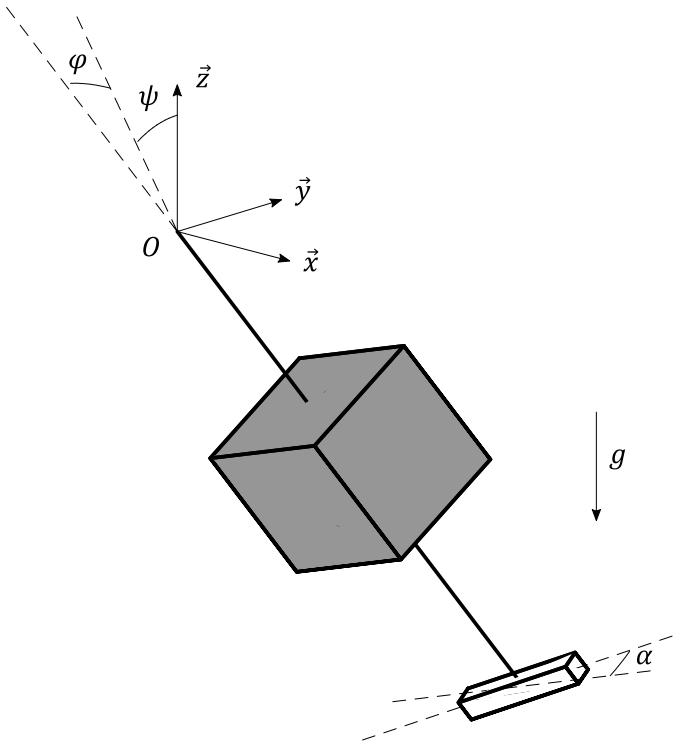
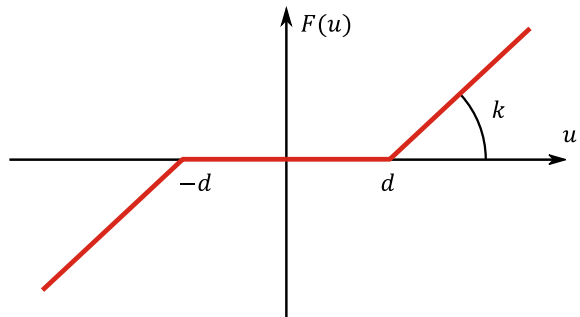


Fig. 1 Two degree-of-freedom pendulum coupled with a NES [8]

Fig. 2 Piece-wise linear restoring force function of the NES [8]



$$E_p = g(Mz_G + mz_m) + S(u) \tag{2}$$

where $\dot{\bullet}$ stands of the time derivation and $\nabla S(u) = F(u)$ where ∇ stands for the gradient operator. We deduct the equations of the system thanks to the Euler–Lagrange equations.

3.2 Assumptions

We assume both natural frequencies of the pendulum are close to each other:

$$\omega_\varphi = \omega_\psi + \sigma\varepsilon \quad (3)$$

where ε is the ratio of mass:

$$\varepsilon = \frac{m}{M} \ll 1 \quad (4)$$

We assume the displacement of the base O is small and periodic, so we can express its coordinates as Fourier series:

$$x_O(t) = \varepsilon \sum_{j=0}^{\infty} x_j e^{ij\Omega t}, \quad y_O(t) = \varepsilon \sum_{j=0}^{\infty} y_j e^{ij\Omega t}, \quad z_O(t) = \varepsilon \sum_{j=0}^{\infty} z_j e^{ij\Omega t} \quad (5)$$

As the excitation is small, we assume the variables of the pendulum are small:

$$\varphi = \varepsilon \underline{\varphi}, \quad \psi = \varepsilon \underline{\psi}, \quad u = \varepsilon \underline{u} \quad (6)$$

Finally, we assume the fundamental frequency of excitation is close to both natural frequencies:

$$\Omega = \omega_\varphi + \sigma_\varphi \varepsilon = \omega_\psi + \sigma_\psi \varepsilon \quad (7)$$

3.3 Multiple Time Scales Method

We introduce the following variables of Manevitch [9]:

$$\Phi e^{i\Omega t} = \underline{\dot{\varphi}} + i\Omega \underline{\varphi}, \quad \Psi e^{i\Omega t} = \underline{\dot{\psi}} + i\Omega \underline{\psi}, \quad U e^{i\Omega t} = \underline{\dot{u}} + i\Omega \underline{u} \quad (8)$$

In the multiple time scales method [10], we used ε as small parameter to decompose the time t in several scales of time:

$$\tau_0 = t, \quad \tau_1 = \varepsilon t, \quad \tau_2 = \varepsilon^2 t, \dots \quad (9)$$

The derivation operator can be redefined:

$$\frac{d}{dt} = \frac{\partial}{\partial \tau_0} + \varepsilon \frac{\partial}{\partial \tau_1} + \varepsilon^2 \frac{\partial}{\partial \tau_2} + \dots \quad (10)$$

We keep only the first harmonics of the response of the system. The following operator does this is done for an arbitrary function of the system $h(\tau_0, \tau_1, \tau_2, \dots)$:

$$H = \frac{\Omega}{2\pi} \int_0^{2\pi} h(\tau_0, \tau_1, \tau_2, \dots) e^{-i\Omega\tau_0} d\tau_0 \tag{11}$$

3.4 Analysis of the System at Fast Time Scale

At the first order $O(\varepsilon)$, corresponding to the fast time scale, the equations read:

$$\frac{\partial \Phi}{\partial \tau_0} = 0 \tag{12}$$

$$\frac{\partial \Psi}{\partial \tau_0} = 0 \tag{13}$$

$$\frac{\partial U}{\partial \tau_0} + \frac{i a \cos(\alpha)(a\Omega^2 - g)}{2\Omega} \Phi + \frac{i a \sin(\alpha)(a\Omega^2 - g)}{2\Omega} \psi + \frac{i\Omega + \lambda}{2} U + i \frac{K}{2\Omega} U S(|U|) = 0 \tag{14}$$

where $\lambda = \frac{c_u}{m}$, $K = \frac{k}{m}$ and

$$S(|U|) = \begin{cases} 0 & \text{if } |U| \leq D \\ \arccos\left(\frac{D}{|U|}\right) - \frac{D\sqrt{|U|^2 - D^2}}{|U|^2} & \text{if } |U| > D \end{cases} \tag{15}$$

where $D = \frac{\Omega d}{\sqrt{\varepsilon}}$. At the asymptotic state (when $\frac{\partial U}{\partial \tau_0}$ tends to 0), with the polar form of variables $\Phi = N_\varphi e^{i\delta_\varphi}$, $\Psi = N_\psi e^{i\delta_\psi}$ and $U = N_u e^{i\delta_u}$, the Eq. (14) describes a slow invariant manifold (SIM):

$$\cos^2(\alpha) N_\varphi^2 + \sin^2(\alpha) N_\psi^2 + 2\sin(\alpha)\cos(\alpha)\cos(\delta) N_\varphi N_\psi = \frac{(K S(N_u) - \Omega^2)^2 + \lambda^2 \Omega^2}{(a\Omega^2 - g)^2} N_u^2 \tag{16}$$

where $\delta = \delta_\varphi - \delta_\psi$. The SIM is represented in Fig. 3 for several values of δ with stable and unstable zones.

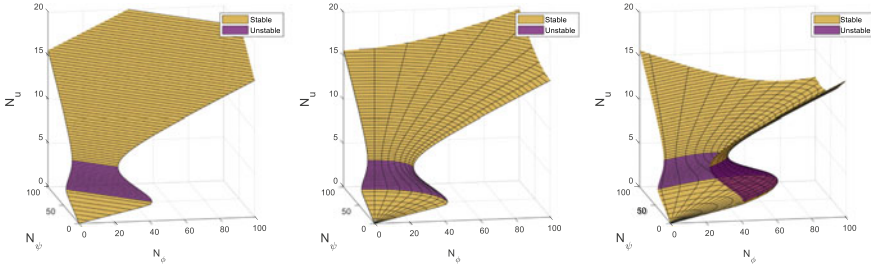


Fig. 3 SIM for $\delta = 0, \frac{\pi}{2}$ and $\frac{4\pi}{5}$

3.5 Analysis of the System at Slow Time Scale

At the next time scale $O(\varepsilon^2)$ corresponding to the first slow time scale, the equations of the system reads:

$$\begin{aligned}
 Lg \frac{\partial \Phi}{\partial \tau_1} + \left(\frac{i2\sigma_\varphi Lg + a\Omega(a\Omega^2 - g)}{2} + \frac{c_\varphi \omega^2}{2} \right) \Phi + \frac{iLg}{16\Omega} |\Phi|^2 \Phi \\
 + \frac{i\cos(\alpha)\Omega(a\Omega^2 - g)}{2} U - x_1 L\Omega^4 - 2iz_2 L\Omega^3 \Phi^* \\
 + i \frac{Lg - 2L^2\omega^2}{8\Omega} \Phi |\Psi|^2 + i \frac{Lg + 2L^2\omega^2}{16\Omega} \Phi^* \Psi^2 = 0
 \end{aligned} \tag{17}$$

$$\begin{aligned}
 Lg \frac{\partial \Psi}{\partial \tau_1} + \left(\frac{i2\sigma_\psi Lg + a\Omega(a\Omega^2 - g)}{2} + \frac{c_\psi \omega^2}{2} \right) \Psi + \frac{iLg}{16\Omega} |\Psi|^2 \Psi \\
 + \frac{i\sin(\alpha)\Omega(a\Omega^2 - g)}{2} U - y_1 L\Omega^4 - 2iz_2 L\Omega^3 \Psi^* \\
 + i \frac{Lg - 2L^2\omega^2}{8\Omega} \Psi |\Phi|^2 + i \frac{Lg + 2L^2\omega^2}{16\Omega} \Psi^* \Phi^2 = 0
 \end{aligned} \tag{18}$$

We can calculate numerically equilibrium points of the system from Eqs. (17), (18) and the Sim Eq. (16). When no stable equilibrium point exists, i.e. equilibrium points are unstable, the system can oscillate between two stable zones of the SIM. This behavior called strongly modulated response [11] is represented on the SIM in Fig. 4. The amplitudes of the system N_φ and N_ψ are pseudo-periodic. Thanks to this phenomenon, the amplitudes stay below a threshold.

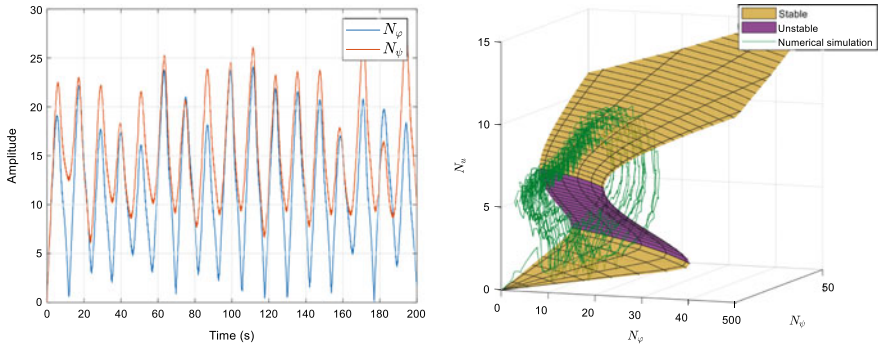


Fig. 4 SMR oscillations of the system: amplitudes and SIM

4 Reduced Model

We built a reduced model in order to estimate the efficiency of the NES experimentally. The pendulum is made with a rod and a steel parallelepiped mass (Fig. 5). It is hung to a frame made with two aluminum-profiled beams. Two close orthogonal pivots linkages constitute the hinge linkage (Fig. 6). The frame is bolted on the shake-table through a PMMA plate to avoid induced current and interference with sensors. The shake table can be set in two different positions in order to excite vertically or horizontally the system.

The mass of the NES is a cylinder translating in two ball rings and stopped with two springs as seen on Fig. 6. It is attached at the extremity of the pendulum.



Fig. 5 Reduced model on the shake table in horizontal and vertical position [8]

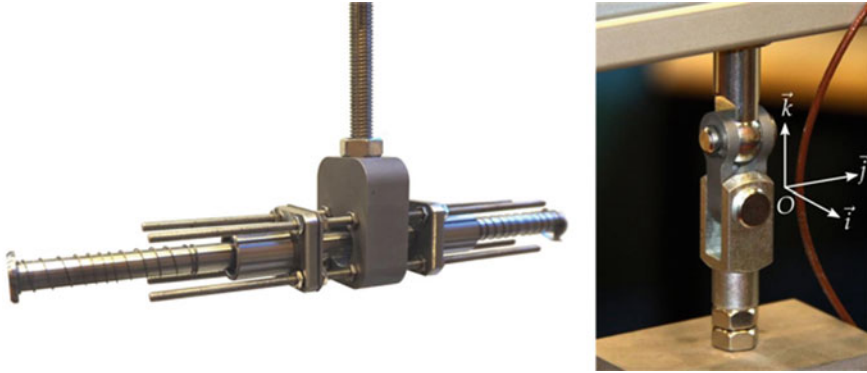


Fig. 6 Non-smooth NES and hinge linkage of the pendulum [8]

5 Test Results

The reduced model is subjected to excitations provided by the shake table. A sine force is provided with a frequency sweep. In order to highlight nonlinear phenomena, we always do ascending and descending sweeps. A control loop enables the shake table to deliver constant velocity whatever the frequency. The response of the system is measured with a triaxle accelerometer located at the extremity of the pendulum.

5.1 *Pendulum Alone*

First, we test the pendulum without NES. Several amplitudes of excitation are provided in Fig. 7. The decreasing frequency of peaks as a function of the amplitude show a softening effect of the system. The difference between increasing and decreasing frequency sweep show that several stable states exist for the same excitation.

5.2 *Horizontal Base Excitation*

Then we excite the structure horizontally with two orientations of the NES:

- $\alpha = 0^\circ$ (Fig. 8)
- $\alpha = 45^\circ$ (Fig. 9)

In both cases the NES provide a good control of the system by dividing by two the amplitudes of oscillation.

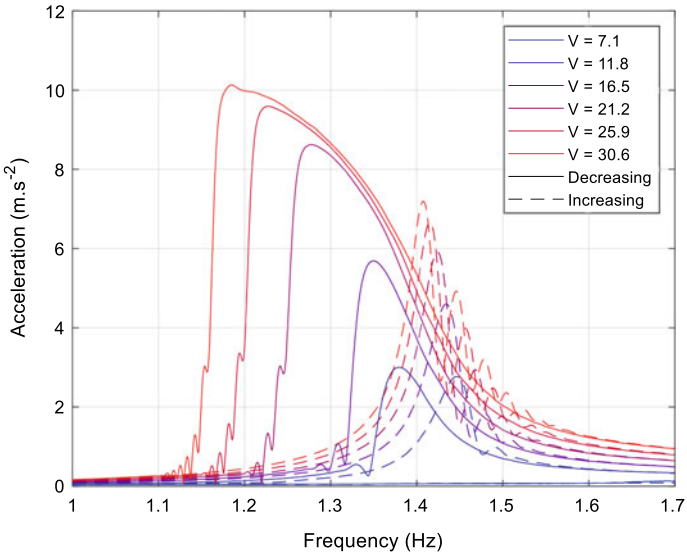


Fig. 7 Nonlinear response of pendulum alone with several velocities of excitation [8]

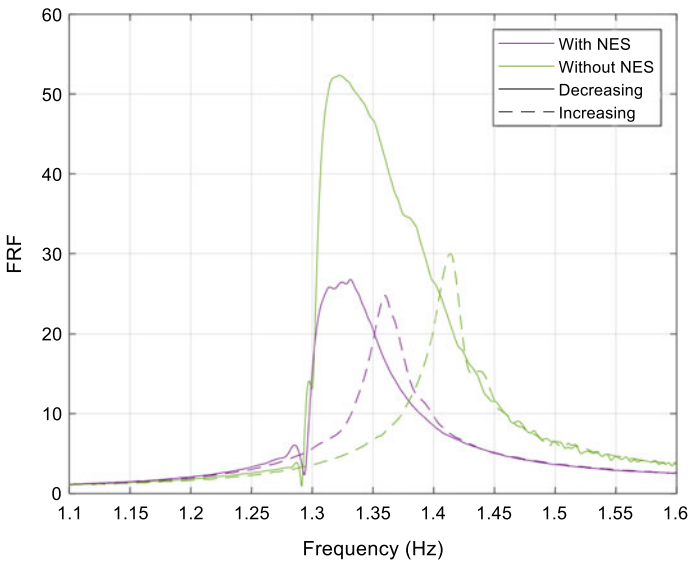


Fig. 8 Efficiency of the NES with horizontal excitation ($\alpha = 0$) [8]

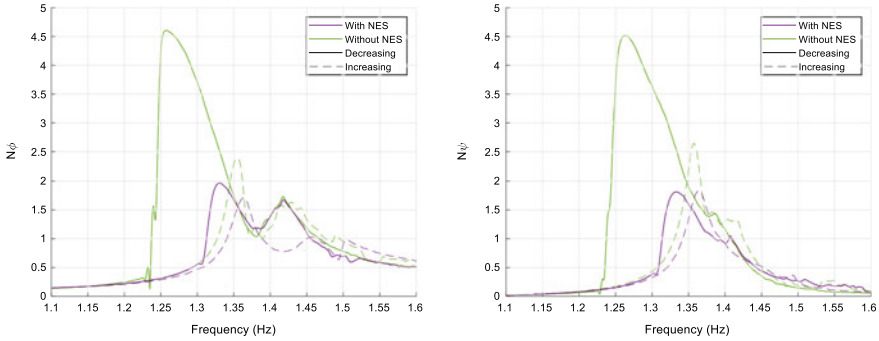


Fig. 9 Amplitude of the system with and without NES ($\alpha = 45^\circ$) [8]

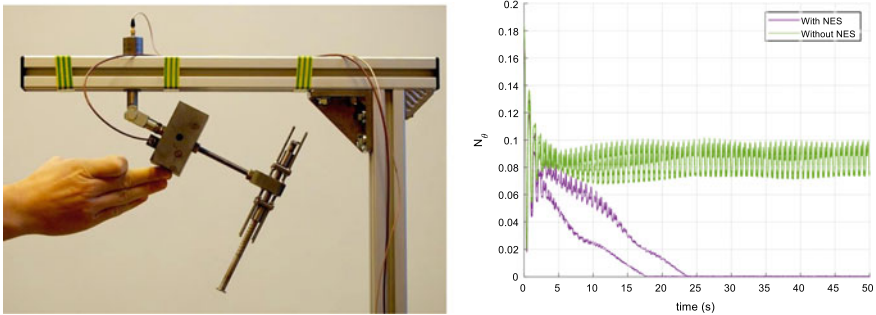


Fig. 10 Response of the system of vertical excitation with initial energy [8]

5.3 Vertical Base Excitation

When the system is subjected to vertical excitation, it does not oscillate if no initial energy is provided. In our test, the initial energy corresponds to an initial angle of the pendulum. The results of Fig. 10 show that without NES, the system continues to oscillate with high amplitude. The NES absorbs the energy of the pendulum, the amplitude of oscillation decreases to reach zero. These results are in agreement with the analytical calculations of [7].

6 Conclusions

We built a reduced model in order to verify and validate the analytical results of the control of a two degrees-of-freedom pendulum. A shake table can excite the system in several configurations. First, we show the nonlinear behavior of the pendulum. Then we show that the NES can control one mode of the pendulum by dividing by

two the amplitude of oscillations. If the orientation of the NES $\alpha = 45^\circ$, both modes are controlled. Finally, with vertical excitation, the NES avoid the pendulum to stay in a state with very high amplitude of oscillation. This experimental study show that the NES is efficient to control a two degrees-of-freedom pendulum in several conditions of excitations.

Acknowledgements This research was funded by “La Région Auvergne Rhone Alpes” in the frame of the CALIPSO project.

1. References

1. Frahm H (1911) Device for damping vibrations of bodies. Patent. *US Patent* 989,958.
2. Roberson RE (1952) Synthesis of a nonlinear dynamic vibration absorber. *J Franklin Inst* 254(3):205–220
3. Vakakis AF, Gendelman O (2001) Energy pumping in nonlinear mechanical oscillators: Part II. resonance capture. *J Appl Mech* 68(1):42
4. Gendelman O, Manevitch LI, Vakakis AF, M’Closkey R (2001) Energy pumping in nonlinear mechanical oscillators: part i dynamics of the underlying hamiltonian systems. *J Appl Mech* 68(1):34
5. Hurel G, Ture Savadkoohi A, Lamarque CH (2019) Nonlinear vibratory energy exchanges between a two degrees-of freedom pendulum and a nonlinear absorber. *J Eng Mech* 145(8):04019058
6. Hurel G, Ture Savadkoohi A, Lamarque CH (2019) Passive control of a two degrees-of-freedom pendulum by a non-smooth absorber. *Nonlinear Dyn* 98(4):3025–3036
7. Hurel G, Ture Savadkoohi A, Lamarque CH (2021) Nonlinear passive control of a pendulum submitted to base excitations. *Acta Mech* 232:1583–1604
8. Hurel G, Ture Savadkoohi A, Lamarque CH (2021) Design of a nonlinear absorber for a two degrees of freedom pendulum and experimental validation. *Struct Control Health Monit*, 2021; 28(11):e2814. <https://doi.org/10.1002/stc.2814>
9. Manevitch LI (2001) The description of localized normal modes in a chain of nonlinear coupled oscillators using complex variables. *Nonlinear Dyn* 25(1):95–109. <https://doi.org/10.1023/A:1012994430793>
10. Nayfeh AH, Mook DT (1995) *Nonlinear oscillations*. Wiley classics library New York: Wiley classics library ed. OCLC:257285431
11. Starosvetsky Y, Gendelman O (2008) Strongly modulated response in forced 2DOF oscillatory system with essential mass and potential asymmetry. *Physica D* 237(13):1719–1733

Hybrid Simulation for Seismic Isolation Effectiveness Assessment of HDR Bearings at Low Temperature



Yuqing Tan, Ji Dang, Akira Igarashi, Takehiko Himeno, Yuki Hamada, and Yoshifumi Uno

Abstract Although the detrimental effects of the low temperature condition on the seismic performance of High Damping Rubber (HDR) bearings are known by the past studies, influence on the dynamic response of structural systems with HDR bearing application and evaluation of consequent seismic performance reduction are yet to be explored. In this research, hybrid simulation for HDR bearings' seismic isolation effectiveness assessment in cold regions was conducted. The testing equipment for elastomeric bearing specimens was modified to enable low-temperature shear loading test under axial load. Shear modulus variation of HDR at different ambient temperatures is shown to diminish as the cyclic loading to HDR bearing progresses, presumably due to the self-heating effect caused by the energy dissipation, as demonstrated by preliminary cyclic loading tests. The effects of low ambient temperature on the dynamic response of the isolated bridge are observed in terms of the increased maximum shear strain of the HDR bearing, amplified maximum load acting on the bridge piers during the seismic excitation, and the consequent increase of pier top displacement.

Keywords Temperature effects · Hybrid simulation · Low temperature · High damping rubber bearing · Self-heating

Y. Tan (✉)

Department of Urban Management, Kyoto University, Kyoto, Japan
e-mail: tan.yuqing.67x@st.kyoto-u.ac.jp

J. Dang

Saitama University, Saitama, Japan

A. Igarashi

Kyoto University, Kyoto, Japan

T. Himeno

Kawakin Core-Tech Co.Ltd, Saitama, Japan

Y. Hamada

Kawakin Core-Tech Co.Ltd, Ibaraki, Japan

Y. Uno

Office U-Tech, Osaka, Japan

1 Introduction

It is known that the mechanical characteristics of High Damping Rubber (HDR) bearing are severely affected by the temperature condition, and the restoring force of the HDR bearing tends to increase as the temperature decreases. On the other hand, stiffness of HDR reduces due to the temperature rise caused by self-heating of the rubber material under cyclic deformation, and this stiffness reduction will further affect the self-heating of the rubber material. As a result, HDR bearing exhibits complicated behavior involving thermo-mechanical interaction.

Okui et al. [1] found that the mechanical behavior of the HDR bearing is governed by the inner temperature of the bearing rather than the ambient temperature. Takaoka et al. [2] investigated the effects of increased temperature on the mechanical behavior of rubber bearings under large cyclic lateral loading. Cardone et al. [3] conducted cyclic loading test to investigate the mechanical properties of elastomeric isolators at seven different air temperatures ranging from 40 °C to −20 °C. These previous studies focused on the hysteretic shear strain—stress relationship of HDR bearing under cyclic loading conditions. Since the earthquake ground motion is different from the cyclic loading in which the shear lateral amplitude is progressively increased or constant, experimental data of the HDR bearing under a more realistic loading condition that reflects the seismic response of isolated bridges under low ambient temperature is of great concern, assuming the implementation of HDR bearings to bridges in earthquake prone cold regions. For this purpose, hybrid simulation is considered to be an effective method to obtain more trustworthy dynamic response of the HDR bearings implemented to an isolated bridge subjected to earthquake ground motion.

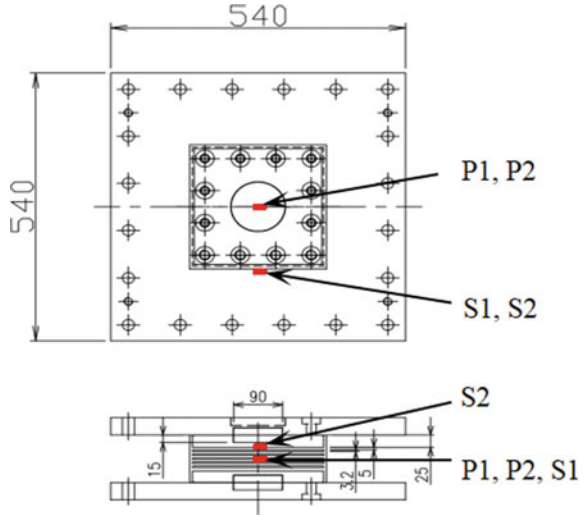
In this study, quasi-static loading tests and hybrid simulation of HDR bearing specimens at room and low ambient temperatures are carried out to investigate the temperature effect on the seismic response of the HDR bearings used in isolated bridges.

2 Test Setup

2.1 Test Specimen

A 1/6-scaled HDR bearing was used as the test specimen in this study. The effective dimensions of the bearing are 240 × 240 mm, and the rubber layer is 5 mm, resulting in a total rubber layer thickness of 30 mm. Shear modulus of the high damping rubber material is 1.2 N/mm². There were four thermocouples used to measure the bearing temperature: two within the specimen in the central section (P1 and P2), and the other two were on the outside surface of the specimen at 1/2 height (S1), and 3/4 height (S2). The HDR bearing specimen and the layout of thermocouples in the plan and elevation views are shown in Fig. 1.

Fig. 1 HDR bearing specimen and layout of thermocouples



2.2 Test Apparatus

A 200tf hydraulic loading system for elastomeric bearings was used in the test, as shown in Fig. 2. The capacity of the loading system is: for the horizontal shear loading, maximum force of ± 400 kN, and maximum stroke of ± 200 mm; for the vertical axial loading, maximum force of $-2000/+1000$ kN and maximum stroke of

Fig. 2 200tf loading system



± 150 mm. The horizontal loading was carried out in the displacement control mode at a constant rate of 10 mm/s (it was actually a sine wave loading, as it is difficult to control the speed when the loading direction changes), maintaining a constant axial stress of 6 MPa in the vertical direction.

2.3 Temperature Control

The hydraulic loading system was modified to enable low-temperature shear loading test. The HDR bearing specimen was placed within a chamber made with heat insulating material, and the ambient temperature of the specimen was controlled to be a predetermined temperature by the delivered cold air through the cooling system during the test. The insulating chamber and cooling system are shown in Fig. 3. Three ambient temperature cases (23 °C, 0 °C and -20 °C) of both the cyclic loading and hybrid simulation were conducted. Before starting each of the loading test, the specimen was stored in the chamber and cold air was provided into the chamber for at least one day until the desired temperature of specimen was reached.

Two insulation plates were installed on the upper and lower surfaces of specimen to prevent the energy loss from the HDR bearing specimen to the loading apparatus, as shown in Fig. 4. However, there was a small amount of energy loss from the specimen to the loading apparatus through the shear key which was installed at the center of upper insulation plate to transmit the shear force to the HDR bearing specimen.

3 Quasi-Static Loading

The shear strain amplitudes in the cyclic shear loading tests were 50, 100, 150, 200 and 250%, in a sequence from the smallest to the largest strain amplitudes, and 5 cycles were repeated for each strain amplitude. The shear strain–stress relationship



Fig. 3 Insulating chamber (left) and cooling system (right)



Fig. 4 Insulation plate (on the upper surface of specimen)

of HDR bearing at different ambient temperatures is shown in Fig. 5. It is observed that the loops at higher strain amplitudes and lower ambient temperatures show larger dissipation and higher stiffness. In addition, the stiffness decreases with increasing

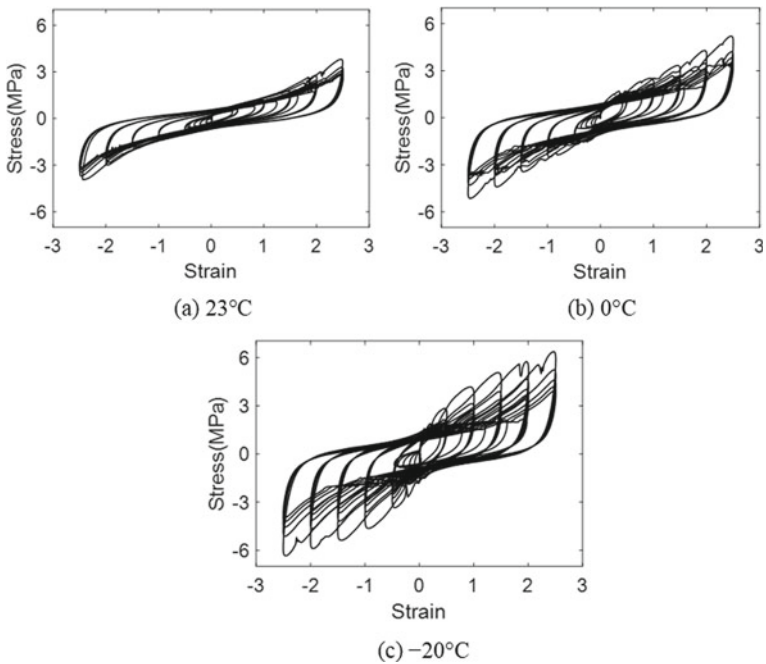


Fig. 5 Shear strain—stress relationship of HDR bearing at different ambient temperatures

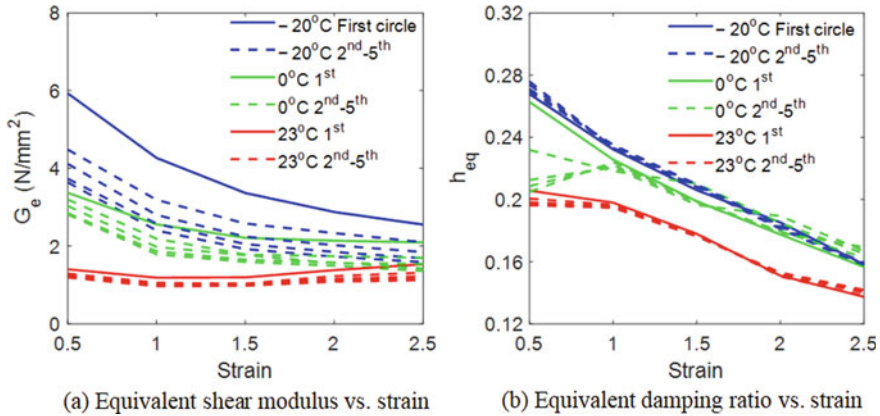


Fig. 6 Results of cyclic loading test

cycle numbers due to the self-heating and drops sharply after the first cycle at each strain amplitude due to the Mullins effect.

The plot of the equivalent shear modulus and the equivalent damping ratio of the HDR bearing against strain amplitude for the five cycles at three different ambient temperatures is shown in Fig. 6. It can be observed that both the equivalent shear modulus and the equivalent damping ratio decrease at higher ambient temperatures and larger strain levels, and the equivalent shear modulus variation due to different ambient temperatures diminishes as the shear strain increases, presumably due to the self-heating effect caused by energy dissipation. The difference of the equivalent shear modulus between the two adjacent cycles decreases at larger cyclic numbers, and consequently the stiffness of HDR decreases by the self-heating of the rubber material. It can also be found that the equivalent damping ratio is less affected by the self-heating of HDR bearing as the equivalent damping ratio is almost identical for different cycles at each ambient temperature.

4 Hybrid Simulation

4.1 Hybrid Simulation Description

The hybrid simulation was conducted on a hypothetical 3-span continuous bridge isolated with HDR bearings, numerically modeled as a simplified 2-DOF system shown in Fig. 7.

There were two HDR bearings installed on the top of each pier, with m_1 and m_2 represent the mass of super-structure and that of the pier, respectively, and the springs k_1 and k_2 represent the stiffness of the rubber bearing and pier, respectively. All the four piers were considered to be linear-elastic and behave identically in the

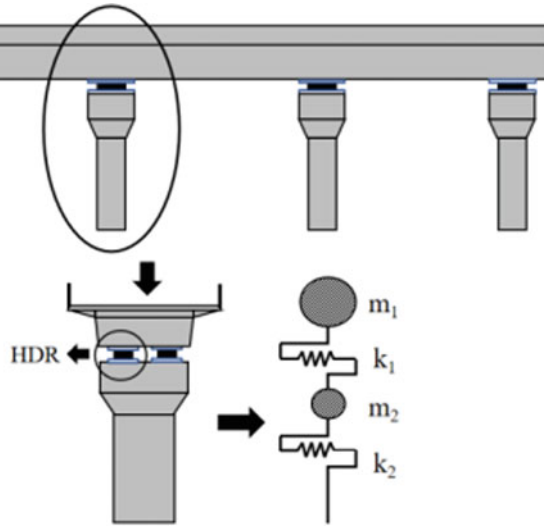


Fig. 7 Assumed bridge model

longitudinal direction. The natural period of the hypothetical isolated bridge model is assumed to be 1.498 s, and the characteristic values of the reduced 2-DOF model are shown in Table 1.

The hybrid simulation system framework is shown in Fig. 8. The test control PC is used to carry out numerical time integration of the equations of motion and generate displacement command signals for the loading device, and the calculated numerical result is sent to the DSP via the LAN cable as command signal, and this signal is then sent to the loading system controller through the terminal block. The loading system is controlled by another PC, and the servo-hydraulic loading jack generates the load following the command signals sent from the control panel. A date logger is connected to the thermocouples to record the temperature value.

The Newmark’s β method was applied as the step-by-step time integration scheme for the 2-DOF system. A value of 1/6 for coefficient β and a time increment Δt of 0.01 s were used, and the similitude law was applied in hybrid simulation. At each time step, the displacement of HDR bearing was calculated and divided by 6, and this predicted displacement was imposed on the HDR bearing specimen, then the

Table 1 Characteristic values of the reduced 2-DOF model

Mass of super-structure, m_1	10,156 (ton)
Mass of pier, m_2	3385 (ton)
Elastic stiffness of HDR bearing, k_1	376 (KN/mm)
Stiffness of pier, k_2	400 (KN/mm)
Damping ratio, h	0.05
Natural period	1.498 (s)

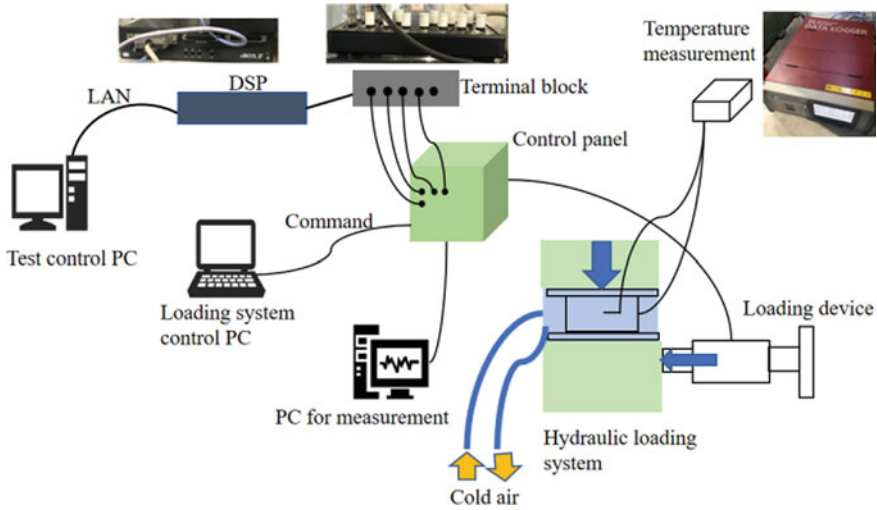


Fig. 8 Hybrid simulation framework

restoring force of the specimen was measured and multiplied by 36 to correct the displacement, velocity and acceleration of the isolated bridge for the next time step integration. These steps were repeated until the end of hybrid simulation.

The ground motion Level 2, Type II, ground type-II accelerogram 1, specified in Design Specification of Highway Bridges (Japan Road Association, 2017) was used as the input accelerogram and is shown in Fig. 9.

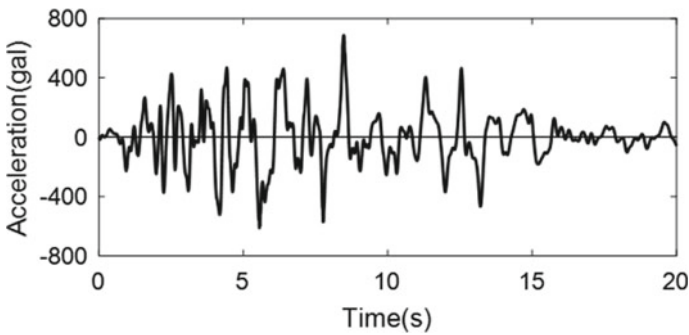


Fig. 9 Earthquake ground motion

4.2 Responses of the HDR Bearing and Pier

The shear strain–stress relationship of HDR bearing obtained by the hybrid simulation is shown in Fig. 10a. It can be observed that the stiffness, shear stress of HDR bearing become higher at lower ambient temperatures. The area of the hysteresis loop significantly increases under lower temperature, indicating increased energy dissipation capacity. The maximum strain becomes larger at lower temperatures in the positive direction while the maximum strain is smaller at lower temperatures in the negative direction.

The maximum absolute shear strain at low ambient temperatures normalized by the maximum absolute shear strain at 23 °C is shown in Fig. 10b. The maximum strain of bearing is reduced by a factor of 0.886 at 0 °C and 0.955 at –20 °C compared with the result at 23 °C, showing a quantitative representation of the reduced effectiveness of the HDR bearing due to low temperature.

The maximum load acting on the bridge piers increases as the restoring force of the HDR bearing increases at low temperature. The pier top displacement obtained from the hybrid simulation at different temperatures is shown in Fig. 11a. It can be

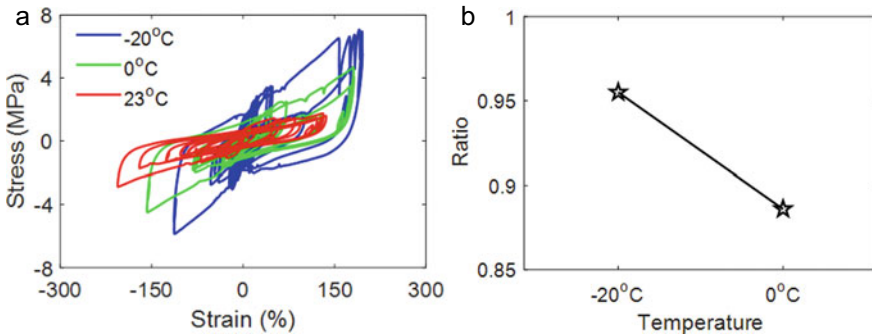


Fig. 10 Hysteresis loops and ratio of maximum shear strain of HDR bearing in hybrid simulation

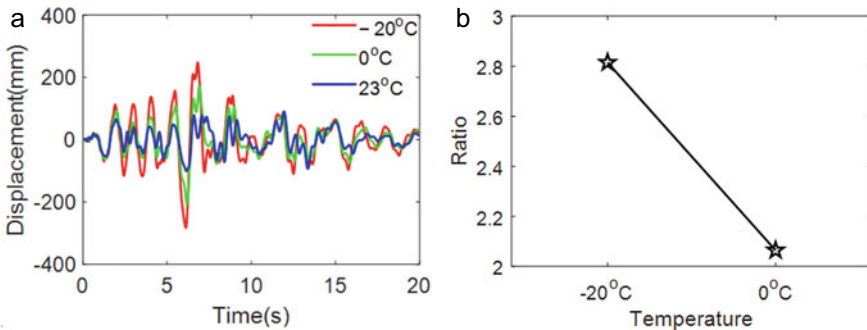


Fig. 11 Pier top displacement obtained from hybrid simulation

observed that the peak pier top displacement increases as the temperature decreases. The maximum absolute pier top displacement at each temperature standardized by the result at 23 °C is shown in Fig. 11b. This result shows that the maximum pier top displacement is increased by a factor of 2.816 at -20 °C and 2.064 at 0 °C compared with the result at 23 °C, implying possible increase of seismic demand due to a low temperature.

4.3 Temperature and Energy Dissipation

The measured temperature time history of the HDR bearing at three different ambient temperatures is shown in Fig. 12, where the loading time domain is marked by solid lines and arrows. The results indicate that the surface temperature (S1 and S2) of the HDR bearing remained almost constant, while the inner temperature (P1 and P2) rose to 27 °C by the end of test for the case of 23 °C and rose to -8 °C for the case of -20 °C; thus, a lower initial ambient temperature corresponds to a larger temperature rise.

In the case of -20 °C, the inner temperature suddenly decreased at approximately 80 s due to a brief interruption regarding safety, as the lateral force was approximately equal to the lateral capacity of the test device, then the hybrid simulation was restarted after a period of time. Except for the case of 0 °C, the inner temperature progressively increased during the loading phase and immediately decreased after the loading was removed. It appears as though the heat was absorbed from the HDR bearing in the case of 0 °C, although the cause of this heat absorption is unclear.

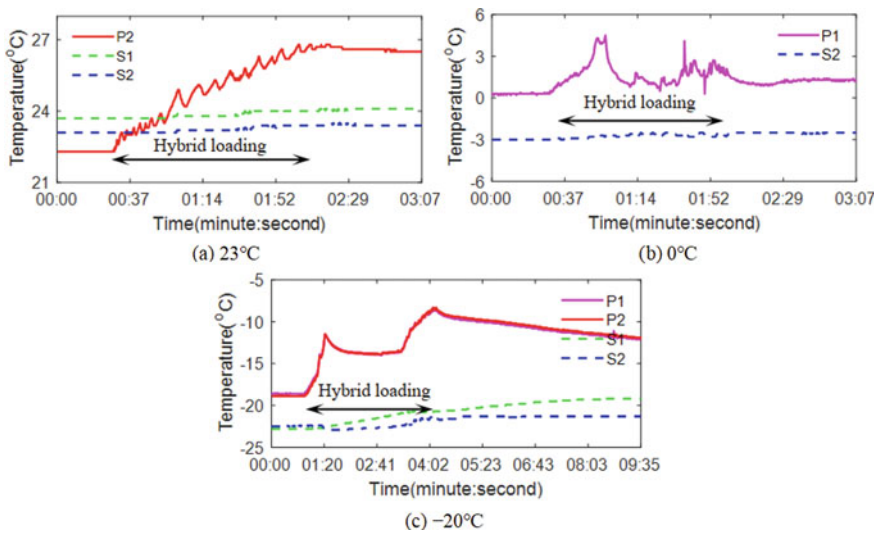
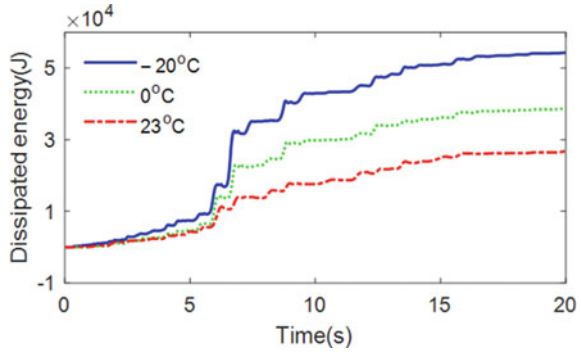


Fig. 12 Temperature time history of HDR bearing at different ambient temperatures

Fig. 13 Dissipated energy of HDR bearing



The dissipated energy at each time step D_n is expressed by Eq. (1), where d is the shear displacement and f is the shear force of the HDR bearing.

$$D_n = \sum_{k=1}^n \frac{(d_k - d_{k-1}) \times (f_k + f_{k-1})}{2} \tag{1}$$

The dissipated energy calculated by Eq. (1) at each ambient temperature is shown in Fig. 13. It is observed that the energy dissipation capacity increases due to the exposure to lower temperatures, which is favorable for earthquake scenarios, as the energy will be absorbed by the HDR bearing and not transferred to the substructure.

5 Conclusions

In this study, cyclic loading test and hybrid simulation were carried out to investigate the seismic performance of the HDR bearings at room and low ambient temperatures. Based on the experimental results, the following main conclusions can be drawn.

In the cyclic loading, the equivalent shear modulus and equivalent damping ratio of bearings increase as the ambient temperature decreases. On the other hand, the equivalent shear modulus variation caused by different temperatures diminishes as the cyclic loading to HDR bearing progresses due to the self-heating effect caused by the energy dissipation.

In the hybrid simulation, it is observed that the maximum strain of bearing is reduced by a factor of 0.886 at 0 °C and the maximum pier top displacement is increased by a factor of 2.816 at -20 °C compared with those at room temperature 23 °C. This result suggests possible decrease of seismic performance of the HDR bearings at low temperature.

References

1. Okui Y, Onoue Y, Sato T, Imai T (2017) Temperature dependence of mechanical behavior of high damping rubber bearings considering self-heating. *J Jpn Soc Civil Eng* 73(1):165–173 (in Japanese)
2. Takaoka E, Takenaka Y, Kondo A, Hikita M, Kitamura H (2008) Heat-mechanics interaction behavior of laminated rubber bearings under large and cyclic lateral deformation. In: *Proceedings of the 14th conference on earthquake engineering*. Beijing, China
3. Cardone D, Gesualdi G, Nigro D (2011) Effects of air temperature on the cyclic behavior of elastomeric seismic isolators. *Bull Earthq Eng* 9(4):1227–1255

A Thermo-Mechanical Coupled Model of Hysteresis Behavior of HDR Bearings



Yuqing Tan, Ji Dang, Akira Igarashi, Takehiko Himeno, and Yuki Hamada

Abstract It has been known that the hysteretic behavior of High Damping Rubber (HDR) bearings is significantly affected by low ambient temperature, while the restoring force gradually reduces under repeated cyclic loading due to self-heating of the rubber material. For seismic response simulation of isolated bridges in cold regions for earthquake events occurring in winter, a nonlinear hysteresis model of HDR bearing with consideration of the thermo-mechanical coupling is necessary for realistic seismic safety assessment of the bridge isolated with HDR bearings. In this study, a thermo-mechanical coupled hysteretic restoring force model of HDR bearing is developed based on the bilinear model. The model is combined with a procedure to estimate the instantaneous inner temperature of the bearing using the information of the hysteretic energy dissipation and heat conduction/radiation, and the mechanical properties of the bearing are updated according to the inner temperature information. The model parameters are identified from quasi-static loading tests of HDR bearing specimens under various ambient temperatures, and the validity of the developed model is discussed based on a comparison of the result of numerical dynamic simulation of a bridge model using HDR bearings subjected to design ground motion with the experimental result obtained by hybrid simulation of the same bridge model using a test system that allows shear loading of HDR bearings under low ambient temperatures.

Y. Tan (✉)

Department of Urban Management, Kyoto University, Kyoto, Japan

e-mail: tan.yuqing.67x@st.kyoto-u.ac.jp

J. Dang

Saitama University, Saitama, Japan

A. Igarashi

Kyoto University, Kyoto, Japan

T. Himeno

Kawakin Core-Tech Co., Ltd., Saitama, Japan

Y. Hamada

Kawakin Core-Tech Co., Ltd., Ibaraki, Japan

Keywords High damping rubber bearing · Restoring force model · Temperature effect · Self-heating · Hybrid simulation

1 Introduction

The shear strain—stress hysteresis behavior of High Damping Rubber (HDR) bearing is highly dependent on the temperature. Stiffness of HDR is increased as the temperature decreases, and self-heating of HDR caused by energy dissipation will lead to reduction of stiffness, as shown in the experimental study by Okui et al. [1]. This heat-mechanical interaction phenomenon is of great concern in modeling of the hysteretic behavior of the HDR bearing. Therefore, for accurate prediction of the seismic performance of isolated bridges with HDR bearing application at low temperature, it is of great significance to develop a thermo-mechanical coupled hysteretic model of HDR bearings.

A few temperature-dependent analytical models for HDR bearings have been proposed in the past researches. For example, Nguyen et al. [2] improved a rheology model to describe the rate-dependent hysteresis behavior for HDR bearings at different ambient temperatures. Hwang et al. [3] improved the fractional derivative Kelvin model and the beginning ambient temperature was considered in the model. Kikuchi et al. [4] developed a non-linear model for HDR bearings including the thermo-mechanical coupled effect under long-period, long-duration ground motions, and a finite volume method was used in the thermal conductivity analysis.

However, only the ambient temperature was considered in most of the temperature-dependent models, while incorporating the self-heating effect in some models makes the calculation of the inner temperature too complicated, which may reduce the practicality in the seismic response simulation of the isolated structures. As an alternative approach, a simple model to describe the thermo-mechanical interaction behavior of HDR bearings is developed in this study.

The thermo-mechanical coupled restoring force model of HDR bearings developed in this study is based on the simple bilinear model, and a formula to calculate the inner temperature of HDR adapted from the method proposed by Okui et al. [1]. Furthermore, accuracy of the developed model is discussed according to the comparison between the result of the seismic response analysis of an isolated bridge model and the experimental result of hybrid simulation using controlled temperature environment.

2 Inner Temperature of HDR Bearing

2.1 Inner Temperature Evaluation

Okui et al. [1] proposed a simple formula to estimate the inner temperature of HDR bearing assuming that the temperature is uniformly distributed within the whole volume of rubber material.

$$\dot{T} = \dot{E}\lambda \quad (1)$$

where $T(t)$ is the inner temperature of the HDR bearing at time t , and the dot symbol denotes the time derivative. On the other hand, the dissipated energy $E(t)$ can be calculated in a manner such that the increase of the dissipated energy per cycle is equal to the area of the hysteresis curve under cyclic loading.

$$E(t) = \int_0^t F(\tau)\dot{\delta}(\tau)d\tau \quad (2)$$

where $F(t)$ and $\delta(t)$ are the restoring force and shear displacement of the bearing in the cyclic reversals at time t , respectively. The constant λ is defined by

$$\lambda = \frac{1}{m_r C_{pr} + m_s C_{ps}} \quad (3)$$

in which m_r and m_s are the mass of rubber layers and steel layers in the bearing, respectively, C_{pr} and C_{ps} are the specific heat capacity of rubber and steel, respectively. In this study, the governing equation for the inner temperature is extended to the form given in Eq. (4) by considering the energy loss due to the heat radiation and conduction from the bearing contact surfaces.

$$\dot{T} = (\dot{E} - \dot{Q})\lambda \quad (4)$$

where $Q(t)$ is the energy loss expressed by

$$\dot{Q} = Ah(T - T_a) \quad (5)$$

where A is the cross sectional area of the shear key, h is the convective heat transfer coefficient given by $W/(m^2 \cdot K)$, in which W , m , K are the convective heat, length and temperature, respectively, and T_a is the ambient temperature. In this formulation, the energy loss is assumed to be equal to the energy of heat transfer from the bearing

Table 1 Material constants

$\rho_r(\text{kg/m}^3)$	$\rho_s(\text{kg/m}^3)$	$C_{pr}(\text{J}/(\text{kg}\cdot\text{K}))$	$C_{ps}(\text{J}/(\text{kg}\cdot\text{K}))$	$A(\text{m}^2)$	$h(\text{W}/(\text{m}^2\cdot\text{K}))$	$\lambda(\text{K}/\text{J})$
1146	7740	1732	432	0.0064	300	1.536e-4

to outside through the shear key at the temperature controlled in the test [5]. In this study, the T_a is set to be either 23 °C, 0 °C or −20 °C. The material constants used for the analysis are presented in Table 1, ρ_r and ρ_s are the density of rubber and steel, respectively.

2.2 Comparison with Temperature Results in Hybrid Simulation

The numerical inner temperature calculated by Eqs. (1) and (4) is compared with the experimental temperature measured by thermocouples installed in the central section of HDR bearing in hybrid simulation at each ambient temperature case, as shown in Fig. 1. All the ambient temperature cases show a similar tendency between the numerical and measured inner temperature except for the case of 0 °C, the heat seemed to be absorbed from the HDR bearing in the case of 0 °C and the reason of this heat absorption is unknown. The difference between the numerical and experimental temperature is considered to be caused by the nonuniform distribution of temperature over the volume of HDR bearing, as the inner temperature is assumed to be uniformly distributed within the volume of rubber material in Eqs. (1) and (4). Furthermore, the inner temperature calculated by Eqs. (1) and (4) is almost consistent, indicating that the area A is small due to the heat insulation measures at each controlled ambient temperature case in hybrid simulation.

3 Thermo-Mechanical Coupled Bilinear Model

The bilinear model, which is a non-linear hysteretic restoring force model for the elastomeric bearings, can be characterized by three parameters: characteristic strength (force intersect at zero displacement) q , the elastic stiffness K_1 , and the post-yield stiffness ratio α , the ratio of the post-yield stiffness K_2 to K_1 .

The restoring force consists of the elastic restoring force F_e and the plastic force F_p , as expressed by

$$F = F_e + F_p \quad (6)$$

F_e and F_p are expressed by Eqs. (7) and (8), respectively, where $\Delta\delta$ is the shear displacement increment of HDR bearing at each time step increment.

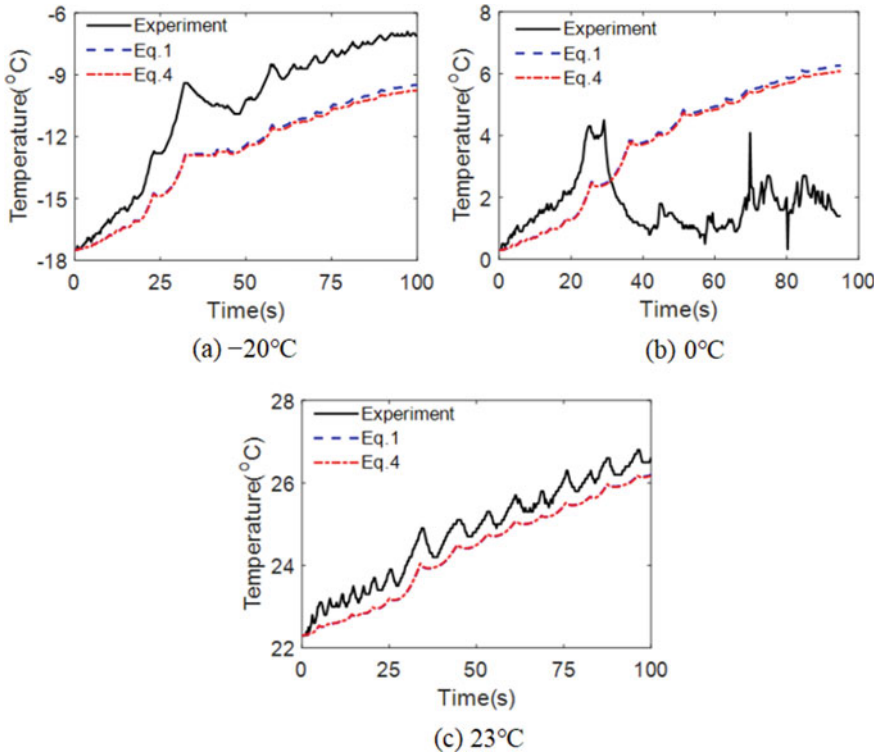


Fig. 1 Comparison between experimental and numerical inner temperature of HDR bearing in hybrid simulation

$$F_e = \alpha K_1 \delta \tag{7}$$

$$F_p = (1 - \alpha) K_1 \Delta \delta + F_p \tag{8}$$

The upper and lower bound values of F_p are determined by Eq. (9), F_p is $+q$ or $-q$ when the absolute value of F_p exceeds q .

$$|F_p| \leq q \tag{9}$$

q is defined by Eq. (10), where δ_0 is the yield displacement.

$$q = (1 - \alpha) K_1 \delta_0 \tag{10}$$

In this study, the characteristic strength q and elastic stiffness K_1 of the bilinear model are updated by the inner temperature T calculated by Eq. (4) with the following equations:

$$q = q_0 e^{c \times \frac{T-23}{100}} \tag{11}$$

$$K_1 = K_{1,0} e^{d \times \frac{T-23}{100}} \tag{12}$$

where q_0 and $K_{1,0}$ are the initial characteristic strength and elastic stiffness, respectively, c and d are constants to be identified from the cyclic loading test. Hereafter, the thermo-mechanical coupled bilinear model expressed by Eqs. (11) and (12) is referred to as the TMC bilinear model. The thermo-mechanical coupled analysis is conducted in the following procedure: (1) the characteristic strength and elastic stiffness are updated by the inner temperature T calculated at the previous time step. (2) seismic response analysis is performed with the updated characteristic strength and elastic stiffness, and the increase of dissipated energy ΔE can be obtained by the displacement and force increment of the HDR bearing after the seismic response analysis. (3) ΔE is used to calculate the inner temperature T by Eq. (4) for the next time step. This procedure is repeated until the end of the analysis.

The variation of characteristic strength and elastic stiffness due to low temperature according to Eqs. (11) and (12) is shown in Fig. 2. The characteristic strength and elastic stiffness increase as the inner temperature of HDR bearing decreases, and the variation rate is higher at lower inner temperature.

The TMC bilinear model at different inner temperatures is shown in Fig. 3, and the area of hysteresis loop is larger at lower inner temperature of the HDR bearing.

Fig. 2 Variation of characteristic strength and elastic stiffness due to low temperature

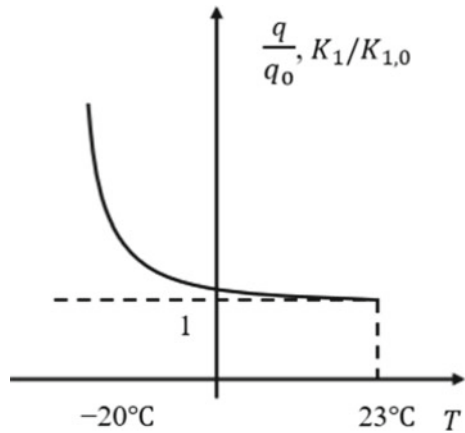
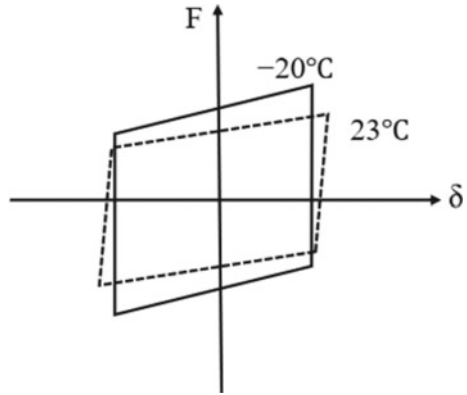


Fig. 3 TMC bilinear model at different inner temperatures



4 Parameter Identification by Cyclic Loading Test Data

The cyclic loading tests were carried out to investigate the hysteresis behavior of the HDR bearing at room and low ambient temperatures of 23 °C, 0 °C and -20 °C, and the 1/6-scaled HDR bearing specimen with effective dimensions of 240 × 240 mm, total rubber layer thickness of 30 mm, and shear modulus of the HDR material of 1.2 N/mm² was used, as shown in Fig. 4. The shear strain were from the smallest 50% to the highest 250%, and 5 cycles were conducted at each shear strain level. The detailed description of the test can be found in [5].

Fig. 4 HDR bearing specimen

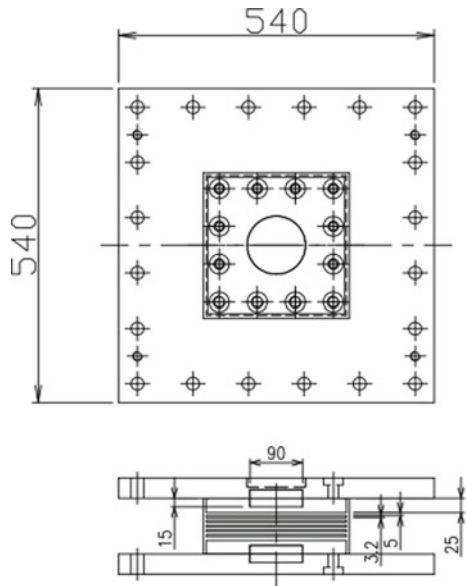




Fig. 5 200tf loading system (left) and cooling system (right)

Table 2 Identified parameters

α	K_1 (KN/mm)	q	c	d
0.322	4.321	31.208	-2.457	-1.132

The 200tf hydraulic loading system and the cooling system are shown in Fig. 5. The displacement controlled loading with a constant rate of 10 mm/s was conducted in the horizontal direction, and an axial stress of 6 MPa was maintained in the vertical direction. During the test, the HDR bearing was wrapped in a chamber made with heat insulating material, and the ambient temperature of the HDR bearing was set to be a predetermined value by delivering cold air through the cooling system.

The model parameters identified from the cyclic loading test results are shown in Table 2.

The hysteresis loops of the HDR bearing obtained from the cyclic loading tests and simulated results using the TMC bilinear model and bilinear model are shown in Fig. 6. The bilinear model and TMC bilinear model are shown to be only capable of capturing the feature of steady-state response at low-to-moderate shear strain levels. Although the TMC bilinear model shows to be superior to the bilinear model in expressing the hardening behavior of the HDR bearing, the hardening phenomenon observed in the experimental results in lower temperature and higher strain level are not well reproduced by the TMC bilinear model. Hence, further improvement of the thermo-mechanical coupled model is to be pursued in the future study.

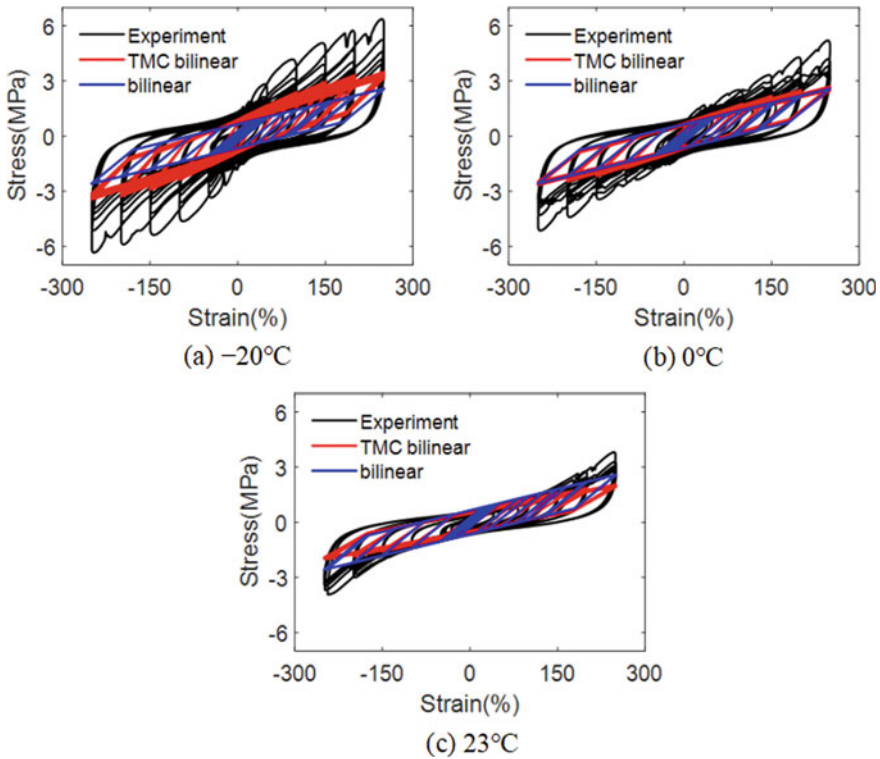


Fig. 6 Hysteresis loops of HDR bearing computed by models and comparison with cyclic loading test result

5 Comparison with Hybrid Simulation Test Results and Discussion

The hybrid simulation was carried out to evaluate the seismic response of a HDR bearing isolated bridge at room and low ambient temperatures of 23 °C, 0 °C and -20 °C [5]. The hypothesized bridge and the simplified two-degree-of-freedom system model are shown in Fig. 7. The natural period of the isolated bridge is 1.498 s, and the design ground motion of Level 2, Type II, ground type-II accelerogram 1, specified in Design Specification of Highway Bridges (Japan Road Association, 2017) was input as the seismic wave.

The hysteresis loops of the HDR bearing obtained from the hybrid simulation, simulated results using the TMC bilinear model and bilinear model are shown in Fig. 8. It can be seen that the hysteresis loops computed by the bilinear model are identical for all ambient temperatures, as the temperature effect is not considered in the conventional bilinear model. In contrast, the TMC bilinear model captures the stiffening occurring at lower temperatures, especially at -20 °C. However, a

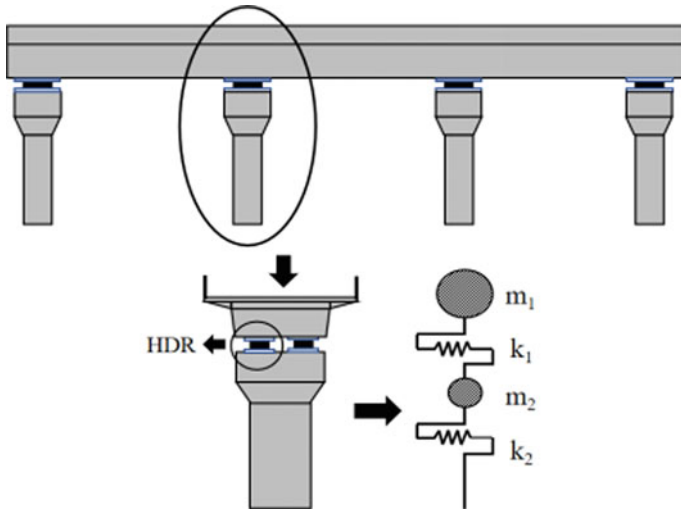


Fig. 7 Hypothetical isolated bridge model

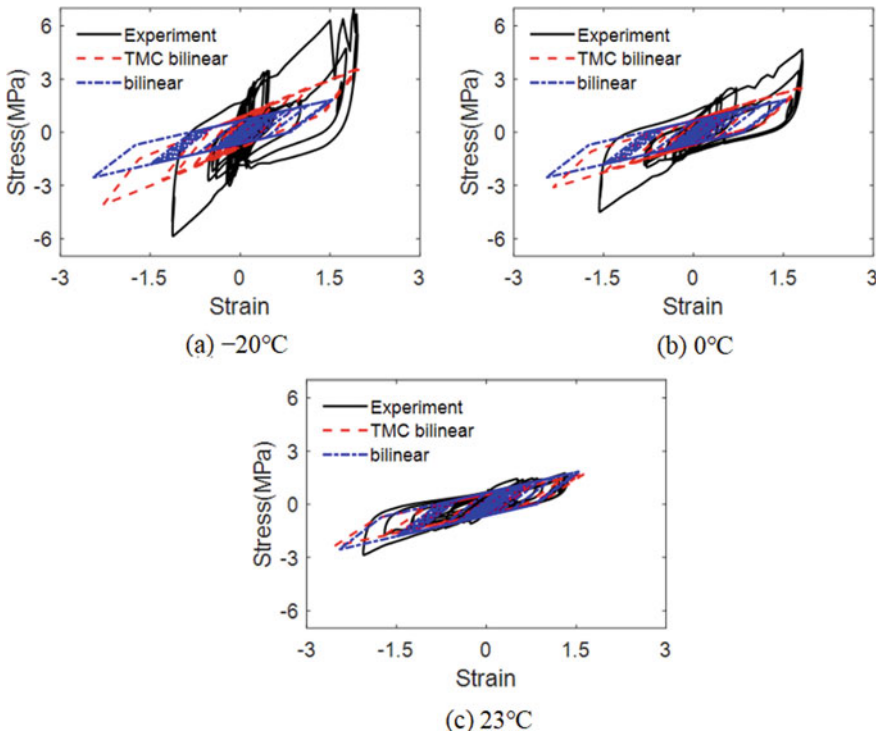


Fig. 8 Hysteresis loops of HDR bearing obtained by the restoring force models and by hybrid simulation

substantial difference between the test result and analytical result using the TMC bilinear model at lower temperatures indicates that the relevance of the temperature dependence of the HDR bearing expressed by the TMC bilinear model is limited.

The comparison between hybrid simulation and numerical results by the TMC bilinear model and bilinear model in terms of the shear strain of the HDR bearing and pier top displacement at different temperatures is also shown in Fig. 9 and Fig. 10, respectively. A close agreement between the hybrid simulation and the analytical results can be seen at 23 °C, while the difference is noticeable for the lower temperature, especially the maximum shear strain of HDR bearing and pier top displacement at -20 °C. Hence, the maximum pier top displacement can be underestimated by the TMC bilinear model and bilinear model at lower temperatures.

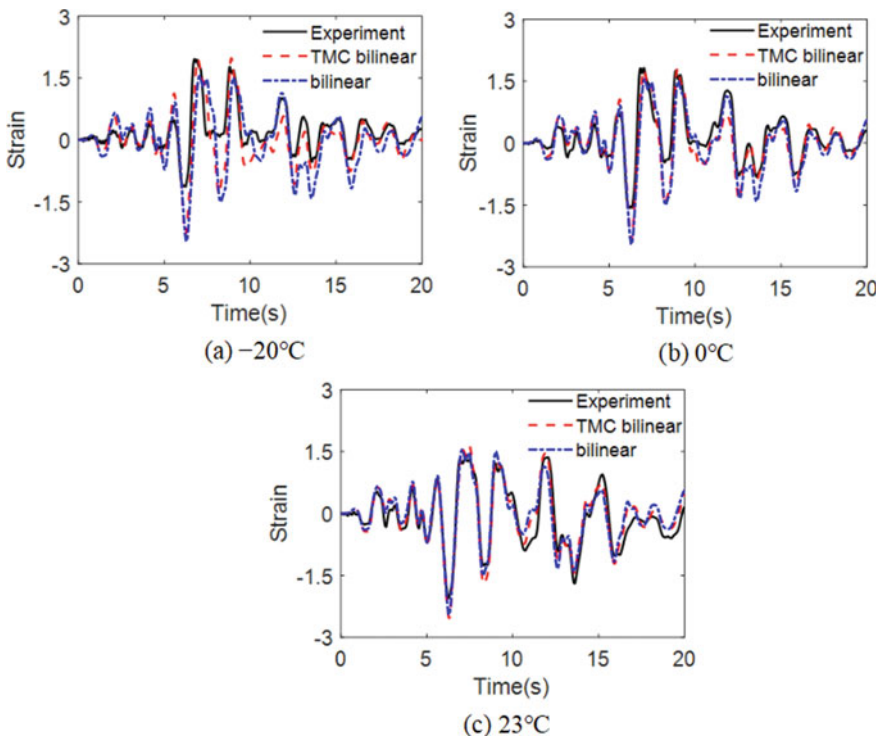


Fig. 9 Shear strain of HDR bearing obtained by the numerical models and by hybrid simulation

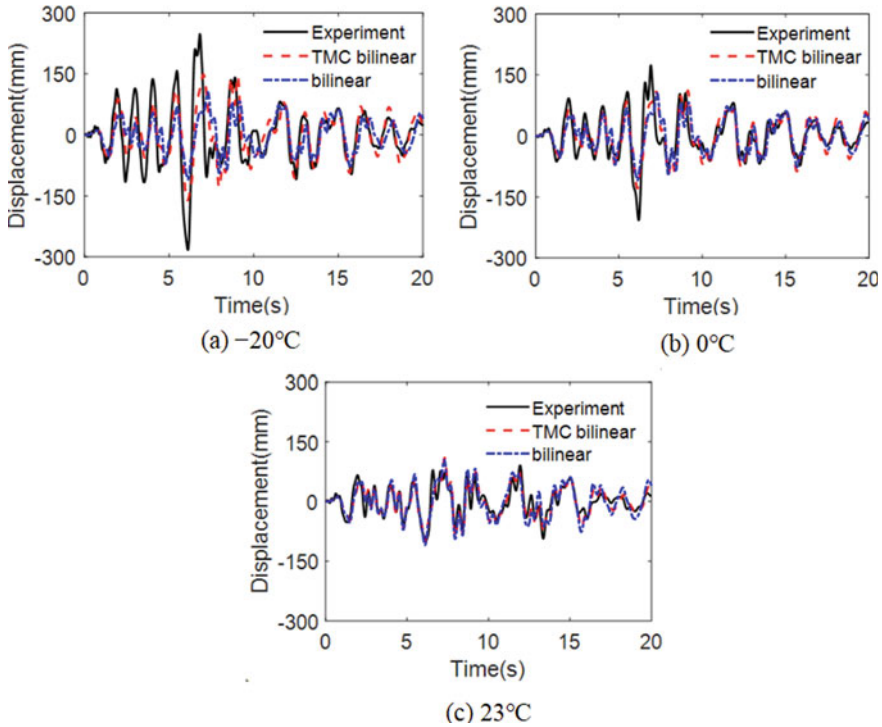


Fig. 10 Pier top displacement obtained by the numerical models and by hybrid simulation

6 Conclusions

In this study, a thermo-mechanical coupled analytical model, referred to as the TMC bilinear model, to express the temperature dependence of HDR bearing at different ambient temperatures is developed. In TMC bilinear model, the characteristic strength and elastic stiffness of bearing are updated based on the instantaneous inner temperature predicted by the information of the hysteretic energy dissipation and heat conduction/radiation. It is found that the accuracy of seismic response analysis of bearing is partially improved by the use of the TMC bilinear model compared with the conventional bilinear model. However, the maximum pier top displacement can be underestimated by the TMC bilinear model at lower temperatures. Further refinement of the thermo-mechanical coupled analytical model is required for improved accuracy of seismic response assessment of isolated bridges.

References

1. Okui Y, Onoue Y, Sato T, Imai T (2017) Temperature dependence of mechanical behavior of high damping rubber bearings considering self heating. *J JSCE Ser A1* 73(1):165–173 (In Japanese)
2. Nguyen DA, Dang J, Okui Y, Amin AFMS, Okada S, Imai T (2015) An improved rheology model for the description of the rate-dependent cyclic behavior of high damping rubber bearings. *J Soil Dyn Earthq Eng* 77:416–431
3. Hwang JS, Hsu TY (2001) A fractional derivative model to include effect of ambient temperature on HDR bearings. *J Eng Struct* 23(5):484–490
4. Kikuchi M, Ishii K (2018) Thermal-mechanical coupled behavior of elastomeric isolation bearings under cyclic loadings. In: 15th European conference on earthquake engineering, Thessaloniki, Greece (in print)
5. Tan Y, Dang J, Igarashi A, Himeno T, Hamada Y, Uno Y (2021) Low temperature hybrid simulations for high damping rubber bearings. In: Proceedings of the 23rd symposium on disaster mitigation and resilience of the infrastructures and lifeline systems. JSCE, pp 215–221

Research on Seismic Response of Single-Tower Cable-Stayed Bridge Across Faults



Feng Jiang, Li-Peng Liu, Feng-Chao Jiang, and Jia-Qi Li

Abstract Near-fault ground motions usually produce irrecoverable permanent ground displacements and trigger various near-fault ground motion effects, which are significantly different from general ground motions and far-field motions. And the structure may be seriously damaged as a result. In order to study the influence of this special type of ground motion, the semi-floating system single-tower cable-stayed bridge is used to cross the fault, and the finite element model is established. Then, the seismic behavior of the structure is analyzed based on the ground motion database. Finally, the aseismic design is carried out. The results show that the ground motion velocity pulse has a significant impact on the seismic response of the structure. The main tower of the cable-stayed bridge is more affected by the velocity pulse than the main beam, and the pulse period and the parity of the number of pulses are important factors in the seismic response of the structure. The installation of longitudinal viscous dampers and transverse E-shaped steel dampers can effectively suppress the seismic response of the structure. The research results of this article can provide reference for related research.

Keyword Cross fault · Velocity pulse · Single tower cable-stayed bridge · Structural seismic response analysis

The Port Hueneme earthquake (1957) in the United States [1] made researchers realize for the first time that the near-fault ground motion is characterized by short ground motion duration, high amplitude, and obvious velocity pulses. In the subsequent Kocaeli and Duzce earthquakes (1999) in Turkey, there were earthquake damages such as surface rupture of faults and bridges' progressive collapse [2, 3] which resulted to great economic losses and human casualties. And with the development of society and economy, it is not feasible for bridge structures to completely avoid faults; therefore, it is necessary to study the seismic response of cross-fault bridge structure.

F. Jiang · L.-P. Liu (✉) · F.-C. Jiang · J.-Q. Li
School of Transportation Science and Engineering, Harbin Institute of Technology, Harbin, China
e-mail: 1429705033@qq.com

In recent decades, many scholars have studied the basic characteristics of near-fault ground motion. Hall et al. [4] (1995) pointed that the directional effect is significant in many near-fault ground motion effects. Malhotra's (1999) research [5] has found that the main characteristics of near-fault ground motion is that the directional effect produces strong velocity pulses, which is the reason for the high ratio of the peak ground velocity (PGV) of near-fault ground motions to the peak ground acceleration (PGA). Domestic scholars have focused on the effects of near-fault ground motion on bridge structure in recent years. Shi Yan et al. [6] (2014) adopted the combination of damping tenons and cable limiters for bridge structures to discuss the seismic performance of bridge structures under the action of near-fault pulse-type ground motion with forward directional effect and sliding effect. Wu Wen-peng, Li-Feng et al. [7] (2015) studied the influence of different bearing layout schemes on the displacement of the main girder, the deformation of the bearing and pier under the actions of near-fault ground motion. As a special near-fault ground motion, the cross-fault ground motion is still at the initial stage in China and abroad. Roussis [8], Park [9], Ucak and Mavroeidis [10] have analyzed the seismic response of Bolu1 Bridge and pointed out that the primary cause of the damage of the bridge was that the relative dislocation on both sides of the fault was not fully considered. Hui Ying-xin et al. [11] (2015) used hybrid simulation to synthesize near-fault ground motions and used a continuous beam bridge across a strike-slip fault as the research object, and used non-uniform excitation input to study the effects of variables such as fault rupture location, crossing angle, and pier height on the seismic response of the continuous beam bridge across a strike-slip fault.

At present, there are still some problems in the field of the seismic response of bridge structures across faults, such as the difference in the characteristics of near-fault pulse-type and pulse-free ground motions, the seismic input mode for simulating the fault motion and the influence of pulse on the seismic response of structures. Based on this, this paper will analyze the near-fault ground motion from the structural point of view, simulate the near-fault ground motion input, carry out the seismic reduction design for the single-tower cable-stayed bridge with semi-floating system across faults, and study the effects of pulse ground motion on the structural response.

1 Research on Characteristics of Near-Fault Ground Motion

Considering the characteristics of velocity pulse contained in near-fault ground motion and the forward directional effect, slip effect, hanging wall effects and vertical effects caused by different types of fault motion, it is reasonable to use the pulse parameter PGV/PGA as the basis for determining whether ground motion contains pulse characteristics [12]. And it is very strongly correlated with the maximum seismic response of the structure [13].

Three pulse ground motion records of different fault types are selected by setting ground motion parameter conditions, and the three near-fault seismic waves without velocity pulse in the same seismic event are selected as the comparison for the following research on the effects of velocity pulse on the structure. The parameters of each ground motion are shown in Table 1, and the comparison of the seismic time history velocity curve is shown in Fig. 1.

From Fig. 1, it can be seen that there are obvious sudden changes in the velocity time history curves of near-fault ground motion with velocity pulse characteristics, and the structure may show more unfavorable structural response under continuous

Table 1 The parameters of near-fault ground motions

Earthquake name	Fault type	Earthquake No	Fault distance (km)	Pulse period (s)	PGA (g)	PGV (cm/s)	PGV/PGA (s)
Irpinia	Normal	RSN292	10.84	3.27	0.3205	71.96	0.229
		RSN289	17.64	–	0.1364	18.78	0.141
Northridge	Reverse	RSN1013	5.92	1.62	0.4263	74.84	0.179
		RSN1042	12.51	–	0.2535	30.80	0.124
Landers	Strike Slip	RSN879	2.19	5.12	0.7252	133.4	0.188
		RSN864	11.03	–	0.2840	42.59	0.153

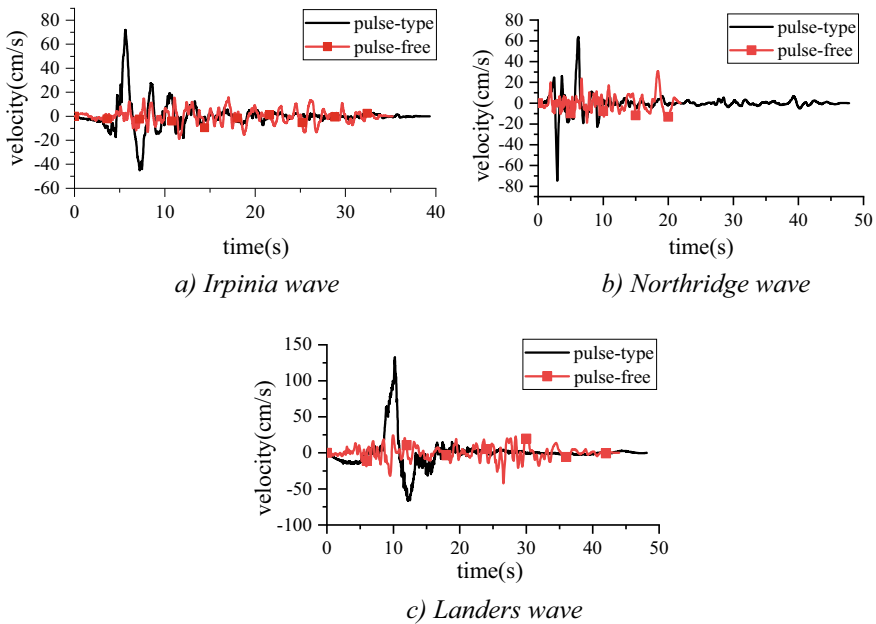


Fig. 1 Time history curves of near-fault seismic wave velocity

unidirectional pulse loading. The period and number of pulses are also completely different in different ground motions. Therefore, the subsequent research needs to carry out relevant structural seismic response analysis.

2 Seismic Response Analysis of Single Tower Cable-Stayed Bridge Across Faults

2.1 Finite Element Model

Based on a crossing fault cable-stayed bridge project, the design load of the main bridge is highway Class I standard, and the two-way six lanes are adopted with the design speed of 80 km/h. The basic seismic intensity in the bridge location area is 8 degrees, and the engineering field category is type II site. The peak design acceleration of seismic level is 0.30 g corresponding to 10% exceedance probability of 50 years. The bridge is a symmetrical floating system cable-stayed bridge without auxiliary piers, and the main bridge adopts 230 m + 230 m two-span single tower steel box girder cable-stayed bridge, as shown in Fig. 2a. The main tower is reinforced concrete structure. The height of the main tower is 151.8 m, and the height of the lower part of the bridge deck is 34 m. The root section size of the main tower is 14 m × 9 m (longitudinal × transverse), as shown in Fig. 2b.

The spine model is used as the calculation model of the cable-stayed bridge. The tower, main girders, cross girders and piers of the cable-stayed bridge are simulated by 3D elastic beam element. The stay cable is simulated by tension-only spar element. In addition, the second phase dead load and 1/2 live load are simulated by centralized mass element. The main bridge is a semi-floating system, the main beams are not restrained in the longitudinal direction and can move freely along the longitudinal

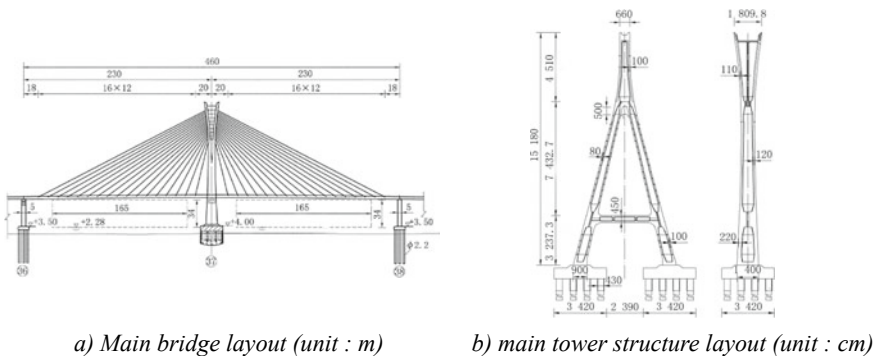


Fig. 2 Main bridge layout and main tower structure layout

direction, coupled with the transverse and vertical degrees of freedom at the connection of the towers, side piers and main girders. The first-order natural frequency of the structure is 0.2178 Hz, and the corresponding period is 4.59 s, which corresponds to the longitudinal drift of the main beam. The second-order natural frequency of the structure is 0.4051 Hz, and the corresponding period is 2.47 s, which corresponds to vertical bending of the main beam and longitudinal bending of the main tower.

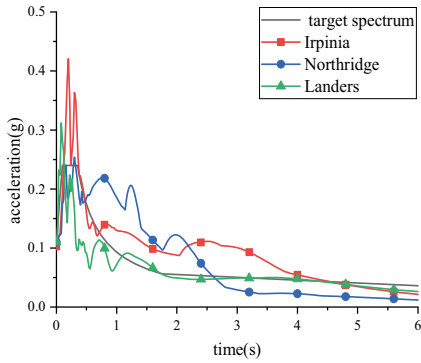
2.2 Effects of Velocity Pulse on the Seismic Response of the Structure

The characteristics of seismogenic faults play a decisive role in earthquake surface rupture [14, 15] and different seismic input methods should be adopted for different fault types. Now the main bridge is all located in the fault footwall and vertical to the fault, according to the motion characteristics of different fault earthquakes, the seismic wave input method for dip-slip fault is a combination of longitudinal + vertical, and that for strike-slip fault is a combination of longitudinal + horizontal. The seismic wave amplitude is 0.11 g at the E1 level, as shown in Fig. 3a. The seismic waves were input by uniform excitation, and the dynamic analysis of the structure was performed to obtain the seismic response of the main tower and the main beam. The average response envelopes of the key sections of the main bridge under pulse-type and pulse-free ground motion are shown in Fig. 3b, c.

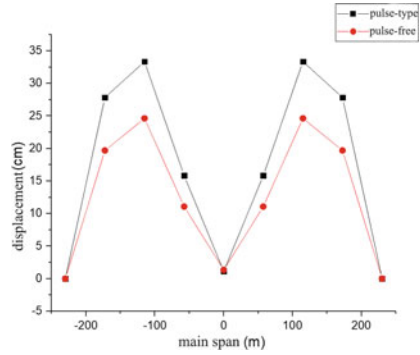
From the analysis results in Fig. 3b, c, it can be concluded that: comparing the displacement response of the main beam under pulse-type and pulse-free ground motion, the maximum displacement response of the main beam due to velocity pulses increased by 36%. Whether it is pulse-type or pulse-free ground motion, the longitudinal displacement of the main tower increases with the increase of the height of the main tower, and the response increases by 2.2 times under the effects of pulse type ground motion, indicating that velocity pulse has a more significant effect on the seismic response of the main tower.

The longitudinal displacement time history curves of the beam end are shown in Fig. 4. The amplitudes of the structural displacement responses under the influence of velocity pulse are all greater than those without pulse, and the following conclusions can be drawn.

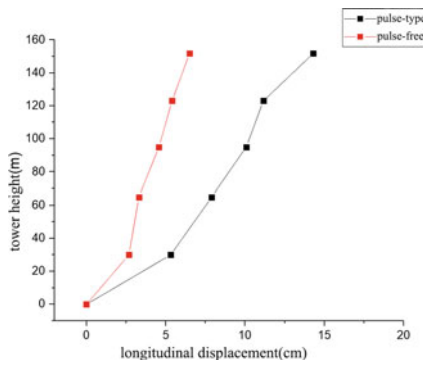
- (1) The maximum longitudinal displacement of beam end caused by Landers ground motion of strike slip fault is significantly larger than that of other two ground motions, and the reason is that the period of the first-order vibration mode (main beam longitudinal drift) is 4.59 s, which is close to the pulse period 5.12 s of Landers seismic wave itself, and the structural response is more significant.
- (2) From Fig. 4, it can be seen that the larger the product of the pulse period and PGV of the near-fault earthquake, the larger the value of its seismic response, i.e., displacement response Landers > Irpinia > Northridge, indicating that the



a) Target spectrum and seismic wave acceleration response spectrum curve



b) Vertical displacement of the main beam



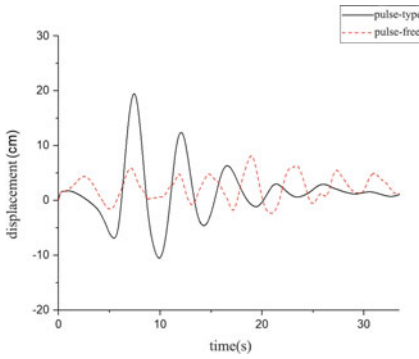
c) Longitudinal displacement of the main tower

Fig. 3 Envelopes of structural seismic response and acceleration response spectrum

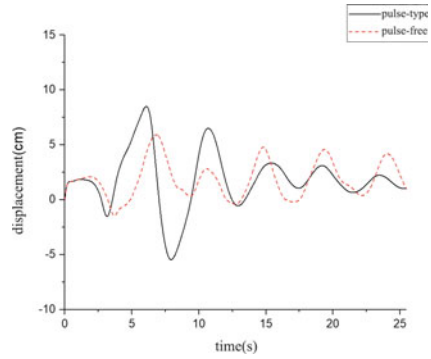
product of the pulse period and PGV can reflect the energy magnitude of the pulse-type ground motion

2.3 Effects of Pulse Period on the Seismic Response of the Structure

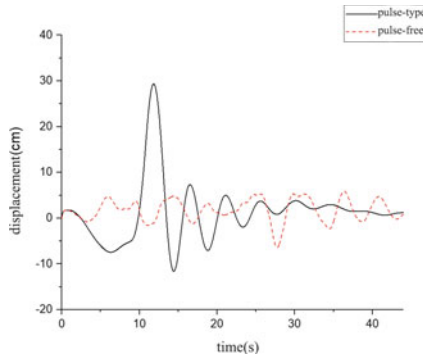
It is known that the pulse period is likely to be an important factor affecting the seismic response of near-fault pulse ground motion to the structure. Therefore, in order to study the effects of near-fault pulsed seismic pulse period on the single-tower cable-stayed bridges, eight seismic waves with different pulse period recorded by different stations in the same earthquake (shown in Table 2) were selected based



a) Time history of the beam end displacement under Irpinia wave



b) Time history of the beam end displacement under Northridge wave



c) Time history of the beam end displacement under Landers wave

Fig. 4 Longitudinal displacement time history curves of beam end under near-fault ground motion

Table 2 Seismic waves at different pulse periods

Earthquake name	Fault type	No	Earthquake No	Fault distance (km)	Pulse period (s)	PGA (g)	PGV (cm/s)	PGV/PGA (s)
Irpinia	Normal	I1	RSN285	8.18	1.713	0.1898	34.71	0.187
		I2	RSN292	10.84	3.27	0.3205	71.96	0.229
Northridge	Reverse	N1	RSN1050	7.01	0.588	0.4158	44.29	0.109
		N2	RSN1086	5.3	2.436	0.8434	129.4	0.157
		N3	RSN983	5.43	3.535	0.5712	76.13	0.136
Landers	Strike slip	L1	RSN879	2.19	5.124	0.7252	133.4	0.188
		L2	RSN900	23.62	7.504	0.2445	51.12	0.213
		L3	RSN838	34.86	9.128	0.1355	25.04	0.189

on PEER seismic database from Irpinia (normal fault), Northridge (reverse fault) and Landers (strike-slip fault) to study the relationship between pulse period and ground motion response. And the peak acceleration is adjusted to 0.11 g. To exclude other influencing factors, only longitudinal uniform excitation input is applied to the structure. The longitudinal displacement time histories of the end of the main bridge under three groups of ground motions with different pulse periods in Table 2 are calculated by dynamic time history analysis, as shown in Fig. 5.

The following conclusions can be drawn from Fig. 5.

- (1) With the change of pulse period of Irpinia and Northridge seismic excitation, the displacement response of the structure under near-fault pulse ground motion increases significantly. The reason for this is that the pulse period is close to

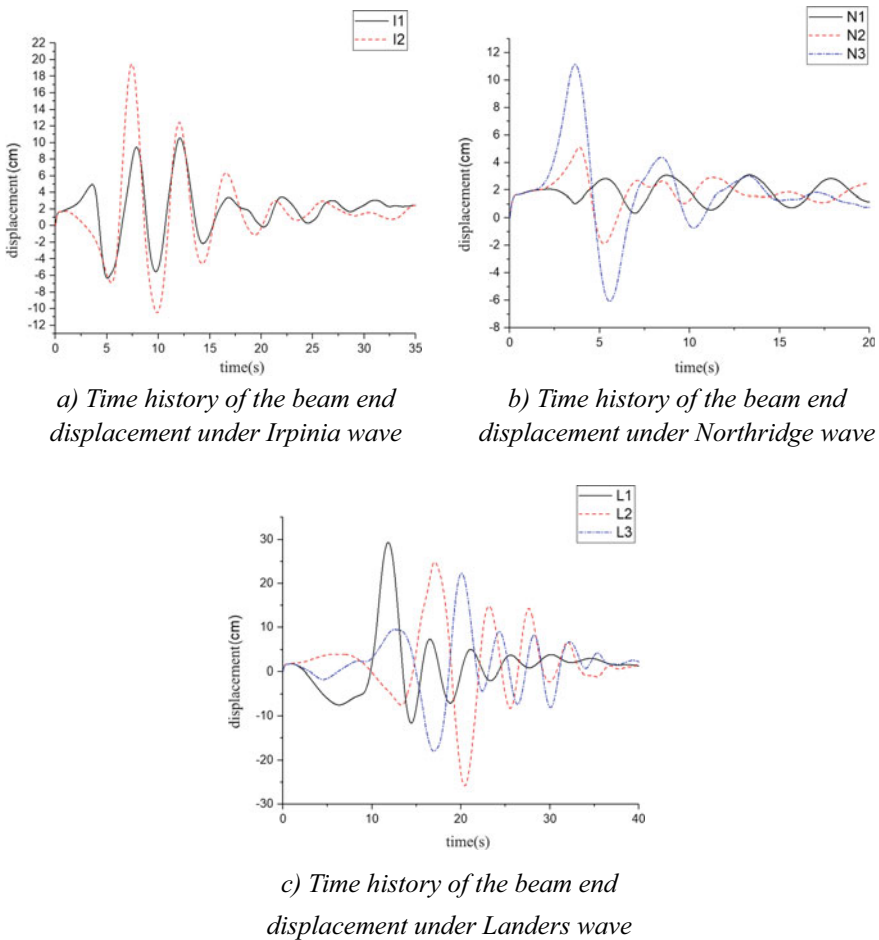


Fig. 5 Longitudinal displacement time history curves of beam end under different pulse periods

the first-order vibration mode period of the structure (longitudinal drift of the main beam), and the longitudinal displacement of the beam end increases significantly.

- (2) With the change of pulse period of Landers (strike-slip fault) seismic wave, the peak values of longitudinal displacement of the main beam decreased by 12% and 13.8% respectively, and the amplitude of the change was significantly reduced compared with the previous two earthquakes. The main reason is that with the pulse period gradually away from the main vibration mode period of the structure, the change of seismic displacement response caused by ground motion is gradually reduced.

2.4 Effects of the Number of Pulses on the Seismic Response of the Structure

Near-fault ground motion effects are different in different regions of the fault, and the components in the vertical direction of the fault may contain multi-directional velocity pulses affected by the directional effect. While the components along the sliding direction of the parallel fault are affected by the slip effect and the ground motion contains one-way velocity pulse. Therefore, to study the effect of velocity pulse number (n) on seismic response of single-tower cable-stayed bridge, the ground motions with $n = 1, 2$ and 3 in 1979 Imperial Valley earthquake are selected according to target spectrum. The original parameters of each ground motion are shown in Table 3. Unified amplitude modulation of velocity pulse peak in finite element analysis is 40 cm/s . Taking the three ground motions in Table 3 as input, the seismic response time histories and envelopes of the main girder and main tower under the ground motions with $n = 1, 2$ and 3 are obtained by using the spatial consistent excitation dynamic time history analysis, as shown in Fig. 6.

The following conclusions can be drawn from Fig. 6: the maximum longitudinal displacement response of the beam end and tower top, the vertical displacement and bending moment response of the main beam when $n = 2$ are significantly greater than those when n is odd, indicating that the parity of the peak number of velocity pulses is the main reason of the seismic response of the main beam and the main tower, rather than the number of pulses. And effect of even pulse peak ground motion on seismic response of main beam is greater than that of main tower.

Table 3 The parameters of ground motions with different number of pulses

Earthquake name	Fault type	Earthquake No	n	PGA (g)	PGV (cm/s)	PGV/PGA (s)
Imperial valley	Strike slip	RSN161	1	0.2195	40.94	0.19
		RSN179	2	0.3704	80.41	0.22
		RSN179	3	0.4843	39.64	0.08

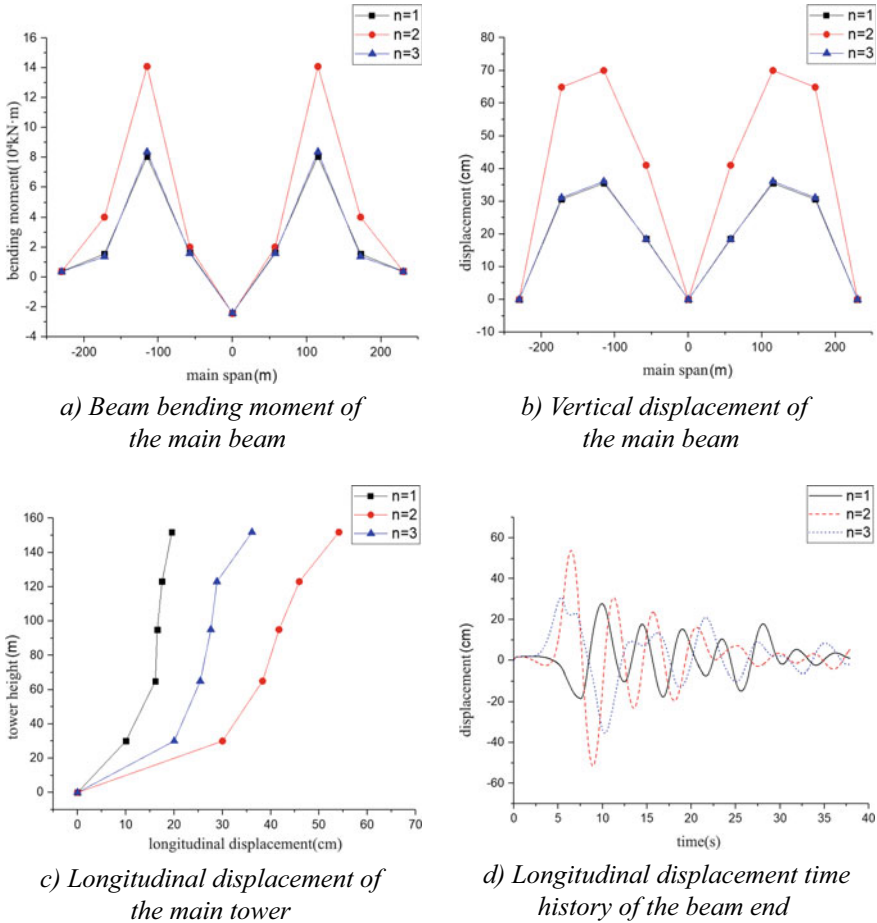


Fig. 6 Seismic response of main bridge under different pulse peak numbers

3 Aseismic Design of Single-Tower Cable-Stayed Bridges Across Faults

The aseismic design is composed of the semi-floating system with dampers. The longitudinal direction reduces the displacement response of the structure by installing viscous dampers to dissipate the seismic energy and achieve the coordination of the seismic displacement and the internal force response. In order to meet the requirements of wind resistance of the structure, the transverse support system is required to provide certain stiffness in the normal use stage and play the role of transverse support, and play the role of dissipation of energy to achieve damping when earthquake occurs. To meet the requirements of seismic and wind resistance of the bridge, E-shaped steel damper is proposed for lateral support. Through trial analysis, a pair

of nonlinear viscous dampers are paralleled between the crossbeam of the bridge tower and the main beam, the damping coefficient C is $5500 \text{ kN(m/s)}^{-0.3}$, and the velocity index α is 0.3. Two E-shaped steel dampers are installed on the main tower and the transverse bridge of the side piers, and their initial stiffness are 3500 and 1250kN/m, respectively.

The model of a single-tower cable-stayed bridge with two types of dampers was established. And taking the Landers ground motion in Sect. 1 as the input, the structural time-history response of the key sections of the main girder and the main tower is analyzed by using the longitudinal + transverse spatial multi-point excitation. The seismic response of bridge components before and after installing longitudinal viscous dampers and transverse E-beam dampers are obtained, as shown in Fig. 7.

From Fig. 7, it can be seen that compared with the floating system without any damping device, the maximum longitudinal displacement of the main beam end of the semi-floating single tower cable-stayed bridge with damping measures is reduced by

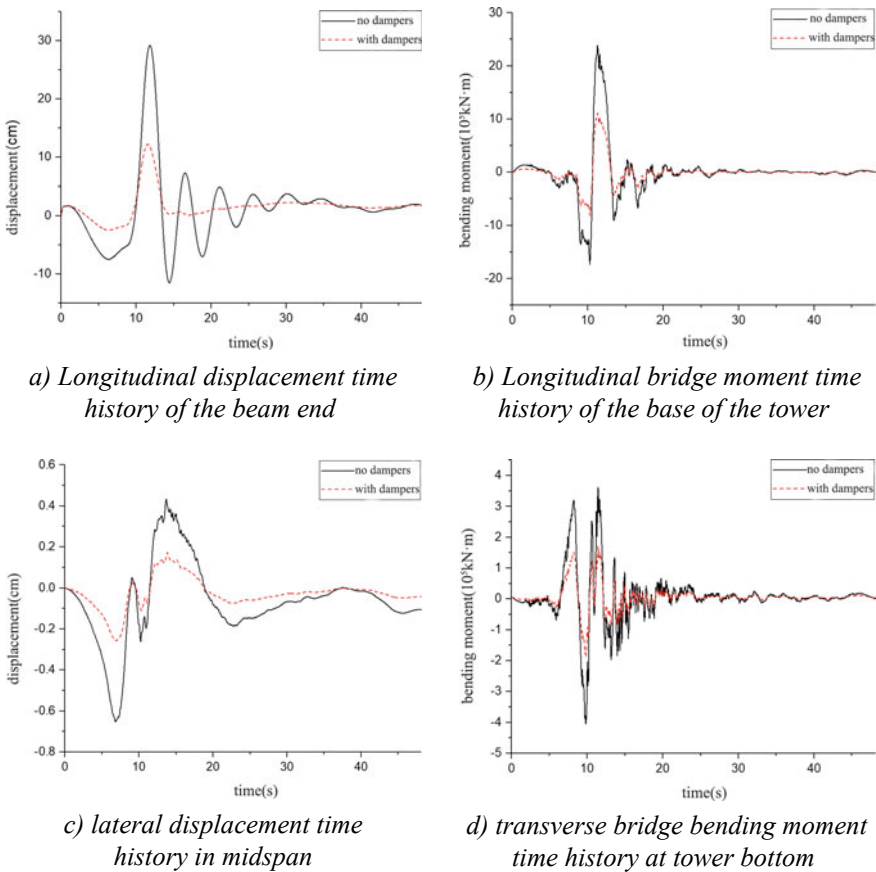


Fig. 7 Seismic response time history curves before and after installing dampers

58%, the maximum bending moment of the tower bottom along the bridge direction is reduced by 54%, and the longitudinal seismic response is significantly reduced. The maximum lateral displacement in the middle of the span is reduced by 60%, the maximum bending moment in the transverse direction of the tower bottom is reduced by 53%, and the seismic response in the transverse direction is significantly reduced. The above results show that the seismic response of the semi-floating single-tower cable-stayed bridge with dampers is effectively suppressed.

4 Conclusions

In this paper, the finite element model of a single-tower cable-stayed bridge across a fault is established based on FEA method according to three common fault types. The effects of velocity pulse, pulse period and pulse number on the seismic response of the structure is studied by dynamic time history analysis method. The main conclusions are as follows.

The velocity pulse, pulse period and the number of pulses have obvious effects on the structural seismic response.

- (1) The seismic response of the main beam is significantly increased by the velocity pulse, and the main tower is more affected by the velocity pulse than the main beam;
- (2) The change of pulse period significantly affects the seismic response of the structure, and it is especially obvious when the pulse period is close to the basic vibration mode period of the structure;
- (3) The parity of the number of pulses is the main reason affecting the seismic response of the main beam and main tower rather, not the number of pulses.

Acknowledgements This work was supported by National Natural Science Foundation of China (Grant No. 52078164).

References

1. Shuang L, Li-Li X (2007) Progress and trend on near-field problems in civil engineering. *Acta Seismologica Sinica* 29(1):102–111
2. Ying-Xin H, Yu-Ji T, Ke-Hai W, Chong L, Gang W (2017) Enlightenment and suggestions for seismic fortification of bridges crossing fault-rupture zones. *World Earthq Eng* 33(02):192–198
3. Ying-xin H, Ming-jie M, Hai-feng L (2018) Zhang Shang-rong Influence of structural seismic response of bridges crossing active fault. *J Jilin Univ (Engineering and Technology Edition)* 48(06):1725–1734
4. Hall JF, Heaton TH, Hailing MW et al (1995) Near-source ground motion and its effects on flexible buildings. *Earthq Spectra* 11(4):569–605
5. Malhotra PK (1999) Response of buildings to near-field pulse-like ground motions. *Earthq Eng Struct Dyn* 28(11):1309–1326

6. Yan S, Dong-sheng W, Zhi-Guo S (2014) Seismic isolation design for high speed railway bridge under near-fault ground motions. *China Railway Sci* 35(6):34–40
7. Wen-Peng W, Li-Feng L, Si-Cong H (2015) Effects of the bearing arrangement on seismic performance of continuous girder bridges under near-fault ground motions. *Earthq Eng Eng Dyn* 35(4):155–163
8. Roussis PC, Constantinou MC, Erdik M et al (2003) Assessment of performance of isolation system of bolu viaduct. *J Bridge Eng ASCE* 8(4):182–190
9. Park SW, Ghasemi H, Shen J et al (2004) Simulation of the seismic performance of the bolu viaduct subjected to near-fault ground motions. *Earthq Eng Struct Dyn* 33(13):1249–1270
10. Ucak A, Mavrocidis GP, Tsopelas P (2014) Behavior of a seismically isolated bridge crossing a fault rupture zone. *Soil Dyn Earthq Eng* 57(2):164–178
11. Ying-xin HUI, Ke-hai WANG, Gang WU (2015) Seismic responses of bridges crossing faults and their best crossing angles. *J Vib Shock* 34(13):6–11
12. Shuai L (2018) Characteristics of near fault records and its influence on the seismic responses of long-span cable-stayed bridges. Southeast University
13. Jia-Qi L (2020) Research on single tower cable-stayed bridge's seismic response crossing faults. Harbin Institute of Technology
14. Qi-fang L, Yi-fan Y, Xing J, Hai-ping D (2006) Basic characteristics of near-fault ground motion. *Earthq Eng Eng Vib* 26(1):1–10
15. Zhang-Ming W, Yan-Guang Y (1990) Characteristics of earthquake surface rupture and seismogenic faults. *J Catastrophology* 1990(04):14–19

Analysis on the Behavior of Seismic Retrofitting Steel Brace Based on Acceleration and Strain Response Measurements



Tsuyoshi Koyama, Jun Iyama, Yoshihiro Fukushima, Shota Miyazaki, and Naoto Kato

Abstract Though great care is taken in the design process, little is considered on verifying that the buildings perform “as designed”. In this paper, the actual structural performance of steel braced frames installed as seismic reinforcement in a nine-story RC building is investigated through highly sensitive semi-conductor strain gauges and MEMS accelerometers under minor earthquakes. The structural performance of the steel braces are evaluated by comparing the measured axial forces, which can be directly estimated from the attached strain gauges, to the computed values from the static analysis of a line element model of the steel braces and surrounding steel frame through Fourier analysis. The ratio between the computed and measured axial forces are evaluated for 403 earthquake records (extracted from 36 earthquakes). The results show that the computed values are more than twice the measured values. The ratio is dispersed for small interstory drifts and converges to a value close to 2 with increasing interstory drift. The cause of the overestimation is investigated through MEMS accelerometers placed at the ends of the steel braces for a single earthquake motion. The Fourier amplitude of the pseudo displacements of the brace ends at the fundamental frequency are obtained from the acceleration measurements. These pseudo displacements suggest a rigid body type of motion of the braced frame, implying a possibility of overestimation of the actual interstory drift. Such an overestimation results in an overestimation of the computed axial force, and may be the reason for the large discrepancy between the measured and structural analysis results. The axial forces estimated from the pseudo displacements of the brace ends show a value approximately 70% of the measured axial force, validating the reliability of the measurements and supporting the possibility of actual rigid body motion of the steel braced frame.

Keywords Structural health monitoring · Interstory drift · Acceleration measurements · Strain measurements · Structural performance verification

T. Koyama (✉)
Tokyo Denki University, Tokyo, Japan
e-mail: tkoyama@mail.dendai.ac.jp

J. Iyama · Y. Fukushima · S. Miyazaki · N. Kato
The University of Tokyo, Tokyo, Japan

1 Introduction

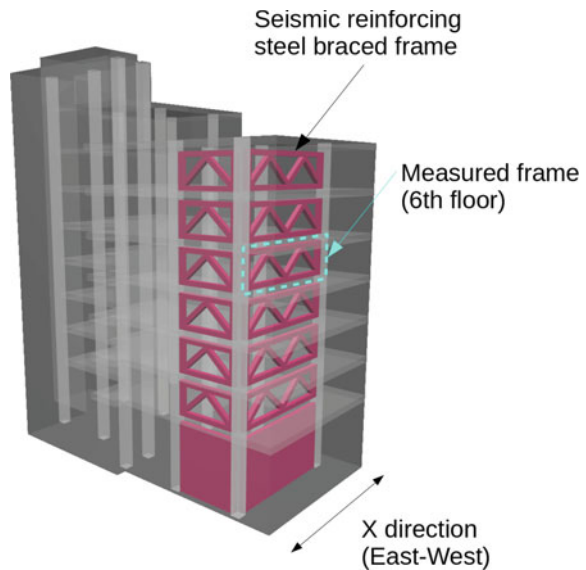
Though great care is taken in the design process of buildings, little is considered on verifying that the buildings perform “as designed”. Structural health monitoring methods involving accelerometers are popular but lack the ability to supply local information on the actual load carrying behavior of individual structural members. In this paper, the structural performance of steel braced frames installed as seismic reinforcement in a nine-story RC building is investigated through highly sensitive semiconductor strain gauges and MEMS accelerometers. The structural performance of the steel braces are investigated via Fourier analysis, by comparing the brace axial forces measured from the strain gauges with those evaluated from the acceleration measurements combined with a structural model.

2 Experimental Setup And Methodology

2.1 Measured Building

The building analyzed in this paper is a 9-story reinforced concrete building (built in 1967), shown in Fig. 1. A seismic retrofit has been conducted in 2005, where steel braced frames employing epoxy resin adhesives [1] have been installed in the 3rd to 8th stories. In this paper, the behavior of the steel braced frame set in the 6th floor providing X (East–West) direction resistance is investigated.

Fig. 1 Perspective of the measured building



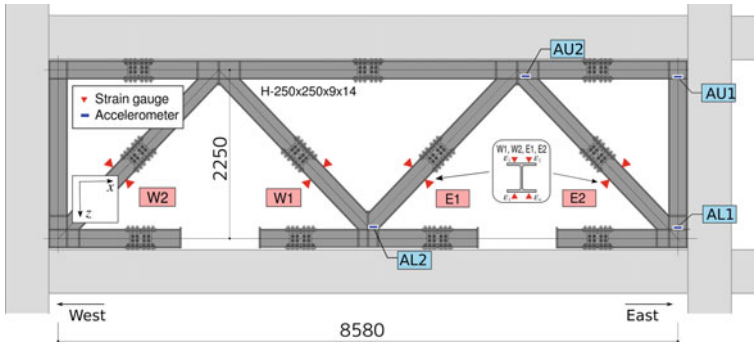


Fig. 2 Location of the strain gauges and accelerometers within the braced frame

2.2 Measurement System

Highly sensitive semi-conductor strain gauges (KSN-2-120-E4-11, Kyowa Electronic Instruments Co., Ltd.) and three-directional MEMS accelerometers (ADXL355, Analog Devices, Inc.) [2, 3] are attached to the steel braced frame at the locations shown in Fig. 2. 4 strain gauges are attached to the flanges of the four braces (E1, E2, W1, W2) in order to measure the axial and bending behavior. Since the data obtained from braces W1 and W2 are almost identical to those obtained from E1 and E2, only the E1, E2 brace data will be further discussed in this paper. Accelerometers are attached to the 4 locations, AU1 through AL2. (Accelerometers AU2, AL2 have been installed in January 2021 and only data after this date is obtained).

2.3 Structural Model

The steel braced frame in Fig. 2, can be represented by the line element model shown in Fig. 3. The size of the columns, beams and braces are H250 × 250x9 × 14. The interaction between the surrounding RC frame and steel braced frame is represented by the distributed load along the top beam.

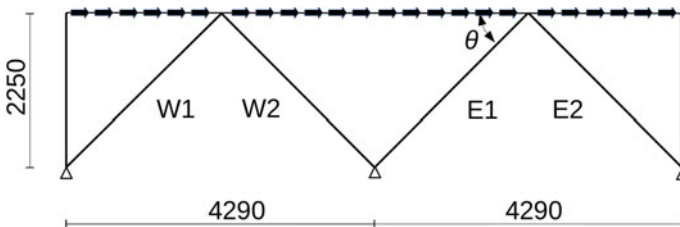


Fig. 3 Structural model of the steel braced frame

2.4 Input Earthquake Measurements

In investigating the relationship between the brace axial force estimations from strain gauges and column interstory drift, 36 earthquakes measured between April 2020 to December 2020 are examined. The time duration of each record is 240[s] starting from the time the earthquake occurred according to the Japan Meteorological Agency (JMA). Since the amplitude of the response is assumed to affect the vibrational characteristics, forty-seven 10[s] duration records are extracted from each earthquake record. The i th 10[s] duration record is obtained by extracting the $[5(i - 1), 5(i + 1)]$ [s] interval of the original earthquake record. From the 1,692 extracted short earthquakes, those with acceleration records with accelerations smaller than a given threshold and those with data acquisition error are removed, resulting in 403 short earthquake data that are analyzed.

In the investigation of the relationship between the brace axial force estimations from the strain gauges and pseudo displacements of the brace ends, the measurement from the earthquake occurring off the coast of Fukushima at around 23:08 AM, February 13th, 2021 is used. The length of the measurement is 180[s] starting at 23:08:30 AM. The JMA intensity scale at the location of the building, Bunkyo ward, Tokyo, was 3.

2.5 Fourier Analysis and Brace Axial Forces

A Fourier analysis is conducted to investigate the structural performance of the steel braces. The acceleration and strain time history records obtained from the accelerometers and strain gauges are Fourier transformed and the component corresponding to the 1st fundamental frequency is extracted and further investigated. As an example, the acceleration time histories and corresponding Fourier amplitude spectrum of AU1 and AL1 are shown in Fig. 4a, b, and the strain time histories and corresponding Fourier amplitude spectrum of E1 are shown in Fig. 4c, d. From Fig. 4b, d, one can observe that the acceleration and strain Fourier amplitude spectrums show a peak at the same frequency. This frequency is referred to as ω_{peak} , and the acceleration and strain components corresponding to this frequency is employed in the calculations.

In order to verify the performance of the steel braces, the axial forces obtained directly from the Fourier amplitude of the strains are compared to those computed from the structural model presented in Sect. 2.3. To validate the reliability of the acceleration measurements and to further understand the structural resisting mechanism of the steel braces, the axial forces from the strain gauges are also compared to the axial forces computed from the pseudo displacements of the brace ends.

(a) Column interstory drift

The Fourier amplitude of the interstory drift, $\hat{\delta}_{peak}$, computed from the top (AU1) and bottom (AL1) acceleration of the column, shown in Fig. 2, is expressed by the

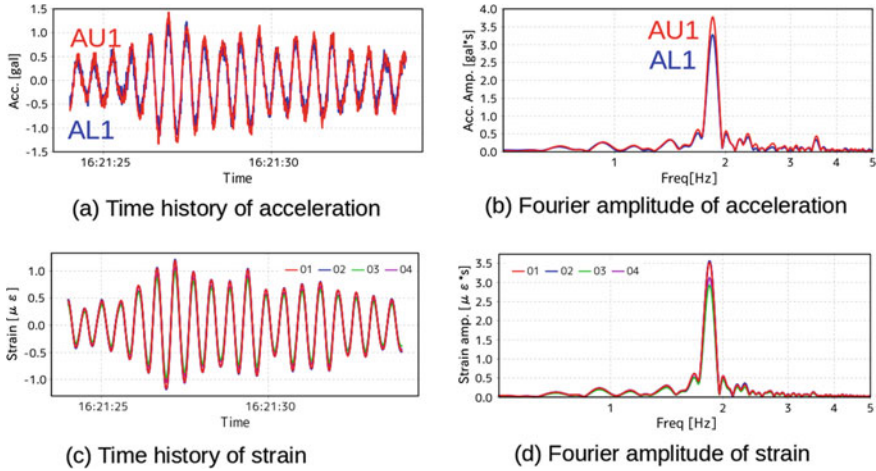


Fig. 4 Acceleration and strain time histories

following equation.

$$\hat{\delta}(\omega_{peak}) = \frac{|a_{\hat{U}1x}(\omega_{peak})| - |\hat{a}_{L1x}(\omega_{peak})|}{\omega_{peak}^2} \tag{1}$$

Here, $\hat{a}_{U1x}(\omega_{peak})$ and $\hat{a}_{L1x}(\omega_{peak})$ are the horizontal direction Fourier amplitude spectrum components of AU1 and AL1 at the frequency ω_{peak} corresponding to the peak values in Fig. 4b. To be precise, the Fourier amplitude of the interstory drift should be calculated by first taking the difference between $\hat{a}_{U1x}(\omega_{peak})$ and $\hat{a}_{L1x}(\omega_{peak})$ and then taking their absolute value. Under the assumption that the phase difference of the two acceleration values are negligible when the system is vibrating near its fundamental frequency, the simplified form in Eq. (1) can be employed.

(b) **Brace axial forces from strain**

The Fourier amplitude of the brace axial forces can be estimated directly from the value of the Fourier amplitudes of the 4 strain gauges attached to the brace by the following equation.

$$\hat{N}_{strain}(\omega_{peak}) = EA \frac{|\hat{\epsilon}_1(\omega_{peak})| + |\hat{\epsilon}_2(\omega_{peak})| + |\hat{\epsilon}_3(\omega_{peak})| + |\hat{\epsilon}_4(\omega_{peak})|}{4} \tag{2}$$

Here E is the Youngs modulus, A is the cross sectional area, and $\hat{\epsilon}_i(\omega_{peak})$ is the Fourier amplitude spectrum component of strain gauge i attached to the beam cross section at the frequency ω_{peak} corresponding to the peak values in Fig. 4d. As in the estimation of the column interstory drift, the phase difference between the strain

values are assumed negligible and their absolute values are taken before computing the average.

(c) **Brace axial forces from structural analysis and column interstory drift**

The Fourier amplitude of the brace axial forces can also be estimated from the column interstory drift by employing the structural model of Sect. 2.3 as shown in Fig. 5c. Since a linear structural model is considered, the brace axial force per unit column interstory drift can be evaluated. Using these values, the Fourier amplitude of the brace axial forces can be estimated for the model in Fig. 3 from the column interstory drift, $\hat{\delta}(\omega_{peak})$, using the following formulas.

$$\hat{N}_{model,E1}(\omega_{peak}) = 369[\text{kN/mm}] \times \hat{\delta}(\omega_{peak}) \tag{3}$$

$$\hat{N}_{model,E2}(\omega_{peak}) = -356[\text{kN/mm}] \times \hat{\delta}(\omega_{peak}) \tag{4}$$

(d) **Brace axial forces from end displacements**

The third method to estimate the Fourier amplitude of the brace axial forces is from the pseudo displacements of the brace ends. The pseudo displacements are computed from the Fourier amplitude spectrum acceleration values at the ends of the braces from the equation $\hat{d} = \hat{a} / \omega_{peak}^2$. In the case of brace E1, AL2 and AU2 are utilized, and in the case of E2, AU2 and AL1. Compared to the evaluation of the column interstory drift which only involves the horizontal (x direction) acceleration, the calculation of the brace elongation involves both horizontal and vertical (z direction) acceleration components.

$$\hat{N}_{disp,E1}(\omega_{peak}) = EA \frac{\left\{ \left| \hat{a}_{AU2x}(\omega_{peak}) \right| - \left| \hat{a}_{AL2x}(\omega_{peak}) \right| \right\} \cos \theta - \left\{ \left| \hat{a}_{AU2z}(\omega_{peak}) \right| - \left| \hat{a}_{AL2z}(\omega_{peak}) \right| \right\} \sin \theta}{\omega_{peak}^2} \tag{5}$$

$$\hat{N}_{disp,E2}(\omega_{peak}) = EA \frac{\left\{ \left| \hat{a}_{AL1x}(\omega_{peak}) \right| - \left| \hat{a}_{AU2x}(\omega_{peak}) \right| \right\} \cos \theta - \left\{ \left| \hat{a}_{AL1z}(\omega_{peak}) \right| - \left| \hat{a}_{AU2z}(\omega_{peak}) \right| \right\} \sin \theta}{\omega_{peak}^2} \tag{6}$$

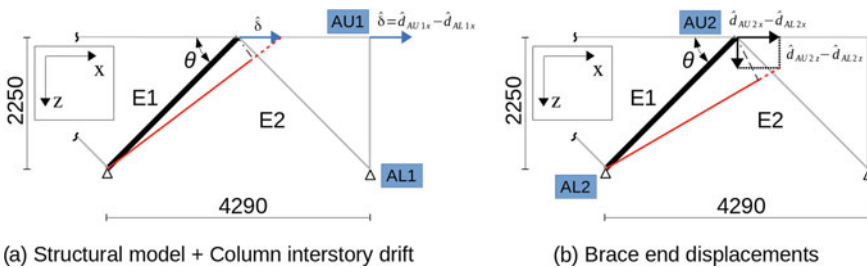


Fig. 5 Schematic of the brace elongation configuration assumed in the brace axial force calculation

Figure 5d illustrates the difference between the brace elongation considered in this calculation and that considered in the brace axial force calculation involving column interstory drift. The two brace axial force values coincide, only in the case where the relative vertical acceleration amplitude is zero.

3 Results and Discussion

3.1 Comparison Between Brace Axial Force Estimations from Interstory Drift and Strain Gauges

The structural performance of the steel braces are investigated by comparing the brace axial forces computed from the strain gauges, $\hat{N}_{strain}(\omega_{peak})$, which should most closely represent the actual axial force, to the axial force computed from the structural model based on the measured column interstory drift, $\hat{N}_{mod\ el}(\omega_{peak})$. The ratio, $\hat{N}_{mod\ el}(\omega_{peak}) / \hat{N}_{strain}(\omega_{peak})$, computed from the 403 earthquake records introduced in Sect. 2.4 for braces E1 and E2 are presented in Fig. 6 with respect to the corresponding column interstory drift $\hat{\delta}(\omega_{peak})$. The ratio is larger than 2.0 over the obtained interstory drift range and is larger than 2.0 and dispersed when the interstory drift is small. For larger interstory drift values, the ratio seems to converge to a value close to 2.0. The results first imply that the steel braces due indeed support forces of the same magnitude as values assumed theoretically from a structural model. They also imply that the structural model overestimates the brace force for the given column interstory drift and seem to behave too stiff compared to the actual force resisting mechanism (Fig. 6).

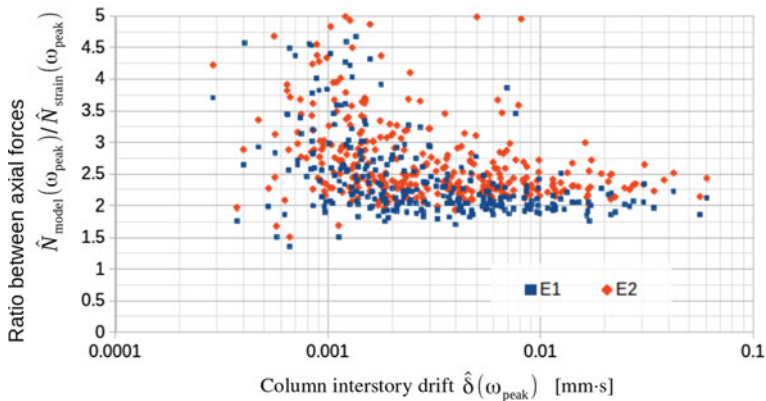


Fig. 6 Ratio of the axial force estimations between the interstory drift and strain gauges with respect to the column interstory drift

3.2 Comparison Between Brace Axial Force Estimations from Strain Gauges and Brace End Displacements

In order to investigate the cause of the discrepancy observed in the previous section between the brace axial force computed from the structural model and the values computed from the strain, the axial force computed from the pseudo brace end displacements (Eqs. (5) and (6)) are presented for the earthquake occurring off the coast of Fukushima at around 23:08 AM, February 13th, 2021. The horizontal and vertical acceleration and strain time histories, as well as their Fourier amplitude spectrum are shown in Figs. 7 and 8. Though the acceleration amplitude spectrums in Fig. 8 do not show one single prominent peak, their shapes are similar and have a peak at 1.7[Hz]. This value is assumed as ω_{peak} and the Fourier amplitude spectrum values corresponding to this frequency are employed in the calculations for the brace axial forces using Eqs. (1)–(6). The pseudo horizontal and vertical displacement amplitudes $\hat{d} = \hat{a} / \omega_{peak}^2$ obtained from the acceleration records of AL1, AU1, AL2, AU2 are shown in Fig. 9. The values from AL2, AU2, AL1 are inserted into Eqs. (5) and (6) to obtain the brace axial force estimations from the brace end displacements. N_{disp} , shown in Fig. 9c. The brace axial forces computed from the strain gauges, N_{strain} , and those from the structural model, N_{model} , are shown in Fig. 9a, b, respectively. A comparison between the three axial forces is presented in Table 1.

The axial force ratio between the model and the strain obtained values are approximately 2, which coincides with the results presented in the previous section. As for

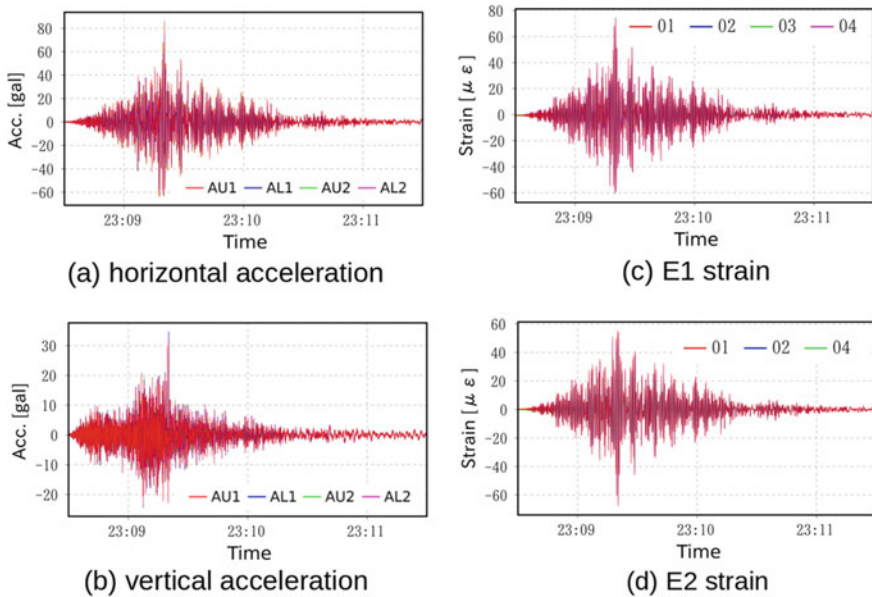


Fig. 7 Time histories of the acceleration and strain

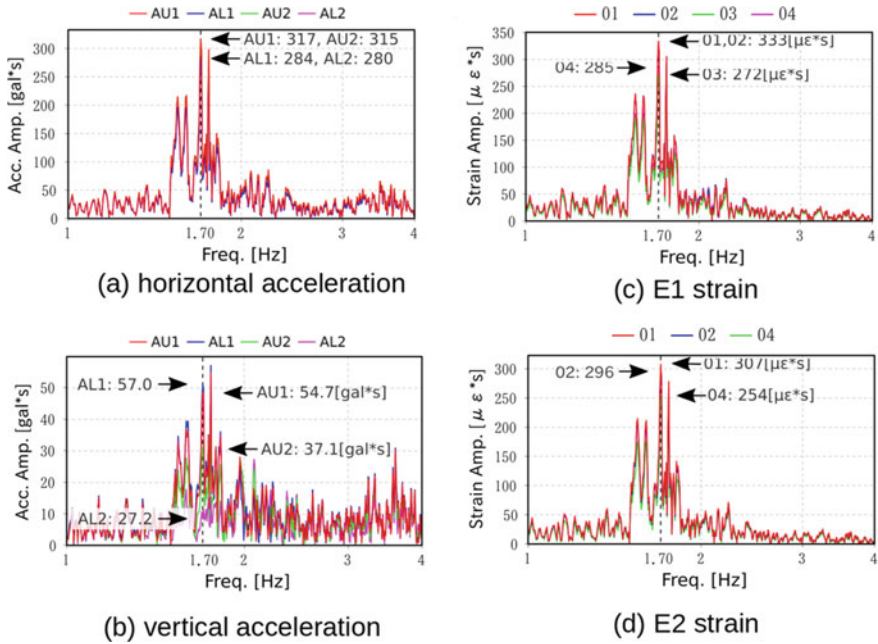


Fig. 8 Fourier amplitude spectra of the acceleration and strain

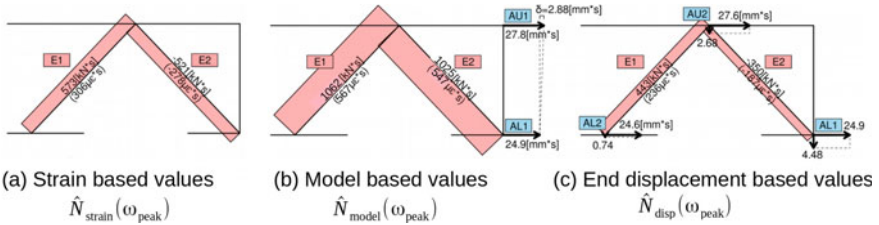


Fig. 9 Comparison of the brace axial forces estimated from three different methods

Table 1 Comparison between obtained brace axial forces

Brace	$\hat{N}_{strain}(\omega_{peak})$ [kNs]	$\hat{N}_{model}(\omega_{peak})$ [kNs]	$\hat{N}_{disp}(\omega_{peak})$ [kNs]
E1	573	1062(185%)	443(77%)
E2	521	1025(197%)	350(67%)

Note The values in the parentheses represent the percentage with respect to N_{strain}

the ratio between the pseudo brace end displacement and strain obtained values, they are 77%(E1) and 67%(E2). Though the brace axial force computed from the end displacements underestimate the measured strain based values, they better estimate the actual measured strain based brace force compared to the structural model. One

reason for the underestimation can be attributed to the lack of accuracy in the vertical component of the acceleration measurements due to the resolution of the equipment and measurement noise. A cause for the overestimation of the axial forces from the structural model may be due to the existence of a rigid body type of motion of the steel braced frame which is neglected in the structural model. A close investigation of the pseudo vertical displacement amplitudes in Fig. 9c reveal that the vertical displacement amplitude increases from AL2, AU2, AL1, implying a rigid body motion centered near the intersection of the two inverted V steel braces. To confirm this claim, acceleration measurements at the ends of the W1, W2 braces are also required. The better estimation of the axial forces from the pseudo brace end displacements is due to the elimination of the rigid body mode in its evaluation.

4 Conclusions

In order to verify the structural performance of the seismic retrofitting steel truss frame installed in the RC building, high-precision semi-conductor strain gauges were attached to the brace cross sections and MEMS accelerometers were attached to the frame to measure the response during small earthquakes. The Fourier transform was employed to obtain Fourier spectrum amplitudes of the acceleration and strain at the fundamental frequency from the time histories. These were then used to obtain the interstory displacement and brace axial forces.

The brace axial force directly calculated from the Fourier amplitudes of the strains, which represents the actual axial force acting in the brace, is compared to the axial force computed from a linear elastic line element structural model combined with the measured column interstory drift, which should represent the amount of axial force the brace is expected to carry. The axial force computed from the structural model is of the same magnitude as the actual axial force calculated in the brace, suggesting that the seismic steel brace is indeed resisting seismic forces even for small earthquakes. The actual ratio between the axial force from the structural model and that from the actual axial force is largely dispersed with a minimum of approximately 2 for small interstory drifts, and converges to a value close to 2 for larger interstory drifts. These results imply that the structural model overestimates the brace force and behaves stiffer than the actual force resisting mechanism.

To investigate the cause of the discrepancy between the computed model and actual brace axial forces, as well as to validate the acceleration measurements, the axial force computed from the pseudo brace end displacements are obtained. The ratio between the pseudo brace end displacement and actual brace axial forces obtained from the strain are 77%(E1) and 67%(E2), which gives a better estimation compared to the structural model. One reason for the underestimation can be attributed to the lack of accuracy in the vertical component of the acceleration measurements due to the resolution of the equipment and measurement noise. A cause for the overestimation of the axial forces from the structural model may be due to the existence of a rigid body type of motion of the steel braced frame which is neglected in the structural

model. A close investigation of the pseudo vertical displacement amplitudes reveal a rigid body motion centered near the intersection of the two inverted V steel braces.

Acknowledgements We would like to express our gratitude to the JFE 21st Century Foundation as well as JSPS KAKENHI(Grant Number 20H02293) for partially supporting this research.

References

1. Ishimura M, Sadasue K, Miyauchi Y, Yokoyama T, Fujii T, Minami K (2012) Seismic performance evaluation for retrofitting steel brace of existing RC building with low-strength concrete. In: 15th world conference on earthquake engineering. Lisbon, Portugal
2. Fukuda T, Iyama J, Fukushima Y, Tsuboi K (2019) Micro-strain response measurements in steel seismic reinforcements. In: Annual meeting of the Japan association for earthquake engineering. Kyoto, Japan
3. Koyama T, Fukushima Y, Iyama J, Fukuda T (2020) Estimation of stress distribution by micro strain measurement in seismic reinforcement steel brace. In: 17th world conference on earthquake engineering, 17WCEE. Sendai, Japan

System and Model Identification

Probabilistic Time-Variant Linear Finite Element Model Updating for Nonlinear Structural Systems



Felipe Mizon, Matías Birrell, José Abell, and Rodrigo Astroza

Abstract This paper presents a method to update linear time-variant finite element (FE) models of civil structures experiencing nonlinear behavior due to earthquake excitation. First, the time-varying modal parameters of the structure are identified using the input–output dynamic data recorded during a damaging seismic event by employing a short-time windowing approach. Then, the identified modal parameters are used to update a linear FE model of the structure using a Bayesian approach. Global sensitivity analysis based on Sobol’ indices is employed to select the most influential parameters for the model updating stage. The evolution of the equivalent stiffness of different elements of the FE model are tracked and their estimation uncertainties are also quantified. The method is verified using numerically simulated data of a two-dimensional nonlinear FE model of a nine-story steel frame.

Keywords System identification · Model updating · Damage · Modal properties

1 Introduction

Minimizing the impact of natural disasters such as earthquakes, tsunamis and hurricanes on civil structures has been one of the main structural engineering challenges on recent decades. One component of this challenge is the assessment of structural health after a disaster. Several damage assessment methods based on qualitative and/or quantitative data have been developed to assess the performance of structures following such extreme events. In structural engineering, people often use finite element (FE) models to design, analyze and evaluate civil engineering structures. For existing structures, FE model updating methods provides tools to calibrate a FE model based on observed structural response [1]. FE model updating usually uses modal properties, such as natural frequencies and mode shapes, obtained from vibration data and is typically applied to the assessment of structural damage, localizing and quantifying it in a nondestructive way [2]. Localized structural damage leads to a

F. Mizon · M. Birrell · J. Abell · R. Astroza (✉)
Faculty of Engineering and Applied Sciences, Universidad de los Andes, Santiago, Chile
e-mail: rastroza@miuandes.cl

© The Author(s), under exclusive license to Springer Nature Switzerland AG 2023
Z. Wu et al. (eds.), *Experimental Vibration Analysis for Civil Engineering Structures*,
Lecture Notes in Civil Engineering 224,
https://doi.org/10.1007/978-3-030-93236-7_30

loss of effective stiffness. Therefore, the updated model parameters usually represent the reduction of equivalent stiffness of the substructure. The main objective of FE model updating is determining the optimal values of a set of the model parameters by minimizing the difference between the predictions of the FE model and the measured data or quantities derived therefrom.

Deterministic methods of model updating cannot take into account the uncertainties associated to identification errors, measurement noise, and modeling errors. During the system identification phase, the measured noise in recorded signals and the assumptions underlying the identification method increases the uncertainty in the estimation. While during the modeling phase, modeling assumptions are made to simplify and discretize the model, which also adds uncertainty to the problem. To consider all the uncertainties associated in FE model updating, a probabilistic framework, based on Bayesian inference, is adopted herein. Bayesian model updating methods are founded on a rigorous stochastic framework, meaning that robust estimation results can be obtained. The computation of different statistics, such as mean and covariance, is common in the study of the posterior probability density function (PDF), which is referred to as resolution analysis. The degree of confidence of the value of an uncertain parameter is expressed by PDFs of the uncertain parameters. Prior PDF reflects the prior knowledge of the parameter before any data is considered. Using Bayes' theorem, the prior PDF is converted into a posterior PDF, taking into account both the uncertainty of prior information and the uncertainty of the model and the experimental data. This transformation is performed via the Likelihood function, which reflects the ability of the FE model to explain the observed data.

Most of the recent research has focused on updating a FE model using the structure's modal characteristics identified before and after damage has occurred. In this paper, the deterministic-stochastic subspace identification (DSI) method is applied to a moving short-time window of input–output acceleration data to extract the structure's "instantaneous" modal characteristics during a seismic test [4–6]. Then, using Bayesian model updating, the identified time-variant model parameters are utilized to estimate the evolution of material parameters of a linear FE of the damage structure during an earthquake event.

2 Damage Identification Based on Bayesian Time-Variant FE Model Updating

2.1 Proposed Approach

Most of earlier investigations on Bayesian model updating and modal parameter identification focused solely on the calibration of the FE model before to and after seismic excitations, in order to locate and quantify structural damage. In this paper,

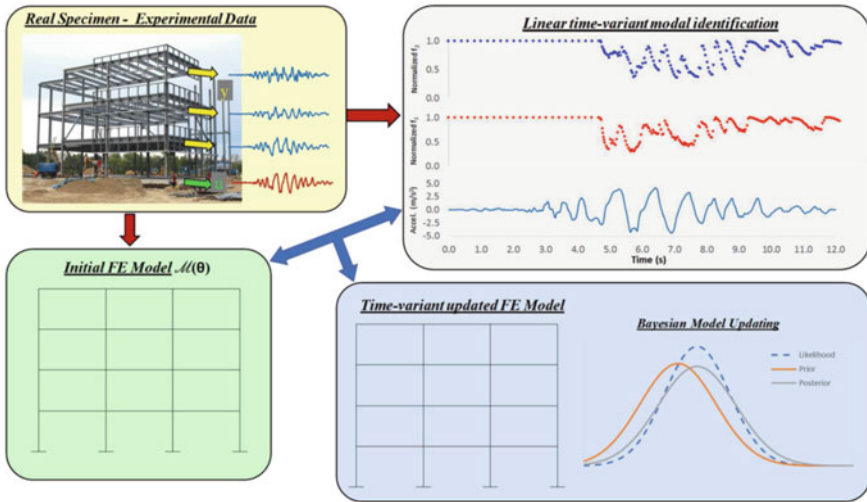


Fig. 1 Proposed probabilistic time-variant linear finite element model updating approach

a novel approach is proposed to identify the damage based on Bayesian time-variant FE model updating.

The first stage involves using sensors to monitor the behavior of a real structure while it is subjected to an earthquake excitation (input) and to record the structure’s response (output). Using the input–output acceleration data, instantaneous modal properties of the structure are identified by applying the DSI method to a moving short-time window, obtaining the modal properties of the structure, i.e., natural frequencies, mode shapes, and damping ratios. Although nonlinear FE models are widely used in a variety of engineering fields due to their ability replicate and simulate phenomena that occur in the real world, they demand significant computational power. An equivalent linear FE model of the structure is considered herein to overcome that problem while also obtaining accurate results. The damage in the structure is considered as a decrease in the equivalent Young’s modulus of the different elements of the structure.

A sensitivity analysis is performed to determine which are the most relevant parameters of the model in terms of choosing the set of parameters θ to calibrate. Then, a linear FE model defined by θ is updated by considering the time-variant modal parameters identified during the earthquake event and a Bayesian approach. The evolution of the equivalent elastic modulus of different zones of the FE model allow modelling the damage in the structure. The initial model parameter values $\theta^{initial}$ are adopted as the most probable point of the model parameters θ in the preliminary updating stage, while for the next updating steps, the maximum a posteriori (MAP) estimate of the model parameters obtained in the previous estimation step is proposed as the mean prior values of the current time, taking into account a

correlation between the damaged produced before and the actual damage. Figure 1 summarizes the approach proposed in this paper.

2.2 Linear Time-Varying System Identification

Time-variant modal properties of a structure during seismic events are identified using the DSI method with input–output acceleration data recorded from the monitored structures. This allows to estimate the structure’s instantaneous modal characteristics using a short-time windowing approach [6] (see Fig. 2).

The purpose of the DSI method is to determine the system’s order (n) and the system matrices ($\mathbf{A}_d, \mathbf{B}_d, \mathbf{C}_d, \mathbf{D}_d, \mathbf{Q}, \mathbf{R}$ and \mathbf{S}) from s measurement samples of the input ($\mathbf{u}_0, \mathbf{u}_1, \dots, \mathbf{u}_{s-1}$) and output ($\mathbf{y}_0, \mathbf{y}_1, \dots, \mathbf{y}_{s-1}$) data. The modal properties of the system can be determined from the eigenvalues and eigenvectors of matrix \mathbf{A}_d , matrix \mathbf{C}_d , and the relationships between the discrete and the continuous state matrices:

$$f_r = \frac{\sqrt{\lambda_r \lambda_r^*}}{2\pi} \quad r = 1, \dots, n/2 \tag{1}$$

$$\xi_r = \frac{-Re(\lambda_r)}{|\lambda_r|} \quad r = 1, \dots, n/2 \tag{2}$$

$$\Phi_r = \mathbf{C}_d \Psi = [\phi_1, \dots, \phi_{n/2}] \tag{3}$$

where f_r are the modal frequencies, ξ_r are the modal damping ratios and Φ_r are the mode shapes, respectively; $\lambda_r =$ eigenvalues of the continuous-time state matrix \mathbf{A}_c (with $\mathbf{A}_d = e^{\mathbf{A}_c \Delta t}$) and Δt is the sampling time, $\Psi =$ eigenvectors and \mathbf{A}_d , and superscript $*$ and $|\cdot|$ denote complex conjugate and magnitude, respectively. The instantaneous modal properties are estimated employing input–output acceleration recorded data divided over short-time windows in order to track the changes of the structure’s dynamic properties.

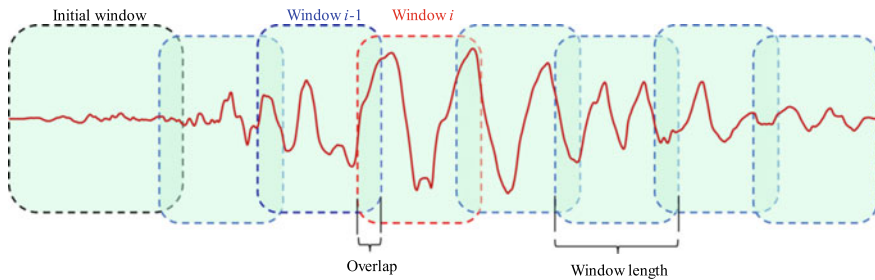


Fig. 2 Short-time windowing approach for linear-time variant system identification

It is noted that the minimum length window, both with and without overlap, was suggested in [6] to conduct the linear-time varying system identification of model properties based on input–output seismic data. In addition, stabilization diagrams [7] are used to distinguish between physical and spurious (mathematical) modes for each short-window data set.

2.3 Global Sensitivity Analysis

Global sensitivity analysis (GSA) on the model response is conducted as a preliminary step towards parameter estimation, to examine the composition of the model response and select the parameters to be estimated. In this section, first (S^I) and total order Sobol’s indices (S^T) [8] are computed for the FE model parameters. These quantify the response variability induced by the variability of each parameter (S^I), and all groups of parameters in which it is contained (S^T).

When dealing with models defined by a high number of parameters, GSA constitutes an important exercise towards identifying those model parameters that have the most influence on model response. With the hierarchy of parameter influence established by GSA, the high dimensionality of the inverse problem in model calibration can be reduced by estimating the parameters that define the model response. In subsequent model calibration, those parameters that do not considerably influence the model response might not be identifiable from experimental data. For this reason, this reduction of dimensionality can help to achieve more confident estimation results and translate into more accurate model predictions afterwards. Additionally, the generation of several thousands of model response samples provides a thorough exploration of the parameter space that partially informs the selection of prior PDFs for model calibration in Sect. 3.5.

Due to the high computational cost of sampling large FE models, a PCE-based computation [9] of Sobol’s indices is presented in Sect. 3.4. To this end, the model is executed 3000 times and a surrogate PCE-model of order 3 is fitted to obtained model responses. The computation of Sobol’s indices for the PCE-model is analytical through the definitions in [8], effectively saving a considerable amount of time over a simulation-based computation of the indices.

2.4 Bayesian Finite Element Model Updating

Bayesian model updating is employed to determine the probability distribution of the selected model parameters. Below is a brief overview of the methodology applied in this study. For a thorough description of Bayesian model updating, more information can be found elsewhere [10]. The Bayes theorem can be written as:

$$p(\boldsymbol{\theta}|\mathbf{d}) = cp(\mathbf{d}|\boldsymbol{\theta})p(\boldsymbol{\theta}) \quad (4)$$

In this equation, $p(\theta|d)$ is the posterior PDF of the updating parameters (modulus of elasticity) based on recorded data, \mathbf{d} (time-variant identified modal properties) and the data evidence is represented in c , which is a normalizing constant which guarantees that the posterior PDF integrates to one, the likelihood function $p(d|\theta)$ reflects the probability of observing the recorded data given the updating parameters and can be interpreted as an indicator of how well a model succeeds in explaining the measurements \mathbf{d} , as well as the contribution of the measured data \mathbf{d} in estimating the updated PDF of the model parameters θ . Finally, $p(\theta)$ refers to the prior PDF which represents the initial understanding of the updating parameters. In most cases, the prior distributions are determined based on engineering criteria and existing prior information. Prior PDFs are considered as a lognormal distribution in this work, assuming independent parameters.

The following error functions are defined, assuming to have zero mean Gaussian distributions in order to determine the likelihood function [11].

$$e_{\lambda_i} = \frac{\tilde{\lambda}_i - \lambda(\theta)}{\tilde{\lambda}_i} \quad (5)$$

$$e_{\Phi_i} = \frac{\tilde{\Phi}_i}{\|\tilde{\Phi}_i\|} - a_i \frac{\Gamma \Phi_i(\theta)}{\|\Gamma \Phi_i(\theta)\|} \quad (6)$$

where e_{λ_i} is the eigenfrequency error, where $\tilde{\lambda}_i = (2 \cdot \pi \cdot \tilde{f}_i)^2$ is the natural frequency extracted from the data, $\lambda(\theta)$ is the model generated natural frequency considering the model parameters θ , e_{Φ_i} is the mode shape error, where $\tilde{\Phi}_i$ is the mode shape vector of the i th mode extracted from the data, and $\Phi_i(\theta)$ is the model generated mode shape vector considering the model parameters θ of the i th mode. Finally, Γ is a mapping matrix which matches the modal coordinates of the model and the sensors utilized to identify the experimental data and a_i is defined as:

$$a_i = \frac{\tilde{\Phi}_i \Gamma \Phi_i(\theta)}{\|\tilde{\Phi}_i\| \|\Gamma \Phi_i(\theta)\|} \quad (7)$$

The posterior PDF can be expressed as follows, based on the chosen likelihood function (error functions) and prior PDF:

$$p(\theta|\mathbf{d}) \propto \exp\left(-\frac{1}{2} J(\theta, \mathbf{d})\right) \quad (8)$$

where $J(\theta, d)$ is:

$$J(\boldsymbol{\theta}, \mathbf{d}) = \sum_{i=1}^m \frac{(e_{\lambda_i})^2}{\sigma_{\lambda_i}^2} + \sum_{i=1}^m \frac{\mathbf{e}_{\Phi_i}^T \cdot \mathbf{e}_{\Phi_i}}{\sigma_{\Phi_i}^2} \tag{9}$$

where m is the number of modes considered, the standard deviation of the i th frequency is denoted by σ_{λ_i} and the standard deviation of mode shape components for i th mode is σ_{Φ_i} .

Computing the posterior joint and marginal PDFs in most common situations involving many parameters requires calculating high-dimensional integrals. In order to solve this problem, asymptotic expressions or sampling methods like Markov-chain Monte Carlo (MCMC) methods and its variants, such as transitional MCMC and delayed-rejections adaptive Metropolis–Hastings MCMC, are frequently employed.

In an initial updating stage, the initial values of the model parameters $\theta^{initial}$ are considered as the most probable prior point for the set of the updating parameters. For the next updating steps, it is proposed to consider the MAP estimate values of the model parameters θ obtained in the previous updating step as the mean of the prior PDF of θ of the current time. This is consistent with the structure’s progressive damage pattern: only data gathered in that particular damage state are used to obtain the posterior PDF of θ in each time t_k , but because the structure was already compromised in the previous time t_{k-1} , it is reasonable to use the previous damage state’s MAP estimate values of the parameters as the mean prior values of the current state. Over the course of the calibration, the form or shape of the prior PDF is maintained. This prevents the prior PDF from getting narrower and narrower, which might lead to skewed results in the updating method.

3 Application Example

3.1 Description of the Structure and Nonlinear FE Model

The structure to be investigated is the SAC-LA9 building, a 9-story special moment resisting frame (SMRF) building researched under the SAC venture [12]. The OpenSees [13] software is used to create a nonlinear FE model of the building, consisting of nine stories, one basement and 5 bays. The story heights, bay widths and cross section of all the elements are represented in Fig. 3. Beams are made of A36 steel while columns are made of A572, and fully constrained beam-to-column connections and rigid end zones are modeled at the ends. To model beam-column elements, a displacement-based (DB) formulation is used, considering Gauss–Lobatto quadrature with 5 integration points (IPs) for plastic hinges (PHs) and 3 IPs for non-PH elements for each member of the building model. The webs of the cross-sections of the columns acting on their strong axis are discretized into six fibers along the length and one fiber along the width, with a single fiber utilized for each flange, while the

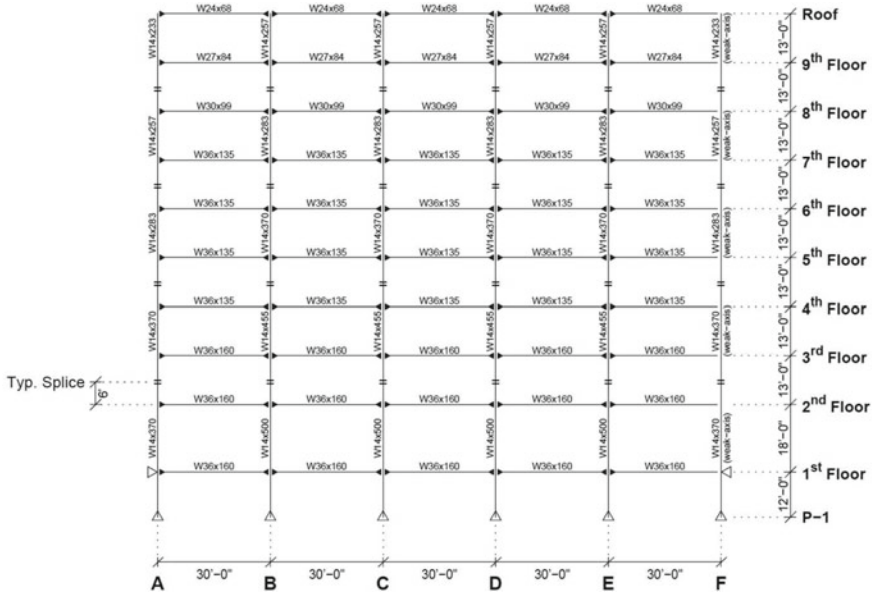


Fig. 3 SAC-LA9 building structure [12]

flanges of the cross-sections of the columns acting on their weak axis are discretized into ten fibers along the length and one fiber across the width, considering the webs with a single fiber. The cross-sections of the beams are discretized into 10 fibers along the length and one fiber across the width, with a single fiber representing each flange.

Modelling the nonlinear response of structural steel using the Giuffre-Menegotto-Pinto (GMP) material constitutive law [14] has proven to be very effective. The GMP model considers ten constant material parameters and material history variables that are modified at every strain reversal. The ten material parameters are divided into four main variables that control the monotonic stress–strain curve and six secondary parameters that control the evolution of cyclic stress–strain behavior, specifically the curvature of the transition from elastic to plastic behavior and isotropic stiffening for each branch of the hysteresis loops produced by the stress–strain cycles. The elastic Young’s modulus (E_0), initial yield stress (σ_y), strain hardening ratio (b), and a parameter (R_0) characterizing the curvature of the transition curve between the elastic and plastic branches during the first loading are the four major parameters. To simulate the uniaxial behavior of steel fibers in columns and beams, the uniaxial GMP material model with the following parameters is used: $E_0^{col} = E_0^{beam} = 200$ GPa, $\sigma_y^{col} = 345$ MPa, $\sigma_y^{beam} = 250$ MPa, $b^{col} = 0.08$, $b^{beam} = 0.05$, $R_0^{col} = 20$, and $R_0^{beam} = 18$. Also, linear elastic section shear force–deformation model is aggregated, but uncoupled with the inelastic flexure-axial behavior, along the element’s length.

The nodal masses on beams are determined from the design dead and live loads specified in FEMA-355C and the P– Δ approximation is used to account for nonlinear

geometry. Besides hysteretic energy dissipated by the material inelastic action, mass and tangent stiffness-proportional Rayleigh damping with a critical damping ratio of 2% for the first two natural periods (gravity loads applied) is assumed. In this nonlinear model, $T_1 = 2.07$ s and $T_2 = 0.70$ s are the periods of the first two initial modes.

3.2 System Identification Results and Earthquake Excitation

As mentioned before, the DSI method is employed to extract the instantaneous structural properties from input–output data collected from a real specimen using sensors. However, in this case, modal properties such as natural frequencies and mode shapes of the building are simulated analytically using the software OpenSees [13]. Note that the nonlinear behavior of the FE model implies variation of the stiffness matrix of the structure, and therefore the modal parameters change along the earthquake loading.

The natural frequencies and mode shapes of the first three modes are the dynamic properties simulated from the 9-story building model. The nodes considered to obtain the modal shapes are the nodes on each level of the building’s left column or the A axis in Fig. 3. The ground-motion measures at Los Gatos station during the Loma Prieta 1989 earthquake is used as seismic base excitation. The total duration of the input motion is 12 s, and the “identification” process is considered with a sampling time $dt = 0.02$ s, with a total of 600 points along the entire duration. Figure 4 shows the input excitation and the variation of the natural frequencies of the structure (normalized by their initial value) along the time.

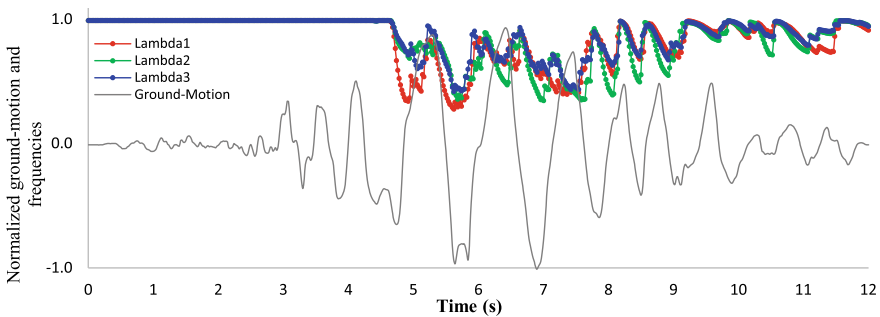


Fig. 4 Normalized input-motion (Los Gatos station) and “identified” natural frequencies

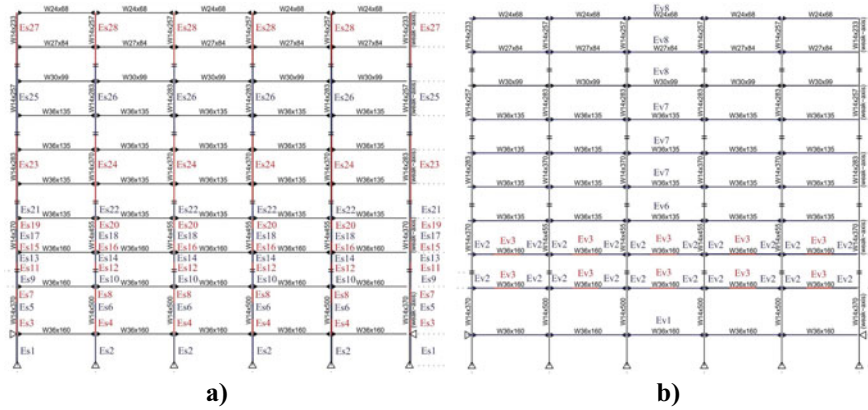


Fig. 5 Element discretization of the linear SAC-LA9 FE model **a** columns, **b** beams

3.3 Linear FE Model

The nonlinear FE model of the SAC-LA9 building detailed in Sect. 3.1, is simplified into an equivalent linear FE model. This linear model is updated using the time-varying modal parameters “identified” from the input–output data recorded in the structure.

All the energy dissipated by hysteretic cycles and non-linearity, as well as the structural damage caused by plastic deformations in some elements produced by the earthquake excitation, is modeled by a degradation in the modulus of elasticity of the damaged elements. The discretization of the linear FE model was based on engineering criteria, which included combining certain elements of the building that shared physical characteristics such as the same cross-section and type of steel, and the elements that are more likely to present damage due to the configuration of the earthquake-resistant design, which is based on a moment resisting frame that is designed to dissipate energy through plastic deformations at the ends of the beams and at the base of the first-floor columns. Considering these aspects, the discretization of the linear FE model of the SAC-LA9 building considers 36 parameters, including column stiffnesses $Es_1, Es_2, \dots, Es_{28}$ and beam stiffnesses Ev_1, Ev_2, \dots, Ev_8 . The distribution of these parameters is shown in Fig. 5.

3.4 Sensitivity Analysis

As introduced in Sect. 2.3, GSA was conducted on the equivalent linear FE model of the SAC-LA9 building, with the purpose of establishing a hierarchy of influence among the model parameters. The Matlab library UQlab [15] was used to handle the execution of the analysis presented in this section.

For simulations, the Young’s modulus of the 36 elements (see Fig. 5) was sampled with a Lognormal distribution with mean of 200 GPa and standard deviation of 40 GPa. The range of modal responses of the model is spread about the mean parameter response as expected because of the linear formulation. Total Sobol’s indices obtained for each parameter for the first three modes (λ and mode shapes) are shown Fig. 6 along with the modal responses simulated for analysis.

It can be observed in Fig. 6 that the beams corresponding to $Ev7$ and $Ev8$ have the most influence in the model variability, with the remaining beams showing this influence on a lesser extent. Due to the design criteria, column sections are notoriously stronger than those of beams. Additionally, the grouping of beams across several stories implies that a potentially larger number of elements was affected by the variations on beam stiffness parameters. For these two reasons, it could be expected that a variation in the stiffness of beams would have a greater impact on the overall stiffness of the linear model. Analogously, in the non-linear model of the building, the yield strength of beams’ reinforcing steel is lower than that of columns’, thus inducing plastic deformations in beams that could notoriously affect the modal properties of the building.

More in detail regarding beam elements, $Ev8$ was assigned to all beams on the upper 3 stories, while $Ev7$ was assigned to stories 5, 6, and 7. As a result, $Ev7$ greatly influenced the first mode shape, while $Ev8$ controlled the second mode shape which depends more on the stiffness of upper stories.

The lower stories of the model were divided into $Ev1$ to $Ev6$; therefore, a smaller portion of the beams was associated with each of them than with the upper-story beams. Nevertheless, the influence of these beams was still relevant to the modal response -especially to the first and third modes as discussed-, and thus they were included in model calibration.

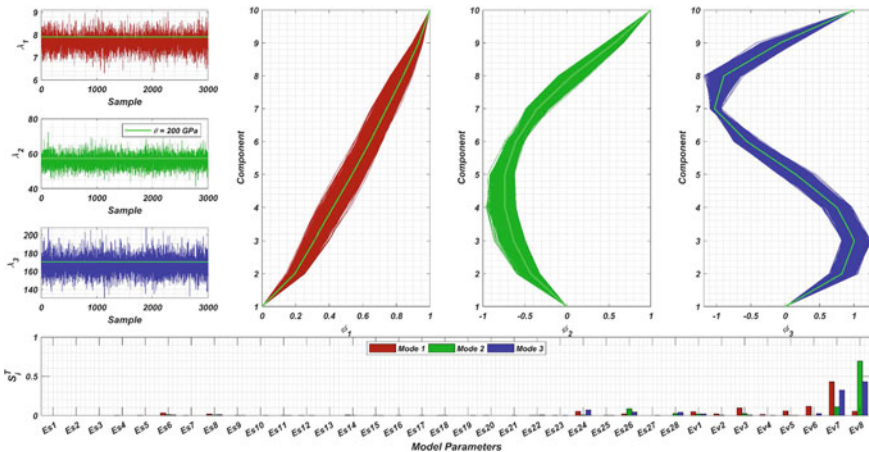


Fig. 6 Total Sobol’s indices for the first three modes (λ and mode shapes) of the linear FE model

With respect to the columns, it can be observed that *Es6*, *Es8*, *Es24*, *Es26*, and *Es28* have the most notorious influence on the modal responses. It is worth noting that *Es6* and *Es8* correspond to the segments of the first story's interior columns, so intuitively the change on their stiffness would induce change on the first mode, which was reflected on their Sobol's indices. Similarly, while *Es14* did not present a high index, it was still noticeable despite the small section associated with it.

Finally, *Es24*, *Es26*, and *Es28* comprise the interior columns of stories 5 to 10, thus making up for most of the column sections in the model. Consequently, the influence of these parameters could be appreciated for the three modes analyzed, with *Es28* having the least influence on mode 1 because it is linked to the upper stories, which was consistent with the indices for the beams in those stories.

A total of 14 out of the 36 parameters were selected for estimation including all beam stiffnesses *Ev1-Ev8*, as well as column stiffnesses *Es6*, *Es8*, *Es14*, *Es24*, *Es26* and *Es28*.

3.5 Model Updating Results

The Bayesian updating technique is performed to quantify the uncertainties and localize the damages in the SAC-LA9 model given a set of parameters. To accomplish so, the modulus of elasticity of steel material of the 14 selected elements of the linear FE model are used as the updating parameters, which are defined as the ratio of updated to initial elastic modulus:

$$\theta_i = \frac{E_i^{Updated}}{E_i^{Initial}} \text{ with } i = 1, \dots, 14 \quad (12)$$

The calibration of the model is considered at every 0.2 s, from $t = 4.6$ s to $t = 11.0$ s of the input ground motion, however, a preliminary calibration is performed in order to determine the initial values $\theta^{initial}$. The priors PDFs are considered as lognormal distributions, assuming independent parameters and $E_i^{initial} = 200$ GPa for all the parameters. As explained before, for the following updating times, the mean of prior PDFs of the current time are constructed using the peak values of the posterior PDFs of the previous updating time, taking into account the degradation produced before. The standard deviation of the parameters θ is considered as the 15% of the initial value of the mean, and is maintained throughout the entire calibration, preventing the use of very narrow PDFs for the prior PDFs. The likelihood data simulated analytically from the nonlinear FE model of the SAC-LA9 building are utilized to calibrate linear model parameters θ , which consists of a number of modal properties, such as natural frequencies and modal shapes of the structure considering the first three modes. In order to do so, Sequential Monte Carlo (SMC) sampling is used with a total of 3200 samples per updating time.

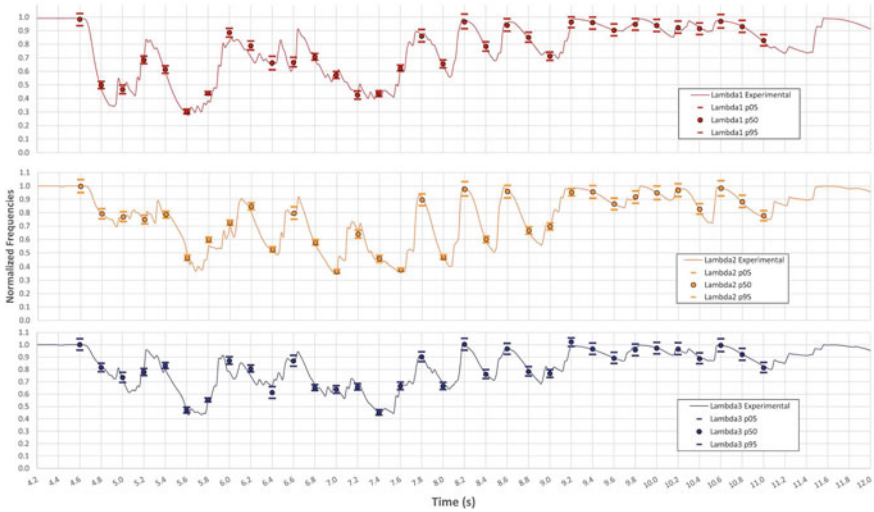


Fig. 7 Model updating results

From the posterior PDFs obtained of the model parameters θ , 1000 responses are generated each updating time in order to propagate the uncertainty of the parameters in the model’s response. The results of the natural frequencies obtained can be seen in Fig. 7, where the “experimental data” (i.e., nonlinear FE model) considered is the continuous line, while the linear model’s response obtained using the model updating results are the values of the percentiles 5, 50, and 95 considering the 1000 responses.

The obtained posterior distributions are less variable than the prior PDFs, indicating that the measured data provides information about the updating parameters. It is also worth mentioning that the data are limited when it refers to the building’s columns. The uncertainty in the modulus of elasticity parameters that characterize this region could not be decreased using the available data. The beam elements, on the other hand, are well resolved by the data, attributed to higher damage level and larger modal curvatures in these parts of the structure, having narrower posterior PDFs than the other parameters. Considering the p50 value obtained versus the experimental data, the average error considering all the time and the three frequencies is 2.17%, with a peak of 14.59% for the first mode at 5.8 s.

4 Conclusions

Bayesian linear finite element model updating in a 9-story steel building subjected to the Los Gatos ground motion is employed to quantify uncertainty and localize damage. To do so, a short-time windowing technique can be used to identify the structure’s instantaneous modal properties employing the deterministic-stochastic

subspace identification method using input–output acceleration data during the earthquake. However, in this case, the first three natural frequencies and mode shapes of the building are simulated analytically using the software OpenSees considering tangent stiffness-proportional Rayleigh damping and a non-linear FE model. The difference between the model-predicted and identified modal parameters is specified as the error function in the Bayesian FE model updating technique and the MAP estimate at the previous updating time t_k is adopted as the mean value of prior PDF of the current updating time. The modulus of elasticity of the elements of the building is chosen as the updating parameter. Finally, the posterior PDF of the parameters is estimated considering the SMC approach.

Even when updating 14 parameters are considered, the Bayesian method agrees quite well with the simulated results. For this study, the results are very similar to the “experimental data” confirming that the approach provides accurate results and is able to identify and localize the damage in the 9-story building while also quantifying the corresponding uncertainties.

Acknowledgements The authors acknowledge the financial support from the Chilean National Agency for Research and Development (ANID), through FONDECYT research grant No. 1200277.

References

1. Friswell M, Mottershead J (1995) Finite element model updating in structural dynamics. Kluwer, Dordrecht
2. Teughels A, Maeck J, De Roeck G (2002) Damage assessment by FE model updating using damage functions. *Comp Struct* 80(25):1869–1879
3. Tobita J, Izumi M, Katukura H (1988) Identification of biration systems and the nonlinear dynamics characteristics of structures under earthquake excitations. In: 9th world conference on earthquake engineering. Tokyo, Japan
4. Moaveni B, Asgari E (2012) Deterministic-stochastic subspace identification method for identification of nonlinear structures as time-varying linear systems. *Mech Syst Signal Process* 31:40–55
5. Astroza R, Gutierrez G, Repenning C, Hernández F (2018) Time-variant modal parameters and response behavior of a base-isolated building tested on a shake table. *Earthq Spectra* 34(1):121–143
6. Peeters B, De Roeck G (2001) One-year monitoring of the Z24-bridge: Environmental effects versus damage events. *Earthq Eng Struct Dyn* 30:149–171
7. Sobol IM (2001) Global sensitivity indices for nonlinear mathematical models and their Monte Carlo estimates. *Math Comput Simul* 55(1–3):271–280
8. Sudret B (2008) Global sensitivity analysis using polynomial chaos expansions. *Reliab Eng Syst Saf* 93:964–979
9. Beck J, Katfygiotis L (1998) Updating models and their uncertainties. *J Eng Mech* 124(4):455–461
10. Akhlaghi M, Bose S, Moaveni B, Stavridis A (2018) Bayesian model updating of a damaged school building in Sankhu, Nepal. *Model Valid Uncertain Quantif* 3:235–244
11. FEMA-335C (2000) State-of-the-art report on systems performance of steel moment frames subjected to earthquake ground shaking, SAC Joint Venture for the Federal Emergency Management Agency, Washington, DC

12. McKenna F, Fenves G, Scott M, Jeremic B (2000) Open system for earthquake engineering simulation (Opensees). University of California, Berkeley, Pacific Earthquake Engineering Research Center
13. Filippou F, Popov E, Bertero V (1983) Effects of bond deterioration on hysteretic behavior of reinforced concrete joints. Report EERC 83-19. University of California, Berkeley, Earthquake Engineering Research Center
14. Marelli S, Sudret B (2014) UQLab: a framework for uncertainty quantification in Matlab. In: 2nd international conference on vulnerability, risk analysis and management (ICVRAM2014). Liverpool (UK)

Ambient Vibration Based Modal Analysis and Cable Tension Estimation for a Cable-Stayed Bridge with Bayesian Approaches



W. J. Jiang, Chul-Woo Kim, Xin Zhou, and Yoshinao Goi

Abstract This study aims to investigate ambient vibration based modal analysis and cable tension estimation with Bayesian approaches, associating with an ambient vibration testing in a cable-stayed bridge. Firstly, a Bayesian fast Fourier transform (FFT) is introduced to the target bridge for operational modal analysis using ambient vibration data. Considering a mixing effect of local modes and global modes in the vibration measurements of cables, the identification is implemented in three scenarios: global modal analysis without data of cables, global modal analysis with data of cables, local modal analysis of each cable. The effects of involving measurements of cables into the global modal analysis of the whole bridge are discussed, and the identification uncertainty of modal frequencies in each scenario is investigated. Then, considering the identified modal frequencies of multiple modes in each cable, a Bayesian cable tension estimation framework including a Bayesian linear regression (BLR) is proposed, with the ability of simultaneously estimating the cable tension and flexural rigidity in a probabilistic way. The estimation is conducted with the identification results by both ambient vibration and hammer test. The results showed different accuracy and uncertainty in the estimation of cable tension and flexural rigidity, as well as among different cable conditions.

Keywords Ambient vibration · Cable-stayed bridge · Modal analysis · Bayesian FFT · Bayesian cable tension estimation

1 Introduction

With excellent performance to realize long-span crossing, cable-stayed bridge is widely constructed around the world in the past few years. The stayed cable, as a crucial component connecting bridge deck with tower in cable-stayed bridge, is always faced with a long-term deterioration caused by traffic, ambient vibration,

W. J. Jiang · C.-W. Kim (✉) · X. Zhou · Y. Goi

Department of Civil & Earth Resources Engineering, Graduate School of Engineering, Kyoto University, Kyoto, Japan

e-mail: kim.chulwoo.5u@kyoto-u.ac.jp

© The Author(s), under exclusive license to Springer Nature Switzerland AG 2023
Z. Wu et al. (eds.), *Experimental Vibration Analysis for Civil Engineering Structures*,
Lecture Notes in Civil Engineering 224,
https://doi.org/10.1007/978-3-030-93236-7_31

365

corrosion, fatigue, etc. Therefore, it is well-acknowledged that the monitoring of cable is of great meaning for the safety and maintenance of cable-stayed bridge. There have been many researches on the structural health monitoring (SHM) of cable-stayed bridge [1, 2]. Among those studies, the dynamic characteristics and cable tension are generally valued as informative features reflecting the condition of cable and whole bridge.

To get the dynamic characteristics of cable and bridge, field test is required. From the view of accuracy in structural identification, a hammer test or a weight-drop-off test may be a choice (despite in some large bridge the artificial excitation may be deficient). However, from the view of convenience in conducting long-term SHM, ambient vibration based modal analysis played a more important role due to its release of artificial excitation and continuity. Various methods have been proposed for ambient vibration based modal analysis, like frequency domain decomposition (FDD), stochastic subspace identification (SSI), a series of Bayesian operational modal analysis (BAYOMA) methods, etc., which make the output-only system identification (general case in ambient vibration) efficient and flexible. Compare to cable dynamics, cable tension is a more intuitional mechanical feature for assessing the cable and bridge state. Thus, based on the relation between modal frequency and cable tension, there are also some studies on the vibration-based cable tension estimation [3, 4].

However, in the entire process as above, some issues remained and heavily affected the reliability of SHM using ambient vibration. Firstly, the cable-stayed bridge is a complex structure incorporating both global modes of bridge and local modes of cable under ambient vibration. The interactive influence between the global modes and local modes will augment the uncertainty in the structural identification, especially in the cable. Secondly, due to lack of input information, low signal-to-noise ratio (SNR), model assumptions, etc., the identification uncertainty may increase in the operational modal analysis and pollute the damage effect. Then, even though the previous study [5] well demonstrated the feasibility of vibration based cable tension estimation using hammer test, the increased uncertainty in ambient vibration based modal analysis may seriously reduce the reliability of cable tension estimation since the estimate tends to be sensitive to the identification uncertainty. Therefore, with a concern on these issues of the uncertainty and accuracy in particular, this paper presents a study on the modal analysis and cable tension estimation in a cable-stayed bridge under ambient vibration and Bayesian framework.

2 Theoretical Basis

2.1 *Fast Bayesian FFT*

As one of the Bayesian operational modal analysis methods possessing the ability of uncertainty measurement, a fast Bayesian FFT approach [6, 7] is introduced here.

By associating Bayesian inference with the FFTs of vibration response, Bayesian FFT gives a basic form as

$$p\left(\theta \mid \left\{ \hat{F}_k \right\}\right) = \frac{p\left(\left\{ \hat{F}_k \right\} \mid \theta\right) p(\theta)}{p\left(\left\{ \hat{F}_k \right\}\right)} \tag{1}$$

where θ denotes the system parameters of the structure to be identified, and \hat{F}_k are the estimated FFTs data at different frequencies f_k .

Then, given that the FFTs are Gaussian and independent at different frequencies, it can be written as

$$p\left(\theta \mid \left\{ \hat{F}_k \right\}\right) \propto p\left(\left\{ \hat{F}_k \right\} \mid \theta\right) = \frac{\pi^{-nN_f}}{\prod_k |E_k(\theta)|} \exp\left[-\sum_k \hat{F}_k^* E_k(\theta)^{-1} \hat{F}_k\right] = e^{-L(\theta)} \tag{2}$$

where

$$E_k(\theta) = E\left[F_k F_k^* \mid \theta\right] + E\left[\varepsilon_k \varepsilon_k^* \mid \theta\right] = \sum_{i=1}^r \sum_{j=1}^r h_{ik} h_{jk}^* S_{ij} \varphi_i \varphi_j^T + S_e I_n \tag{3}$$

is the theoretical power spectral density (PSD) matrix of data at the kth FFT for given θ . And

$$L(\theta) = nN_f \ln \pi + \sum_k \ln |E_k(\theta)| + \sum_k \hat{F}_k^* E_k(\theta)^{-1} \hat{F}_k \tag{4}$$

is the ‘negative log-likelihood function’ (NLLF), and the most probable value (MPV) $\hat{\theta} = \arg \min_{\theta} L(\theta)$.

Here, the system parameter θ comprises modal frequencies $f_{i=1}^r$ and modal damping ratios $\zeta_{i=1}^r$ denoted in transfer functions h_{ik}^r corresponding to each mode, partial mode shapes $\varphi_{i=1}^r$, PSD matrix of modal forces $S = [S_{ij}]_{r \times r}$, and the PSD matrix of prediction errors $S_e I_n$. In addition, r represents the number of dominant modes in a specified frequency band where the estimation is conducted. n is the number of sensors to collect the ambient vibration response. N_f is the number of FFT points in the specified frequency band.

It has been demonstrated that the posterior PDF can be well approximated as a Gaussian form for typical data size. Au [7] showed that a second-order Taylor approximation of the NLLF at the MPV engenders a Gaussian approximation of the posterior PDF as

$$p(\theta | \{\hat{F}_k\}) \approx (2\pi)^{-n_\theta/2} |\hat{C}|^{-1/2} \exp\left[-\frac{1}{2}(\theta - \hat{\theta})^T \hat{C}^{-1}(\theta - \hat{\theta})\right] \quad (5)$$

where $\hat{\theta}$ is the MPV, and \hat{C} denotes the posterior covariance matrix which is the inverse of the Hessian of NLLF at the MPV. Also, n_θ represents the number of parameters in θ . The posterior covariance matrix \hat{C} can provide useful information reflecting the identification uncertainty.

2.2 Modal Frequency Versus Cable Tension

Given some assumptions, the relation between modal frequency of cable and cable tension can be derived from the free vibration differential equation of cable as below.

$$m \frac{\partial^2 v(x, t)}{\partial t^2} + EI \frac{\partial^4 v(x, t)}{\partial x^4} - T \frac{\partial^2 v(x, t)}{\partial x^2} - h(t) \frac{\partial^2 v(x, t)}{\partial x^2} = 0 \quad (6)$$

where $v(x, t)$ denotes the vertical vibration deflection, x is the cable longitudinal coordinate and t denotes time. The symbol m is the mass of cable per unit length, EI denotes the flexural rigidity of cable and T is the cable tension force. The notation $h(t)$ is the derivative cable tension force caused by vibration.

According to [3], the influence of vibration-induced derivative cable tension $h(t)$ and the cable sag is generally small and ignorable for simplicity. Then, given that the boundary condition is hinged support, the solution of Eq. (6) can be presented as follows.

$$\left(\frac{f_i}{i}\right)^2 = \frac{\pi^2 i^2}{4ml^4} EI + \frac{1}{4ml^2} T \quad (7)$$

where i is mode order and f_i denotes the i th modal frequency of cable; l is the length of cable.

Then, when the cable vibration is more similar to a string (the contribution of EI on modal frequency is rather small), the equation can be further simplified as

$$\left(\frac{f_i}{i}\right)^2 = \frac{1}{4ml^2} T \quad (8)$$

Generally, Eqs. (7) and (8) can be regarded as hinged beam model and string model, respectively, depending on the feature of cable vibration. To see whether the cable performs like a beam or a string, a parameter can be referred as below.

$$\xi = \sqrt{\frac{T}{EI}} \cdot l \tag{9}$$

where, the larger the value of ξ is, the more similar to a string the cable performs.

2.3 Bayesian Cable Tension Estimation

With multiple modal frequencies of cable identified, the estimation of cable tension from Eqs. (7) and (8) can be treated as a regression issue.

Given that a basic form of Bayesian linear regression (BLR) model can be denoted as below.

$$y = X\beta + \varepsilon, \varepsilon \sim N(0, \sigma^2) \tag{10}$$

where y is a $n \times 1$ vector of response variable; X is a $n \times d$ matrix of predictor variables; β is a $d \times 1$ vector of coefficients; ε denotes the *iid* error term which obeys a normal distribution with zero mean and variance σ^2 for each observation; n is the number of observations, and d is the number of predictor variables.

Then, the posterior distribution of (β, σ^2) can be obtained by Bayesian reference like

$$p(\beta, \sigma^2 | y, X) = \frac{p(y | X, \beta, \sigma^2) \cdot p(\beta, \sigma^2)}{p(y | X)} \tag{11}$$

Further, the marginal posterior of β can be given as

$$p(\beta | y, X) = \int p(\beta, \sigma^2 | y, X) d\sigma^2 \tag{12}$$

Given a Jeffreys non-informative prior

$$p(\beta, \sigma^2) \propto \frac{1}{\sigma^2} \tag{13}$$

the marginal posterior of β is analytically tractable and follows a d dimensional *t-location-scale* distribution as

$$\beta \left| y, X \sim t_d \left(\hat{\beta}, \frac{(y - X\hat{\beta})'(y - X\hat{\beta})}{n - d} (X'X)^{-1}, n - d \right) \tag{14}$$

where the three parts in the right hand are the location parameter, scale parameter, degree of freedom, in sequence. The notations (y, X, β, n, d) are the same as before, while $\hat{\beta}$ is the least-squares estimate of β with a form as follows.

$$\hat{\beta} = (X'X)^{-1} X'y \tag{15}$$

Without loss of generality, taking Eq. (7) into the form as Eq. (10), a Bayesian cable tension estimation framework can be established with

$$y = \left\{ \left(\frac{f_i}{i} \right)^2 \right\}_{n \times 1}, X = \begin{bmatrix} \frac{\pi^2 i^2}{4ml^4} & \frac{1}{4ml^2} \end{bmatrix}_{n \times 2}, \beta = \begin{Bmatrix} EI \\ T \end{Bmatrix}_{2 \times 1} \tag{16}$$

and the posterior distribution of β contributes to a simultaneous estimation of cable tension and flexural rigidity, along with a depiction of the estimation uncertainty.

3 Vibration Test on Cable-Stayed Bridge

3.1 Field Experiment

The target bridge is a single-tower cable-stayed bridge shown in Fig. 1. The span length of the bridge is about 124 m and tower height is about 48 m (see Fig. 2). A short-term field test including forced excitation test and ambient vibration test was carried out in November, 2020. The corresponding sensor setup and structural layout are shown in Fig. 2. Vibration signals from cables at anchor, cables at bridge deck, bridge deck nodes and a tower node were collected during the test. The forced excitation test was conducted just on the cables, while the ambient vibration test was implemented on the whole bridge involving cables, bridge deck and tower.

Fig. 1 A side view of investigated bridge



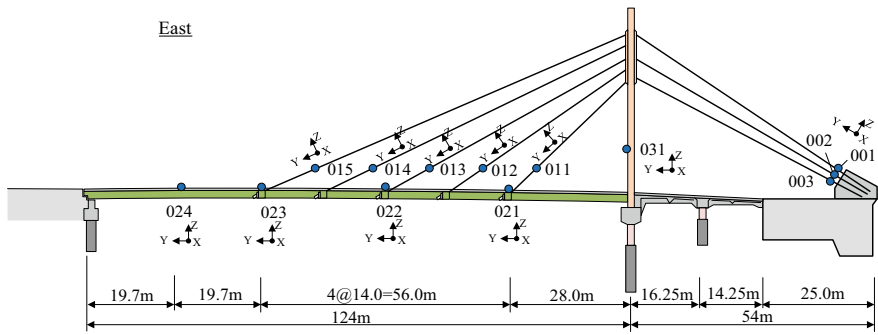


Fig. 2 Bridge layout and sensor deploying map

3.2 Operational Modal Analysis of Bridge

As discussed before, there is an interactive influence between global modes of bridge and local modes of cables. Thus, operational modal analysis (OMA) of the bridge is conducted in two signal scenarios: bridge with cable channels, and bridge without cable channels. To specify a prior set including initial value and frequency band for the optimization algorithm of the fast Bayesian FFT, a singular value spectrum (SVS) as shown in Fig. 3 is used. A peak in the highest spectral line of SVS indicates a possible modal frequency. More information about use of SVS in the fast Bayesian FFT can be found in [7].

Figure 4 showed a comparison of the identified modal frequencies of the whole bridge with and without signals from cable channels. It can be noted that the identification uncertainty is low, and the error between two signal scenarios is also small in lower modes while increasing in some higher modes. This phenomenon indicated

Fig. 3 Singular value spectrum of signal set from bridge deck nodes

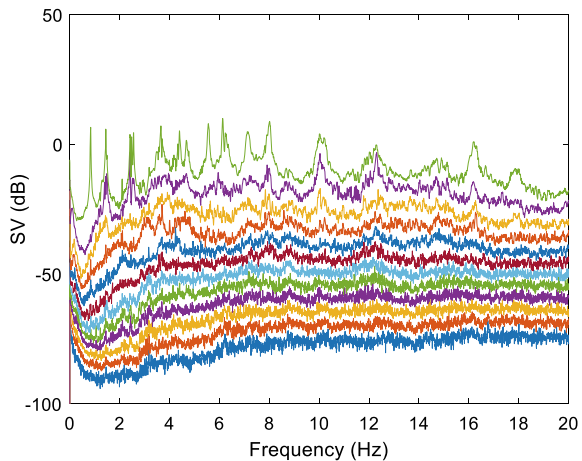
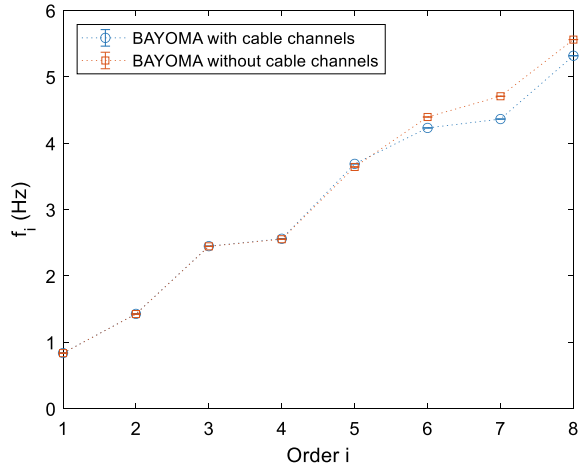


Fig. 4 Comparison of OMA results for bridge with and without signal from cables



that the OMA of the whole bridge under ambient vibration is of efficacy, and the interference from the local modes of cables only makes a clear difference in some higher global modes of bridge under ambient vibration.

3.3 Modal Analysis of Cables

Three cables with sensors are considered in this paper to simplify the discussion even though vibrations of all the cables were examined. A cable at the anchor, the shortest cable at bridge deck and the longest cable at bridge deck are selected, and each cable is named as cable 001, cable 011, cable 015 respectively as shown in Fig. 2.

To specify a prior set about the initial value and frequency band for the fast Bayesian FFT, a power spectral density (PSD) plot along with the highest spectral line in SVS of bridge to help eliminate some fake peaks caused by the global modes of bridge is given as shown in Fig. 5. Comparing with the SVS, it can be noted that some global modes in SVS also appear in the PSD of cables, which will affect the identification about local modal frequency of cables and further affect the accuracy of vibration-based cable tension estimation. In addition, observations on the PSDs of three cables show different SNRs in three groups of cables, and further different accuracy of OMA. The PSD curve of the cable at anchor indicated a low SNR due to weak ambient excitation comparing to the cables at the bridge deck. The short cable at bridge deck performs better since the higher ambient excitation comparing to the cable at the anchor. The long cable at bridge deck shows clear PSD peaks as a result of higher ambient excitation.

As mentioned previously, the forced excitation test was also conducted in the cables. Generally, the forced excitation test is believed to offer a modal identification with higher accuracy and lower uncertainty compared to the ambient vibration test,

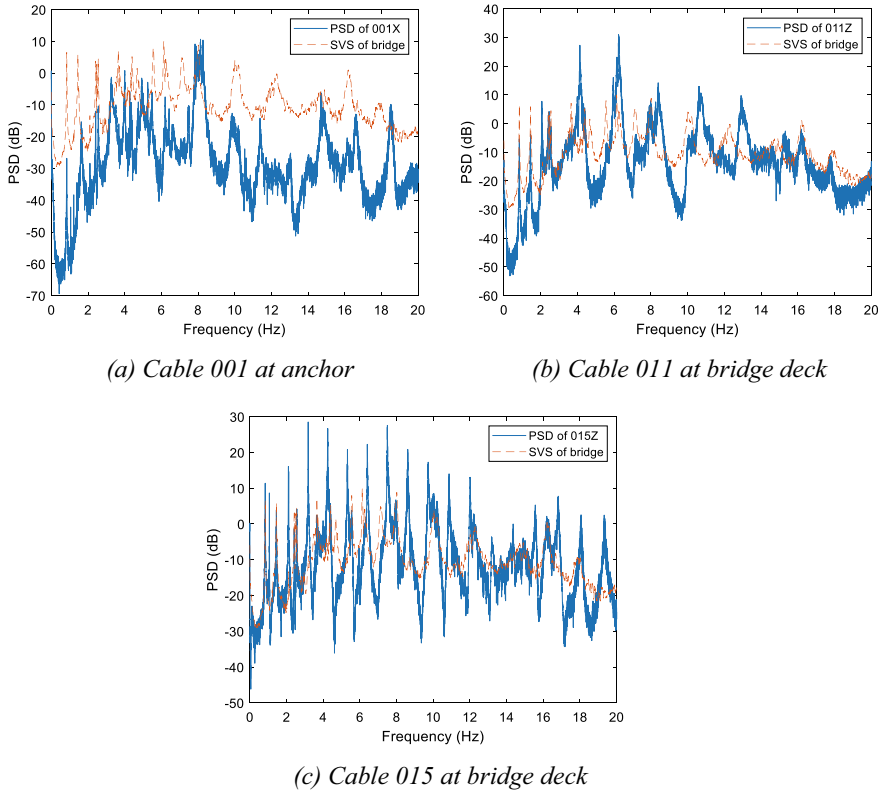


Fig. 5 PSDs of three cables under ambient vibration

since the strength and frequency domain feature of the forced excitation is more ideal than the ambient vibration test. Another reason is that, the forced excitation test just excites local vibration of cable, while ambient vibration of cable is mixed with interference from global vibration for the bridge. Therefore, taking the forced excitation test results as a reference, the fast Bayesian FFT results of cables under ambient vibration are summarized in Fig. 6.

As shown in Fig. 6, the identification performances of each cable by means of the fast Bayesian FFT were different in comparison to the forced excitation test results. Generally, the identification uncertainty from the ambient vibration was rather small, but clear difference between the fast Bayesian FFT (denoted as BAYOMA in Fig. 6) and the forced excitation test was in some higher modes: 8, 9 and 10th modes of Cable 001 at the anchor and Cable 011 at the bridge deck. Good consistency was observed in lower modes of the cables at bridge deck, except for the identified 1st modal frequency by the fast Bayesian FFT which is close to the global modal frequency of the bridge deck. This phenomenon indicated the 1st modal frequency in the cable at the bridge deck is apt to be polluted by the global vibration of the bridge under

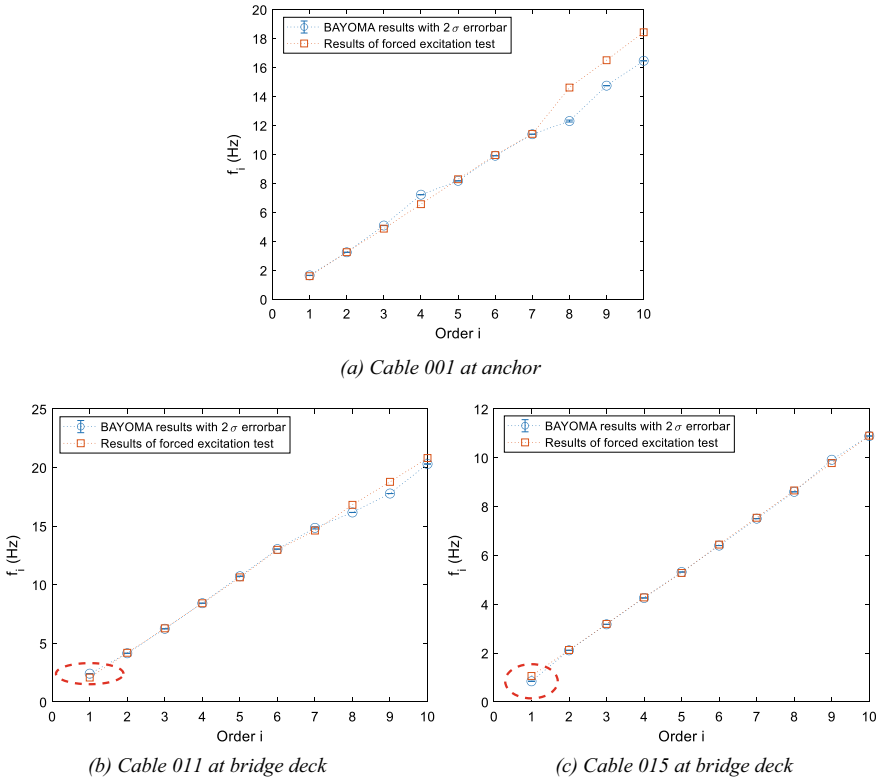


Fig. 6 Identified modal frequency w.r.t. mode order for three cables

ambient vibration. In further research of cable tension estimation, these polluted results need to be removed. Hence, modal frequencies from 2nd to the 6th modes are considered in the cable tension identification. On the other hand, it is noted that while the interference of global vibration of the bridge deck is small in the cable at the anchor, the inconsistency in lower modes indicated a lower accuracy of identification in this cable.

3.4 Estimation of Cable Tension

With the identified modal frequencies of cables, Bayesian cable tension estimation is carried out. Because there is no direct and real-time cable tension measurement of the target bridge, the original design value of cable tension and calculated flexural rigidity with approximate cross-section are taken as a reference value. In addition, since the good performance of the forced excitation test in the modal analysis, the estimation from data of the forced excitation test is taken as another reference values.

Those two reference values from design and the forced vibration test are named as “R1” and “R2” respectively.

According to Eq. (7), there is a linear relation between $(f_i/i)^2$ and i^2 for the hinged beam model. Then, with the BLR model, cable tension and flexural rigidity can be simultaneously estimated. Figure 7 showed the observations and fitted line by BLR in three cables. It can be noted that generally a linear relation can be observed in both the Bayesian FFT results and the forced excitation test results, except for the Bayesian FFT results in the cable at the anchor which indicated a high identification uncertainty.

The posterior estimate of flexural rigidity EI and cable tension T is summarized in Tables 1 and 2, respectively. It can be noted that generally the MPV of posterior estimate of EI showed a large deviation to the value of both R1 and R2, while the posterior estimate of T performed much better. This observation indicated that the estimate of EI is more sensitive to the uncertainty in the ambient vibration based modal analysis than T , which indicates the cable vibration of the bridge is more similar to a string model than to the hinged beam model when we consider the frequencies up to 10th modes.

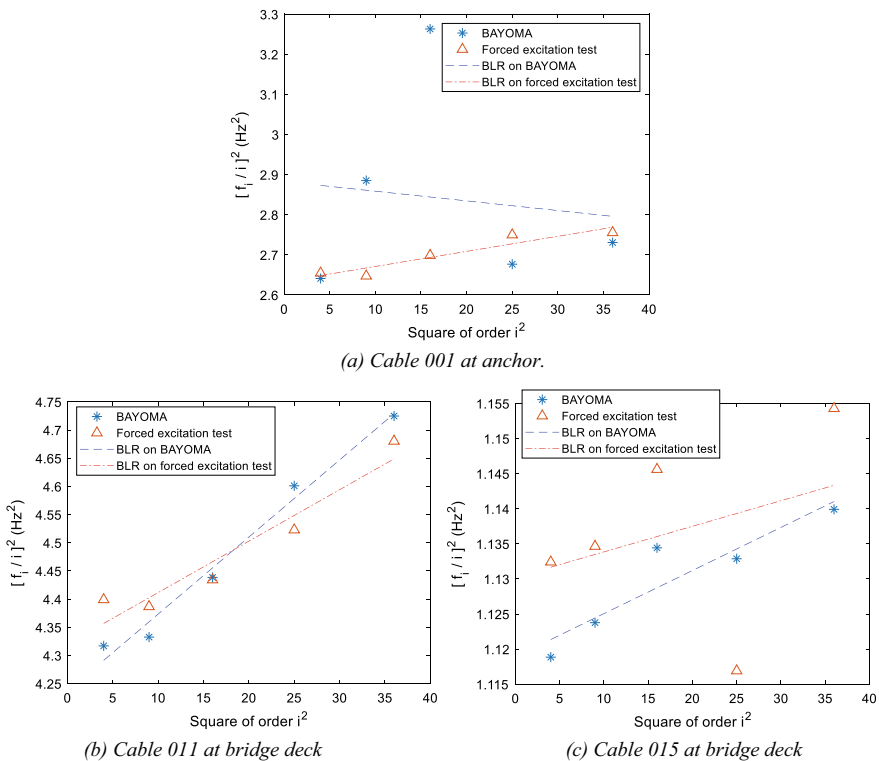


Fig. 7 Observations and BLR fitted line with a hinged beam model in three cables

Table 1 Posterior estimate of flexural rigidity in three cables using hinged beam model

Cable	Bayoma		Forced excitation test (R2)		Design (R1)	Relative error R2 (%)	Relative error R1 (%)
	EI (kN·m ²)	std (kN·m ²)	EI (kN·m ²)	std (kN·m ²)	EI (kN·m ²)		
001	-1702	13,947	2655	933	10,048	-164.1	-116.9
011	520	70	347	102	2337	49.9	-77.8
015	1174	486	697	1999	6273	68.5	-81.3

Table 2 Posterior estimate of cable tension in three cables using hinged beam model

Cable	Bayoma		Forced excitation test (R2)		Design (R1)	Relative error R2 (%)	Relative error R1 (%)
	T (kN)	std (kN)	T (kN)	std (kN)	T (kN)		
001	4605	673	4206	45	4312	9.5	6.8
011	978	9	997	13	1332	-1.9	-26.5
015	2465	12	2490	49	3057	-1.0	-19.4

The MPV of posterior estimate of T of the cables at the bridge deck resulted in differences of 20–26% comparing to the design values (R1), and that of the cable at the anchor showed 7% difference comparing to the design value (R1). However, those estimated tensions were highly comparable to the estimate from vibrations of the forced excitation test (R2). Meanwhile, a difference between the cable tensions at the anchor and at the bridge deck was observed. For the Cable 011 and Cable 015 at bridge deck, the estimated T showed low posterior uncertainty and was very consistent to those from vibrations of the forced excitation test (R2). But on the other hand, for Cable 001 at the anchor, the estimated of both EI and T showed large posterior uncertainty. Therefore, for the target bridge, it can be concluded that the ambient vibration-based cable tension estimation in the cable at the bridge deck may be more feasible due to higher SNR and accuracy in OMA.

Table 3 showed the posterior estimate of cable tension T using string model (Eq. (8)). It is noted there is no obvious difference compared to the estimate using hinged beam model (see Table 2), which implied a low contribution of flexural rigidity

Table 3 Posterior estimate of cable tension in three cables using string model

Cable	Bayoma	Forced excitation test (R2)	Design (R1)	Relative error R2 (%)	Relative error R1 (%)
	T (kN)	T (kN)	T (kN)		
001	4536	4315	4312	5.1	5.2
011	1034	1035	1332	0.0	-22.3
015	2489	2504	3057	-0.6	-18.6

EI to the modal frequencies of these cables. Besides, the MPV of T using string model resulted in a lower error to both design value R1 and forced excitation test result R2. Actually, unsatisfactory estimate of EI may further decrease the accuracy in estimate of T using hinged beam model. Therefore, string model may be more suitable for the ambient vibration-based Bayesian cable tension estimation in these cables.

4 Conclusions

This paper investigated the performance and uncertainty quantification of ambient vibration based modal analysis and cable tension estimation in a cable-stayed bridge under a Bayesian framework. The uncertainty sources and propagation in this process from original vibration response to operational modal analysis, and further to vibration-based cable tension estimation was discussed. Based on the above investigation, it can be concluded as follows.

- (1) An interactive interference exists between the global modal analysis of bridge and the local modal analysis of cable under ambient vibration, which should be considered in the long-term SHM study using ambient vibration. In particular, the global vibration of bridge affects the accuracy of OMA in 1st modal frequency of cables at the bridge deck.
- (2) Under ambient vibration, the performance of OMA and further cable tension estimation also differs with the cable conditions in cable-stayed bridge. Generally, cable at the bridge deck shows higher accuracy and lower uncertainty in OMA and cable tension estimation than cable at anchor except for a situation that cable at the bridge deck is easy to be perturbed by the global vibration of bridge.
- (3) Under ambient vibrations, the proposed Bayesian cable tension estimation approach shows different accuracy and uncertainty between the posterior estimate of flexural rigidity and cable tension. Generally, the posterior estimate of flexural rigidity presents high uncertainty and low accuracy, while the estimate of cable tension performs better and almost consistent with the estimate by the forced excited vibration. It is noted that when the string model was applied, the difference between design and estimate values were reduced to around 20% for cables at the bridge deck and around 5% for cables at the anchor, which indicates that the cable vibration in target bridge is more similar to a string model than to the hinged beam model.

To sum up, ambient vibration-based SHM in cable-stayed bridge is a complicated issue encountered with various sources affecting the accuracy and uncertainty such as low SNR, deviation with the idealized frequency domain feature of ambient excitation in the fast Bayesian FFT, interference from global vibration of bridge, simplification in the model of cable tension estimation, and so on. It is noted that the environmental variation should be considered as a source of uncertainty in the long-term SHM campaign, which will be discussed in further study.

Acknowledgements This study is partly sponsored by a Japanese Society for the Promotion of Science (JSPS) Grant-in-Aid for Scientific Research (B) under project No.19H02225. That financial support is gratefully acknowledged.

References

1. Sun M, Alamdari MM, Kalthori H (2017) Automated operational modal analysis of a cable-stayed bridge. *J Bridge Eng* 22(12):05017012
2. Ni YC, Alamdari MM, Ye XW, Zhang FL (2021) Fast operational modal analysis of a single-tower cable-stayed bridge by a Bayesian method. *Measurement* 174:109048
3. Zui H, Shinke T, Namita Y (1996) Practical formulas for estimation of cable tension by vibration method. *J Struct Eng* 122(6):651–656
4. Papadimitriou C, Giakoumi K, Argyris C, Spyrou LA, Panetsos P (2016) Bayesian estimation of tension in bridge hangers using modal frequency measurements. *Struct Monitor Mainten* 3(4):349–375
5. Yamagiwa I, Utsuno H, Sugii K, Honda Y (1999) Simultaneous identification of tension and flexural rigidity of cables. Report 49(2). Kobe Steel Engineering Reports
6. Au SK, Zhang FL, Ni YC (2013) Bayesian operational modal analysis: theory, computation, practice. *Comput Struct* 126:3–14
7. Au SK (2017) Operational modal analysis: modeling, bayesian inference, uncertainty laws. Springer, Singapore

Tension Estimation Method for Cable with Damper and Its Application to Real Cable-Stayed Bridge



Aiko Furukawa, Katsuya Hirose, and Ryosuke Kobayashi

Abstract In the maintenance of cable structures, such as cable-stayed bridges and extra-dosed bridges, it is necessary to estimate the tension acting on the cables. The safety of a cable is assessed by comparing the tension acting on the cable and the allowable value. In current Japanese practice, the tension of a cable is estimated using the vibration method or the higher-order vibration method, which considers the natural frequencies of the cable. However, in recent years, the aerodynamic vibration of cables caused by wind has become a problem owing to the recent increase in the cable length and low damping performance of the cable itself. In such a case, dampers are installed onto the cables to suppress the aerodynamic vibration of cables. Because the damper changes the cable's natural frequencies, the vibration and higher-order vibration methods are inappropriate for estimating the tension of a cable with a damper. With this background, the authors developed a tension estimation method for a cable with a damper where a cable is modeled with a tensioned Bernoulli–Euler beam. The theoretical equation is derived, which relates the natural frequencies with the tension and bending stiffness of the cable and damper parameters. The method inversely estimates the tension and bending stiffness of the cable and damper parameters simultaneously from the natural frequencies. In this paper, the authors' tension estimation method is first introduced. Then the validity of the method is shown through numerical simulations. Then the method is verified through a laboratory experiment. Moreover, the field measurements of a cable-stayed bridge in Japan were conducted to verify the method. It was found that the method could estimate the tension of a cable with the damper with high accuracy. In this way, the validity of the method was confirmed.

Keywords Tension estimation · Cable · Damper · Natural frequency · Experiment verification

A. Furukawa (✉) · K. Hirose
Department of Urban Management, Kyoto University, Kyoto, Japan
e-mail: furukawa.aiko.3w@kyoto-u.ac.jp

R. Kobayashi
Kobelco Wire Company, Ltd, Hyogo, Japan

1 Introduction

A cable is known as an efficient structural member to support structures. In civil engineering structures, cables are used for long-span bridges such as cable-stayed bridges and suspension bridges. Since each cable has its strength, the load-bearing capacity of the cable is assessed by comparing the cable's tension with its strength. Therefore, it is necessary to estimate the cable's tension to assess the structural safety in the maintenance. There are two methods to measure cable's tension: a direct measuring method using a load cell or hydraulic jack and a vibration-based estimating method using cable's natural frequencies. Currently, the latter method is used because it is easy to implement, and estimation accuracy is high.

In recent years, since the length of the bridge has increased, the aerodynamic vibration has become a problem owing to the low damping nature of cables. In order to suppress the aerodynamic vibrations, a damping device called a damper is installed. However, since the vibration characteristics of the cable change due to the presence of the damping device, the natural frequencies required for tension estimation also change. Therefore, the damper is detached, the cable's natural frequencies are estimated, and the cable's tension is estimated by the vibration method. The damper has to be attached again to the cable after the measurements. This detachment and attachment of dampers are time and labor-consuming.

As a cable's tension estimation method, Shinke et al. [1] proposed a vibration-based practical formula. They derived the equation to estimate the cable's tension using the natural frequency of the cable from the string theory. However, this method needs to know the value of bending stiffness in advance, which is difficult as a practical problem. So, a higher-order vibration method was then proposed by Yamagiwa et al. [2]. They proposed an estimation method of cable's tension and bending stiffness simultaneously by using natural frequencies of multiple modes based on the tensioned Bernoulli–Euler beam theory. In their proposed estimation equation, the natural frequency was expressed by a polynomial of mode order with bending stiffness and tension as coefficients. When this method is used, the bending stiffness need not be known prior. Currently, this method is often used for tension estimation.

Previous studies on cables with dampers have mostly focused on optimal design methods for dampers to suppress the cable amplitude [3, 4, 5, 6] and have not dealt with the tension estimation method. Krenk [7] derived a theoretical equation to obtain the complex eigenfrequencies, from which the natural frequencies and the damping ratios were obtained. However, the cable was modeled as a string, and the cable's bending stiffness was ignored. Therefore, these equations cannot be used to estimate the tension of a cable with bending stiffness.

With this background, the authors developed a tension estimation method for a cable with a damper [8]. Using the higher-order vibration method based on the tensioned Bernoulli–Euler beam theory, the authors derived a theoretical equation for estimating the natural frequencies with a damper. The method's validity should be checked by various measures, such as numerical simulations, laboratory experiments, and field measurements of real cable-stayed bridges. Especially, it is desirable to

verify the method through the field measurement of real existing bridges. However, the authors' method has not been verified by the field measurement.

In this paper, the authors' tension estimation method is first introduced. Then the validity of the method is shown through numerical simulations. Then the method is verified through a laboratory experiment. Moreover, the field measurements of a cable-stayed bridge in Japan were conducted to verify the method. It was found that the authors' method can estimate cable's tension with the damper with high accuracy. In this way, the validity of the method was confirmed.

2 Tension Estimation Method

2.1 Higher-Order Vibration Method for a Cable Without a Damper

This section introduces the higher-order vibration method currently used in practice. If the cable is regarded as a tensioned Bernoulli–Euler beam, the following differential equation is established.

$$EI \frac{\partial^4 y}{\partial x^4} + \rho A \frac{\partial^2 y}{\partial t^2} - T \frac{\partial^2 y}{\partial x^2} = 0 \quad (1)$$

where T is tension, EI is bending stiffness, A is cross-section area, and ρ is density. Solving Eq. (1) under the boundary condition of simple support at both ends, the following equation is derived.

$$f_i^2 = \frac{\pi^2 EI}{4\rho AL^4} i^4 + \frac{T}{4\rho AL^2} i^2 \quad (2)$$

where L is cable length, i is mode number and f_i is a natural frequency of mode i . Equation (2) is called the tension estimation formula of the higher-order vibration method. In this method, the tension is estimated as follows. Accelerometers are attached to the cable. The cable with the accelerometer is vibrated by hitting the cable with a hammer, for example. The acceleration response of the free vibration is measured, the acceleration time history is Fourier transformed, and natural frequencies of cables are obtained. Substituting two or more natural frequencies into Eq. (2), two unknowns, T and EI , can be estimated by the least-squares method.

2.2 Authors' Method for a Cable with a Damper

This section explains the tension estimation method proposed by the authors. The model of a cable with a damper is shown in Fig. 1. Let us assume that the cable length is L , the length between the left end and the damper position is L_1 , the damper's spring constant is k , and the damper's damping constant is c . Similar to the higher-order vibration method, the cable is regarded as a tensioned Bernoulli–Euler beam. Solving Eq. (2) under the boundary condition of simple support at both ends and continuity equations at the damper position, Eqs. (3) and (4) are derived. Equation (3) is the equation to estimate the theoretical natural frequencies of the cable with a damper. f_i^t is a theoretical natural frequency of mode i . Comparing Eq. (3) with Eq. (2), the natural frequency with a damper is larger than that without a damper owing to θ_i satisfying Eq. (4). α_i , β_i , and k_i^* in Eq. (4) are obtained by Eqs. (5), (6), and (7).

$$f_i^t = \sqrt{\frac{\pi^2 EI}{4\rho AL^4} \left(i + \frac{\theta_i}{\pi}\right)^4 + \frac{T}{4\rho AL^2} \left(i + \frac{\theta_i}{\pi}\right)^2} \quad i = 1, 2, \dots \tag{3}$$

$$\theta_i = \tan^{-1} \frac{\frac{k_i^* \sin^2 \alpha_i L_1}{EI \alpha_i}}{(\alpha_i^2 + \beta_i^2) + \frac{k_i^*}{EI} \left\{ \frac{\sin \alpha_i L_1 \cos \alpha_i L_1}{\alpha_i} - \frac{\sinh \beta_i L_1 \sinh \beta_i (L - L_1)}{\beta_i \sinh \beta_i L} \right\}} \tag{4}$$

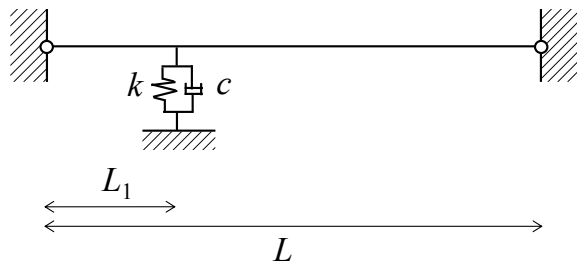
$$\alpha_i = \sqrt{\sqrt{\left(\frac{T}{2EI}\right)^2 + \frac{\rho A (2\pi f_i^t)^2}{EI}} - \frac{T}{2EI}} \tag{5}$$

$$\beta_i = \sqrt{\sqrt{\left(\frac{T}{2EI}\right)^2 + \frac{\rho A (2\pi f_i^t)^2}{EI}} + \frac{T}{2EI}} \tag{6}$$

$$k_i^* = \begin{cases} k + j(2\pi f_i^t)c & \text{(viscous shear damper)} \\ ku + jkv & \text{(high-damping rubber damper)} \end{cases} \tag{7}$$

k^* is the complex stiffness of a damper. Different models are available for different types of dampers. In this study, a viscous shear damper and a high-damping rubber

Fig. 1 Analytical model of a cable with a damper



damper are assumed. The viscous shear damper is modeled by Eq. (7), where k is the spring constant, and c is the damping coefficient of the damper. The high-damping rubber damper is modeled by Eq. (7b), where ku and kv are the real and imaginary parts of the complex stiffness of the damper. j is the imaginary unit. If k^* is 0, θ_i is 0. Therefore, Eq. (3) matches Eq. (2).

Using Eqs. (3)–(7), the theoretical natural frequencies of each mode f_i^t can be calculated using the following parameters: the mass per unit length of the cable ρA , the cable length L , the length from one end of the cable to the damper position L_1 , the cable’s tension T , the cable’s bending stiffness EI , and the two parameters of damper’s stiffness k and c , or ku and kv .

By using this theoretical equation as an inverse problem, the four parameters, such as cable’s tension, cable’s bending stiffness, and two parameters of damper’s stiffness, can be inversely estimated from the mass per unit length of the cable, the cable length, the length from one end of the cable to the damper position, and the natural frequencies for each mode. The bending stiffness of the cable and two damper parameters are simultaneously estimated with the cable’s tension, so they need not be known prior. It is noted that f_i^t is the complex value, and the real part of f_i^t is the natural frequencies obtained by the experiment. Therefore, tension and other three parameters are estimated assuming that the natural frequencies obtained by the measurement match the real part of f_i^t .

3 Numerical Simulations

First, the validity of the authors’ method is shown using the numerical simulation results. Table 1 shows the cable parameters, and Table 2 shows the damper parameters. The high-damping rubber damper is assumed. The values of u and v are obtained by $u = 1/\sqrt{1 + \gamma^2}$ and $v = \gamma/\sqrt{1 + \gamma^2}$, where γ is the loss factor shown in Table 2. Fifty numerical models with the combinations of five cables and ten dampers are considered. The model number will be defined as the sum of the cable number and the damper number. The real part of the theoretical natural frequencies, namely, the measured natural frequencies, are computed by the finite element analysis.

Table 1 Cable parameters

Cable No	Mass per unit length ρA (kg/m)	Length L (m)	Tension (kN)	Bending stiffness (kN·m ²)
10	30.1	25	1650	106.4
20	30.1	25	3300	106.4
30	30.1	200	1650	106.4
40	30.1	200	3300	106.4
50	30.1	200	5340	1111

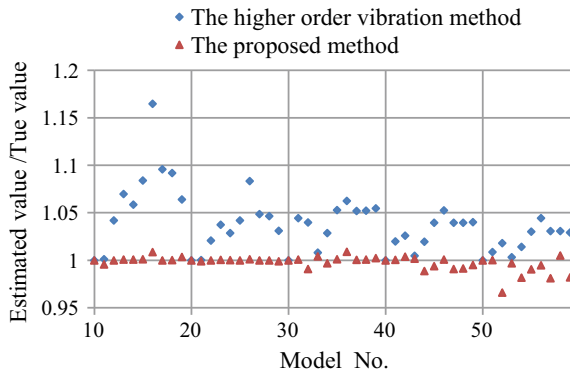
Table 2 Damper parameters

Damper No	Spring constant k (kN/m)	Loss factor γ (-)	Damper position L_1 (m)
0	0	0	0
1	0	0.63	7
2	280	0.63	7
3	560	0.63	2
4	560	0.63	4.5
5	560	0.63	7
6	1120	0.63	7
7	560	0	7
8	560	0.33	7
9	560	1.3	7

Then the four unknown parameters, T , EI , ku , and $are estimated so that the real part of the theoretical natural frequency in Eq. (3) matches the measured natural frequencies by using the least-squares method. Since there are four unknowns, four or more natural frequencies are required. The natural frequencies of the first seven modes are computed and used for estimation.$

The tension estimation result is shown in Fig. 2. The vertical axis is the ratio between the estimated tension value and the assumed tension value. If the vertical axis value is close to 1, the accuracy is high. For comparison, the result by the higher-order vibration method is shown. It is confirmed that the accuracy of tension estimation by the authors' proposed method is higher than that of the higher-order vibration method, and the tension estimation error is within $\pm 5\%$. The bending stiffness and two damper parameters could not be estimated with good accuracy due to their low sensitivity.

Fig. 2 Tension estimation result of numerical simulations



4 Laboratory Experiment

Next, the validity of the authors' method is checked by the laboratory experiment results. An experimental setting is shown in Fig. 3. A load cell is installed at the lower end, and the tension was measured. The tension measured by the load cell was regarded as the true tension value. Cable parameters are shown in Table 3. First, the cable without a damper was hit by a hammer, and the acceleration histories are measured. Natural frequencies are measured by reading the predominant frequencies of the acceleration Fourier spectra. Then the viscous shear-type damper was installed, and the natural frequencies of a cable with a damper were estimated twice. The measured natural frequencies are shown in Table 4. As for case No.1 without a damper, the natural frequencies of the first seven modes could be read, and they are used for tension estimation. However, as for cases No.2 and 3 with damper, the seventh mode could not be estimated. Therefore, the natural frequencies of the first six modes are used for tension estimation.

Figure 4 shows the tension estimation results by the authors' proposed method and the higher-order vibration method. First, the damper was modeled with Eq. (7a), but the result was not good. Considering that the cable length is short and the mass of the damper is not negligible, the effect of damper mass was introduced. The damper was modeled by $k_i^* = k + j(2\pi f_i^t)c - (2\pi f_i^t)^2 m$ instead of Eq. (7a). In this damper model, the unknown parameters are $T, EI, k, c,$ and m .

Fig. 3 Experimental setting

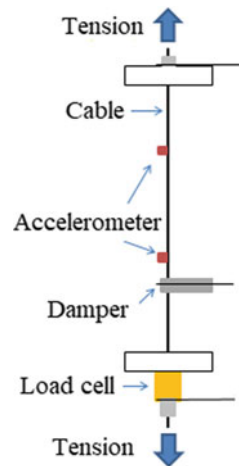


Table 3 Cable dimensions

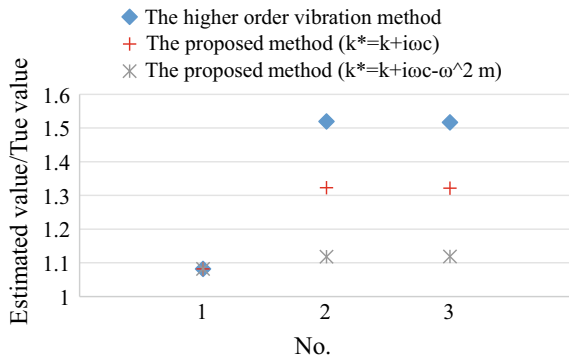
Mass per unit length ρA (kg/m)	Length L (m)	Damper position L_1 (m)	Tension T (kN)
0.3	3.518	0.3518	19.004

Table 4 Measured natural frequencies of laboratory experiment

Case No	Damper	Natural frequencies (Hz)						
		1st	2nd	3rd	4th	5th	6th	7th
1	Without damper	37.188	74.500	112.063	150.00	188.250	227.188	266.500
2	With damper (1st)	43.875	88.188	132.937	177.875	224.125	270.563	–
3	With damper (2nd)	43.875	88.063	132.688	177.813	224.125	270.375	–

(–indicates that the corresponding natural frequency could not be measured)

Fig. 4 Tension estimation result of laboratory experiment



In case No.1 without a damper, the results of the three methods are almost the same, and the estimation error is about 10%. The method assumes both ends are pinned support. The actual boundary condition may be close to a fixed support. Therefore, the tension was overestimated with an error of 10%. In the cases with a damper, the tension estimated by the authors’ proposed method has the highest accuracy and close to the tension of case No.1. The tension was overestimated with an error of 10% because both ends are modeled as pinned support. Since the cable is short, the effect of the boundary condition became large. In the future study, we would like to develop a modified method considering the arbitrary boundary condition.

5 Field Measurements

5.1 Overview

Next, the authors’ method is verified using the field measurement results. A target bridge is a cable-stayed bridge in Japan. A diagram of the bridge is shown in Fig. 5. The cables from C1 to C5 on the downstream side and cable C3 on the upstream

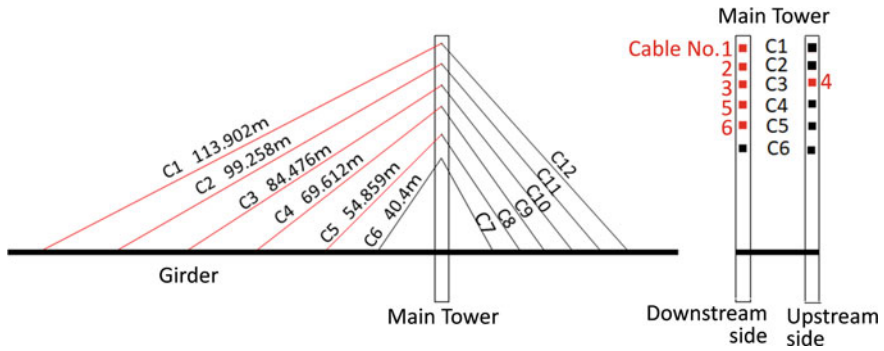


Fig. 5 Diagram of a real cable-stayed bridge

Table 5 Cable dimensions of a real cable-stayed bridge

Cable No	Mass per unit length ρA (kg/m)	Length L (m)	Damper position L_1 (m)
1	70.8	113.902	6.024
2	143	99.258	5.578
3	143	84.476	5.273
4	143	84.476	5.273
5	70.8	69.612	4.954
6	56.7	54.859	4.443

side were measured. The cable dimension is shown in Table 5. The high-damping rubber-type dampers are installed.

The natural frequencies of these cables with a damper were measured as follows. The nylon sling was hooked to the cable, and the cable’s vibration was excited by pulling the nylon sling. The acceleration histories are measured, Fourier transformed, and the natural frequencies are estimated by reading the predominant frequencies. Since the actual tension is unknown, the damper was removed from the cable, and the natural frequencies without a damper were measured. Then the tension of the cables without a damper was estimated by the higher-order vibration method and regarded as the true values.

5.2 Tension Estimation Results

Table 6 shows the measured natural frequencies of cables with and without a damper. The first natural frequencies of cable No.1 without the damper and the sixth natural frequency of cable No.3 without the damper could not be measured since the clear peak could not be seen. Tension was estimated using the measured natural frequencies shown in Table 6.

Table 6 Measured natural frequencies of a real cable-stayed bridge

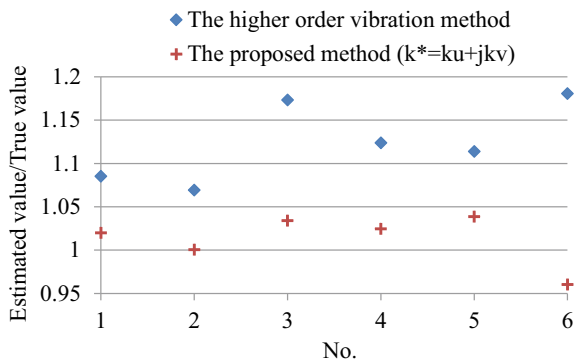
Cable No	Damper	Natural frequencies (Hz)						
		1st	2nd	3rd	4th	5th	6th	7th
1	Without damper	–	1.133	1.68	2.227	2.813	3.359	3.867
	With damper	0.664	1.172	1.758	2.344	2.93	3.516	4.063
2	Without damper	0.781	1.563	2.305	3.086	3.867	4.688	5.313
	With damper	0.859	1.68	2.5	3.32	4.141	4.922	5.859
3	Without damper	1.016	1.953	3.086	3.828	4.805	–	6.758
	With damper	1.016	2.031	3.047	4.219	5.156	6.172	7.109
4	Without damper	1.094	2.109	3.203	4.219	5.234	6.328	7.383
	With damper	1.133	2.227	3.32	4.453	5.664	6.641	7.852
5	Without damper	0.977	1.836	2.813	3.633	4.492	5.273	6.25
	With damper	1.211	1.953	2.891	3.867	4.844	5.82	6.875
6	Without damper	1.367	2.695	4.023	5.391	6.602	7.969	9.336
	With damper	1.445	2.852	4.18	5.703	7.227	8.516	9.883

(–indicates that the corresponding natural frequency could not be measured)

The tension estimation result is shown in Fig. 6. The cable’s tension with a damper was estimated by the authors’ proposed method and the higher-order vibration method, and the results were compared. The estimation error of the proposed method is quite small and within 4%. On the other hand, the estimation error of the higher-order vibration method is between 7 to 18%. The increase of natural frequencies due to damper installation is evaluated as the overestimation of tension.

However, the real tension could not be measured using the load cell, and the tension without a damper estimated by the higher-order vibration method was used as the true value. Therefore, it can be said that the proposed method for a cable with a damper provides estimation results comparable to the higher-order vibration method for a cable without a damper without removing the damper.

Fig. 6 Tension estimation result of a real cable-stayed bridge



It was shown that the authors' method enables estimating the tension of a cable with a damper with high accuracy without removing the damper from the cable. Therefore, the reinstallation of the damper after the measurement is unnecessary. The proposed method contributes to the efficiency of the inspection work.

6 Conclusions

The authors have been studying a tension estimation method for a cable with a damper without removing the damper. The authors have derived a theoretical equation for the natural frequency of a simply-supported cable with a damper. By using this equation, the natural frequencies of each mode order can be calculated using the following parameters: the mass per unit length of the cable, the cable length, the length from one end of the cable to the damper position, the tension, the bending stiffness, and the two parameters of damper's stiffness. By using this theoretical equation as an inverse problem, the four parameters, such as tension, bending stiffness, and two parameters of damper's stiffness, can be inversely estimated from the mass per unit length of the cable, the cable length, the length from one end of the cable to the damper position, and the natural frequencies for each mode. Since the sensitivity of the bending stiffness and two parameters of damper's stiffness is smaller than the cable's tension, estimation of cable's tension only is considered. The purpose of this paper is to verify the validity of the authors' proposed method by laboratory experiment and field measurement of a real cable-stayed bridge.

In this paper, the authors' tension estimation method is first introduced in Sect. 2. Then the validity of the method is shown through numerical simulations in Sect. 3. Then the method is verified through a laboratory experiment in Sect. 4. Finally, the field measurements of a cable-stayed bridge in Japan were conducted to verify the method in Sect. 5. It was found that the authors' method could estimate the cable's tension with the damper with high accuracy.

In the current practice in Japan, the damper is detached from the cable; then, the natural frequencies of the cable without a damper are measured, and the damper is attached to the cable again. However, the process of detaching and attaching the damper is time-consuming and labor-intensive. The authors' proposed method is useful since it can estimate the tension of a cable with a damper without detaching the damper from the cable. The fact that the damper does not have to be detached is a great advantage in terms of work efficiency.

References

1. Shinke T, Hironaka K, Zui H, Nishimura H (1980) Practical formulas for estimation of cable tension by vibration method. *J Jpn Soc Civil Eng* 294:25–32
2. Yamagiwa I, Utsuno H, Endo K, Sugii K (2000) Identification of flexural rigidity and tension of the one-dimensional structure by measuring eigenvalues in higher order. *Trans Jpn Soc Mech Eng* 66(649):2905–2911
3. Pacheco BM, Fujino Y, Sulekh A (1993) Estimation curve for modal damping in stay cables with viscous damper. *J Struct Eng* 119(6):1961–1979
4. Lazar IF, Neild SA, Wagg DJ (2016) Vibration suppression of cables using tuned inerter dampers. *Eng Struct* 122:62–71
5. Shi X, Zhu S (2018) Dynamic characteristics of stay cables with inerter dampers. *J Sound Vib* 423:287–305
6. Javanbakht M, Cheng S, Ghrib F (2019) Control-oriented model for the dynamic response of a damped cable. *J Sound Vib* 442:249–267
7. Krenk S (2000) Vibration of a taut cable with an external damper. *J Appl Mech ASME* 67:772–776
8. Furukawa A, Hirose K, Kobayashi R (2021) Tension estimation method for cable with damper using natural frequencies. *Front Built Environ* <https://doi.org/10.3389/fbuil.2021.603857>

Evaluation of Damping Ratio of Buildings Using Seismic Interferometry Method



Zheng Zhang, Xin Wang, and Masayuki Nagano

Abstract Seismic interferometry method is applied to evaluate the internal attenuation of buildings regarding the building as the sedimentary layers of one-dimensional layered medium. The original wave field is reconstructed to be a new wave field expressed by deconvolved waves with virtual source at the top, consisting single up-going wave and single down-going wave reflected at the top. The damping ratio is evaluated from the transfer functions of up-going and down-going waves of the deconvolved wave at the 1st-floor of a building. The feasibility of this method is investigated using a homogeneous model, a 2-layer model, and a heterogeneous model, imaging 10 story buildings. We found that the damping ratios of those models extracted from the transfer functions were consistent with the preset values.

Keywords Damping ratio · Seismic interferometry method · Wave propagation · Transfer function · Deconvolution

1 Introduction

In order to evaluate the seismic responses of buildings with high accuracy, it is very important to properly identify the dynamic response characteristics, i.e., natural periods and damping ratios. Natural periods can be estimated from the transfer function between the top and the base of a building or can be simply detected from the Fourier spectra of response records at top including the soil-structure interaction effect. However, it is difficult to evaluate damping property accurately, because various kinds of damping are included in a building system, e.g., the friction

Z. Zhang (✉)

Department of Architecture, Tokyo University of Science, Noda, Chiba, Japan

e-mail: 7116071@ed.tus.ac.jp

X. Wang

Ashikaga University, Ashikaga, Tochigi, Japan

M. Nagano

Tokyo University of Science, Noda, Chiba, Japan

damping, scattering damping, dissipation damping due to the dynamic soil-structure interaction.

In general, the building response is considered as the superposition of plural shaking modes with different frequencies. On the other hand, the building response can be regarded as consequence of the wave propagation within the building. Therefore, by applying seismic interferometry to the response of buildings, single wave propagating in the vertical direction in the building can be extracted. Seismic interferometry is a method to obtain the Green's function regarded as impulse responses between two observation points, which enable us to construct a new wave field. If the virtual source is assumed at the top of a building, the impulse response at each floor only consists with single up-going wave and single down-going wave, which make it easy to separate the up-going wave and down-going wave and then to obtain the transfer function between them. Fukushima et al. [1, 2] have examined the validity of the transfer function between the down-going wave and up-going wave to estimate the S-wave attenuation characteristics (Q_S^{-1} values) of sedimentary layers, and estimated the Q_S^{-1} between the borehole and surface observation points at some stations of KiK-net of Japan.

Moreover, for a building system, there are cases that the soil-structure interaction is attributed as additional damping due to radiated energy to unbounded media, which will contaminate the pure damping evaluation of the upper structure [3]. In the new wave field obtained from seismic interferometry, the boundary condition will be changed and the effect of soil-structure interaction can be excluded [4]. Therefore, it is possible to investigate the internal attenuation of the upper structure without the effect of soil-structure interaction. Recently, wave interferometry has been applied to evaluate the shear wave velocity V_s of each story of buildings [5].

In this study, we applied the principle of the seismic wave interferometry to deconvolution analysis of the calculated waveforms in buildings. For simplicity, buildings are regarded to be the one-dimensional layered medium by converting mass and shear stiffness into mass density and S-wave velocity. By extracting the waves propagating up and down in the building, we could calculate the propagation time and attenuation of the waves from the incident and reflection inside the building. The specific attenuation inside the building is estimated from transfer function between up-going and down-going waves.

2 Methodology and Fundamental Study Using a Homogeneous Model

2.1 Reconstruction of Wave Field

The vibration of upper structure can be regarded as the wave propagation within the building traveling in the vertical direction. However, it is difficult to separate the up-going and down-going waves from the original waveforms. Alternatively, from the

impulse response functions, which is a new wave field generated by a virtual pulse source at the base or at the top, it is easier to distinguish the up-going waves and the down-going waves. Snieder and Şafak [4] have proved that for the impulse response to the virtual source at the top of a building is the new wave field only consisting of one up-going wave and one down-going wave and that the effect of soil-structure interaction can be excluded.

We try to apply the impulse response to the virtual source at the top of a building to evaluate the internal attenuation of buildings from the transfer function between the up-going wave and the down-going wave. Specifically, the feasibility of the seismic interferometry method to extract the internal damping ratio of buildings will be verified in this study. The deconvolution method in Eq. (1) is used to obtain the impulse response, which is also called the deconvolved wave.

$$D(\omega) = \frac{u_i(\omega)u_t^*(\omega)}{|u_t(\omega)|^2 + \varepsilon} \tag{1}$$

where $D(\omega)$ is the deconvolved wave in frequency domain. $u_i(\omega), u_t(\omega)$ are the Fourier transform of the middle and the top of the building, respectively. Parameter ε was initially set to 10% of the average power spectrum by referring [4].

2.2 Fundamental Study Using a Homogeneous Model

As a fundamental study using seismic interferometry method, we used a homogeneous soil model of 30 m height with fixed base in Fig. 1a. The S-wave velocity V_S was set to 480 m/s in order to keep the natural frequency at 4 Hz, which is roughly equivalent to the natural frequency of a 10-story RC building. The damping ratio was set to 0.01 with frequency-independent hysteretic damping. Observed points were set at 3 m depth intervals. White noise was input as acceleration time history at the

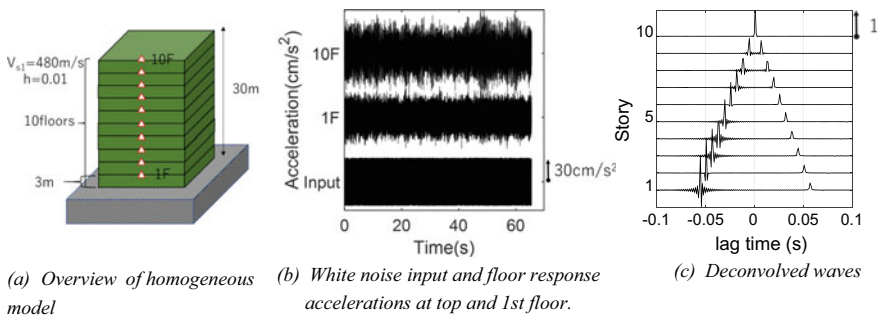


Fig. 1 a Overview of homogeneous model. b White noise was input to bottom of the model. c Floor response accelerations are plotted along with deconvolved waves at ten floors

bottom. Time interval was set to 0.001 s with time steps $N = 65,536$. Floor responses at top and 1st floor were obtained as presented in Fig. 1b.

Deconvolved waves in Fig. 1c were calculated by Eq. (1), the ε was set to be 0.01. Amplitude for each floor was normalized so that maximum value at the top floor was set to 1. In the deconvolved waves in Fig. 1c, the up-going wave can be recognized as the incident wave. The up-going wave was reflected at the top of the building and travelling as the down-going wave.

2.3 Extraction of Internal Attenuation from Transfer Function

Amplitude of the down-going wave in Fig. 1c was smaller than the up-going wave, implying that the interval attenuation played an important role in the middle stories during wave propagation. The time difference between the up-going and the down-going wave (τ') is the travel time of a pulse taken to start from a point and then return to that point, which depends on the wave velocity and the travel distance. Travel distance here is the twice of the height from the start floor to the top of the building.

Transfer function between the down-going wave and the up-going wave can be expressed as the Eq. (2),

$$H(f) = \frac{S_{xy}(f)}{S_{xx}(f)} \quad (2)$$

In which $S_{xy}(f)$ means the cross spectrum between the up-going wave and down-going wave, and $S_{xx}(f)$ is the power spectrum of the up-going wave, f means frequency. For homogeneous medium, the frequency-dependent S-wave attenuation $Q_s(f)$ and $h(f)$ can be estimated using the transfer function $H(f)$ by the Eq. (3).

$$Q_s(f) = -\frac{\pi f \tau'}{\ln[H(f)]} = \frac{1}{2h(f)} \quad (3)$$

In Eq. (3), the τ' presents the two-way travel time between the bottom and the top of a building. Usually, because the τ' of the deconvolved wave at the base is the largest, it is easier to separate the incident wave and the reflected wave. Therefore, usually the deconvolved wave at the base is commonly used to detect the damping ratio $h(f)$.

Fukushima et al. [2] analyzed seismic waveforms recorded at the bottom and seismic waveforms recorded at the surface of the borehole to examine the S-wave attenuation of ground. In [2], incident and reflected waves were considered to be equal and were initially selected based on a coefficient factor C related to the coherence between the incident and reflected waves as shown in Eq. (4).

$$C = \int_{1.0}^{10.0} S_{xx}(f) \text{coh}^2(f) df \quad (4)$$

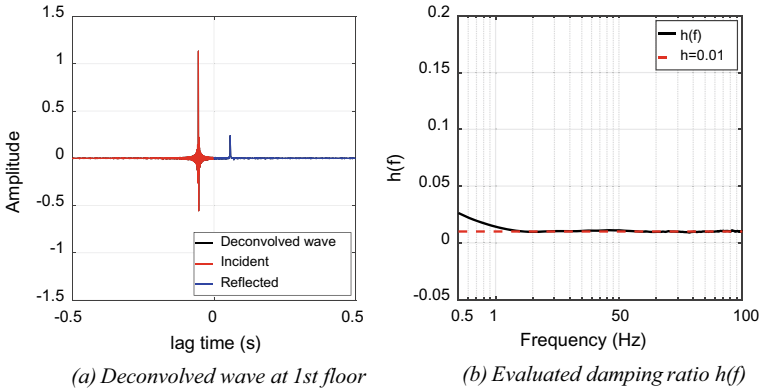


Fig. 2 **a** Deconvolved wave at 1st floor and **b** damping ratio inferred from incident and reflected waves

Evi et al. [6] presented a different time-based time-window of the up-going and down-going wave. In which coherence-based and travel time-based time-window was compared in a homogeneous soil model. And in this research, since travel time-based selection of upgoing and down going wave windows has a remarkable improvement in accuracy, we investigated the range of time-window’s influences in a similar way with Evi et al. [6] of various models.

In this study, we used a homogeneous model shown in Fig. 1a to test the validity of the results extracted from the damping ratio using wave interferometry initially. Travel time-based deconvolution waves was used same as Evi et al. [6] to calculate the damping ratio in this study. The length of incident and reflected waves we used was set in 8.192 s and ϵ was set to be 0.01. The results shown in Fig. 2b which is calculated by using deconvolved wave in the bottom of the homogeneous soil model shown in Fig. 2a are corresponds to the set value with high accuracy as planned. The damping ratio in the low frequency range is distinctly overestimated, within the range of 2–100 Hz, and within a range close to the natural frequency of the building, the accuracy of the calculated damping ratio is very precise. As the frequency increases, the tendency to converge to a set value ($h = 0.01$) is distinctly.

2.4 Analysis of Influences to Internal Attenuation

At the same time, we found that modification in the range of bottom deconvolution wave used and the ϵ can also cause drastic fluctuation in accuracy of damping ratio. So initially we have added an investigation of the used range of bottom deconvolution wave with ϵ set to be 0.01. An integer power of 2 for the length of time was used to ensure that the FFT is computed. And then we found that as the data length of incident and reflected waves used for calculating damping ratio become larger, the effect on

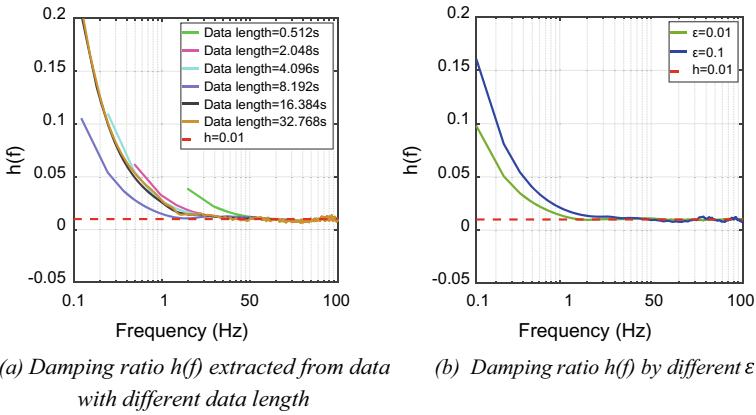


Fig. 3 **a** Damping ratio $h(f)$ extracted from data with different data length; **b** damping ratio $h(f)$ by different ϵ

accuracy of the damping ratio becomes more pronounced. Since the accuracy of the results (Fig. 3a) for a quarter of the length of the upward wave is the best, both the upward and downward waves in this study are evaluated for the damping ratio using data with a length of 8.192 s.

Secondly, the accuracy of the damping evaluation was evaluated for different settings of ϵ . We set ϵ to 0.1 and 0.01 for comparison with used data length in 8.192 s. As shown in Fig. 3b, the results calculated with ϵ set to 0.01 showed a small difference from the result with 0.1 in the range of 3 Hz and below, and the results with ϵ set to 0.01 were in better agreement with the set value in comparison. All the subsequent studies in this research will be investigated with ϵ set to be 0.01.

3 Analysis Using a Two-Layer Model

The feasibility of internal damping ratio’s calculation in a two layers model was investigated. Model overview is shown in Fig. 4a. The additional layer, which is different from the top and to assume a natural frequency close to 4 Hz, the S-wave velocity V_S was set to a different value in 400 and 500 m/s and the damping ratio was same in 0.01. Same as the investigation of homogeneous model, White noise was input at the bottom, and the damping ratio was calculated by the amplitude ratio of the deconvolution wave at the top and bottom. Measurement points were set at 3 m depth intervals.

As the result of simulation in two-layer model, it is obviously to find the reflected peaks of two-layers’ interfaces, which is shown in Fig. 4b. Even for a two-layer model with different V_S velocities, the damping ratio of the model can be extracted using wave interferometry with the same accuracy as homogeneous soil model’s result,

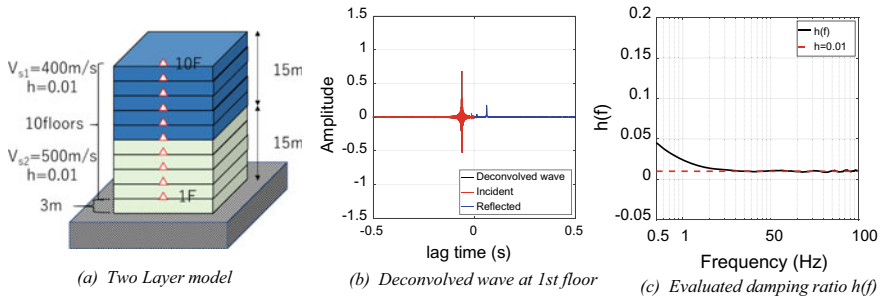


Fig. 4 a Two-layer model, b deconvolved wave at 1st floor, and c damping function

and especially the calculated damping ratio is highly accurate matched with the set value in 2–100 Hz, which is shown in Fig. 4c.

4 Analysis Using a Heterogeneous Model

After validating the results with homogeneous and two-layer soil models, we examined the feasibility and accuracy of calculating damping ratio in a heterogeneous building model. To validate on a real building model, 10-story building model is used. The natural period is set to $T = 0.025 N$ assuming a walled RC structure, N is the number of floors here (Fig. 5).

Details of the 10-story building model are shown in Table 1. The table shows the shear stiffness K , the equivalent density ρ and the equivalent shear wave velocity V_s ($=\sqrt{G/\rho}$) of each layer for a 10-story walled RC building. We set the primary mode as an inverted triangle distribution and set the stiffness of each layer. Figure 6a, b

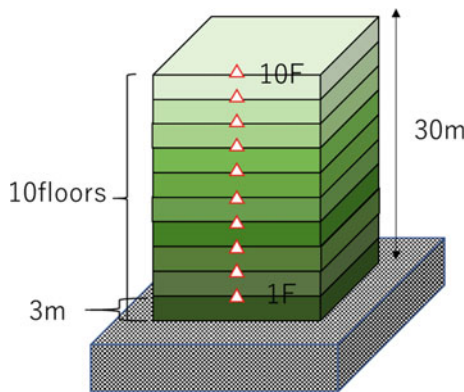


Fig. 5 Overview of heterogeneous model

Table 1 Profile of the heterogeneous model

Story	K (kN/m)	ρ (t/m ³)	Vs (m/s)
10	3.98×10^6	0.467	238
9	7.56×10^6	0.467	329
8	1.07×10^7	0.467	392
7	1.35×10^7	0.467	440
6	1.59×10^7	0.467	477
5	1.79×10^7	0.467	506
4	1.95×10^7	0.467	528
3	2.07×10^7	0.467	544
2	2.15×10^7	0.467	554
1	2.19×10^7	0.467	559

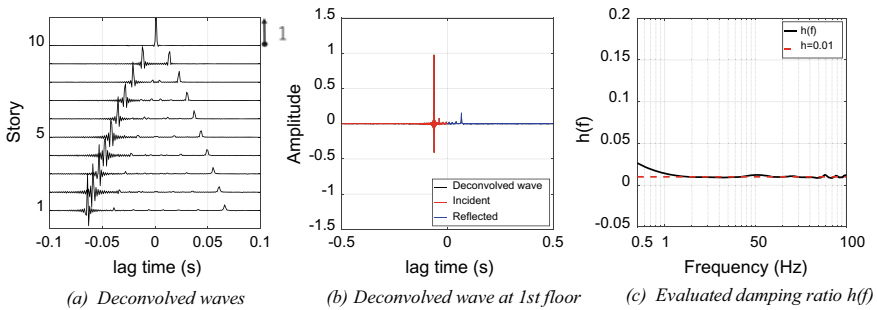


Fig. 6 **a** Deconvolved waves at all floors, **b** incident and reflected waves of the deconvolved wave at the 1st-floor, and **c** damping ratio $h(f)$

shows all and 1st story’s deconvolved waveform of acceleration data that used for calculating damping ratio $h(f)$.

Even the calculation is using a 10-story heterogeneous model to simulate a building model, the results shown in Fig. 6c are still converging in 20% above and below the set value, reached a satisfactory accuracy. But same to the homogeneous model, $h(f)$ in the low frequency range is obviously overestimated in the 0–3 Hz range and reaches a set value as the frequency increases. Within the frequency region of 0–2 Hz and the high frequency range in 50–100 Hz, the accuracy of $h(f)$ is not good as $h(f)$ in 2–50 Hz, but generally, the validity of the wave interferometry was verified in the case of using a similar building model.

5 Conclusions

In this study, we applied the seismic interferometry method to extract the internal attenuation of buildings by regarding buildings as one-dimensional layered medium. Firstly, we have verified the feasibility of extracting the damping ratio of a homogeneous soil model using seismic interferometry method, which used the deconvolution wave at the 1st-floor and top of model. As a result, it is able to calculate the damping ratio $h(f)$ for both the homogeneous soil model and the two-layer soil model. Within the frequency region of 0–2 Hz, the accuracy of $h(f)$ is not satisfactory compared to the set value, however with good agreement with the set value for the frequency range of 2–100 Hz. This trend was also reported by Evi et al. [6]. The natural frequency of each model was set to around 4 Hz, and all the damping ratio at 4 Hz reached a satisfactory accuracy to the set value. There are still several factors that can affect this result, such as the ϵ setting when deconvoluting, and the accuracy of the acceleration data. The causes of influence in accuracy of $h(f)$ will be the subject of future research. Furthermore, for the 10-layer heterogeneous building model, the results of using the data of the first layer and the top of building model corresponded well with the expected values.

In future research, it is necessary to examine the effect of soil-structure interaction to the evaluation of internal damping ratio of the upper structure using the building model including the rocking and sway components. Also, we are going to summarize the results of the calculation of building attenuation using wave propagation characteristics, verify the wave interferometry using a multi-modal general-purpose building model, and finally calculate and verify the accuracy of building damping ratio using actual seismic motion data of the building.

References

1. Fukushima Y, Kinoshita S, Sato H (1992) Measurement of Q_S^{-1} for S waves in mudstone at Chikura, Japan: comparison of incident and reflected phases in borehole seismograms. *Bull Seismol Soc Am* 82:148–163
2. Fukushima R, Nakahara H, Nishimura T (2016) Estimating S-wave attenuation in sediments by deconvolution analysis of KiK-net borehole seismograms. *Bull Seismol Soc Am* 106:552–559
3. Cruz C, Miranda E (2021) Insights into damping ratios in buildings. *Earthquake Eng Struct Dyn* 50:916–934
4. Snieder R, Şafak E (2006) Extracting the building response using seismic interferometry: theory and application to the Millikan library in Pasadena, California. *Bull Seismol Soc Am* 96:586–598
5. Wang X, Masaki K, Irikura K (2015) 1D Wave propagation analysis and shear-wave velocity extraction of super high-rise buildings based on vertical microtremor observation array. *J Struct Constr Eng (Trans AIJ)* 718:1859–1868 (in Japanese)
6. Evi R, Fabrice H, Zafeiria R (2019) Assessing the applicability of deconvolution of borehole records for determining near-surface shear-wave attenuation. *Bull Seismol Soc Am* 109:621–635

Structural Parameter Identification of a Reinforced Concrete Frame Using Constrained Unscented Kalman Filter



Dan Li

Abstract Field dynamic test on an as-built structure usually provides responses which are different from those generated by a corresponding finite element (FE) model. To update parameters in the FE model according to measured data, nonlinear Kalman filters, especially the unscented Kalman filter (UKF), can be applied by treating the model parameters as augmented system states. The UKF propagates the first two moments of the system states based on unscented transform, in which a set of sigma points approximating the state distribution are generated and transferred through the system equation. Although the UKF is a powerful tool for parameter identification, ignoring parameter constraints during the identification process may result in unreliable estimates. To address this challenge, this research investigates the application of constrained UKF (CUKF) on structural parameter identification. Different from the UKF, the proposed CUKF suitably generates sigma points in each iteration and make sure that all the sigma points locate within feasible region. As the weighted average of the constrained sigma points, the state estimates are guaranteed to follow the applied constraints. This paper also discusses the importance of weighting factors for sigma points for achieving second-order accuracy. Effectiveness and robustness of the proposed method are validated using experimentally measured data from a full-scale reinforced concrete frame structure. The identification results demonstrate that with properly applying parameter constraints, the proposed CUKF provides more reasonable estimation than the UKF. Finally, the updated FE model with identified model parameters is shown to achieve closer dynamic responses to experimental measurements than the initial model.

Keywords Parameter identification · Unscented Kalman filter · Constraints · Dynamic analysis · Full-scale experiment

D. Li (✉)

School of Civil Engineering, Southeast University, Nanjing, China

e-mail: danli@seu.edu.cn

1 Introduction

The finite element method (FEM) has been widely used for numerically solving problems arising from structural analysis. Based on design data and engineering judgement, a carefully developed FE model can capture static and dynamic characteristics of the corresponding structure and predict its responses to a certain degree of accuracy. In practice, however, there are always uncertain material properties and boundary conditions which are some of the main contributors to mismatch between the structure and FE model [1]. To improve the reliability of the FE model, critical parameters need to be identified based on measurement data.

Model updating is the process of tuning parameter values in an FE model to match with experimentally measured structural responses. Updating model parameters according to measured data is of practical importance to verifying modeling techniques and improving the predictive performance of models [2]. Various approaches have been proposed and developed for model updating, among which recursive filtering techniques, such as extended Kalman filter (EKF), unscented Kalman filter (UKF), and particle filter (PF), have found applications on identifying structural parameters from noisy measurements [3–5]. It is noted that the inherent flaws of the EKF due to linearization could result in large estimation errors, especially for highly nonlinear systems [6]. On the other hand, the PF suffers from high computational cost and sample impoverishment issue which limit the applicability in updating large-scale structures [5].

As a powerful alternative to the EKF and the PF, the UKF utilizes a deterministic sampling approach to calculate mean and covariance of system states which undergo a nonlinear transformation. In this way, the UKF can achieve accuracy to the third order for Gaussian inputs, while maintaining computational complexity comparable to the EKF [7, 8]. Despite that the UKF has shown promising results for structural parameter identification, the deficiency of not considering bounds or other constraints on state variables may cause inaccurate estimation results and even divergence of identification process [9, 10]. To address this issue, this paper proposes a constrained UKF (CUKF) method which confines the state estimates within feasible domain by adjusting the generated sigma points. In addition, the weighting factors are re-evaluated to maintain second order accuracy of the probability distribution of the states.

The rest of paper is organized as follows. Section 2 briefly reviews the UKF for parameter identification and presents details of the CUKF algorithm. Section 3 shows structural parameter identification of a full-scale reinforced concrete frame using the proposed approach. In the end, Sect. 4 provides a summary.

2 UKF for Parameter Identification

2.1 Standard UKF

As an extension of the Kalman filter, the UKF relies on a set of sigma points to calculate the mean and covariance of system states which undergo nonlinear transformation. In order to estimate structural parameters θ , an augmented state vector $\mathbf{x} = [\mathbf{q}; \dot{\mathbf{q}}; \theta]$ is formed. Here, \mathbf{q} and $\dot{\mathbf{q}}$ are displacement and velocity vectors, respectively; the semicolons denote the concatenation of vectors to lighten notations. In this way, parameters θ can be estimated together with system states \mathbf{q} and $\dot{\mathbf{q}}$ from the measurement results.

Consider a general dynamic system governed by a nonlinear process equation:

$$\dot{\mathbf{x}} = \mathbf{f}(\mathbf{x}, \mathbf{u}, \mathbf{w}) \tag{1}$$

where \mathbf{u} is known excitation and \mathbf{w} is a zero-mean white Gaussian process noise with $\mathbb{E}[\mathbf{w}(t)\mathbf{w}^T(t + \tau)] = \Sigma_{\mathbf{w}}\delta(\tau)$. At time $t = k\Delta t$, the measurement \mathbf{y}_k is given by the equation:

$$\mathbf{y}_k = \mathbf{h}(\mathbf{x}_k, \mathbf{u}_k, \mathbf{v}_k) \tag{2}$$

where \mathbf{v}_k is the zero-mean white Gaussian measurement noise with $\mathbb{E}[\mathbf{v}_k\mathbf{v}_{k+l}^T] = \Sigma_{\mathbf{v}}\delta_l$.

In order to deal with the noises $\mathbf{w} \in \mathbb{R}^{n_w}$ and $\mathbf{v}_k \in \mathbb{R}^{n_v}$, the state vector \mathbf{x}^a is redefined as concatenation of the original state vector $\mathbf{x} \in \mathbb{R}^{n_x}$ and noises variables:

$$\mathbf{x}^a = [\mathbf{x}; \mathbf{w}; \mathbf{v}] \in \mathbb{R}^N \tag{3}$$

where $N = n_x + n_w + n_v$ is the dimension of \mathbf{x}^a .

At time $t = k\Delta t$, the a posteriori estimate $\hat{\mathbf{x}}_{k|k}^T$ and its covariance matrix $\Sigma_{\mathbf{x}_{k|k}}$ are known by induction. As a result, the estimate of the augmented state vector is formed as:

$$\hat{\mathbf{x}}_{k|k}^a = \begin{bmatrix} \hat{\mathbf{x}}_{k|k}^T \\ 0 \\ 0 \end{bmatrix} \tag{4}$$

with covariance matrix:

$$\Sigma_{\mathbf{x}_{k|k}^a} = \begin{bmatrix} \Sigma_{\mathbf{x}_{k|k}} & 0 & 0 \\ 0 & \Sigma_{\mathbf{w}} & 0 \\ 0 & 0 & \Sigma_{\mathbf{v}} \end{bmatrix} \tag{5}$$

To propagate the mean and covariance through the process equation, $2N + 1$ sigma points $\mathbf{x}_{k|k,i}^a, i = 0, 1, \dots, 2N + 1$, are generated first:

$$\begin{aligned} \mathbf{x}_{k|k,0}^a &= \hat{\mathbf{x}}_{k|k}^a \\ \mathbf{x}_{k|k,i}^a &= \hat{\mathbf{x}}_{k|k}^a + \left(\sqrt{(N + \kappa) \Sigma_{\mathbf{x}_{k|k}^a}} \right)_i, \quad i = 1, 2, \dots, N \\ \mathbf{x}_{k|k,N+i}^a &= \hat{\mathbf{x}}_{k|k}^a - \left(\sqrt{(N + \kappa) \Sigma_{\mathbf{x}_{k|k}^a}} \right)_i, \quad i = 1, 2, \dots, N \end{aligned} \quad (6)$$

where $(\cdot)_i$ refers to the i th column of the matrix and $\sqrt{\cdot}$ is the matrix square root. The scaling parameter κ can be any number as long as $N + \kappa > 0$ [8].

The weighting factors associated with sigma points are calculated by the following equation:

$$\begin{aligned} W_0 &= \frac{\kappa}{N + \kappa} \\ W_i &= \frac{1}{2(N + \kappa)} \quad i = 1, 2, \dots, 2N \end{aligned} \quad (7)$$

Each sigma point is propagated through the nonlinear process equation to yield sigma point for the next time step:

$$\mathbf{x}_{k+1|k,i}^x = \mathbf{x}_{k|k,i}^x + \int_{k\Delta t}^{(k+1)\Delta t} \mathbf{f}(\mathbf{x}_{k|k,i}^x, \mathbf{u}, \mathbf{x}_{k|k,i}^w) dt \quad i = 0, 1, \dots, 2N \quad (8)$$

Using the calculated sigma points, the a priori estimate $\hat{\mathbf{x}}_{k+1|k}$ and its covariance matrix $\Sigma_{\mathbf{x}_{k+1|k}}$ can be evaluated as:

$$\begin{aligned} \hat{\mathbf{x}}_{k+1|k} &= \sum_{i=0}^{2N} W_i \mathbf{x}_{k+1|k,i}^x \\ \Sigma_{\mathbf{x}_{k+1|k}} &= \sum_{i=0}^{2N} W_i (\mathbf{x}_{k+1|k,i}^x - \hat{\mathbf{x}}_{k+1|k})(\mathbf{x}_{k+1|k,i}^x - \hat{\mathbf{x}}_{k+1|k})^T \end{aligned} \quad (9)$$

Similarly, the predicted measurement $\mathcal{Y}_{k+1|k,i}$ of each sigma point are obtained according to the measurement equation:

$$\mathcal{Y}_{k+1|k,i} = \mathbf{h}(\mathbf{x}_{k|k,i}^x, \mathbf{u}_k, \mathbf{x}_{k|k,i}^v) \quad i = 0, 1, \dots, 2N \quad (10)$$

The predicted measurement $\hat{\mathbf{y}}_{k+1|k}$ of state \mathbf{x}_{k+1} , the innovation covariance matrix $\Sigma_{\mathbf{y}_{k+1|k}}$, and the cross-covariance matrix $\Sigma_{\mathbf{xy}_{k+1|k}}$ can be calculated as:

$$\begin{aligned}\mathbf{Q}_{k+1|k} &= \sum_{i=0}^{2N} \mathbf{W}_i \mathcal{Y}_{k+1|k,i} \\ \Sigma_{\mathbf{y}_{k+1|k}} &= \sum_{i=0}^{2N} \mathbf{W}_i (\mathcal{x}_{k+1|k,i} - \mathbf{Q}_{k+1|k}) (\mathcal{Y}_{k+1|k,i} - \mathbf{Q}_{k+1|k})^T\end{aligned}\quad (11)$$

The Kalman gain \mathbf{K}_{k+1} can then be obtained by:

$$\mathbf{K}_{k+1} = \Sigma_{\mathbf{x}\mathbf{y}_{k+1|k}} (\Sigma_{\mathbf{y}_{k+1|k}})^{-1}\quad (12)$$

Upon measurement \mathbf{y}_{k+1} being available, the a posteriori estimate $\hat{\mathbf{x}}_{k+1|k+1}$ can be calculated according to the measurement residual $\mathbf{r}_{k+1} = \mathbf{y}_{k+1} - \hat{\mathbf{y}}_{k+1|k}$:

$$\hat{\mathbf{x}}_{k+1|k+1} = \hat{\mathbf{x}}_{k+1|k} + \mathbf{K}_{k+1} \mathbf{r}_{k+1}\quad (13)$$

Along with the measurement update of the state, the covariance matrix $\Sigma_{\mathbf{x}_{k+1|k+1}}$ for the a posteriori estimate can be evaluated as:

$$\Sigma_{\mathbf{x}_{k+1|k+1}} = \Sigma_{\mathbf{x}_{k+1|k}} - \mathbf{K}_{k+1} \Sigma_{\mathbf{y}_{k+1|k}} \mathbf{K}_{k+1}^T\quad (14)$$

In this way, the UKF recursively update system states based on measurement results.

2.2 Constrained UKF

Constraints on states serve as a remediation for inaccurate system modeling and thus play an important role in reliable parameter identification using the UKF. The basic strategy of implementing constraints is to adjust the sigma point x_i outside of the feasible domain back within the boundary along its direction $(\sqrt{\Sigma_{\mathbf{x}}})_i$ to the state estimate. In this research, a backtracking line search method is utilized to adjust the sigma point which fails to satisfy general constraints $\mathbf{g}(\mathbf{x}) \geq 0$ implemented on the system. Starting with $d_i = \sqrt{N + \kappa}$, the method keeps reducing d_i by a scaling factor $\alpha \in (0, 1)$ until $x_i = \hat{\mathbf{x}} + d_i (\sqrt{\Sigma_{\mathbf{x}}})_i$ and $x_{i+N} = \hat{\mathbf{x}} - d_i (\sqrt{\Sigma_{\mathbf{x}}})_i$ satisfy constraints $\mathbf{g}(\mathbf{x}) \geq 0$. Here, x_{i+N} in the pair is also adjusted to preserve the symmetric distribution of the set of sigma points. The scaling factor α controls speed of the adjusting procedure, with a lower value corresponding to a fast but crude search and a higher value corresponding to a slow but fine search.

In order to achieve second-order accuracy of approximation of the probability distribution by the sigma points, the weighting factors need to be updated according to the new set of sigma points:

$$W_i = \frac{1}{2d_i^2} \quad i = 1, 2, \dots, 2N$$

$$W_0 = 1 - \sum_{i=1}^{2N} W_i \tag{15}$$

It can be proved that the weighted mean and covariance of the sigma points match with the those of the state distribution. The proposed constraint implementing algorithm is summarized below:

Algorithm Implement constraint during UKF iteration
Given constraints $\mathbf{g}(\mathbf{x}) \geq 0$, state estimate $\hat{\mathbf{x}}$, direction $(\sqrt{\Sigma_{\mathbf{x}}})_i$, dimension N , and scalar factors $\kappa, \alpha \in (0, 1)$
Initialize $d_i = \sqrt{N + \kappa}$
 1. while $\mathbf{g}(\hat{\mathbf{x}} + d_i(\sqrt{\Sigma_{\mathbf{x}}})_i) < 0$ or $\mathbf{g}(\hat{\mathbf{x}} - d_i(\sqrt{\Sigma_{\mathbf{x}}})_i) < 0, d_i := \alpha d_i$
 2. **output** $x_i = \hat{\mathbf{x}} + d_i(\sqrt{\Sigma_{\mathbf{x}}})_i, x_{i+N} = \hat{\mathbf{x}} - d_i(\sqrt{\Sigma_{\mathbf{x}}})_i, W_i = 1/2d_i^2, W_0 = 1 - \sum_{i=1}^{2N} W_i$

3 Application

The proposed CUKF algorithm is applied to parameter identification of a reinforced concrete frame. A set of four full-scale two-story two-bay concrete frames were constructed and tested to investigate performance of different seismic retrofitting methods [11]. As shown in Fig. 1a, each frame was built independently with a gap from its neighboring frames. A 75-kip hydraulic linear inertial shaker was installed on the frame and provided excitation for testing. The frame is of 24 ft in height and 36 ft in length. During construction, concrete pouring was conducted in five stages, indicated by five different colors shown in Fig. 1b.

To provide excitation, the hydraulic linear inertia shaker generated a scaled El Centro earthquake signal on the frame inducing in-plane vibration of the structure.

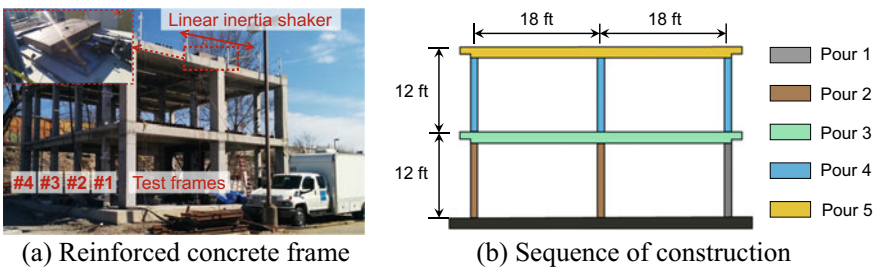


Fig. 1 Full-scale test frame and pour sequence

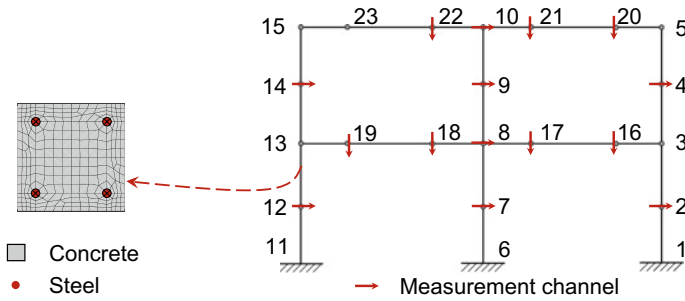


Fig. 2 FE model for the reinforced concrete frame

An accelerometer was installed on the moving mass of the shaker for calculating the exact shaker force during the test. In addition, a total of 44 acceleration channels were instrumented on the structure to measure the dynamic response of the frame. There were 27 channels along longitudinal direction, and 17 channels along vertical direction. Specifically, the accelerometers were instrumented at mid-length and quarter length locations of each component of the frame. Structural acceleration responses were sampled at 200 Hz and were filtered by a Butterworth filter to remove phase distortion. Experimental data from frame #1 is used for the parameter identification.

To simulate the dynamic behaviors of the reinforced concrete frame, a 2D FE model is built based Euler–Bernoulli beam theory as shown in Fig. 2. There are 23 nodes and 24 elements in the model which neglects axial deformation of elements. As illustrated in the figure, composite sections consisting concrete and steel rebars are adopted for each element. The base nodes are fixed according to the design drawing. Considering both the sensor instrumentation and node locations of the FE model, it is assumed that 15 DOFs are measured by sensors, as annotated by red arrows in the figure.

In the initial model, nominal values of Young’s moduli of the concrete and steel rebars are adopted, as listed in Table 1.

The FE model is divided into five parts according to the construction phases which may influence their mechanical characteristics. Five stiffness variables $\theta \in \mathbb{R}^5$ representing the relative change from the nominal values are selected for updating. Besides stiffness variables, two damping ratios $\zeta \in \mathbb{R}^2$ are also updated to construct a Rayleigh damping matrix. The FE model is further condensed to the 15 measured DOFs based on Guyan model reduction technique. Newmark-beta method is adopted to solve the dynamic responses of the frame structure. The initial values of model parameters are set as $\theta_{i,0|−1} = 0$ and $\zeta_{i,0|−1} = 0.02$. To confine parameter estimates

Table 1 Nominal values of Young’s moduli of concrete and steel (Unit: kips/in²)

Material	Young’s moduli
Concrete	3,800
Steel	28,000

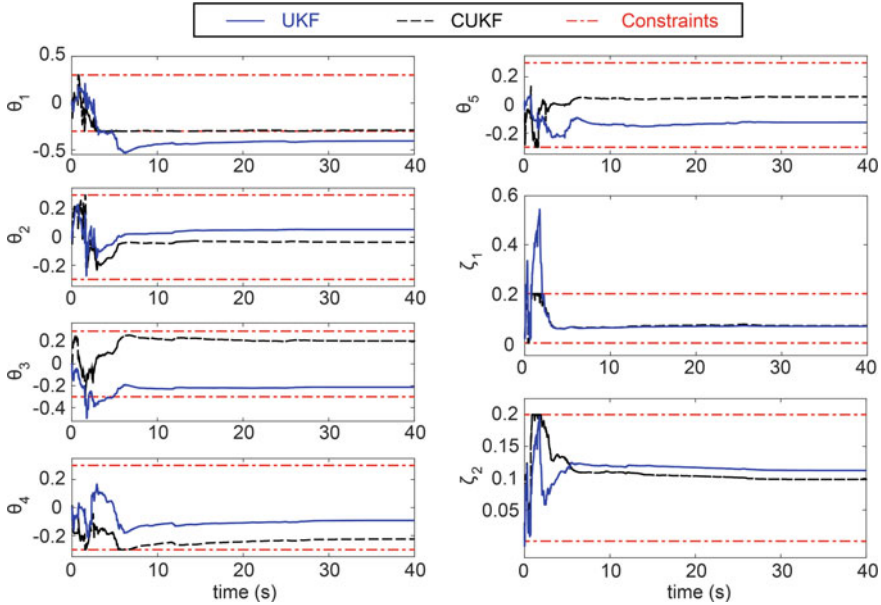


Fig. 3 Identified stiffness variables and damping ratios from UKF and CUKF

within reasonable range, bound constraints are applied during identification process:

$$-0.3 \leq \theta_i \leq 0.3, 0.001 \leq \zeta_i \leq 0.2 \tag{16}$$

Both the standard UKF and the proposed CUKF are utilized to identify parameters of the frame structure. Figure 3 plots the time histories of the a posteriori parameter estimates updated from experimental measurements. The figure shows that model parameters undergo strong fluctuations during the beginning 5 s of identification process, and gradually converge to constant values. It should be noted that the estimates of the CUKF always stay within the pre-set feasible domain, but some of the UKF estimates violate the constraints. For example, the UKF estimate of θ_1 drops below -0.3 and reaches a value about -0.4 at the end of identification process, indicating a quite large decrease of member stiffness. In addition, the UKF estimate of ζ_1 rises up to about 0.5, which is far beyond reasonable range of damping ratios of concrete structures.

Table 2 summarizes final identification results provided by the UKF and the CUKF for the reinforced concrete frame structure. Both UKF and CUKF results show that the stiffness values of members constructed by the 1st and 4th pouring decrease from the nominal value. On the other hand, the two identification methods give opposite trends for the other stiffness parameters. The decrease in stiffness values of column members (θ_1, θ_2 and θ_4) may be caused by the $P - \Delta$ effect. In terms of damping ratios, the values provided by the CUKF are reasonable for reinforced concrete structures,

Table 2 Identification results using the UKF and the CUKF of the reinforced concrete frame structure

Parameter	UKF	CUKF
θ_1	-0.4045	-0.2895
θ_2	0.0542	-0.0358
θ_3	-0.2127	0.2094
θ_4	-0.0913	-0.2247
θ_5	-0.1236	0.0585
ζ_1	0.0696	0.0720
ζ_2	0.1122	0.0982

whose damping ratios typically range from 0.05 to 0.10 [12]. However, the value of ζ_2 identified by the UKF is slightly higher than the typical range.

To further investigate performance of the UKF and the CUKF, updated FE models using identified parameters are built to simulate the dynamic response of the structure. Using the same excitation signal, dynamic responses of the structure are calculated and compared with measured data. Acceleration responses of the frame structure at Node 7 and 10 simulated by models using initial parameters and the updated parameters are given in Fig. 4. It is clear that the initial model could not generate accurate simulation results of structural behaviors. Using parameters identified by the UKF and the CUKF, FE models could predict structural behaviors close to the experimental measurements. It should be emphasized that although FE models updated by the UKF and the CUKF provide similar dynamic responses, the parameters identified by the CUKF are more reasonable in the engineering sense.

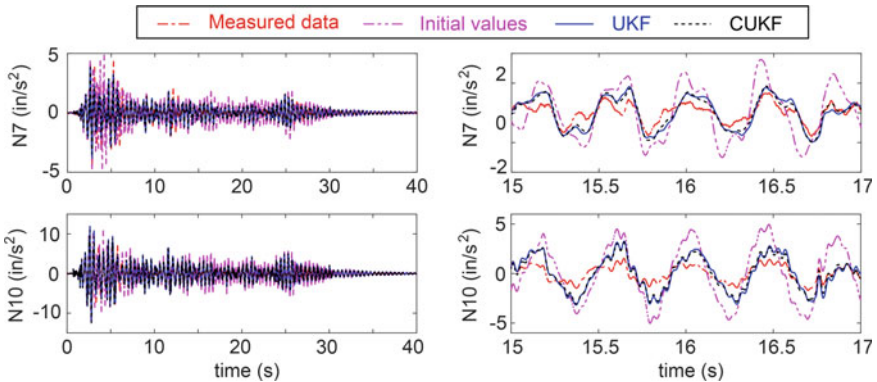


Fig. 4 Simulated acceleration using different model parameters

4 Conclusions

In this paper, a CUKF method is proposed and developed for identifying structural parameters from noisy measurements of dynamic responses. In this method, the parameter constraints are implemented by adjusting the sigma points generated in each iteration. A simple but effective backtracking line search method is adopted to ensure that the sigma points satisfy bounds or other types of constraints. The weighting factors of the new set of sigma points are recalculated to achieve a second order accuracy of the state probability distribution. To verify the effectiveness of the proposed method, parameter identification of a full-scale reinforced concrete frame is conducted. Stiffness parameters of different structural members and damping ratios are identified from the measured acceleration responses using the UKF and the CUKF. The identification results demonstrate that the CUKF can effectively confine state estimate within pre-set feasible domain, and provide reasonable parameter estimates. Compared to initial model, the updated FE model can better capture characteristics of the structure and give response predictions closer to experimental measurements.

Acknowledgements This research was partially funded by the Fundamental Research Funds for the Central Universities (#3205002103A2). Any opinions, findings, and conclusions or recommendations expressed in this publication are those of the authors and do not necessarily reflect the view of the sponsors.

References

1. Astroza R, Alessandri A (2019) Effects of model uncertainty in nonlinear structural finite element model updating by numerical simulation of building structures. *Struct Control and Health Monit* 26(3):e2297
2. Friswell M, Mottershead JE (2013) *Finite element model updating in structural dynamics*. Springer Science & Business Media
3. Astroza R, Ebrahimian H, Conte JP (2019) Performance comparison of Kalman—Based filters for nonlinear structural finite element model updating. *J Sound Vib* 438:520–542
4. Song M, Astroza R, Ebrahimian H, Moaveni B, Papadimitriou C (2020) Adaptive Kalman filters for nonlinear finite element model updating. *Mech Syst Signal Process* 143:106837
5. Olivier A, Smyth AW (2017) Particle filtering and marginalization for parameter identification in structural systems. *Struct Control Health Monit* 24(3):e1874
6. Wu M, Smyth AW (2007) Application of the unscented Kalman filter for real-time nonlinear structural system identification. *Struct Control Health Monit* 14(7):971–990
7. Van Der Merwe R, Wan EA (2001) The square-root unscented Kalman filter for state and parameter-estimation. In: 2001 IEEE international conference on acoustics, speech, and signal processing. Proceedings (Cat. No. 01CH37221). IEEE
8. Simon D (2006) *Optimal state estimation: Kalman, H infinity, and nonlinear approaches*. Wiley, Hoboken, NJ
9. Calabrese A, Strano S, Terzo M (2018) Adaptive constrained unscented Kalman filtering for real-time nonlinear structural system identification. *Struct Control Health Monit* 25(2):e2084
10. Wu B, Wang T (2014) Model updating with constrained unscented Kalman filter for hybrid testing. *Smart Struct Syst* 14(6):1105–1129

11. Wright TR (2015) Full-scale seismic testing of a reinforced concrete moment frame using mobile shakers. Ph.D., Civil and Environmental Engineering, Georgia Institute of Technology, Atlanta, GA, USA
12. Chopra AK (2011) Dynamics of structures: theory and applications to earthquake engineering, 4th edn. Pearson Prentice Hall, Upper Saddle River, NJ

Dynamic Response Evaluation of an Existing Bridge Structure Based on Finite Element Modeling



Muhammad Rashid and Mayuko Nishio

Abstract Seismic excitation poses a serious risk to the road infrastructure network, particularly when it comes to the dynamic behavior of bridge structures. In order to assess the safety and serviceability of these structures, the dynamic response must be evaluated. In this regard, the finite element modeling is one of the widely used accepted methods which is equally applicable for the response evaluation of existing bridge structures. This paper focuses on the dynamic response evaluation of an existing highway bridge structure. The target system is a curved, box girder steel bridge, resting on soil type-II. For this purpose, a detailed 3D analytical modeling was carried out based on the recommended design guidelines, while considering the nonlinearities in the material and structural properties. The high intensity and low probability occurring, level-II type, accelerograms were retrieved and applied for dynamic response simulations. The parameters of interest analyzed were modal shapes, resonant frequencies, the response of substructure, and the laminated rubber bearings (LRBs). The resonant frequency associated with the fundamental mode observed was 0.978 Hz in the transverse direction. The displacement time histories were plotted at the selected node for the super and substructure. The reduction in relative displacement observed was ranging from 50.64% to 96.90%, which shows the effectiveness of LRBs in reducing the displacement demand on piers. It is worth mentioning, that despite a higher reduction rate in displacement, the bearings did not exceed the ultimate capacity limit state. Finally, the relative degree of vulnerability was described by developing the fragility functions for the pier and bearings, based on nonlinear time history analysis. The results showed that, for the given intensity demand, the reinforced concrete (RC) pier is highly sensitive to failure as compared to the rubber bearings.

Keywords Finite element modeling · Seismic fragility · Level-II type earthquake · Existing bridge · Laminated rubber bearing

M. Rashid (✉)

Department of Engineering Mechanics and Energy, University of Tsukuba, Tsukuba, Japan

M. Nishio

University of Tsukuba, Tsukuba, Japan

1 Introduction

Bridges in the road network behave like fuse elements during high-intensity dynamic excitations. The performance of bridges during previous earthquakes has proven that bridges are extremely sensitive to damages during earthquakes [1]. A considerable contribution has been made in the past few decades to assess the safety-based performance of these structures. For the most accurate response simulation, the analytical modeling approach is widely recognized. This method enables the practitioners and researchers to reproduce the inherent dynamic response of any structural system. After the disastrous major seismic events like Northridge 1994, and Kobe 1995, most of the existing bridges were damaged due to large deformation or displacement of the columns and bearings, resulting in collapse and unseating of the superstructure. Following that, the need for seismic evaluation and design methods that explicitly take into consideration the material and geometrical nonlinearities became the topic of interest to many researchers. In the more recent seismic regulation and guidelines, the dynamic response evaluation of the three-dimensional bridge model is recommended for the structures located in high-intensity seismic regions, extended to the planning and selection of appropriate strengthening approaches. The finite element (FE) analysis allows for a more systematic analytical approach to be implemented for the design and assessment of bridge infrastructure for safety and reliability evaluation. The wide applications include, structural health monitoring, repair and strengthening design, up-gradation and maintenance are among some of them [2]. The underlying principles can be used to model analytically the intrinsic non-linear characteristics of a particular structural system subjected to dynamic excitation. A real-time experimental investigation based on large-scale testing is still needed to ensure enough credibility of these models for assessment purposes. However, sometimes due to unavailability or capacity limitations of the available testing facilities and equipment, the problem is tackled by analytical modeling with some numerical approximation and physical assumptions. The accuracy of these models can further be upgraded by incorporating field data for the subsequent structural analysis or health monitoring.

The seismic performance of bridge structures is usually expressed in terms of fragility functions, which expresses the probability of reaching or exceeding a certain damage state level during any seismic event. Usually, for the simplest type of system, the system fragility is described based on the most vulnerable component. This approach may be appropriate for the system where the seismic response is largely governed by the most fragile component. The study by Nielson and DesRoches [3], showed that a bridge as a system is more fragile than any one of the individual components. It was reported that the results alter approximately by 50% when the column fragility is considered as the representative of the system fragility. When the most fragile component reaches its capacity level, there is a probability that the rest of the components will be at some fraction of the damage state for the same input seismic demand. This provides enough support to the consideration of multiple components for the derivation of the system fragility. Moreover, response in complex

bridge systems is affected by the change in input loading direction in conjunction with the change in the direction of the bridge system. To develop a representative system's fragility functions, all these complexities and the individual component response should be considered.

This study is divided into several steps, which include the development of finite element representative model, dynamic response evaluation, component, and system fragility evaluation, consideration to uncertainty quantification in structural, material, and loading properties, and their resultant effect on the global system fragility. This paper primarily focuses on the development of the FE model and dynamic response evaluation of a testbed seismically isolated steel box girder bridge structure, subjected to level-II type lateral loading. Dynamic response of structural components is evaluated both in the longitudinal and transverse direction with laminated rubber bearings as isolation devices. A detailed finite element modeling was carried out and dynamic simulations were performed using the incremental dynamic analysis (IDA) approach. The displacement response histories of the pier and bearings are compared for evaluation purposes. The bearing hysteresis response history shows that they are highly effective in reducing the displacement demand on the pier while remaining within the safe limit of the ultimate capacity. For different damage state values, the fragility curves are developed for the pier and bearing components, which later on, in the next phase of this study, will be combined to estimate the global fragility of the bridge system.

2 Description of the Target Bridge System

2.1 Structural and Geometric Configuration

The target bridge in this study is a highway bridge, located in Yokohama city Japan, shown in Fig. 1. The total span of the bridge is 327.9 m, the width is 16.95 m to 13 m for the mainline, and 5.4 m to 5.2 m for the ramps. Structurally it is a composite type of system, consisting of steel and RC sections. The geometric complexities are due to the presence of the on-off ramps and horizontal curvature in the mainline. The total length is divided into six unequal spans and is supported by five steel and



Fig. 1 Panoramic view of the study bridge structure

Table 1 Structural details of the target bridge

Description	Superstructure	Substructure		
Geometry	6 span continuous steel box girders	Piers	Steel pier	P7, P8, P9, P10, P11
			Reinforced Concrete (RC) pier	P6
		Foundation	Shallow foundation	P8, P9, P10, P11
			Pile foundation	A2, A3, A4
Concrete	$\sigma_{ck} = 30 \text{ N/mm}^2$	$\sigma_{ck} = 24 \text{ N/mm}^2$		
Structural steel	SM 490Y, SM400, SS400			
Steel bar	SD 345			

one RC piers and abutments at the end. Gate shape piers, consisting of twin piers, are provided at the wider zones, where the ramps are joining the main structure. The bridge is standing on soil type-II, which is hard soil with a predominant period of $0.2 \leq T_G < 0.4$ s. The characteristic strength of the concrete used in superstructure and substructure are 30 and 24 N/mm², respectively. Throughout the structure, the SM 490Y, 400, and SS 400 steel framing sections are employed, which are super heavy steel plates used for welded structure of bridges in highway construction. For the seismic isolation, the LRBs are provided at the top of the piers. The structural details are summarized in Table 1.

2.2 Numerical Modeling

For understanding the dynamic response of the bridge system, the analytical 3D modeling of the structure was carried out using a finite element software *Engineer's Studio* Forum-8 [4]. The superstructure was modeled as a linear beam element because of the relatively higher stiffness value and without changing the geometrical properties to alter the mass. Similarly, the abutments were represented by elastic beam elements. For the non-linear response of the piers, the piers are modeled as Fiber-elements. Two basic types of fibers were used for the composite sections, the confined concrete, and the unconfined steel sections. Each single fiber unit is associated with a unique non-linear constitutive material model for confined and unconfined regions, as shown in Fig. 2c. The bent-top beams are modeled as linear elastic beam elements. The plastic hinge element is employed for RC pier-6 and represented by Takeda nonlinear model. Figure 2b. Subsequently, the material constitutive models are defined, and the section's discretization was carried out.

The link between the superstructure and bents are LRBs, which are primarily responsible for resisting the shear forces during lateral loading. Bi-linear shear spring elements are used to simulate the mechanical characteristics of the LRB. Additionally, since the direction of the bridge is continuously changing in the horizontal plane, the bearings are represented by multi shear springs (MSS) elements, such that

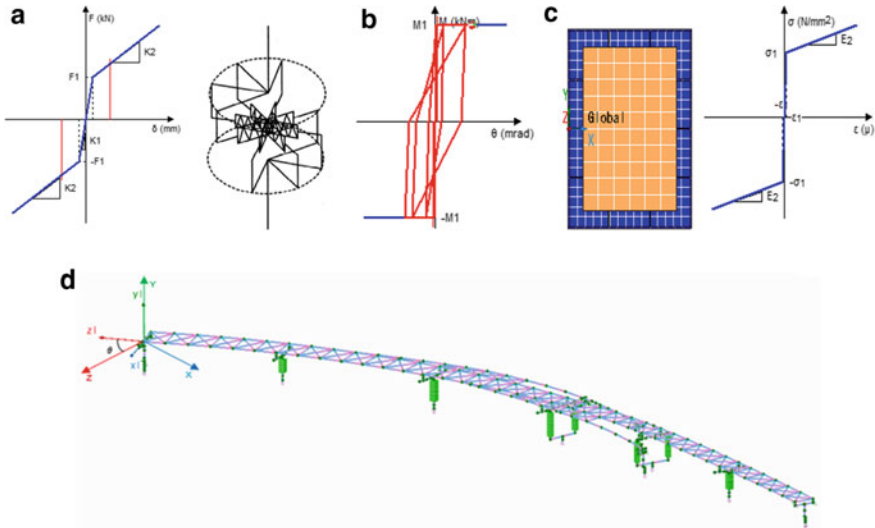


Fig. 2 Analytical model of the bridge **a** Bi-linear shear spring with MSS characteristics **b** Takeda model for the concrete pier **c** Pier’s fiber section with material constitutive model **d** Bridge model

it shows the same non-linear characteristics throughout the horizontal plane. In this model, a total of 12 springs are combined in the MSS element at a 15-degree interval, as shown in Fig. 2a.

To account for the soil-structure interaction, equivalent linear translational and rotational springs were defined to model the piers and abutment foundations. The stiffness values were calculated based on the foundation type and soil characteristics based on the Japanese highway design documentation. The 3D finite model of the bridge is shown in Fig. 2.

2.3 Modal Characteristics

Generally, the natural vibration modes characterize the dynamic response of the structure. For the current case, the resonant frequencies and the associated modal shapes are retrieved and presented in Fig. 3. The fundamental mode was a transverse vibration-based mode having a frequency of 0.97 Hz. The first four modes showed that the structure undergoes larger displacement in the horizontal plane, which is the same as described in the reference design document. Table 2 describes the comparison of the resonant frequencies with the reference design document values. The relative difference is due to the approximations made in analytical modeling.

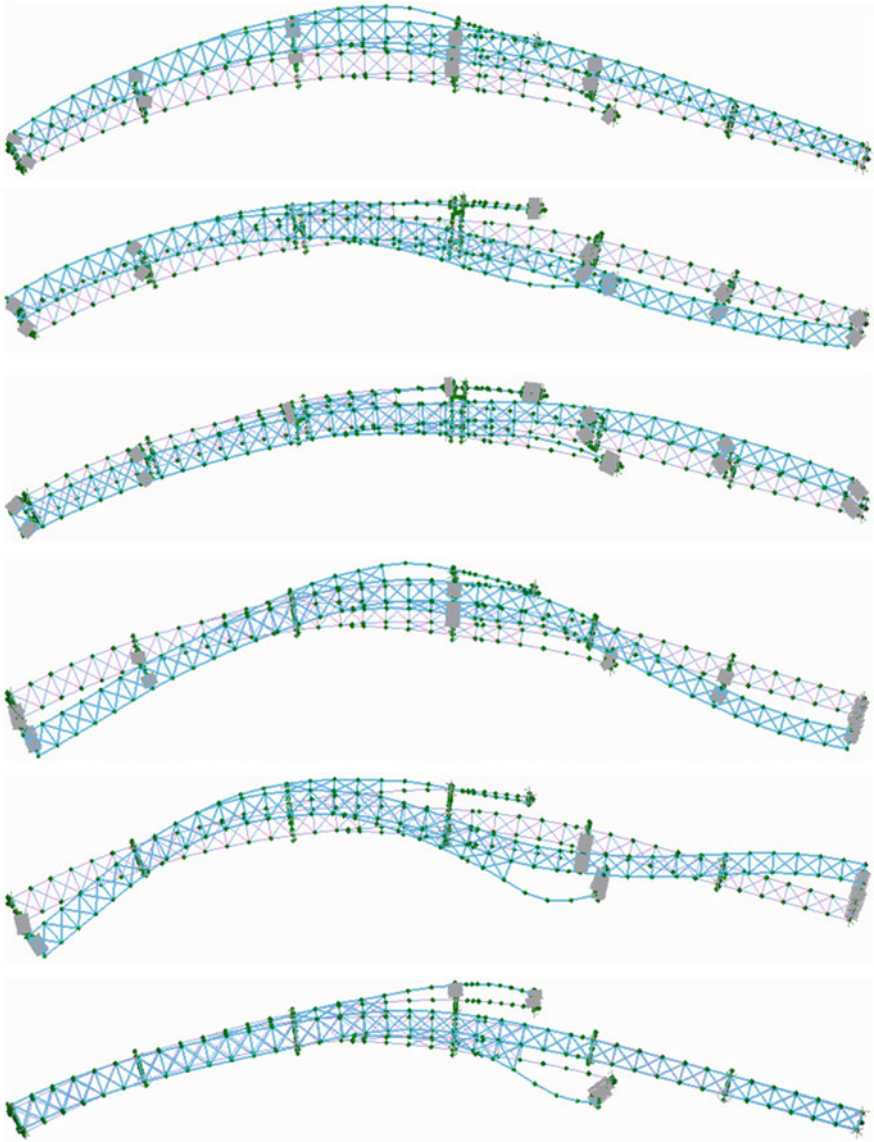


Fig. 3 First six modal shapes

Table 2 Comparison of the analytical and the design reference resonant frequencies

Mode #	1	2	3	4	5	6
Analysis result (Hz)	0.97	1.06	1.10	1.26	1.54	1.71
Reference value (Hz)	0.65	0.67	0.72	0.88	1.16	1.24

2.4 Non-Linear Time History Analysis

The non-linear time history analysis was performed using the Newmark- β method with an integration time step of 0.01 s. Using the design standards, the damping coefficient of 3% and 5% are used for the steel and concrete elements, respectively. Following the 1995 Kobe earthquake, the design guidelines were revised for the bridge infrastructures. According to this, the high intensity and low probability occurring (level-II) design earthquakes must be taken into considerations. These types of earthquakes are rarely occurring with high intensity at tectonic boundaries, which have excessive acceleration vibrations, and hence are more destructive in nature. Since, the bridge is resting on the ground with soil type-II characteristics, for which the level-II type acceleration waveforms on soil type-II were retrieved from Strong Ground Motion Network database (K-Net and KiK-net) Japan [5]. The selected accelerograms and the associated response spectra are presented in Fig. 4, for which the PGA ranges from 0.69 g to 0.75 g.

3 Dynamic Response Evaluation

3.1 Structural Components Response

Due to geometrical irregularities and variation in the loading direction, the basic elements and their properties were defined in local coordinates, therefore for response evaluation, initially the global responses are transformed into the local coordinate system by employing the coordinate transformation relationship presented in Eq. (1).

$$\begin{bmatrix} x \\ y \end{bmatrix} = \begin{bmatrix} \cos(\theta) & -\sin(\theta) \\ \sin(\theta) & \cos(\theta) \end{bmatrix} \begin{bmatrix} X \\ Y \end{bmatrix} \quad (1)$$

where θ is the relative measure of the angle between the two coordinates system, x, y and X, Y represents the response in the local and global coordinate system, respectively.

Since the structure is designed as seismically isolated, the response of the piers and superstructure are considerably varying for the same input excitation. For instance, the peak displacement responses at the selected nodes are compared for the longitudinal and transverse input loading direction in Table 3. The relative reduction in displacement ranges from 50.64% to 96.90%, which shows that the bearings are highly effective in reducing the displacement demand on the piers. The response variation of the pier 6 and the associated rubber bearing shows that for the longitudinal direction of loading, the relative peak displacement for the pier is reduced by 76.66% and 75.64% in longitudinal and transverse directions, respectively. For the transverse direction, the relative difference in displacement was 80.64% and

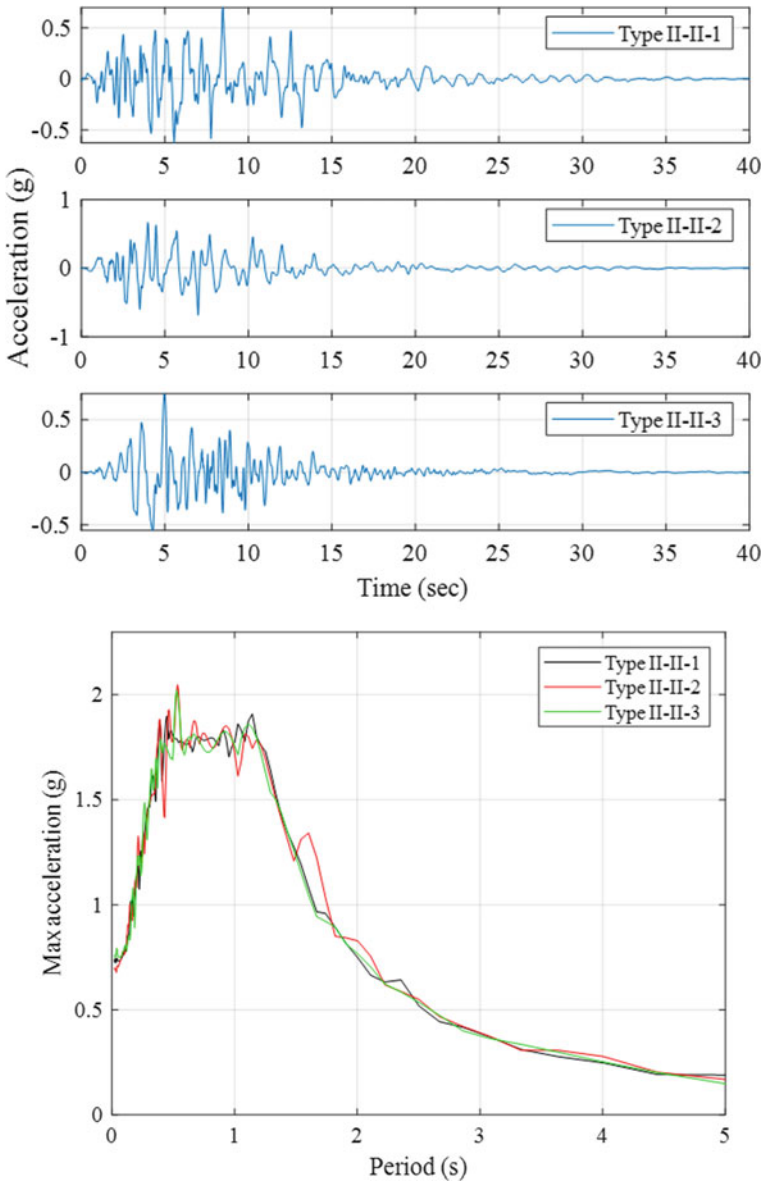


Fig. 4 Level-II type accelerograms and their response spectra

Table 3 Displacement response for the piers and the associated bearings

ID	0° loading						90° loading					
	Longitudinal displacement (mm)			Transverse displacement (mm)			Longitudinal displacement (mm)			Transverse displacement (mm)		
	Pier	Bearing	% Diff	Pier	Bearing	% Diff	Pier	Bearing	% Diff	Pier	Bearing	% Diff
6	86.21	369.333	76.66	30.66	125.85	75.64	26.95	139.19	80.64	74.52	269.94	72.39
7	23.44	218.34	89.26	27.31	237.96	88.52	27.10	243.60	88.88	25.17	181.33	86.12
8	58.70	190.10	69.12	61.28	194.90	68.56	70.06	217.22	67.75	61.47	184.88	66.75
9	78.09	158.21	50.64	81.44	178.48	54.37	30.96	282.49	89.04	30.79	239.90	87.17
10	45.59	288.07	84.17	15.44	148.65	89.61	5.25	169.16	96.90	23.24	346.81	93.30
11	26.43	251	89.47	21.99	218.42	89.93	24.65	213.99	88.48	29.31	226.10	87.04

72.39% in longitudinal and transverse directions, respectively. The % difference in displacement responses of the piers and the associated bearings, subjected to the same loading direction, are almost the same in the longitudinal and transverse direction. For different loading directions, the relative %- difference in response is attributed due to the change in the relative stiffnesses of the pier and the associated bearing in each direction. The effect of loading direction is also evident from the relative response values. The displacement time histories for the pier (P6) top and the associated bearings in the longitudinal and transverse directions are presented in Fig. 5 for the longitudinal and transverse loading direction, which demonstrates that the columns and bearings undergo permanent relative residual deformation.

Figure 6a shows the orbit displacement of the rubber bearing at P6, which describes the relative displacement profile of the pier top and the superstructure. The maximum relative displacement of about 370 mm is observed in the longitudinal direction which is almost three-fold of the maximum relative displacement in the transverse direction for the 0° loading. With the change in loading direction, the dominating response direction also changes, like for the same bearing subjected to 90° loading direction, the transverse displacement is dominating, which is almost double of the longitudinal displacement. The relative comparison of the hysteresis profile, in Fig. 6b for two different loading directions, shows that higher energy dissipation demand is associated with the 0° loading direction because of relative larger displacement in the longitudinal direction. For any time range, connecting the maximum and minimum loads by a straight line shows the approximate effective stiffness of the LRB. As the time duration increases, the decrease in effective stiffness can be observed from the hysteresis profile. The shear strain results are summarized in Table 4 for all the bearings at the pier's top, which shows the effect of change in direction on the shear strain demand. The maximum shear strain of 248.83% is observed for B9, which is lower than the failure limit of 250%.

4 Seismic Vulnerability Assessment of Bridge Components

Seismic fragility assessment is a widely accepted useful technique for the safety evaluation of critical infrastructure. The main applications include emergency response planning in disasters, functionality loss evaluation, seismic design, retrofit design and prioritization, and economic loss assessment for a particular seismic event. Usually, the seismic vulnerability is expressed in terms of fragility functions, which describe the conditional probability of exceeding a seismic demand for a specific damage level [6, 7]. Different methodologies have been devised for fragility development, where some of them are based on expert opinions like ATC [8], others are empirically derived based on the actual damage field data from past earthquakes [9, 10], while some are derived based on the analytical modeling [7, 11, 12]. Among them, the analytical method is widely adopted since they are more rapidly applicable to all the bridge types and regions where there is no sufficient damage record available.

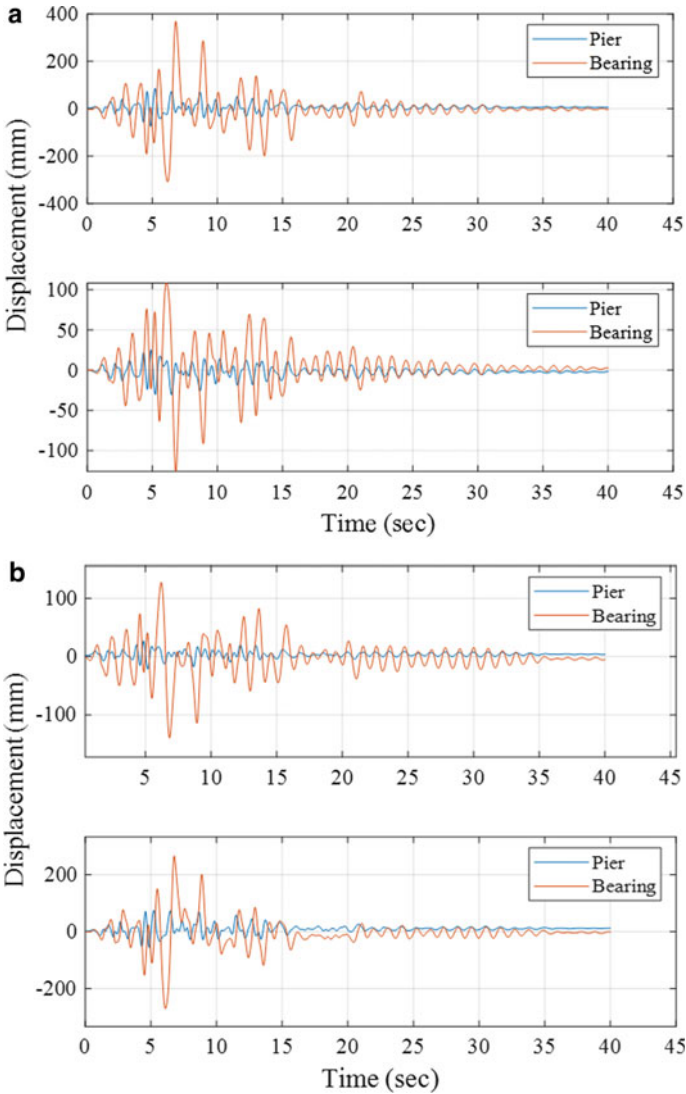


Fig. 5 Displacement response histories for the pier and bearing in longitudinal and transverse directions **a** 0° loading, **b** 90° loading

In probabilistic terms, the fragility can be described by Eq. (2), which expresses the condition of reaching or exceeding the damage state DS for the intensity demand value of x . using the nonlinear time history analysis, the probabilistic seismic demand model (PSDM) is developed, which relate the engineering demand parameter (EDP) and the intensity demand. The PSDM approach adopted here is based on the cloud method [3, 7, 11]. Ductility demand and shear strain parameters are considered as

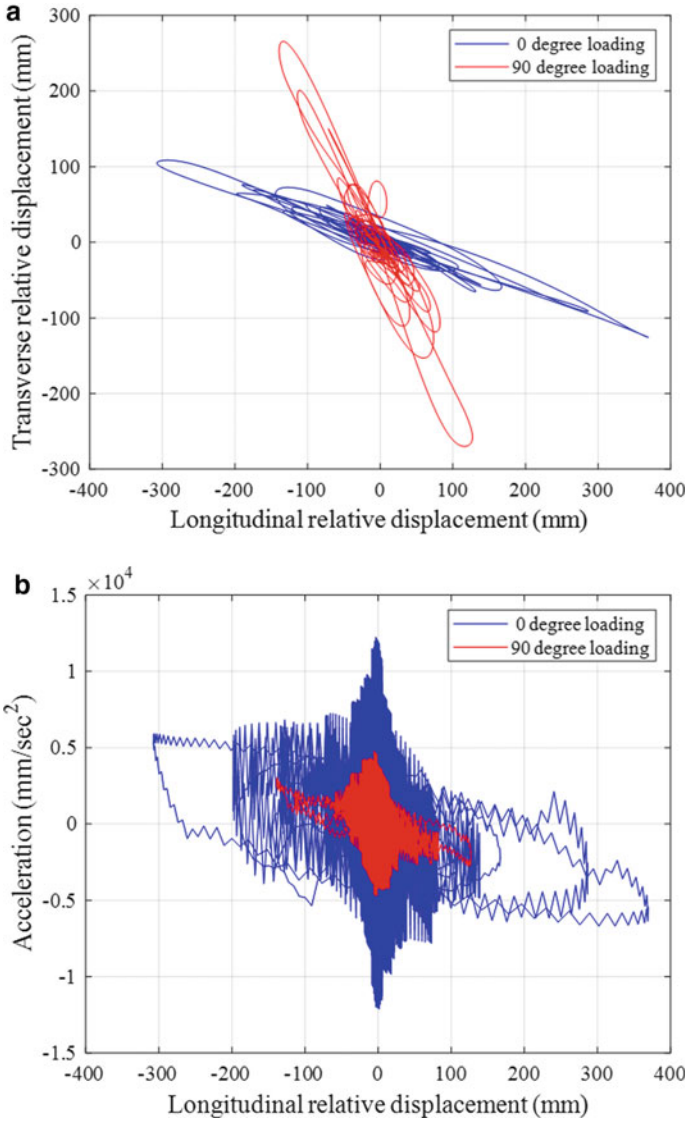


Fig. 6 Response of the bearing at P6 (a) Orbit motion of the LRB showing relative displacement between the pier and the bearing top (b) Hysteresis characteristics of the LRB

Table 4 Maximum shear strain values for the bearings in the longitudinal and transverse loading direction

Bearing ID	B6	B7	B8	B9	B10	B11
0° load (%)	179.80	171.49	144.67	165.45	147.29	173.24
90° load (%)	137.19	162.79	170.01	248.83	175.30	162.11

the EDPs for fragility development for the RC pier and bearings, respectively. Using the power law in Eq. (3), the mean and standard deviation for each limit state are calculated through regression analysis.

$$Fragility = P(DS|IM = x) \tag{2}$$

$$EDP = a(IM)^b \tag{3}$$

where a and b are regression coefficients. The IDA was carried out to obtain sufficient data points for the regression analysis, where the selected ground motions were scaled up to double of the actual PGA values. The fragility curves are derived based on Eq. (4) [13].

$$P[LS|IM = x] = \Phi \left[\frac{\ln\left(\frac{x}{\lambda_c}\right)}{\sqrt{\beta_d^2 + \beta_c^2}} \right] \tag{4}$$

where $\Phi[\]$ represents the standard normal cumulative distribution function, λ_c is the median value of the intensity measure IM and the term in denominator represents the cumulative dispersion for a particular damage state. For the damage state characterization, the HAZUS-MH (FEMA, 2003) criteria are employed, where a total of four damages states are defined for each component as described in Table 5 [14].

The seismic vulnerability of the bridge components is described in terms of fragility functions, which are based on the nonlinear response history analysis. Using pre-determined damage indices, a damaged state is assigned to each component. The probabilistic seismic demand models are developed using the peak response of the components obtained from IDA. Figure 7a, b shows the PSDMs developed for P6 in term of ductility and B9 in term of shear strain, respectively. The regression coefficients and demand dispersion parameters are obtained from the regression analysis. The fragility curves for the RC pier and bearing are developed using Eq. (4) and presented in Fig. 7c, d.

The fragilities are developed for transverse loading direction, which provides enough evidence about the higher damage probability of pier than the bearings. The seismic vulnerability of the pier in a slight, moderate and extensive damage state

Table 5 Damage state definition for the bridge components

Component	Damage state	Slight	Moderate	Extensive	Complete collapse
	Failure mode	Spalling	Moderate cracking	Moderate crushing	Severe crushing and collapse
Pier	Displacement ductility	$\mu_d > 1$	$\mu_d > 1.2$	$\mu_d > 1.76$	$\mu_d > 4.76$
LRB	Shear strain (%)	$\gamma > 100$	$\gamma > 150$	$\gamma > 200$	$\gamma > 250$

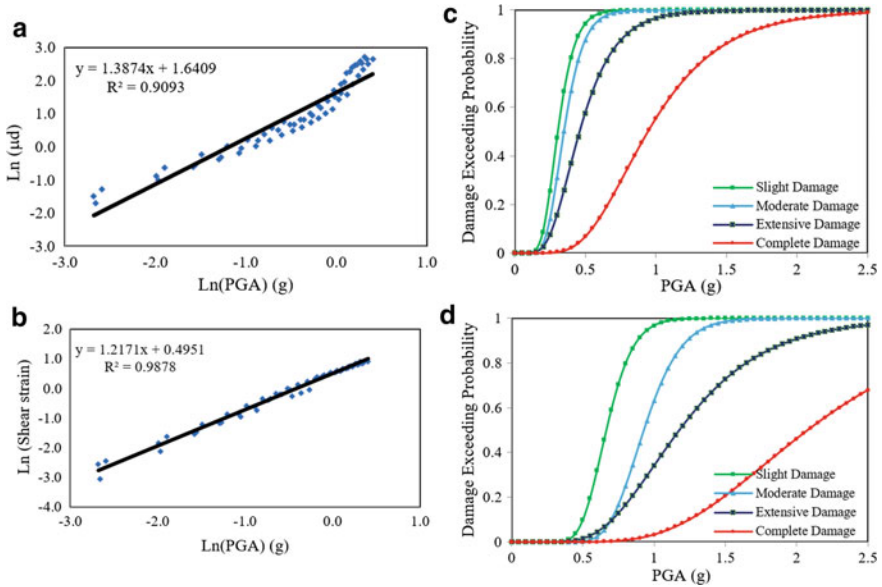


Fig. 7 PSDM and Fragility curves for loading in the transverse direction (a–c) Pier_6 (b–d) Bearing_9

is higher than the complete collapse state, which indicates the higher probability of minor cracking and spalling, even during low-intensity earthquake events. In contrast, the bearing response shows less vulnerability for the same demand associated with ground motion.

5 Conclusions

The dynamic response of an existing highway steel bridge was presented in the previous sections. For this purpose, a detailed nonlinear finite element modeling was carried out. The dynamic response of the bearings showed enough reduction in the displacement demand on the piers. The hysteresis behavior demonstrates that bearings are highly effective in dissipating the energy demand while remaining within the ultimate capacity limits for the given intensity of ground motion. The analytical fragility curves are developed for the pier and bearings using incremental dynamic analysis while considering level-II type earthquakes. The results showed that the bridge piers are highly vulnerable to possible damage for the medium to strong ground motions compared to the laminated rubber bearings. The response results can be used in assessing the structural vulnerability to estimate the potential loss associated with the high-intensity seismic events, retrofit design, retrofit prioritization, and seismic up-gradation.

In the next phase of this study, the components level fragility will be used in developing the global system fragility. Special attention will be made to consider the most fragile response based on the critical loading direction. Finally, the effect on system-level fragility will be quantified while considering the material, geometrical, and input loading uncertainties.

Acknowledgements The first author would like to acknowledge the support from the Japanese government through MEXT. We are also thankful to Prof. Gaku Shoji for his valuable comments and suggestions during the lab seminar activity.

References

1. Pan Y, Agrawal AK, Ghosn M, Alampalli S (2010) Seismic fragility of multispan simply supported steel highway bridges in New York State. I: Bridge modeling, parametric analysis, and retrofit design. *J Bridge Eng* 15(5):448–461. [https://doi.org/10.1061/\(asce\)be.1943-5592.0000085](https://doi.org/10.1061/(asce)be.1943-5592.0000085)
2. Nishio M, Marin J, Fujino Y (2012) Uncertainty quantification of the finite element model of existing bridges for dynamic analysis. *J Civ Struct Heal Monit* 2(3–4):163–173. <https://doi.org/10.1007/s13349-012-0026-z> Dec
3. Nielson BG (2005) Analytical fragility curves for highway bridges in moderate seismic zones. *Environ Eng* December, 400. <https://doi.org/10.1016/j.engstruct.2017.03.041>
4. Civil & Structural Engineering | FORUM8 | 3D VR & Visual Interactive Simulation. <https://www.forum8.com/solutions/engineers-studio/>. Accessed 09 Jun 2021
5. Strong motion seismographs network. <https://www.kyoshin.bosai.go.jp/>
6. Lins G (2001) Seismic fragility analysis of highway bridges
7. Choi E, DesRoches R, Nielson B (2004) Seismic fragility of typical bridges in moderate seismic zones. *Eng Struct* 26(2):187–199. <https://doi.org/10.1016/j.engstruct.2003.09.006>
8. Applied Technology Council—ATC (1985) Earthquake Damage Evaluation Data for California, ATC-13 Report, Applied Technology Council, Redwood City. - References - Scientific Research Publishing. [https://www.scirp.org/\(S\(351jmbntvnsjt1aadkposzje\)\)/reference/ReferencesPapers.aspx?ReferenceID=1276600](https://www.scirp.org/(S(351jmbntvnsjt1aadkposzje))/reference/ReferencesPapers.aspx?ReferenceID=1276600). Accessed 29 Jun 2021
9. Shinozuka M, Feng MQ, Lee J, Naganuma T (2000) Statistical analysis of fragility curves. *J Eng Mech* 126(12):1224–1231. [https://doi.org/10.1061/\(asce\)0733-9399\(2000\)126:12\(1224\)Dec](https://doi.org/10.1061/(asce)0733-9399(2000)126:12(1224)Dec)
10. Basoz N, Mander JB (2021) Seismic fragility curve theory for highway bridges. https://www.researchgate.net/publication/292691534_Seismic_fragility_curve_theory_for_highway_bridges. Accessed 26 Jun 2021
11. Nielson BG, DesRoches R (2007) Analytical seismic fragility curves for typical bridges in the central and southeastern United States. *Earthq Spectra* 23(3):615–633. <https://doi.org/10.1193/1.2756815>
12. Billah AHMM, Alam MS (2013) Seismic fragility assessment of multi span continuous concrete highway bridges in British Columbia. *Proc Annu Conf - Can Soc Civ Eng* 5(January):4053–4062
13. Tavares DH, Padgett JE, Paultre P (2012) Fragility curves of typical as-built highway bridges in eastern Canada. *Eng Struct* 40:107–118. <https://doi.org/10.1016/j.engstruct.2012.02.019>
14. Hazus @-MH User Manual. Accessed 28 Jun 2021. www.msc.fema.gov

A New Attempt at Estimating Natural Vibration and Bending Deformation Characteristics of Super High-Rise Buildings Using Wave Interferometry



Xin Wang, Testushi Watanabe, and Masayuki Nagano

Abstract In this paper, we attempt to estimate the bending-shear ratio of super high-rise buildings using the wave interferometry method. Firstly, some basic examinations on the relationship between the fundamental period and shear-wave travel time from the base to the top of buildings was performed. Then the bending-shear ratios of super high-rise buildings were estimated based on the ratios of the period of bending-shear vibration and the period of vibration only in shear mode. We found that, in the heterogeneous shear model, four times of the travel time from the base to the top is about 1.33 times of the fundamental period regardless of the number of stories. In the bending-shear models, the difference between four times of the travel time and the fundamental period becomes larger with the increasing number of stories. The bending-shear ratio of super high-rise buildings over 120 m can be estimated accurately.

Keywords Bending-shear ratio · Super high-rise building · Wave propagation · Shear-wave travel time · Natural period

1 Introduction

In response analysis of super high-rise buildings, it is necessary to consider the change in eigen periods of higher-order modes due to the growing overall bending deformation with the increase of overturning moment. However, it is difficult to evaluate the effect directly by strong-motion observation or microtremor measurement [1]. In the previous studies, the seismic interferometry was applied to super high-rise buildings

X. Wang (✉)

Department of Structural Engineering, Ashikaga University, Tochigi, Japan

e-mail: wang.xin@g.ashikaga.ac.jp

T. Watanabe

Taisei Corporation, Tokyo University of Science, Chiba, Japan

M. Nagano

Tokyo University of Science, Chiba, Japan

to evaluate the propagation time and shear-wave velocity V_s from the waves propagating vertically between the layers of the building [2]. If the wave propagation time obtained by the seismic interferometry is attributed only to the shear component of the whole building, it may be possible to extract the bending component generated by the overturning moment.

In this study, firstly, the relationship between wave travel time obtained from the reconstructed wave field by the deconvolution method and the fundamental natural period was reviewed. Also, the effect of the frequency characteristics of the input wave on the accuracy of the travel time and the velocity are investigated using a 10-story building model. Then, the relationships between travel time and natural periods are investigated using a generic shear multi-degree-of-freedom model (generic S model) and a generic bending-shear multi-degree-of-freedom model (generic BS model) that reflect the average structural characteristics of existing super high-rise RC buildings in Japan. In addition, the effect of the bending component in the seismic interferometry is investigated, and the evaluation accuracy of the bending-shear ratio calculated is examined using a vibration analysis model.

2 Relationship Between Propagation Time and Fundamental Period

2.1 Examination Using Homogeneous Building Model

As a basic study, a ten-story building model with uniform stiffness of each story is used to examine the commonly accepted relationship between shear-wave travel time (τ) and the fundamental period (T_1), i.e., $T_1 = 4\tau$. Also, shear-wave travel times extracted from deconvolved waves are compared with the theoretical values and the values from the pulse travel time. The building plane area is $A = 15 \text{ m} \times 30 \text{ m}$, the floor height is 3 m, and the mass is calculated by $1.4 \times A = 630t$. The shear-wave velocity traveling within each story is set to be $V_s = 500 \text{ m/s}$. The attenuation is Rayleigh attenuation, and the first- and second-order attenuation factors are both 3%. Figure 1a shows the acceleration response waveforms of each floor under an incident Ricker wavelet (central frequency 10 Hz, sampling rate 1000 Hz) from the foundation. Figure 1b shows the transfer function between the top and the foundation, where the first order eigen period is 0.24 s. Figure 1c shows the deconvolved wave at the top and inter floors with respect to the wave at the top [3], which include one up-going wave (pulse) and down-going wave (pulse). It can be seen that the travel time from the foundation to the top is 0.6 s, which is 1/4 of the fundamental period of the building model. In Fig. 1d, the shear wave travel times from foundation to the inter floors and the top are compared among the values extracted from deconvolved waves (red closed circles), the impulse travel time (black closed circles), and the theoretical values (gray closed circles). Because the superposition of up-going and down-going waves of deconvolved waves at the 8F and 9F, the travel time cannot

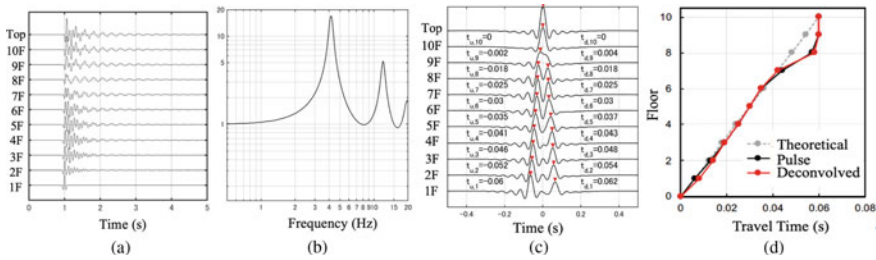


Fig. 1 **a** Acceleration response at each floor; **b** transfer function between top and the base; **c** deconvolved waves; **d** comparison among the travel time extracted from deconvolved waves, impulse response, and the theoretical values

be read. However, the travel times are almost identical on other floors. Therefore, it can be confirmed that the shear-wave travel time can be accurately extracted by deconvolution, and the relationship $T_1 = 4\tau$ is corroborate when the stiffness of each story is uniform.

2.2 Examination Using Heterogeneous Building Model

A building model of ten-story wall-mounted RC building with story stiffness in inverted triangular distribution is used. The natural period is $T = 0.025 N$ (N is the number of stories). Table 1 shows the shear stiffness K , equivalent density ρ , and equivalent shear wave velocity $V_s (= \sqrt{G/\rho})$ for each story. In order to examine the effect of precision of extraction of travel time and the accuracy of shear wave velocity extraction, the center frequency of input Ricker wavelet the is set to 10 Hz, 50 Hz, and sampling rates of 1000 Hz and 10,000 Hz. The deconvolved waves corresponding to different center frequency and sampling rates are shown in Fig. 2a. Shear-wave

Table 1 Overview of the heterogeneous building model

Story	$K(\text{kN/m})$	$\rho(\text{t/m}^3)$	$V_s(\text{m/s})$
10	3.98×10^6	0.467	238
9	7.56×10^6	0.467	329
8	1.07×10^7	0.467	392
7	1.35×10^7	0.467	440
6	1.59×10^7	0.467	477
5	1.79×10^7	0.467	506
4	1.95×10^7	0.467	528
3	2.07×10^7	0.467	544
2	2.15×10^7	0.467	554
1	2.19×10^7	0.467	559

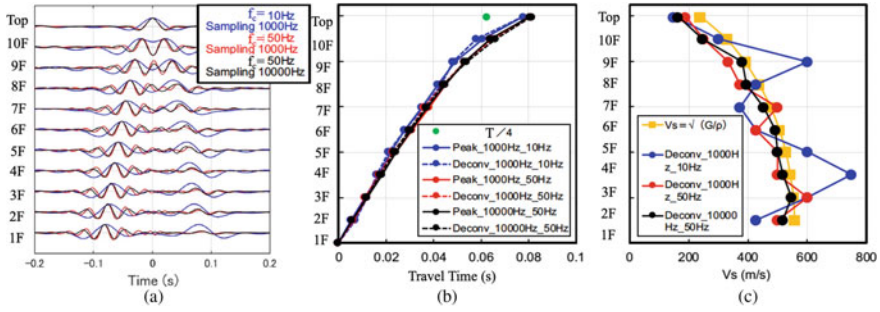


Fig. 2 **a** Deconvolved waves corresponding to different center frequency (f_c) of Ricker Wavelet and different sampling rate; **b** trave time from base to top; **c** shear-wave velocity within each story

travel time from base to top and the shear-wave velocity of each story are shown in Fig. 2b. Figure 2c, respectively. Regardless of the frequency characteristics of the input wave, the propagation time from the foundation to each layer calculated from the inverse superimposed wave is almost the same, and the accuracy of V_s is almost the same as the set value when the center frequency is 50 Hz and the sampling rate is 10000 Hz. The accuracy of V_s is almost equal to the set value when the central frequency is 50 Hz and the sampling rate is 10000 Hz. The response analysis will be conducted at the central frequency of 50 Hz and the sampling rate of 10,000 Hz in the following examination. The first-order eigenperiod of the building model is 0.25 s, and the four times of the propagation time from the base to the top is 0.33 s. Therefore, in the case of heterogeneous building models where the shear stiffness of each story is not uniform, the fundamental natural period of the building and four times of the propagation time from base to top are not consistent.

2.3 Examination Using Generic Models of Super High-Rise Buildings

A shear generic multi-degree-of-freedom (MDOF) model [4] (generic S model) and a generic bending-shear MDOF model [5] (generic BS model), which reflect the average of the structural properties of 39 existing super high-rise RC residential buildings in Japan, are used to investigate the relationship between shear-wave propagation time and natural periods. The number of floors is in the range of 20F ~ 50F. The outlines of the generic building models are shown in Table 2. Figures 3a, b show the comparison between the natural period (T_{deconv}) calculated from the four times of the shear-wave travel time from the base to the top and the first order natural period (T_{eigen}) calculated from the eigenvalue analysis. Figure 3c shows the ratio between T_{deconv} and T_{eigen} for both the generic S model and the generic BS model. In the generic S model, T_{deconv} is about 1.33 times larger than T_{eigen} , regardless of the number of floors. On the other hand, in the generic BS model, the difference

Table 2 Overview of generic models

<i>Generic shear model</i>	
Plane shape	30 m*30 m
Story height	3 m
Natural frequency	$T = 0.02H$
<i>Generic bending-shear model</i>	
Plane shape	Calculated by aspect ratio
Story height	5 m(1F),4 m(2F) 3 m(3 m~)
Natural frequency	$T = 0.02H$

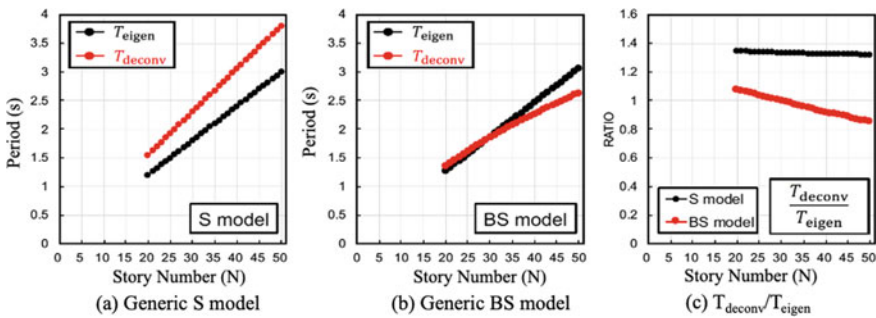


Fig. 3 Relationship between story number and the periods (T_{deconv} and T_{eigen}) for (a) the generic S model and (b) the generic BS model; (c) shows the ratio of period T_{deconv} and T_{eigen}

between T_{deconv} and T_{eigen} becomes larger at higher elevations because of the bending component.

3 Effect of Bending Component in Wave Interferometry

To investigate the effect of the bending component in the shear-wave interferometry, we compare the propagation time of the generic BS model and a pure S model by setting the bending stiffness EI multiplied by 1000. Figure 4 shows the comparison of the T_{deconv} and T_{eigen} in the generic BS model and the pure S model. There is a big difference between the T_{eigen} calculated from BS model and the pure S model. However, the T_{deconv} in the generic BS model and the pure S model are almost the same. That is to say that there is no effect of bending component to the extraction of shear-wave travel time from the deconvolved waves.

Inter-story shear velocity (V_s) calculated from the story height and the travel time in the generic S model, generic BS model, and pure S model with 20 stories and 50 stories are shown in Fig. 5. The inter-story V_s calculated from the shear stiffness of

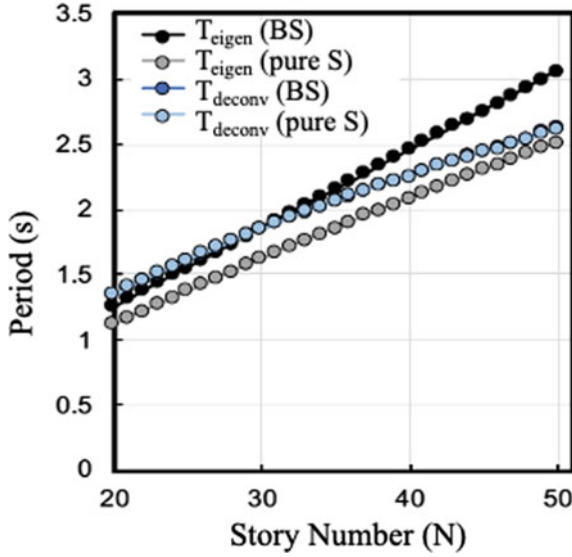


Fig. 4 Relationship between story number and the periods calculated from generic BS model and the pure S model

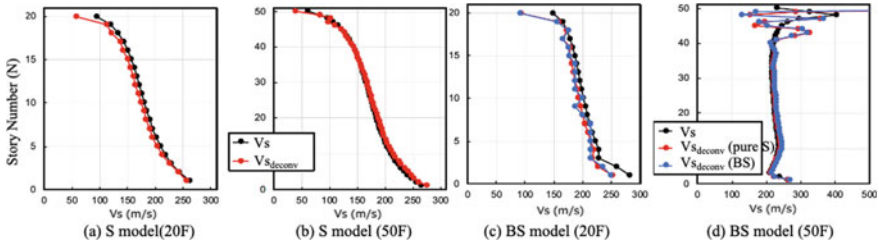


Fig. 5 Inter-story shear-wave velocity (V_s) calculated from the S model with (a) 20 stories(20F) and (b) 50 stories(50F); and from BS models and pure S model with (c) 20F and (d) 50F. the black closed circle present the V_s directly calculated from the parameters of the models

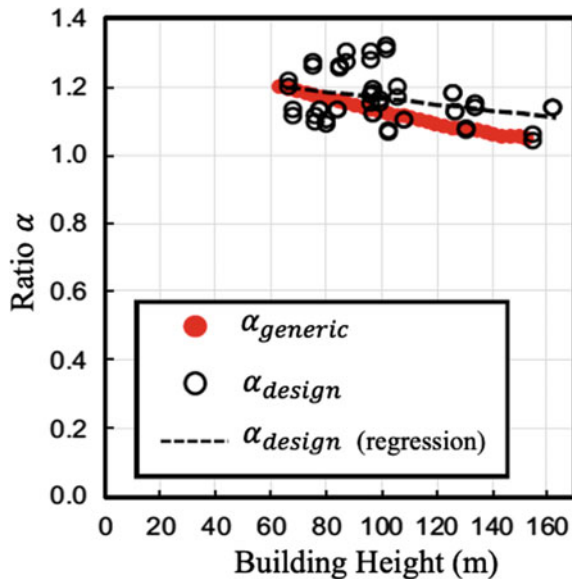
the building model are also shown in Fig. 5 with black closed circles. In the generic S model, where only the shear stiffness is set, V_s can be calculated more accurately than the propagation time. On the other hand, in the generic BS model and the pure S model, the shear stiffness becomes apparently larger due to the inverse shear caused by the bending deformation near the top. Moreover, the variation of V_s becomes larger due to the inability to extract the propagation time accurately, but it generally agrees with the set value. In addition, the distribution of V_s in the BS model and the pure S model is almost the same, which indicates that the wave interferometry can exclude the effect of bending component.

4 Calculation of Bending Shear Ratio Based on Propagation Time

From the previous section, it was confirmed that the wave interferometry can exclude the effect of the bending component. Therefore, it is possible to estimate the flexural shear ratio of the building from the propagation time. Let the natural period of the bending-shear model be T_{BS} and that of the pure shear model be T_S , according to the relationship between the natural period and the shear stiffness, the bending-shear ratio can be expressed as $\alpha^2 = T_{BS}^2/T_S^2$. In this study, we use the bending-shear models for seismic design of 24 existing high-rise buildings to study the relationships between the building height and bending-shear ratios. For the generic model, the ratio α is presented as $\alpha_{generic}$, and for the design model it is presented as α_{design} . The relationships between building height and $\alpha_{generic}$ and α_{design} are shown in Fig. 6. In the case of building height less than 100 m, $\alpha_{generic}$ and α_{design} are almost the same, while the difference becomes larger for buildings over 100 m.

Using $\alpha_{generic}$ and α_{design} shown in Fig. 6, we estimate the natural period T_S of the pure S model. Bending-shear ratios are calculated using the estimated T_S and the period T_{BS} of the BS model calculated from the eigenvalue analysis. The estimated bending-shear ratios based on the $\alpha_{generic}$ and α_{design} are shown in Fig. 7a, b, respectively, with the blue circles. In these figures, the black and red circles present the bending-shear ratios of the generic models and the design models, respectively, which were calculated from the eigenvalue analysis. The ratios of the bending-shear ratios of design models between the values from eigenvalue analysis (red circles) and the values from the $\alpha_{generic}$ and α_{design} (blue circles) are shown in Fig. 7c, d,

Fig. 6 Relationship between building height and ratio α for the generic building models and design models



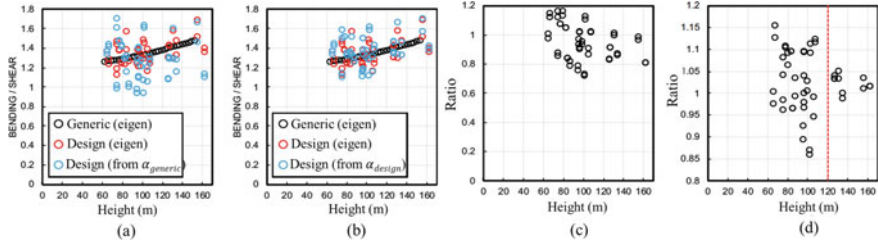


Fig. 7 Bending-shear ratios calculated by the eigenvalue analysis of generic models (black circles) and design models (red circles), and those from (a) ratio $\alpha_{generic}$ and (b) α_{design} (blue circles); (c) and (d) presents the ratio of bending-shear ratios of design models between the values from eigenvalue analysis (red circles) and those (blue circles) from ratio $\alpha_{generic}$ and α_{design} , respectively

respectively. It can be seen that the bending-shear ratios estimated from $\alpha_{generic}$ is more variable than those estimated from α_{design} . This is because the generic model reflects the general structural characteristics of existing buildings, and it is difficult to reproduce the structural characteristics of actual buildings individually. In Fig. 7d, if we focus on the high-rise buildings with height more than 120 m, the variation in the evaluation accuracy of the bending-shear ratio is relatively small.

In Fig. 8a, the new regression of α_{design} using only the values of buildings with height more than 120 m ($\alpha_{over120}$) are shown in the black broken line, which is higher than the values from the red line which is regressed using the $\alpha_{generic}$ models. The bending-shear ratios of design models estimated using the $\alpha_{over120}$ are shown in Fig. 8b with blue circles. In this figure, the red circles and black circles are the same with those in the Fig. 7b for the values of buildings with height more than 120 m. In order to compare the variations of the shear-bending ratios between the values estimated from α_{design} and those from the $\alpha_{over120}$, the ratios of bending-shear ratios

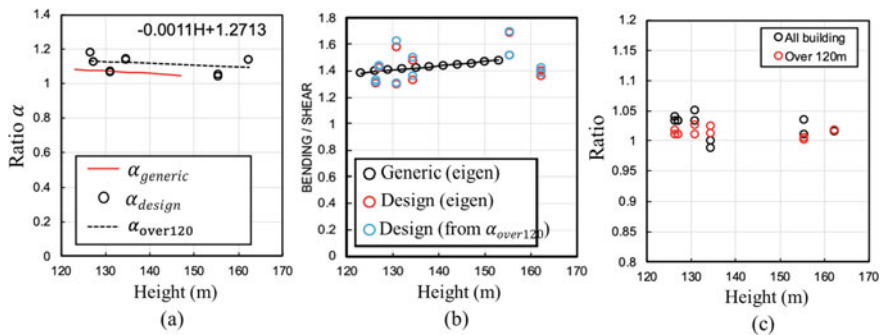


Fig. 8 a Ratio $\alpha_{generic}$, α_{design} and the regression of the height and the α_{design} for buildings over 120 m ($\alpha_{over120}$); b bending shear ratios from eigenvalue analysis of generic models (black circles) and design model (red circles), and the values estimated from $\alpha_{over120}$ (blue circles); c the ratios of the bending-shear ratios estimated from the α_{design} (black circles) and those from $\alpha_{over120}$ (red circles)

calculated from eigenvalue analysis and the regressed α are shown in Fig. 8c. the black circles are the same as the ones in Fig. 7d for buildings with height more than 120 m. It can be seen that for super high-rise buildings over 120 m the bending-shear ratios can be estimated with higher precision. In conclusion, it is possible that the bending-shear ratio can be estimated accurately for high-rise buildings above 120 m.

5 Conclusions

In this study, we attempt to evaluate the bending deformation characteristics using the wave interferometry method. Firstly, some basic examinations on the shear-wave travel time and fundamental periods of buildings were performed. The shear-wave travel time from the base to the top of buildings can be extracted regardless of the frequency characteristics of the input motions. However, if a higher sampling frequency of response data and wider frequency range of input motions is used, a more accurate inter-story shear-wave velocity can be obtained. In the homogeneous shear model that the inter-story shear stiffnesses are unify, fundamental period is consistent with the four times of the shear-wave travel time from the base to the top. On the other hand, in the heterogeneous shear model that the inter-story shear-stiffnesses are varying vertically, four times of the travel time from the base to the top is about 1.33 times of the fundamental period. Moreover, in the heterogeneous bending-shear models, because of the effect of bending deformation, the difference between four times of the travel time and the fundamental period is not constant, which becomes larger with the increasing number of stories. Secondly, the bending-shear ratio which is defined as the ratio of the fundamental period of bending-shear coupled vibration and the fundamental period of the pure shear vibration. The period of the pure shear vibration can be estimated based on the empirical ratio α . The variation of α obtained from the generic model of super high-rise building is wider than those obtained from the design models. Moreover, the bending-shear ratio of buildings with height over 120 m can be estimated with relatively higher accurate.

References

1. Asahina R, Tobita Y, Wang X, Nagano M (2020) Flexural deformation of a high-rise RC building Based on strong motion records and microtremor data. In: 17th world conference on earthquake engineering, Sendai, Japan
2. Wang X, Masaki K, Irikura K, Motosaka M, Hisada Y (2015) 1D wave propagation analysis and shear-wave velocity extraction of super high-rise buildings based on vertical microtremor observation array. *J Struct Constr Eng, AIJ*, 80, 718:1859–1868. (in Japanese with English abstract)
3. Sineder R, Şafak E (2006) Extracting the building response using interferometry: theory and applications to the Millikan Library in Pasadena, California. *Bull Seismol Soc Am* 96(2):586–598,4

4. Hinoura Y, Nagano M, Suzuki K, Hida T, Kitahori T, et al (2018) Construction of nonlinear multi-degree-of-freedom system models for super high-rise buildings and estimation of seismic responses during 2016 Kumamoto Earthquake. *J Struct Constr Eng AIJ*, 83(749):963–973. (in Japanese)
5. Murata M, Nagano M, Hinowura M et al (2019) Statistical analysis of bending deformation components of vibration analysis models and construction of generic bending shear multi-mass models for super high-rise buildings. *AIJ J Technol Des* 25(59):91–96 (in Japanese)

Structural Damage Identification Using Spectral Finite Element Modeling for Extended Timoshenko Beams



Krishna Modak, T. Jothi Saravanan, and Shanthanu Rajasekharan

Abstract This paper introduces a finite spectral element method for a single edge notch cracked extended Timoshenko beam for wave propagation analysis and damage detection. The crack introduced is a transverse open and non-propagating crack. The cracked region is discretized in a mass-less and dimension-less spring element. The quantity of damage implemented is expressed in terms of crack flexibility based on fracture mechanics. In the damage region, the compatibility conditions are satisfied. This procedure is approached by the spectral element method to solve the wave propagation difficulties in structures. This method is the best fit for wave propagation analysis and computing modal parameters. Periodic large lattice structures like frames, truss, etc., may experience extension-transverse shear-bending couple vibrations, which the extended Timoshenko beam theory can well describe. This paper developed a spectral element model for the classical extended Timoshenko beam element and cracked extended Timoshenko beam element. The change in wave propagation process is studied in the presence of crack by comparing responses from damaged and undamaged extended Timoshenko beams. In this paper, the effect of crack depth and crack location for wave propagation is examined. The responses collected from different points are presented. The extended Timoshenko beam element was excited with different signals to observe the effects of signals in the wave propagation process. The differences in wave propagation and proper analysis of these responses point to the damage location very accurately.

Keywords Spectral element method · Wave propagation · Non-propagation crack · Damage detection · SHM

K. Modak · T. J. Saravanan (✉)

School of Infrastructure, Indian Institute of Technology Bhubaneswar, Bhubaneswar, Odisha, India

e-mail: tjs@iitbbs.ac.in

S. Rajasekharan

Aster Co., Ltd, Tokyo, Japan

1 Introduction

There is an urgent need to monitor the integrity of structural systems to improve safety, reliability, and service life. Over the last few decades, there has been a great deal of interest in infrastructure monitoring and damage detection [1–3]. Many analytical methods have been developed to solve wave propagation problems [4–6]. This includes Fourier synthesis (or spectrum analysis). Spectral analysis is a way to represent a dynamic solution as a series of solutions at different frequencies [7–9]. The structure of a spectral element scheme is very similar to that of a common finite element program until assembly and solution are considered. First, excitation activity using Fast Fourier Transform (FFT) is divided into several frequency components. The dynamic stiffness matrix is then generated and converted to all frequencies as part of the larger frequency two-loop (instead of the two-loop in the time steps of traditional FEM formation). This will be resolved. It directly provides the frequency response function (FRF) of the analyzed problem. The frequency domain is converted to response time using the inverse Fourier Transform (IFFT).

Various elements have been developed for finite and quasi-infinite domain structural components. Inertia properties are modeled accurately, so limited elements are required to model a large area. Generalized nodes should only be placed in a structural inconsistency. Multiple spectral elements can simultaneously model structures containing segments with different widths or physical properties. The solution is obtained as a normalized displacement, and subsequent velocity calculations, acceleration, strain, and strain per applied load can be calculated in inexpensive post-processing calculations. The spectral element method (SEM) straight calculates the frequency response of the structure and delivers extra info to bridge the gap between the modal method based on free vibration and the time reconstruction based on direct integration [10]. Several spectral models of the structure are currently available in the literature. Spectral models of rods, beams, and plates can be found without loss. Cracked rod elements are shown in reference [11], while cracked Timoshenko beam can be found in reference [12]. The model described provides satisfactory results for determining crack parameters by propagating wave analysis.

This article introduces a new ETB SEM with an open non-propagating transverse single edge crack opening. This element can be used for modal analysis and study of wave propagation processes. Some numerical examples show the effect of crack formation on modal parameter changes and wave propagation analysis. The proposed elements have been shown to analyze damaged structures and identify and evaluate crack's location.

2 Spectral Element Formulation

2.1 Finite Length Element

Based on the discrete Fourier transform (DFT) theory to construct the spectral elements of the ETB [13], we convert the governing equations in the frequency domain:

$$\begin{bmatrix} EA & C_1 & C_2 \\ C_1 & \rho A & C_3 \\ C_2 & C_3 & EI \end{bmatrix} \begin{bmatrix} \bar{u}'' \\ \bar{w}'' \\ \bar{\theta}'' \end{bmatrix} + \begin{bmatrix} 0 & 0 & -C_1 \\ 0 & 0 & -GA \\ C_1 & GA & 0 \end{bmatrix} \begin{bmatrix} \bar{u}' \\ \bar{w}' \\ \bar{\theta}' \end{bmatrix} - \begin{bmatrix} 0 & 0 & 0 \\ 0 & 0 & 0 \\ 0 & 0 & GA \end{bmatrix} \begin{bmatrix} \bar{u} \\ \bar{w} \\ \bar{\theta} \end{bmatrix} + \omega^2 \begin{bmatrix} \rho A & 0 & \rho R \\ 0 & \rho A & 0 \\ \rho R & 0 & \rho I \end{bmatrix} \begin{bmatrix} \bar{u} \\ \bar{w} \\ \bar{\theta} \end{bmatrix} = \begin{bmatrix} 0 \\ 0 \\ 0 \end{bmatrix} \quad (1)$$

ρA , ρR , and ρI are the effective mass per length, the first-order moment of inertia, and the second-order moment of inertia.

$$\rho A = \int \rho dA, \quad \rho R = \int \rho z dA, \quad \rho I = \int \rho z^2 dA, \quad (2)$$

Assuming general solution of Eq. (1) as

$$\bar{u}(x) = \alpha W e^{-ikx}, \quad \bar{w}(x) = W e^{-ikx}, \quad \bar{\theta}(x) = \beta W e^{-ikx} \quad (3)$$

where k is the wavenumber. Substitution of Eq. (3) into Eq. (1) we get

$$X(k)W \begin{bmatrix} \alpha \\ 1 \\ \beta \end{bmatrix} = \begin{bmatrix} 0 \\ 0 \\ 0 \end{bmatrix} \quad (4)$$

where,

$$X(k) = \begin{bmatrix} -k^2 EA + \omega^2 \rho A & -k^2 C_1 & ikC_1 - k^2 C_2 + \omega^2 \rho R \\ -k^2 C_1 & -k^2 GA + \omega^2 \rho A & ikGA - k^2 C_3 \\ -ikC_1 - k^2 C_2 + \omega^2 \rho R & -ikGA - k^2 C_3 & -k^2 EI + \omega^2 \rho I - GA \end{bmatrix} \quad (5)$$

From Eq. (5), we get the dispersion equation as

$$X(k) = a_1 k^6 + a_2 k^4 + a_3 k^2 + a_4 = 0 \quad (6)$$

where,

$$\begin{aligned}
 a_1 &= EIC_1^2 - 2C_1C_2C_3 + GAC_2^2 + EAC_3^2 - EAEIGA \\
 a_2 &= 2C_1C_3\rho R\omega^2 - C_3^2\rho A\omega^2 - C_1^2\rho I\omega^2 - 2C_2GA\rho R\omega^2 \\
 &\quad + EAEI\rho A\omega^2 + EAGA\rho I\omega^2 + EIGA\rho A\omega^2 \\
 a_3 &= GA\rho R^2\omega^2 - EI\rho A^2\omega^4 - C_1^2\rho A\omega^2 \\
 &\quad + EAGA\rho A\rho R\omega^4 - EA\rho A\rho I\omega^4 + EIGA\rho A\omega^2 \\
 a_4 &= \rho I\rho A^2\omega^6 - GA\rho A^2\omega^4 - \rho A\rho R^2\omega^6
 \end{aligned} \tag{7}$$

We can obtain the six roots of Eq. (6) as

$$k_1 = -k_4k_2 = -k_5k_3 = -k_6 \tag{8}$$

From Eq. (4), α_n and β_n are determined as

$$\begin{aligned}
 \alpha_n &= \left(\frac{\rho A\rho R\omega^4 - C_1C_3k^4 + C_2GAk^4 - C_2k^2\rho A\omega^2}{-GAk^2\rho R\omega^2 + iC_1k\rho A\omega^2} \right) / \Delta \\
 \beta_n &= (C_1^2k^4 - \rho A^2\omega^4 - EAGAk^4 + EAk^2\rho A\omega^2 + GAk^2\rho A\omega^2) / \Delta \\
 \Delta &= \left(k \left(iC_1^2k^2 - C_2C_1k^3 + \rho RC_1k\omega^2 + C_3EAk^3 \right) \right)
 \end{aligned} \tag{9}$$

By using the six wavenumbers, we can express the general solution for an element in the form of:

$$\begin{aligned}
 \bar{u}(x) &= \alpha_1 W_1 e^{-ik_1x} + \alpha_2 W_2 e^{-ik_2x} + \alpha_3 W_3 e^{-ik_3x} + \alpha_4 W_4 e^{-ik_1(L-x)} \\
 &\quad + \alpha_5 W_5 e^{-ik_2(L-x)} + \alpha_6 W_6 e^{-ik_3(L-x)} \\
 \bar{w}(x) &= W_1 e^{-ik_1x} + W_2 e^{-ik_2x} + W_3 e^{-ik_3x} + W_4 e^{-ik_1(L-x)} \\
 &\quad + W_5 e^{-ik_2(L-x)} + W_6 e^{-ik_3(L-x)} \\
 \bar{\theta}(x) &= \beta_1 W_1 e^{-ik_1x} + \beta_2 W_2 e^{-ik_2x} + \beta_3 W_3 e^{-ik_3x} + \beta_4 W_4 e^{-ik_1(L-x)} \\
 &\quad + \beta_5 W_5 e^{-ik_2(L-x)} + \beta_6 W_6 e^{-ik_3(L-x)}
 \end{aligned} \tag{10}$$

Substituting the boundary conditions of nodal displacements shown in Fig. 1, we get

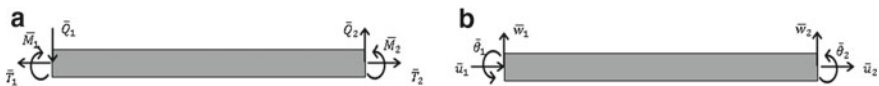


Fig. 1 Sign conventions defined for **a** Nodal forces, **b** Nodal displacements

$$\begin{bmatrix} \bar{u}_1 \\ \bar{w}_1 \\ \bar{\theta}_1 \\ \bar{u}_2 \\ \bar{w}_2 \\ \bar{\theta}_2 \end{bmatrix} = \begin{bmatrix} \bar{u}(0) \\ \bar{w}(0) \\ \bar{\theta}(0) \\ \bar{u}(L) \\ \bar{w}(L) \\ \bar{\theta}(L) \end{bmatrix} = [\mathbf{T}_1] \begin{bmatrix} W_1 \\ W_2 \\ W_3 \\ W_4 \\ W_5 \\ W_6 \end{bmatrix} \quad (11)$$

Substituting the Eq. (10) into Eq. (1), balancing nodal forces for an element we get

$$\begin{bmatrix} \bar{T}_1 \\ \bar{Q}_1 \\ \bar{M}_1 \\ \bar{T}_2 \\ \bar{Q}_2 \\ \bar{M}_2 \end{bmatrix} = \begin{bmatrix} -\bar{T}(0) \\ -\bar{Q}(0) \\ -\bar{M}(0) \\ \bar{T}(L) \\ \bar{Q}(L) \\ \bar{M}(L) \end{bmatrix} = [\mathbf{T}_2] \begin{bmatrix} W_1 \\ W_2 \\ W_3 \\ W_4 \\ W_5 \\ W_6 \end{bmatrix} \quad (12)$$

From Eqs. (11) to (12), we get a frequency-dependent dynamic stiffness matrix for a finite element

$$S(\omega) = [\mathbf{T}_2][\mathbf{T}_1]^{-1} \quad (13)$$

2.2 Throw-Off (Semi-Infinite) Element

Similarly, we can derive a frequency-dependent dynamic stiffness matrix for the throw-off element. From Eq. (10), the general solution reduces to: (as $L = \infty$)

$$\begin{aligned} \bar{u}_t(x) &= \alpha_1 W_1 e^{-ik_1 x} + \alpha_2 W_2 e^{-ik_2 x} + \alpha_3 W_3 e^{-ik_3 x} \\ \bar{w}_t(x) &= W_1 e^{-ik_1 x} + W_2 e^{-ik_2 x} + W_3 e^{-ik_3 x} \\ \bar{\theta}_t(x) &= \beta_1 W_1 e^{-ik_1 x} + \beta_2 W_2 e^{-ik_2 x} + \beta_3 W_3 e^{-ik_3 x} \end{aligned} \quad (14)$$

Following the same procedure from above, we get a frequency-dependent dynamic stiffness matrix:

$$\begin{bmatrix} \bar{T}_t \\ \bar{Q}_t \\ \bar{M}_t \end{bmatrix} = [\mathbf{T}_{t2}][\mathbf{T}_{t1}]^{-1} \begin{bmatrix} \bar{u}_t \\ \bar{w}_t \\ \bar{\theta}_t \end{bmatrix} \quad (15)$$

3 Cracked Extended Timoshenko Beam

Figure 2 shows a finite element of a spectral extended Timoshenko beam with an open transverse crack that does not propagate. The length of the element is L , and its cross-sectional area is A . The crack is replaced by a dimensionless-massless spring, the flexibility of which is calculated using Castigliano Theorem and laws of fracture mechanics; This is briefly presented in the next section.

The spectral nodal displacements are presumed for the left and right parts of the beam as follows:

$$\begin{aligned}
 \bar{u}_1 &= A_1\alpha_1e^{(-ik_1x)} + B_1\alpha_2e^{(-ik_2x)} + C_1\alpha_3e^{(-ik_3x)} + D_1\alpha_4e^{(-ik_1(L_1-x))} \\
 &\quad + E_1\alpha_5e^{(-ik_2(L_1-x))} + F_1\alpha_6e^{(-ik_3(L_1-x))} \text{ for } x \in (0, L_1) \\
 \bar{w}_1 &= A_1e^{(-ik_1x)} + B_1e^{(-ik_2x)} + C_1e^{(-ik_3x)} + D_1e^{(-ik_1(L_1-x))} \\
 &\quad + E_1e^{(-ik_2(L_1-x))} + F_1e^{(-ik_3(L_1-x))} \text{ for } x \in (0, L_1) \\
 \bar{\theta}_1 &= A_1\beta_1e^{(-ik_1x)} + B_1\beta_2e^{(-ik_2x)} + C_1\beta_3e^{(-ik_3x)} + D_1\beta_4e^{(-ik_1(L_1-x))} \\
 &\quad + E_1\beta_5e^{(-ik_2(L_1-x))} + F_1\beta_6e^{(-ik_3(L_1-x))} \text{ for } x \in (0, L_1) \\
 \bar{u}_2 &= A_2\alpha_1e^{(-ik_1(L_1+x))} + B_2\alpha_2e^{(-ik_2(L_1+x))} + C_2\alpha_3e^{(-ik_3(L_1+x))} + D_2\alpha_4e^{(ik_1(L_1-L+x))} \\
 &\quad + E_2\alpha_5e^{(ik_2(L_1-L+x))} + F_2\alpha_6e^{(ik_3(L_1-L+x))} \text{ for } x \in (0, L - L_1) \\
 \bar{w}_2 &= A_2e^{(-ik_1(L_1+x))} + B_2e^{(-ik_2(L_1+x))} + C_2e^{(-ik_3(L_1+x))} + D_2e^{(ik_1(L_1-L+x))} \\
 &\quad + E_2e^{(ik_2(L_1-L+x))} + F_2e^{(ik_3(L_1-L+x))} \text{ for } x \in (0, L - L_1) \\
 \bar{\theta}_2 &= A_2\beta_1e^{(-ik_1(L_1+x))} + B_2\beta_2e^{(-ik_2(L_1+x))} + C_2\beta_3e^{(-ik_3(L_1+x))} + D_2\beta_4e^{(ik_1(L_1-L+x))} \\
 &\quad + E_2\beta_5e^{(ik_2(L_1-L+x))} + F_2\beta_6e^{(ik_3(L_1-L+x))} \text{ for } x \in (0, L - L_1)
 \end{aligned}
 \tag{16}$$

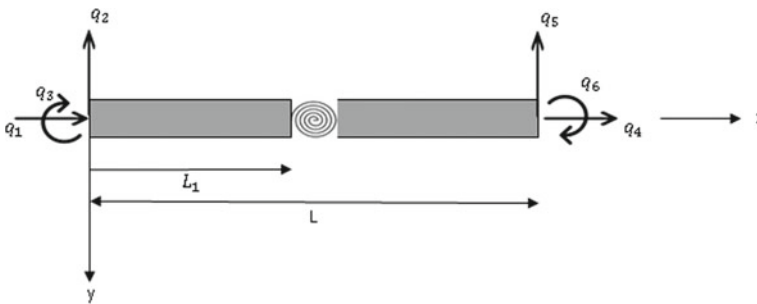


Fig. 2 Numerical model of extended Timoshenko beam with a transverse open and non-propagating crack represented by an elastic hinge

where L_1 is the location of the crack from the left. $A_1, B_1, C_1, D_1, E_1, F_1, A_2, B_2, C_2, D_2, E_2, F_2$ can be calculated from the boundary conditions:

- At the left end of the element ($x = 0$)

$$\begin{aligned} u_1(x) &= q_1 \\ w_1(x) &= q_2 \\ \theta_1(x) &= q_3 \end{aligned} \quad (17a)$$

- At the right end of the element ($x = L$)

$$\begin{aligned} u_2(x) &= q_4 \\ w_2(x) &= q_5 \\ \theta_2(x) &= q_6 \end{aligned} \quad (17b)$$

- At crack location ($x = L_1$ for $u_1(x), w_1(x), \theta_1(x)$ and $x = 0$ for $u_2(x), w_2(x), \theta_2(x)$)

$$\begin{aligned} u_2(x) - u_1(x) - \phi \frac{\partial u_1(x)}{\partial x} &= 0 \\ EA \frac{\partial u_1(x)}{\partial x} + C_1 \left(\frac{\partial w_1(x)}{\partial x} - \theta_1(x) \right) + C_2 \frac{\partial \theta_1(x)}{\partial x} \\ - \left(EA \frac{\partial u_2(x)}{\partial x} + C_1 \left(\frac{\partial w_2(x)}{\partial x} - \theta_2(x) \right) + C_2 \frac{\partial \theta_2(x)}{\partial x} \right) &= 0 \\ w_2(x) - w_1(x) - \xi \left(\frac{\partial w_1(x)}{\partial x} - \theta_1(x) \right) &= 0 \\ C_1 \frac{\partial u_1(x)}{\partial x} + GA \left(\frac{\partial w_1(x)}{\partial x} - \theta_1(x) \right) + C_3 \frac{\partial \theta_1(x)}{\partial x} \\ - \left(C_1 \frac{\partial u_2(x)}{\partial x} + GA \left(\frac{\partial w_2(x)}{\partial x} - \theta_2(x) \right) + C_3 \frac{\partial \theta_2(x)}{\partial x} \right) &= 0 \\ \theta_2(x) - \theta_1(x) - \Omega \frac{\partial \theta_1(x)}{\partial x} &= 0 \\ C_2 \frac{\partial u_1(x)}{\partial x} + C_3 \left(\frac{\partial w_1(x)}{\partial x} - \theta_1(x) \right) + EI \frac{\partial \theta_1(x)}{\partial x} \\ - \left(C_2 \frac{\partial u_2(x)}{\partial x} + C_3 \left(\frac{\partial w_2(x)}{\partial x} - \theta_2(x) \right) + EI \frac{\partial \theta_2(x)}{\partial x} \right) &= 0 \end{aligned} \quad (17c)$$

From Eq. (23), we can write the boundary conditions in the form of a matrix as follows:

$$[cT_1]_{12 \times 12} \begin{bmatrix} A_1 \\ B_1 \\ C_1 \\ D_1 \\ \cdot \\ \cdot \\ C_2 \\ D_2 \\ E_2 \\ F_2 \end{bmatrix}_{12 \times 1} = \begin{bmatrix} q_1 \\ q_2 \\ q_3 \\ q_4 \\ q_5 \\ q_6 \\ 0 \\ \cdot \\ \cdot \\ 0 \end{bmatrix}_{12 \times 1} \tag{18}$$

The nodal spectral forces (P axial force, T shear force, M bending moment) can be obtained by differentiating the spectral displacements; and formerly can be written in the matrix system as

$$[cT_2]_{6 \times 12} \begin{bmatrix} A_1 \\ B_1 \\ C_1 \\ D_1 \\ \cdot \\ \cdot \\ C_2 \\ D_2 \\ E_2 \\ F_2 \end{bmatrix}_{12 \times 1} = \begin{bmatrix} P_1 \\ V_1 \\ M_1 \\ P_2 \\ V_2 \\ M_2 \end{bmatrix}_{6 \times 1} \tag{19}$$

From $[cT_1]$ and $[cT_2]$, the square matrix (6×6), representing the frequency-dependent dynamic stiffness for the extended Timoshenko beam spectral element with transverse open and non-propagating crack, can be obtained.

3.1 Flexibilities at the Crack Region

Flexibilities at the crack region can be obtained from Castigliano’s theorem:

$$C_{ij} = \frac{\partial^2 U}{\partial P_i \partial P_j} \quad i = 1, 2, \dots, 6, \quad j = 1, 2, \dots, 6 \tag{20}$$

where U represents the elastic strain energy and P represents nodal forces.

$$U = \frac{1}{E} \int_A (K_I^2 + K_{II}^2) dA \tag{21}$$

where K_I and K_{II} denotes stress intensity factors corresponding to the first and second mode of crack growth [14] and A denotes crack area (refer to Figs. 3 and 4).

$$\text{Axial flexibility: } c_a = \frac{2}{Eb} \int_0^{\bar{a}} \bar{\alpha} F_I^2(\bar{\alpha}) d\bar{a}$$

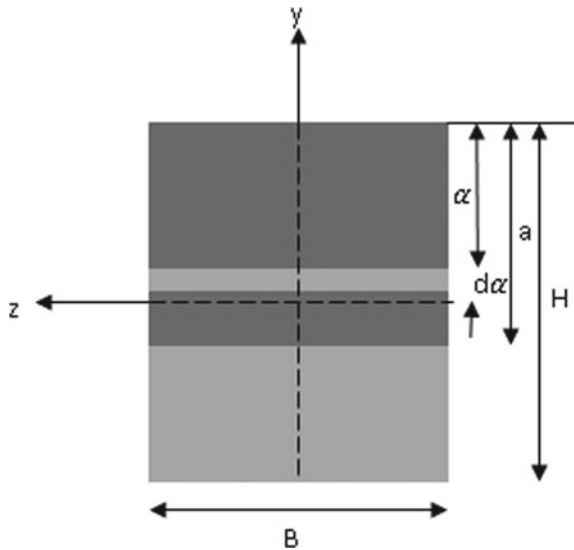
$$\phi = E A c_a \tag{22}$$

where c_a is the axial flexibility due to the presence of a crack.



Fig. 3 I and II crack propagation modes

Fig. 4 Cross-section of beam element at the crack site



$$\begin{aligned} \text{Bending flexibility: } c_b &= \frac{72\pi}{BH^2} \int_0^{\bar{a}} \bar{\alpha} F_I^2(\bar{\alpha}) d\bar{a}, \quad c_s = \frac{2\beta\pi}{B} \int_0^{\bar{a}} \bar{\alpha} F_{II}^2(\bar{\alpha}) d\bar{a} \\ \Omega &= \frac{EIc_b}{L}, \quad \xi = \frac{GAc_s}{L} \end{aligned} \tag{23}$$

where c_b denotes bending flexibility and c_s denotes shear flexibility. β is the shear factor [15]. F_I and F_{II} are correction function expressed as:

$$\begin{aligned} F_I\left(\frac{\alpha}{H}\right) &= \sqrt{\frac{\tan(\pi\alpha/2H)}{\pi\alpha/2H} \frac{0.752+2.02(\alpha/H)+0.37[1-\sin(\pi\alpha/2H)]^3}{\cos(\pi\alpha/2H)}} \\ F_{II}\left(\frac{\alpha}{H}\right) &= \frac{1.30-0.65(\alpha/H)+0.37(\alpha/H)^2+0.28(\alpha/H)^3}{\sqrt{1-(\alpha/H)}} \end{aligned} \tag{24}$$

4 Numerical Investigations

The first numerical test was done to show if the proposed model would help capture forward and backward moving waves. To make the numerical simple and easier to understand, in numerical test, all the coupling coefficients were zero ($C_1, C_2, C_3 = 0$) and the first moment of inertial is zero ($\rho R = 0$). The numerical test model consists of two elements, one classical ETB element, and a throw-off element. The model was excited at one end of the beam. Figure 5 shows the wave propagation for the model in the bending part of the ETB beam. The next numerical test shows the influence of a crack in the wave propagation, as shown in Fig. 6. The crack is located at 25% of the beam length, and the crack depth is 15% of the depth of the beam. The model is excited at one end of the beam. The results have been compared with a cracked rod [11] for the axial part, and a cracked Timoshenko beam [12] for the bending part.

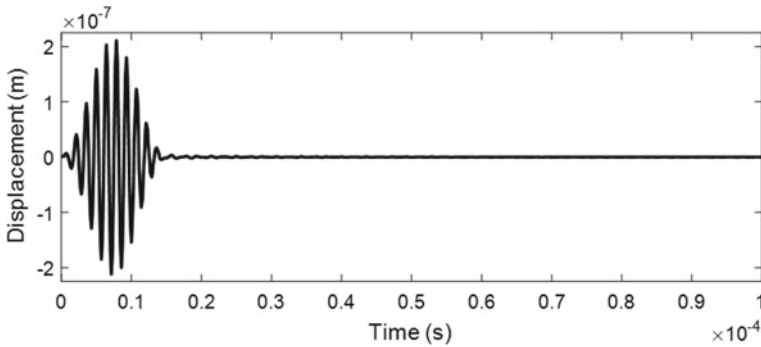


Fig. 5 Wave propagation in the first numerical test for bending part

Fig. 6 Model for second numerical test

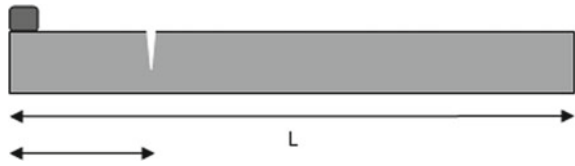


Figure 7 shows the response of the beam. Here, again to make the numerical investigation simple and easier to understand, in numerical test, all the coupling coefficients were zero ($C_1, C_2, C_3 = 0$) and the first moment of inertial is zero ($\rho R = 0$). The model consists of three elements: one cracked extended Timoshenko beam element at the middle and two throw-off elements at both ends. Figure 7b also shows the presence of a second propagating mode [16], which is faster than the first mode.

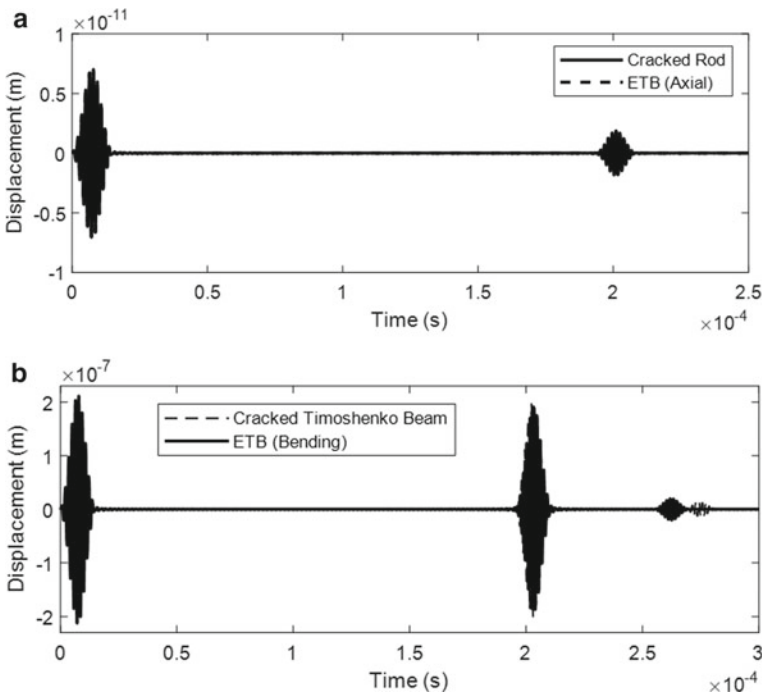


Fig. 7 Wave propagation in **a** axial, **b** bending part of second numerical test

5 Conclusions

This paper presents a new model of the extended Timoshenko Spectral finite beam element with single and non-propagating cracks. The fundamental difference between the classical approach and the spectral method is clearly shown. It is easy to see that the spectral approach provides more information and is more appropriate for detecting damage. Spectral elements can be used not only for simple modal analysis but also for wave analysis. The results obtained show that the current approach can calculate higher natural frequencies without additional time-consuming numerical calculations. It can provide information about the crack location and the effect of various locations on the crack on the wave propagation of the damaged structure. We can conclude that it is better to use a packet signal with a short time and excite as wide a frequency as possible. One can use the difference in the answers to accurately estimate the location of the crack. Future research will focus on extending the spectral element system to damaged structures of more complex shapes, such as structures constructed from structures such as plates and beams.

References

1. Krawczuk M, Palacz M, Ostachowicz W (2004) Wave propagation in plate structures for crack detection. *Finite Elements Anal Des* 40(9–10):991–1004
2. Saravanan TJ, Gopalakrishnan N, Rao NP (2015) Damage detection in structural element through propagating waves using radially weighted and factored RMS. *Measurement* 73:520–538
3. Kumar KV, Saravanan TJ, Sreekala R, Gopalakrishnan N, Mini KM (2017) Structural damage detection through longitudinal wave propagation using spectral finite element method. *Geomechan Eng* 12(1):161–183
4. Saravanan TJ, Gopalakrishnan N, Prasad Rao N (2018) Experiments on coupled axial–flexural wave propagation in a sagged rod with structural discontinuity using piezoelectric transducers. *J Vib Control* 24(13):2717–2731
5. Thiyagarajan JS (2020) Non-destructive testing mechanism for pre-stressed steel wire using acoustic emission monitoring. *Materials* 13(21):5029
6. Saravanan TJ (2021) Elastic wave methods for non-destructive damage diagnosis in the axisymmetric viscoelastic cylindrical waveguide. *Measurement* 177:109253
7. Shi D, Wang Q, Shi X, Pang F (2015) An accurate solution method for the vibration analysis of Timoshenko beams with general elastic supports. *Proc Inst Mech Eng C J Mech Eng Sci* 229(13):2327–2340
8. Wang K, Wang B (2015) Timoshenko beam model for the vibration analysis of a cracked nanobeam with surface energy. *J Vib Control* 21(12):2452–2464
9. Saravanan TJ, Gopalakrishnan N, Prasad Rao N (2017) Detection of damage through coupled axial–flexural wave interactions in a sagged rod using the spectral finite element method. *J Vib Control* 23(20):3345–3364
10. Doyle JF (1997) *Wave propagation in structures*. Springer, New York
11. Palacz M, Krawczuk M (2002) Analysis of longitudinal wave propagation in a cracked rod by the spectral element method. *Comput Struct* 80(24):1809–1816
12. Krawczuk M, Palacz M, Ostachowicz W (2003) The dynamic analysis of a cracked Timoshenko beam by the spectral element method. *J Sound Vib* 264(5):1139–1153

13. Lee U, Lee C (2009) Spectral element modeling for extended Timoshenko beams. *J Sound Vib* 319(3–5):993–1002
14. Tada H, Paris P, Irwin G (2000) *The analysis of cracks handbook*, vol 2, no 1. ASME Press, New York
15. Cowper GR (1966) The shear coefficient in Timoshenko's beam theory. *J Appl Phys* 33(2):335–340
16. Gopalakrishnan S, Martin M, Doyle JF (1992) A matrix methodology for spectral analysis of wave propagation in multiple connected Timoshenko beams. *J Sound Vib* 158(1):11–24

Experimental Study on Identification of Structural Changes Using Wavelet Energy Features



Xiaobang Zhang, Yong Lu, Zachariah Wynne, and Thomas P. S. Reynolds

Abstract Wavelet packet transformation has been used widely in the damage identification and structural health monitoring communities. In particular, the use of wavelet packet node energy (WPNE) as damage sensitive features has attracted much research interest in more recent years. WPNE features tend to contain detailed information which can be highly sensitive to local damage or other forms of structural changes. However, most of the existing studies in the literature on using wavelet energy based features have been numerical and involved idealised assumptions such as perfect and identical excitations among different tests. This paper presents an experimental investigation into the viability of WPNE based techniques for detection and localisation of the structural changes in a real measurement environment. Vibration signals are acquired firstly from the test structures with different alterations to the structural states, realized mainly through the use of additional masses, and WPNE features are extracted. These features and the corresponding structural states form a dataset, from which supervised machine learning with neural network is carried out. The trained neural network is subsequently tested for its prediction capability. The experimental structures include a free-ended steel I beam, a flat beam with fixed ends and MX3D Bridge, the world's first 3D-printed metal bridge. Different forms of excitation are involved for different test structures, including hammer impact and controlled heel drops and impacts from pedestrian footfall. Results indicate that the WPNE based neural network approach is capable of detecting and localising the structural changes in all tested structures. The accuracy is generally higher in a better controlled excitation situation, where structural changes at a level equivalent to incipient damage is detectable.

Keywords Vibration testing · Damage identification · Wavelet packet transform (WPT) · WPT energy features · Machine learning

X. Zhang · Y. Lu (✉) · Z. Wynne · T. P. S. Reynolds
Institute for Infrastructure and Environment, School of Engineering, University of Edinburgh,
Edinburgh EH9 3JL, UK
e-mail: yong.lu@ed.ac.uk

© The Author(s), under exclusive license to Springer Nature Switzerland AG 2023
Z. Wu et al. (eds.), *Experimental Vibration Analysis for Civil Engineering Structures*,
Lecture Notes in Civil Engineering 224,
https://doi.org/10.1007/978-3-030-93236-7_38

1 Introduction

In vibration based structural damage identification, wavelet energy based features are deemed to contain detailed information which can be highly sensitive to local damages. Yen and Lin [1] introduced wavelet packet transform (WPT) energy as an alternative means of extracting time-frequency information from vibration signals and integrated it with neural network in classification. Statistical-based feature selection criteria were employed to yield a reduced dimensional feature. The feasibility of the classification technique was examined through numerical simulations of a helicopter gearbox. The results demonstrated that WPT features outperformed FFT features and excellent classification was achieved with eight sensors. Since then, WPT features have been widely studied in damage identification and classification for civil engineering structures as well. Many numerical and experimental studies have demonstrated the strong ability of wavelet transform based features in detecting, localising and quantifying damages. Han et al. [2] proposed wavelet energy rate index as a measure of damage based on WPT energy extracted from 29 acceleration signals, and illustrated the method with a numerical simulated simply supported beam and an experimental steel beam to detect damage locations. Both simulated and experimental investigations demonstrated that the index was sensitive to structural local damage. Two assumptions were adopted in their study, namely a) reliable undamaged and damaged structural models are available, and b) all excitation are identical and repeatable. Mikami et al. [3] used the power spectrum density of WPT components as a damage detection index and verified the identification method using numerical and experimental data extracted from a steel beam. It was shown that the proposed index was sensitive to damages.

Damage identification based on merely the feature proxy usually requires a large number of sensors with spatial information. With the assistance of machine learning tools in classification and identification, some studies have looked into the improved mapping of the relationships between feature proxy and structural state with a limited number of signal sources. For example, Sun and Chang [4] investigated the use of WPT and the neural network model for damage assessment by numerical simulations of a three-span continuous bridge under impact excitation. The results showed that WPT energies extracted from one signal source could be used for various levels of damage assessment including identifying damage occurrence, location and severity.

However, most of the studies so far on using wavelet energy based features have been numerical and involved idealized assumptions such as perfect and identical excitations among different tests. This paper presents an experimental investigation into the viability of WPNE based techniques for detection and quantification of the structural changes in a real measurement environment. Vibration signals are acquired firstly from the test structures with different alterations to the structural states, realized mainly through the use of additional masses, and WPNE features are extracted. These features and the corresponding structural states form a dataset, from which supervised machine learning with neural network is carried out. The trained neural network is subsequently tested for its prediction capability. The experimental

structures include a free-ended steel I beam, a flat beam with fixed ends and MX3D Bridge, the world’s first 3D-printed metal bridge. Different forms of excitation are involved for different test structures, including hammer impact and controlled heel drops and impacts from pedestrian footfall.

2 Background Theories and Methodology

2.1 WPT Energy-Based Damage Sensitive Feature

Wavelet transform (WT) is a signal processing technique which has been commonly used in various areas of engineering. It overcomes the limitations of Fourier transform and reveals signal properties in both time and frequency domains. By shifting and dilating a basis function, which is called ‘mother wavelet’, wavelet transform describes a signal with coefficients which represent the direct proportions between mother wavelet and the original signal [5]. WPT has a tree structure where the original signal is decomposed into approximations and details at every level. Hence a higher resolution in the frequency domain is achieved. An example tree structure of wavelet packet transform is shown in Fig. 1.

The signal is decomposed by the following standard expressions:

$$\begin{cases} u_{2n}^{(j)}(t) = \sqrt{2} \sum_k h(k)u_n^{(j)}(2t - k) \\ u_{2n+1}^{(j)}(t) = \sqrt{2} \sum_k g(k)u_n^{(j)}(2t - k) \end{cases} ; n, k = 0, 1, 2 \dots \quad (1)$$

where $u_0^{(0)}(t) = \varphi(t)$ is the scaling function, $u_1^{(0)}(t) = \psi(t)$ is the wavelet function, j is the decomposition level, k is the translation parameter and n is the modulation parameter. The terms $h(k)$ and $g(k)$ are quadrature mirror filters and the corresponding function sets $H = \{h(k)\}_{k=z}$ and $G = \{g(k)\}_{k=z}$ denote the low pass filter and the high pass filter, respectively. After being decomposed for j times, 2^j

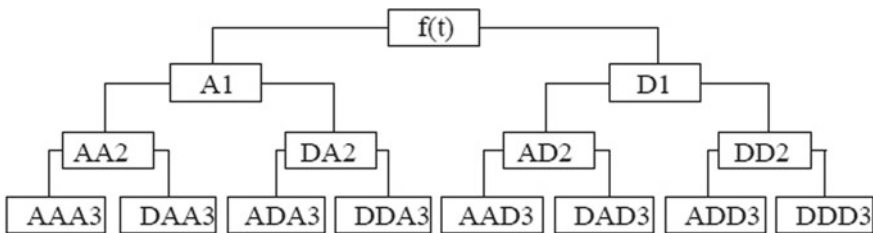


Fig. 1 Three-level wavelet packet transform

signal components are obtained. The sum of the component signals can represent the original signal $f(t)$ as:

$$f(t) = \sum_{i=1}^{2^j} f_j^i(t) \quad (2)$$

$$f_j^i(t) = \sum_{k=1}^{2^j} C_j^i(t) \psi_{j,k}^i(t) \quad (3)$$

where $f_j^i(t)$ denotes the i th component signal at the j th decomposition level, $C_j^i(t)$ denotes the wavelet packet coefficients and $\psi_{j,k}^i(t)$ denotes wavelet packet functions. Then, wavelet packet node energies (WPNEs) can be calculated as:

$$E_j^i = \int_{-\infty}^{\infty} f_j^i(t)^2 dt \quad (4)$$

The WPNE denotes the energy content in a specific frequency band without taking into account the time-variant characteristic. Normalised wavelet packet node energy (NWPNE) E_i in i -frequency band is expressed as:

$$E_i = \frac{E_j^i}{E_f} \quad (5)$$

where E_f denotes the sum of all terminal WPNEs, and it represents the total signal energy. The normalization can largely eliminate the effects of gross variation especially in the magnitudes of the excitations. The NWPNE is therefore chosen as the damage sensitive feature and integrated with neural networks as inputs. In this study, WPT level is determined with entropy-based selection method [6].

2.2 Backpropagation (BP) Neural Network

The relation between NWPNE and the dynamic properties of a structure cannot be directly interpreted due to its high nonlinearity. Existing studies have demonstrated that Back-Propagation (BP) neural networks can generally be applied to implement pattern recognition in damage identification for civil engineering structures. Thus, feedforward BP neural networks are used in this study which include an input layer for receiving input data, a hidden layer for processing data and an output layer for decision making and indicating the results. In this study, the extracted NPWNEs are used as inputs. The training algorithm of BP neural network consists of forward

and back propagation. In the forward propagation, the inputs are transmitted through layers and the error is resulted. In the back propagation, the weights and biases are iteratively adjusted based on the error feedback. The training process will be terminated when the loss measured by validation data stops improving. Cross entropy loss is used in this case which is defined as:

$$H(p, q) = - \sum_u p(u) \log q(u) \quad (6)$$

where $p(u)$ denotes one-hot encoding vector of the true label and $q(u)$ denotes the corresponding output. A BP neural network is trained by scaled conjugate gradient algorithm to perform classification where each structural state is regarded as a class. The structural states include intact and damage at various locations. Therefore the output indicates the existence and the location of the added mass. In this study, logistic sigmoid functions and softmax functions are used in the hidden layers and output layer respectively. Cross entropy function is used on top of the softmax output as the loss function. One-hot encoded vector is used as the label. For example, a vector of [0,1,0,0,0,0,0,0,0] represents the class of damage at segment 2. The number of hidden neurons is estimated by the empirical formula as follows:

$$L = \sqrt{m + n} + k \quad (7)$$

where L is the number of hidden layer nodes, m is the number of input nodes, n is the number of output nodes, and k is a constant, $k \in [1,10]$.

2.3 WPT Energy and Neural Network Integrated (WPNE-NN) Approach

The key procedures of WPNE-NN approach are explained as follows. Firstly, the vibration response signals from the structure under an excitation are obtained. As is commonly the case, herein the signals are taken in the form of acceleration time histories. Secondly, WPNE features are constructed by wavelet packet transform of the vibration measurements. It has been demonstrated that Daubechies mother wavelets are the best choices to analyse acceleration signals [7]. Thus herein ‘Daubechies 4’ is selected as the mother wavelet in wavelet packet analysis. Through the feature extraction process, the vibration signals are transformed into feature vectors formed by WPNEs. Thirdly, supervised training of neural network is conducted. Fourthly, to identify the structural state, a new measurement is transformed into WPNE feature and input into the trained neural networks. The output of the neural networks will indicate the occurrence and location of the structural change.

The collected samples are randomly split into training, validation and test sets. Training set is used to train the neural networks and the validation set is used to

provide an unbiased evaluation of a model fit on the training set while tuning model hyperparameters. The ratios of training, validation and test data sizes are set as 70%, 15% and 15%. For simplicity in the demonstration of the procedure, it is assumed that damage occurs only in a single segment of the structure, and this may be regarded as consistent with the stated aim of the current approach in detecting incipient damage.

3 Experimental Investigations

The viability of the WPNE-NN approach towards real-life applications is looked into through experimental investigations. Experiments have been conducted on two laboratory structures and a real-life sized steel bridge.

3.1 Laboratory Set up

An instrumented impact hammer (B&K type 8206-002) was used to induce and measure the impact excitations. An aluminium impactor head was selected which had a capacity of generating a flat force spectrum in the range of 0–2000 Hz. Modal testing accelerometers (B&K Delta Tron® 4508 B 003 type) were used to measure the vibration response of the beam. The accelerometers have a measuring range of $\pm 700 \text{ m/s}^2$ and 0.3–8000 Hz. The weight of the accelerometers (4.9 g) is small enough compared to the unit weight of the beam (per segment of interest), therefore the influence of transducer mass on modal testing results is negligible. The impact force and acceleration response signals were acquired with a data acquisition module via a lab view control interface. During the test, the maximum acceleration and the frequency spectrum of the impact were monitored to ensure the beam was properly excited.

3.2 Free Ended I Beam

The test specimen was a 3 m long standard IPE 80 steel beam which has a parallel internal surface of the flanges and dimensions according to EN 10,365. The beam was hung on two springs located at 300 mm from each end of the beam as shown in Fig. 2. As is common in similar laboratory studies [8], the structural changes were simulated by placing additional mass at varying locations. Two accelerometers were mounted on the top surface of the beam at 1300 and 1000 mm (or about 1/2.3 and 1/3 of the beam length) from the left end and labelled as accelerometer A1 and A2, respectively. The impact excitation was applied at the location of 1450 mm measuring from left end.

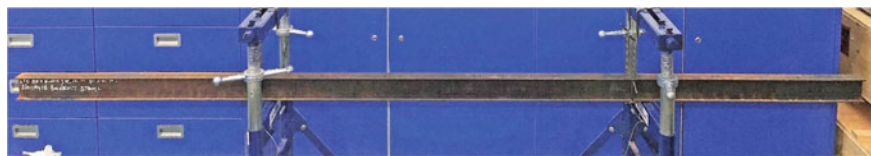


Fig. 2 Spring-hung IPE 80 steel beam

A measurement array was arranged by dividing the beam into 10 segments with equal length, giving 10 segmental midpoints which were labelled as points 1 to 10. 10 ‘damaged’ states were created by attaching a mass of 200 g at points 1–10 sequentially. The mass was approximately equal to 1% of the beam weight. Including the original state of the beam with no mass attached, there were totally 11 states being studied in the damage detection and localisation process. In each of the states, the beam was excited 20 times and in total 220 samples are recorded.

The vibration response was recorded for a duration of 9 s counting from the start of the impact action until it fully dies out, and the sampling rate was 2560 Hz. A time-series signal collected from sensor A1 at intact state is shown in Fig. 3a as an example. The magnitudes and durations of the recorded impact forces vary within ranges of 3–7 N and 0.8–1.2 ms, respectively. Based on the entropy analysis, the level of WPT decomposition is determined as 7. Therefore, from each recorded signal, a feature vector consisting of 128 NWPNEs was extracted at the 7th level of WPT. The NWPNE feature extracted from the signal in Fig. 3a is shown in Fig. 3b as an example.

Hence, the 220 samples were transformed from time-series signals into 128-dimensional feature vectors, which were used as inputs of the neural network for training, validation and testing. A BP neural network was established and the number of neurons in hidden layer was set as 20 based on Eq. (7). The labels of the 220 samples are 11-dimensional one-hot encoded vectors indicating the structural state from the 11 scenarios of interest. In this case, class 1 represents intact state and class 2–11 represent states of added mass at segments 1–10, respectively. Thus, the numbers of neurons in the input layer, hidden layer and output layer are 128, 20 and 11 respectively.

The training, validation and test datasets were formed whose sizes were 154, 33 and 33 respectively based on the ratio stated in Sect. 2. The neural network was trained by scaled conjugate gradient algorithm. The training process terminates after 41 iterations when generalization stops improving, resulting in a cross-entropy error of 1.28×10^{-7} . The loss in training is nearly 0 which indicates the parameters in the neural network have been tuned to a state that the relationship between input and target of the training samples can be very accurately mapped.

To examine the performance in the real measurement environment, in fact only one response source is needed in the present scheme. Therefore, the datasets collected by A1 and A2 are tested independently. It has been found that the results from using either of the two datasets are comparable, so only the results using the dataset from

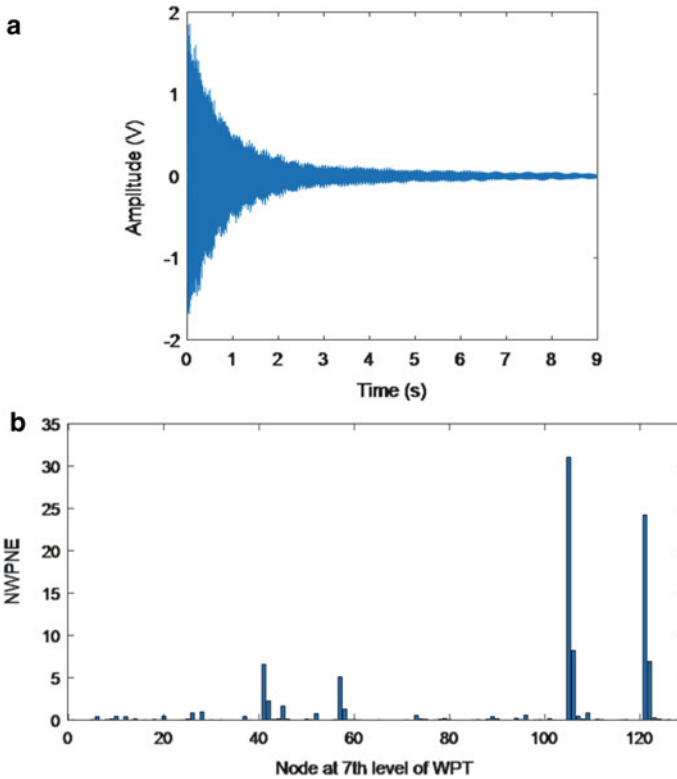


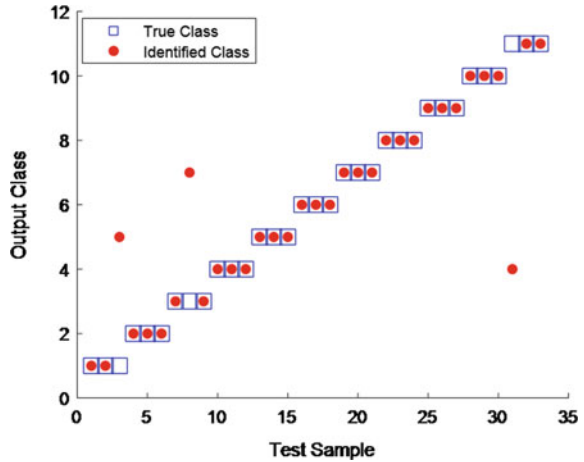
Fig. 3 **a** Time series of a signal collected from sensor A1 at intact state (left); **b** NWPNE feature of the signal (right)

one sensor is presented. Figure 4 shows the identification result using the dataset from A1, where the output class of 33 test samples are marked as red dots. It can be seen that only 3 of them fall out of the target classes which are indicated as blue squares. This means 30 out of 33 tests are correct in the structural state identification and the accuracy is 90.9%. In conjunction with additional tests on the same beam which are not included here, the WPNE-NN approach has demonstrated good sensitivity and robustness on a physical structure in real excitation and measurement environment.

3.3 Flat Beam with Fixed Ends

In order to further examine the performance of the approach on a laboratory structure with more realistic support conditions, an experiment was conducted on a flat steel beam under a fixed-end condition. Steel clamping plates and bolts were used to fix two ends of the beam on strong steel supports. The stiffness of the supports is deemed

Fig. 4 Added mass identification result using the dataset from A1



considerably larger than the testing specimen so that it can be regarded as a fixed support. The beam had a length of 1020 mm and a cross-section of width 50 mm and depth 6 mm. A sketch and a photo of the set-up are shown in Fig. 5.

A measurement array was arranged by dividing the beam into 10 segments along its length, giving 9 joints in between the two supports which were labelled as points 1–9. To avoid nodal points in any of the first few mode shapes the beam was excited by vertical impacts between points 4 and 5 and an accelerometer is located at point 6. The record duration was set at 6 s, which is adequate to cover the useful signal and maintain a manageable data size. The sampling rate was set at 1651 Hz. All hammer impact points were within a 2 cm by 2 cm square area at the middle point between node 4 and 5. All excitation forces were within a range of 10–20 N. A mass of 12 g which approximately equals 0.5% of the beam weight was used as the

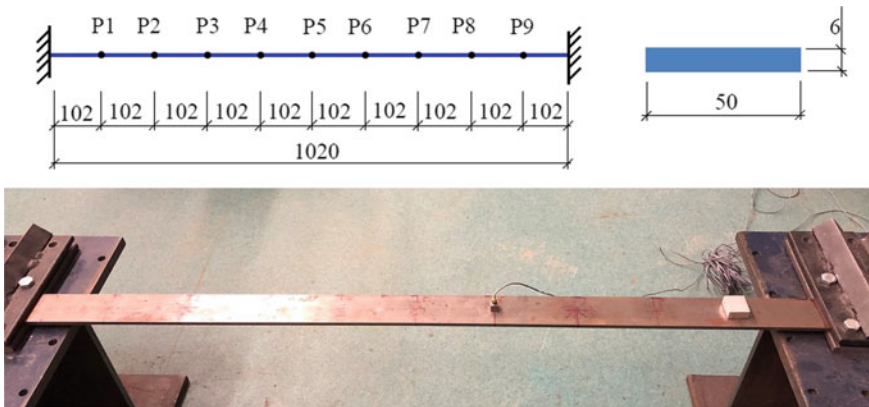
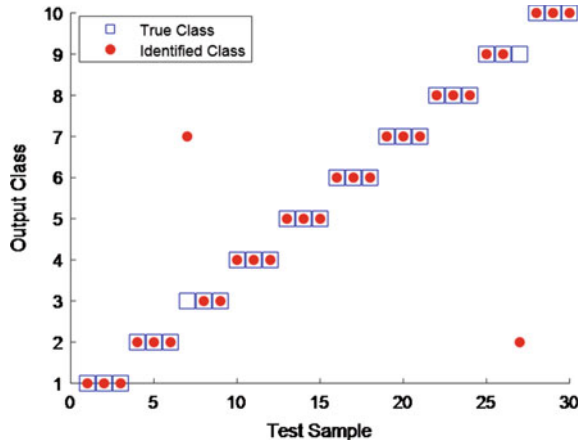


Fig. 5 a Sketch of the flat beam with fixed ends (top). b Flat steel beam (bottom)

Fig. 6 Added mass identification result



additional mass in the structure. 9 structure states were created by attaching the mass at points 1–9. Including the case of no mass attached, there were totally 10 states studied. Similar to the I beam test, in each state the beam was excited 20 times and 200 samples were recorded in total.

Based on entropy analysis, the level of WPT decomposition is determined at 7. From the measured signals, the 128-dimensional feature vectors consisting of NWPNEs at the 7th level of WPT are extracted and used as the inputs of the neural network.

Similar to the I beam case, the number of neurons in hidden layer is set as 20. The outputs are 10-dimensional one-hot encoded vectors. Thus, the structure of the neural network in terms of neuron numbers in each layer is 128–20–10. The sizes of training, validation and test datasets in this case are 140, 30 and 30 respectively based on the same division ratio mentioned above. The training of the neural network completes with 36 iterations and a cross-entropy error is 8.34×10^{-5} .

The test (prediction) result is illustrated in Fig. 6 showing a satisfactory accuracy of 93.3% in structural state identification for this fixed-end beam case.

3.4 MX3D Bridge

To extend the experimental investigation into more realistic structural settings, a similar structural state identification is performed on data collected from testing of a 3D steel footbridge. This steel bridge is the world’s first metal 3D printed bridge manufactured by Dutch company MX3D in 2018. The bridge has an overall span of 10.5 m and a mass of 7.8 t with steel main structure and a non-slip deck coating. Figure 7a shows an overall view of the bridge.

During the vibration test, the bridge was fully instrumented with various sensors. Seven tri-axial accelerometers (model MX1601B-R) labelled A01 to A07 were

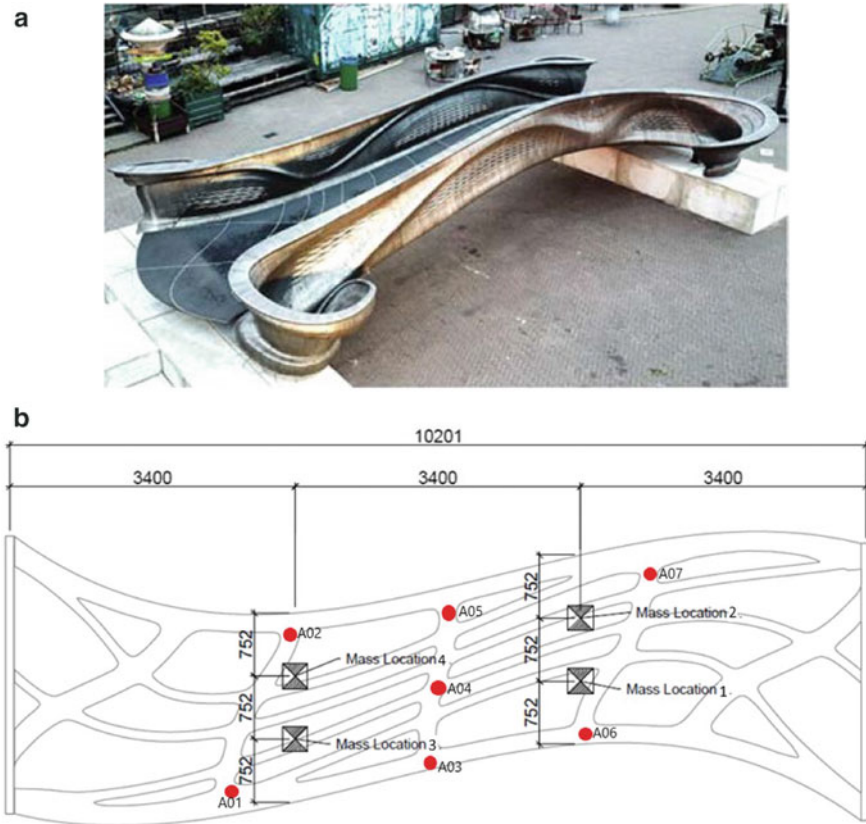


Fig. 7 a Overall view of MX3D Bridge (left); b locations of loading and accelerometers (right)

mounted on the bottom surface of the main beams. Added mass, which consisted of eight pieces of slabs with a total weight of 95 kg, was applied at one of the four specified locations each time, creating 4 different loading scenarios. Including the no added mass scenario, 5 structural states are to be identified. It is worth noting that the added mass was approximately 1.2% of the total weight of the structure. Hence the extent of structural change is commensurate with that in the previous laboratory tests. The locations of mass and accelerometers are shown in Fig. 7b.

In each structural state, the bridge was excited by a person walking and performing heel drops on the structure. The procedures were as follows: a person weighing 84.2 kg wearing running sneakers walked across the bridge 10 times at a pace of 100 steps per minute. After that, the same person performed heel drops 5 times at location 1 with 30 s rest between each heel drop. The whole test was repeated another 3 times on the second day allowing exposures to various ambient influence in the measurements. The time of tests included early morning, mid-day and evening with readings of thermistors varying from 15 to 47 °C. Therefore, in each structural state,

40 sets of walking signals and 20 sets of heel-dropping signals are sampled at a rate of 100 Hz. Each walking signal and heel-dropping signal lasted for 20 and 8 s respectively. The recorded time series of a walking signal and a heel-dropping signal are shown in Fig. 8a. In this study, only vertical acceleration signals are utilised since walking and heel-dropping excitations are considered as vertical loads. The power spectral density of a walking signal and a heel-dropping signal are shown in Fig. 8b as an example. WPNEs are extracted at the 8th level of the WPT decomposition. Examples of NWPNE features extracted are shown in Fig. 9. In order to allow a larger testing dataset, the data are split with an adjusted ratio of 60%, 10% and 30% to form training, validation and testing dataset, respectively.

From the frequency spectrums it can be seen that high frequency components have been significantly interfered in the measurements and clear peaks can only be observed in the first few modes. Responses of walking excitations appear even vaguer. To investigate the effects of the two types of excitations, the walking and heel-dropping signals sets are tested separately with the WPNE-NN approach.

Besides, signal sets from 7 accelerometers are tested individually to examine the performance of the approach with single data source, following which a few combination cases of multiple data sources are tested to examine the effect of data fusion. The fusion of the features from multiple sources is achieved by combining them into a higher dimensional vector. The combination cases include (1) A04 + A05 (2) A04 + A05 + A02 (3) A02 + A05 + A07 (4) all 7 sensors. Since the input and output vectors of the neural network are 256 and 5 in dimension, the number of neurons in the hidden layer is determined as 20, resulting in a network structure of 256-20-5 in terms of the number of neurons in each layer.

The identification results based on various data sources and signals types are compared in Table 1. Cases 1–13 represent tests with different data sources involved. Results from signals collected under two types of excitations (heel-dropping and walking) are compared in these 13 cases. It can be seen that with any single data source, the approach can hardly identify the structural state with most of the accuracies under 50%. When more data sources are involved, apparent improvements can be observed in both results based on data from heel-dropping and walking. Particularly, the identification based on heel-dropping data appears to be highly accurate although variation in accuracy exists with different combinations of data sources. On the other hand, the results based on walking data cannot be improved to a satisfying extent even with a combination of more data sources.

4 Conclusions

Through an experimental investigation on two laboratory structures and a real-life steel bridge, the viability of the WPNE-NN approach in detecting and localising incipient structural changes under realistic structural and measurement conditions is examined. In the test on free-ended I beam, the WPNE-NN approach has

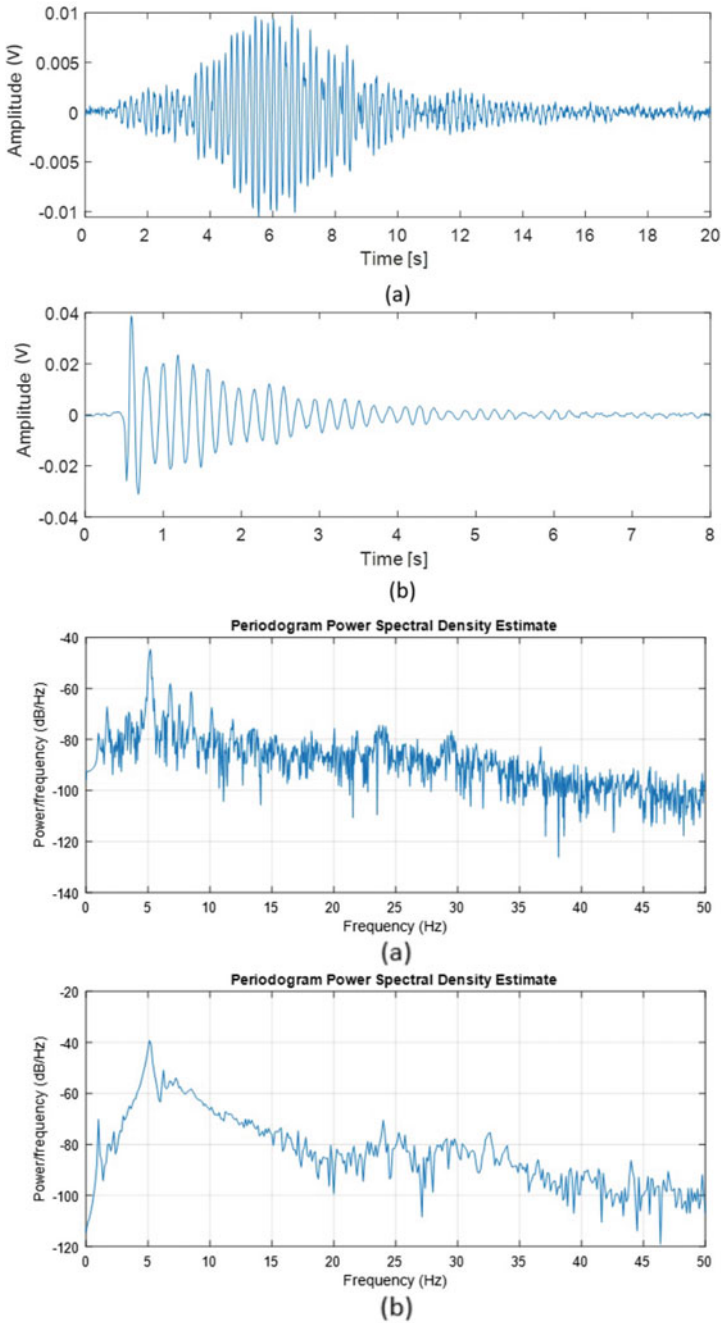


Fig. 8 Left: time histories of a signal excited by **a** walking, **b** a heel drop; right: The corresponding power spectral density plots

Fig. 9 Examples of NWPNE features from **a** a signal collected from A04 excited by walking, **b** a signal collected from A04 excited by a heel drop

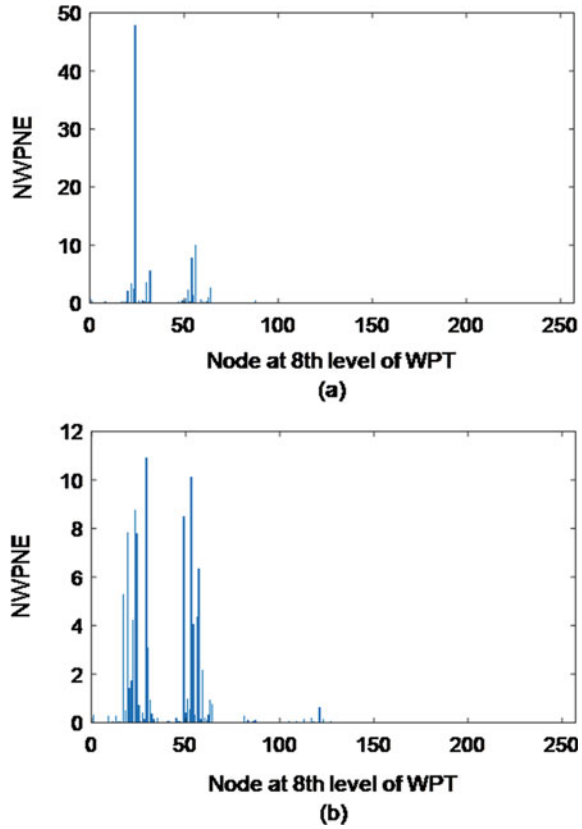


Table 1 Detection and localization results of test on MX3D Bridge

Case	Heel dropping		Walking	
	Data source	Accuracy (%)	Data source	Accuracy (%)
1–8	A01, ..., A08	13.3–66.7	A01, ..., A08	13.3–33.3
9	A04 + A05	86.70	A04 + A05	46.70
10	A04 + A05 + A02	100	A04 + A05 + A02	53.30
11	A02 + A05 + A07	73.30	A02 + A05 + A07	50.00
12	A02 + A03 + A07	100	A02 + A03 + A07	50.00
13	A01 to A07	100	A01 to A07	56.70

demonstrated satisfactory sensitivity and robustness in identifying incipient structural changes with just a single data source. The results from testing a beam with fixed ends further confirm the applicability of the approach under a practical boundary condition. Further application of the approach on data collected from testing of the

MX3D Bridge indicates that, as the complexity of the structure and the measurement increases, using a single data source may no longer be sufficient, and data fusion from multiple sources becomes essential. The results from using a combination of data from multiple sensors have yielded satisfactory classification accuracy even with the complex 3D bridge. In general, the identification accuracy is higher in a better controlled excitation situation, where structural changes at a level equivalent to incipient damage are detectable.

Acknowledgements The experimental study on data from the MX3D Bridge dynamic testing has been made possible thanks to funding and support from the Data-Centric Engineering programme at the Alan Turing Institute, funded by the Lloyd's Register Foundation. The authors would also like to thank Autodesk, the BRIDE Project, Force Technology, Imperial College London, and the University of Twente, for their contributions to the MX3D Smart Bridge Project. Special thanks are given to the University of Twente for hosting the experimental testing from which the original vibration data used in this paper has been generated, and Professor Roland Kromanis for overseeing collection of the ambient acceleration data.

References

1. Yen GG, Lin KC (2000) Wavelet packet feature extraction for vibration monitoring. *IEEE Trans Industr Electron* 47(3):650–667
2. Han JG, Ren WX, Sun ZS (2005) Wavelet packet based damage identification of beam structures. *Int J Solids Struct* 42(26):6610–6627
3. Mikami S, Beskhyroun S, Oshima T (2011) Wavelet packet based damage detection in beam-like structures without baseline modal parameters. *Struct Infrastruct Eng* 7(3):211–227
4. Sun Z, Chang CC (2002) Structural damage assessment based on wavelet packet transform. *J Struct Eng ASCE* 128(10):1354–1361
5. Graps A (1995) An introduction to wavelets. *IEEE Comput Sci Eng* 2(2):50–61
6. Coifman RR, Wickerhauser MV (1992) Entropy-based algorithms for best basis selection. *IEEE Trans Inf Theory* 38(2):713–718
7. Mallat S, Peyre G (2009) A wavelet tour of signal processing the sparse way preface to the, sparse. *The Sparse Way, Xv-+, Wavelet Tour of Signal Processing*
8. Xu BT, Zhang XZ, Jiang JF, Liu K, Wang S, Fan XJ, Liu TG (2019) Method of damage location determination based on a neural network using a single fiber Bragg grating sensor. *Appl Opt* 58(26):7251–7257

Identification of the Dynamic Properties of the Residential Tower New Orleans



A. J. Bronkhorst, D. Moretti, and C. P. W. Geurts

Abstract This paper describes the application of the Frequency Domain Decomposition (FDD) technique on measured acceleration data on the residential tower *New Orleans* in Rotterdam, the Netherlands. The goal of this study is to determine and analyse multiple natural frequencies and mode shapes of this tower. A measurement campaign was setup on the 158 m high *New Orleans* tower. Accelerations were measured at the 15th, 34th and 44th floor. Modal properties are obtained using the FDD method. A total of 11 modes are identified, of which 7 modes have a clear dominant direction. The first mode, with the lowest natural frequency, is observed in X-direction, which corresponds with the lower bending stiffness of the *New Orleans* tower in this direction compared to the Y-direction. The second mode in X-direction has a higher natural frequency than the second mode in Y-direction. This suggests that the foundation stiffnesses in X-direction are larger than those in Y-direction. The obtained modal properties provide a good basis for further work, in which the properties of an Euler-Bernoulli beam with rotational and translational springs at the base can be determined by matching the measured modal properties.

Keywords High-rise building · Acceleration measurements · Frequency domain decomposition · Natural frequencies · Mode shapes

1 Introduction

Reliable prediction of the dynamic characteristics of high-rise buildings requires accurate estimation of the structural building properties (i.e. stiffness and mass). Accurate estimation of these properties in the design phase is difficult. Bronkhorst and Geurts [1] showed that the predicted natural frequency of several Dutch high-rise buildings deviates significantly from the estimated value. This is attributed to an inaccurate estimation of the building and foundation properties during the design

A. J. Bronkhorst (✉) · D. Moretti · C. P. W. Geurts
Department of Structural Dynamics, Unit Building, Infrastructure and Maritime, TNO, Delft,
Netherlands
e-mail: okke.bronkhorst@tno.nl

© The Author(s), under exclusive license to Springer Nature Switzerland AG 2023
Z. Wu et al. (eds.), *Experimental Vibration Analysis for Civil Engineering Structures*,
Lecture Notes in Civil Engineering 224,
https://doi.org/10.1007/978-3-030-93236-7_39

phase. It is unclear which properties (i.e. building mass, building stiffness and/or foundation stiffness) are incorrectly estimated and by how much. To determine to what extent the estimated building properties are responsible for the inaccurate estimation of the natural frequency, these properties need to be determined via in-situ measurements. One approach to determine structural properties via measurements is to measure several modes (i.e. natural frequencies and mode shapes) of the building and match these with the modes of a model by tuning its structural properties. In previous measurement studies on Dutch high-rise buildings [1–3], the first three natural frequencies were determined through picking of peaks in the measured output spectra of measurements on one floor. This measurement setup does not allow to obtain information on the mode shapes. According to van den Berg en Steenbergen [2], information on both natural frequencies and mode shapes for more modes is needed for accurate estimation of the building properties. The Frequency Domain Decomposition (FDD) technique is a well-established method, see for example [4–6], to determine natural frequencies and mode shapes from output-only acceleration measurements, also known as Operational Modal Analysis (OMA). This paper describes the application of the FDD technique on measured acceleration data on the *New Orleans* residential tower. The goal of this study is to determine and analyse multiple natural frequencies and mode shapes of this tower. Section 2 describes the measurement setup on the *New Orleans* tower. Section 3 explains the methods used to analyse the data, and to assess the obtained modal properties. The results of this study are presented in Sect. 4. Section 5 gives the conclusions of this study. The obtained modal properties provide the basis for ensuing work, in which the structural properties of an analytical model (i.e. an Euler–Bernoulli beam with rotational and translational spring at the base) are estimated by matching the measured modal properties.

2 Measurement Setup

Measurements were performed on the residential tower *New Orleans* in Rotterdam, shown in Fig. 1a. This building is equipped with a permanent monitoring system. The original reason for setting up this monitoring system was a research project on local wind loads on façade elements, and the influence of pressure equalization on these loads. Details about the setup of the permanent monitoring system can be found in [1, 7, 8].

The permanent monitoring system on the 34th floor was supplemented with additional acceleration sensors (Sundstrand, type QA-700) on the 15th and 44th floor. Figure 1b–d shows the position of the 8 accelerometers of the permanent monitoring setup on the 34th floor, and the additional accelerometers placed on the 15th and 44th floor. The data applied in this study was recorded on 29/03/2020. A total of 129 10-min records were used, which were sampled with 20 Hz. The mean wind velocity ranged between 5 and 16 m/s and the average wind direction varied between 0 and 40°.

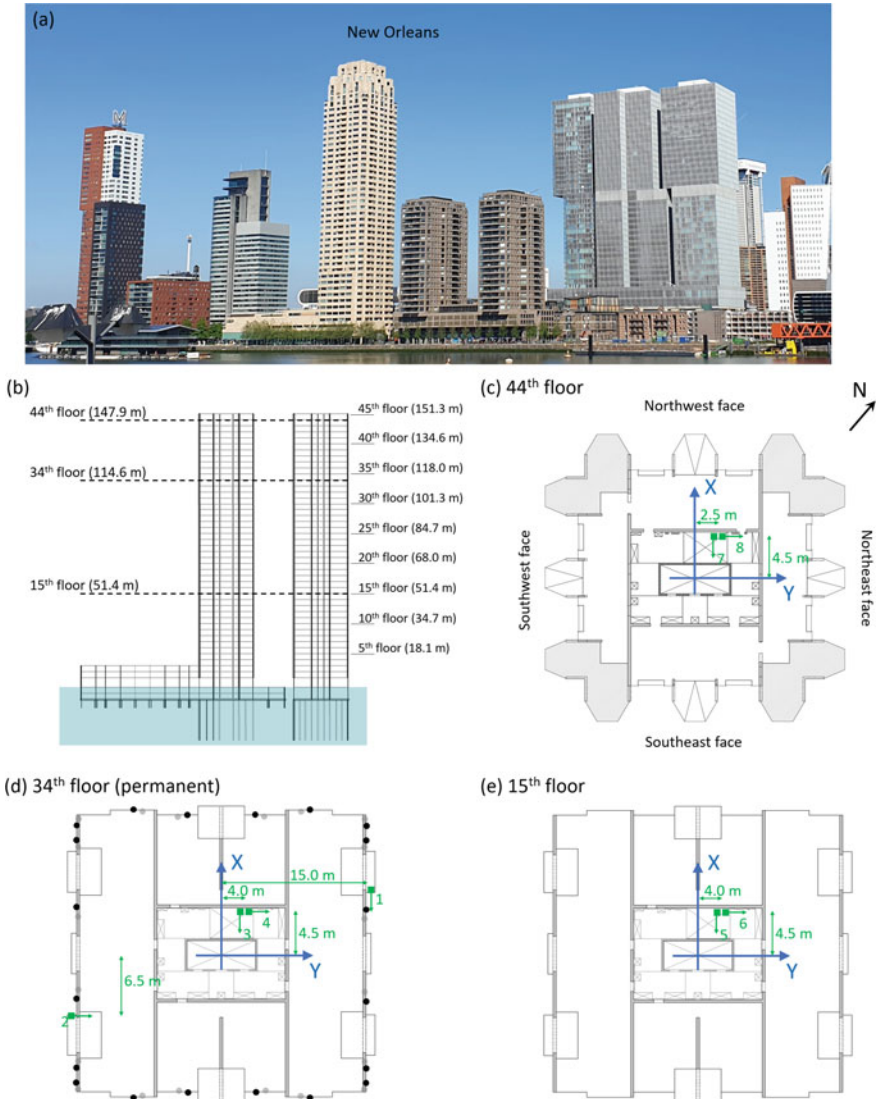


Fig. 1 a, b Picture and schematic of the New Orleans tower and positions of the acceleration sensors (green squares) on the New Orleans residential tower on c the 44th floor, d the 34th floor, and e the 15th floor. The green arrows indicate the directions of the acceleration sensors

3 Data Analysis

This section describes the methods used to process the measured acceleration data and analyse the obtained mode shapes. The first paragraph explains the processing steps in the Frequency Domain Decomposition, with which the modes of the *New Orleans*

are determined. The second paragraph explains the applied scaling procedure for the obtained mode shapes. The last paragraph describes the Modal Assurance Criterion (MAC), which is a technique to assess whether mode shapes are sufficiently well identified to differentiate them from other modes.

3.1 Frequency Domain Decomposition

The Frequency Domain Decomposition (FDD) method was first presented by Brincker et al. [4]. It is a frequency domain technique with which natural frequencies and mode shapes can be estimated from measured acceleration signals on a structure excited by ambient vibrations closely representing white noise.

First the power spectral density matrix G_{yy} of the measured time series is obtained by determining the cross and auto power spectra of all measured signals. The power spectra are computed after detrending the time series by removing the average. Power spectral densities for all measured 10 min time traces were obtained with Welch's averaged, modified periodogram method (cpsd in Matlab R2019a). The applied window size was chosen equal to the number of samples in the measured signal (number of samples in 10 min) and no overlap was applied; zero-padding was used to increase the FFT resolution. Averaging was applied over the 129 power spectra obtained with this procedure.

After obtaining the averaged 8×8 power spectral density matrix G_{yy} , for each frequency instance ω in the spectrum, these matrices were decomposed using the singular value decomposition [4]:

$$G_{yy} = USU^{*'} \quad (1)$$

where U is an orthonormal matrix (i.e. $U'U = UU' = I$) containing the singular vectors and S is a diagonal matrix with the singular values at each frequency instance ω . The singular values of S are the ordinates of scalar spectra of single degree of freedom systems. The singular vectors in matrix U can be associated with mode shapes of the tested structure. In particular, in this study the column in U corresponding to the first singular value in S for each frequency that can be identified as a natural frequency (see Fig. 2) is used as mode shape. This may lead to more mode shapes than can be described by the limited set of sensors. Section 3.3 describes how to determine which modes are not sufficiently well described.

3.2 Mode Shape Scaling

The obtained mode shapes φ_i from the matrix U at the identified natural frequencies are scaled using degree of freedom (DOF) scaling; the DOF scaled mode shape is

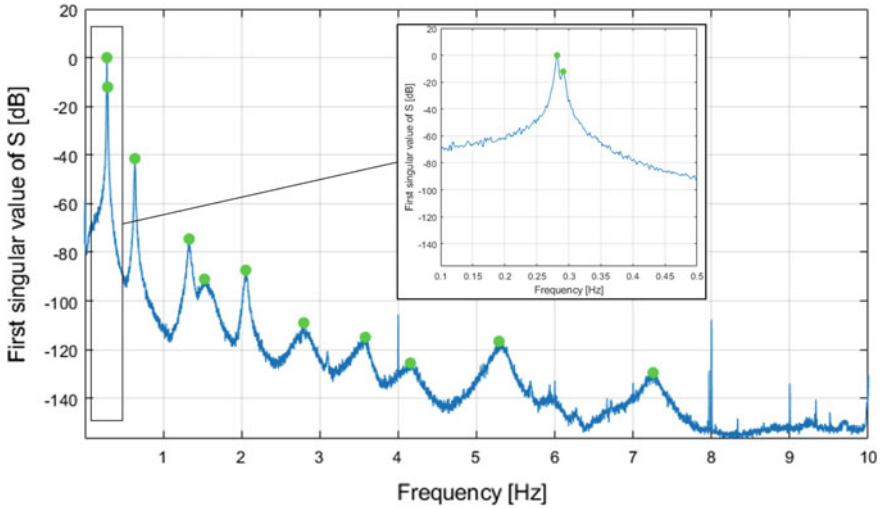


Fig. 2 Dimensionless spectrum of the first singular value of S for each frequency. Indicated in green are the natural frequencies of the New Orleans tower

defined as [9]:

$$\varphi_{i,D} = \frac{\varphi_i}{\varphi_{i,D_n}} \tag{2}$$

where φ_{D_n} is the considered DOF used for scaling; in this study the DOF with the largest component was used.

3.3 Modal Assurance Criterion

To assess whether the obtained modes are orthogonal (i.e. the correlation between the mode shapes is low), the Modal Assurance Criterion (MAC) is applied here. The MAC gives the correlation coefficient between two mode shape vectors, and is defined as [10]:

$$MAC = \frac{(\varphi_1^{*T} \varphi_2)^2}{(\varphi_1^{*T} \varphi_1)(\varphi_2^{*T} \varphi_2)} \tag{3}$$

Normalization is not relevant here and the original mode shapes φ_i can be used. The MAC values of mode shape vectors describing different modes should generally be small; Heylen et al. [10] suggest a value less than 10%. If the MAC is high (larger than 35%), this can mean two things:

- If the modes are at close frequencies, this could indicate the two modes are actually the same mode;
- If the modes are at distant frequencies, this is a strong indication that the number of sensor positions is not sufficient to differentiate sufficiently between the two modes.

4 Results and Discussion

This section discusses the results obtained from the measurements on the *New Orleans* tower. The first paragraph presents the obtained modal frequencies and the DOF-scaled modal displacements, and discusses the orthogonality of the obtained modes. The second paragraph discusses the dominant directions of the obtained mode shapes.

4.1 Orthogonal Modes

Figure 2 shows the dimensionless spectrum of the first singular value of S . The peaks indicated in this graph correspond with the natural frequencies specified in Tables 1 and 2. These tables also specify per mode the dominant direction and the DOF-scaled modal displacements of each sensor. Table 3 gives the MAC values determined for each combination of mode shapes. Table 3 shows that modes 1, 2, 4, 5, 7 and 8 have MAC values which are all smaller than 35%. This indicates the applied measurement setup is sufficient for observability of these modes. It furthermore shows that these modes are orthogonal modes of the *New Orleans* tower.

Table 1 Properties of the modes defined from the singular value spectrum (modes 1–6)

Mode	1	2	3	4	5	6
Dominant direction [–]	X	Y	θ	Y	X	θ
Natural frequency [Hz]	0.282	0.291	0.638	1.332	1.527	2.054
<i>Modal displacement [–]</i>						
Sensor 5 (51.4 m)	–0.30	–0.05	–0.13	0.00	0.89	0.29
Sensor 6 (51.4 m)	–0.02	–0.29	–0.15	–0.90	0.05	0.50
Sensor 1 (114.6 m)	–0.71	–0.10	–1.00	–0.02	–0.23	–1.00
Sensor 2 (114.6 m)	–0.03	–0.78	0.43	0.19	0.02	0.45
Sensor 3 (114.6 m)	–0.67	–0.11	–0.28	0.00	–0.06	–0.24
Sensor 4 (114.6 m)	–0.03	–0.76	–0.30	0.06	–0.02	–0.21
Sensor 7 (147.9 m)	–1.00	–0.12	–0.23	–0.04	–1.00	–0.25
Sensor 8 (147.9 m)	–0.09	–1.00	–0.38	1.00	–0.11	–0.61

Table 2 Properties of the modes defined from the singular value spectrum (modes 7–11)

Mode	7	8	9	10	11
Dominant direction [-]	Y		Y		
Natural frequency [Hz]	2.771	3.560	4.155	5.300	7.250
<i>Modal displacement [-]</i>					
Sensor 5 (51.4 m)	0.02	0.33	0.03	0.08	-0.16
Sensor 6 (51.4 m)	-0.73	0.22	0.18	-0.03	-0.06
Sensor 1 (114.6 m)	-0.11	-1.00	-0.12	-1.00	-1.00
Sensor 2 (114.6 m)	0.83	0.11	1.00	0.15	0.20
Sensor 3 (114.6 m)	-0.06	-0.80	-0.08	-0.58	-0.51
Sensor 4 (114.6 m)	0.99	-0.38	0.95	-0.29	-0.13
Sensor 7 (147.9 m)	0.01	0.41	-0.06	0.16	0.16
Sensor 8 (147.9 m)	-1.00	0.39	0.35	0.14	0.11

Table 3 Modal assurance criterion (MAC) values for the modes of Tables 1 and 2

Mode	1	2	3	4	5	6	7	8	9	10	11
1	1.00										
2	0.04	1.00									
3	0.44	0.06	1.00								
4	0.00	0.20	0.01	1.00							
5	0.24	0.01	0.06	0.00	1.00						
6	0.27	0.03	0.69	0.24	0.19	1.00					
7	0.00	0.00	0.09	0.00	0.00	0.04	1.00				
8	0.11	0.00	0.32	0.01	0.00	0.30	0.06	1.00			
9	0.00	0.73	0.01	0.05	0.00	0.02	0.26	0.00	1.00		
10	0.27	0.00	0.63	0.01	0.01	0.43	0.00	0.88	0.00	1.00	
11	0.30	0.00	0.68	0.02	0.00	0.39	0.00	0.74	0.02	0.94	1.00

Colour legend: 0–0.25; 0.25–0.5; 0.5–0.75; 0.75–1

Mode 3, 6, 9, 10 and 11 have more than 35% correlation with some lower modes (e.g. mode 3 with mode 1). According to Heylen et al. [10], this is a strong indication that the sensor setup violates the base assumption of observability for these modes. This means the applied setup is not sufficient to properly distinguish the mode shapes of these modes from the mode shapes of lower modes. It is noted that when mode 3

is not considered, mode 6 does meet the 35% correlation criterion. Measurements at additional floor levels with a minimum of 3 sensors on each floor are needed to meet the observability criterion for these modes. The best floor levels should be based on the expected mode shapes of these higher modes (i.e. mode 3, 6 and 8–11). The analytical model that will be fitted on the obtained modal properties in ensuing work could be used to determine the floor levels at which additional measurements should be performed to properly assess the higher modes.

Although the setup is not enough to properly distinguish the mode shapes of mode 3 and mode 6, it is sufficient to determine that these modes are (dominant) torsional modes. The next paragraph provides more information about the dominant direction of the measured modes.

4.2 Dominant Direction

The dominant direction is determined from the DOF-scaled modal displacements specified in Tables 1 and 2. The modal displacements obtained for the sensors that are oriented in the direction opposite to the dominant direction are indicated in light grey. For example, the modal displacements of mode 1 for the sensors in X-direction are clearly larger than for the sensors in Y-direction. For a number of modes (mode 1, 2, 3, 4, 5, 7 and 9) a clear dominant direction (translational or torsional) of the mode shape is found. For these modes, relatively small modal displacements are observed in the non-dominant direction.

Table 2 shows that for modes 8, 10 and 11 no clear dominant direction can be determined from the modal displacements. The modes appear to consist of a combination of torsion and translation in X-direction. This could have implications when fitting a model on these measured mode shapes. The modes with a clear dominant direction can be fitted with a simpler model (only considering the dominant direction), while the modes with combined directions require a more complex model that considers all directions (both translations and rotation).

The dominant direction of the torsional modes can be established by considering the position of the sensor with respect to the neutral axis of the building. Because the torsional movement of the tower is very small, the angular modal displacements can be determined by dividing the modal displacement with the distance between the sensor and the building axes (see Fig. 1). Table 4 gives the DOF-scaled angular modal displacements per sensor for mode 3 and 6. For mode 3, the modal displacements are similar for each set of sensors per floor, with an average value of -0.36 for the 15th floor (51.4 m), -0.71 for the 34th floor (114.6 m), and -0.98 for the 44th floor (147.9 m). Figure 3 shows that mode 3 gradually increases in angular modal displacement with height. The variability in angular modal displacements between different sensors at the same floor is small compared to those observed for mode 6. This shows mode 3 is a well-defined torsional mode around the neutral axis of the *New Orleans* tower. The larger variability observed for mode 6 indicates this mode shape is not as well-defined as mode 3, but the main contribution is torsional.

Table 4 The DOF-scaled angular modal displacements for mode 3 and mode 6

Mode	1	6
Sensor 5 (51.4 m)	-0.34	0.48
Sensor 6 (51.4 m)	-0.38	0.83
Sensor 1 (114.6 m)	-0.71	-0.44
Sensor 2 (114.6 m)	-0.70	-0.46
Sensor 3 (114.6 m)	-0.73	-0.39
Sensor 4 (114.6 m)	-0.71	-0.31
Sensor 7 (147.9 m)	-0.96	-0.66
Sensor 8 (147.9 m)	-1.00	-1.00

Figure 3 shows the DOF-scaled mode shapes of mode 1–7. The top row of graphs shows the modes with the main contribution in X-direction, the middle row the modes mainly in Y-direction, and the bottom row the modes in torsional direction. The first mode with the lowest natural frequency of 0.282 Hz is observed in X-direction. This corresponds with the lower bending stiffness of the *New Orleans* tower in this direction compared to the Y-direction. The second mode in X-direction (mode 5) has, however, a higher natural frequency than the second mode in Y-direction (mode 4). Because the mass of the building is the same for both directions, the foundation stiffness (rotational and/or translational) appears to be responsible for this difference in natural frequencies.

The obtained natural frequencies and mode shapes provide a good first basis for a study on the identification of the structural properties of an analytical beam model of the *New Orleans* tower. The mode shapes determined for mode 1 to mode 7 indicate that the *New Orleans* tower can be well-represented by an Euler-Bernoulli beam with rotational and translational springs at the base.

5 Conclusion

This paper described a study on the application of the Frequency Domain Decomposition (FDD) technique on acceleration data measured on the *New Orleans* residential tower. A total of 11 modes were identified. Application of the Modal Assurance Criterion showed that 6 of the identified modes (i.e. mode 1, 2, 4, 5, 7 and 8) meet the requirement for orthogonality. For these modes the applied measurement setup is sufficient for observability. The other modes (mode 3, 6, 9, 10 and 11) do not meet the MAC requirements to properly distinguish them from lower modes. Measurements at additional floor levels are needed to meet the observability criterion for these modes.

For a number of modes (mode 1, 2, 3, 4, 5, 7 and 9) a clear dominant direction (translational or rotational) of the mode shape is observed. For these modes, relatively small modal displacements are found in the non-dominant direction. For the other

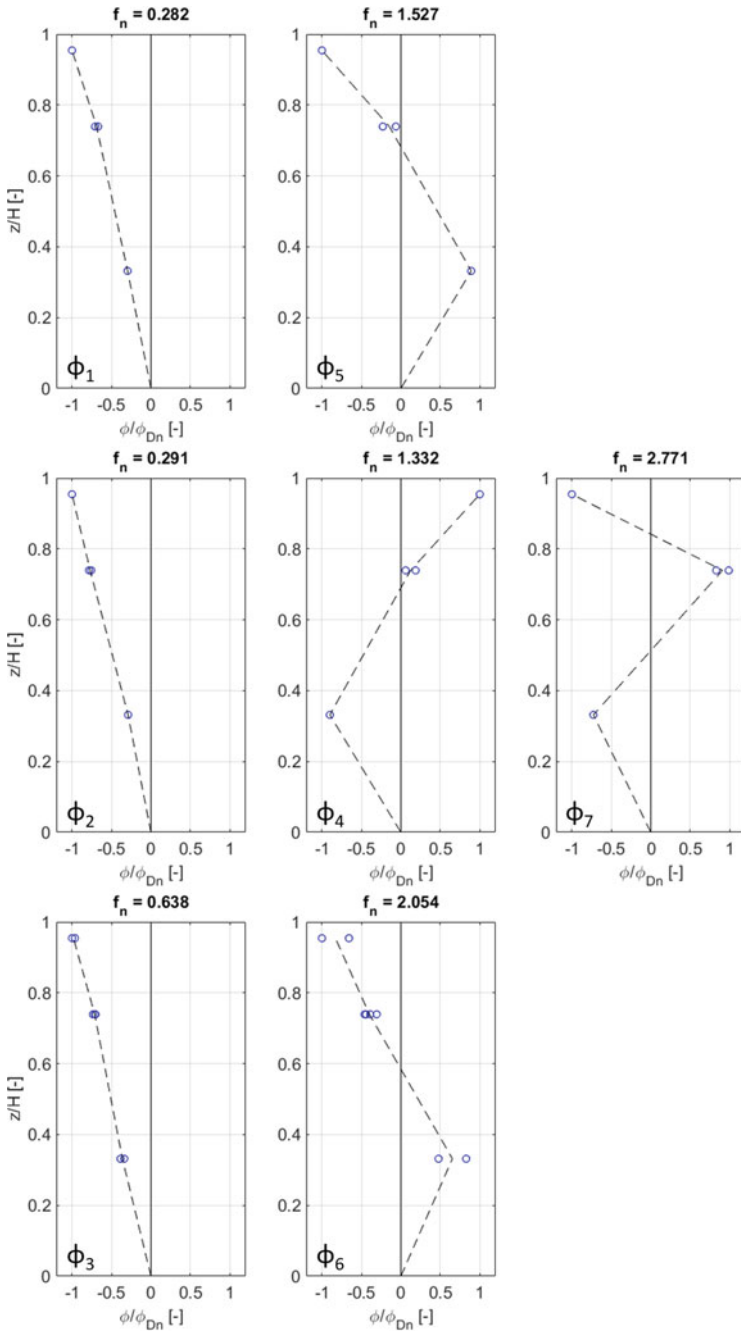


Fig. 3 DOF-scaled mode shapes of mode 1–7: (top row) mode 1 and 5 with dominant X-direction, (middle row) mode 2, 4 and 7 with dominant Y-direction, (bottom row) mode 3 and 6 with dominant torsional direction

modes (mode 6, 8, 10 and 11), the mode shapes do not have a clear dominant direction, but consist of a combination of directions. This could have implications for the required model setup to estimate the structural properties of the *New Orleans* tower.

The obtained modal properties obtained in this study provide a good first basis for the estimation of the structural properties (i.e. building mass, building stiffness and foundation stiffness) of the *New Orleans* tower by fitting an Euler–Bernoulli beam with rotational and translational springs at the base.

Acknowledgements This work was performed in the research project “HIVIBE”. The authors wish to acknowledge the participation of the partners in this research: Aronsohn, BAM, Besix, Fugro, IMd, Peutz, SCIA Engineer, Kennisoverdracht Windtechnologie, Structure Portante Grimaud, and Zonneveld Ingenieurs.

The “HIVIBE” project is financially supported by the Ministry of Economic Affairs and falls under the Topsector Water & Maritime, contract number T-DEL/2021/024.

References

1. Bronkhorst AJ, Geurts CPW (2020) Long-term vibration and wind load monitoring on a high-rise building. In: Proceedings ISMA2020, Leuven, Belgium
2. Van den Berg RLJ, Steenbergen RDJM (2013) Identifying the damping contribution of building components based on measured top vibration. In: 4th ECCOMAS thematic conference on Computational methods in structural and earthquake engineering, Greece
3. Gómez SS, Geurts CPW, Metrikine A (2018) On the importance of soil damping for tall buildings loaded by wind. *Eng Struct* 163:426–435
4. Brincker R, Zhang L, Andersen P (2000) Modal identification from ambient responses using frequency domain decomposition. In: Proceedings of the IMAC 18, International modal analysis conference, San Antonio, USA
5. Brincker R, Zhang L (2009) Frequency domain decomposition revisited. In: Proceedings of the IOMAC 3, International operational modal analysis conference, Portonovo, Italy
6. Magalhães F, Cunha Á (2011) Explaining operational modal analysis with data from an arch bridge. *J Mech Syst Signal Process* 25:1431–1450
7. Van Bentum CA, Kalkman IM, Geurts CPW (2014) Field tests to study the pressure equalization on air permeable façade elements. In: Proceedings ICBEST 2014: Building for a changing world, Aachen, Germany
8. Van Bentum CA, Geurts CPW (2015) Full scale measurements of pressure equalization on air permeable façade elements. In: Proceedings 14th international conference on wind engineering, Porto Alegre, Brazil
9. Aenlle M, Juul M, Brincker R (2020) Modal mass and length of mode shapes in structural dynamics. *Hindawi Shock Vib* 2020, article ID 8648769, 16 p. <https://doi.org/10.1155/2020/8648769>
10. Heylen W, Lammens S, Sas P (2007) Modal analysis theory and testing. KU Leuven, Belgium

Coupled Dynamical Systems

Response Spectrum Method for Vehicle-Induced Bridge Vibration Serviceability Design



Haoqi Wang and Tomonori Nagayama

Abstract The vehicle-induced bridge vibration, which is mainly caused by the dynamic part of the load, has many negative influences on the serviceability of the bridge including bridge fatigue, driving safety, and pedestrian's comfort, etc. At the design stage, the prediction of the vibration level of the bridge to be constructed is an important task. This paper proposes a novel method to predict the bridge vibration due to single vehicle passage using the idea of response spectrum inspired from the research field of seismic engineering. The procedure of this response spectrum method is demonstrated through a numerical example. Possible factors that may affect the shape of the response spectrum are also discussed. This proposal provides an applicable method to predict the acceleration response under vehicle's passage.

Keywords Vehicle-induced load · Bridge vibration · Response spectrum · Design criteria · Infrastructure serviceability

1 Introduction

Among many types of loads, including seismic movement, wind, etc., the vehicle-induced load is one of the most common excitation that a bridge may encounter during its service life. Because the bridge pavement is usually uneven, the bridge surface provides excitation to the mechanical system of the vehicle, which, in return, exerts dynamic load on the bridge deck, leading to vibration of the bridge. Effects of this vehicle-induced vibration include fatigue of the structural components like girders or cables. The vehicles' driving safety and the pedestrians' comfort are also affected if the vibration of the bridge is not well controlled, even resulting in a negative social influence. If the unpleasant vibration occurs after the construction

H. Wang (✉)

College of Civil Engineering, Tongji University, Shanghai, P.R. China

e-mail: 12wanghaoqi@tongji.edu.cn

T. Nagayama

Department of Civil Engineering, The University of Tokyo, Tokyo, Japan

has been completed, the time and cost expenses on vibration mitigation are supposed to be high. Therefore, the bridge vibration caused by passing vehicles needs to be carefully considered during the design stage.

The dynamic effect of the passing vehicles is usually reflected by an amplification factor in the current design methods, which is related with either the bridge fundamental frequency [1] or the bridge span [2] in which the dynamic response of the bridge is considered as a fixed amplified static response. This method, although simple and straightforward, could not directly evaluate the vibration level of the bridge because it does not consider the properties of the vehicle-induced load as well as its stochastic features. On the other hand, the idea of responses spectrum has been proposed for a long time since 1920s, when Suyehiro analyzed the movement of different pendulums under one earthquake [3]. This idea was then developed by researchers including Biot [4], Housner [5], and Newmark [6], and was later adopted as the standard method for seismic design [7]. Although the concept of the response spectrum is proposed and developed in the field of earthquake engineering, the responses spectrum is not limited to seismic load, and has already been extended to wind load [8] and human-induced activities [9].

However, there is still not much investigation on the possibility of using responses spectrum method for bridge vibration serviceability design. To the authors' understanding, the main difficulties are about the measurement of real vehicle dynamic load and the affecting factors that need to be considered, e.g., pavement roughness, driving speed. In recent years, with the development of the moving force identification technique, the indirect measurement or identification of the passing vehicle's load becomes possible [10], providing foundation for the derivation of the vehicle-induced response spectrum. Moreover, the pavement roughness, which is the main excitation source of the vehicle-bridge system, has become possible to be detected and evaluated through a recently-developed algorithm [11, 12]. Therefore, the vehicle-induced responses spectrum and corresponding design strategy is ready to be developed.

In this paper, the procedure of developing the response spectrum model is given after a brief introduction on the concept of response spectrum. Factors that may affect the responses spectrum model is discussed. Steps for the use of the proposed method are summarized. Some future work that requires further investigation on the vehicle-induced responses spectrum model is also given.

2 Vehicle Dynamic Load

It is well known that to develop the response spectrum model, it is crucial to obtain a large amount of time histories of vehicle-induced load. For example, without the database of recordings of seismic acceleration input, it is not even possible to develop the response spectrum model for seismic design. Unfortunately, for the vehicle-induced load, large-scale measurement of real vehicle dynamic load remains difficult, if not impossible [13]. In this manner, it is important to develop indirect identification technique and conduct field tests to establish the database of vehicle-induced load

time histories. Note that this paper mainly focuses on the procedure of the development of the response spectrum rather than moving force identification. Therefore, the vehicle-induced load time histories used in this paper are simulated ones, rather than extracted from a field test. However, it is clear that a correct and reliable response spectrum should be based on the vehicle loads from in-situ measurement.

The vehicle-induced dynamic load is related on two aspects, the pavement roughness and the vehicle dynamic parameters. The pavement roughness in this section is extracted from a field test [14], and is shown in Fig. 1a. For the vehicle parameters, a half-car model is adopted with all its parameters considered as random variables. The probability distribution of these parameters are listed in Table 1, where $N(\mu, \sigma)$ means the variable follows a normal distribution with a mean value of μ and a standard deviation of σ , and $U(a, b)$ indicates the uniform distribution with lower limit a and upper limit b . The physical meanings vehicle parameters shown in Table 1 are illustrated in Fig. 1b.

Fig. 1 Pavement roughness and half-car model. **a** Pavement roughness extracted from a field test. **b** Illustration of a half-car model

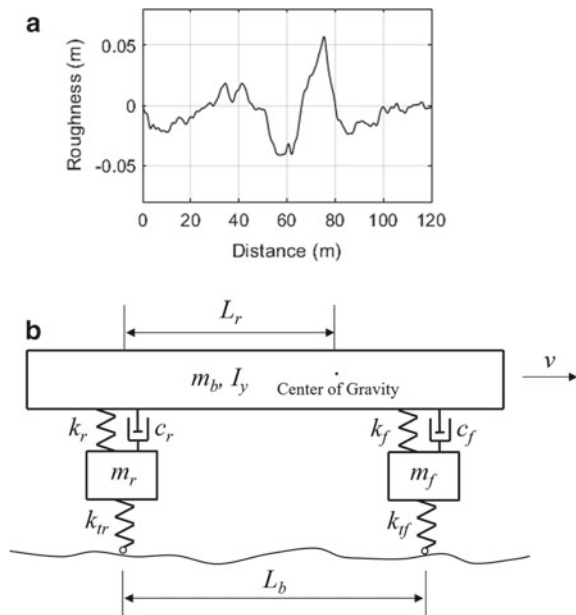


Table 1 Parameter distribution of a half-car model

m_b (kg)	m_f (kg)	m_r (kg)	I_y	k_f (N/m)	k_r (N/m)
$N(2000,300)$	$N(100,10)$	$N(150,10)$	$N(2000,500)$	$N(10,000,1000)$	$N(13,000,1000)$
k_{ff} (N/m)	k_{tr} (N/m)	c_f (Nm/s)	c_r (Nm/s)	L_b (m)	L_r (m)
$N(200,000,5000)$	$N(200,000,5000)$	$N(2500,200)$	$N(2700,200)$	$N(2.5,0.1)$	$N(2.05,0.02)$
v (m/s ²)					
$U(30,50)$					

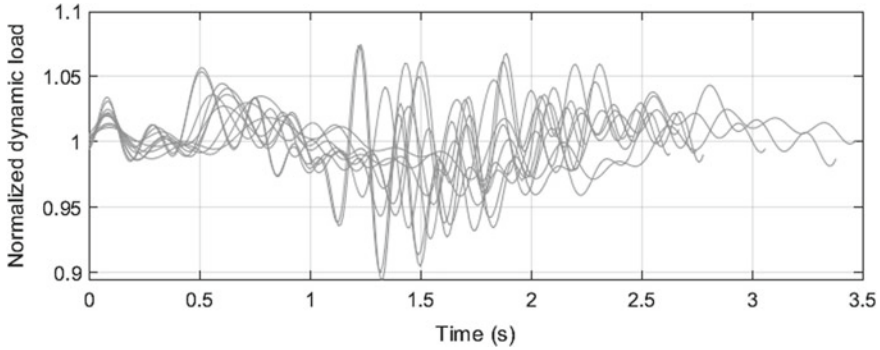


Fig. 2 Simulated normalized dynamic load

With the pavement roughness and vehicle parameters decided, the vehicle responses are calculated through Eq. (1)

$$\mathbf{M}\ddot{\mathbf{U}}(t) + \mathbf{C}\dot{\mathbf{U}}(t) + \mathbf{K}\mathbf{U}(t) = \mathbf{P}(t) \tag{1}$$

where \mathbf{M} , \mathbf{C} , \mathbf{K} , \mathbf{U} , and \mathbf{P} are mass matrix, damping matrix, stiffness matrix, response vector, and input vector of the half-car model system, whose detailed definition could be found in Ref. [15]. The vehicle dynamic load are thus calculated through Eq. (2)

$$\begin{aligned} F_f(t) &= k_{if}(u_f(t) - h_f(t)) \\ F_r(t) &= k_{ir}(u_r(t) - h_r(t)) \end{aligned} \tag{2}$$

in which F_f , F_r , u_f , u_r , h_f , h_r indicates the dynamic force, displacement, and pavement roughness of the front and rear tire, respectively. Moreover, for most two-axle vehicles, the wheel base is usually negligibly smaller than the bridge span. Therefore, the total dynamic load $F(t)$ on the bridge is expressed by the summation of $F_f(t)$ and $F_r(t)$. Figure 2 shows 10 vehicle dynamic load generated following the process described above.

3 Derivation of Response Spectrum

3.1 Generalized Single-Degree-of-Freedom System

A responses spectrum is defined as a plot of maximum responses of single-degree-of-freedom (SDOF) systems with various fundamental frequencies and damping ratios. The mass of the SDOF system is usually normalized to 1. The equation of motion

of the SDOF system is shown by Eq. (3)

$$\ddot{z}(t) + 2\omega\xi\dot{z}(t) + \omega^2z(t) = p(t) \quad (3)$$

where $z(t)$, ω , and ξ are the displacement response, circular frequency, and damping ratio of this SDOF system, and $p(t)$ is the external load. With ω and ξ determined, the responses could be calculated by solving Eq. (3) and the corresponding maximum or RMS value are obtained for each frequency and damping ratio.

3.2 System Input Considering Moving Effect

One main difference between the vehicle excitation and seismic excitation is that the vehicle-bridge contact point moves along the bridge while the seismic excitation is input on a fixed point of the structure. In this paper, the moving effect is considered by modifying the input of the generalized SDOF system. The vehicle dynamic load is multiplied by a half-sine wave, as expressed by Eq. (4)

$$p(t) = F(t) \cdot \sin(\pi vt/L) \quad (4)$$

where L is the bridge span. The half-sine wave here represents the first vibration mode shape of a simply-supported beam.

3.3 Representative Vehicle-Induced Response Spectra

For each vehicle passage, the response spectrum can be extracted following the procedure described above by changing the fundamental frequency and the damping ratio of the generalized SDOF system. The vehicle dynamic load is a random process affected by pavement roughness and the vehicle parameters. Representative response spectra of 100 simulated vehicle dynamic loads are calculated and plotted together in Fig. 3. The damping ratio is chosen to be 0.01. Note that in this figure, the vertical axis represents the maximum acceleration response of the SDOF system. If other physical quantities are of interest, the vertical axis could be adjusted accordingly, e.g., RMS value of the displacement.

It is observed that most spectra have peaks near 2–3 Hz, indicating that most simulated half-car models have their fundamental frequencies around this range. Note that the above dominant frequency range is in accordance with the findings in Reference [16], in which real vehicle loads were directly measured by load cells, showing that the vehicle parameters adopted in this study are reasonable. However, this dominant frequency range may vary according to the adopted vehicle load, which shows again the importance of in-situ vehicle load identification. Moreover, for each

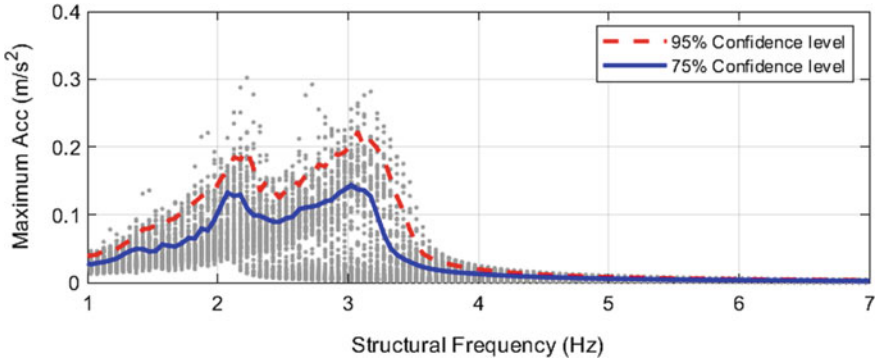


Fig. 3 Response spectra of 100 simulated vehicle loads (damping ratio = 0.01)

frequency component, the value that covers 95% and 75% of all data is calculated and plotted in the same figure, showing the curves corresponding to each confidence level.

4 Mathematical Model of Design Spectrum

For each vehicle passage, a response spectrum could be extracted through the above process. However, to use the response spectrum, the idea of design spectrum needs to be developed. In the field of earthquake engineering, the design spectrum is obtained from the response spectra of a series of seismic input recordings. Similarly, the design spectrum of vehicle-induced load could also be developed.

From Fig. 3, it is observed that the value of the spectrum first increases within the range of 1–2 Hz, reaches its highest value near 2–3.5 Hz and then decrease with the structural frequency towards a very small value. Inspired by this phenomenon, the mathematical model of the design spectrum is shown in Fig. 4. The corresponding formula describing this design spectrum is given in Eq. (5).

$$R(f) = \begin{cases} a_{1st}f, & 0 < f \leq 2 \text{ Hz} \\ a_{1st}, & 2 \text{ Hz} < f \leq 3.5 \text{ Hz} \\ a_{1st}(3.5/f)^\gamma, & 3.5 \text{ Hz} < f \leq 5 \text{ Hz} \\ a_{2nd}, & f > 5 \text{ Hz} \end{cases} \quad (5)$$

where $R(f)$ is the value of the design spectrum at frequency f , a_{1st} , a_{2nd} indicates the value of the first and second plateau of the curve, respectively, and γ is the exponential index of the descending curve. For each confidence level, the value of a_{1st} , a_{2nd} , and γ could be optimized from the datasets. For the curves shown in Fig. 3, the optimized values are listed in Table 2.

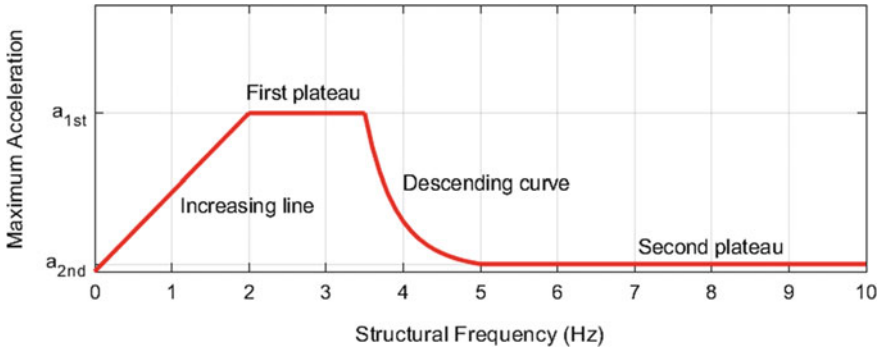


Fig. 4 The shape of the design spectrum

Table 2 Optimized parameters for design spectrum (damping ratio = 0.01)

Confidence level	Design spectrum parameter		
	a_{1st}	a_{2nd}	γ
95%	0.171	0.008	8.586
	0.115	0.006	8.280

5 Factors Affecting the Design Spectrum

5.1 Pavement Roughness

It is straightforward that if the bridge pavement becomes higher, the vehicle will also encounter vibration, leading to larger dynamic force on the bridge, and the bridge vibration becomes larger accordingly. Therefore, the pavement roughness needs to be considered in the response spectrum model. Assuming that the vehicle-bridge coupling system remains linear during vehicle passage, the bridge responses could be expressed as the product of a series of transfer functions in the frequency domain, which is shown by Eq. (6)

$$S_{acc}(\omega) = H_b(\omega) \cdot H_v(\omega) \cdot S_r(\omega) \tag{6}$$

where $S_{acc}(\omega)$ is the power spectrum of the bridge acceleration response, $H_v(\omega)$, $H_b(\omega)$ is the transfer function of the vehicle and the bridge, respectively, and $S_r(\omega)$ is the power spectrum of the pavement roughness in the temporal frequency domain, which satisfies the following relationship expressed by Eq. (7) according to ISO 8608 [17]

$$S_r(\omega) = v\lambda/\omega^2 \tag{7}$$

where λ is the degree of roughness defined by ISO 8608. For the pavement roughness used in this paper that is shown by Fig. 1, the value of λ is 41×10^{-6} . Combination of Eqs. (6) and (7) indicates that the bridge vibration level is proportional to the pavement roughness index λ . In this manner, a modification factor β_r is proposed to account for the effect from different pavement roughness, as expressed by Eq. (8)

$$\beta_r = \lambda_{design} / \lambda_{test} \quad (8)$$

in which λ_{test} is the roughness degree of the bridge where the vehicle dynamic loads are collected, and λ_{design} is the degree of roughness of the bridge to be designed, respectively.

5.2 Driving Speed

The driving speed also has an influence on the bridge vibration level. As expressed by Eqs. (6) and (7), the relation between the bridge vibration and driving speed is also linear. Therefore, a similar modification factor β_v is given by Eq. (9)

$$\beta_v = v_{design} / v_{test} \quad (9)$$

in which v_{test} is the driving speed of the vehicles whose dynamic loads are used in the design spectrum calculation. Ideally, it is better to use vehicles with similar driving speed to avoid inaccuracy.

6 Application Procedure of the Response Spectrum Method

The procedure to use the response spectrum method to calculate the bridge acceleration is described as follows.

- (1) Obtain the natural frequency f_j , damping ratio ξ_j , modal mass M_j for the j th vibration mode of the bridge to be constructed from the finite-element model or from the design documents
- (2) Decide the confidence level P , and calculate the value of the design spectrum through Eq. (5). Note that the design spectrum value is related with f_j , ξ_j , and P .
- (3) Calculate the modification factors from Eqs. (8) and (9).
- (4) Select the point of interest where the vibration level is to be predicted, and obtain the mode shape value φ_j of this point.
- (5) Decide a gross weight value G for the passing vehicle.

- (6) Calculate the predicted response level of the bridge acceleration under single vehicle passage following Eq. (10) including all vibration modes

$$\text{Acc} = \sqrt{\sum_j \left(\frac{G\varphi_j\beta_r\beta_m}{M_j} a_j(f_j, \xi_j P) \right)^2} \quad (10)$$

7 Conclusions

The contribution of this paper is that the procedure to develop a design-oriented response spectrum model is proposed for the prediction of the bridge vibration during the design stage. The factors affecting the shape of the design spectrum, including pavement roughness, and driving speed, are discussed and considered in the calculation process. Finally, the application steps of the proposed method are summarized. The proposed response spectrum method is capable to calculate the bridge vibration level under vehicle's passage.

Acknowledgements This work was partially supported by Council for Science, Technology and Innovation, "Cross-ministerial Strategic Innovation Promotion Program (SIP), Infrastructure Maintenance, Renovation, and Management" (funding agency: JST) and JSPS KAKENHI Grant Number 17H03295. This work was also sponsored by Chenguang Program (Grant Number: 20CG27) supported by Shanghai Education Development Foundation and Shanghai Municipal Education Commission.

References

1. The Ministry of Transport of the People's Republic of China (2015) General specifications for design of highway bridges and culverts
2. Japan Road Association (2017) Specifications for highway bridges
3. A Seismic Vibration Analyzer and the Records Obtained Therewith in the Bulletin of the Earthquake Research Institute, vol 1 (1926)
4. Biot MA (1942) Analytical and experimental methods in engineering seismology. ASCE Trans 108:365–408
5. Housner GW (1959) Behavior of structures during earthquakes. J Eng Mech Div ASCE. 85(EM 4):109–129
6. Newmark NM, Blume JA, Kapur KK (1973) Seismic design criteria for nuclear power plants. J Power Div ASCE 99:287–303
7. United States Atomic Energy Commission (1973) Design response spectra for seismic design of nuclear power plants. Regulatory guide no. 1.60
8. Solari G (1989) Wind response spectrum. J Eng Mech 115:2057–2073
9. Chen J, Xu R, Zhang M (2014) Acceleration response spectrum for predicting floor vibration due to occupant walking. J Sound Vib 333:3564–3579
10. Wang H, Nagayama T, Su D (2021) Static and dynamic vehicle load identification with lane detection from measured bridge acceleration and inclination responses. Struct Control Health Monit. <https://doi.org/10.1002/stc.2823>

11. Xue K, Nagayama T, Zhao B (2020) Road profile estimation and half-car model identification through the automated processing of smartphone data. *Mech Syst Signal Process* 142:106722
12. Zhao B, Nagayama T, Xue K (2019) Road profile estimation, and its numerical and experimental validation, by smartphone measurement of the dynamic responses of an ordinary vehicle. *J Sound Vib* 457:92–117
13. Yu Y, Cai CS, Deng L (2016) State-of-the-art review on bridge weigh-in-motion technology. *Adv Struct Eng* 19:1514–1530
14. Wang H, Nagayama T, Zhao B, Su D (2017) Identification of moving vehicle parameters using bridge responses and estimated bridge pavement roughness. *Eng Struct* 153:57–70
15. Wang H, Nagayama T, Nakasuka J, Zhao B, Su D (2018) Extraction of bridge fundamental frequency from estimated vehicle excitation through a particle filter approach. *J Sound Vib* 428:44–58
16. Wang H, Nagayama T, Su D (2019) Estimation of dynamic tire force by measurement of vehicle body responses with numerical and experimental validation. *Mech Syst Signal Process* 123:369–385
17. ISO-8608 (1995) Mechanical vibration-road surface profiles-reporting of measured data

A Railway Vibration Simulation Considering Contact Conditions Between Structures and Ground



Toru Gondo, Hidefumi Yokoyama, and Yuta Mitsuhashi

Abstract To clarify mechanisms of railway vibration, we have been using railway vibration simulation method developed by Railway Technical Research Institute. However, a result by using this simulation method sometimes leads to overestimation of railway vibration in high frequency bands. We suppose that one of the possible causes of the overestimation is contact conditions between structures and ground. In the simulation method, force-displacement relationship between structures and ground is completely continuous. However, in actual ground, there exist some loose areas nearby structures, and the force-displacement relationship between structures and ground is not completely continuous. Therefore, in this paper, we study influence of contact conditions between structures and ground on the estimation of ground responses. To simulate the looseness between structures and ground, spring elements are set on nodes between structures and ground in the analysis model. We examine five contact conditions consisted of sufficiently high stiffness spring elements and sufficiently low stiffness spring elements. The results of the study show that ground responses decrease in the frequency band of 20 Hz or higher under contact conditions that sufficiently low stiffness spring elements are set on some of nodes between structures and ground. Therefore, using the railway vibration simulation method, we can improve the simulation accuracy by incorporating the influence of contact conditions between structures and ground into the simulation method.

Keywords Railway vibration · Contact condition · Dynamic interaction analysis · Girder viaduct · Flexible volume method

T. Gondo (✉) · H. Yokoyama
Geology Laboratory, Railway Technical Research Institute, Tokyo, Japan
e-mail: gondo.toru.20@rtri.or.jp

Y. Mitsuhashi
Disaster Reduction and Environmental Engineering Department, Kozo Keikaku Engineering Inc,
Tokyo, Japan

© The Author(s), under exclusive license to Springer Nature Switzerland AG 2023
Z. Wu et al. (eds.), *Experimental Vibration Analysis for Civil Engineering Structures*,
Lecture Notes in Civil Engineering 224,
https://doi.org/10.1007/978-3-030-93236-7_41

1 Introduction

Ground vibration arising from railways (hereinafter, railway vibration) sometimes causes environmental problems. To take appropriate countermeasures against railway vibration, it is important to clarify generation and propagation mechanisms of railway vibration.

To clarify the mechanisms of railway vibration, we have been using railway vibration simulation method developed by Railway Technical Research Institute [1]. This simulation method is combination of two dynamic interaction analyses. First, to calculate excitation force induced by a train running, we conduct the dynamic interaction analysis of a train running, tracks and structures. Secondly, the calculated excitation force is input into the dynamic interaction analysis of structures and ground to estimate railway vibration. We use programs named DALIA (Kozo Keikaku Engineering Inc. (KKE)) for the former analysis, and Super FLUSH/3DS (KKE)) for the latter one.

However, a result by using the simulation method mentioned above sometimes leads to overestimation of railway vibration in high frequency bands. We suppose that one of the possible causes of the overestimation is contact conditions between structures and ground. In the simulation method, force-displacement relationship between structures and ground is completely continuous. However, in actual ground, there exist some loose areas nearby structures, and the force-displacement relationship between structures and ground is not completely continuous.

In this paper, we study influence of contact conditions between structures and ground in the railway vibration simulation method on the estimation of ground responses. To simulate the looseness between structures and ground, spring elements are set on nodes between structures and ground in the analysis model. Then, we conduct parametric studies of these spring elements.

2 Dynamic Interaction Analysis of Structures and Ground

We describe the dynamic interaction analysis of structures and ground in the railway vibration simulation method. We model girder viaduct section.

2.1 Outline of Analysis Model

Figure 1 shows the analysis model. All girders are simply supported box girders. The span of the girder (T2) is 49 m, and the span of the other girders (T1, T3, T4) is 33 m. The piers (P2, P3) are round piers, and the other piers (P1, P4, P5) are wall-type piers. To prevent unbalanced dynamic loads on the piers at both ends, 33 m dummy girders are added to each end of the analysis model. The foundation type of P2 and

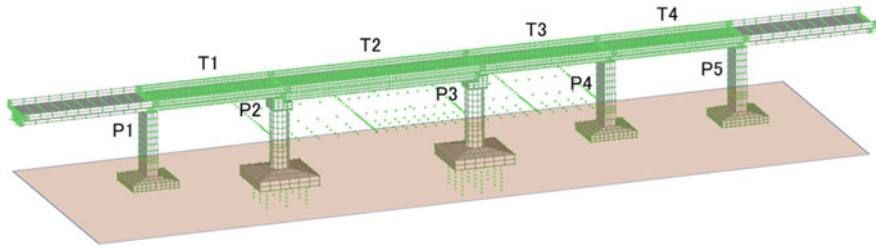


Fig. 1 The dynamic interaction analysis model of structures and ground

Table 1 The material properties of structures

Parts of the structures	Young's modulus (kN/m ²)	Unit volume weight (kN/m ³)	Poisson's ratio
Girder	4.00×10^7	24.5	0.200
Pier	$3.42E \times 10^7$	24.5	0.200
Footing and pile	$3.03E \times 10^7$	24.5	0.200

P3 is pile foundation, while that of P1, P4 and P5 is direct foundation. The railway tracks are slab tracks.

The analysis model consists of structures based on 3D FEM models and ground based on thin layered element method models. The physical constrains of the bridge bearings on P1, P3 and P5 are hinge-supported, and those of the bridge bearings on P2 and P4 are roller-supported.

After referring to design standards, material properties of the structures are adjusted to match the natural frequency of the first bending mode on T4 identified by an experimental modal analysis. Physical properties of the ground are obtained from geologic columnar sections and S-wave velocity structures estimated by a surface wave method. Tables 1 and 2 show the material properties of structures and the physical properties of ground. Damping ratio of the structures and the ground is 2%.

2.2 Conventional Contact Conditions

In the dynamic interaction analysis of structures and ground, the force–displacement relationship between structures and ground is evaluated by a flexible volume method. Under conventional contact conditions, the force–displacement relationship is completely continuous. The number of nodes is 14211 and the number of elements is 15296.

Table 2 The physical properties of ground

Depth (m)	Shear modulus (kN/m ³)	Density	Poisson's ratio
0 ~ 0.9	4.70×10^3	1.50×10^3	0.499
0.9 ~ 1.9	8.66×10^3	1.50×10^3	0.499
1.9 ~ 2.9	1.08×10^4	1.50×10^3	0.498
2.9 ~ 4.9	1.15×10^5	1.50×10^3	0.487
4.9 ~ 6.9	2.38×10^4	2.00×10^3	0.497
6.9 ~ 8.9	1.19×10^5	1.80×10^3	0.486
8.9 ~ 10.9	6.15×10^4	1.90×10^3	0.493
10.9 ~ 12.9	1.30×10^5	1.90×10^3	0.485
12.9 ~ 14.9	5.36×10^4	2.00×10^3	0.494
14.9 ~ 16.9	2.96×10^5	1.90×10^3	0.463
16.9 ~ 20.9	1.41×10^6	1.90×10^3	0.301
20.9 ~ 120.9	2.20×10^6	2.20×10^3	0.100

2.3 Improved Contact Conditions

Under improved contact conditions, we incorporate influence of contact conditions between structures and ground into the dynamic interaction analysis of structures and ground. Nodes of the structures existing below the ground surface except the piles are separated into two types of nodes: the node to make up the structures, and the node to set the ground impedance. These separated nodes are double-nodes, and spring elements are set on these separated nodes. The number of spring elements is 2203, the number of nodes is 16414, and the number of elements is 17499.

We examine five conditions (a)–(e) shown in Table 3. These conditions consist of sufficiently high stiffness spring elements (Property Type1) and sufficiently low stiffness spring elements (Property Type2). Table 4 shows physical properties of spring elements Type1 and Type2. The contact conditions of separated nodes with spring

Table 3 The setting of spring elements

Setting of spring elements	Condition (a)	Condition (b)	Condition (c)	Condition (d)	Condition (e)
Pier at ground surface	Type 1	Type 2	Type 2	Type 2	Type 2
Pier	Type 1	Type 1	Type 2	Type 2	Type 2
Upper part of footing	Type 1	Type 1	Type 1	Type 2	Type 2
Middle part of footing	Type 1	Type 1	Type 1	Type 1	Type 2
Lower part of footing	Type 1	Type 1	Type 1	Type 1	Type 1

Table 4 The physical properties of spring elements Type1 and Type2

Spring elements	Longitudinal (kN/m)	Transverse (kN/m)	Vertical (kN/m)
Type 1	9.8×10^{10}	9.8×10^{10}	9.8×10^{10}
Type 2	9.8×10^0	9.8×10^0	9.8×10^0

elements Type1 are close to the conventional contact conditions, which the force–displacement relationship between structures and ground is completely continuous. On the other hand, under the contact conditions of separated nodes where spring elements Type 2 are set, the force–displacement relationship between structures and ground is almost non-continuous. This simulates the looseness between structures and ground.

Under condition (a), spring elements Type 1 are set on all the separated nodes. Under condition (b), spring elements Type 2 are set on the separated nodes between piers and ground surface, and spring elements Type 1 are set on the other separated nodes. Under condition (c), spring elements Type 2 are set on the separated nodes between piers and ground, and spring elements Type 1 are set on the other separated nodes. Under condition (d), spring elements Type 1 are set on the separated nodes between upper and lower parts of footings and ground, and spring elements Type 2 are set on the other separated nodes. Under condition (e), spring elements Type 1 are set on the separated nodes between lower part of footings and ground, and spring elements Type 2 are set on the other separated nodes. For example, Fig. 2 shows the setting of spring elements at P4 under each condition.

2.4 Analysis Conditions

We input unit excitation force into the analysis model for both the conventional contact conditions and the improved contact conditions. The excitation points are positions of left and right fastening devices just above P4. The calculated receiving points on the ground are 4.2 m, 9.5 m, 27.2 m, 52 m away from P4 in transverse direction.

3 Results and Consideration

Railway vibration is generally evaluated by magnitude of vertical vibration, so that we organize transfer functions in vertical direction.

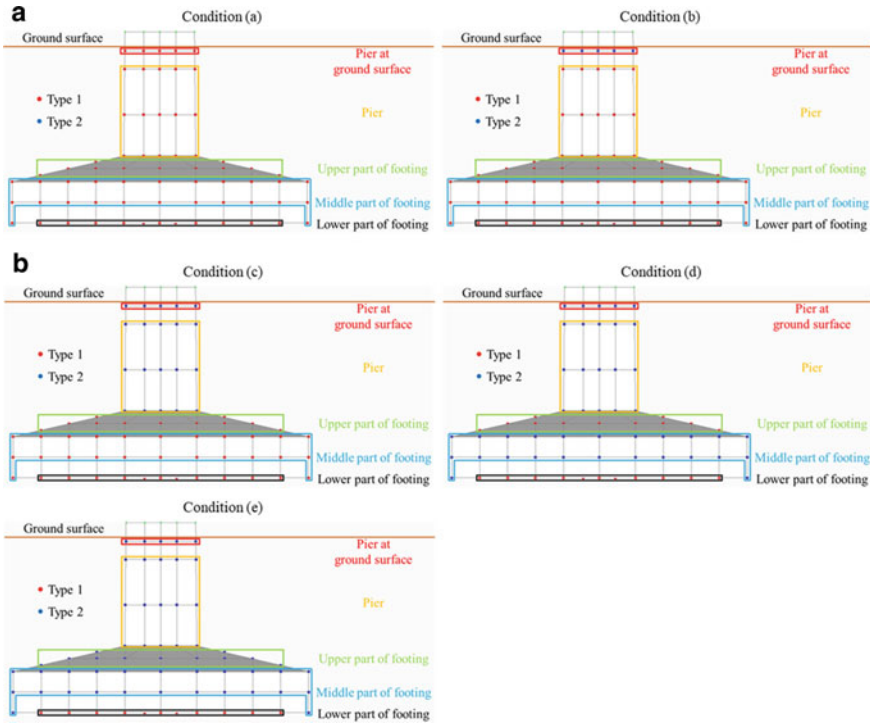
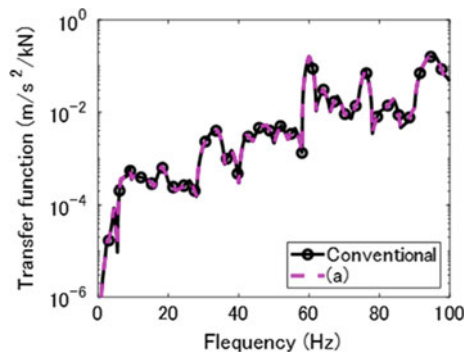


Fig. 2 The setting of spring elements at P4 (Longitudinal cross section)

3.1 Contact Conditions and Ground Responses

Figure 3 shows ground responses at 9.5 m point under the conventional contact conditions and condition (a). The results of condition (a) match well with the results of the conventional contact conditions. Therefore, the contact conditions between the

Fig. 3 The ground responses at 9.5 m point



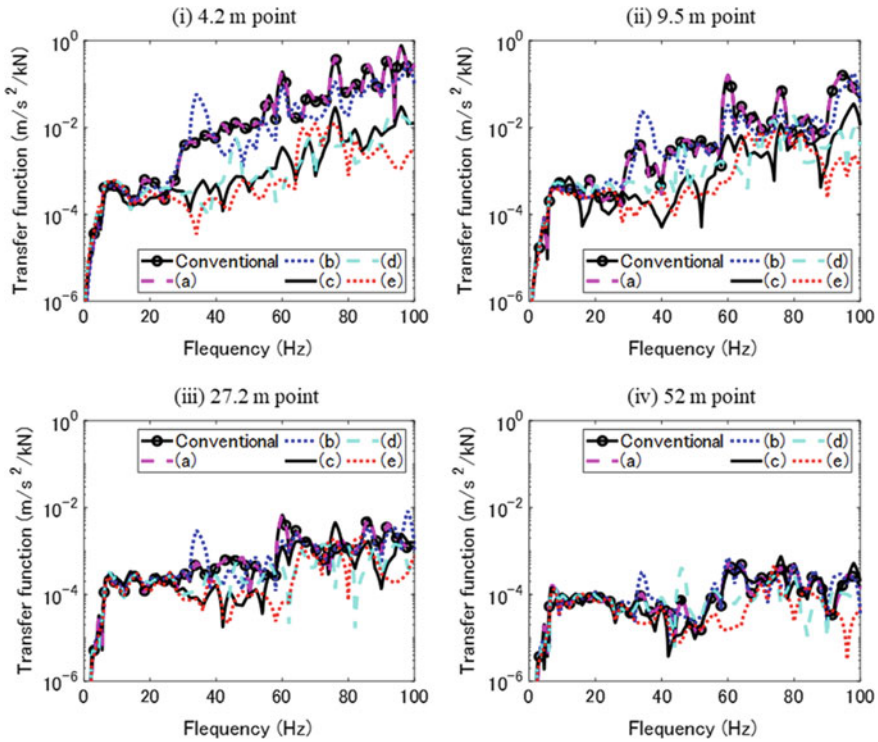


Fig. 4 The ground responses

structures and the ground under condition (a) are close to the conventional contact conditions.

Figure 4 shows ground responses under conditions (a)–(e) and the conventional contact conditions. The results of conditions (a)–(e) are roughly the same in the frequency band of 20 Hz or lower. In the frequency band of 20 Hz or higher, the results of condition (b) tend to be smaller than the results of condition (a), and the results of conditions (c)–(e) tend to be smaller than the results of condition (b). There is no magnitude relationship in the results of conditions (c)–(e). From these results, in the frequency band of 20 Hz or higher, ground responses become smaller due to the contact conditions between structures and ground.

Since the ground near the structures is directly affected by the contact conditions, the difference of contact conditions on ground responses is clear. On the other hand, as the distance from structures increases, it becomes unclear.

In the frequency band of 20 Hz or lower, the results of condition (e) and other conditions are roughly the same. Under condition (e), spring elements Type 1 are set on the separated nodes only between lower part of footings and ground. From this, vibration propagation from lower surface of footings to ground may be dominant in the frequency band of 20 Hz or lower.

3.2 Contact Conditions and Responses of Structures

The contact conditions between structures and ground should affect not only the ground responses confirmed above but also the responses of structures. The contact conditions will change vibration characteristics of piers and footings. These can affect the ground responses.

Figure 5 shows the responses of P4 at 60.1 Hz to examine the influence of contact conditions on piers and footings. The results of condition (a) are in good agreement with the results of conventional contact conditions. The contact conditions of condition (a) are close to the conventional contact conditions, which is also confirmed in the ground responses shown in Fig. 3.

Except for condition (b), the smaller responses of P4 become, the smaller the ground responses shown in Fig. 4 become. The results of condition (b) are larger than the results of condition (a) at upper and lower ends of piers, ground surface and footings. The results of condition (b) are greater than the results of condition (a) in the responses of P4. However, the results of condition (a) are greater than the results of condition (b) in the ground responses. This may be because there is almost no vibration propagation from structures to ground at ground surface under condition (b). Under condition (b), spring elements Type 2 are set on the separated nodes between piers and ground surface.

The distribution of transfer functions under conditions (a)–(c) and conditions (d), (e) are different. This indicates that the vibration modes of P4 differ under conditions (a)–(c) and conditions (d), (e). The reason for this is probably that subgrade reaction at the middle part of footings is small under conditions (d) and (e). Under conditions (d) and (e), spring elements Type 2 are set on the separated nodes between middle part of footings and ground. It is possible that this change of vibration characteristics at structures makes the ground responses particularly small.

4 Conclusion

In this paper, we studied the influence of contact conditions between structures and ground on the estimation of ground responses. To simulate the looseness between structures and ground, we set spring elements on nodes between structures and ground in the analysis model. Then, we conducted parametric studies of these spring elements. The following findings were obtained.

- The conditions that sufficiently high stiffness spring elements are set on all nodes between structures and ground are close to the conventional contact conditions where force–displacement relationship between structures and ground is completely continuous.
- Under the conditions that sufficiently low stiffness spring elements are set on some of nodes between structures and ground, ground responses decrease in the frequency band of 20 Hz or higher.

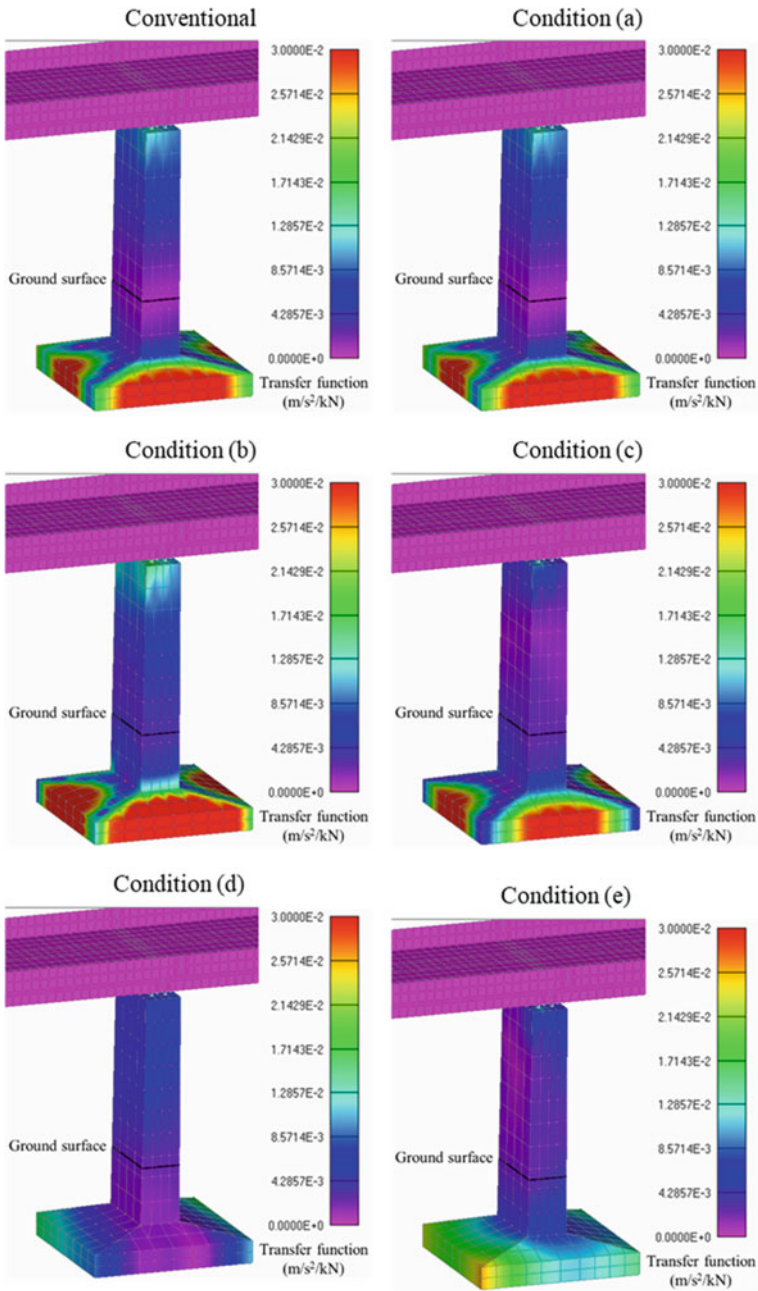


Fig. 5 The responses of P4

- In the frequency band of 20 Hz or lower, vibration propagated from the lower surface of footings to ground may be dominant of ground responses.
- The contact conditions affect not only ground responses but also responses of structures. As responses of piers and footings become small, ground responses decrease. However, this relationship does not always hold. This is because only parts where vibration propagates from structure to ground affect ground responses.
- Contact conditions may change vibration modes of piers and footings. This Changes of vibration characteristics at structures can greatly affect ground responses.

From the above results, it is possible that the overestimation of railway vibration in high frequency bands can be solved by incorporating the influence of contact conditions between structures and ground into the simulation method. In this paper, we examined five contact conditions consisted of sufficiently high stiffness spring elements and sufficiently low stiffness spring elements. In the future, to improve the accuracy of the simulation method, it is necessary to examine physical properties and installation positions of spring elements.

Reference

1. Hidefumi Y, Yasuhiko I, Tsutomu W (2016) A numerical simulation method for ground and building vibration based on three dimensional dynamic analysis. Quality Report of RTRI, RTRI 57(2):151–157

Vortex Induced Vibration Analysis of a Triangle Prism at Different Velocities



Johny Shaida Shaik and Putti Srinivasa Rao

Abstract In this Paper the Flow-induced motion (FIM) and power conversion of triangular prism in cross-flow is numerically investigated using 2-Dimensional fluid domain with spring mounted oscillators and study the effects at wakes. Flow velocities between 0.05–0.15 m/sec, Reynolds number 2250–7500 and spring stiffness of 125 and 250 N/m are used for the simulation cases. The results show that in Vortex Induced Vibration (VIV) region the response of dynamic characteristics is high with a maximum amplitude and maximum power. The maximum amplitude of the oscillation, maximum co-efficient of lift force and displacement have been calculated mathematically for plotting a graph and theoretical and simulated efficiencies are compared for validation of the analysis.

Keywords Dynamic characteristics · Vortex Induced Vibration (VIV) · Flow induced motion (FIM) · Mounted oscillators · Numerical analysis

1 Introduction

Triangular prisms are widely used in different applications such as deep water channels, pipelines, dams, flow streams, bridges etc. By arranging this in flexible method with sufficient under water the fluid flow strikes the prism thereby vortex induced vibration (VIV) is generated. In this paper the VIV of Triangular Prism with different combinations of mass ratio and frequency were performed. In order to solve this, the double degree of freedom (DOF) of vibration of the prism along with the Navier–stokes equations is used. Kang et al. [1] has investigated that by increasing range of Re number the VIV characteristics changes and also some effects absorbed when Re number vibration characteristics changes under different mass and frequency

J. S. Shaik (✉)

Research Scholar, Department of Mechanical Engineering, Andhra University, Visakhapatnam 530003, India

P. S. Rao

Professor, Department of Mechanical Engineering, Andhra University, Visakhapatnam 530003, India

ratio which helps in research of VIV. Zhang et al. [2] studied on flow over spring mounted cylinder at moderate number over normal cylinder for same fluid at lag between displacement and coefficient of lift at 0° called initial branch over 180° lower branch. Finally we came to know that the vibration at wavy cylinder is less compared with normal cylinder due to high structural damping. In this paper a hydrokinetic power conversion investigation is done on two rough tandem cylinders at Reynold's number to increase power and efficiency of Vortex Induced Vibration (VIV). By using Navier stokes equation numerical simulations are performed. The results are compared experimentally with the same tandem cylinder that how to increase the power. Finally Ding et al. [3] concluded that at $Re = 60,000$ the amplitude, frequency, power harness and efficiency is same at upstream whereas at downstream it is less due to shedding effect. Similarly at galloping region $Re = 110,000$ the downstream is less due to impingement and the upstream has higher energy and power harness. Ou et al. [4] investigated on the Vortex Induced Vibration (VIV) for three elastic cylinders in triangle arrangement with same mass and natural frequency at high Reynold's number are simulated. The analysed results of displacement and lift forces are displayed informing that the cylinder at downstream undergoes fluctuation at lift forces. Gohel et al. [5] made a prediction on circular cylinder with triangular array numerically by allowing to vibrate at high Reynold's number and the effects on drag and lift force are studied to solve. Hence, the cylinder displacement is validated analytically and experimentally. For this a program is developed to calculate and solve the displacement. Liu et al. [6] performed simulations on triangular prism using numerical and simulation software. For this some cases are considered. In one case according to flow three different models and at each model drag, lift and Strouhal number was discussed. For the second case the prism rotates periodically by this vortices separating the surface which satisfy the lift and drag coefficients.

2 Procedure for Simulation

A domain with rectangular as shown in Fig. 1 is created so that the water can flow over triangular prism using ANSYS Fluent 2D solver. To simulate the 2-way fluid –solid interaction Six-DOF solver is built. Prism mass, spring stiffness and six degree

Fig. 1 Rectangular domain with triangular prism

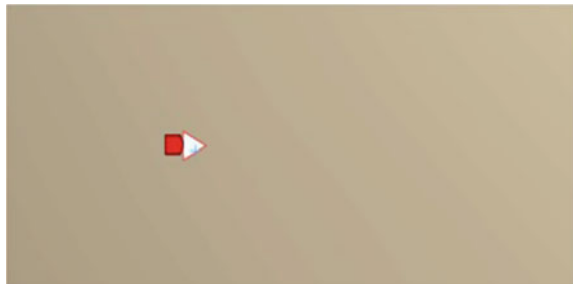


Table 1 Specifications for VIVACE simulation

Parameter	Present Work
Base	0.06 m
Height	0.06 m
Mass ratio (m*)	4.2 kg (considered)
Free stream velocity (U)	0.05–0.15 m/s
Reynolds number (Re)	2.5×10^3 – 7.5×10^3
Spring stiffness (k)	125–250 N/m

of freedom (DOF) constraints are specified using user defined function in Visual C programming language so that the movement will be free in vertical remaining all DOFs restricted. By doing this the pressure which is developed on the prism surface as vertical force which helps in giving input to prism motion and displacement by solving motion equation back propagate the updates mesh for the next step. To begin this a flow model in viscous laminar which is fundamental used to eliminate complexity, 3 to 15 s time is chosen for total simulation depending upon the response for coefficient of lift. According to this the specification are listed below.

2.1 Specifications

Prism base side is considered as 6 cm and length as 1 m and hence the ANSYS Fluent 2D solver is more consistent with unit thickness (1 m). Viscous damping constant of oscillating constant of oscillating triangular prism (Mass-spring damper system) in the six degree of freedom (DOF) solver is not specified during motion, but may be present because of Fluid–Solid interaction. The other specifications are listed in Table 1.

2.2 ANSYS Fluent and Mesh Setup

Using ANSYS a triangular element mesh is generated as shown in Fig. 2 and inflation layers starting with 0.1 mm as shown in Fig. 3 to display the effective simulation of viscous vortex shedding and boundary layer effects on the surface of prism.

Method: All Triangles Method

Max Face Size: 10 mm

Inflation Layers: 20

First Layer Height: 0.1 mm

Growth Rate: 1.2

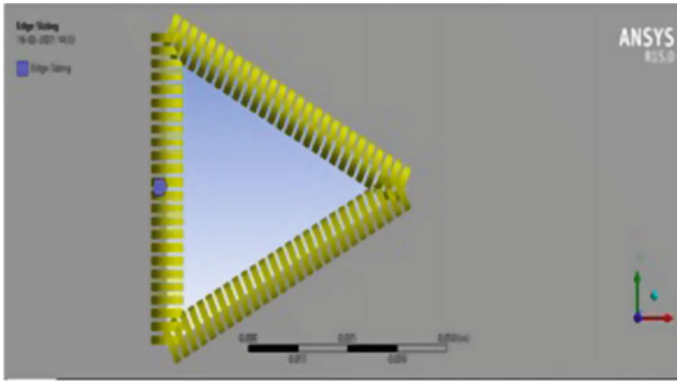


Fig. 2 2D Mesh in ANSYS

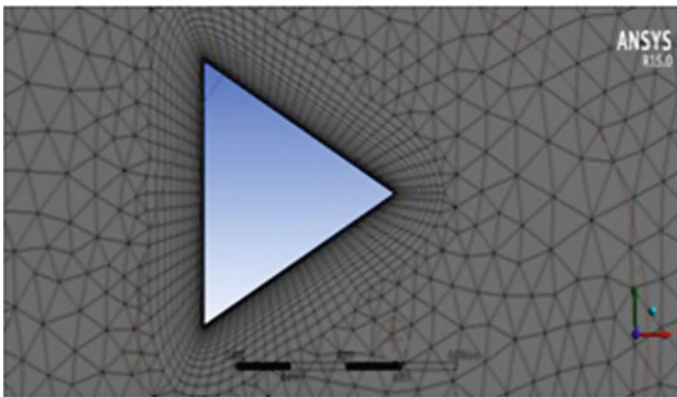


Fig. 3 Inflation layers

2.3 Schematic View of VIVACE Converter

Totally six simulations are conducted at flow velocities 0.05 m/sec, 0.075 m/sec, 0.15 m/sec with spring stiffness of 125 N/m similarly 0.05 m/sec, 0.075 m/sec, 0.15 m/sec flow velocities at 250 N/m spring stiffness. The main objective of each simulation to obtain amplitude of oscillation, F_{OSC} , amplitude versus time, lift force versus time and Mechanical Power versus time by running ANSYS Fluent. As an example to illustrate this, the **Simulation 1–3** is selected to present in Sect. 3 for lift coefficient variation with time, dynamic mesh deformation, velocity and power curve with time and velocity contour and displacement.

3 Simulation Results of 1–3

Spring stiffness with 125 N/m and flow velocity of 0.15 m/sec is allowed to run at simulation 1–3 (Sim 1–3). We observed approximately for about 10 s coefficient of lift (C_L) fluctuates between -2.5 to $+2.5$ as shown in Fig. 4 as the fluctuation generates forces on the triangular prism due to shedding of vortices on bottom half and top half surfaces of prism. The contour velocity, contour statics pressure and dynamic mesh during the prism is at top extreme and bottom extreme as shown in Figs. 5, 6 and 7. Mesh cells with blue decreased in size whereas the mesh cells with red indicate increased in size. According to the deformations the cell size indicates the mesh surrounding the moving prism. The prism displacement in cm and the value of lift force in N are plotted in time scale as shown in Fig. 8.

Using MATLAB function the power developed is obtained in VIVACE converter by instantaneous prism velocity from amplitude. The velocity which is obtained in (m/sec) is multiplied with lift force to get the mechanical power. Mechanical power = lift force \times velocity.

The power developed fluctuation is shown in Fig. 9. The RMS value of power obtained from Fig. 9 which is at 0.0103 watts is considered as capacity for VIVACE at flow velocity of 0.15 m/sec. Thus the power at simulation data obtained is 0.028 watts

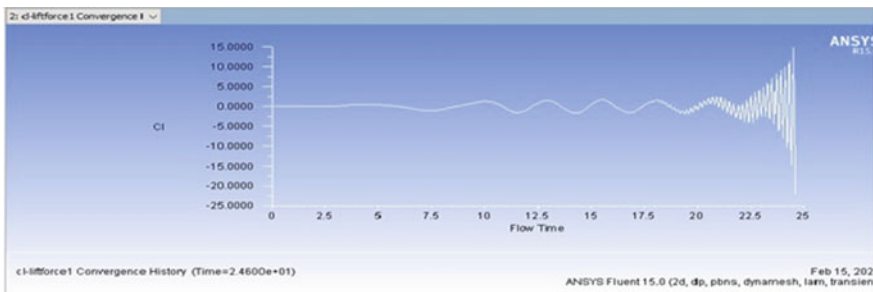


Fig. 4 Coefficient of lift force

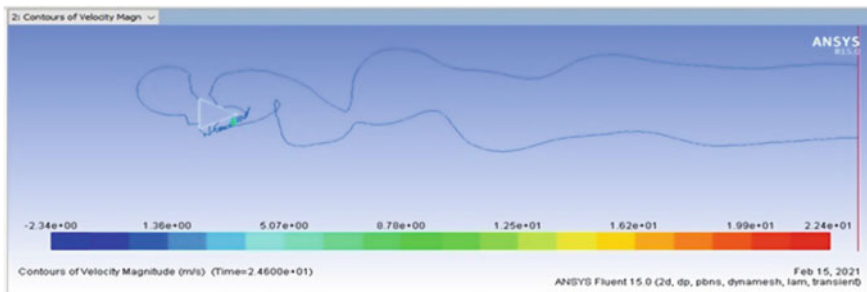


Fig. 5 Contours of velocity

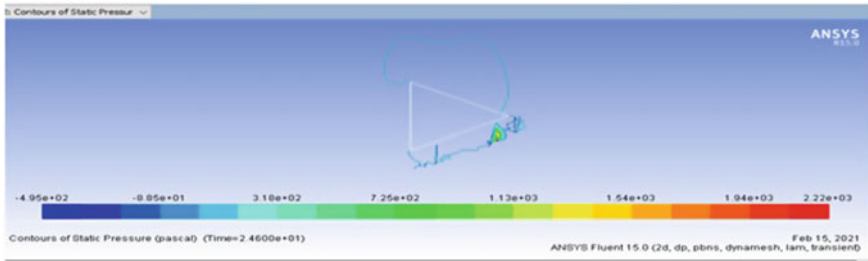


Fig. 6 Contours of static pressure

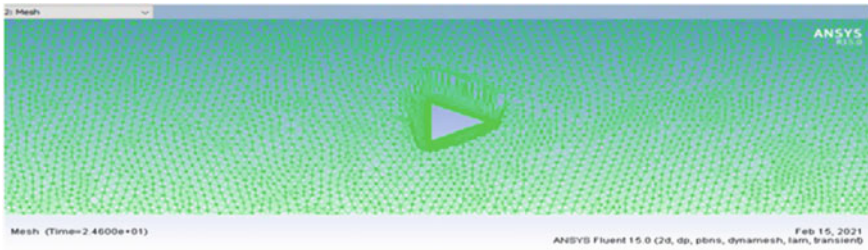


Fig. 7 Contours of dynamic mesh

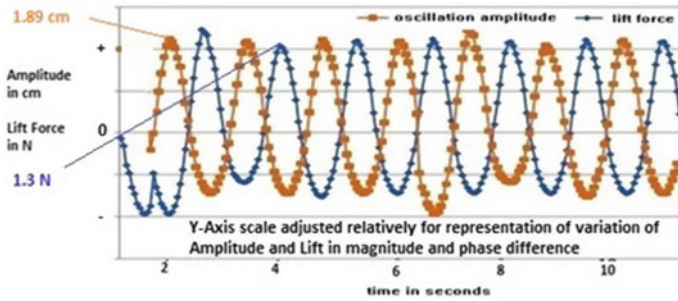


Fig. 8 Oscillation amplitude and lift force versus time at 0.15 m/Sec $k = 125$ N/m

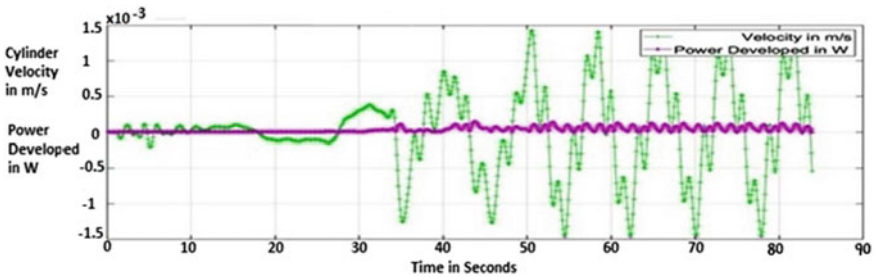


Fig. 9 Oscillation velocity and power versus time $U = 0.15$ m/sec, $k = 125$ N/m

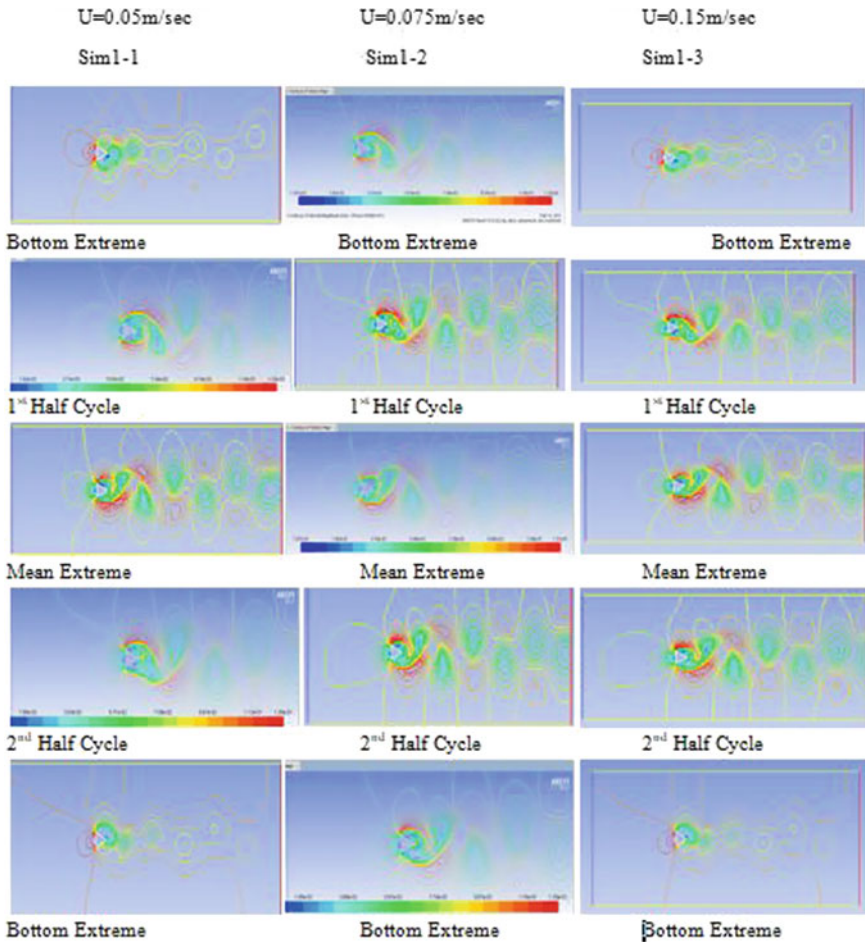


Fig. 10 Velocity contours Sim1-1, Sim1-2 and Sim1-3 at 0.05 m/sec, 0.075 m/sec and 0.15 m/sec

at peak stable power. Power (simulation data MATLAB) = 0.028 watts. Shedding vortices at top and bottom surfaces of prism in detail are shown in Fig. 10.

4 Results and Discussion

4.1 Simulation Results

In Table 2 the simulation results are presented. A graph between Oscillation amplitude/Prism Base Side length (A/D) with Reynolds's number (Re) is plotted as shown

Table 2 Simulation analysis numbering and corresponding data

SIM No	U (m/s)	Re	f_{str} (Hz)	k (N/m)	f_n (Hz)	U*	C_L	F _{osc} HZ	F*	A (cm)	A/D	Amp Dev (%)	Power W	Sync
1-1	0.05	2.5×10^3	0.16	125	0.730	1.14	1.90	0.120	0.164	1.95	0.325	65	0.0040	No
1-2	0.075	3.7×10^3	0.25	125	0.730	1.71	1.877	0.192	0.263	1.56	0.260	70	0.0025	No
1-3*	0.15	7.5×10^3	0.5	125	0.730	3.42	1.942	0.380	0.520	1.897	0.315	8	0.0103	Yes
2-1	0.05	2.5×10^3	0.16	250	1.032	0.80	1.858	0.225	1.45	1.963	0.327	36	0.00135	No
2-2	0.075	3.7×10^3	0.25	250	1.032	1.21	1.533	0.128	0.124	1.635	0.272	33	0.0030	No
2-3	0.15	7.5×10^3	0.5	250	1.032	2.42	1.135	0.312	0.302	0.992	0.165	52	0.0041	No

1-3* Maximum Amplitude and consistency in the oscillation cycles is observed in this simulation values.

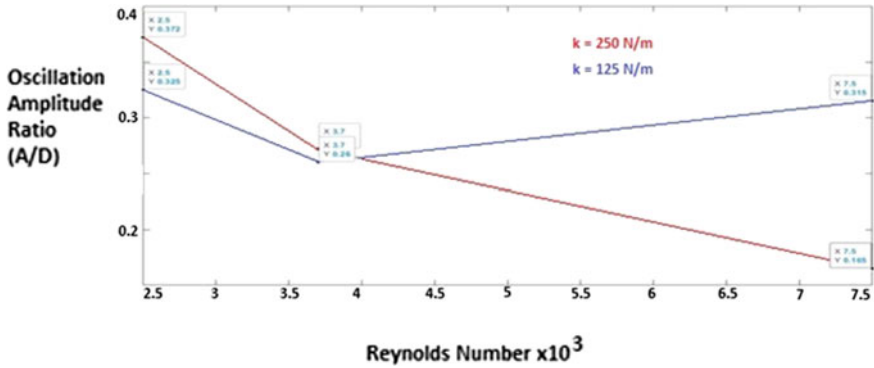


Fig. 11 Oscillation amplitude/Prism base side length (A/D) with reynolds number

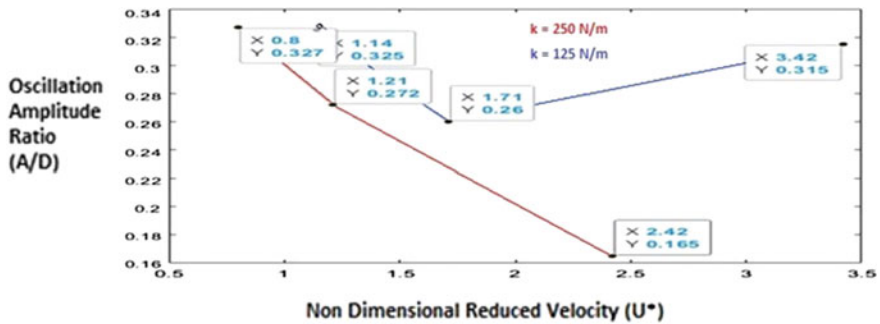


Fig. 12 Oscillation amplitude/Prism base side length (A/D) with non dimensional reduced velocity (U^*)

in Fig. 11 and with non-dimensional reduced velocity (U^*) is shown in Fig. 12 for spring stiffness of 125 and 250 N/m.

The power developed versus non-dimensional reduced velocity (U^*) is plotted as shown in Fig. 13 and power developed versus Reynold’s number as shown in Fig. 14. In order to get the power peaks consistent in magnitude in the case of simulation in Fig. 10. The vanished lift force during power drop and mean points at triangular prism are only accepted.

The results at each simulation are summarized at Table 2. The stable oscillation amplitude which produces consistent power curve and expressed by comparing each cycle with oscillation amplitude and average amplitude. The time versus amplitude at each values of U and U^* are shown in Figs. 15 and 16 for $K = 125$ & 250 N/m.

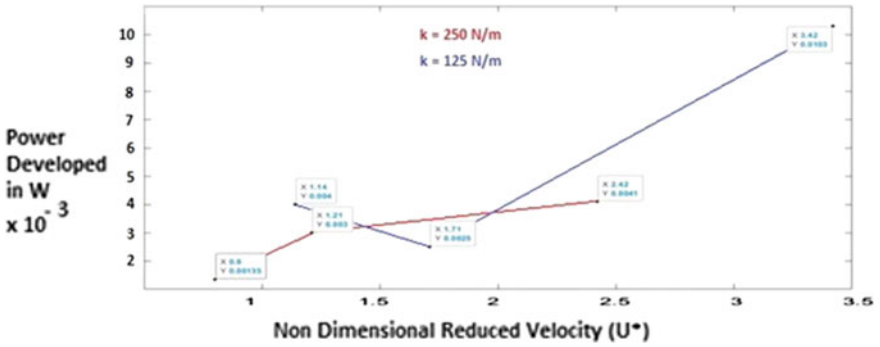


Fig. 13 Power developed versus reduced velocity

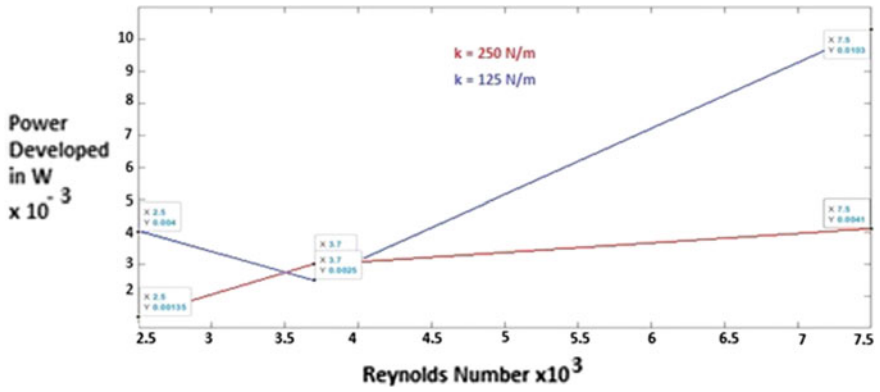


Fig. 14 Power developed versus reynolds number

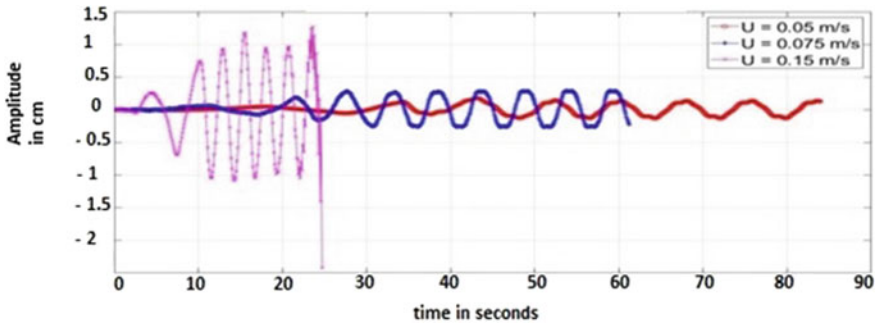


Fig. 15 Oscillation amplitude versus Time at $k = 125 \text{ N/m}$

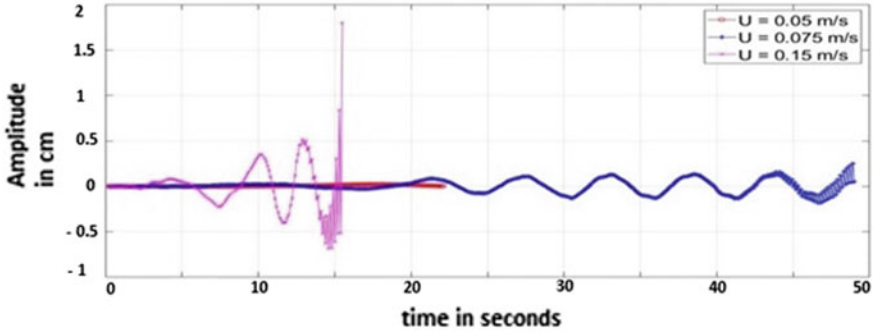


Fig. 16 Oscillation amplitude versus Time at $k = 250 \text{ N/m}$

4.2 Establishing a Power Estimation Theory

Assumptions in the Power Estimation Theory are given below

1. Maximum amplitude occurs when U^* is between 3 and 4.
2. Maximum Power occurs when U^* is between 3 and 4.
3. Amplitude of oscillation (A) is a fraction of Prism Base Side Length (D).
4. Frequency of oscillation (f_{osc}) is a function of Strouhal frequency (f_{str}).
5. Strouhal number (St) is a function of Free stream velocity (U) and D , and is constant equal to 0.2 over the range $Re = 10^3 - 10^5$ as found in literature.
6. Lift Force is a function of Coefficient of lift (C_L) and free stream velocity U .
7. Reduced Velocity (U^*) is a function of U , D and f_n .
8. Natural Frequency of the prism (f_n) is a function of Stiffness (k), mass of prism (m) and mass of the displaced fluid (m_d).

Based on the above, a Power equation can be formulated as shown below

$$\begin{aligned}
 \text{Power} &= [\text{Lift Force} \times \sin(\omega_{osc}t)] \times [\text{Velocity}] \\
 &= [1/2.C_L \rho A_f.U^2. \sin(\omega_{osc}t)] \times [\text{times differential of displacement}] \\
 &= [1/2.C_L \rho.D.L.U^2. \sin(\omega_{osc}t)] \times [\text{time differential of } A. \sin(\omega_{osc}t + \pi)] \\
 &= [1/2.C_L \rho.D.L.U^2. \sin(\omega_{osc}t)] \times [A.\omega_{osc} \cos(\omega_{osc}t + \pi)] \\
 &= [1/2.C_L \rho.D.L.U^2. \sin(\omega_{osc}t)] \times [(A/D).D.(2\pi f_{osc}) \cos(\omega_{osc}t + \pi)] \\
 &= [1/2.C_L \rho.D.L.U^2 \times (A/D).D.(2\pi f_{osc}) \times \sin(\omega_{osc}t). \cos(\omega_{osc}t + \pi)] \\
 &= [1/2.C_L \rho.D.L.U^2 \times (A/D).D.(2\pi f^0 f_{str}) \times \sin(\omega_{osc}t). \cos(\omega_{osc}t + \pi)] \\
 &= [1/2.C_L \rho.D.L.U^2 \times (A/D).D.(2\pi f^0.(0.2.U/D)) \times \sin(\omega_{osc}t). \cos(\omega_{osc}t + \pi)] \\
 &= [C_L.(A/D).2\pi f^0.(0.2). \sin(\omega_{osc}t). \cos(\omega_{osc}t + \pi) \times [1/2.\rho.D.L.U^3]
 \end{aligned}
 \tag{1}$$

Table 3 Efficiency reports of the VIVACE convertor

Work and year	Method	Efficiency	Remarks
Present work (2021)	Theoretical-Equations (a)	28.05%	When triangle base is perpendicular to horizontal
	ANSYS FLUENT SIM (b) (Simulation-logged Power Data)	27.65%	When triangle base is perpendicular to horizontal

Dimensions of the Prism in the present work is $D = 0.06$ m, $L = 1$ m, $U = 0.15$ m/s and maximum value of the combined sin and cos term ‘ $\sin(\omega_{osc}t).cos(\omega_{osc}t + \pi)$ ’ = 0.5. Taking $CL = 1.942$, $A/D = 0.315$, $f_0 = f_{osc}/f_{str} = 0.730$ from Sim-1–3 in Table 3 and using Eq. (1), the Theoretical Power obtained is 0.0284 W (See point (a) below). The Input Fluid Energy @ $U = 0.15$ m/s, $D = 0.06$ m, $L = 1$ m = $[1/2.\rho.D.L.U^3] = 0.10125$ W. Now we need to compare theoretical efficiency with the ANSYS Fluent simulated efficiency.

(a))Theoretical Efficiency = $[C_L.(A/D)0.2\pi f^0.(0.2). \sin(\omega_{osc}t).cos(\omega_{osc}t + \pi)]/[1/2.\rho.D.L.U^3] = 0.0284/0.10125 = 28.05\%$

Now calculating Simulated Efficiency (From the simulated results of Sim 1–3), we have the Power (Simulation data MATLAB) = 0.0280 W (Peak),

(b))ANSYS Fluent Simulated Efficiency = 0.0280 W / 0.10125 W = $0.2765 = 27.65\%$

4.3 Design Recommendations for VIVACE Power Plant

In this present work each simulation is performed at a specific speed with a specific value of spring stiffness. But experimentally the flow velocity varies either in Ocean/river. Hence, it is necessary to tune the VIVACE converter to gain the power irrespective with flow velocity. For this stiffness of spring should be adjusted in a way that the reduced velocity $U^* = 3-4$. This can be control (spring stiffness) using computer control systems.

5 Conclusion

The performance of the VIVACE Triangular prism is expressed in:

- (i) Oscillation amplitude (A) and oscillation amplitude ratio (A/D)
- (ii) Coefficient of lift force (CL)
- (iii) Ratio between f_{osc} and f_{str} (f_0)
- (iv) Stability in oscillations from cycle to cycle,
- (v) Stability in power generated

(vi) Non-dimensional reduced velocity (U^*).

The first three points (i, ii, iii) influence directly upon efficiency of power where as the remaining two (iv, v) express oscillation and power, the sixth (vi) implies maximum A/D ratio to ensure oscillation and power as follow (a, b, c).

- (a) At each cycle Triangular prism are constant (% variation is last) at values of U^* near 3.42 outside the range. Thereby oscillation varies one cycle to another as shown in Table 2.
- (b) Vibration of amplitude is maximum at U^* near 3.42.
- (c) At U^* near 3.42 power curve is continuous and stable with fluctuations rising only. In order for design considerations of VIVACE power generation, diameter, natural frequency and velocity of flow should lies near 3.42. In Table 2 the entire analysis gives the result to obtain the power.

Acknowledgements Author would like to thank his Professor & research guide of Andhra University, Visakhapatnam, India.

References

1. Kang Z, Zhang C, Chang R, Ma G (2019) A numerical investigation of the effects of Reynolds number on vortex-induced vibration of the cylinders with different mass ratios and frequency ratios. *Int J Naval Archit Ocean Eng* 11(2):835–850. <https://doi.org/10.1016/j.ijnaoe.2019.02.012>
2. Zhang K, Katsuchi H, Zhou D, Yamada H, Zhang T, Han Z (2017) Numerical simulation of vortex induced vibrations of a flexibly mounted wavy cylinder at subcritical Reynolds number. *Ocean Eng* 133:170–181. <https://doi.org/10.1016/j.oceaneng.2016.11.025>
3. Ding W, Sun H, Xu W, Bernitsas MM (2019) Numerical investigation on interactive FIO of two-tandem cylinders for hydrokinetic energy harnessing. *Ocean Eng* 187:106215. <https://doi.org/10.1016/j.oceaneng.2019.106215>
4. Ou, J. P., Xu, F., & Xiao, Y. Q. (2009). "Numerical simulation of vortex induced vibration of three cylinders in regular triangle arrangement". *7th Asia-Pacific Conference on Wind Engineering, APCWE-VII*.
5. Gohel HR, Shah BA, Lakdawala AM (2013) Numerical investigation of flow induced vibration for the triangular array of circular cylinder. *Procedia Eng* 51:644–649. <https://doi.org/10.1016/j.proeng.2013.01.091>
6. Liu X, Gui N, Wu H, Yang X, Tu J, Jiang S (2020) Numerical simulation of flow past a triangular prism with fluid–structure interaction. *Eng Appl Comput Fluid Mech* 14(1):462–476. <https://doi.org/10.1080/19942060.2020.1721332>

Effect of the Deterioration Degree of the Backside Weak Zone on the Seismic Response of the Tunnel and Surrounding Ground



Saddy Ahmed and Ying Cui

Abstract The surrounding ground of the tunnel can deteriorate with weathering, erosion, etc., and the seismic stability of the tunnel may be affected by the presence of the weak zone whose mechanical properties have been decreased. In this study, a two-dimensional shaking table apparatus was developed to investigate the tunnel and ground response around a tunnel subjected to seismic excitation, as well as the impact of the weak zone. Aluminum rods were used to generate model ground, and the weak zone was created by increasing the void ratio of the ground. The effect of size and stiffness of the weak zone was investigated in this research. The weak zone was created at tunnel crown positions, and the size of the weak zone was defined by the internal angle and the height above the tunnel surface. The sizes of the weak zone were tested by varying the internal angles, and the stiffness was controlled by varying the void ratio. A high-speed camera was used to capture the displacements of the ground particles, and these images were then analyzed to estimate the ground movement using the Particle Image Velocimetry (PIV) method. The lining response was recorded in terms of internal strain measured by installing the strain gauges at a regular interval of 45° around the tunnel. It has been seen that the presence of the weak zone significantly altered the tunnel response as well as the ground strains. The presence of a weak zone causes strain accumulation as more soil tends to move towards the weakened zone. When the size of the weak zone was increased, the volumetric and deviatoric strain spread over a large area. Moreover, the decrease in the stiffness of the weak zone caused more strains in the model ground. The produced strains in the ground exert more strains to the tunnel lining observed in terms of the internal strain. Thus, the changes observed in the ground response can potentially change the liner's stress state, resulting in concrete cracking, spalling, and maybe complete failure.

S. Ahmed (✉)

Department of Urban Innovation, Yokohama National University, Yokohama, Japan

e-mail: saddy-ahmed-zf@ynu.jp

Y. Cui

Faculty of Urban Innovation, Yokohama National University, Yokohama, Japan

Keywords Weak zone · Deterioration · Particle image velocimetry · Seismic response · Shaking table test

1 Introduction

Tunnels are essential structures built to avoid surface obstacles. The response of the tunnel against external forces is very much dependent on the surrounding ground in which they are constructed. Usually, we thought that the tunnels are string against the seismic loadings; however, the recent earthquakes, e.g., 1995 Kobe earthquake [1], 1999 Chi-Chi earthquake [2], 1999 Turkey earthquake [3], and 2008 Wenchuan earthquake [4] revealed that the tunnels could also be severely damaged during earthquake shaking. Yashiro et al. [5] indicated that the mountain tunnels are vulnerable to seismic damages when the tunnels are lying close to the earthquake fault or subjected to massive seismic excitation. Thus, it is essential to understand how surrounding ground deforms when subjected to earthquake forces [6] to study underground engineering problems. The ground deformation behavior changes over time due to soil degradation and changes in the soil properties. The soil degradation caused by swelling, slacking, water erosion, and dynamic loading can appear in weak zones behind the liner. The presence of such weak zones can change the ground and tunnel response under static and dynamic conditions. Many researchers (e.g., [7–10]) have explored the effect of weak zones behind the lining on the lining response. In this study, the effect of weak zones behind the lining on the ground deformation behavior under dynamic conditions has been explored.

2 Experimental Setup

2.1 *Shaking Table Apparatus*

The main experimental setup used in the research is a two-dimensional shaking table apparatus, tunnel model, and the model ground. The details of each experimental component and its specifications have been listed in the following sections. A two-dimensional shaking table apparatus was used to produce the seismic excitation. Figure 1 shows the outline of the apparatus. The size of the table is 0.5×0.5 m which comprises twenty blocks with equal heights racked on each other. Two vertical supports have been placed on the blocks' backside to keep the horizontal blocks at the correct position. The moving table is attached to a fixed platform through frictionless hinge supports, and the fixed platform is further embedded in the ground. A horizontal beam is placed at the top connected with fixed columns through connecting nuts. The table can oscillate in the horizontal direction with the help of an electric motor. Different accelerometers and displacement sensors have been attached to the table to

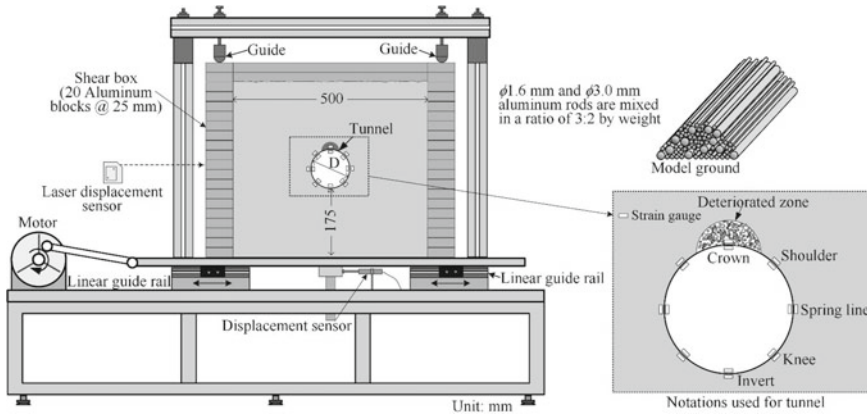


Fig. 1 Schematic diagram of two-dimensional shaking table apparatus

check the applied force and position of the table. The table was excited in a sinusoidal manner at a frequency of 1 Hz with an amplitude of 25 mm displacement.

The movement of the ground was captured by a high-speed camera during the whole testing process. The high-speed camera was set on a frame fixed on the shaking table; thus, the camera can only capture the relative movement of the ground. Several strain gauges were attached to the lining model to measure the tunnel lining deformation, and a laser transducer was set to measure the horizontal displacement of the shaking box at the height of the crown. In this paper, only the ground movement captured from the high-speed camera will be introduced.

2.2 Tunnel Model

In this study, a circular tunnel model made of acrylic resin has been used. The important characteristics of the model tunnel have been listed in Table 1. The different

Table 1 Characteristics of model tunnel

Item	Unit	Value
Diameter	mm	100
Thickness	mm	2
Length	mm	60
Bending stiffness	N mm ²	1.26 × 10 ⁵
Elastic modulus	Gpa	3.41
Axial rigidity	N	3.76 × 10 ⁵
Flexural strength	Mpa	45
Tensile strength	Mpa	40

notations used have been illustrated in エラー! 参照元が見つかりません。1. The topmost location is regarded as the crown, horizontal ass spring lines, lowermost as invert, and diagonal as shoulders and knees. To record the response of the tunnel model has been equipped with strain gauges at a regular interval of 45° around its periphery.

2.3 Model Ground and Weak Zone Preparation

The model ground has been prepared using aluminum rods with a uniform length of 50 mm. Two types of particles having sizes of 3 mm and 1.6 mm have been mixed in 3 : 2 by weight. The main properties of the model ground have been listed in Table 2. Biaxial tests conducted on the model ground show the behavior of dense sand [11]; however, the higher void ratio converts its behavior from dense to loose material, as shown in Fig. 2. Before starting the testing procedure, several tests were conducted to check the effect of the bottom boundary effect, and it was found that the 175 mm height above the table surface is enough to avoid the effect of the bottom boundary. The ground has been prepared in a layer-by-layer fashion by keeping the lift thickness as 50 mm. The density of each layer was checked and kept constant throughout the experimental process to ensure the preparation of the homogeneous ground. While placing the groundmass on the shaking table, a plastic board was placed in the model ground’s backside and removed after finishing the ground.

Table 2 Properties of model ground

Item	Unit	Value
Density	KN/m ³	22.3
Void ratio	–	0.18
Elastic modulus	Gpa	7.5
Cohesive strength	MPa	0
Frictional angle	(°)	31

Fig. 2 Model ground behavior under biaxial test

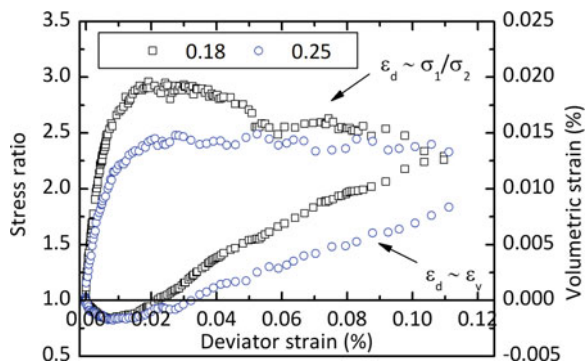


Fig. 3 Definition of the weak zone

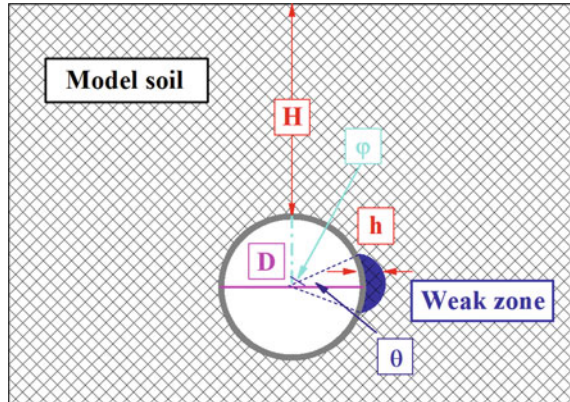


Table 3 Experimental cases

Location of weak zone	Height (mm)	Internal angle	Void ratio
-	-	-	0.18
Crown	20	50°	0.30
			0.45
			0.60
		90°	0.30
			0.45
			0.60

The weak zone around the tunnel was created by reducing the ground stiffness obtained by increasing the void ratio of that position. It was obtained after extracting the calculated amount of ground from the specific position. While removing the particles, care was exercised to remove them uniformly to get a weak zone with a homogeneous void ratio. Two different sizes were tested to check the effect of the size of the weak zone. Here in this study, the size of the weak zone was defined with the help of the internal angle (θ) and the height (h) above the tunnel surface, as explained in Fig. 3. The detailed experimental plan has shown in Table 3.

2.4 Particle Image Velocimetry

Particle image velocimetry (PIV) is a surface visualization measuring tool to calculate the deformations by comparing the consecutive images. Originally, the method was developed in the field of fluid mechanics, but many researchers have employed it in soil mechanics as well [12]. To estimate the strains in the model ground, the movement of particles was captured in the form of consecutive images. These image

series were then analyzed, and the displacements vectors $\{u\}$ were established. These displacement vectors were then used to calculate the strains $\{\varepsilon\}$ in the groundmass using Eq. 1 where $[B]$ matrix is the derivation of shape function.

$$\{\varepsilon\} = [B]\{u\} \quad (1)$$

3 Results and Discussion

The results presented here are obtained by testing the tunnel under the soil cover of 2D, where D is the tunnel's diameter. The results have been summarized in terms of ground and tunnel response. The ground response includes the deviatoric and volumetric strain, while the tunnel response includes the internal strain of the lining.

3.1 Ground Response

During the shaking, the photos were captured continuously for 30 s at a rate of 60 photos per second. After recording the data, the strain distributions for different time intervals were drawn, and the effect of the weak zone was checked. It was found that the response of the tunnel and the surrounding ground results obtained at the maximum shear displacement seems to be more comprehensive, and, in this paper, the results evaluated at the time of maximum shear displacement have been presented. The photo at the maximum shear displacement was compared with the initial photo to estimate the ground strains, i.e., the deviatoric and volumetric strains. The initial state of this experiment was set as just before the cyclic shear.

Figure 4 shows the deviatoric and volumetric strain distribution for no weak zone case. For the deviatoric strain, only the deviatoric strain values larger than 2.5% were drawn for all cases. For the distribution of the volume expansion higher than 2%etric strain, the black color represents compression higher than 2%, and the grey color shows the.

It can be seen that for no weak zone, both the deviatoric and volumetric strain appears around the tunnel boundary and at some part around the spring line locations. The concentrated strain around the tunnel boundary is due to the soil-tunnel boundary effect. The deviatoric strain around the spring line shows that the ground squeezes the tunnel inside due to lateral pressure. The camera was placed closer to the moving ground because the main focus was the weak zone; hence, only 16% area of the shaking ground was captured, and due to this reason, the development of the shear band cannot be observed.

Figure 5 represents the distribution of the deviatoric strain and shows the effect of the weak zone stiffness and size. The deviatoric strain plots indicate that the presence of the weak zone caused the development of more deviatoric strain as compared to

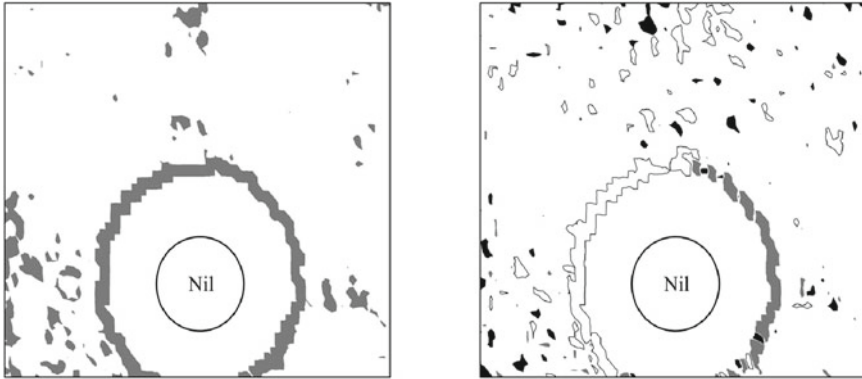


Fig. 4 Strain distribution for no weak zone (Left: deviator strain (larger than 2.5%), Right: volumetric strain (black color shows compression higher than 2%, grey color shows expansion higher than 2%))

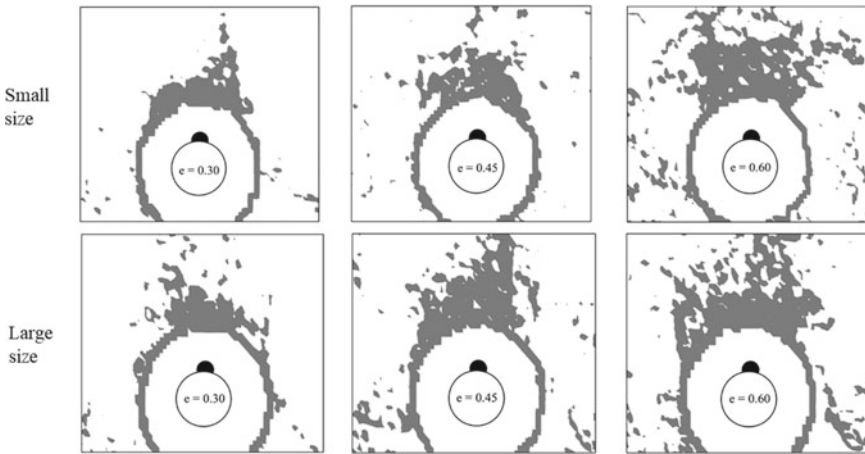


Fig. 5 Effect of the weak zone on deviator strain distribution (larger than 2.5%)

the no weak zone case. The first row in Fig. 5 shows the small size weak zone while the second row contains graphs for the large size weak zone; however, moving from left to right, the void ratio increased from 0.30 to 0.60. By comparing the effect of the void ratio, it is evident that the higher void ratios show more deviatoric strains. The increase in deviatoric strain is due to ground loosening caused by a higher void ratio, and the ground has lost some of its shear strength. Furthermore, the deviatoric strains for large size weak zone show that the development of the deviatoric strain increases with the increase of the void ratio. The development of the deviatoric strain is very significant around the weak zone’s vicinity compared to the rest of the analyzed area. The plotted data shows that when the stiffness of the weak zone

was reduced, the compression and expansion strains increased simultaneously. The increase in the void ratio of the weak zone gives more space for the ground to settle, which causes ground compression. While moving towards the weak zone, the ground is compressed, and the other parts will expand that as shown with grey color. For volume change, the effect of the ground stiffness shows a similar tendency with the deviatoric strain distribution. While comparing the effect of the weak zone, it was found that with the increase in the size of the weak zone, the ground volume change occurred over a larger area compared to the smaller size.

In conclusion, it can be stated that the results plotted for different sizes show that the larger size has a more deviatoric and volumetric strain, and their spread is also on the more area around the tunnel as compared to the smaller area. The loosened area in the form of a weak zone provides extra space for the tunnel to bend towards it. The bending of the tunnel will further impose more stresses on the lining structure. As the size of the weak zone grows, the deviatoric stresses increase which means that the weak zone can even cause the complete collapse of the tunnel if it keeps on growing in its size and void ratio. The process starting from the appearance of the weak zone to lining failure can be split into three stages. In 1st stage, a small weak zone will appear, which will produce a crack in the concrete lining. In the 2nd stage, the crack will grow and allow the moisture to infiltrate the tunnel, hence increasing its size. In the 3rd stage, the increase of weak zone will produce more cracks and ultimately complete failure of the tunnel lining (Fig. 6).

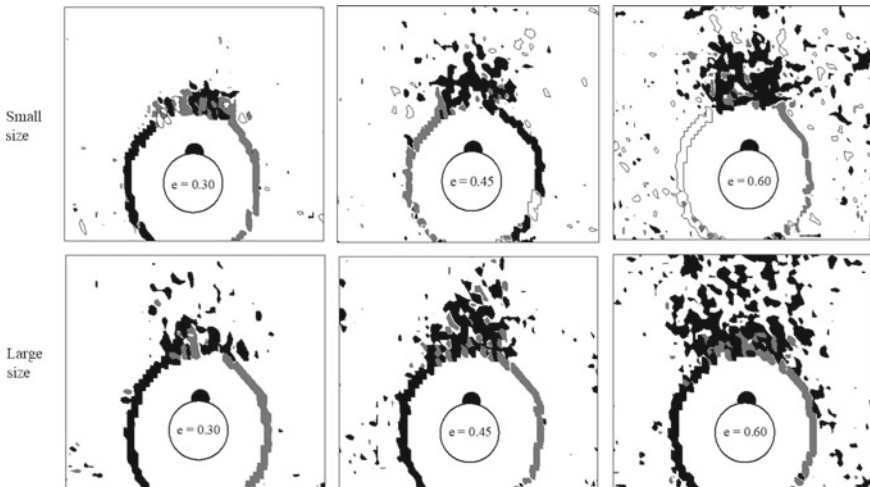


Fig. 6 Effect of the weak zone on volumetric strain distribution (black color shows compression higher than 2%, grey color shows expansion higher than 2%)

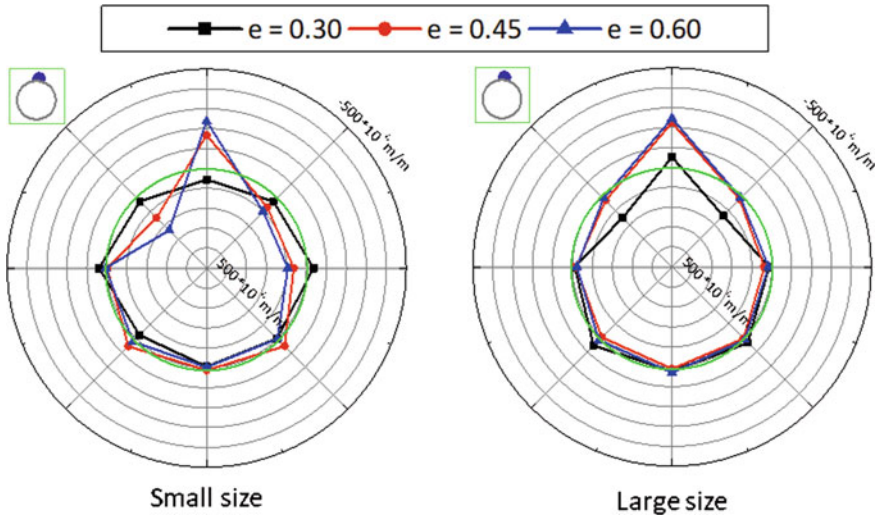


Fig. 7 Internal strain before shaking (initial state)

3.2 Tunnel Response

The tunnel response has been measured in terms of the internal strain and was measured by installing the strain gauges. The results have been presented for two different scenarios, i.e., before shaking and during shaking. After completion of the tunnel construction process, the data was recorded to measure the effect of the overburden pressure. After recording the data, the weak zone was created, and the values were recorded again. These values were then subtracted from the effect of the overburden to get the effect of the weak zone. The tunnel response to the weak zone before shaking has been illustrated in Fig. 7. From the graph, it can be seen that as the void ratio of the weak zone was increased, the internal strain increased. When the void ratio was increased from 0.30 to 0.45, the change was very significant; however, when it was increased from 0.45 to 0.60, the change was not so significant. The reason is the arching effect which has developed after the void ratio of 0.45. Initially, when the stiffness was reduced, the tunnel bends outward due to the availability of the space. However, the ground around the weak zone has formed an arch that will not weaken the ground further. As the values are the incremental values, therefore, the other points show values closer to zero. By comparing the effect of the size, it shows that for a larger size weak zone, the increase in the strain is higher. Figure 8 shows the results for the tunnel response during the shaking process. Similar to the ground strain, the internal strain has also been estimated at the maximum shear displacement of the ground, and the values are the incremental values considering only the effect of the shaking. During shaking, the tunnel bending behavior depends on the movement of the surrounding ground. As there was a weak zone at the crown position, the ground will be pushed directly towards the crown position hence exerting more

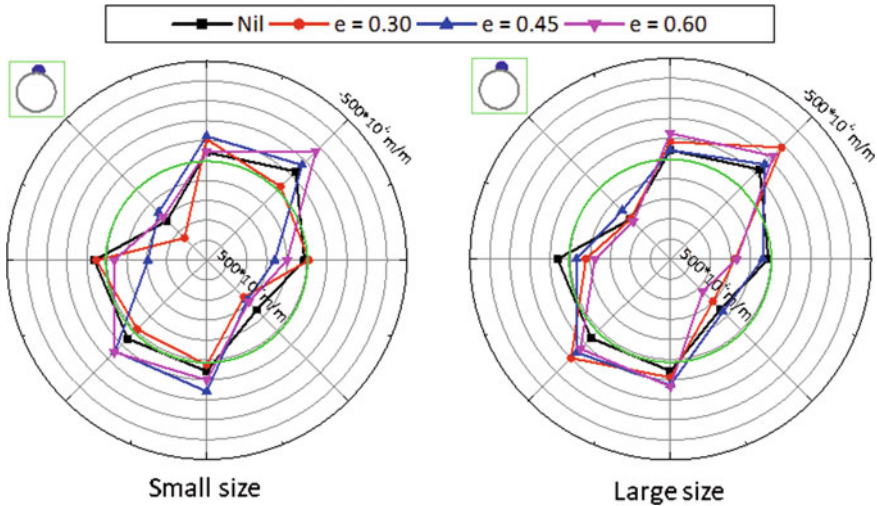


Fig. 8 Internal strain at maximum shear displacement

pressure on the tunnel crown. This additional pressure from the incoming ground will force the tunnel to bend at the crown location and elongation along the diagonal axis. As the void ratio of the weak zone was increased, more bending at the crown position and more elongation along the diagonal axis were observed.

4 Conclusions

The effect of the weak zone on the seismic response of the tunnel and the surrounding ground was discussed in this study. For this purpose, two sizes of the weak zone and three stiffness types have been explored in the crown position. Following conclusions have been drawn from the above study.

- The presence of a weak zone substantially changes the internal tunnel strain and the strains in the ground compared to the no weak zone case.
- Keeping the weak zone's size constant and increasing the void ratio of the weak zone have increased the deviatoric and volumetric strains and intensifies the tunnel bending.
- The larger size of weak zones has more ground strains, which spread over a larger area than the smaller size.
- The ground strains that develop around the weak zone can put extra stress on the lining, leading to the degradation of the concrete structure. The development of the ground strains and tunnel bending behavior have strong correlations.
- The growing size of the weak zone is very critical as it can be responsible for the damage or complete collapse of the structure. Therefore, efforts should be

made to detect the weak zones' position and deterioration degree and repair them timely to avoid their further advancement.

Acknowledgements This work was supported by JSPS KAKENHI Grant Number 19K04594.

References

1. Asakura T, Sato Y (1996) Damage to mountain tunnels in hazard area. *Soils Found.*, no. Special:301–310
2. Wang WL, Wang TT, Su JJ, Lin CH, Seng CR, Huang TH (2001) Assessment of damage in mountain tunnels due to the Taiwan Chi-Chi Earthquake. *Tunn Undergr Sp Technol* 16(3):133–150
3. Sung YC et al (2009) Enhancing the structural longevity of the bridges with insufficient seismic capacity by retrofitting 1(1):1–16
4. Li T (2012) Damage to mountain tunnels related to the Wenchuan earthquake and some suggestions for aseismic tunnel construction. *Bull Eng Geol Environ* 71(2):297–308
5. Yashiro K, Kojima Y, Shimizu M (2009) Historical earthquake damage to tunnels in Japan and case studies of railway tunnels in the 2004 Niigata-ken-Chuetsu earthquake. *Q. Rep. RTRI (railway. Tech. Res. Institute)* 48(3):136–141
6. Zamani R, Motahari MR (2015) The effect of soil stiffness variations on Tunnel Lining Internal Forces under seismic loading and Case comparison with existing analytical methods. *Ciência e Nat* 37:476
7. Meguid MA, Dang HK (2009) The effect of erosion voids on existing tunnel linings. *Tunn Undergr Sp Technol* 24(3):278–286
8. Meguid MA, Kamel S (2014) A three-dimensional analysis of the effects of erosion voids on rigid pipes. *Tunn Undergr Sp Technol* 43:276–289
9. Yasuda N, Tsukada K, Asakura T (2017) Elastic solutions for the circular tunnel with a void behind lining, *Tunn Undergr Sp Technol* 70(November 2016):274–285
10. Yasuda N, Tsukada K, Asakura T (2019) Three-dimensional seismic response of a cylindrical tunnel with voids behind the lining. *Tunn Undergr Sp Technol* 84(November 2018): 399–412
11. Shahin et al (2011) Behavior of ground and response of existing foundation due to tunneling. *Soils Found* 51(3):395–409
12. Adrian RJ (1991) Particle-imaging techniques for experimental fluid mechanics. *Annu Rev Fluid Mech* 23(1):261–304

Application of Artificial Intelligence Techniques

Machine Learning Enhanced Nonlinear Model Parameter Selection from HDR-S Cyclic Loading Test



Katrina Montes, Ji Dang, Yuqing Tan, Akira Igarashi, and Takehiko Himeno

Abstract The accuracy of new types of seismic rubber bearing's properties selection mainly depends on the engineer's experience and might be subjected to bias, reliability, and some uncertainties. This was a trial-and-error process which takes a lot of time specifically on the assumption of the nonlinear model and initial parameters and might encounter problem on the parameter optimization depending on the optimization method used. The parameters from the HDR-S cyclic loading test data should be evaluated precisely to have a more accurate results on the bearing's behavior on structure for nonlinear dynamic simulation. This study proposed a method that accelerated the selection process of the nonlinear parameters using machine learning and KH Method. The developed neural network model predicted the nonlinear parameters of an HDR-S bearing at three different temperature under bilinear model. The parameters was the initial input data for KH Method, which accelerated the process and solved the initial value problem. The proposed method imposes to use artificial intelligence which can serve as an initial guide and will greatly help the engineers in the evaluation of the nonlinear parameters of seismic isolators prior structural design.

Keywords Machine learning · HDR-S cyclic loading test · Bilinear model · Nonlinear parameters · KH Method

K. Montes (✉) · J. Dang

Department of Civil and Environmental Engineering, Saitama University, Saitama, Japan
e-mail: montes.k.m.s.886@ms.saitama-u.ac.jp

Y. Tan · A. Igarashi

Department of Civil and Environment Engineering, Kyoto University, Kyoto, Japan

T. Himeno

Kawakin Core Tech Co. Ltd, Saitama, Japan

1 Introduction

In 2011, a large earthquake in Tohoku ($M_w = 9.0$) caused a huge devastation in Japan. The main damaged occurred in seismic isolators, expansions joints, and structural members supporting horizontal loads [1]. This questioned the reliability of the seismic isolators and serves as a wakeup call that the design process must be more reliable. In response to that, the Design Specification for Highway Bridges was published last 2012 [2] and constantly updating every after 5 years to improve the standard of seismic isolator design. It was proposed that the seismic performance of structural members with seismic isolators should be checked thoroughly using reliable numerical analysis methods. However, past studies show's that bridges seismic isolator's nonlinear behavior can be influenced by temperature, loading rate, strain rate, etc. and several nonlinear models were proposed. A study includes pinching effect on the shear-strain behavior of High Damping Rubber bearing (HDR) and proposed modified Park-Wen model in biaxial direction [3]. A rheology model was proposed that includes the strain rate effect on high damping rubber bearings [4]. In Japan, there were existing guide for engineers about the range of these nonlinear parameters however the seismic isolators listed were limited and only bilinear model was considered. Currently, the need for a high-performance elastomeric isolator leads to the development of new types of seismic rubber bearings like SPR-S. In parallel to this, the development of new isolators needs new nonlinear models to interpret its nonlinear behavior prior to structural design. The more uncertainties considered means that the numerical model becomes more complicated, and the nonlinear parameter identification accuracy highly depends on the engineer's expertise, which can be subjected to bias, time consuming, a trial-and-error process, and highly dependent on the optimum algorithm used. A developed algorithm named KH method was commonly used for nonlinear parameter identification [5], but the optimum algorithm convergence was highly dependent on the initial parameter assumption which makes it a trial-and-error process. Therefore, this study developed an artificial neural network model (ANN) that can understand the nonlinear behavior of seismic isolators through the use of existing nonlinear model like Bilinear model. The developed ANN model can identify the nonlinear parameters based on the shear strain and shear stress input data. An actual super high damping rubber (HDR-S) bearing's nonlinear parameter was predicted using the developed ANN model and compared to KH method. The proposed method makes the nonlinear model identification process faster and overcome the initial parameter assumption problem of KH Method, which can greatly help the engineers in identification of nonlinear parameters prior to structural design.

2 Proposed Method

This study developed a neural network model that can understand the nonlinear behavior of seismic isolators using bilinear model. The developed neural network can suggest nonlinear parameters based on the shear strain and shear stress input values. The proposed methodology was shown in Fig. 1 and the process starts from:

- (1) Data generation using the normalized shear strain data of an HDR-S cyclic loading test data and numerically simulated shear stress based on bilinear model.
- (2) Training and evaluation of the artificial neural network (ANN) model. The output data was the nonlinear parameter of Bilinear model which was initial stiffness, stiffness ratio, and yielding force.
- (3) An actual HDR-S force and displacement data was converted to shear strain and shear stress, and the developed ANN model was used to predict the nonlinear parameters.
- (4) The ANN model suggested parameters was combined to KH method and compared to nonlinear parameter identification using KH method only. The contribution rate and total number of steps was compared. The initial parameter assumption problem using KH method was highlighted.

The nonlinear model was limited to bilinear model, but the process can be repeated with other nonlinear models. However, as the nonlinear parameter and parameter range increases, the neural network model can be more complicated.

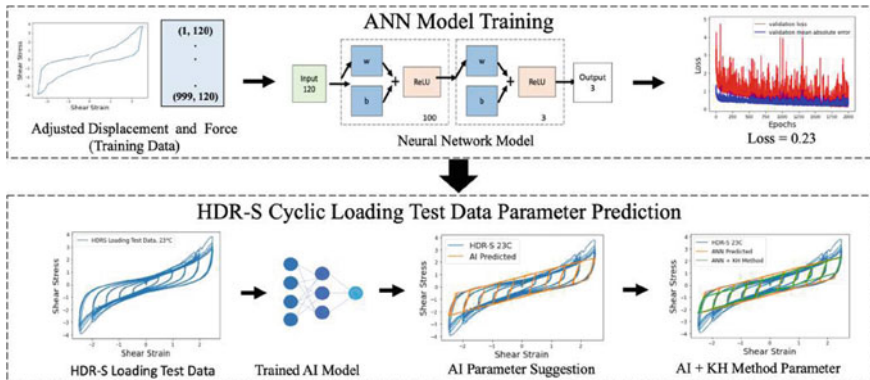


Fig. 1 Proposed methodology

3 Artificial Neural Network (ANN) Model Training

The HDR-S data at three different temperature was shown in Fig. 2. The training of the ANN model consists of data generation, data normalization, and the development of the neural network model. The training of neural network model was highly dependent on the data, hyperparameters, optimizers, activation and loss functions, which needs to be carefully specified.

3.1 Data Generation

The data set for the development of neural network model consisted of the normalized shear stress from the HDR-S cyclic loading test data at 23 °C and 250% amplitude. This shear stress was used to produce the shear strain using numerical simulation of bilinear model and the parameter range was shown in Tables 1 and 2. The parameter ranges as shown in Table 1, was determined by conducting KH method on the three

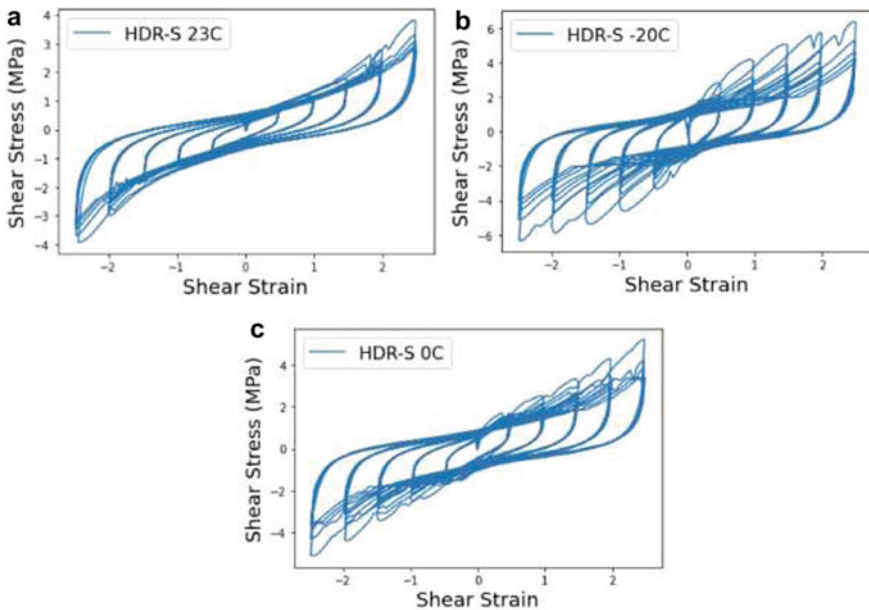


Fig. 2 HDR-S loading test data a 23 °C, b -20 °C, c 0 °C

Table 1 Parameter range of bilinear model by KH method

α	$k(\frac{N}{mm^2})$	q_c
0.05–0.12	8–20	0.5–2.0

Table 2 Parameter range of bilinear model from bridge seismic control design method draft (HDR and HDR-S)

α	$k(\frac{N}{mm^2})$	q_c
0.09–0.12	1–35	0.01–2.0

HDR-S data. Comparing to the standard range as shown in Table 2, it can be observed that the stiffness ratio range was larger, because during the KH method fitting for the HDR-S data at low temperature, the stiffness decreased. Also, the development of the standard was based on a standard room temperature (23 °C). The data size was 60 shear strain and 60 shear stress per data set. In numerical simulation, the dataset was iterated for 1000 times in preparation for the ANN model training. Then, the data was separated into training and testing, the training data was 120 by 900, and the testing data was 120 by 100.

3.2 Data Normalization

The HDR-S cyclic loading data consist of 5 amplitudes, each amplitude has 5 loops. The loops were separated and normalized to 60 data points of shear strain and shear stress using nearest neighbor method for the ANN training and testing preparation. The normalized shear strain and shear stress were shown in Fig. 3. The 60 data points was the optimum value that was resulted to a trial-and-error training process conducted. The determination of the optimum dataset size reduces the ANN model training time.

3.3 Numerically Simulated Data

After the data normalization, the shear strain data at HDR-S 23 °C and 250% amplitude was used to numerically simulated the shear stress under bilinear model for the ANN training preparation. The range of parameters was shown in Table 1, each parameter was randomly selected to generate each dataset. The sample numerically simulated data was shown in Fig. 4.

3.4 Artificial Neural Network (ANN) Model

The fundamental parts of the neural network model consists of input data, hidden layers, and output data. In this study, the input data was the normalized shear strain

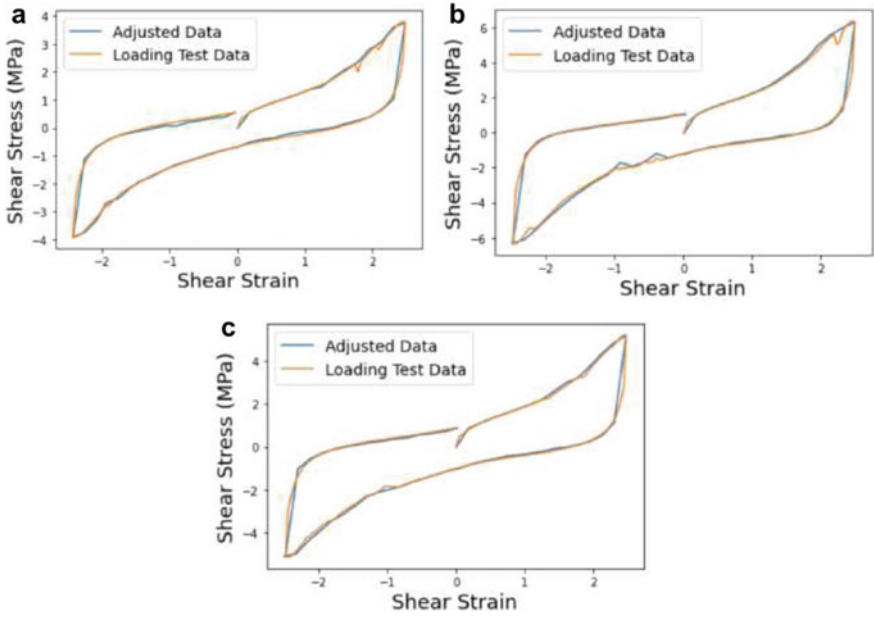


Fig. 3 Shear strain and shear stress data normalization at 250% amplitude a 23 °C, b -20 °C, c 0 °C

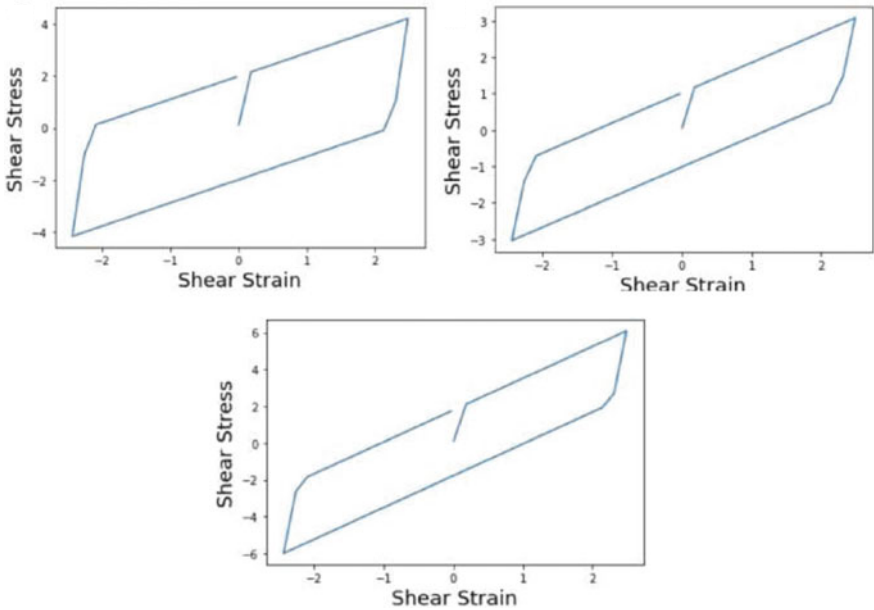


Fig. 4 Shear strain and shear stress data from bilinear model numerical simulation

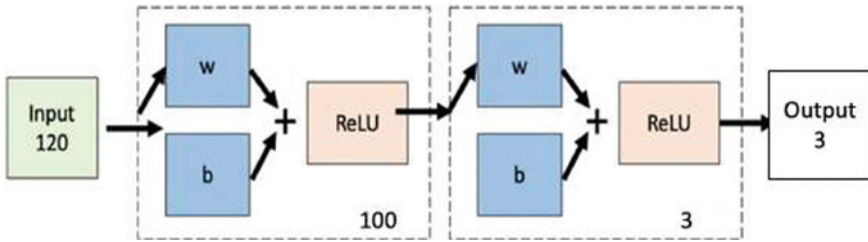


Fig. 5 Neural network mode

from the 250% amplitudes at three different temperatures, and the numerically simulated shear stress using bilinear model. The hidden layer was 100, and the activation function was rectified linear activation function (ReLU) which was commonly used for regression problem. The optimizer was RMSProp with a learning rate of 0.001, it helps to eliminate the vanishing gradient problem of obtaining the optimum regression value. The output was three nonlinear parameters of bilinear model which were stiffness ratio, initial stiffness, and yielding force. The neural network model was shown in Fig. 5.

4 ANN Model Evaluation

The training data was 120 by 900, and the testing data was 120 by 100. Before the ANN training, the training data was separated into 90% training and 10% validation using validation split function. The important key point of the ANN model evaluation was the loss should approach to zero.

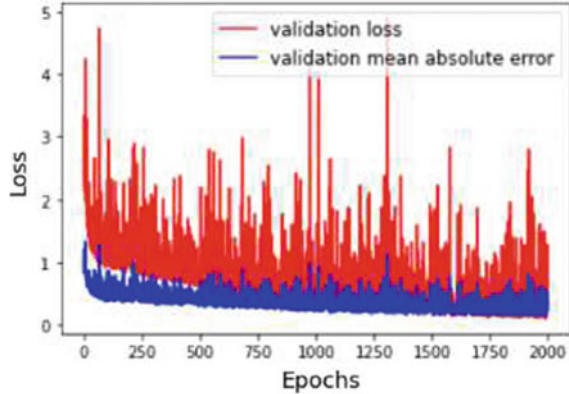
4.1 Loss Functions

The loss functions were mean squared error (MSE) and mean average error (MAE) as shown in Eqs. (1) and (2), where in, n is the total number of data, y_i is the simulated value, and y_p was the predicted value.

$$\text{MSE} = \frac{1}{n} \sum_{i=0}^n (y_i - y_p)^2 \quad (1)$$

$$\text{MAE} = \frac{1}{n} \sum_{i=0}^n |y_i - y_p| \quad (2)$$

Fig. 6 ANN model evaluation



After 2000 epochs, the mean squared error was 0.23 as shown in Fig. 6. The loss approached to zero which indicated that the ANN model was good.

4.2 Validation

To visualize the accuracy of the trained ANN model, the simulated and predicted data was shown in Fig. 7. The most critical parameter was found out to be the stiffness ratio.

5 HDR-S Loading Test Data Nonlinear Parameter Prediction

The HDR-S cyclic loading data consist of force and displacement values at five different amplitudes: 50%, 100%, 150%, 200%, and 250%. The data was converted into shear stress and shear strain to eliminate the effect of the bearing's cross section properties. Also, the HDR-S bearing data at three different temperature was considered. However, only the 250% amplitude data at each temperature was used in the prediction because it greatly represents the final shape of the hysteresis curve.

5.1 ANN Model Prediction

The ANN model predicted nonlinear parameter for the HDR-S cyclic loading data at 250% amplitude was shown in Fig. 8, the blue line represents the HDR-S loading data while the yellow represents the ANN model prediction. The same nonlinear

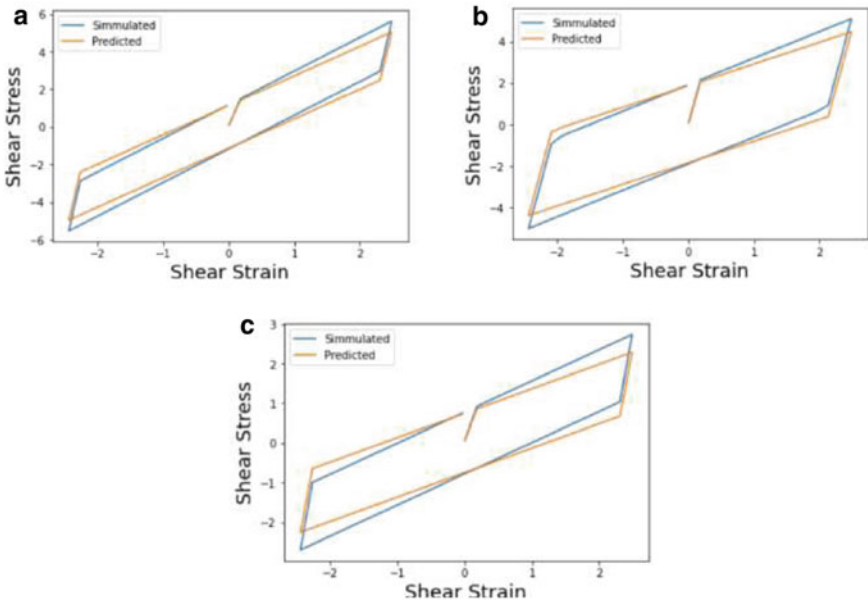


Fig. 7 ANN model predicted parameter at 50%, 150%, and 250% amplitude

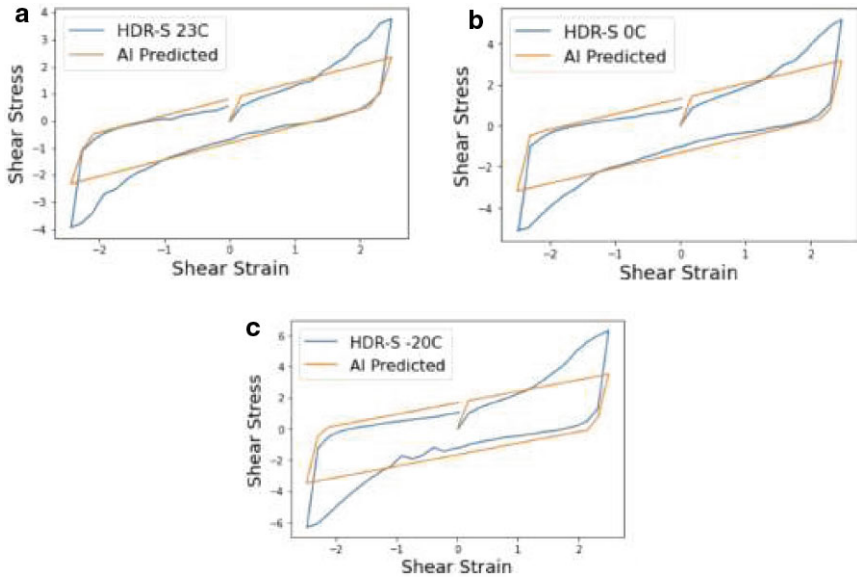


Fig. 8 ANN model predicted parameter for 250% amplitude of HDR-S data at a 23 °C, b 0 °C, c -20 °C

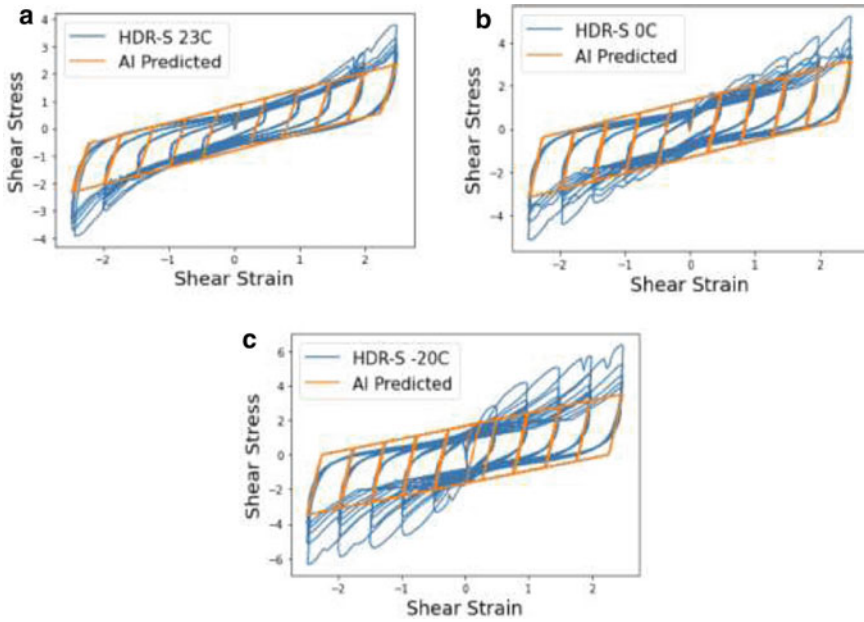


Fig. 9 ANN model predicted parameter for all amplitude of HDR-S data at **a** 23 °C, **b** 0 °C, **c** – 20 °C

Table 3 ANN predicted bilinear parameter at HDR-S data

HDR-S	α	k	q_c	R (250% Amplitude)	R (All Amplitude)
23 °C	0.087	7.097	0.814	0.944	0.944
0 °C	0.056	13.423	1.313	0.945	0.938
–20 °C	0.046	15.874	1.665	0.916	0.921

parameters were compared to all of the data amplitude as shown in Fig. 9. It can be observed that the stiffness ratio is directly proportional to the decrease of temperature while the initial stiffness and yield force was inversely proportional. The initial stiffness and yield force increases as the temperature decreases. The contribution rate was similar to both the 250% amplitude data and comparing to all of the amplitude (Table 3).

5.2 ANN Model and KH Method

The predicted nonlinear parameters from the ANN model were used as the initial parameter for KH method which makes the process faster and the contribution rate

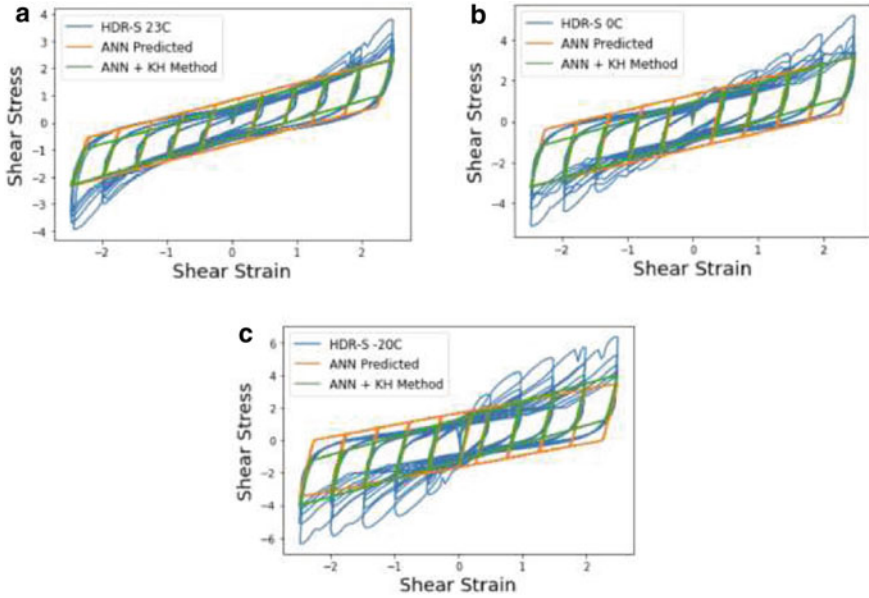


Fig. 10 ANN model and KH model predicted parameters for all amplitude of HDR-S data at **a** 23 °C, **b** 0 °C, **c** -20 °C

Table 4 ANN predicted bilinear parameter at HDR-S data

HDR-S	α	k	q_c	R (ANN + KH METHOD)	Steps
23C	0.097	7.159	0.594	0.966	13
0C	0.062	14.745	0.948	0.97	20
-20 °C	0.065	16.839	1.286	0.956	20

increased. Figure 10 shows the comparison of ANN prediction and the ANN prediction with KH method for HDR-S data at three different temperatures. Table 4 shows the list of the updated nonlinear parameters, the contribution rate was improved by 2.2% for the HDR-S at 23 °C, 3.2% for the HDR-S at 0 °C, and 3.5% for HDR-S at -20 °C.

5.3 KH Method

Using the optimization algorithm of KH Method, the nonlinear parameters of HDR-S cyclic loading under Bilinear model was obtained. As shown in Table 5, the contribution rate was 0.966 for the three trials and the updated nonlinear parameters had a similar values. By using KH method, initial random parameters were required, and

Table 5 KH method HDR-S nonlinear parameters predicted

Initial random parameters			R	Adjusted parameters			R	Steps
α	k	q_c		α	k	q_c		
0.01	16	0.03	0.910	0.073	9.655	0.589	0.966	955
0.04	20	0.1	0.944	0.073	9.655	0.589	0.966	770
0.07	17	0.04	0.932	0.073	9.671	0.589	0.966	457

this was bounded by the range specific in the code for reference. The time required for the convergence of the curve fitting depends on the initial parameters, and it was shown in the table that the total number of steps ranges from 457 up to 955. There was a significant time difference between the ANN model which has only 1 step compare to KH method alone. Even the combination of the ANN model and KH method shows a significant reduction in the total number of steps and the contribution rate was same as using KH method alone.

6 Conclusion

This study developed an artificial neural network (ANN) model that can understand the nonlinear behavior of an HDR-S bearing and predict the nonlinear parameters under bilinear model. The ANN model successfully identified the nonlinear parameters of the HDR-S bearing's cyclic loading data at three different temperatures.

- (1) The parameter range considered for the numerical data generation was revised specifically for the value of stiffness ratio compared to the standard. After conducting KH method for HDR-S loading data at low temperature, the stiffness ratio decreases and became lower than the standard's lower limit.
- (2) Using KH method alone, the step size ranges from 457 up to 955, and was highly dependent on the random initial parameter assumption. This takes time and might be more complicated on other nonlinear models.
- (3) The nonlinear parameter suggested by the ANN model serves as the initial parameter for KH method, the total steps decreased compared to KH method alone. The contribution rate increased by 2–3% compared to ANN model.
- (4) It was shown that the developed ANN model can make the nonlinear parameter prediction faster because it only requires one step, and through the improvement of training, the contribution rate may increase and KH method can be disregarded.
- (5) The nonlinear parameter obtained by the ANN model helps to solve the initial problem assumption of KH method.

This study highly suggests to incorporate machine learning to help in the seismic structural design.

References

1. Takashi Y, Hoshikuma J (2013) Damage to road bridges induced by ground motion in the 2001 great east japan earthquake. *J JSCE* 1:398–410
2. Bridge Seismic Control Design Method Draft (2012) Seismic isolation structure research committee for road and bridges
3. Dang G, Igarashi A, Murakoshi Y (2013) Nonlinear numerical hysteresis model for bi-directionally loaded elastomeric isolation bearings. *JAEE* 2
4. Nguyen DA, Dang J, Okui Y, Amin AFMS, Okada S, Imai T (2015) An improved rheology model for the description of the rate-dependent cyclic behavior of high damping rubber bearings. *Soil Dyn Earthq Eng* 77:416–431
5. Kuroda H (2001) Visual basic engineering calculation program. Tokyo CQ Press, Tokyo, pp 69–70

Autonomous Multiple Damage Detection and Segmentation in Structures Using Mask R-CNN



Sal Saad Al Deen Taher and Ji Dang

Abstract There are approximately 730,000 road bridges in Japan. As of 2020, more than 23% of them have been aged over 50 years or more and the percentage will go over 50% within the year 2030. Over the last decade there are numerous bridge accidents all over the world that have cost both monetary values and human lives significantly. Thus, regular inspection of bridges is very important to check the overall condition. However, the inspection is predominantly maintained manually which depends on person's expertise and often the task is cumbersome, expensive and error prone. Over the years, different deep learning-based techniques, such as Convolutional Neural Network (CNN), have been utilized to detect the damages automatically. However, most of them concentrate on damage detection and often been used for single class of detection only. Instance segmentation is a method where each object is detected as separate instance and by adopting a Region-based CNN model, such as Mask R-CNN, the instances can be shown separately. Though instance segmentation has been applied extensively for the detection of common objects in the real world, the application for multiple structural damage detection is very limited so far. Specially, the training and testing of the R-CNN model for multiple structural damage detection is different and challenging than common objects. This study is a step towards the feasibility and application of instance segmentation for multiple damage detection in structures and to evaluate the feasibility for real time detection with complex background.

Keywords Deep learning · Damage detection · Instance segmentation · Mask R-CNN · CNN

S. S. Al Deen Taher (✉)

Department of Civil and Environment Engineering, Saitama University, Saitama, Japan

J. Dang

Saitama University, Saitama, Japan

1 Introduction

According to the Ministry of Land, Infrastructure, Transport and Tourism (MLIT), as of 2017, there are approximately 730,000 road bridges across Japan. Of which 520,000 bridges, which account for 70% of all bridges, are situated on municipal roads. 10 years later, 48% of all bridges will be 50 years or older [1]. Over the last decade, more than 50 bridge collapses due to deteriorating related issues in Europe, North America, and South America caused human death, more than 150 fatalities and close to 20 billion USD in overall monetary value affecting nearly a million people [2]. Hence, early maintenance of the bridges is necessary to ensure the integrity of these structures.

Regular and periodic bridge inspection is required to find out the damages in them. To prevent any further losses in their structural capacity, early detection of the damages in the bridges is the most important thing. The inspection and monitoring of bridges to find damages in them are predominantly maintained manually. The process depends upon the inspector's assessment. Experience plays a significant role in these situations. As the inspection is done only visually, there is always a chance of error in the process. Omission of detecting damages is common for visual inspection. While the process takes a lot of time and due to the nature of the inspection, it is often cumbersome and expensive to arrange all the necessary tools and machinery. And the shortage of experienced engineers in this type of works significantly hampers the regular inspection of the bridges.

Due to the shortcomings of manual inspection, over the years, researchers are concentrating to develop new methods using Machine Learning techniques to effectively detect damages from images. Most of the time the developed models perform well for the dataset they are trained for but for real world scenario they do not perform well due to the presence of complex background, different lighting condition and due to the inadaptability of the trained model for different image dataset. Furthermore, the original machine learning models are developed for large-scale common objects like persons, cars, trees, animals etc. whereas in structural health monitoring the task is changed for the models.

As there are different types of structural damages are present, the models need to be adjusted in their hyper parameters and other consideration must be selected to adjust the models for the structural damage detection. And most of the time these models are trained for single type of damages whereas in structures there are multiple types of damage. To address these issues, a Deep Learning based multiple damage detection and segmentation method is proposed. The chosen model for this task is Mask R-CNN model. [3]

There is numerous CNN based classification models been developed over the years, but they are basically trained and tested on laboratory-based images and cannot be tested on real world application such as Unmanned Aerial Vehicle (UAV) images, as damage can be small or may be in a corner or there are too many variations with complex background. Thus, objective detection and instance segmentation methods can be considered as more practiced method for bridge inspection using robot or UAV.

This research focuses on the preliminary study of using Mask R-CNN on multiple damages.

As the original Mask R-CNN model has been proposed for standard database such as MS COCO [4] dataset, but it is unknown how to detect structural damages. The damage target such as corrosion or cracks are different from the standard database and do not have some shape feature or specific contour profile, it is easy to be missed with background. Thus, basic setting of training parameters is the key to find a better recognition model.

2 Background Information and Related Works

2.1 Machine Learning Based Damage Detection

Traditional Machine Learning based damage detection began almost 40 years ago when researchers dealt with large quantities of nonstructured image data. Thus, before training the models, a predefined feature extraction stage was required [5]. Further on, researchers utilized machine learning techniques like Support Vector Machine (SVM) [6], Artificial Neural Network (ANN) [5], and Random Forest [7] to classify damages in structures, mainly cracks.

In 2012, Krizhevsky et al. [8] developed a deep Convolutional Neural Network (CNN) that superseded the best methods by precision and accuracy that can classify images from the ImageNet dataset. Ever since, CNN is extensively used to classify objects from images. And researchers begin to use CNN to classify damages from images.

CNN based object detection are developed broadly to three categories- (a) Classification (b) Object Detection (c) Segmentation. The classification is simply separating the damage patches in the image from the non-damage patches. Most researchers used patch level classification [9] which separates every image into small patches with the advantages of generating more data from the small patches and localized information of damages in images. The object detection task is to generate bounding boxes around the areas that contain the damage. There are some object detection models developed over the years, such as Faster R-CNN [10], Single Shot Detector (SSD) [11], You Only Look Once (YOLO) [12] etc. In contrast, SSD and YOLO are single-stage detectors that require less training time than Faster R-CNN, which is a double state detector. Object detection tasks is popular among the researchers who want to classify damages from the images. Zhang et al. [13] conducted a study using YOLOv3 for detecting four types of concrete bridge damages i.e. crack, pop-out, spalling and exposed rebar. The original model is further improved to enhance the detection accuracy by adopting transfer learning. Cha et al. [14] proposed a Faster R-CNN based structural visual inspection method where five types of structural damages- concrete crack, steel corrosion with two levels (medium and high), bolt corrosion, and steel delamination can be detected.

The segmentation task predicts the classification in image pixel-wise that is each pixel is classified as damage or non-damage. The precise location of damages and separation generated by segmentation is useful for both damage classification and damage features. For this reason, to detect damages, recently the segmentation is gaining popularity among researchers. Hsieh et al. [15] reviewed 68 papers to identify the development trend in Machine Learning based crack detection algorithm. They found that since 2016 CNN based crack detection from images are on the rise. While initially the classification task was popular among researchers, the object detection and segmentation tasks took over it. Yang et al. [16] proposed a FCN model that can detect cracks concurrently at pixel level. The model is trained by feeding multiple types of cracks to semantically identify and segment pixel-wise cracks at different scales. Li et al. [17] proposed also a FCN model that can detect multiple damages including crack, spalling, efflorescence, and hole images in concrete structures. Wang et al. [18] proposed a Mask R-CNN model to identify and assess superficial damages on roof tiles of historic buildings in Palace Museum in China.

3 Methodology

The proposed framework is based on a mask and region-based convolutional neural net Mask R-CNN. Overall architecture is shown in Fig. 1. Mask R-CNN consists of two stages. The first stage is like Faster R-CNN. In the first stage, the Region Proposal Network (RPN) proposes a set of Region of Interests (ROIs) with probabilistic scores, which indicate if they contain an object within them. The only difference is that Mask R-CNN uses ROIAlign [3], which is an improvement of the ROI Pool operation. In the second stage, the Faster R-CNN classifier is combined with an additional mask prediction head to predict the object's class within the ROIs and corresponding mask. The proposed framework is based on Matterport Mask R-CNN implementation, free to use under MIT License.

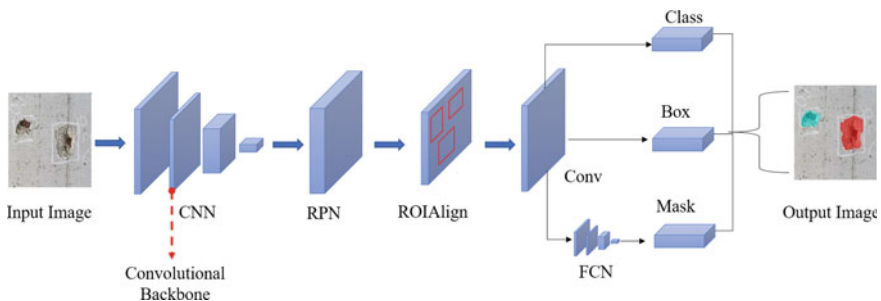


Fig. 1 Overall architecture of mask R-CNN

3.1 Backbone

A standard Convolution Neural Network (CNN) that serves as a feature extractor constitutes the backbone architecture of the Mask R-CNN. Lower level features are detected in the early layers of the network, whereas higher level features are successively detected in the later layers. Generally, this network acts as a good backbone, but employing a Feature Pyramid Network (FPN) improves the feature extraction of Mask R-CNN significantly. A second pyramid is added that extracts the higher level features from the first pyramid and passes them to lower layers, allowing features at all levels to access both lower and higher level features. Our proposed framework uses ResNet-101 architecture.

3.2 Region Proposal Network

The Region Proposal Network (RPN) is a lightweight neural network predicts multiple region proposals using a sliding window technique. RPN extracts relevant anchor boxes from feature maps. Anchor boxes are precalculated fixed sized bounding boxes of various sizes that are placed throughout the image and represent approximate bounding box predictions to save time.

3.3 ROIAlign

Features of objects are extracted from the object proposal results from the RPN using ROIAlign. ROIAlign is a feature map operation that aligns the candidate box feature extraction result with the input image.

3.4 Network Heads

The feature map extracted by ROIAlign is fed to a classification layer, bounding box refinement layer and a mask branch to output the class, bounding box and mask of the object respectively. The mask branch is an Fully Convolutional Network (FCN) that do the segmentation in an image in the pixel level.

3.5 Loss Function

The loss function for Mask R-CNN is shown in Eq. (1)

$$L = L_{cls} + L_{bbox} + L_{mask} \quad (1)$$

The $L_{cls} = (L_{cls1} + L_{cls2})$ is the classification loss, indicates how close the predictions are to the true class, and $L_{bbox} (L_{bbox1} + L_{bbox2})$ is the bounding box loss, which indicates the model localization accuracy. The mask prediction loss L_{mask} , is calculated by taking the binary cross-entropy between the predicted mask and the ground truth. This loss penalizes wrong per-pixel binary classifications.

3.6 Transfer Learning

Our dataset is relatively small. Thus, for robust training of the model transfer learning methodology has been adopted. The model was initialized with pre-trained weights from training on the COCO dataset. Fine tuning of the model is possible by tweaking several hyperparameters. For example, learning rate, learning momentum, weight decay, train ROIs per image etc. can be changed according to the user's choice.

3.7 Data Augmentation

Data Augmentation has been considered for training as the dataset size is small. The data augmentations strategies considered here are horizontal flips, random crops, small gaussian blur with random sigma between 0 and 0.5 about 50% of all images, strengthen or weaken the contrast in each image, make some images brighter and some darker, affine transformations to each image, scale/zoom them, translate/move them, rotate them and shear them.

4 Dataset Preparation and Training Details

4.1 Dataset Preparation

For the proposed framework, the Mask R-CNN model has been trained and tested to detect three types of structural damages-(i) Crack, (ii) Corrosion, and (iii) Spalling. A dataset of total 1,950 images has been used. The images are separated according to their class and randomly split into 80% training and 20% validation data. The details is given on Table 1. All the images have been collected from the inspection report of

Table 1 Details of the dataset

Type of damage	Crack	Corrosion	Spalling	Total
Training images	595	402	445	1442
Testing images	149	100	111	360
Total	744	502	556	1802

structures prepared by General Incorporated Foundation Bridge Survey Committee, Japan. There is no fixed resolution of the dataset images.

4.2 Data Annotation

Some image was annotated by the open-source program VGG Image Annotator (VIA) which is a simple and standalone manual annotation software for image, audio and video. An example of Annotated image by VIA has been shown on Fig. 2. The annotated images are exported to MS COCO format which are stored in a json file.

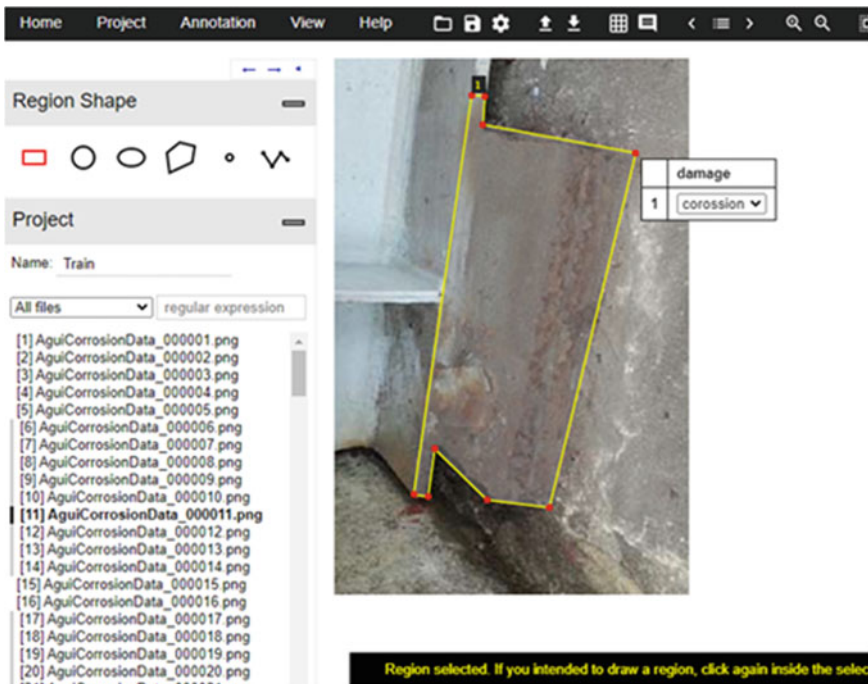


Fig. 2 Annotation by VGG Image Annotator (VIA)

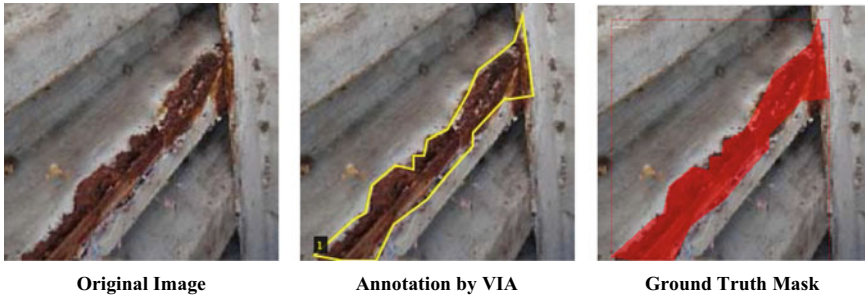


Fig. 3 Sample ground truth mask

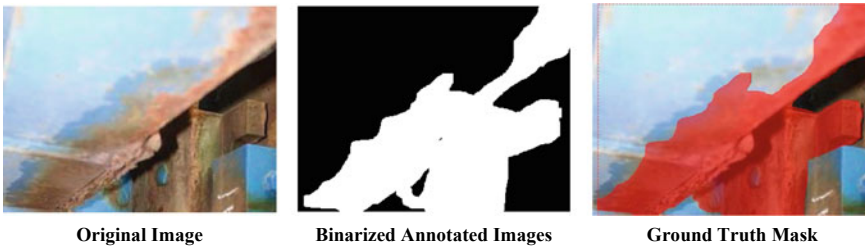


Fig. 4 Converted annotated images

The corresponding ground truth can be visualized by the Mask R-CNN’s own visualization program. (Fig. 3) Other images were previously annotated on MATLAB which produced their corresponding greyscale mask images separately. The mask images then converted into desired MS COCO format by developed Python program using OpenCV library. The conversion has been shown in Fig. 4.

4.3 Training Details

For the testing, we have used Python 3.6, Tensorflow Version 1.15.2, Keras Version 2.1.5. The training was carried cloud-based Google Collaboratory with integrated GPU supports. Each mini-batch had one image per GPU. Three different training strategies were selected for this dataset.

The Mask R-CNN models have been initialized with pre-trained weights from training on the COCO dataset, with learning rate, weight decay, and momentum were set as 0.001, 0.0001, and 0.9, respectively. Stochastic Gradient Descent (SGD) was chosen as the optimizer. The details of the training strategies have been shown in Table 2.

Table 2 Details of training

Parameter	Training A	Training B	Training C
Backbone	ResNet-101	ResNet-101	ResNet-101
Batch size	2	2	2
Optimizer	SGD	SGD	SGD
Learning rate	0.001	0.001	0.001
Learning momentum	0.9	0.9	0.9
Weight decay	0.0001	0.0001	0.0001
Training steps per epoch	100	100	100
RPN anchor scales	32, 64, 128, 256, 512	32, 64, 128, 256, 512	32, 64, 128, 256, 512
RPN train anchors per image	256	256	256
Train ROIS per images	200	200	200
Layers trained	Only Heads	Only Heads	All Layers
No of epochs trained	120	120	120
Data augmentation applied	No	Yes	Yes
Training time	7 h	4 h	4 h

5 Result and Discussion

5.1 Result

The training and validation loss for the three different training approach has been shown in Fig. 5. From the figure it can be shown that both the training and validation loss has been decreasing at a steady rate with the increment of time. The training loss is decreased to almost 1.5 for Training A whereas the training loss for Training C decreased to 1.75. The loss value should be decreased further for better training. Possible improvement can be done by increasing the number of training epochs and also number of images in the dataset.

Some detection result has been shown in Figs. 6, 7, and 8. From Fig. 6, in the validation images we can see that, Training A and Training B models are able to detect the corrosion damage correctly while Training C model completely ignores the corrosion damage class. In Fig. 7, three models were not able to detect the crack damages correctly. This is probably due to the quality of the images that contain the crack damages are not annotated properly. Most of the images that are annotated as

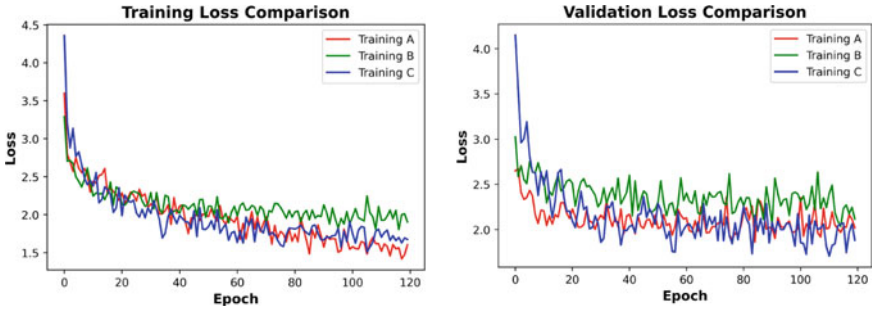


Fig. 5 Comparison of training and validation loss

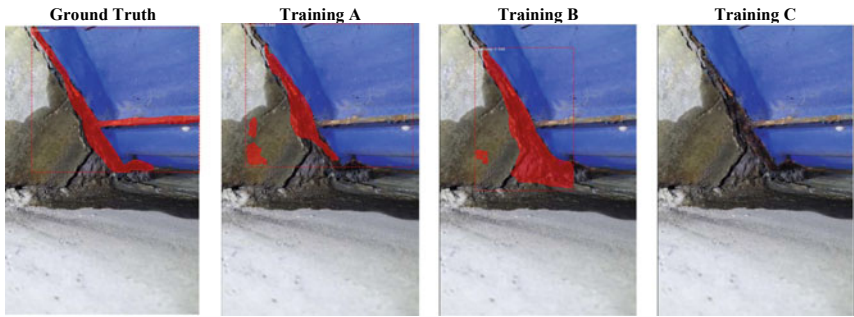


Fig. 6 Validated images for corrosion damage

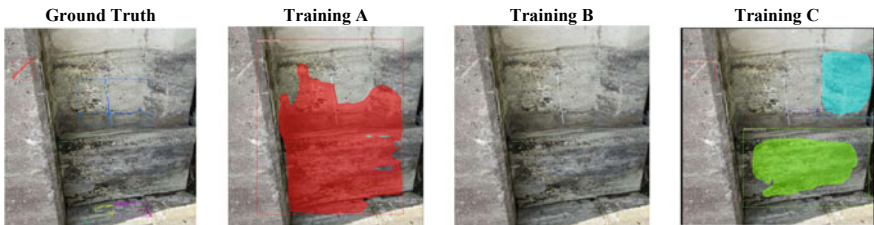


Fig. 7 Validated images for crack damage

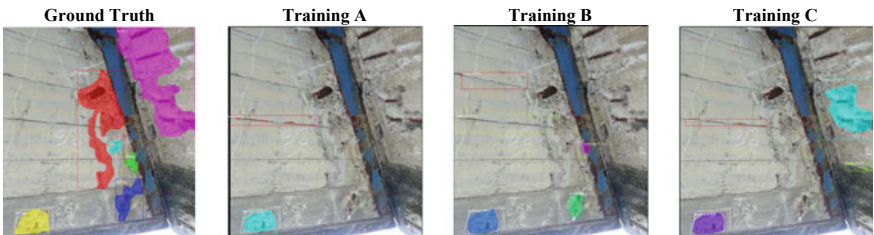


Fig. 8 Validated images for spalling damage

crack have chalk marks around the cracked regions which may have been repaired. Thus it made the training of this class difficult. For spalling damage, all three models have detected a part of the spalling but yet a large part is missed by all models. These detected results indicate the need for improvement in training on the dataset.

5.2 Future Works

Three training strategy was implemented for the dataset. The detection results for all three models were not satisfactory. To improve the training process some initiatives can be taken into action. The number of images can be increased for each damage class. The images should be selected with clearly visible damages. Some images in the current dataset that contain the crack damages are not clearly visible.

The number of training epochs should also be increased as from Fig. 5, we can see that the training and validation losses are decreasing with the increment of time. Also, the number of steps in each epoch can be increased though it is not an important task.

Finetuning the model through transfer learning can also be adopted. In the same model, the training schedule can be divided into training the heads, selected layers of the CNN and also all the layers with different learning rate data augmentation and number of epochs. The improvement can be evaluated by incorporating evaluation metrics set for instance segmentation.

6 Conclusions

Detection of damages in structures manually with complex background is a time consuming, labor intensive work. In this paper, an automated approach to detect multiple damages using machine learning technique is proposed. The proposed framework is based on Mask R-CNN model. Key points can be summarized as below.

- Three types of damages named crack, corrosion and spalling were intended to be detected by the proposed framework. Total 1802 images were annotated for this task and split in to 80% training and 20% validation data.
- Three different Mask R-CNN models were trained and tested.
- Models were initialized with pre-trained weights from training on the COCO dataset adopting transfer learning.
- The training and validation losses for all three models decreased with the increment of training time.
- The detection results were not satisfactory which posed the space for improvement of the training of the proposed model.

- For the improvement of the training and models, the quantity and quality of the training images can be improved. Also the training epochs can be increased. Fine tuning of the models can be achieved by combining different training strategies together.

References

1. MLIT (2020) Ministry of Land, Infrastructure, Transport and Tourism Website. https://www.mlit.go.jp/road/road_e/s3_maintenance.html
2. Ayele YZ, Aliyari M, Griffiths D, Droguett EL (2020) Automatic crack segmentation for UAV-Assisted bridge inspection. *Energies* 13:6250
3. He K, Gkioxari G, Dollár P, Girshick R (2020) Mask R-CNN. *IEEE Trans Pattern Anal Mach Intell* 42:386–397
4. Lin TY, Maire M, Belongie S, Bourdev L, Girshick R, Hays J, Perona P, Ramanan D, Zitnick CL, Dollár P (2015) Microsoft COCO: common objects in context
5. Kaseko MS, Ritchie SG (1993) A neural network-based methodology for pavement crack detection and classification. *Transp Res Part C* 1:275–291
6. Li N, Hou X, Yang X, Dong Y (2009) Automation recognition of pavement surface distress based on support vector machine. In: *ICINIS 2009 - Proceedings of the 2nd International Conference on Intelligent Networks and Intelligent Systems*, pp 346–349
7. Shi Y, Cui L, Qi Z, Meng F, Chen Z (2016) Automatic road crack detection using random structured forests. *IEEE Trans Intell Transp Syst* 17:3434–3445
8. Krizhevsky A, Sutskever I, Hinton GE (2012) ImageNet classification with deep convolutional neural networks. In: *Advances in Neural Information Processing Systems*
9. Schmutge SJ, Rice L, Nguyen NR, Lindberg J, Grizzi R, Joffe C, Shin MC (2016) Detection of cracks in nuclear power plant using spatial-temporal grouping of local patches. In: *2016 IEEE winter conference on applications of computer vision, WACV 2016*
10. Ren S, He K, Girshick R, Sun J (2017) Faster R-CNN: towards real-time object detection with region proposal networks. *IEEE Trans Pattern Anal Mach Intell* 39:1137–1149
11. Liu W, Anguelov D, Erhan D, Szegedy C, Reed S, Fu CY, Berg AC (2016) SSD: Single Shot MultiBox Detector. In: *Computer vision – ECCV 2016, Cham*
12. Redmon J, Divvala S, Girshick R, Farhadi A (2016) You only look once: Unified, real-time object detection. In: *Proceedings of the IEEE Computer Society Conference on Computer Vision and Pattern Recognition, Vols. 2016-December*, pp 779–788
13. Zhang C, Chen Chang C, Jamshidi M (2020) Concrete bridge surface damage detection using a single-stage detector. *Comput Aided Civil Infrastr Eng* 35:389–409
14. Cha YJ, Choi W, Suh G, Mahmoudkhani S, Büyüköztürk O (2018) Autonomous structural visual inspection using region-based deep learning for detecting multiple damage types. *Comput Aided Civil Infrastr Eng* 33:731–747
15. Hsieh Y-A, Tsai YJ (2020) Machine learning for crack detection: Review and model performance comparison. *J Comput Civ Eng* 34:04020038
16. Yang X, Li H, Yu Y, Luo X, Huang T, Yang X (2018) Automatic pixel-level crack detection and measurement using fully convolutional network. *Comput Aided Civil Infrastr Eng* 33:1090–1109
17. Li S, Zhao X, Zhou G (2019) Automatic pixel-level multiple damage detection of concrete structure using fully convolutional network. *Comput Aided Civil Infrastr Eng* 34:616–634
18. Wang N, Zhao X, Zou Z, Zhao P, Qi F (2020) Autonomous damage segmentation and measurement of glazed tiles in historic buildings via deep learning. *Comput Aided Civil Infrastr Eng* 35:277–291

Nonlinear Model Classification of HDR-S Bearing Under Low Temperature Using Artificial Neural Network



Katrina Montes, Ji Dang, Yuqing Tan, Akira Igarashi, and Takehiko Himeno

Abstract The seismic isolation design for bridges mainly focused on increasing the damping properties of the seismic isolator under controlled period. To adopt to the demand of high damping properties, there were newly developed isolators and dampers nowadays. However, in Japan, the seismic isolator's design standard for bearing's nonlinear parameter standard was limited to some existing isolator types and was fitted to bilinear model under controlled experiment environment settings. Furthermore, in actual environment, the nonlinear behavior of some key members like bearings and dampers were somewhat complicated, that's why there was a need to select the proper nonlinear model carefully to represents the bearing's nonlinear behavior more realistic. The nonlinear model selection can be difficult considering the new types of isolators and different external factors which makes it a trial-and-error process and highly depends on the engineer's expertise. Therefore, inversion process was proposed for structural key member's nonlinear model selection using neural network. The AI model was trained using four existing nonlinear models which was capable to identify the nonlinear model of an HDR-S bearing under low temperature. The training data used the displacement of an actual bearing's experimental data while the force was numerically simulated using different existing nonlinear models. The proposed method will greatly help to guide the engineers on nonlinear model classification which was important prior to nonlinear parameter identification and seismic isolation design.

Keywords Neural networks · Rubber bearing · Nonlinear models · Low temperature · HDR-S bearing

K. Montes (✉) · J. Dang

Department of Civil and Environmental Engineering, Saitama University, Saitama, Japan
e-mail: montes.k.m.s.886@ms.saitama-u.ac.jp

Y. Tan · A. Igarashi

Department of Civil and Environment Engineering, Kyoto University, Kyoto, Japan

T. Himeno

Kawakin Core Tech Co. Ltd, Saitama, Japan

1 Introduction

The mostly adopted type of isolation devices after the Kobe Earthquake were Lead Rubber Bearings (LRB) and High Damping Rubber Bearings (HDR-S). In seismic isolation design, the determination of nonlinear behavior of those bearings should be identified carefully to simulate a more realistic structure response. However, the nonlinearity of those seismic isolators was influenced by different factors like temperature, deterioration, loading rate, different loading conditions, strain rate, combination of different materials, etc. Therefore, there was a need to deeply understand the nonlinear behavior of seismic isolators and numerous numerical models was proposed but as the process becomes somewhat more complicated. The structural design with seismic isolator starts from the assumption of the type of bearing and its nonlinear properties [1]. The existing standard focuses on fitting the experimental cyclic loading data to bilinear model and the limited to some seismic isolator bearing types. In addition to that, there were newly developed seismic isolators that does not have guide for nonlinear model identification that needs further numerical method. The process can be difficult, and the accuracy was highly dependent on engineer's expertise. Therefore, this study proposed a method that can automate the nonlinear model classification through the utilization of machine learning. This study developed an artificial neural network (ANN) model that can classify the nonlinear model depending on the pair of force and displacement input data. The displacement used was from a super high damping rubber bearing (HDR-S) cyclic loading data and was normalized to fit the ANN training input. The force was generated through numerical simulation of the four nonlinear models namely bilinear, modified bilinear, Bouc-wen, and modified Park-Wen model. After the ANN model training and evaluation, the actual HDR-S at three different temperature was tested and the nonlinear model at each amplitude was classified. The results of the classified nonlinear model at different temperature were later compared. The use of machine learning for the nonlinear model selection will greatly help and serves as an initial guide for the engineers in the initial process prior to structural design with seismic isolators specifically for the newly developed seismic isolators.

2 Proposed Method

This study developed an artificial neural network (ANN) model that suggest the similarity of the HDR-S cyclic loading data based on the four nonlinear models namely Bilinear (BL), Modified Bilinear (MBL), Bouc-Wen (BW), and Modified Park-Wen (MPW). The proposed methodology was shown in Fig. 1 which starts from:

- (1) The generated input data for artificial neural network model development came from the displacement values of the HDR-S bearing at 23 °C, while the force was numerically simulated using the four nonlinear models stated. The dataset

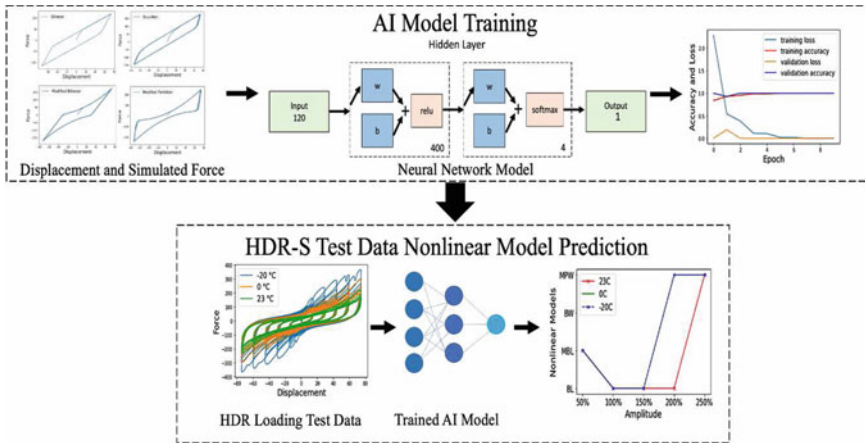


Fig. 1 Proposed methodology

consists of 60 displacement and 60 force values. Each nonlinear model data set was iterated by 500 times.

- (2) The dataset was separated into training and testing. The neural network model was defined, and the training took 10 epochs.
- (3) After the development of the ANN model, the HDR-S data at three different temperature was tested. The ANN model classified the most probable nonlinear model based on the HDR-S data input.

3 Nonlinear Models

The nonlinear models used in this study consisted of Bilinear (BL), Modified Bilinear (MBL), Bouc-Wen (BW), and Modified Park-Wen (MPW). Each nonlinear model was explained as follows.

3.1 Bilinear Model

This nonlinear model covers the changes in stiffness from elastic to plastic. The restoring force F is the combination of the elastic force F_e , and plastic force F_p as shown in Eq. (1). The elastic force is the product of the initial stiffness k_1 , and the displacement as shown in Eq. (2). During the plastic stage, the initial stiffness changes to secondary stiffness k_2 , with stiffness ratio α as shown in Eq. (3). x is the displacement in mm.

$$F = F_e + F_p \tag{1}$$

$$F e = k_1 x \quad (2)$$

$$k_2 = \alpha k_1 \quad (3)$$

The restoring force F was the combination of elastic force and plastic force as shown in Eq. (4).

$$F = (1 - \alpha)k_1 \Delta x \quad (4)$$

The loading and unloading behaviour of the hysteresis curve was controlled by the yielding force q_c as shown in Eqs. (5) and (6)

$$\text{If } F_p > q_c, F_p = q_c \quad (5)$$

$$\text{If } F_p < -q_c, F_p = -q_c \quad (6)$$

3.2 Modified Bilinear Model

The modified bilinear (MBL) has the same parameters as Bilinear model (BL) but with an additional parameter x as shown in Eq. (7), which controls the pinching effect. The pinching effect has a direct effect on the yielding force.

$$q_c = q_{c_0} + bx^2 \quad (7)$$

3.3 Bouc-Wen Model

Bouc-Wen model includes the continuous change in stiffness due to yielding. It represents the hardening and softening due to the degradation in stiffness. The formula of this model was shown in Eqs. (8) and (9).

$$F = \alpha kx + (1 - \alpha)kz \quad (8)$$

$$\dot{z} = A\dot{x} - \beta|\dot{x}||z|^{n-1}z - \gamma\dot{x}|z|^n \quad (n = 2) \quad (9)$$

where F is the restoring force, z is the displacement of the hysteresis, k is the coefficient of stiffness, α is the ratio of initial to post yield stiffness. n , β , γ , A controls the

shape of the hysteresis [2], Specifically, β and γ controls the softening and hardening of the hysteresis shape, n is for the curve smoothness transition. A is equal to 1.0 and n is 2.0.

3.4 Modified Park-Wen Model

Modified Park-Wen model includes pinching effect which can be observe on the parameter b and stiffness degradation.

$$F = \alpha kx + (1 - \alpha)k(1 + bx^2)z \quad (10)$$

$$\dot{z} = A\dot{x} - \beta|\dot{x}z|z - \gamma\dot{x}z^2 \quad (11)$$

where F is the restoring force, x are displacement, z is the plastic component, k is the initial elastic stiffness, b is caused by the shearing deformation which result to the change of critical force and produce pinching effect. β and γ are based on the yield displacement d_y , while A is generally equal to 1. This model was tested to fit the nonlinear response of a high damping rubber (HDR) bearing under unidirectional load test [3].

4 Training of the Artificial Neural Network (ANN) Model

The development of the artificial neural network model starts from the data generation and normalization, building the neural network model with different parameters, and ANN model training and evaluation. The developed artificial neural network (ANN) aims to classify the nonlinear model from an HDR-S experimental loading test data.

4.1 Data Generation

The displacement of the HDR-S loading of 23 °C, amplitude was used to generate the different force from the four nonlinear models through numerical simulation as shown in Fig. 2. The displacement data of the HDR-S experiment at 100% amplitude and first loop was normalized to reduce the size to 60 data points using nearest neighbor method. It was simulated to produce a 60 data points of restoring force using different nonlinear models.

In the numerical simulation, the parameters of each nonlinear model were identified by conducting KH Method (Kuroda, 2001) in each HDR-S data at three different temperatures. Bilinear model has a parameter range standard based on the road and

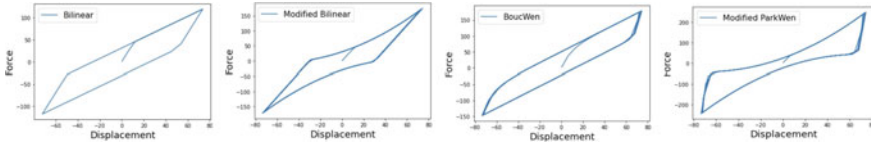


Fig. 2 Nonlinear models

Table 1 Parameter range of bilinear model

α	$k(\frac{N}{mm^2})$	$q_c(N)$
0.3–0.4	2–9	30–40

Table 2 Parameter range of modified bilinear model

α	$k(\frac{N}{mm^2})$	$q_c(N)$	b
0.3–0.4	2–9	30–40	0.01–0.02

Table 3 Parameter range of Bouc-Wen model

α	$k(\frac{N}{mm^2})$	β	γ
0.2–0.3	4–7	-0.3–-0.2	-0.15–-0.1

bridge seismic design draft [1]. However, for other nonlinear models like modified bilinear model, Bouc-Wen model, and modified Park-Wen model, the parameter range was difficult. Therefore, in identifying the parameter range, KH method was used for curve fitting and determined the nonlinear parameters as a preliminary step [4]. The parameters obtained from KH method was adjusted and created a range near to it, as shown from Tables 1, 2, 3 up to 4.

4.2 Artificial Neural Network (ANN) Model

The artificial neural network model consists of input layer, hidden layers, and output layer. The input data was from the displacement data of the HDR-S cyclic loading data at 100% amplitude reduced to 60 data points. The force was numerically simulated using the four nonlinear models. The input data was the combined displacement and force on each nonlinear model. The hidden layer was 400, the activation was rectified linear activation function (ReLU) at the first hidden layer, and softmax for the output layer which gives a score of 1.0 to the highest probable non-linear model.

Table 4 Parameter range of modified park-wen model

α	$k(\frac{N}{mm^2})$	β	γ	b
0.2–0.3	4–7	0.15–0.2	-0.15–-0.1	0.00055–0.00065

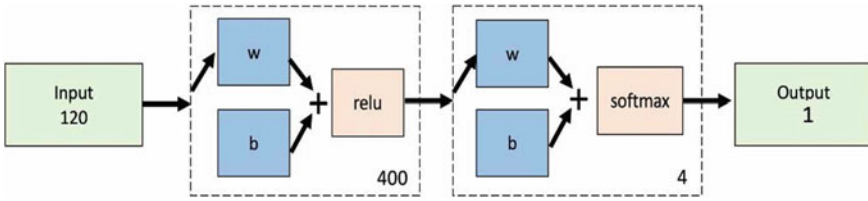


Fig. 3 Artificial Neural Network (ANN) model

Table 5 Artificial neural network model key points

Optimizer	Adam, learning rate = 0.001
Activation function	ReLU and Softmax
Loss function	Categorical cross entropy
Platform	Google colabratory
Epochs	10

The output was 1, which was the classified nonlinear model based on the force–displacement input data. The loss function was categorical cross entropy, this was used for classification problem with classes more than 1. The platform used was google colabratory using python language. The optimizer was Adam with learning rate of 0.001, this study used few different optimizers for comparison but Adam shows the best result (Fig. 3; Table 5).

5 ANN Model Evaluation

After 10 epochs, the validation accuracy was 1.0 and the loss was approaching to zero as shown in Fig. 4, which shows a good result. The confusion matrix was shown

Fig. 4 Accuracy and loss

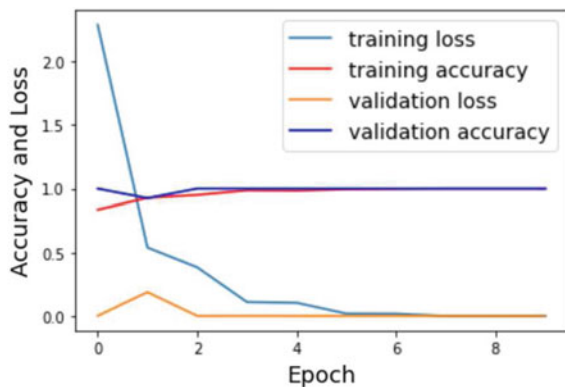
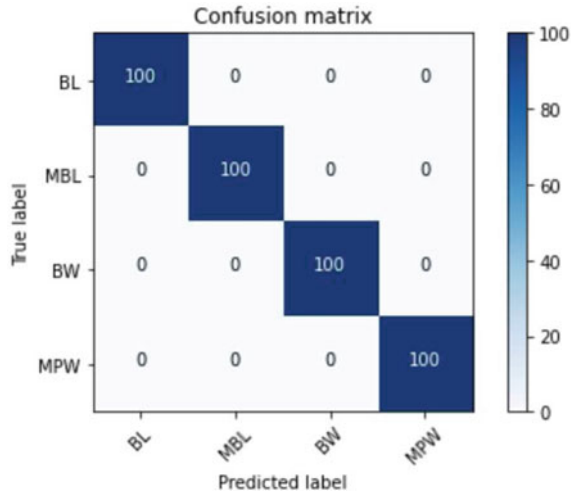


Fig. 5 Confusion matrix



in Fig. 5, this serves as visualization of the predicted label and true label of the testing data. Each nonlinear model consisted of 100 testing data, and the confusion matrix shows that all of the testing data was classified correctly.

6 HDR-S Cyclic Loading Test Data

The Super High Damping Rubber (HDR-S) bearing data came from the cyclic loading test at different ambient temperature specifically at -20°C , 0°C , and 23°C . The data was shown in Fig. 6. Each cyclic loading result consist of force and displacement data at five different amplitude which ranges from 50%, 100%, 150%, 200%, and 250%.

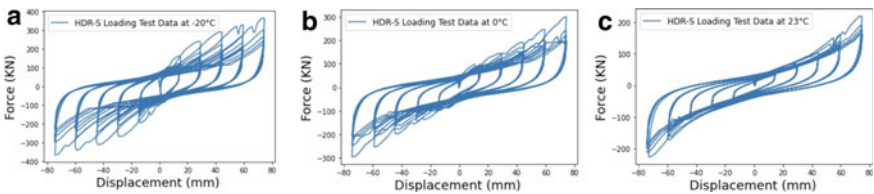
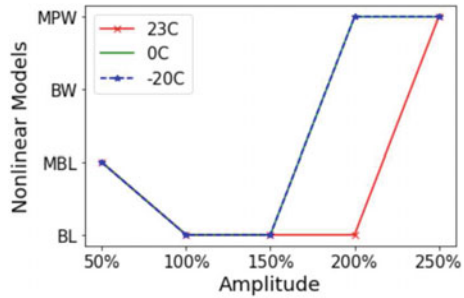


Fig. 6 HDR-S Cyclic Loading Test Data at **a** -20°C , **b** 0°C , **c** 23°C

Fig. 7 Nonlinear model classification at different temperature of the HDR-S data



7 HDR-S Bearing Nonlinear Model Evaluation

Using the developed ANN model, HDR-S loading data at the first loop at each amplitude was tested. The nonlinear model was classified as shown in Fig. 7. The data at 0 °C and –20 °C, shows a totally similar pattern which starts from modified bilinear (MBL) at 50% amplitude, then bilinear model (BL) at 100% and 150% amplitude, while the classification goes to Modified Park-Wen (MPW) model at 200% and 250% amplitude. On the contrary, the data at 23 °C shows a different prediction at 200% amplitude which stays at Bilinear model (BL) but eventually goes to Modified Park-Wen (MPW) at 250% amplitude. Majority of the classification was Bilinear Model (BL) but during higher amplitude, the nonlinear model becomes Modified Park-Wen (MPW).

8 Conclusion

This study developed an artificial neural network model that aimed to classify the nonlinear model of a super high damping rubber (HDR-S) bearing experiment result at three different temperatures. The nonlinear models used from training were bilinear model (BL), modified bilinear model (MBL), Bouc-Wen model (BW), and Modified Park-Wen Model (MPW). The neural network model showed a high accuracy of 1.0 and loss of 0.0028 after 10 epochs. The testing data of the four nonlinear models were all categorized correctly by the ANN model. The HDR-S data was separated by amplitude and was normalized to reduced size of 60 data points of displacement and 60 data points of force for the ANN model input data. Based on the classification result, the HDR-S data at 0 °C and –20 °C, shows the same pattern on the nonlinear model classification which was bilinear model until 150% amplitude, but became Modified Park-Wen model at 200% and 250% amplitude. However, for the HDR-S data at 23 °C, at 200% amplitude, it stays as bilinear model, but eventually becomes modified Park-Wen model at 250% amplitude. Therefore, at lower amplitudes, Bilinear model (BL) was the mostly classified model, but on higher amplitude, Modified park-Wen (MPW) governs. The parameter range of each nonlinear model

for the data generation in the training the ANN model was limited and customized for the cross section of the HDR-S bearing because it was expressed in force and displacement values. However, the development of the neural network model shows that it can successfully classify the experiment data into different nonlinear model. This will be helpful to the engineers and can be a guide in deciding the nonlinear model to be used prior to structural design using seismic isolators. This study recommend the use of machine learning enhanced method which will help the engineers in seismic design.

References

1. Bridge Seismic Control Design Method Draft (2012) (Seismic Isolation Structure Research Committee for Road and Bridges)
2. Zhu X, Lu X (2011) Parametric identification of bouc-wen model and its application in mild steel damper modeling. In: The twelfth Earth Asia-Pacific conference on structural engineering and construction, Vol 14, pp 318–324
3. Dang G, Igarashi A, Murakoshi Y (2013) Nonlinear numerical hysteresis model for bi-directionally loaded elastomeric isolation bearings. JAEE 2
4. Kuroda H (2001) Visual basic engineering calculation program, CQ Press, Tokyo, pp 69–70

Automatic Top-View Transformation and Image Stitching of In-Vehicle Smartphone Camera for Road Crack Evaluation



Jose Maria G. Geda, Kai Xue, and Tomonori Nagayama

Abstract Current technology for road crack evaluation uses precision profilers with line scan cameras and manual detection of road cracks from captured images. In Japan, the crack ratio is evaluated using a top-view photo by the coverage of the area of 0.5 m rectangular grid traversed by cracks usually over a 20 m span of road. Previous research using in-vehicle smartphone camera were conducted but the crack ratio cannot be calculated based on the definition. This paper proposes an automatic top-view transformation and image stitching algorithm for road crack evaluation by utilizing video captured of an in-vehicle smartphone camera. A vision-based approach for camera calibration is proposed since camera parameters cannot be easily obtained. Four conditions are used to perform the parameter calibration. (1) horizontal manhole axis, (2) parallel lane line, (3) circular manhole, (4) vertical lane line conditions. A frame with straight lane lines and a circular manhole is automatically selected by object detection. Top-view transformation is performed on these images and parameters are adjusted until both conditions are satisfied. The same parameters are then applied to the other frames assuming that the camera parameters (i.e., location, orientation, and settings remain the same). After the successful top-view transformation of frames, feature matching is conducted to pairs of successive frames to calculate the homography matrix between the two images. This is used for the image stitching of successive frames and obtain the translation offset between the images. Based on the calculated translation offset and the extracted frame distance interval the pixel-to-real-distance conversion factor is calculated. A fine resolution image of road top-view can be produced that can be used for the evaluation of road cracks.

Keywords Road condition assessment · Crack ratio · Top-view transformation · Image stitching · AI

J. M. G. Geda · K. Xue · T. Nagayama (✉)
Department of Civil Engineering, The University of Tokyo, Tokyo, Japan
e-mail: nagayama@bridge.t.u-tokyo.ac.jp

K. Xue
SmartCity Research Institute, Tokyo, Japan

© The Author(s), under exclusive license to Springer Nature Switzerland AG 2023
Z. Wu et al. (eds.), *Experimental Vibration Analysis for Civil Engineering Structures*,
Lecture Notes in Civil Engineering 224,
https://doi.org/10.1007/978-3-030-93236-7_47

567

1 Introduction

Limited coverage of road assessment and the increasing number of aging roads are the two fundamental problems in road condition assessment. In Japan, the approximate total length of the road network is about 1.22 million kilometers [1]. These road networks include municipal roads, prefectural roads, national roads, and expressways. As of 2017, most of the roads assessed by precision profilers are the national roads managed by the Ministry of Land, Infrastructure, Transport, and Tourism (MLIT) which are only about 2% of the total road network [1]. MLIT requires three years to implement precision profiler surveys to cover the 24,000 km length of national roads. With a monitoring capacity of 8,000 km per year, many aging road networks in Japan remain unassessed or manually assessed. Manual road assessment is time-consuming and highly depends on the subjective visual skills of road inspectors, while high profilers are expensive and have limited coverage. Therefore, road management officials are continuously seeking accurate and affordable road assessment solutions.

Road management officials use pavement inspection in studying road defects, maintenance procedures, and repair priority. In the Japanese guideline for pavement testing [2], the crack ratio is calculated in the top-view of a 50 × 50 cm grid over a 20 m span of the road. The crack ratio is defined as the percentage of the total crack area over the area of the pavement section, as expressed in Eq. (1). A sample road segment with detailed crack classification is shown in Fig. 1. The conventional method to calculate the crack ratio is to obtain top-view images from road profiler with line scan camera. This method is accurate but is also expensive and time consuming.

$$C(\%) = \frac{\text{Cracking Area(m}^2\text{)}}{\text{Survey Target Section Area(m}^2\text{)}} \times 100 \tag{1}$$

Alternative methods are proposed using in-vehicle smartphone camera as shown in Fig. 2 and machine learning. Crack ratio calculation by object detection of road crack on the pavement from in-vehicle smartphone camera images was developed

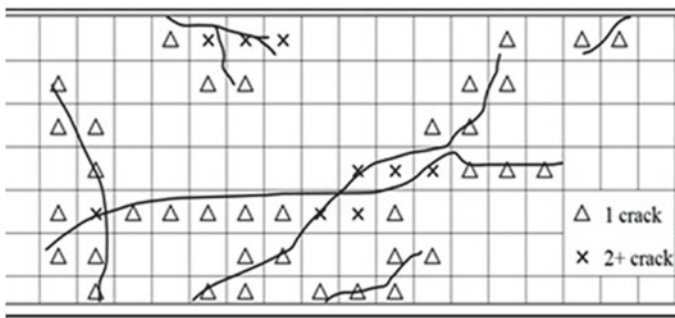


Fig. 1 Road crack inspection method



Fig. 2 In-vehicle smartphone setup

[3]. In this method, images from in-vehicle smartphone camera were utilized to capture road pavements. Then, object detection is used to identify the details of road pavement. The crack ratio calculation was determined by summing up the total area contribution of each detected crack divided by the target area for evaluation, as shown in Fig. 3. Since the crack area is calculated using the rectangular area of the bounding box from the object detection, the accuracy is limited. Also, the crack ratio cannot be calculated based on the definition.

Perspective transformation of an image requires knowing the camera parameters, which are used to calculate the transformation from the camera-view to the top-view. Camera calibration estimates the parameters of a lens and image sensor of an image or a video camera. These parameters can be used for lens distortion correction, measuring the object’s size in real-world units, and determining the camera’s location in the scene. The camera parameters are usually estimated in the laboratory or by analyzing a set of images of a calibration object taken from different viewpoints [4]. These camera parameters are not easy to obtain; hence, an automatic process for parameter calibration is proposed. In this paper, we are proposing an automatic top-view transformation and image stitching procedure for images captured from an in-vehicle smartphone camera for road crack evaluation.

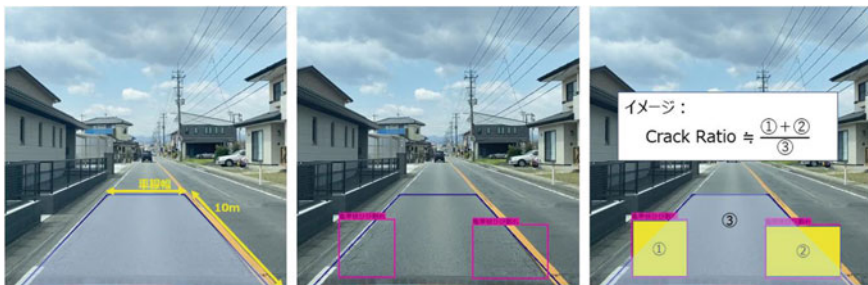


Fig. 3 The procedure of crack ratio calculation using object detection

2 Top-View Transformation

2.1 Transformation Principle

The top-view transformation coordinate system is shown in Fig. 4 [5]. $O_W - X_W Y_W Z_W$ is defined as the vehicle coordinate, $O_C - X_C Y_C Z_C$ and $O_{VC} - X_{VC} Y_{VC} Z_{VC}$ is defined as the camera-view coordinate and top-view coordinate, respectively. The viewpoint O_C , whose location is (t_x, t_y, t_z) , rotates by θ about the X_W axis, by ρ about the Y_W axis, and by φ about the Z_W axis. H_C is the height of the camera from the surface of the road obtained during measurements. H_{VC} is the height of the virtual camera from the road’s surface, which affects the zoom ratio of the image. Additionally, all the objects in the image are also assumed to be planar objects. The top-view image is obtained by transforming the in-vehicle view image from Eqs. (2) and (3).

$$x' = \frac{f'}{H_{vc}} \cdot \frac{H_c(x - x_0(d))}{f \sin\theta - y \cos\theta} \tag{2}$$

$$y' = \frac{f'}{H_{vc}} \cdot \left\{ \frac{H_c(f \cos\theta + y \sin\theta)}{f \sin\theta - y \cos\theta} - D_{vc} \right\} \tag{3}$$

where x and y are the pixel coordinates from the camera view in the $X_C - Y_C$ plane with the origin $O_C - X_C Y_C$ set the bottom middle of the image by default. x' and y' are the corresponding top-view coordinates after transformation. f and f' are the focal lengths (in pixels) of the in-vehicle camera and virtual camera, respectively. The previous study assumes that the camera parameters f and θ are known and

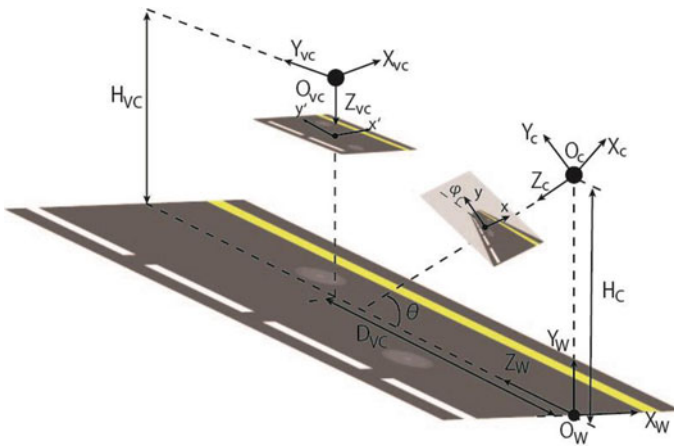


Fig. 4 Top-view transformation coordinate system

other parameters such as φ and the camera position $x - x_0(d)$ were not considered. A vision-based approach is proposed for the camera parameter calibration.

2.2 Proposed Top-View Transformation

Interior and exterior camera parameters necessary for coordinate transformation are obtained in a rigorous procedure. Hence, an automatic process for parameter calibration is proposed. To successfully perform a top-view transformation, camera parameters f and θ should be identified to solve the top-view transformation described in Eqs. (2) and (3). When these two parameters are known, the equations can be applied to all the other frames obtained from the same measurement, assuming that θ did not change through the course of the measurements. A vision-based approach for parameter identification is proposed.

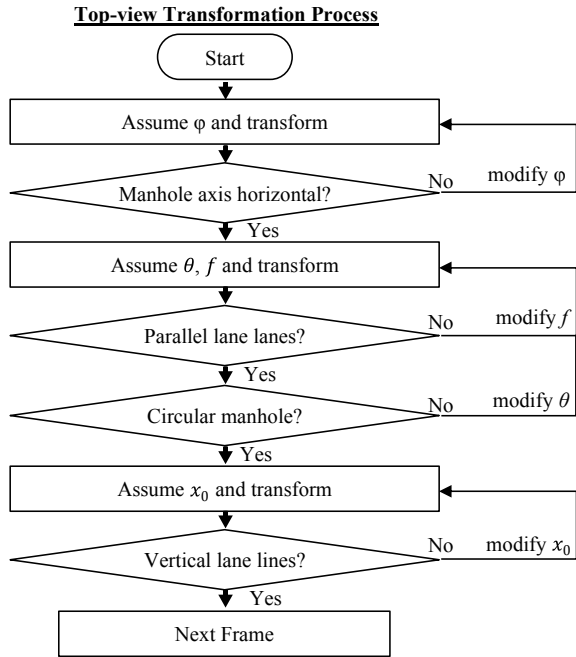
3 Parameter Identification

There are four parameters in total needing calibration, $[f, \theta, \varphi$ and $x_0]$. These parameters are automatically calibrated using the images captured from an in-vehicle smartphone camera when driving on a normal road. The vision-based approach eliminates the need to obtain the camera parameters directly and will also be able to adapt to any setup position inside the vehicle. Four conditions were set to obtain these parameters. First, parallel straight lane lines on the road should be parallel after transformation, and second, the aspect ratio of the image should be consistent. All this process is summarized in Fig. 5.

3.1 Horizontal Manhole Axis Condition (φ)

The first parameter to be identified is the angle of rotation about the Z_w axis, φ . The proposed method is divided into three main steps. First, the manhole detection is conducted by object detection from the camera view. Approximately 16,000 images of round and rectangular manholes were carefully annotated. The state-of-the-art YOLOv5 [6] object detector is utilized to achieve the manhole detector. Second, the manholes with bounding box areas larger than 3500 pixel² are cropped from the dataset. Approximately 1700 cropped manhole images are pixel-labeled into two classes, or round manhole and rectangular manhole for semantic segmentation. An implementation of deep learning-based image semantic segmentation [7] is used in this study. The feature pyramid network (FPN) [8] architecture with the VGG19 [9] encoder is applied as the segmentation model. Third, ellipse estimation is conducted. An ellipse detection algorithm is implemented based on the method proposed by Xie

Fig. 5 Top-view transformation process



and Ji [10]. This method takes advantage of the major axis of an ellipse to find the ellipse parameter fast and efficiently. A one-dimensional accumulator array is used to accumulate the length information for the ellipse’s minor axis. The Canny edge detector is applied to the manhole semantic segmentation after converting the image into grayscale. Then the ellipse detection is implemented, and the ellipse angle orientation φ is determined. The process is showed in Fig. 6.

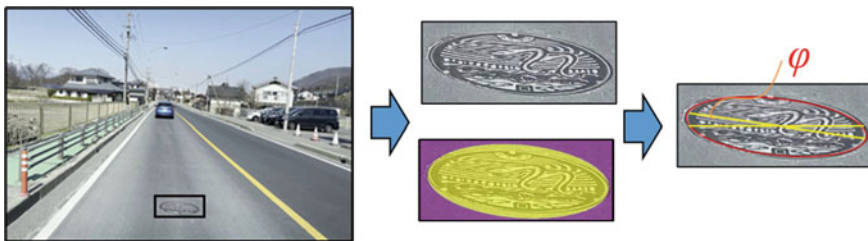


Fig. 6 Manhole object detection (left). Semantic segmentation (middle). Ellipse detection (right)

3.2 Parallel Lane Line Condition (F)

After the parameter φ is identified, f and θ initial values are assumed and transformed coordinates were calculated using Eqs. (2) and (3). Then the parallel lane line condition is verified. Parallel lane line condition is selected because this condition can be achieved based solely on the f parameter. An object detection method is developed for straight lines detection to test the parallel lane line condition. Four types of road lane lines are defined as straight left, straight right, curve left, and curve right. Each class and its corresponding annotation are illustrated in the examples in Fig. 7. Approximately 8000 images of 640×640 pixels are prepared as the dataset, and the bounding boxes were carefully annotated. The state-of-the-art YOLOv5 [6] object detector is utilized for this road straight lane lines detection.

The four coordinates of the bounding box for each detected object were obtained. Then, only the straight left and straight right classes are chosen as candidates. The straight lane lines are processed by drawing a line connecting the bottom-left with the top-right corner of the bounding box for the straight left class and the bottom-right with the top-left corner for the straight right class. In cases where multiple left or right straight lane lines are detected, the line with the endpoint nearest to the bottom-left for the left straight lane line and bottom-right for the straight right lane line will be selected as shown in Fig. 7.

After the lane lines were detected, two points were selected from each lane at a specified y coordinate. The four points obtained are: (x_1, y_1) , (x_2, y_2) , (x_3, y_2) , and (x_4, y_1) as shown in Fig. 8 (left). By setting an initial value to f and θ , transformed coordinates (x'_1, y'_1) , (x'_2, y'_2) , (x'_3, y'_2) , and (x'_4, y'_1) can be calculated from Eqs. (2) and (3) as shown in Fig. 8 (right). Then the slope is calculated for the left and right lane lines after transformation, which are m'_1 and m'_2 respectively. The parallel lane line condition would be $m'_1 = m'_2$.



Fig. 7 Four classes for road lane line detection

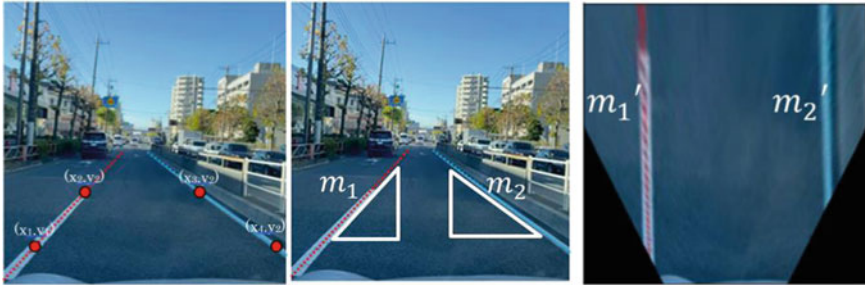


Fig. 8 Road lane lines detected after post-processing

3.3 Circular Manhole Condition (ϕ)

The aspect ratio of an image is defined as the ratio of the width to the height. When resizing an image or performing a perspective transform, ignoring the aspect ratio of an image can lead to resized images that look distorted, squished, and crunched. After the transformation of images to top-view, the consistent aspect ratio is not automatically adjusted. The images produced can have different scaling in x and y directions. Road information such as the manhole with a known aspect ratio was used for scaling in x and y directions. The same process from Sect. 3.1 was used. After the manhole is detected using object detection and semantic segmentation, top-view transformation is performed, and the resulting manhole image is obtained. The ellipse detection algorithm is then applied to the transformed image, and the ellipse parameters a, b (where a is the radius of the major axis of the estimated ellipse and b is the radius of the minor axis) and orientation is obtained. The transformation is calculated for a range of θ values. The range is determined based on previous experiments (e.g., θ range is set to 25° – 35° at an interval of 1 degree). For each θ , a corresponding f value is calculated to comply with the parallel lane line condition. Then the θ that produced the transformation that meets the condition $a/b \leq 1.05$ or the θ that produced the closest the ratio to 1.0 is selected. The process is showed in Fig. 9.



Fig. 9 Manhole semantic segmentation (left). Top-view manhole segmentation (middle). Ellipse detection (right)

3.4 Vertical Lane Line Condition ($x - x_0(d)$)

After the camera parameters, f and θ were obtained, these parameters are applied to all the frames extracted from the same measurement. During measurement, the camera position with respect to the road may be offset from the center of the road, and the top-view image will produce inclined lanes. The condition is corrected by adjusting the position of the camera along the x -axis, $x - x_0(d)$. The origin axis is adjusted until the condition $x'_1 = x'_2$ and/or $x'_3 = x'_4$ is achieved. This process is repeated for all extracted frames. Figure 10 shows the same frame extracted from the video; the left one has no adjustment (i.e., $x_0(d) = 0$) while the right one has the shifting of $x - x_0(d)$. Each frame will produce slight to moderate adjustment, and this is dependent on how the driver positions within the lane.

After all the parameters were identified, the road top-view image is produced, as shown in Fig. 11. The quality of the image on the farther part from the camera has poor resolution, and crack evaluation can be complex. Hence, a good resolution portion of the image was used, and an image stitching algorithm is implemented.

4 Image Stitching

From the transformed top-view images, the crack ratio can now be calculated based on the definition but actual length scale may not be known. Also, image resolution from the top-view images becomes very poor at the farther part of the image. Thus,

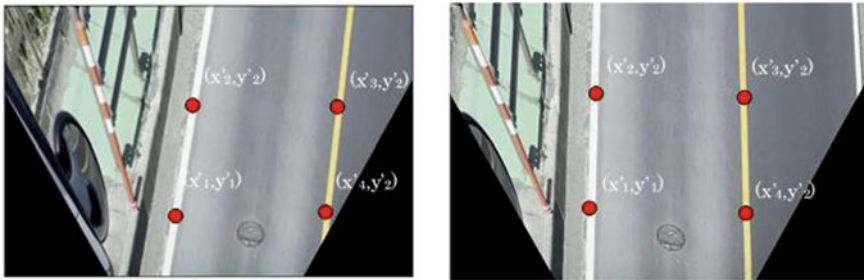
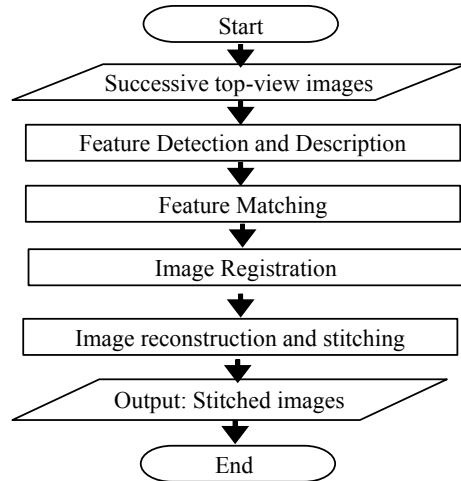


Fig. 10 Inclined road after transformation (left). Straight lane lines after adjustment (right)



Fig. 11 Road top-view image

Fig. 12 Image stitching process



an image stitching algorithm is proposed to calculate the pixel-to-distance ratio from the transformed top-view images and produce fine resolution images for crack ratio calculation. Successive frames were extracted from the measurement video at a specified distance interval based on the GPS information. The basic structure of a stitching algorithm is shown in Fig. 12.

4.1 Feature Detection and Description

The first step in the image stitching algorithm is to extract and match features between all the images. The features KAZE [11] and A-KAZE [12] based on the calculation of the determinant of Hessian Matrix in the nonlinear scale space were used. A-KAZE means Accelerated-KAZE improves upon the KAZE features to dramatically speed up the calculations by introducing Fast Explicit Diffusion (FED) schemes embedded in a pyramidal framework. It was observed that the A-KAZE feature detection provided similar results with SIFT and SURF algorithms but at a much faster rate.

4.2 Feature Matching

Once the features have been extracted, features from the successive images are matched to each other. First, a Brute Force Matcher [13] is used for matching the features of the first image with another image. It takes one descriptor of the first image and matches all the descriptors of the second image, and then it goes to the second descriptor of the first image and matches all the descriptors of the second image

and so on. The characteristics of each corresponding descriptor are compared. Each comparison gives a distance value, and the best result is considered to be a match. After obtaining the matches produced by the Brute-Force matcher, the k -nearest neighbor (k -NN) algorithm is used to return the k best matches (we use $k = 2$) [14]. David Lowe's ratio test is used to increase the probability that a match is correct and to get rid of the points that are not distinct enough [15]. Lowe's test checks that the two distances are sufficiently different by taking the ratio of the distance from the closest neighbor to the distance of the second closest. If they are not, then the keypoint is eliminated and will not be used for further calculations (we use Lowe ratio = 0.75).

4.3 Image Registration

Features matched from both images can now be used to find the perspective transformation of that object. The technique discussed in Sect. 4.2 using four correct points is used to find the transformation, but there can be some possible errors while matching, which may affect the result. Random sample consensus (RANSAC) is used to avoid errors. RANSAC can separate feature matches that are geometrically consistent called inliers and those inside the area of overlap but not consistent called outliers. A threshold is set as a maximum allowed reprojection error to treat a point pair as an inlier or an outlier (we use threshold = 4). This step produces four pairs of points each and is used to estimate the homography matrix as discussed in Sect. 4.3. The quality/goodness of the computer homography is calculated based on the number of inliers from the RANSAC algorithm. The best subset is then used to produce the homography matrix. After top-view transformation, it is assumed that the resulting images are from the same plane. With this assumption, the calculated homography matrix is in the form of a 3×3 matrix as in Eq. (4). From the assumption that the successive frames are obtained from a car moving only along the road, the homography matrix is reduced to the translation matrix. Wherein R is the rotation matrix, T is the translation matrix, and P is the scaling matrix.

$$H = \begin{bmatrix} R_{11} & R_{12} & T_1 \\ R_{21} & R_{22} & T_2 \\ P_1 & P_2 & 1 \end{bmatrix} = \begin{bmatrix} 1 & 0 & T_1 \\ 0 & 1 & T_2 \\ 0 & 0 & 1 \end{bmatrix} \quad (4)$$

Since the aspect ratio of the top-view is consistent on both sides, the pixel-to-distance ratio for the x and y-axis can be calculated from Eq. (5), where T is the pixel offset between two frames and $d_i - d_{i-1}$ is the GPS distance between the frames.

$$\text{pixel-to-distance ratio, } r_i = \frac{T_{1n}}{d_i - d_{i-1}} \quad (5)$$

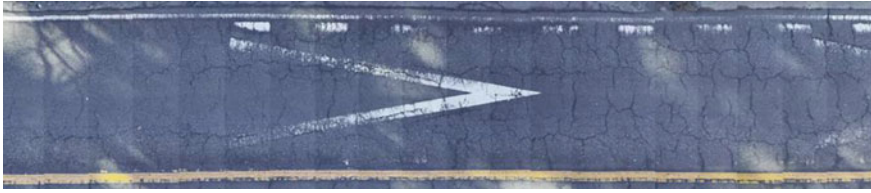


Fig. 13 Fine resolution road top-view image

4.4 Image Reconstruction and Stitching

Once the homography matrix is calculated, the images are transformed and stitched together. Road top-view image from the high-resolution parts of the frames was stitched and produced a fine-resolution image for 20 m road segment for road crack evaluation as shown in Fig. 13.

5 Conclusions

An automatic top-view transformation and image stitching method are proposed for road crack evaluation. Straight lane lines detection and manhole detection through object detection and semantic segmentation are developed for the camera parameters calibration. The parameters are optimized such that the detected lane lines are parallel and the cropped round manhole is circular after the top-view transformation. After successful frame transformation, the successive frames were stitched. AKAZE feature detection algorithm was used, which is based on the determinant of the Hessian Matrix. Features detected from the images were matched using the k-nearest neighbors algorithm (k-NN), and the suitable matches are filtered using the Lowe's ratio test to obtain the best match. Random sample consensus (RANSAC) was used to select a set of inliers compatible with a homography between the images. After that, the homography matrix was calculated. The translation offset from the matrix was obtained along with the GPS information when extracting the frame. Then, the pixel-to-distance ratio is calculated. A fine resolution image was produced that can be used for the evaluation of road cracks. The effectiveness and robustness of the proposed methods are verified by a large number of practical road images. For the aspect ratio, manholes were used, but other known pavement features and markings can be used as a reference.

Acknowledgements A part of this research is supported by a research fund by Kanto Regional Development Bureau, MLIT.

References

1. Ministry of Land, Infrastructures, Transport and Tourism (2017) Pavement Maintenance in Japan. Road Conference 2017 International
2. Japan Road Association (2010) Manual for Pavement Testing Method
3. Smart City Research Institute (2021) Crack ratio classification by object detection. <https://www.smc-tech.com/en/>
4. Zhang Z (2000) A flexible new technique for camera calibration. *IEEE Trans Pattern Anal Mach Intell* 22(11):1330–1334. <https://doi.org/10.1109/34.888718>
5. Tanaka S, Yamada K, Ito T, Ohkawa T (2011) Vehicle detection based on perspective transformation using rear-view camera. *Int J Vehic Technol* 2011:1–9. <https://doi.org/10.1155/2011/279739>
6. Jocher G, Stoken A, Borovec J, et al (2021) Ultralytics/yolov5: “V4.—Activations, weights & biases logging, PyTorch Hub integration.” Zenodo. <https://doi.org/10.5281/zenodo.4418161>
7. Yakubovskiy P (2021) Qubvel/segmentation_models. https://github.com/qubvel/segmentation_models
8. Lin TY, Dollár P, Girshick R, He K, Hariharan B, Belongie S (2017) Feature pyramid networks for object detection. [Cs]. <http://arxiv.org/abs/1612.03144>
9. Simonyan K, Zisserman A (2015) Very deep convolutional networks for large-scale image recognition. [Cs]. <http://arxiv.org/abs/1409.1556>
10. Xie Y, Ji Q (2002) A new efficient ellipse detection method. *Object Recognition Supported by User Interaction for Service Robots* 2:957–960. <https://doi.org/10.1109/ICPR.2002.1048464>
11. Alcantarilla PF, Bartoli A, Davison AJ (2012) KAZE Features. In Fitzgibbon A, Lazebnik S, Perona P, Sato Y, Schmid C (Eds) *Computer Vision – ECCV 2012* (Vol 7577, pp 214–227). Springer Berlin Heidelberg. https://doi.org/10.1007/978-3-642-33783-3_16
12. Alcantarilla P, Nuevo J, Bartoli A (2013) Fast explicit diffusion for accelerated features in nonlinear scale spaces. *Proceedings of the British Machine Vision Conference 2013*, 13.1–13.11. <https://doi.org/10.5244/C.27.13>
13. OpenCV modules. Accessed 16 July, 2021. <http://docs.opencv.org/3.1.0>
14. Brown M, Lowe DG (2007) Automatic panoramic image stitching using invariant features. *Int J Comput Vision* 74(1):59–73. <https://doi.org/10.1007/s11263-006-0002-3>
15. Lowe DG (2004) Distinctive image features from scale-invariant keypoints. *Int J Comput Vision* 60(2):91–110. <https://doi.org/10.1023/B:VISI.0000029664.99615.94>

Assessment of Damage in Composite Beams with Wavelet Packet Node Energy Features and Machine Learning



Yu Gu and Yong Lu

Abstract Composite structures are commonly used in bridge and building construction. A typical example is a bridge deck comprising of concrete slab and steel beam girders, with shear connectors linking the concrete slab and the steel beams to form the composite effect. The behaviour of a composite structure is dependent not only on the condition of the main constituent components, namely concrete slab and the steel beams, but also on the effectiveness of the shear connectors. In fact, the influences of damage to the main components (herein called flexural damage) and damage to the shear connectors on the overall structural performance are distinctively different. Therefore it is important that damages in a composite structure be distinguished between these two types of parameters. However, not much attention has been paid in differentiating the flexural and shear connector damages in the existing damage identification literature. In this paper we will provide an overall discussion on the distinctive effects of flexural and shear-connector damages to the rigidity and its distribution in a composite beam. A vibration based approach is then presented for the identification of the mixed presence of flexural and shear-link damage parameters by means of supervised machine learning. The wavelet packet node energy (WPNE), which has been shown to be sensitive to structural changes in previous studies, is chosen as input features. Appropriate selection of the wavelet packet transformation levels in the case using a single measurement sensor, as well as using multiple sensors, are discussed. Results demonstrate that with WPNE features combined with supervised machine learning, it is possible to differentiate and identify flexural and shear-connector damages, and hence the actual structural condition, of a composite beam.

Keywords Damage assessment · Composite beams · Flexural damage · Shear-link damage · Wavelet packet transform · Machine learning

Y. Gu · Y. Lu (✉)

Institute for Infrastructure and Environment, School of Engineering, University of Edinburgh,
Edinburgh EH9 3JL, UK

e-mail: yong.lu@ed.ac.uk

1 Introduction

Many critical structures, including road bridges and viaducts, often involve composite elements such as bridge decks. The monitoring or assessment of this type of structures is still largely based on bending deformation, which in turn depends upon the gross flexural properties: globally as flexural stiffness and locally flexural rigidity [1]. However, the correlation between the gross “flexural” stiffness and changes in the composite conditions, i.e. damage to shear connectors and bonded interface, is far more complicated than typical flexural damage such as a crack. Up to now, although there are many studies that relate to condition assessment of composite beams, there is a lack of systematic information and guidance with regard to determining damage to the shear connector properties, in addition to the more conventional flexural damage, especially in the vibration-based structural health monitoring literature.

In the present study, we will provide an overview on the distinctive effects of flexural and shear-connector damages to the rigidity and its distribution in a composite beam, and how these transpire in the changes of the natural frequencies and mode shapes. Then, a vibration-based method is proposed to identify the mixed existence of damage parameters of bending and shear connector by supervised machine learning. The wavelet packet node energy (WPNE), which has been shown to be sensitive to structural changes in previous studies [2, 3], is chosen as the input feature. Appropriate selection of the wavelet packet transformation levels in the case of using a single measurement sensor, as well as using multiple sensors, are discussed. Results demonstrate that with WPNE features combined with supervised machine learning, it is possible to differentiate and identify flexural and shear-connector damages, and hence the actual structural condition, of a composite beam.

2 General Effects of Flexural and Shear Link Damage on Stiffness Distribution, Modal Frequencies and Mode Shapes

Vibration based identification of structural damage commonly relies on the transverse vibration properties, which are effectively governed by the gross flexural rigidity and its distribution along the member length. In the case of a composite beam, the gross stiffness and its distribution are affected not only by the typical “flexural” damages such as a crack, but also by the condition of the shear connectors due to their effect on the degree of the composite effect. For a concrete slab-steel section composite beam, in general, the degradation of the shear connectors will result in a decrease in the composite effect, and thereby the gross flexural rigidity and stiffness. However, the involvement of the shear connector at a particular location is actually directly determined by the shear slip tendency at the interface between the concrete slab and the steel section, and the shear slip tendency in turn depends upon locally on the presence of the shear force and globally the effectiveness of the adjacent

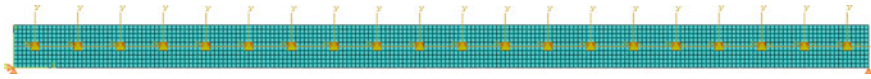


Fig. 1 FE model of a representative composite beam

shear connectors. Therefore in terms of the shear connector effect, the gross flexural rigidity at a particular location is affected not only by the connector at or closest to this location, but also by adjacent shear connectors.

Figure 1 shows a finite element model of a simple composite beam consisting of two rectangular beam sections of the equal depth of 0.05 m and width of 0.3 m, and the length of the beam is 2 m. Totally 20 discrete shear links are arranged uniformly along the beam length, and the beam is supported by pin-roller supports. The FE model uses 2000 elements of type CPS4R, with 10 layers over the beam depth. The cross-section rigidities for the top beam and bottom beam are equally $8.125 \times 10^4 \text{ N} \cdot \text{m}^2$. The density of the beam is set as 2300 kg/m^3 . The stiffness of each shear link is assumed to be 40 kN/mm according to typical shear link properties in the literature. For convenience, the shear links are numbered 1 to 20 in sequence from the left to right. For the sake of simulating the direct flexural damage, the upper part of the composite beam is equally divided into 10 segments along the length, such that direct flexural damage can be assigned by reducing the stiffness (Young's modulus) at any one or more of these segments, these segments are numbered 1 to 10 in sequence from the left to right as well for the clear demonstration.

For demonstration, two shear damage scenarios and one beam section (flexural) damage are selected to be presented here. For the first scenario, the shear links No. 5 and No. 6 are removed. For the second scenario, the shear links No. 10 and No. 11 are removed. For the third scenario, the beam stiffness of Sect. 5 is reduced to 30% of the intact stiffness.

The first mode shape curvature of these three damage scenarios are compared with that of the intact composite beam in Fig. 2. It can be clearly observed that the first mode shape curvature of the first damage scenario has a significant difference from the first mode shape curvature of the intact composite beam, and furthermore the effect extends beyond the positions where the two damaged shear links locate. On the contrary, the removal of shear links No. 10 and No. 11 influences little the mode shape curvature. In comparison, the direct damage to the beam section has an immediate effect on the mode shape curvature at the location where the flexural damage occurs.

As discussed earlier, the effect of shear links on the gross beam stiffness depends upon the internal force (shear) condition as well as the effectiveness of the adjacent shear links. It is therefore anticipated that the same shear link damage will have different effects on the gross flexural stiffness of the beam in different vibration modes. This is indeed confirmed by the FE modelling results as shown in Table 1, where the first 4 mode frequencies of these three damage scenarios are compared to the those of the intact composite beam. The shear links No. 5 and No. 6 are located at one-fourth of the beam from the left end, which is almost at the displacement peak

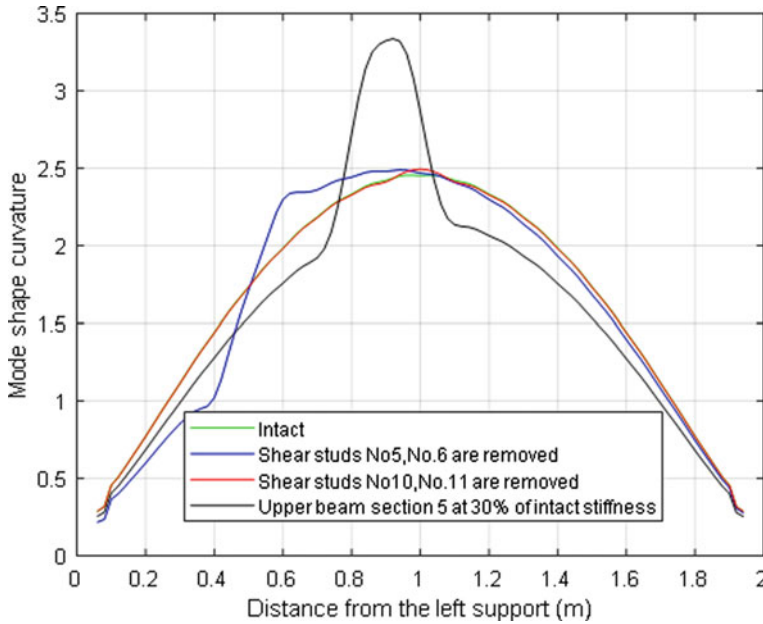


Fig. 2 Comparison of the first mode shape curvature of 4 scenarios

Table 1 Mode frequency comparison between selected damage scenario and intact situation

	Intact (Hz)	S5, S6 = 0	Percentage difference to the intact situation (%)	S10, S11 = 0	Percentage difference to the intact situation (%)	Section 5 at 30% of intact stiffness (Hz)	Percentage difference to the intact situation (%)
Mode 1	28.59	27.62 Hz	-2.10	28.59 Hz	0.00	27.21	-4.83
Mode 2	90.83	89.70 Hz	-0.07	87.77 Hz	-3.37	90.18	-0.72
Mode 3	184.5	184.3 Hz	-1.14	184.3 Hz	-0.11	178.7	-3.14
Mode 4	310.7	310.0 Hz	-1.29	306.6 Hz	-1.32	305.1	-1.80

of mode 2. Hence, despite the significant influence on the first mode, the influence of the damage is quite limited for mode 2. The shear links No. 10 and No. 11 are located at the midsection of the beam, which is at the displacement peak of mode 1 and mode 3 and inflection points on mode 2 and mode 4. Hence the percentage difference to the intact beam are almost zeros under mode 1 and mode 3, but the difference is significant under mode 2 and mode 3. On the other hand, in the case of beam section (flexural) damage, as the damage is located near the middle of the beam, the difference brought by the beam section damage is significant in mode 1 and mode 3.

The above observations indicate that the effect of damage to the shear connectors on the overall structural performance is distinctively different from flexural damage. In spite of these, damages to shear links still tend to present distinctive patterns, albeit more complex, in the mode shape and modal frequency information. This suggests that transverse vibration data should contain pertinent information that could allow the separation of the two groups of parameters in a composite beam. In this study, the wavelet packet node energy (WPNE) is incorporated with a neural network to differentiate and identify flexural and shear-connector damages.

3 Overview of Wavelet Packet Transformation and WPNE Features

3.1 Wavelet Packet Transform

By recursively filtering and decimating a signal, the Wavelet packet transform (WPT) separates it into successive low- and high-frequency components [4]. As an example, the binary tree up to the third level wavelet packet decomposition (WPD) of the time-domain signal $f(t)$ is shown in Fig. 3. After the decomposition of the j -th level, the original signal $f(t)$ can be constructed by the sum of 2^j components as:

$$f(t) = \sum_{i=1}^{2^j} f_j^i(t) \tag{1}$$

where $f_j^i(t)$ is the wavelet packet component signal that can be expressed by a linear combination of wavelet packet functions as follows:

$$f_j^i(t) = \sum_{k=-\infty}^{\infty} c_{j,k}^i \psi_{j,k}^i(t) \tag{2}$$

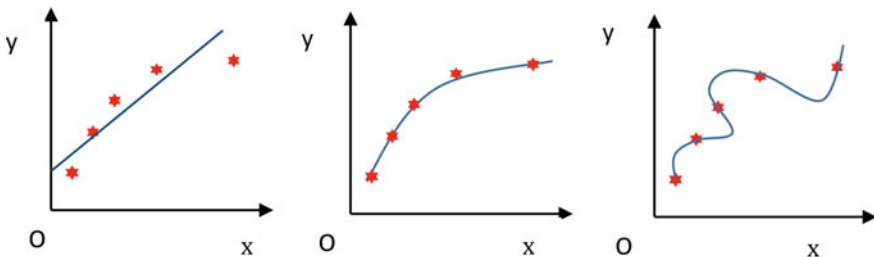


Fig. 3 Fitness of a model on a sample set of data. **a** Underfitting (high bias) using a linear model. **b** Adequate fitting using a quadric model. **c** Overfitting (high variance) with a high order model

where i, j and k are integers, which are defined as the modulation, scale and translation parameter, respectively $c_{j,k}^i$ and $\psi_{j,k}^i(t)$ are defined as wavelet packet coefficients and wavelet packet functions. The wavelet packet coefficients $c_{j,k}^i$ can be obtained from:

$$c_{j,k}^i = \int_{-\infty}^{\infty} f(t)\psi_{j,k}^i(t)dt \tag{3}$$

The wavelet packet function is defined as:

$$\psi_{j,k}^i(t) = 2^{j/2}\psi^i(2^j t - k) \tag{4}$$

with $\psi^0(t) = \varphi(t)$ and $\psi^1(t) = \psi(t)$. The first wavelet $\psi^1(t)$ is called the mother wavelet function [4]. One of the widely used mother wavelet functions is Daubechies wavelet. And Daubechies is continuously differentiable, which makes it a good smoothing function for signal analysis and effectively analyses the vibration signal. In the present study, Daubechies 3(DB3) is adopted in the wavelet packet transform operation.

The wavelets ψ^i are obtained from the following recursive relationships:

$$\psi^{2i}(t) = \sqrt{2} \sum_k h(k)\psi^i(2t - k) \tag{5}$$

$$\psi^{2i+1}(t) = \sqrt{2} \sum_k g(k)\psi^i(2t - k) \tag{6}$$

The discrete filters $h(k)$ and $g(k)$ are quadrature mirror filters associated with the scaling function and the mother wavelet function.

Every component in the WPD tree can be regarded as the output of a filter, which is tuned to a specific basis function. At the top of the WPT tree with a low decomposition level, better resolution in the time domain can be obtained, but the resolution in the frequency domain is poor. At the bottom of the WPD tree which is a relatively high decomposition level, the resolution in the frequency domain is good, but the time domain resolution is poor. That is to say, wavelet packet transform can be a multi-level signal band division in the whole band, thereby improving the time–frequency domain resolution. Therefore, the frequency band signal contains abundant information of the original signal [5].

3.2 Wavelet Packet Component Energy

Yen and Lin [6] defined the wavelet packet node energy (WPNE) index and it measures the signal energy contained in certain specific frequency bands. The total signal energy E_f is defined as:

$$E_f = \int_{-\infty}^{\infty} f^2(t)dt = \sum_{m=1}^{2^j} \sum_{n=1}^{2^j} \int_{-\infty}^{\infty} f_j^m(t)f_j^n(t)dt \tag{7}$$

Substituting Eq. (2) into Eq. (7) and using the orthogonal condition when $m \neq n$:

$$\psi_{j,k}^m(t)\psi_{j,k}^n(t) = 0 \tag{8}$$

Gives

$$E_f = \sum_{i=1}^{2^j} \int_{-\infty}^{\infty} f_j^i(t)^2 dt \tag{9}$$

It can be seen that the component signal $f_j^i(t)$ is a superposition of wavelet functions $\psi_{j,k}^m(t)$ of the same scale as j but translated into the time domain ($-\infty < k < \infty$). This indicates that the component $E_{f_j^i}$ is the energy stored in the component signal frequency band $f_j^i(t)$ determined by the wavelet function $\psi_{j,k}^i(t)$, which is evaluated by:

$$E_{f_j^i} = \int_{-\infty}^{\infty} f_j^i(t)^2 dt \tag{10}$$

The WPNE features used in the presented study are all normalized WPNE features, which is the percentages of energy corresponding to the terminal nodes of the tree:

$$E_{f_j^i}^{\%} = \frac{E_{f_j^i}}{E_f} \tag{11}$$

4 Using WPNE Based Neural Network for Identification of Damage in Composite Beams

The artificial neural network (ANN) is a powerful supervised learning algorithm. Inspired by the function of the human brain, ANN consists of a group of artificial neurons (called processing units) connected with other neurons, and these neurons depend on the weights of the neural network, and these weights represent the connections between the neurons, which determine the effect of one neuron on another neuron. Typically an ANN consists of three kinds of neuron layers, namely the input layer, one or more hidden layers, and one output layer. The neurons in the input layer receive the data and transfer them to neurons in the first hidden layer through the weighted links. The data is processed mathematically, and the result is transmitted to the neurons in the next layer. The output of the network is produced by the neurons in the last layer.

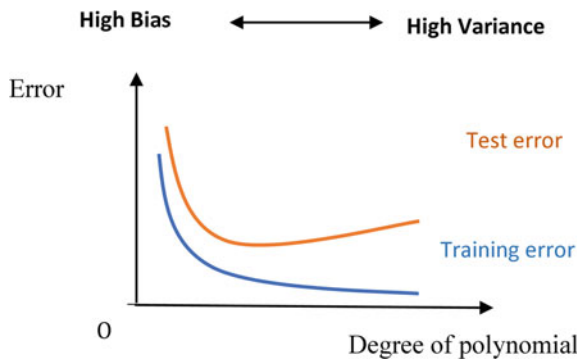
The goal of a neural network is to have a final model, which performs well in both the training dataset and test dataset. The learning and generalization ability are two concepts to describe the performance of a neural network model. Learning capability describes how well can a neural network perform in a training dataset, and generalization capability describes how well can a neural network predict the unseen data. And bias and variance play an essential role in understanding the fundamental issue of learning and generalization in neural network modelling.

Dietterich and Kong [7] give detailed explanations on the concept of “Bias” and “Variance” from statistical and machine learning perspectives. In machine learning, “Bias” is the amount that a model’s prediction differs from the target value, “Variance” describes how much a random variable differs from its expected value. In a “high bias” situation, the hypothesis space of an improper absolute bias does not contain any good approximations to the objective function. In a “high variance” situation, there is a good approximation to the target function in the hypothesis space; however, the expected value of the squared difference between any particular hypotheses and the average hypothesis is large.

A case of using a polynomial function to fit 5 samples of data on a quadric line (the red points) is used to demonstrate these concepts, as shown in Fig. 3. In Fig. 3a, it is too simple of using a linear model, which is represented by the blue line, to learn and predict these data. Increasing the number of data samples will not improve the training and predictive performance of the model. Conversely, in Fig. 3c, the chosen model represented by the blue line is too complex, although all of the 5 points are located on the predicted line, which means training performance is good, the predictive performance could be poor. As it is shown, the model cannot predict more data that follow a quadric line. Therefore, a bias-variance trade-off is needed to yield a suitable model [8], for example, a quadratic model in Fig. 3b is suitable to train and predict the object function.

According to these concepts, it can be understood that the performance of bias and variance problems has different features under the same training samples size, as schematically illustrated in Fig. 4.

Fig. 4 Error for test and training versus degree of the polynomial



For a given structure of a neural network, the required model complexity, as represented by the input–output configurations, fundamentally depends on the inherent complexity of the physical problem, as manifested in the implicit relationship between the selected set of input and the output parameters. Since the output configuration is usually pre-defined in accordance with the particular damage identification approach, the neural network model complexity is mainly controlled by the input layer configuration and the input information used. Therefore in the present study, the neural network model's complexity is adjusted by means of adjustment to the input layer configuration and the input data.

Before adjusting the model complexity, the bias and variance situations are diagnosed. To do so, the test error and training error are compared using different sizes of the dataset for observing how they change with the increase of the dataset size. For a high bias situation, the test and training error will not be reduced with increasing the training set size. On the other hand, for a high variance situation, the training set size needs to be larger than that for a proper fit situation to bring the test error down to the training error level. Therefore, it can be understood that the required number of data samples can be minimized by finding a proper degree of complexity of the model that would yield a desirable fitness state.

4.1 Damage Assessment Procedure

In the present study, the degree of damage in individual elements of a structure is determined directly as the output layer of the neural network model. In this way, the location and degree of damage are determined at the same time. The WPNE features extracted from the translational acceleration signals are employed as the input layer of the neural network model. For the network training, the “Bayesian regularization” algorithm, which is known to be robust, is employed.

The wavelet packet transform (WPT) contains a complete decomposition at every level. However, a higher level of decomposition can achieve a higher resolution in the frequency region. Subsequently, the wavelet packet node energy (WPNE) calculated from these specific frequency bands have a higher resolution as well, which naturally could carry more information. However, higher level decomposition could be more susceptible to small disturbances such as measurement errors. Therefore, the choice of an appropriate decomposition level is a subject that requires careful consideration. A strategy using a trial process based on the bias and variance evaluation is proposed in the present study. In this process, first, a wavelet packet decomposition level is selected. Different training set sizes are then chosen to train the neural network model using the WPNEs at the selected decomposition level, and the corresponding training and test error are compared. If both errors are found to be large even with a sufficient training dataset, the neural network model is judged to suffer from a high bias problem. On the other hand, if the training error is small but the test error is large even with a sufficient training dataset, the model suffers from a high variance problem.

If the model is found to suffer from high bias, the model complexity degree should be increased, which means a deeper decomposition level is needed. On the contrary, if the model is found to suffer from high variance, the model complexity degree as controlled by the decomposition level needs to be decreased.

Besides the selection of the WPT decomposition level from a single sensor to adjust model complexity degree, the fused WPNE information obtained from multiple sensors located at different locations can be used to form the input of the neural network, which provide another dimension to adjust the model's complexity.

4.2 Numerical Simulation Study on Composite Beam

The previously introduced FE model is used here to demonstrate the damage identification procedure. To extract the feature of wavelet packet node energy, an excitation is assumed to be an impact force of 100 N applied at the position of 0.35 m from the right end. Two accelerometers, sensor 1 and sensor 2, are set at the position of 0.6 m and 1.2 m from the left end of the beam bottom side. To excite a wide frequency range, a short pulse is employed, which has a triangle shape with a duration of 0.0016 s. For the acceleration responses, the "recorded" time duration is 2 s, and the sampling rate is set at 1250 Hz, which is found to be sufficient to cover the first 4 modes of vibration of the composite beam.

For demonstration purpose, the scenario with a single beam flexural damage plus a single shear link damage is investigated herein. As mentioned earlier, the upper part of the composite beam is equally divided into 10 segments, and similarly, the 20 shear links are divided into 10 groups, each containing two adjacent shear links of the same condition.

For the damaged samples, only half of the beam is involved in the assessment, which means there are 5 damage cases in shear links groups and 5 damage cases in the beam sections. Subsequently, there are $5 \times 5 = 25$ combinations of one shear damage plus one beam section damage scenarios. The stiffness of the "damaged" shear links ranges from 5 to 95% of the intact shear stiffness, with 5% representing effectively a total damage. For the beam section damage, the stiffness of the "damaged" beam section ranges from 30 to 95% of the intact beam section. The interval stiffness for damage section are set as 20%, 10%, 5%, respectively. Hence, there are 3, 7, 14 damage levels for each beam damage position and 4, 9, 19 damage levels for each shear damage position respectively. In correspondence, 300, 1575, 6650 cases of damage scenarios are generated respectively to form the training and test datasets.

Level 6 to level 8 of WPT decomposition are carried out on the acceleration signals acquired from sensor 1. Correspondingly, 64, 128, 256 component energy values are used as the input layer of the neural network. The hidden layer is assigned 50 neurons. The 5 groups of shear link stiffness plus the 5 beam section stiffness value are used as the output of the neural network.

The mean squared errors for the training and test datasets with different levels of WPT decomposition are presented in Fig. 5, where x-axis is the number of samples,

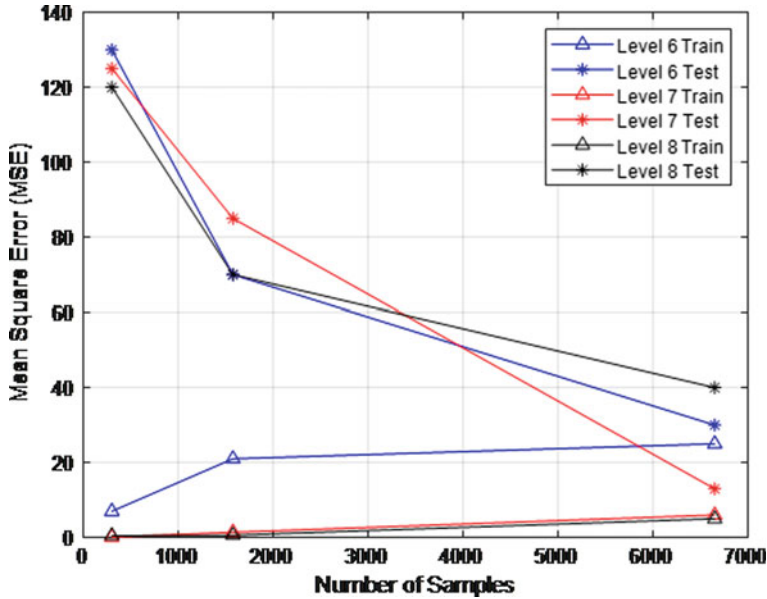


Fig. 5 Learning curve for training and test dataset of assessing single damages using different decomposition levels

and y-axis is the mean square error (MSE). The mean square error is the average squared difference between outputs and targets, and it is defined as follows:

$$MSE = \frac{1}{n} \sum_{i=1}^n (Y_i - \hat{Y}_i)^2 \tag{12}$$

where n is the number of data points, Y_i denotes the target values, which represent the percentage of target section stiffness to the intact stiffness, \hat{Y}_i is predicted values, which represent the percentage of neural network predicted section stiffness to the intact stiffness. Therefore, the smaller the MSE, the better the performance of the neural network is. In this study, MSE is one of the main indices to measure the performance of the neural network model, and a satisfying level is chosen as 10 (which is roughly equivalent to an absolute stiffness error of about 3%). When the MSE is lower than 10, the neural network model is considered to have a satisfactory prediction.

It can be observed from Fig. 5 that the MSE trend of the training dataset and test dataset for level 6 to level 8 are typical “high bias”, “just-fit” and “high variance” situations, respectively. When using the WPNE data from level 6 decomposition to train the neural network, it can be seen that with an increase of dataset size, the MSE for the training dataset gradually increases and maintains at an unsatisfied level, exceeding 30. Conversely, when using the WPNEs of level 8 decomposition,

although the MSE for the training dataset is low, the MSE for the test dataset is over 40 when the dataset size reaches 6650. Therefore, to further decrease the test error, more data samples are needed. Different from these two cases, the MSE of the test data set using level 7 WPNEs information can be reduced to 13, and the MSE of train data is still lower than 5. This indicates the fact that the required number of data samples can be minimized by finding a proper fit situation of complexity.

Figure 6 shows the performance of the neural network model, where x-axis represents the target stiffness, and y-axis represents the output of the neural network model. Although a few points were incorrectly predicted, the regression R values of the training and test data sets were 0.99 and 0.98, respectively, and this means that most of the results were correctly predicted.

To have a more detailed observation, a comparison between target and predicted stiffness values of a selected damage scenario in the test data set is shown in Fig. 7. In this damage scenario, the stiffness of the 3rd shear link group and 3rd beam section both were reduced to 40% of the respective intact stiffness, as shown with the blue

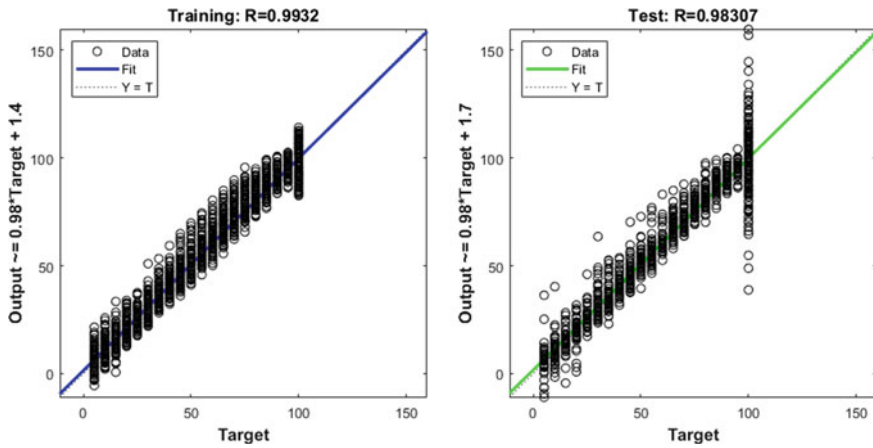


Fig. 6 Regression plot of NN results for one shear-link plus one flexural damage using WPNE of level 7: Left = Training dataset; Right = Test dataset

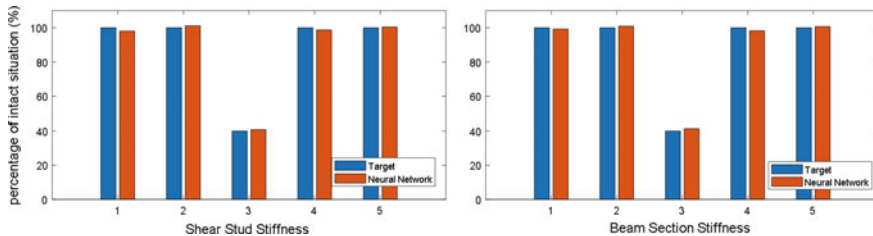


Fig. 7 Comparison between target and predicted stiffness values of selected damage scenarios in test data set

bars. The predicted stiffness values are shown in orange bars. All the stiffness values including the damaged shear links and the damaged beam section are predicted accurately. This indicates that using the proposed WPNE-based neural network it is possible to differentiate and identify flexural and shear-connector damages in a composite beam.

Furthermore, using the fused WPNEs information acquired from sensor 1 and sensor 2 with decomposition Level 7 as the input layer of the neural network can further improve the test (prediction) performance, with the MSE for the test dataset dropping from 13 to 8. This indicates that a combination of WPNE data from different sensors tend to bring more information pertaining to damage and hence provides further scope for improving and optimizing the use of WPNE data and the performance of the neural network.

5 Concluding Remarks

The distinctive effects of flexural and shear-connector damages on the rigidity and its distribution in the composite beam, and therefore on the transverse vibration properties, have been investigated. It is found that shear link damage has an extended effect in a wider area (beyond the damaged shear link location) and the equivalent effect on the gross flexural stiffness also depends on the deformation (mode) shapes. Therefore, the shear connectors on the overall structural performance are distinctively different from flexural damage. As such, the transverse vibration data can be deemed to contain pertinent information that could allow the separation of the two groups of parameters in a composite beam. A WPNE based machine learning approach has been put forward for the identification of the mixed flexural and shear link damages in composite beams. Results show the effectiveness of the proposed method is promising, with the damages in shear links and beam section being identified with good accuracy. From the numerical investigations, it is also shown that the strategy for selection of decomposition level via examining bias and variance is workable and it can help achieve good learning and generalization performance. Further study will be required to investigate the robustness of the proposed method against noise, and to that end, physical experiments on composite beams should be conducted.

References

1. Avci O, et al (2021) A review of vibration-based damage detection in civil structures: from traditional methods to Machine Learning and Deep Learning applications. *Mech Syst Signal Process.* 147: p. 107077
2. Sun Z, Chang C (2002) Structural damage assessment based on wavelet packet transform. *J Struct Eng* 128(10):1354–1361

3. Diao YS, Li HJ, Wang Y (2006) A two-step structural damage detection approach based on wavelet packet analysis and neural network. In: 2006 International conference on machine learning and cybernetics. IEEE
4. Peng X-L, Hao H, Li Z-X (2012) Application of wavelet packet transform in subsea pipeline bedding condition assessment. *Eng Struct* 39:50–65
5. Chen G, Zheng Q (2018) Online chatter detection of the end milling based on wavelet packet transform and support vector machine recursive feature elimination. *Int J Adv Manuf Technol* 95(1):775–784
6. Yen GG, Lin K-C (2000) Wavelet packet feature extraction for vibration monitoring. *IEEE Trans Industr Electron* 47(3):650–667
7. Dietterich TG, Kong EB (1995) Machine learning bias, statistical bias, and statistical variance of decision tree algorithms. Citeseer
8. Mehta P et al (2019) A high-bias, low-variance introduction to machine learning for physicists. *Phys Rep* 810:1–124

Scalable and Probabilistic Point-Cloud Generation for UAS-Based Structural Assessment



Qingli Zeng and ZhiQiang Chen

Abstract Many critical civil structures serve in areas that are subject to extreme events, such as earthquakes and tropical cyclones. To achieve systematic resilience (hence rapid restoration to its designed functionality), the critical action is to assess the structures rapidly and intelligently. As machine vision systems become more low-cost and cognitively powerful as they are equipped to many unmanned vehicles, robotics, and wearable platforms, machine vision systems can be deployed autonomously to explore, scan, and assess the integrity of structures. The reality is that one cannot expect a single imaging campaign can accomplish the inspection task once and for all. More realistically, such imaging activities need to be conducted on an event-driven or as-need basis in the service life of a structure. In this work, by combining visual simultaneous localization and mapping (SLAM) and Structure-from-Motion algorithms in a wearable augmented reality system (HoloLens), we propose a scalable and probabilistic point-cloud generation procedure. With this procedure, the point cloud as a probabilistic occupancy model is dynamically updated by integrating visual SLAM and SFM point clouds. We vision that this procedure can be further semantically classified and combined with a building information model to facilitate digital twin generation.

Keywords Visual—slam · SFM · Point cloud · COLMAP · HoloLens

1 Introduction

SLAM is the abbreviation of simultaneous localization and mapping; it is a technique for estimating the movement of the sensor and reconstructing the structure in an

Q. Zeng

Department of Civil and Mechanical Engineering, University of Missouri - Kansas City, Kansas City, MO, USA

Z. Chen (✉)

School of Computing and Engineering, University of Missouri - Kansas City, Kansas City, MO, USA

e-mail: chenzhiq@umkc.edu

unknown environment. SLAM using cameras is called visual SLAM due to it is based only on visual information. The origin of Monocular SLAM is Andrew Davison's MonoSLAM [1] based on the EKF model. Later, his teacher in Oxford, David Murray, published Keyframe based PTAM [2], which is the cornerstone of most SLAM systems today. There are two popular monocular SLAMs in the last two years. One is LSD-SLAM [3] from TU Munich. This work is not based on image feature point matching and motion estimation, but directly extracts regions with obvious gradient changes in the contrast image and create a semi-dense map. The second one is ORB-SLAM [4] and ORB-SLAM2 [5] of University of Zaragoza. This work is essentially not different from PTAM, but the author has made the system the most functional at present through strong code implementation capabilities. ORB-SLAM uses high-speed ORB image feature points, adds the important re-localizing and loop closure modules in the SLAM system, and uses g2o to minimize global errors.

Structure from motion (SFM) is a popular strategy for 3D reconstruction from a collection of unordered images. SFM methods can be divided into incremental, global, hybrid, hierarchical, and semantic-based SFM (Semantic SFM). Incremental SFM method [6–12] is currently the most widely used method. Most methods are based on the pipeline in [6] and have been improved. We chose COLMAP [12] as the SFM method which was published in CVPR in 2016 by J. L. Schonberger. COLMAP has been improved for the steps of triangulation and BA in incremental SFM, which can significantly improve the robustness and reconstruction integrity of SFM.

In the past few decades, the structure of motion (SFM) and visual SLAM technology has aroused great interest in the computer vision and robotics communities. Many variants of these technologies have begun to have an impact on a ubiquitously range of applications, including robotics and UAV technology and augmented reality. Therefore, it makes sense to compare the point cloud generated by visual slam and SFM. As we all know, HoloLens is an excellent AR platform developed by Microsoft, and the role of visual slam in AR is pivotal, which means HoloLens is an excellent platform for studying visual slam. The visual slam algorithm used by HoloLens is a highly customized version of PTAM, but the algorithm is not open source yet.

However, despite some remarkable results in many areas, most SFM and visual SLAM technologies operate on the assumption that the observed environment is static. However, when facing moving objects, the accuracy of the entire system may be threatened. In this article, we introduce for the first-time research of visual SLAM and SFM technologies for operating in two different motion scenarios.

In general, we use HoloLens as an input device to obtain a point cloud through the internal visual slam algorithm of HoloLens. Moreover, we use HoloLens as a recording device to generate a point cloud using the COLMAP algorithm and compare two different workflows generated in the same motion scenario. Additionally, compare the point clouds generated by the same workflow in different motion scenarios.

2 Experiment

2.1 Point Cloud Extraction

a. From HoloLens

Visual slam is regarded as the most important part of the AR algorithm leads to HoloLens, as an excellent AR platform, can provide an exceptionally remarkable real-time point cloud. In this article, we used the Microsoft HoloLens camera and its internal visual slam algorithm to extract the real-time point cloud, as shown in Fig. 1. It can be seen from the figure that we have chosen an indoor scene as our research object since HoloLens works better indoors.

b. From COLMAP

HoloLens is equipped with many cameras, so it is also used as an excellent recording device. In the point cloud extraction part of SFM, we choose to use the COLMAP algorithm to generate the point cloud of the recorded video. Figure 2 shows the result of point cloud extraction.

Fig. 1 Real-time point cloud of the building with HoloLens

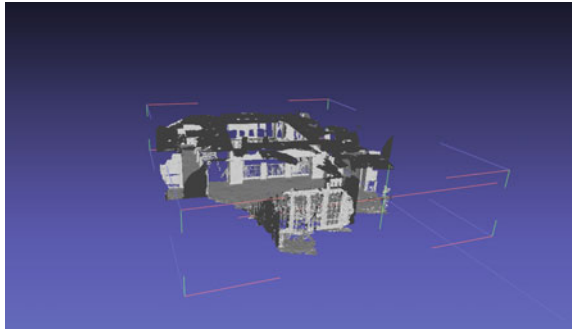
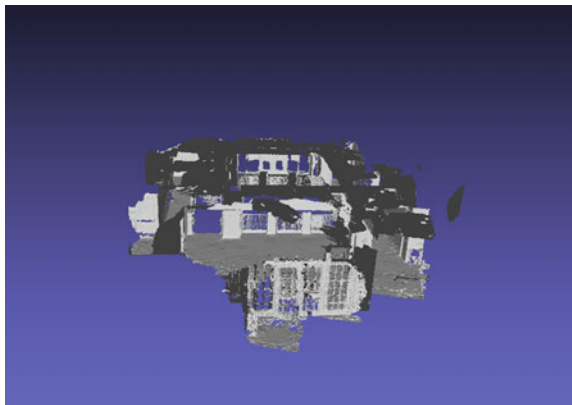


Fig. 2 Point cloud of the building with SFM (COLMAP)



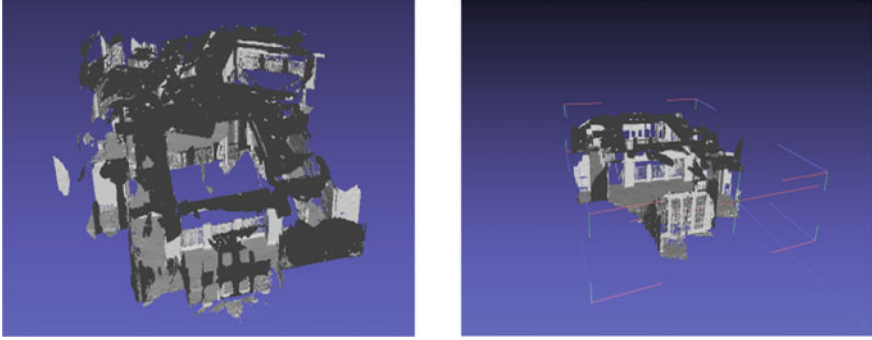


Fig. 3 Quick motion(left) and slow motion(right) point cloud of the building with HoloLens

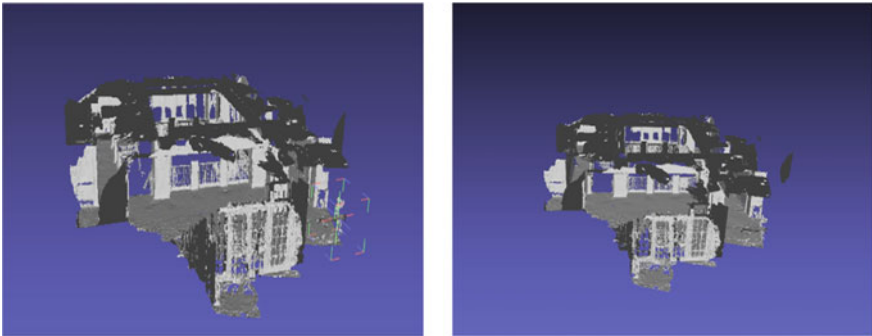


Fig. 4 Quick motion(left) and slow motion(right) point cloud of the building with SFM (COLMAP)

c. With different motion scenarios

Since the moving speed of the camera also plays a decisive role in the quality of the point cloud, it is meaningful to study the quality comparison of the point cloud in different sports motion scenarios. In this part, we simulated the different speeds of human movement. The HoloLens was moved in two different forms, fast and slow respectively. To get point cloud models at different speeds. The result is shown in Fig. 3. We did the same for COLMAP. The result is shown in Fig. 4.

2.2 Point Cloud Registration

To compare different point clouds, we adopted point cloud registration. That is, given two points sets $P = \{p_i\}$, $Q = \{q_i\}$, initial transformation R, t, p_i and q_i corresponds to the same point in the world.

$$\bar{p} := \frac{1}{m} \sum_{i=1}^m p_i \quad \bar{q} := \frac{1}{m} \sum_{i=1}^m q_i \tag{1}$$

$$\hat{p}_i := p_i - \bar{p} \quad \hat{q}_i := q_i - \bar{q} \tag{2}$$

We need to Estimate the best R^* , t^* between P and Q . Translation matrix can be calculated as

$$t^* = \bar{p} - R\bar{q} \tag{3}$$

Rotation can be calculated as

$$R^* = VU^T \tag{4}$$

The rotation matrix R and the translation matrix T is obtained through registration, and the error is calculated to compare the matching results. For the three-dimensional point set registration problem, researchers have proposed many solutions but the most widely used, but the most widely used, and the most influential is the Iterative Closest Point (ICP) [13] algorithm proposed by Paul J. Bed and Neil D. Mckay in 1992. It is a three-dimensional object alignment algorithm based on a pure geometric model. Because of its powerful functions and high accuracy, it quickly became the mainstream algorithm in surface registration (Fig. 5).

The key thoughts of Iterative closest point (ICP) are Given two points sets, estimate R , t to align two points. And the main process is: Find point correspondences, Estimate R , t , Based on R , t , compute errors and scores, iteratively run the aforementioned steps until converged. Figure 6 shows the modular of ICP. In this point cloud matching, the main tool we use is PCL (Point Cloud Library).

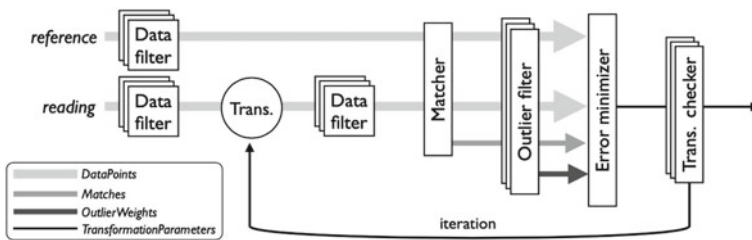


Fig. 5 Modular ICP

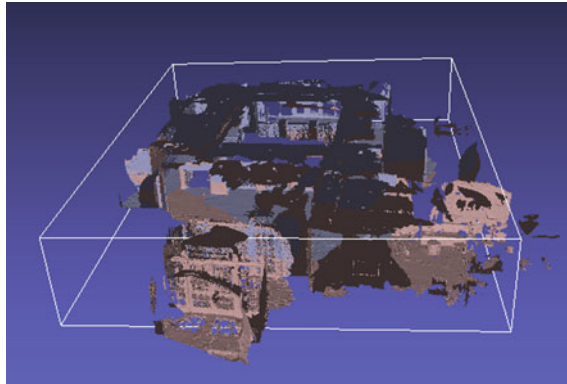


Fig. 6 Point cloud after registration with different workflows

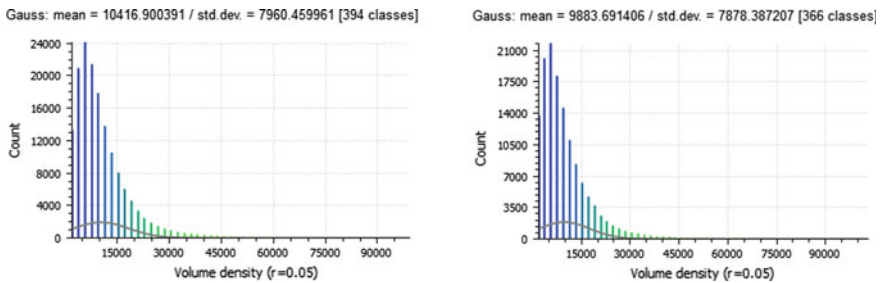


Fig. 7 Quick motion (left) and slow motion (right) point cloud density map with HoloLens

2.3 Comparison of Points Clouds with Different Workflows

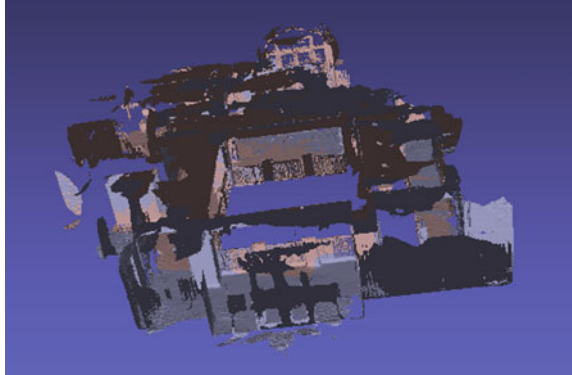
In this part, we try to compare the quality of point clouds generated by different workflows. One of the point clouds is from the real-time point cloud generated by HoloLens, and the other is the point cloud generated by the COLMAP algorithm. To control the variables, we have adopted the same movement speed of the camera.

We use the ICP algorithm to perform point cloud matching on the two points clouds. Figure 7 shows the point cloud image after Registration. It can be seen from the picture that they are almost coincident.

2.4 Comparison of Points Clouds with Different Motion Scenarios

In this part, we tried to compare the quality of the point cloud generated by the same algorithm in different sports scenes. It is divided into two parts, that is, we moved

Fig. 8 Point cloud after registration with different motion scenarios



the HOLOLENS device at different speeds, and extracted the real-time point cloud and the point cloud generated by the COLMAP algorithm.

First, we calculated the density of the point cloud due to the density is an intuitive standard to measure the quality of the point cloud. The greater the density, the greater the number of points, and the more information stored. According to the Gaussian density curve in Fig. 7, the density of the point cloud generated under quick motion scenario is less than the density of point cloud generated by slow motion scenario.

We use the ICP algorithm to perform point cloud matching on the two points clouds. Figure 8 shows the point cloud image after Registration. It can be seen from the figure that they are highly coincident.

3 Results

We obtained the transformation matrix through point cloud registration, namely the rotation matrix R and the translation matrix T and calculated the error. The result is as follows.

3.1 Comparison of Different Workflows

Through calculation, we get that the rotation matrix of the real-time point cloud extracted by HoloLens are show in (5). We get that the rotation matrix and translation matrix of the real-time point cloud extracted by HoloLens is. Since we use this point cloud as a reference point cloud, its transformation matrix is an identity matrix.

Table 1 Registration error with different workflows

Avg Err	Median	Error bound
0.028	0.028	0.0010

$$\begin{bmatrix} 1.000000 & 0.000000 & 0.000000 & 0.000000 \\ 0.000000 & 1.000000 & 0.000000 & 0.000000 \\ 0.000000 & 0.000000 & 1.000000 & 0.000000 \\ 0.000000 & 0.000000 & 0.000000 & 1.000000 \end{bmatrix} \tag{5}$$

The transformation matrix of the point cloud obtained by the SFM method is (6)

$$\begin{bmatrix} 0.999390 & -0.031802 & -0.014452 & 2.201854 \\ 0.031262 & 0.998857 & -0.036158 & -0.279066 \\ 0.015585 & 0.035684 & 0.999242 & 3.087117 \\ 0.000000 & 0.000000 & 0.000000 & 1.000000 \end{bmatrix} \tag{6}$$

The obtained point cloud registration error is shown in Table 1.

3.2 Comparison of Different Motion Scenarios

After calculation, we get the transformation matrix and registration error of point cloud matching under fast motion and slow motion.

We take the point cloud obtained during fast motion as the reference, so its transformation matrix is the same as (5).

$$\begin{bmatrix} 0.999390 & -0.031802 & -0.014452 & 2.201854 \\ 0.031262 & 0.998857 & -0.036158 & -0.279066 \\ 0.015585 & 0.035684 & 0.999242 & 3.087117 \\ 0.000000 & 0.000000 & 0.000000 & 1.000000 \end{bmatrix} \tag{7}$$

Table 2 shows the registration error obtained in different motion scenarios.

Table 2 Registration error with different motion scenarios

Avg err	Median	Error bound
0.005	0.005	0.0010

4 Conclusions

Significant progress has been made in the past few decades to solve the problem of visual simultaneous localization and reconstruction in motion environments. At the same time, excellent AR/VR platforms like Microsoft HoloLens have emerged, and they are all equipped with excellent SLAM or SFM algorithms. In this article, our work is to use PCL as an analysis tool and do two main studies. While controlling the variables, it explored the point cloud quality changes for different sports scenes and different workflows. After experimenting, we found that for the same workflow, the speed of the camera affects the quality of the point cloud, especially the density. The slower the camera moves, the more information the point cloud contains, but the difference in information content is within an acceptable range. At the same movement speed, we mainly explored the quality of point clouds generated under different workflows. We used an AR platform as a SLAM and recording device. For the SLAM algorithm, we use Microsoft's Spatial Mapping algorithm, and for the SFM algorithm, we use the COLMAP algorithm. The result of point cloud registration shows that the error of the point cloud map obtained by modeling the same scene in different workflows is not particularly large, especially the better the algorithm, the smaller the error of the point cloud registration. To enable practical implementations of simultaneous localization and reconstruction in dynamic environment. further research is needed since for most of the technologies discussed, dealing with lost, noisy, and outlying data remains a future challenge. Most technologies also have difficulty dealing with degradation and related movements. This will be our future work.

Acknowledgements The authors would like to thank anonymous reviewers for their helpful suggestions towards improving our paper.

References

1. Davison AJ et al (2007) MonoSLAM: real-time single camera SLAM. *IEEE Trans Pattern Anal Mach Intell* 29(6):1052–1067
2. Klein G, Murray D (2007) Parallel tracking and mapping for small AR workspaces. In 2007 6th IEEE and ACM international symposium on mixed and augmented reality. 2007. IEEE.
3. Engel J, Sturm J, Cremers D (2013) Semi-dense visual odometry for a monocular camera. In: *Proceedings of the IEEE international conference on computer vision*
4. Mur-Artal R, Montiel JMM, Tardos JD (2015) ORB-SLAM: a versatile and accurate monocular SLAM system. *IEEE Trans Rob* 31(5):1147–1163
5. Mur-Artal R, Tardós JD (2017) Orb-slam2: an open-source slam system for monocular, stereo, and rgb-d cameras. *IEEE Trans Rob* 33(5):1255–1262
6. Snavely N, Seitz SM, Szeliski R (2006) Photo tourism: exploring photo collections in 3D. In: *ACM siggraph 2006 papers*, pp. 835–846
7. Agarwal S et al (2011) Building rome in a day. *Commun ACM* 54(10):105–112
8. Snavely KN (2008) Scene reconstruction and visualization from internet photo collections. University of Washington

9. Frahm J-M et al (2010) Building rome on a cloudless day. In: European conference on computer vision. Springer
10. Wu C (2013) Towards linear-time incremental structure from motion. In: 2013 international conference on 3D vision-3DV 2013. 2013. IEEE
11. Moulon P, Monasse P, Marlet R (2012) Adaptive structure from motion with a contrario model estimation. In: Asian conference on computer vision. Springer
12. Schonberger JL, Frahm J-M (2016) Structure-from-motion revisited. In: Proceedings of the IEEE conference on computer vision and pattern recognition
13. Besl PJ, McKay ND (1992) Method for registration of 3-D shapes. in Sensor fusion IV: control paradigms and data structures. International Society for Optics and Photonics

Drive-By Technology

Drive-By Detection of Midspan Cracking and Changing Boundary Conditions in Bridges



Robert Corbally and Abdollah Malekjafarian

Abstract Bridges are critical to the functioning of any transport network and the failure of a bridge can have devastating effects, not only in relation to fatalities or damage associated directly with the collapse, but also to the functioning of the transport network in the aftermath. Traditional methods for inspection and monitoring of bridges are labor-intensive and time consuming and cannot feasibly be applied to monitor all of the bridges on a large transport network. This paper proposes an approach which utilizes vibration measurements from a vehicle driving across a bridge, to monitor changes in its condition over time. In-vehicle vibrations have successfully been used in the past to identify the dynamic properties of the bridge; however, the vehicle speed and the pavement conditions have a big influence on the measured response and can often mask any changes which might occur due to damage in the bridge. This paper demonstrates an approach which combines these in-vehicle vibration measurements with an Artificial Neural Network to identify bridge damage for varying vehicle speeds. The algorithm is shown to be successful in identifying cracking in the deck and changes in the boundary conditions due to seized bearings. The impact of pre-existing damage on the ability of the algorithm to detect further deterioration in bridge condition is also examined. The results show that the sensitivity to further increases in the existing damage is slightly reduced, however the detection of other types of damage is not negatively impacted. The results of the simulations performed in this paper provide a good indication that the application of machine learning to drive-by bridge monitoring represents a promising step towards making large-scale monitoring of bridges feasible.

Keywords Bridge · Structural health monitoring · Machine learning · Damage detection · Artificial neural network

R. Corbally (✉) · A. Malekjafarian
Structural Dynamics and Assessment Laboratory, School of Civil Engineering, University College
Dublin, Dublin, Ireland
e-mail: robert.corbally@ucdconnect.ie

© The Author(s), under exclusive license to Springer Nature Switzerland AG 2023
Z. Wu et al. (eds.), *Experimental Vibration Analysis for Civil Engineering Structures*,
Lecture Notes in Civil Engineering 224,
https://doi.org/10.1007/978-3-030-93236-7_50

607

1 Introduction

Transport infrastructure managers are faced with the challenge of operating and maintaining large networks which are comprised of various civil infrastructure assets. In the modern era, many countries face situations where their roads or railways have been built many years ago and these assets are in need of regular maintenance to ensure that roads and railways can remain serviceable. Bridges are of particular importance to infrastructure managers. The failure of a bridge can have significant consequences, both in terms of the cost of repair and the associated traffic delays, but also in relation to the risk of fatalities or injuries.

With limited budgets available for monitoring and maintenance of ageing bridge stocks, there is a push for cheaper and faster methods to inspect, monitor and assess the condition of bridges [1]. The use of in-vehicle sensors to monitor bridge behavior has gained a lot of attention in recent years [2, 3]. It has been shown that the dynamic properties of a bridge can be obtained purely from sensors inside a passing vehicle [4]. These dynamic properties are generally sensitive to damage and various attempts have been used to monitor natural frequencies [5], mode-shapes [6] and bridge damping [7] to develop approaches for drive-by condition monitoring of bridges.

Despite the significant body of research in this area, there are still a number of limitations in making the drive-by approach a commercially viable solution for bridge condition monitoring. One of the primary concerns relates to the fact that the dynamic properties of a bridge are not only sensitive to damage but are also sensitive to environmental and operational factors. The changes in frequency caused by temperature, for example, can often be as significant as any change that might occur due to damage, which means that it is difficult to be certain whether changes in the structural response are actually caused by changes in the condition of the bridge [8, 9]. In addition, there are added complications when trying to infer the bridge response using in-vehicle measurements. For example, the speed of the vehicle will influence the measured bridge frequency [10] and the pavement roughness will also have a significant effect on the vehicle vibrations [11]. Various attempts have been made to develop new approaches to mitigate these influences, such as using the contact-point response to give a better measure of bridge vibration [12–14] or examining the time-varying nature of the bridge properties during the vehicle crossing [15, 16] to better understand the factors which will influence the bridge behavior.

The growing area of machine learning and artificial intelligence provides promising approaches which could be leveraged to learn and account for the influences of these external factors, providing a greater degree of certainty for damage detection. Whilst machine learning approaches have been widely adopted for direct bridge monitoring strategies [17], where sensors are installed directly on the bridge, there have only been a limited number of attempts to adopt these approaches for drive-by condition monitoring [18–21]. This paper presents a machine learning algorithm for drive-by monitoring of bridges. The algorithm adopts an Artificial Neural Network (ANN) which is trained to recognize the frequency content of measured in-vehicle response as it drives over the bridge at different speeds. The ANN is then

used to identify the presence of different damage scenarios on the bridge, showing that cracking and changes in the boundary conditions can be detected for varying speeds of the vehicle. The results provide a good indication that the application of machine learning to drive-by bridge monitoring represents a promising step towards making large-scale monitoring of bridges feasible.

2 Numerical Modelling Approach

2.1 Modelling Vehicle-Bridge Interaction

In this paper a numerical Vehicle-Bridge Interaction (VBI) model was used to simulate the dynamic response of both the vehicle and the bridge during a vehicle crossing. A Finite Element (FE) beam model was adopted to represent a 15 m long simply supported concrete slab bridge as presented by Malekjafarian et al. [19]. The properties of the bridge are listed in Table 1. The FE model consisted of 20 no. beam elements, 0.75 m long, with 2-degrees of freedom per node, representing rotational and vertical displacements.

The quarter car model, as shown in Fig. 1, consists of two degrees of freedom, with two lumped masses, representing the vertical motion of the (i) vehicle body and (ii) the axle (including the wheel). The two masses are connected using a spring and dashpot representing the stiffness and damping properties of the vehicle suspension and the axle degree of freedom is connected to the bridge using a spring to represent the tyre stiffness. While the quarter-car is a simplified representation of the actual behaviour of a vehicle, it has been widely adopted to represent the two primary modes

Table 1 Properties of the bridge model

Property	Value
Length (L)	15 m
Young's Modulus (E)	35 GPa
Cross Sectional Area (A)	7.5 m ²
Second Moment of Area (I)	0.352 m ⁴
Material Density (ρ)	2,500 kg/m ³

Fig. 1 Vehicle-bridge interaction model

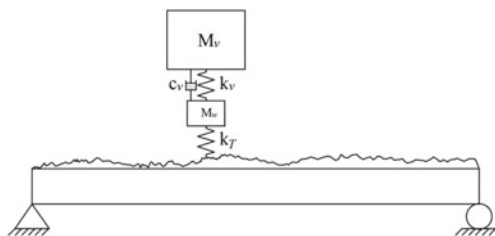


Table 2 Quarter-car properties

Property	Value
Body Mass (M_v)	8,900 kg
Axle Mass (M_w)	1,100 kg
Suspension Stiffness (k_v)	2×10^6 N/m
Suspension Damping (c_v)	40,000 Ns/m
Tyre Stiffness (k_T)	3.5×10^6 N/m
First Frequency (body bounce)	1.9 Hz
Second Frequency (axle-hop)	11.3 Hz

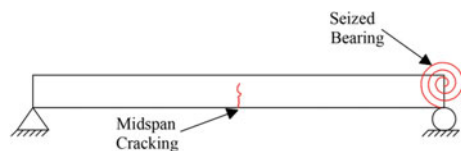
of vibration of a vehicle, i.e. ‘bounce’ of the vehicle body and axle ‘hop’ [22]. The properties used in the quarter-car model and the natural frequencies of the model are included in Table 2 and were chosen to represent a typical truck with single-axle air suspensions [23].

The analysis involved simulating the passage of the quarter-car over the bridge at a constant speed and finding the dynamic response of the vehicle and the bridge. Rayleigh damping of 3% was adopted to represent structural damping of the bridge.

2.2 Modelling Bridge Damage

In order to examine the ability of the algorithm to detect bridge damage, two different damage types were modelled, as shown in Fig. 2. Midspan cracking was represented as a loss of stiffness at the location of the crack following the approach of Sinha et al. [24]. This approach reduces the I-value of the elements in the region of the crack to represent the reduction in stiffness which would occur for a given depth of cracking. Two different crack depths were considered, representing 10 and 20% cracking at midspan. In addition to midspan cracking, a rotational spring was introduced at the right-hand support to represent the effect of the bearings at that location becoming seized. Two different damage levels were also considered for the seized bearing, representing a partially seized bearing, and a fully seized bearing. The partially seized damage case used a rotational spring to limit the rotation at the right-hand support by 50%, while the fully seized damage case considered a situation where the right-hand support was completely fixed against rotation.

Fig. 2 Bridge damage modelling approach



2.3 Artificial Neural Network and Damage Detection Algorithm

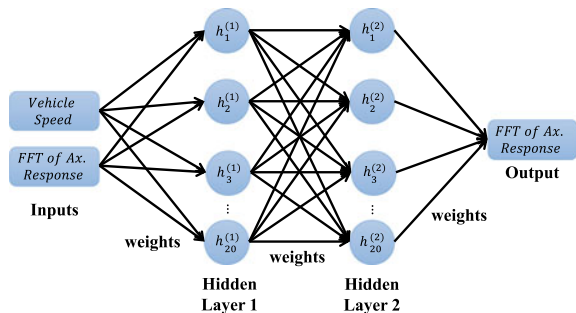
Figure 3 shows the architecture of the ANN used to test for the presence of bridge damage. The ANN has an input layer with 2 input neurons, two hidden layers, each containing 20 neurons and an output layer with a single output which is the predicted frequency content of the acceleration response of the vehicle’s axle. The two inputs, vehicle speed and the frequency content of the axle response, are fed into the hidden layers using pre-defined weights. When the ANN is being trained, the optimal values of these weights are calculated through a learning process such that the difference between the output predictions and the input training data are minimized. A Levenberg–Marquardt backpropagation (LMBP) algorithm is used to train the ANN, with the hidden layers of the ANN containing hyperbolic tangent activation functions and the output layer containing a linear activation function.

3 Damage Detection Using Artificial Neural Network

The proposed approach uses acceleration measurements taken on the axle of a passing vehicle to infer the condition of the bridge by monitoring any changes over time. The idea is based upon the fact that the dynamic response of the bridge contributes to the vibration of the vehicle as part of the complex vehicle-bridge-interaction process. If the structural condition of the bridge changes, for example—due to damage or deterioration, this affects the bridge vibrations, and these changes should also become visible in the measured response on the vehicle.

It has been shown that measurements on the axle of the vehicle give a better indication of the bridge vibration than those recorded on the body of the vehicle [14] and hence the axle response is used in this study. More specifically, the frequency content of the axle response is used to monitor the various frequencies contained in the axle response which will include the fundamental frequency of the bridge. It is intuitive, and well established, that the vibrations recorded on the axle of the vehicle

Fig. 3 ANN architecture



will not just be sensitive to changes in bridge damage, but they will also be highly sensitive to the surface roughness on the pavement and the speed of the vehicle. The fact that the vehicle speed will likely be different for each individual vehicle passage means that it is important to be able to understand how the axle response will behave under different vehicle speeds. This is where the ANN is extremely beneficial. The ANN learns to predict this behavior for varying vehicle speeds and gives a more robust understanding of changes which are caused by damage. The proposed approach uses a series of ‘training runs’ of the vehicle over the bridge, when it is in an undamaged condition, to train the ANN to predict the frequency content of the axle response for different vehicle speeds. Once the ANN has been trained, monitoring of the bridge can begin. During the monitoring phase, the predicted frequency content is compared to the actual frequency content for each individual vehicle passage, these differences are monitored over time and are used to identify when changes occur, which could be indicative of damage.

3.1 Numerical Testing Approach

In order to examine the ability of the algorithm to detect damage, a series of passages of the quarter-car across the bridge model were simulated. The vehicle speeds were varied using a normal distribution with a mean value $\mu_{vel} = 15\text{m/s}$ and a standard deviation $\sigma_{vel} = 1.7\text{m/s}$ to account for variations in vehicle speeds during normal traffic conditions. In order to consider the influence of the pavement roughness, a ‘Class A’ pavement was simulated in accordance with ISO8608 [25] and included in the vehicle-bridge-interaction model. To consider the effects of measurement noise which would be experienced when taking real measurements from inside a vehicle, 2% random noise was added to the simulated axle-acceleration signals.

During the training phase, the ANN was trained using the Fast Fourier Transform (FFT) of the axle-response, along with the associated vehicle speeds, for 200 simulated vehicle passages over the bridge in an undamaged condition. Following the training of the ANN, the ‘monitoring phase’ was carried out, where a series of 100 vehicle passages were simulated over the bridge in various damage states as outlined in Table 3.

For each vehicle passage during the monitoring phase the difference between the simulated frequency content of the axle response and that predicted by the ANN was used as a measure of damage. The prediction error, pe_j , for each vehicle passage, j , was evaluated using Eq. (1), where $pred_i$ & y_i represent the predicted and actual frequency content for each frequency, i , in the FFT spectrum of the axle response, which was evaluated in the range of 0–8 Hz. Equation (1) represents the root-mean square error between the two frequency spectra with the mean being evaluated based on the n frequency samples contained in the 0–8 Hz range of the FFT.

Table 3 Bridge damage scenarios considered

Damage type	Description
A	Midspan cracking (10%)
B	Midspan cracking (20%)
C	Partially seized bearing at right-hand support (50%)
D	Fully seized bearing at right-hand support (100%)
E	Midspan cracking (20%) & Partially seized bearing at right-hand support (50%)
F	Midspan cracking (20%) & Fully seized bearing at right-hand support (100%)

$$pe_j = \sqrt{\frac{1}{n} \sum_{i=1}^n (pred_i - y_i)^2} \tag{1}$$

The prediction error was used to give an indication of the presence of damage and a ‘Damage Index’ (DI_j) was evaluated for each vehicle passage as per Eq. (2), where μ_{tr} and σ_{tr} are the mean and standard deviations of the training errors, respectively.

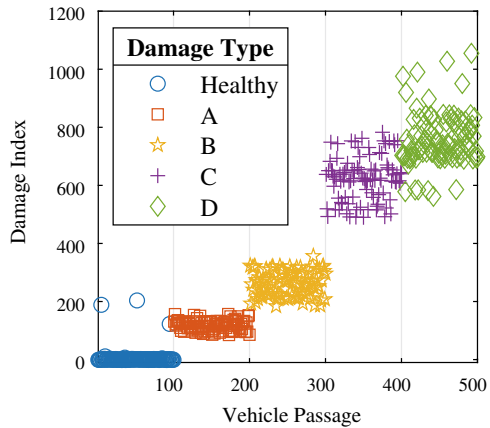
$$DI_j = \frac{pe_j - \mu_{tr}}{\sigma_{tr}} \tag{2}$$

Normalizing the prediction errors in this way reduces the variation in errors for the case when the bridge is in a healthy condition and means that the DI will be close to zero while the bridge is undamaged.

3.2 Detection of Individual Damage Scenarios

Initially, the algorithm was tested to examine the Damage Indices for different types and different levels of damage. The ANN was initially trained using the simulated responses from 200 passages of the quarter-car. Once the training process had been completed, 500 subsequent vehicle passages were simulated, and the Damage Index evaluated for each passage. For the first of these 100 passages, the bridge remained in an undamaged condition and then 4 sets of 100 passages were simulated with damage types A-D (as per Table 3) to examine the Damage Indices for each type and extent of damage. Figure 4 shows the results of the simulations and it can be seen that while the bridge remained in a healthy condition, the Damage Indices were

Fig. 4 Damage indices for cracking (A & B) or seized bearings (C & D)



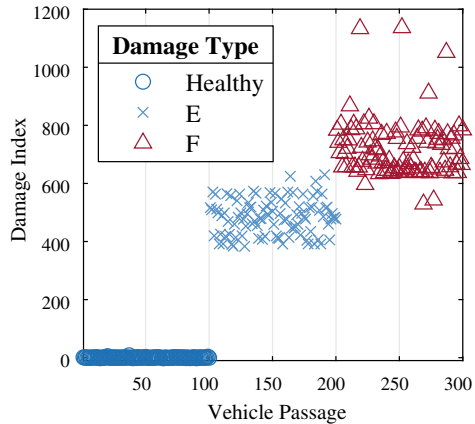
approximately zero, with the exception of a few outliers, where the speeds were quite far from 15 m/s. In these cases, the ANN was not very well trained to predict the expected response as there was limited training data at these speeds.

For the case of midspan cracking, it was seen that when 10% cracking was experienced (Damage Type A), there was a distinct increase in the Damage Indices, which further increased, when the crack depth increased to 20% (Damage Type B). The Damage Indices for changes in boundary conditions at the right-hand support (Damage Type C & D) proved to be much more sensitive to damage, with the Damage Indices for both partial (Type C) and fully (Type D) seized bearings being approximately 3 times larger than for the cases of midspan cracking. While the level of fixity, especially for the case of a fully seized bearing, is likely too conservative to represent what would really be experienced if the bearings were to seize, the results clearly demonstrate that the methodology is sensitive to both cracking in the structure and to changes in the boundary conditions.

3.3 Combined Cracking and Seized Bearings

The next set of simulations followed the same approach, whereby the ANN was trained using signals from 200 passages over the bridge in an undamaged condition. Once the ANN had been trained, 300 vehicle passages were subsequently simulated to monitor the condition of the bridge when combination of midspan cracking and seized bearings occurred. Again, for the first 100 monitoring runs, the bridge remained in a healthy condition, and subsequently the bridge was damaged with a combination of 20% midspan cracking and partially or fully seized bearings at the right-hand support (Type E or F). Figure 5 shows the Damage Indices for the case of combined damage types.

Fig. 5 Damage indices for simultaneous cracking and seized bearings



Again, it can be seen that while the bridge remained healthy, the Damage Indices were close to zero. However, when damage was induced in the bridge, the Damage Indices were typically in the range of 400–600 for Damage Type E, and 600–800 for Damage Type F. It is clear, that the algorithm can detect the simultaneous presence of both damage types. Comparing the Damage Indices to those shown in Fig. 4, however, it can be seen that the Damage Indices in the presence of combined cracking and bearing seizure are actually slightly lower than the situation where the bearings had seized but there was no cracking in the deck (Damage Type C & D). This is due to the fact that midspan cracking reduces the natural frequency of the bridge, whereas the rotational restraint at the support increases the fundamental frequency of the bridge. As such, when both damage types are present, the combined effect reduces the Damage Indices rather than making them increase. Despite this reduction, the algorithm can still clearly identify the damaged scenarios, however if the bridge were to experience cracking for more subtle levels of rotational restraint, then it might partially mask the effect.

3.4 Detection When Cracking Has Occurred Prior to Monitoring

The simulations in the previous two sections utilized an ANN which was trained using data from a healthy bridge, however in reality, there may already be damage to the bridge before drive-by monitoring has commenced. As the proposed approach is based on detecting changes in the bridge condition, it is not possible to detect any existing damage using this approach, however in this section, the simulations were run again to examine the impact which existing damage might have on the ability of the approach to detect further changes in the bridge condition. In this case, the ANN was trained using 200 vehicle passages over the bridge which already had

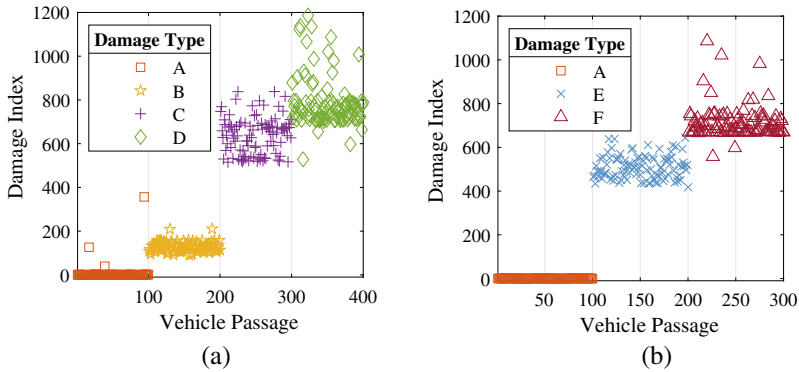


Fig. 6 Damage indices for **a** individual damage types and **b** simultaneous cracking and seized bearings, when the ANN is trained after a 10% crack at midspan has already occurred

experienced 10% midspan cracking (i.e. Damage Type A). Then individual damage types (A-D) and simultaneous damage scenarios (E & F) were induced in the bridge model and the Damage Indices for 100 passages of the quarter car in each damage state were evaluated, with the results shown in Fig. 6.

As would be expected, the presence of the 10% midspan cracking (Damage Type A) cannot be identified and the Damage Indices are approximately zero as this was the baseline condition for which the ANN was trained. The presence of 20% midspan cracking (Damage Type B) or seized bearings (Damage Type C & D) are clearly visible from the Damage Indices shown in Fig. 6a. The Damage Indices for the case of 20% midspan cracking are slightly lower than before, as would be expected, as the 20% level of cracking now represents a less significant change in bridge frequency from the baseline condition. Interestingly, the Damage Indices for the cases of seized bearings (C & D) are not reduced, and are in fact, slightly higher than was seen previously. This is because the presence of cracking does not have an influence on how much the bridge frequency changes when the bearings start to seize. A similar situation can be seen in Fig. 6b, where the Damage Indices for combined cracking and seized bearings do not reduce even though the ANN has been trained following the occurrence of cracking.

4 Discussion

From the results of numerical testing, it can be seen that the application of machine learning to drive-by bridge monitoring represents a promising development. The results clearly show that the algorithm is capable of detecting changes in bridge condition which are caused by damage through the use of a well-trained ANN which can model the expected frequency response of the axle acceleration for various vehicle speeds. Midspan cracking and changes to the boundary conditions can clearly be

identified using the proposed method. In addition, the presence of simultaneous cracking and seized bearings can also be easily detected, however it is observed that when both types of damage are present, the change in bridge frequency is smaller than when the bearings are seized without the presence of any cracking. While the algorithm can still clearly identify the simultaneous presence of both damage types, if the bridge were to experience cracking for more subtle levels of rotational restraint, then it might partially mask the effect.

When midspan cracking has already occurred prior to training the ANN it is seen that the case of 20% midspan cracking is less distinct than it was when the ANN was trained using vehicle passages over a healthy bridge. Despite this, it can be concluded that while pre-existing damage may reduce the sensitivity of the Damage Indices to increased levels of the existing damage, the detection of other types of damage which might subsequently occur should not be adversely affected.

Of course, the numerical simulations presented in this paper cannot account for some of the factors which will inevitably influence the results in a real-life scenario, including external factors which may influence the response of the vehicle and the bridge (e.g. temperature, other vehicles on the bridge, the lateral location of the vehicle, localized effects etc.). However, it is envisaged that further development of this algorithm to also learn and account for these external factors will allow some of the major technical challenges faced by drive-by bridge monitoring to be overcome.

5 Conclusion

This paper presents a bridge monitoring algorithm which utilizes vibration data measured inside a passing vehicle along with an Artificial Neural Network, to identify changes in bridge condition which occur due to damage. Numerical simulations are used to examine the effectiveness of the approach and it is demonstrated that midspan cracking and changes in the boundary conditions due to seized bearings can clearly be identified from the Damage Indices. The impact of pre-existing damage on the ability of the algorithm to detect further deterioration in bridge condition is also examined and the results show that the sensitivity to further increases to existing damage is slightly reduced, however the detection of other types of damage is not negatively impacted. While much work has been done in the field of drive-by monitoring, there are still many technical challenges which have not yet been successfully overcome. The introduction of machine learning approaches, such as the method proposed in this paper, into drive-by bridge monitoring campaigns, represents significant potential to overcome these challenges and move towards a commercially viable approach for large-scale bridge monitoring.

References

1. Favai P et al (2014) Bridgemon: Improved monitoring techniques for bridges. In: Nanukuttan S, Goggins J (eds) *Civil engineering research in Ireland*, Civil Engineering Research Association of Ireland: Belfast, UK, pp 179–184
2. Malekjafarian A, McGetrick PJ, O'Brien EJ (2015) A review of indirect bridge monitoring using passing vehicles. *Shock Vib* 2015:1–16
3. Yang YB, Yang JP (2018) State-of-the-art review on modal identification and damage detection of bridges by moving test vehicles. *Int J Struct Stab Dyn* 18(02)
4. Yang YB, Lin CW, Yau JD (2004) Extracting bridge frequencies from the dynamic response of a passing vehicle. *J Sound Vib* 272(3–5):471–493
5. Kariyawasam KD et al (2020) Assessment of bridge natural frequency as an indicator of scour using centrifuge modelling. *J Civ Struct Health Monit*
6. Malekjafarian A, Prendergast L, O'Brien EJ (2019) Use of mode shape ratios for pier scour monitoring in two-span integral bridges under changing environmental conditions. *Can J Civ Eng*
7. ElHattab A, Uddin N, O'Brien E (2017) Drive-by bridge damage detection using non-specialized instrumented vehicle. *Bridg Struct* 12(3–4):73–84
8. Gillich G-R et al (2019) A robust damage detection method based on multi-modal analysis in variable temperature conditions. *Mech Syst Signal Process* 115:361–379
9. Jin C et al (2016) Damage detection of a highway bridge under severe temperature changes using extended Kalman filter trained neural network. *J Civ Struct Heal Monit* 6(3):545–560
10. Sitton JD et al (2020) Frequency estimation on two-span continuous bridges using dynamic responses of passing vehicles. *J Eng Mech* 146(1)
11. Hester D, González A (2017) A discussion on the merits and limitations of using drive-by monitoring to detect localised damage in a bridge. *Mech Syst Signal Process* 90:234–253
12. Yang YB et al (2018) Contact-point response for modal identification of bridges by a moving test vehicle. *Int J Struct Stab Dyn* 18(05)
13. Nayek R, Narasimhan S (2020) Extraction of contact-point response in indirect bridge health monitoring using an input estimation approach. *J Civ Struct Heal Monit* 10(5):815–831
14. Corbally R, Malekjafarian A (2021) Examining changes in bridge frequency due to damage using the contact-point response of a passing vehicle. *J Struct Integr Maint* 6(3):148–158
15. Li J et al (2020) Time-varying characteristics of bridges under the passage of vehicles using synchroextracting transform. *Mech Syst Signal Process* 140
16. Cantero D et al (2019) Experimental monitoring of bridge frequency evolution during the passage of vehicles with different suspension properties. *Eng Struct* 187:209–219
17. Avci O et al (2021) A review of vibration-based damage detection in civil structures: from traditional methods to Machine Learning and Deep Learning applications. *Mech Syst Signal Process* 147
18. Cerda F, Chen S, Bielak J, Garrett JH, Rizzo P, Kovacevic J (2014) Indirect structural health monitoring of a simplified laboratory-scale bridge model. *Smart Struct Syst* 13(5):849–868
19. Malekjafarian A et al (2019) A machine learning approach to bridge-damage detection using responses measured on a passing vehicle. *Sensors* 19(18)
20. Locke W et al (2020) Using drive-by health monitoring to detect bridge damage considering environmental and operational effects. *J Sound Vib* 468
21. Corbally R, Malekjafarian A (2022) A data-driven approach for drive-by damage detection in bridges considering the influence of temperature change. *Eng Struct* 253, 113783
22. Jazar NR (2008) *Vehicle dynamics, theory and application*. Springer
23. Cebon D (1999) *Handbook of vehicle-road interaction*. Taylor & Francis
24. Sinha JK, Friswell MI, Edwards S (2002) Simplified models for the location of cracks in beam structures using measured vibration data. *J Sound Vib* 251(1):13–38
25. ISO, I. (2016) ISO 8608 Mechanical vibration-road surface profiles-reporting of measured data. BSI Standards Publication, London, UK

Load Carrying Capacity and Vibration Characteristics of PC Box Girders with Damage



K. Takemura, Chul-Woo Kim, G. Hayashi, and E. Yoshida

Abstract This study is intended to examine changes in modal parameters PC box girders due to defective grouting and failures in PC tendons through a laboratory experiment. In the laboratory experiment, three PC box girders, which have different damage scenarios, are examined. Both static loading and vibration experiments were conducted. The static loading experiment was performed with 4-point bending loading, and as vibration experiment, the impact hammer test was applied. This study investigates the relationship between the energy-based bending performance adopted as a load carrying capacity, and frequencies of the PC box girders. The static loading test showed that local cracks were dominated around the location of defective grouting and failure of PC tendons, and energy-based bending performance evaluated from load–displacement curve, decreased according to loading process. Frequencies of bending modes showed a decreasing tendency but showed fluctuations as loading progresses. A moderate correlation was observed between the energy-based bending performance and the natural frequency of 1st and 2nd bending modes.

Keywords Load carrying capacity · PC box girder · PC tendon cut · Vibration test

1 Introduction

In 2023, around 39% of Japanese bridges will reach more than 50 years since commenced, and it has been reported that a lot of bridges have deteriorated [1]. Although it is necessary to inspect and maintain these bridges efficiently, one of

K. Takemura (✉) · C.-W. Kim

Department of Civil and Earth Resources Engineering, Graduate School of Engineering, Kyoto University, Kyoto, Japan

e-mail: takemura.kouhei.82a@st.kyoto-u.ac.jp

G. Hayashi

Bridge Engineering Laboratory, Graduate School of Engineering, Osaka City University, Osaka, Japan

E. Yoshida

Public Works Research Institute, Tsukuba, Japan

© The Author(s), under exclusive license to Springer Nature Switzerland AG 2023
Z. Wu et al. (eds.), *Experimental Vibration Analysis for Civil Engineering Structures*,
Lecture Notes in Civil Engineering 224,
https://doi.org/10.1007/978-3-030-93236-7_51

619

the major maintenance methods has been the visual inspection. However, structural integrity assessment based on the visual inspection is limited in objective decision-making. Since July 2014, local governments have been obliged to visually inspect road bridges of longer than 2 m once every five years, despite few experts involved in bridge maintenance work are available in local governments. Therefore, there is a limit to managing a huge number of bridges only by the visual inspection. In order to overcome the limitations of visual inspection, vibration-based health monitoring, which focuses on the vibration characteristics of bridges, has been proposed.

Among the bridge stock, prestressed concrete bridges (PC bridges), which are the subjects of this study, account for about 44% of all bridges in Japan [2]. As examples of deterioration of PC bridges, grout filling failure and PC tendon damage have been reported. Many studies have investigated grout filling failure, PC tendon damage, and corrosion evaluation as well as quantitative evaluation of the residual performance of PC bridges with such damages [3]. On the other hand, it has been reported that changes in bridge performance due to damage are unlikely to appear as change in vibration characteristics, even though comprehensive investigations on the mechanism between structural performance and vibration characteristics of PC bridges were not enough. Therefore, this study investigates the relationships between structural performance and vibration characteristics of PC bridges, in order to clarify feasibility of vibration-based damage detection of PC bridges.

In this study, three PC box girders which imitate grout filling failure and PC tendon damage are examined. Laboratory static loading and vibration experiments are conducted in order to examine the relationships between structural performance and vibration characteristics of PC box girders. 4-point bending experiment and a vibration experiment using an impact hammer were conducted to examine the effect of damage on the load carrying capacity and vibration characteristics of the PC box girder. In addition, based on these experimental results, it is considered about the correlation between the load carrying capacity and vibration characteristics of PC box girders.

2 Research Method

2.1 Target PC Box Girders

The static-loading experiment and vibration experiment are conducted to understand the load carrying capacity of the PC box girder due to damage which imitates grout filling failure and PC tendon cut. Three 1/2 scale PC box girders are designed and investigated in the laboratory experiment: one intact girder (BG-INT); and two damage girders (BG-DMG1 and BG-DMG2) as shown in Table 1 and Fig. 1 The PC box girders have a length of 8500 mm, a span length of 7500 mm, a height of 1000 mm, an upper floor slab width of 1300 mm, and a lower floor slab width of 1300 mm. In order to imitate the unfilled grout, as shown in Fig. 1, a tube is wrapped

Table 1 Detail of specimen

Height	1000 mm (thickness of web 200 mm)	
Width of upper lower slab	2300 mm (thickness 150 mm), 1300 mm (thickness 180mm)	
Rebar	SD345 D10	
PC tendon	SWPR7BL 1S 12.7 (sheath ϕ 35 mm) \times 12	
Rebar ratio of Axial direction	0.3% (web), 0.2% (upper slab), 0.5% (lower slab)	
Vertical restraining reinforcement rebar ratio	0.2% (stirrup)	
Failure type	Bending fracture BG-INT, BG-DMG1: shear strength > bending strength BG-DMG2: bending strength > shear strength	
Span length	7500 mm	
Girder length	8500 mm	
Concrete (BG-INT)	Compressive strength	51.1 (N/mm ²)
	Young's modulus	34.12 (kN/mm ²)
	Poisson's ratio	0.201
Concrete (BG-DMG1)	Compressive strength	52.7 (N/mm ²)
	Young's modulus	32.31 (kN/mm ²)
	Poisson's ratio	0.207
Concrete (BG-DMG2)	Compressive strength	44.5 (N/mm ²)
	Young's modulus	30.76 (kN/mm ²)
	Poisson's ratio	0.205
Rebar	Yielding stress	354 (N/mm ²)
	Young's modulus	192 (kN/mm ²)
PC tendon	Yielding stress	1600 (N/mm ²)
	Young's modulus	200 (kN/mm ²)
Prestress strength	About 1000 (N/mm ²)	

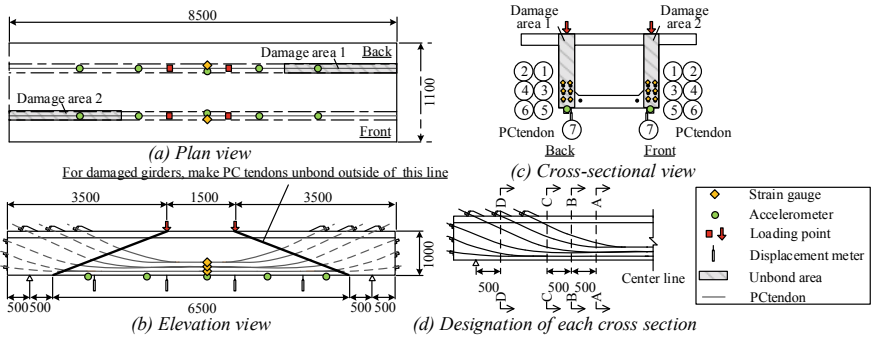


Fig. 1 Specimen

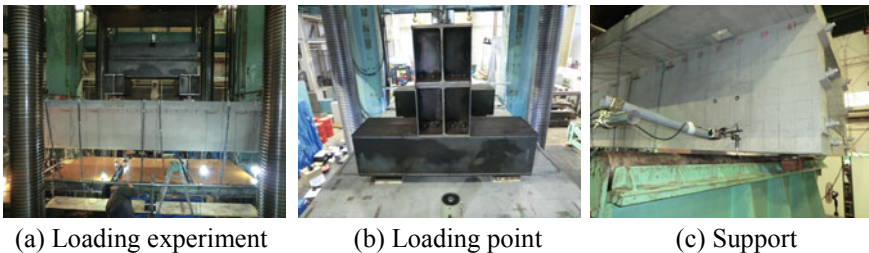
Table 2 Shear strength/bending strength at each section designated in Fig. 1d

	Shear strength/bending strength			
	A-A	B-B	C-C	D-D
BG-INT	1.03	1.16	1.25	1.41
BG-DMG1	1.06	1.12	1.16	1.2
BG-DMG2	0.89	0.87	0.86	0.83

around the PC tendon and unbonded section is installed at the bent-up part of the PC tendon placed on the web. BG-DMG1 has an unbonded section (Damage area 1) on one side, and BG-DMG2 has an unbonded section (Damage area 1 and Damage area 2) on both sides. Assuming that the PC tendon of the lower floor flange of damaged girders is corroded and broken early due to salt damage caused by flying salt, it is considered that the PC tendon is damaged before the PC tendon of web. Therefore, PC tendon was uninstalled in the place of the PC tendon 7, and only the sheath is placed. As shown in Fig. 1 b and c, there are a total of 12 PC tendons, six on each side, and in only BG-INT, PC tendons were also placed on the lower flange. As shown in Fig. 1b, the outside of the line connecting the loading point and the point 500 mm inside the fulcrum is unbonded. In addition, as shown in Table 2, the ratio of shear strength to bending strength is calculated for each cross section in order to confirm which fracture is likely to occur in which cross section. As can be seen, the fracture types are designed so that shear fracture precedes in BG-INT and BG-DMG1 girders and bending fracture preceded in BG-DMG2 girders.

2.2 Static Loading and Vibration Experiments

A static loading experiment is conducted for each girder using a 30 MN loading device with 4-point loading as shown in Fig. 2. In order to measure the static response of the PC box girder, 16 displacement measurements are placed on the lower deck of the PC box girder, and strain gauges are installed above and below each PC tendon at the span center. In the vibration experiment, impact force was applied using an

**Fig. 2** Static loading experiment

impact hammer during the unloading of the static loading step of each girder. As shown in Fig. 1a, 10 accelerometers are placed on the lower floor flange of the PC box girder. The impact point was the surface of the upper flange directly above each acceleration sensor. In each vibration step, 10 ~ 20 consecutive impact tests for each hit point were conducted on BG-INT and BG-DMG1 PC box girders. It should be noted that after confirming decay of the vibration due to structural damping 10 ~ 20 consecutive impact tests were conducted.

10 randomly selected data sets from the data of each hit point are examined, which means a total of 100 acceleration response data sets of 10 hit points are examined. Since BG-DMG2 has a large damage level and is considered to have a large variation, vibration test is performed more than 20 times for each hit point after confirming decay of the vibration due to structural damping. Therefore, for the BG-DMG2 girder, 20 data were randomly selected from the data of each hit point, and a total of 200 acceleration data of 10 hit points were investigated. The vibration characteristics were identified from each acceleration data and their average values are used. The sampling frequency was 2000 Hz.

2.3 Static Loading Step

Figure 3 shows the process of the static loading experiment and vibration experiment for each girder. In BG-INT, as shown in Fig. 3a, four cyclic loadings are carried out, and the vibration experiment is carried out in three stages. For easy of comparison, the loading step was named in accordance with loading steps in damage girders: i.e., the loading step is Load1 → Load4 → Load5 → Load6. Load1 denotes the loading step of a static load that is 10% higher than the initial crack load, Load 4 is a shear crack load, Load5 is a stirrup yield load, and Load6 is the load up to the final load. For the vibration test step, it was also named in accordance with loading steps in damage girders such as St.1 → St.8 → St.9. The vibration experiment is carried out before the loading experiment and after the unloading of each static loading step. Figure 3b shows the loading process in BG-DMG1 and BG-DMG2 girders. The static loading of occurring initial crack load increased by 10% is repeated three times (Load1, Load2, Load3). Load4 is the shear crack load, Load 5 is the stirrup yield load, and

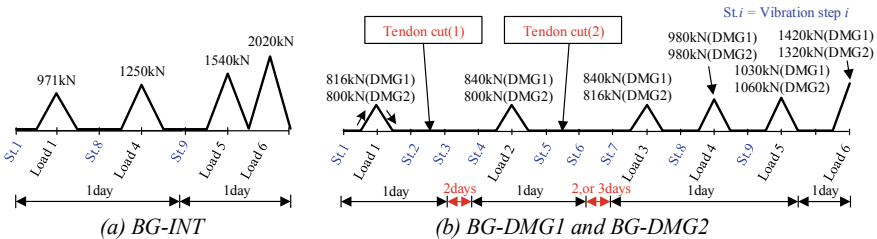


Fig. 3 Process of experiment

Load 6 is the ultimate loading stage. The vibration experiment is carried out before the loading experiment and after unloading (Load1 to Load4), immediately after cutting the PC tendon, and several days after the PC tendon cut. The PC tendon was cut in two steps by gas cutting. In BG-DMG1, the first cut was for three PC tendons 1–3 located in unbonded area on one side (Fig. 1c), and the second cut was for three PC tendons 4 to 6 on the same side. A total of six PC tendons were cut. For the BG-DMG2 girder, the first cut was for three PC tendons 1 to 3 located in unbonded area on both of sides, and the second cut was for three PC tendons 4 to 6 on the both of sides. A total of 12 PC tendons were cut.

2.4 Identification of Modal Parameters Using FRF

In order to identify modal parameters from the acceleration data, the frequency response function (FRF) derived from the excitation force and the vibration response is used. The frequency response function generally expresses the ratio of the vibration response $X(f)$ of the system to the exciting force $F(f)$ as a function of frequency, and is defined as the transfer function $H(f)$ as shown in the following equation [4].

$$H(f) = \frac{X(f) \cdot X^*(f)}{F(f) \cdot X^*(f)} = \frac{G_{XX}(f)}{G_{XF}(f)} \quad (1)$$

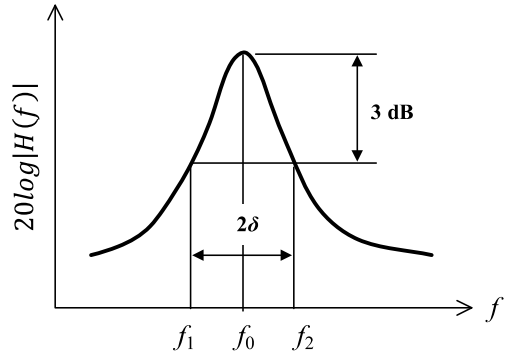
where, * indicates complex conjugate.

The vibration response of a structural system is measured as displacement, velocity, or acceleration. When evaluating a structural system, FRF are generated. The system transfer function is defined by the ratio of the linear Fourier spectrum of the output time domain function to the linear Fourier spectrum of the input time domain function. However, since noise exists in all systems, the auto power spectrum $G_{XX}(f)$ and cross power spectrum $G_{FX}(f)$ of the vibration response were used to reduce the influence of the noise. In this study, the SIMO (single-input multiple-output) shown in Eq. (2) is used to return the multiple output from multiple accelerometers in response to the input of external force by one impact hammer.

$$\begin{Bmatrix} X_1(f) \\ X_2(f) \\ X_3(f) \\ \vdots \\ X_n(f) \end{Bmatrix} = \begin{Bmatrix} H_1(f) \\ H_2(f) \\ H_3(f) \\ \vdots \\ H_n(f) \end{Bmatrix} \cdot F(f) \quad (2)$$

From this FRF, the modal parameters are identified using the peak picking method. The peak picking method is based on the assumption that each sharp peak of the frequency response function corresponds to exactly one natural frequency mode. As

Fig. 4 Peak picking method



shown in Fig. 4, if the frequency showing the sharp peak of the frequency response function is the damped natural frequency f_0 . When the two frequencies 3 dB lower than the peak are f_1 and f_2 respectively, the damping ratio ζ and the natural frequency f_r are derived as in Eqs. (3) and (4) respectively.

$$\zeta = \frac{(f_2 - f_1)}{2f_0} \tag{3}$$

$$f_r = \frac{f_0}{\sqrt{1 - \zeta^2}} \tag{4}$$

3 Result of Static Loading Experiment

3.1 Load–displacement Curve

Figure 5 shows the load–displacement curve at the span center of each girder with dimensionless axis in which F_y denotes the load when the slope of the load–displacement curve starts to change and δ_y denotes the displacement corresponding to F_y . It is noted that during the experiment for BG-INT and BG-DMG2, the displacement transducer was removed in the middle of the final loading step and the unloading of Load6 was not reflected in the load–displacement curve. In BG-INT, the static load at the slope change was 1020kN and the displacement was 3.5 mm. In Load5 and Load6, the curve under loading passes the unloading points of Load4 and Load5 respectively, which means that it has sufficient prestress of PC tendons and even in areas where bending cracks occur in concrete, there is little decrease in resistance to bending deformation. The maximum load was 2033kN. In BG-DMG1 with a fracture of PC tendon on one side, the static load at the slope change was 868kN and the displacement was 3.3 mm. One possible reason of smaller load of BG-DMG1 at the slope change than that of the BG-INT is that the PC tendon of lower flange was not

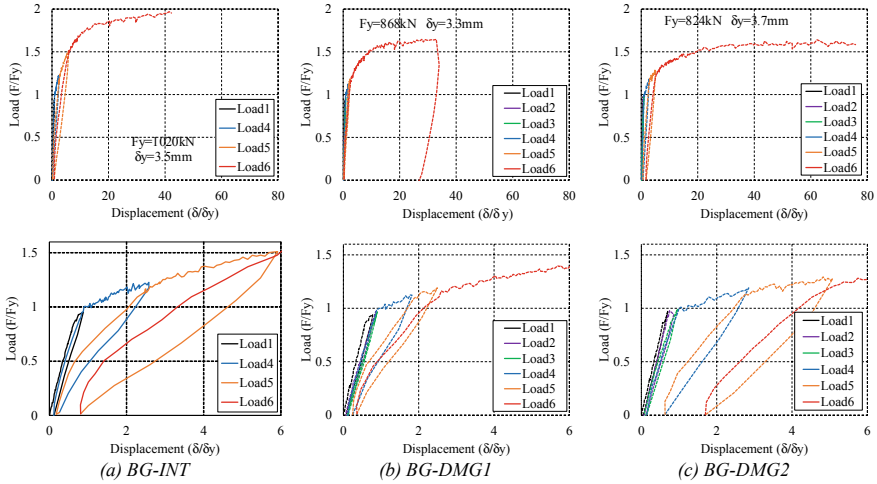


Fig. 5 Load–displacement curve (upper: whole, below; enlarged)

installed in the BG-DMG1 girder and that it is also affected by the cutting the PC tendons. In the BG-INT girder, the load–displacement curve of the next loading step passed that of the unloading point of the previous loading, but in BG-DMG1, the load–displacement curve passed lower loading point than the unloading point of the previous load step due to cutting the PC tendons. The maximum load was 1427kN.

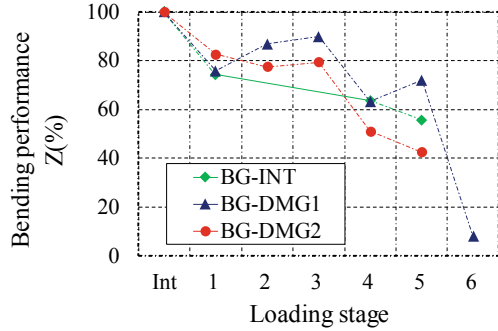
3.2 Energy

For the bridge performance evaluation, a response feature, Z , is estimated using the load–displacement curve. In static load test of concrete bridge, energy is dissipated with respect to crack propagation: the larger the crack, the larger the dissipation energy ($\Delta W_{i,n}$). Energy dissipation is defined by the area surrounded by the loading and unloading curves. In addition, the potential energy ($W_{i,n}$) of the concrete member during loading is defined by the load displacement curve and the area surrounded by the horizontal axis without considering the unloading curve. The response feature ($Z_{i,n}$) measured at each station is defined as in Eq. (5).

$$Z_{i,n} = (1 - \psi_{i,n}) \cdot 100\% \tag{5}$$

$$\psi_{i,n} = \frac{\Delta W_{i,n}}{W_{i,n}} \tag{6}$$

Fig. 6 The response characteristics to bending moment (Z)



where, “ n ” indicates the loading step, and “ i ” indicates each measurement point. Since the response feature Z in Eq. (5) does not take residual strain into consideration, $\varsigma_{i,n}$ representing the effect of residual strain is introduced into Eq. (5) to consider the residual strain, as shown in Eq. (7).

$$Z_{i,n} = \left(1 - \varsigma_{i,n} \frac{\Delta W_{i,n}}{W_{i,n}} \right) \cdot 100\% \quad (7)$$

$$\varsigma_{i,n} = 1 + \left(\frac{\varepsilon_n}{\varepsilon_{lim}} \right) \quad (8)$$

where, $\varsigma_{i,n}$ indicates the residual strain remaining after loading steps, and ε_{lim} is the upper limit of the compressive concrete strain (in this study, 0.002). Considering the BG-INT and BG-DMG2, the vertical displacement at the span center was not measured at the final unloading step as previously mentioned. The response feature (Z) before loading is assumed to be 100%. As shown in Fig. 6, Z of BG-INT gradually decreases as loading step progresses, and Z of BG-DMG1 and BG-DMG2 also generally decreased, although temporarily increases at Load2 and Load3 are observed.

4 Result of Vibration Experiment

Figure 7 shows the results of the identification of the natural frequencies of the 1st bending mode and 2nd bending mode from acceleration data of the impact excitation experiment. The red solid circle in the figure indicates the mean value of the identified natural frequencies, and the error bars indicate the standard deviation.

In BG-INT, the natural frequencies of both the 1st bending mode and 2nd bending mode tend to decrease as loading step progresses because of the decrease in stiffness due to crack propagation following loading steps. The change rate of decrease in the natural frequency from St.1 to St.8 was larger than that from St.8 to St.9

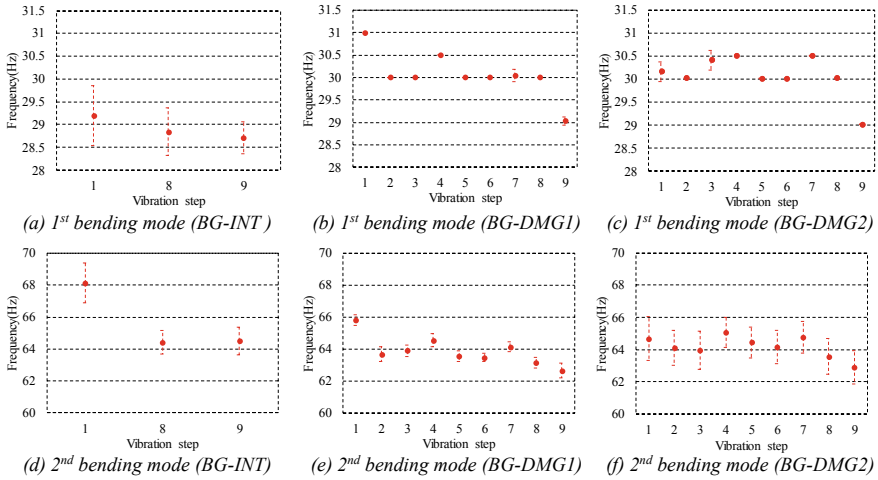


Fig. 7 The natural frequency

as the effective cross-section area was reduced due to initial cracking at Load1 although the reduction in stiffness was small as shown in Fig. 5b. In BG-DMG1, the natural frequencies of both the 1st bending mode and 2nd bending mode also showed decreasing tendency as loading step progresses. However, the natural frequency was increased temporarily in St.4 and St.7, which were measured after two days of cutting the PC tendon. In BG-DMG2, the natural frequency generally decreased as loading step progresses, but the rate of decrease before and after the first loading (St.1 and St.2) was smaller than that of BG-DMG1. However, similar to the BG-DMG1, the natural frequency increased at St.4 and St.7 two days after PC tendon cutting.

Although it is expected that the natural frequency would decrease due to the damage caused by the static loading, the natural frequency increased after loading. This phenomenon is considered to be caused by the restoring force due to the prestressing force of PC tendon. Another possible reason is that changes in location of neutral axis due to the smoothing of stress in the cross-section of during two days resulted in the frequency increase.

5 Comparison of Bridge Performance and Vibration Characteristics

To consider the correlation between bridge performance and modal parameters, relationship between response feature and bending frequency is investigated as shown in Fig. 8 in which the vertical axis indicates the response feature (Z) and the horizontal axis shows the natural frequency. Linear regression lines, the correlation coefficient is R and the coefficient of determination R^2 for BG-DMG1 and BG-DMGs girders

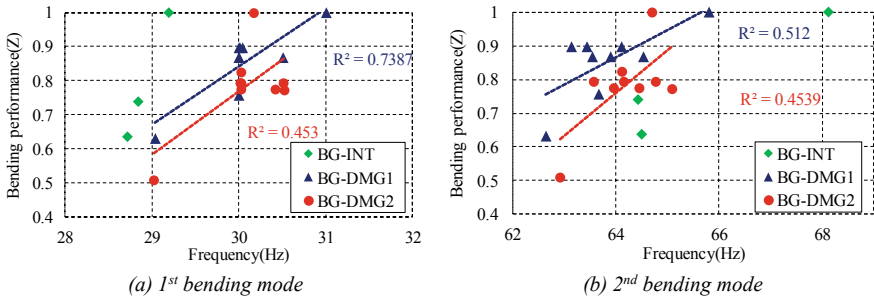


Fig. 8 Correlation between bending performance and natural frequency

are also shown in Fig. 8. For the BG-INT, the linear regression was not estimated because of the small numbers of data. For BG-DMG1, R^2 of 1st bending mode and the response feature (Z) was 0.7387, and R^2 of 2nd bending mode and the response feature (Z) was 0.512. From this result, it is obvious that there exists correlation between bending performance (response feature (Z)) and natural frequency. For BG-DMG2, R^2 of 1st bending mode and the response feature (Z) was 0.453 and R^2 of 2nd bending mode and the response feature (Z) was 0.454.

6 Conclusions

Static loading and vibration experiments on PC box girders are conducted in order to clarify the relationships between structural performance and vibration characteristics of PC box girder. The response feature of the PC box girder as a bending performance is estimated from static loading experiment, and the modal parameters are estimated from the impact hammer test. Observations from the study are summarized as follows.

For the PC box girder without damage (BG-INT girder), the load–displacement curve passed through the unloading point of the previous loading step. On the other hand, for the damaged PC box girders (BG-DMG1 and BG-DMG2), when the PC tendons were cut, the load–displacement curve did not pass through the unloading point because cut the PC tendons led to reduced stiffness against bending deformation.

The response feature (Z) for bending performance estimated from the load–displacement curve decreased with loading in all girders. It is confirmed that in BG-DMG2, the rate of decrease in bending performance was greater, because more PC tendons were cut than BG-DMG1.

The natural frequency generally decreased as static loading step progresses. However, increased frequency was observed after a period of time from cutting the PC tendons because of the restoring force of the remaining PC tendon.

However, the effects of grout filling failure and PC tendon cutting on changes in natural frequency were not so strong, even though it was observed that both of

the bending performance and the natural frequency decreased as the loading step progresses.

In order to suggest the relationship between structural performance and modal parameters of PC box girders, it is important to accumulate more data and to consider the change of the natural frequency under various conditions. Moreover, analytical studies utilizing updated FE model using experimental data are needed to understand mechanism of the change in structural performance and modal parameters clearly. Those remaining issues to be solve are left for the future study.

Acknowledgements This work is supported by JSPS Grant-in-Aid for Scientific Research (B) (Grant No: 19H0225). These financial supports are greatly acknowledged. The authors also would like to thank the researchers who participated in the experiments.

References

1. Ministry of Land, Infrastructure, Transport and Tourism, Road Bureau (2020) Annual Report on Road Maintenance (in Japanese)
2. Ministry of Land, Infrastructure, Transport and Tourism, Road Bureau (2019) Annual Report on Road Statistics (in Japanese)
3. Kenta T, Yasushi T, Hiroaki I, Takuya O, Kiyotaka T, Norio H Evaluation of structural performance of continuous PC box girder bridge affected by corrosion of reinforcement-Case of Mykoohashi bridge (in Japanese)
4. Brüel & Kjær (2003) Experimental modal analysis

The Validation of Sensor On-Vehicle for Evaluation of Actual Bridges with Signal Processing



Yuta Takahashi, Naoki Kaneko, Ryota Shin, and Kyosuke Yamamoto

Abstract Bridge has a diversity. Various environments and backgrounds create a uniqueness of the bridge, making inspection and evaluation difficult. In Japan, the number of bridges 50 years after construction has been increasing, on the other hands, regular inspections have become mandatory, however the efficiency was not high because of visual inspection. This study focuses on vibration of vehicle going on the bridge. Since it is difficult to estimate accurate bridge vibration from vehicle vibration because the vehicle-bridge interaction is complex dynamics problem, the technology is applied as a screening technique. Screening technique can optimize the resource (e.g.: human and sensor) for inspection, evaluation and repair by carrying out of the triage of bridges which have to be inspected in detail. The vehicle sensor is designed based on a common concept considering in future installation on bridges. Due to detect the effects of structural changes, it is necessary that the quantization bit rate of the Analog-Digital converter (ADC) is high. Previous study uses 12 t16 bits commonly, thus this study developed several acceleration sensor devices which mount an ADC of 17 and 23 bits and experimented on actual bridge. Sensors were installed on both the vehicle and the bridge, and the vibrations of both sensors were compared and evaluated. The criterion for identification uses Spatial Singular Mode Angle (SSMA) which assumes bridge vibration from interpolated vehicle ones by singular values decomposition. SSMA has been proved as damage detection criterion for bridge through previous study. Although it is difficult for vehicle sensors to completely reproduce bridge vibrations, it was suggested that statistical analysis of

Y. Takahashi (✉)

Yachiyo Engineering Co.Ltd, Taito, Tokyo, Japan

e-mail: yt-takahashi@yachiyo-eng.co.jp

N. Kaneko

College of Engineering Systems, University of Tsukuba, Tsukuba, Ibaraki, Japan

R. Shin

Masters Program in Service Engineering, University of Tsukuba, Tsukuba, Ibaraki, Japan

K. Yamamoto

Faculty of Engineering, Information and Systems, University of Tsukuba, Tsukuba, Ibaraki, Japan

SSMA etc... may capture structural change of actual bridge. The validation of sensor on-vehicle for evaluation of actual bridges with signal processing.

Keywords Vehicle-bridge interaction(VBI) · MEMS · Spatial singular mode angle(SSMA) · Drive-by bridge inspections

1 Introduction

Recent years in Japan, inspections only which can perform as same as visual inspection have been accepted legally, for instance sensor or UAV. Inspections by sensors have the capacity to directly capture structural changes. However, installation of sensor on the bridge directly is hard, and the cost for detection of the slight influence from structural changes becomes often high. For example, change of natural frequency is depended to rigidity of bridge, thus the detection of small damage need extreme accurate and robust sensors if before the rigidity change becomes larger. A lot of sensors is necessary for modal analysis, and the robustness to numerical integration is required for calculation of accurate deflection. They causes the growth of total cost for bridge maintenance, and it can be assumed that the feasibility will become lower. Additionally, it is consider that the power supply and communication system are necessary for realization of long term bridge monitoring.

Putting sensor on bridge often does it only becomes cost labor, but also power supply problem is occurred. Ones on vehicle doesn't become expensive, and not measure accurately. The spec of sensor on vehicle and the index based on the measure data should be validate considering this problem. Yan et al proposed the method to estimate the bridge natural frequency from vehicle vibration with solved the Vehicle-Bridge Interaction (VBI), however, their study didn't consider the road profile [1]. Nagayama et al estimated the natural frequency of bridge with considered the road profile [2]. The bridge natural frequency can't be estimated easily because the effect of damage is small and they is disturbed by measurement noise, thus the cost of sensor becomes high to capture them. On the other hands, the method using mode shape for damage detection is proposed [3–5]. SSMA, which is one of the damage index for bridge damage based on estimated mode shape, use the Singular Value Decomposition (SVD), hence the mode is expected to be robust for time space. Continuous SSMA is proposed to detect the structural change [6]. This index is calculated from continuous vehicle vibration data, with shift of a fixed calculation length. However, the amplitude of bridge response is smaller than the vehicle one, the estimated mode shape is often affected from quantization bit rate of analog-digital converter (ADC). This study evaluates the effect to frequency or SSMA from the difference in bitrate of ADC. The vehicle put on two sensor systems which has 17 or 23 bit resolution is used for measurement experiment on three actual bridge, and the frequency analysis and calculation SSMA based on the data measured by both of sensor systems. The effect of ADC bitrate to mechanical index for bridge screening technology based on signal processing such as frequency or SSMA. SSMA

is validated based on bridge length which is structure characteristic and vehicle velocity.

2 Vehicle-Bridge Interaction Theorem

2.1 Vehicle Model and Spatial Singular Mode Angle

The mathematical theorem of SSMA is shown. Calculation needs vibration and position at the front, rear axles of vehicle. The vibration should be obtained from mass points under the spring. The assumed vehicle (Half Car) model is shown in Fig. 1. This model has a rigid body as sprung-mass system, of which mass is m_s , and of which inertia moment is I_s . The point G indicates the centre of gravity, and the distances from the point G to the front and the rear axles are L_1 and L_2 , respectively. In this figure, it is noted that L_1 and L_2 described as if as equal, however they are ordinary different because the engine often put near front wheel. The subscript i ($= 1, 2$) represents the front and rear axles. $z_{si}(t)$ and $z_{ui}(t)$ are the vertical displacements of the sprung-mass and the unsprung-mass. $u_i(t)$ is the forced displacement input under the i th axle. k_{si} and c_{si} are the spring stiffness and the damping of the spring-mass at the i th axle. m_{ui} , k_{ui} and c_{ui} are the mass, spring stiffness and damping of the unsprung-mass at the i th axles, respectively. The equation of motion of the vehicle can be described by the following.

$$\mathbf{M}_V \ddot{\mathbf{z}}(t) + \mathbf{C}_V \dot{\mathbf{z}}(t) + \mathbf{K}_V \mathbf{z}(t) = \mathbf{C}_P \dot{\mathbf{u}}(t) + \mathbf{K}_P \mathbf{u}(t) \tag{1}$$

where

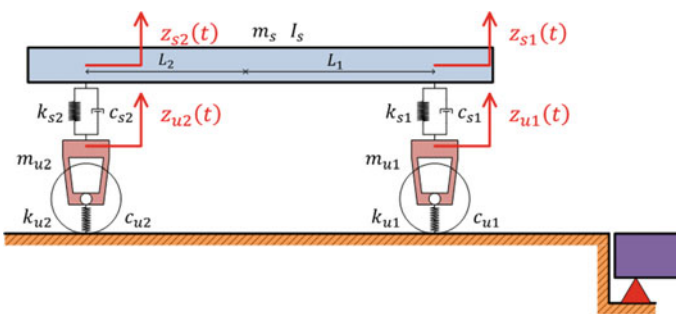


Fig. 1 Vehicle (half car) model

$$\mathbf{z}(t) = \begin{Bmatrix} z_{s1}(t) \\ z_{s2}(t) \\ z_{u1}(t) \\ z_{u2}(t) \end{Bmatrix} \tag{2}$$

$$\mathbf{u}(t) = \begin{Bmatrix} u_1(t) \\ u_2(t) \end{Bmatrix} \tag{3}$$

$$\mathbf{M}_V = \begin{bmatrix} \frac{L_2 m_s}{L_1 + L_2} & \frac{L_1 m_s}{L_1 + L_2} \\ \frac{I_s}{L_1 + L_2} & -\frac{I_s}{L_1 + L_2} \\ & m_{u1} \\ & & m_{u2} \end{bmatrix} \tag{4}$$

$$\mathbf{C}_V = \begin{bmatrix} c_{s1} & c_{s2} & -c_{s1} & -c_{s2} \\ L_1 c_{s1} & -L_2 c_{s2} & -L_1 c_{s1} & L_2 c_{s2} \\ -c_{s1} & 0 & c_{s1} + c_{u1} & 0 \\ 0 & -c_{s2} & 0 & c_{s2} + c_{u2} \end{bmatrix} \tag{5}$$

$$\mathbf{K}_V = \begin{bmatrix} k_{s1} & k_{s2} & -k_{s1} & -k_{s2} \\ L_1 k_{s1} & -L_2 k_{s2} & -L_1 k_{s1} & L_2 k_{s2} \\ -k_{s1} & 0 & k_{s1} + k_{u1} & 0 \\ 0 & -k_{s2} & 0 & k_{s2} + k_{u2} \end{bmatrix} \tag{6}$$

$$\mathbf{C}_P = \begin{bmatrix} 0 & 0 \\ 0 & 0 \\ c_{u1} & 0 \\ 0 & c_{u2} \end{bmatrix} \tag{7}$$

$$\mathbf{K}_P = \begin{bmatrix} 0 & 0 \\ 0 & 0 \\ k_{u1} & 0 \\ 0 & k_{u2} \end{bmatrix} \tag{8}$$

respectively. $\dot{(\)}$ and $\ddot{(\)}$ denote the first-order and second-order time differentiation.

Since the number of sensors are same with that of estimated mode shapes, when we set a sensor on each axle, only the first and second modes can be obtained. When we use only lower mode shapes, their variation can be explained only from two factors: the measurement environment and the structural change. The latter is, in other word, a damage. On the other hand, when we use more sensors, the main factor of variation becomes the ill condition problem, which means that the results depend only on noise, not on the status of the structure.

On the other hand, the bridge displacement at position x and time t can be decomposed as follows:

$$y(x, t) = \sum_k \phi_k(x) q_k(t) \quad (9)$$

$\phi_k(x)$ is the k th order mode shape, and $q_k(t)$ is the k th order basis coordinates. Substituting each axle position $x_i(t)$ into Eq. 9, the bridge displacement just under the i th axle is shown below:

$$y_i(t) = \sum_k \phi_k(x_i(t)) q_k(t) \quad (10)$$

Assuming that the road roughness at the position of x is $R(x)$, the input component of the i th axle of the vehicle at the time of t is shown below:

$$r_i(t) = R(x_i(t)) \quad (11)$$

Then, the forced displacement inputs can be described by

$$\mathbf{u}(t) = \mathbf{y}(t) + \mathbf{r}(t) \quad (12)$$

Where

$$\mathbf{y}(t) = \begin{Bmatrix} y_1(t) \\ y_2(t) \end{Bmatrix} \quad (13)$$

$$\mathbf{r}(t) = \begin{Bmatrix} r_1(t) \\ r_2(t) \end{Bmatrix} \quad (14)$$

On the other hand, assuming that

$$\Phi(t) = \begin{bmatrix} \phi_1(x_1(t)) & \phi_2(x_1(t)) \\ \phi_1(x_2(t)) & \phi_2(x_2(t)) \end{bmatrix} \quad (15)$$

$$\mathbf{q}(t) = \begin{Bmatrix} q_1(t) \\ q_2(t) \end{Bmatrix} \quad (16)$$

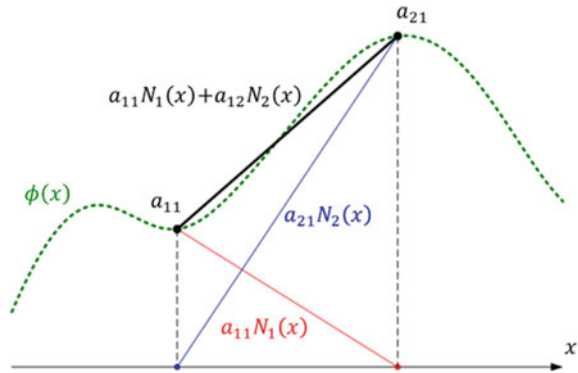
Equation 12 can be rewritten in

$$\mathbf{u}(t) = \Phi(t)\mathbf{q}(t) + \mathbf{r}(t) \quad (17)$$

Next, $\phi_k(x_i(t))$ can be discretized by interpolation as below:

$$\phi_k(x) = \sum_{j=1}^n a_{jk} N_j(x) \quad (18)$$

Fig. 2 Concept of interpolation



When the base function $N_j(x)$ is the Lagrangian function, the coefficient a_{kj} indicates the amplitude of k th order mode shape at the discretized position x_j . Fig. 2 shows the concept of this interpolation.

When $n = 2$ and $x_1 = L/3$ and $x_2 = 2L/3$, the Lagrangian function is

$$N_1(x) = -\frac{3}{L}x + 2 \tag{19}$$

$$N_2(x) = \frac{3}{L}x - 1$$

$$\begin{bmatrix} \phi_1(x_1(t)) & \phi_2(x_1(t)) \\ \phi_1(x_2(t)) & \phi_2(x_2(t)) \end{bmatrix} = \begin{bmatrix} N_1(x_1(t)) & N_2(x_1(t)) \\ N_1(x_2(t)) & N_2(x_2(t)) \end{bmatrix} \begin{bmatrix} a_{11} & a_{12} \\ a_{21} & a_{22} \end{bmatrix} \tag{20}$$

By using Eqs. 19 and 20, 18 becomes

$$\Phi(t) = \mathbf{N}(t)\mathbf{A} \tag{21}$$

where the (k, j) component of the matrix \mathbf{A} is a_{kj} . Assuming that the unsprung-mass parameters of the front and rear axles are same, which means that $k_{u1}/m_{u1} = k_{u2}/m_{u2} = k_u/m_u$ and $c_{u1}/m_{u1} = c_{u2}/m_{u2} = c_u/m_u$, the vertical acceleration vibrations of the unsprung-mass can be described by

$$\ddot{\mathbf{z}}_u(t) = \begin{Bmatrix} \ddot{z}_{u1}(t) \\ \ddot{z}_{u2}(t) \end{Bmatrix} = \mathbf{N}(t)\mathbf{A}\boldsymbol{\sigma}(t) + \bar{\boldsymbol{\epsilon}}(t) \tag{22}$$

$$\boldsymbol{\sigma}(t) = \frac{k_u}{m_u}\mathbf{q}(t) + \frac{c_u}{m_u}\dot{\mathbf{q}}(t) \tag{23}$$

$$\bar{\boldsymbol{\epsilon}}(t) = -\frac{1}{m_u} \begin{bmatrix} -c_{s1} & c_{s1} + c_u \\ -c_{s2} & c_{s2} + c_u \end{bmatrix} \mathbf{z}(t) \tag{24}$$

$$-\frac{1}{m_u} \begin{bmatrix} -k_{s1} & k_{s1} + k_u \\ & -k_{s2} & k_{s2} + k_u \end{bmatrix} \dot{\mathbf{z}}(t) + \frac{k_u}{m_u} \mathbf{r}(t) + \frac{c_u}{m_u} \dot{\mathbf{r}}(t)$$

where

If the position of each axle $x_j(t)$ are available, the interpolation matrix $\mathbf{N}(t)$ can be calculated. Since the unsprung-mass vibrations $\ddot{\mathbf{z}}_u(t)$ and the interpolation matrix $\mathbf{N}(t)$ are known, we obtain

$$\mathbf{N}^{-1}(t)\ddot{\mathbf{z}}_u(t) = \mathbf{A}\boldsymbol{\sigma}(t) + \boldsymbol{\epsilon}(t) \tag{25}$$

$$\boldsymbol{\epsilon}(t) = \mathbf{N}^{-1}(t)\bar{\boldsymbol{\epsilon}}(t) \tag{26}$$

The left side of Eq. 25 is the spatial correction of vehicle vibrations. Based on Eq. 25, the mode shape \mathbf{A} can be estimated by SVD (Singular Value Decomposition) of $\mathbf{N}^{-1}(t)\ddot{\mathbf{z}}_u(t)$. By SVD, the mode shape \mathbf{A} and the bridge vibration component $\boldsymbol{\sigma}(t)$ are calculated at the same time. The bridge components includes only information about the bridge vibration and unsprung-mass characteristics of the vehicle. Others are included in the error term $\boldsymbol{\epsilon}(t)$: the vehicle responses: $\mathbf{z}(t)$, $\dot{\mathbf{z}}(t)$ and the road roughness: $\mathbf{r}(t)$ and $\dot{\mathbf{r}}(t)$. Since $\mathbf{N}^{-1}(t)\ddot{\mathbf{z}}_u(t)$ is time function, it can be described as data matrix $\mathbf{D} \in R^{2 \times T}$. T means the number of the measured data. The SVD of \mathbf{D} is described by the product of an orthogonal matrix $\mathbf{U} \in R^{2 \times 2}$, a diagonal matrix $\boldsymbol{\Sigma} \in R^{2 \times 2}$ and an orthogonal matrix $\mathbf{V} \in R^{T \times 2}$ ($\mathbf{V}^T\mathbf{V} = \mathbf{I}$: the unit matrix) as below:

$$\mathbf{D} = \mathbf{U}\boldsymbol{\Sigma}\mathbf{V}^T \tag{27}$$

where \mathbf{U} is the estimation of \mathbf{A} , and $\boldsymbol{\Sigma}\mathbf{V}^T$ is the estimation of $\boldsymbol{\sigma}(t)$ in the form of data matrix. In order for SVD of \mathbf{D} to accurately estimate the bridge mode shape \mathbf{A} , the following conditions need to be satisfied:

- (a) $\boldsymbol{\sigma}(t)$ is uncorrelated.
- (b) Error term $\boldsymbol{\epsilon}(t)$ is white noise.

The bridge vibration components $\mathbf{q}(t)$ and $\dot{\mathbf{q}}(t)$ are transient responses induced by the traffic loads, in this case. Thus, it is considered that the real values of $\boldsymbol{\sigma}(t)$ does not satisfy the condition of a). While the SVD process gives the estimated bridge vibration components $\boldsymbol{\Sigma}\mathbf{V}^T$, they are just uncorrelated signals near $\boldsymbol{\sigma}(t)$. The error due to this affects on the estimated mode shape \mathbf{U} . This means that the estimation mode shape \mathbf{U} and the succeeding index SSMA deviate slightly from the correct mode shape. This effect on SSMA, however, can be expected to be unchanging under the same measurement condition.

Generally, a local damage on a bridge never influence the dynamic indices of the global system of the structure. Thus, it is expected that \mathbf{A} remains unchanged even after the damage. However, because the local bridge responses are easily affected by the damage, the component $\sigma(t)$ changes. The estimation for it is $\Sigma \mathbf{V}^T$ and it cannot trace the transition. This error is included in the error of \mathbf{U} . This is the mechanism of SSMA to react a bridge's local damage.

The error term $\epsilon(t)$ does not include the bridge vibrations, but the vehicle vibrations $z(t)$, $\dot{z}(t)$ and the road profile $r(t)$, $\dot{r}(t)$. Because the influence of the damage on the bridge vibrations is a kind of pulse, the impact of the damage on the bridge vibration is not transmitted strongly to the vehicle. The error term may affect the result, but the effect is constant and can be ignored. It is noted that the property, which affects SSMA, is the running speed of the vehicle, because the conversion process in Eq. 11 depends on time space.

From the above consideration, although \mathbf{U} , the estimated bridge mode shape in Eq. 27, is different from the actual value \mathbf{A} , it can be used as an evaluation index for the bridge health. It also suggests that SSMA is a possible indicator for bridge screening, because it is more sensitive than the actual mode shape.

3 Experiment on Actual Bridge

Experiment is carried out on PC and Steel bridges. They are two PC and one steel and called as PC1, PC2 and S1. Acceleration and their power spectrum (PS) on 17 and 23 bit rate are shown in Fig. 3. The vehicle vibration over bridge is identified from GPS position of sensor on vehicle and bridges entrance and exit. Blue shows the front unsprung z axis vibration, and orange shows the rear one. Gravity direction is negative. SSMA uses the unsprung vibration, thus this study focuses them. The bridges and vehicle parameter are shown in Table 1. The velocity of vehicle is decided by actual traffic speed. Other vehicles which go through the same bridge then is ignored because the experiment vehicle weight is very heavy (13.8t) and it is confirmed that the similar weight vehicle didn't go with the experiment vehicle when the data in this study are measured. All bridges are evaluated as level I by Japanese bridge inspection expert. The sensor position on vehicle is shown in Fig. 4.

Acceleration amplitude is different with 17 and 23 bit ADC, because they can be affected from the position or eccentricity.

The PS of 17bit has peaks on low frequency (~10Hz). The shorter bridge often has around 10 Hz as natural frequency, thus the result is proper. Notice the short PC bridge are ordinary more rigid than similar steel ones.

On the other hands, the acceleration of 23 bit ADC captures the peaks which is seems to have been when going over joint. The PS on high bitrate has more peaks on higher frequency although there are small peaks in lower 10 Hz. This result can be caused by high bitrate noise because the higher bitrate ADC is more affected from electrical or heat disturbance. However, notice the SSMA is robust for high time frequency noise because it calculated from the assumed bridge vibration by

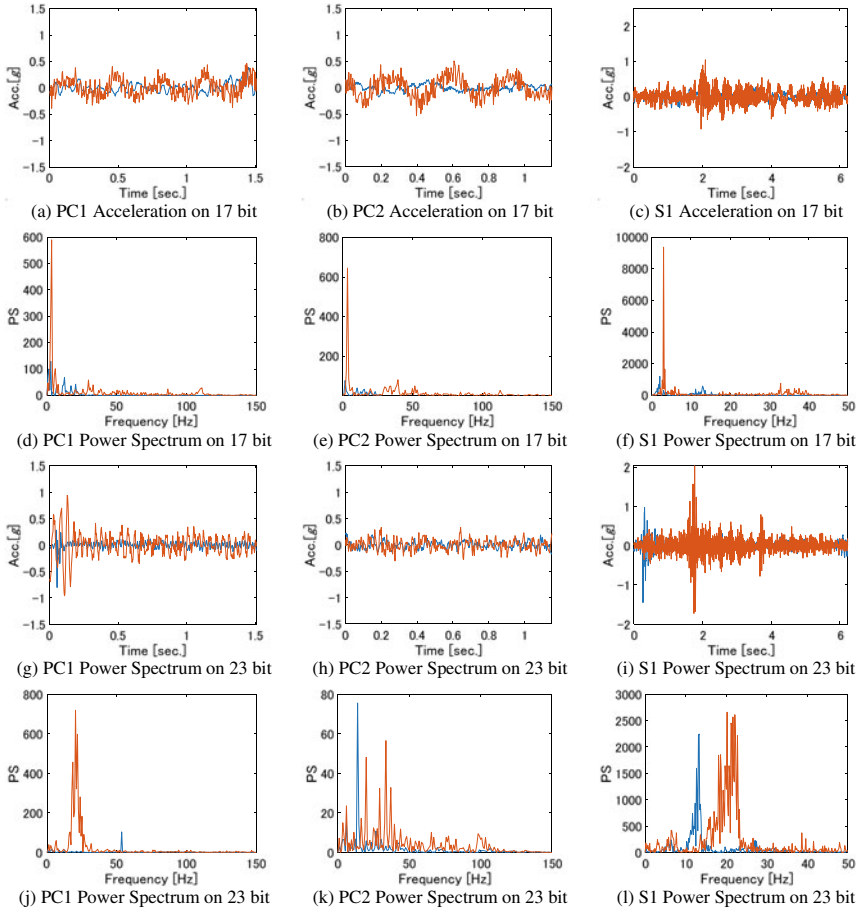


Fig. 3 Acceleration and Power Spectrum on experiment bridges (17 and 23 bit ADC).

Table 1 The parameter in experiment

	PC1	PC2	S1
Span [m]	12.6	14	30
Girder Type, Number	I	T, 4	Steel, 4
Vehicle Weight [t]	13.8		
Vehicle Velocity [km/h]	17.3	43.6	30.0

Singular Value Decomposition (SVD) which can decompose the signal to time or spatial frequency domain.

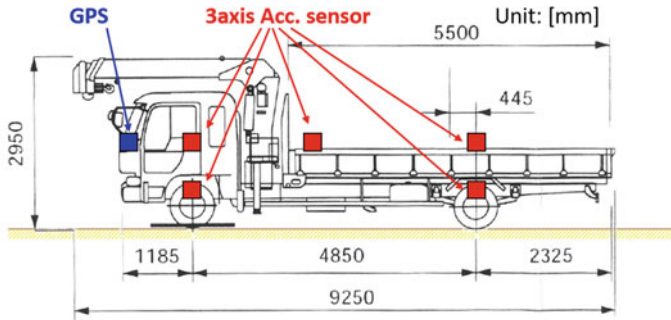


Fig. 4 The position of sensor on vehicle

4 Analysis and Discussion

The SSMA is the index for capture of structural change. However, previous study shows that the calculation is affected from vehicle velocity [6]. Therefore, it is desirable that SSMA should be robust for velocity change and sensitive for structural change. SSMA calculated from experiment result plot with vehicle velocity or span length for horizontal axis. The velocity—SSMA 2D plot are shown in Fig. 5, and the length—SSMA 2D plot are shown in Fig. 6. Blue crosses are the SSMA on low (17 bit) bitrate, and the red ones are high (23 bit) bitrate. In this study, the length change is assumed as most dominant structural change.

The variance of velocity is 126. The variance of SSMA on 17 bit is 123.5 and the variance on 23 bit result is 7.22. The variance of SSMA with velocity change is desirable to be small because previous study [6] suggests bridge damage makes the variance of SSMA greater. The SSMA on 17 bit is changed with velocity and the change seems to be independent on the length change. The change on 23 bit with velocity is smaller than result in 17 bit, and it seems to depend on length change

Fig. 5 Vehicle velocity—SSMA

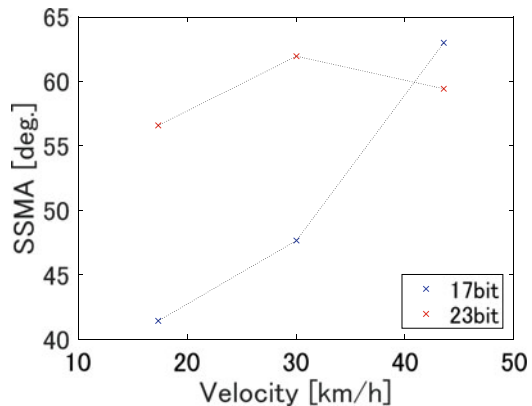
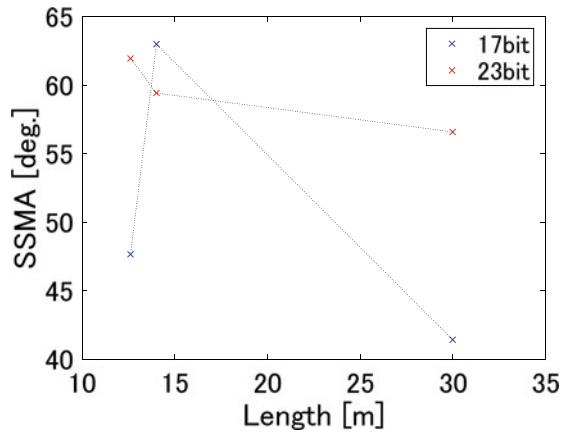


Fig. 6 Span length—SSMA



than the result in 17 bit. Since SSMA should behavior along with structural change rerated to bridge mode, this suggest the result on 23 bit is preferable. The trends of ADC (i.e. low frequency components) which can affect to mode angle estimation is generated from the accumulation of quantization error, and the error becomes more greater by the calculation length change with velocity change when the bitrate is lower. Therefore, this result suggests that the index using vehicle vibration on VBI such as SSMA can require the high bitrate ADC.

5 Conclusions

This study validates that the difference of Analog Digital Converter bitrate affect the performance of the bridge damage index such as natural frequency or Spatial Singular Mode Angle by comparison of the result in three actual bridges experiment. The findings is shown as below:

For validation of the effect of ADC bitrate to the bridge damage index, two bitrate (17 and 23 bit for low and high) ADC is prepared for experiment on actual bridges. The measured acceleration amplitudes are different because the position or eccentricity, however, peaks which are considered as the bridges natural frequency is appear.

Lower bitrate acceleration and their power spectrum is seems to have a strong low frequency component. This can be caused by the calculation length change expanded the effect of quantization error when the bitrate is lower.

Higher bitrate and their power spectrum has a strong high frequency component which may be generated from the electrical and heat disturbance. However, SSMA which can expect as a robust index to high time frequency noise are also robust to the vehicle velocity change. On the other hands, the change with length change

which was assumed as the most dominant structural change in this study reacts more linearly than the lower bitrate result.

In this experiment, the vehicle running was repeated and the data could be obtained on the other bridge. For future works, the validity of this study analysis is verified through the statistical analysis. In addition, the feasibility of the screening (in the future, inspection) using SSMA will be verified in the field experiment at large area.

Acknowledgments This study is supported by MEXT/JSPS KAKENHI Grant Number JP19H02220. The experiments shown in this paper were carried out in cooperation with Ibaraki Prefecture in Japan.

References

1. Yang Y-B, Lin CW, Yau JD (2004) Extracting bridge frequencies from the dynamic response of a passing vehicle. *J Sound Vib* 272:471–493
2. Nagayama T, Reksowardojo AP, Su D, Mizutani T (2017) Bridge natural frequency estimation by extracting the common vibration component from the responses of two vehicles. *Eng Struct* 150:821–829
3. Yang YB, Chang KC (2009) Extraction of bridge frequencies from the dynamic response of a passing vehicle enhanced by the EMD technique. *J Sound Vib* 322(718–739):2009
4. O'Brien EJ, Malekjafarian A (2016) A mode shape-based damage detection approach using laser measurement from a vehicle crossing a simply supported bridge. *Struct Control Health Monit* 23(10):1273–1286
5. Yamamoto K, Ishikawa M (2016) Numerical verification of bridge screening technology based on vehicle vibration. In: *Lecture notes in engineering and computer science: proceedings of the world congress on engineering, London, U.K.*, pp 933–938
6. Takahashi Y, Yamamoto K (2019) The application of drive-by bridge damage detection based on continuous SSMA to the field experimental data. *Int J Lifecycle Perform Eng* 3(3–4):310–330

Inverse Analysis for Road Roughness Profile Identification Utilizing Acceleration of a Moving Vehicle



Soichiro Hasegawa, Chul-Woo Kim, Naoya Toshi, and Kai-Chun Chang

Abstract A road roughness profile of pavement surface is one of the important indicators for status of bridges and roads, and regular pavement monitoring and repairing directly link to the life span of the bridge and road. This research proposes a dynamic regularized least square minimization to identify the road roughness profile directly by regularized least square minimization with dynamic programming. A new discrete-time linear state-space model of a vehicle dynamics which has a road roughness profile as an external input to the system is also proposed. Kalman filter is also a widely researched method of road roughness profile identification. The identification accuracy of dynamic regularized least square minimization was compared to that of Kalman filter. Observations showed that dynamic regularized least square minimization showed a reasonable accuracy and the accuracy was higher than that of Kalman filter in respect of Power Spectral Density (PSD) and International Roughness Index (IRI).

Keywords Road roughness profile identification · Vehicle acceleration · Inverse analysis · Dynamic regularized least square minimization · Drive-by inspection

1 Introduction

A roadway roughness profile is one of the important indicators for status of bridges and roads. If the road roughness condition becomes worse, it could cause decrease in riding comfort of vehicles and shorten the lifespan of the bridge caused by large vibrations of vehicles. In order to prevent from such situations, it is needed to inspect the road roughness profile and repair them regularly [1]. There are a number of methods to measure the road roughness profile. For example, to measure the road roughness profile manually using laser displacement sensors is one of the most basic methods. In recent years, a specially equipped inspection car with laser displacement sensors is developed and used in inspection. The inspection car has high identification

S. Hasegawa (✉) · C.-W. Kim · N. Toshi · K.-C. Chang
Department of Civil and Earth Resources Engineering, Kyoto University, Kyoto, Japan

© The Author(s), under exclusive license to Springer Nature Switzerland AG 2023
Z. Wu et al. (eds.), *Experimental Vibration Analysis for Civil Engineering Structures*,
Lecture Notes in Civil Engineering 224,
https://doi.org/10.1007/978-3-030-93236-7_53

accuracy and needs only short time to measure the road roughness profile although operating the inspection car is high in cost.

If road roughness profile can be identified by using only vehicle accelerations especially by the bounce motion, it could save cost and labor drastically. Methods to obtain a various information of bridges or roads using vibrations of a running vehicle is called as “drive-by inspection”, and using accelerations of vehicle has been focused on in recent years [2–10] because accelerometers are relatively low-cost sensors. However, the ill-posedness in the inverse analysis of the road roughness profile identification makes it difficult to identify in high accuracy only using accelerations of vehicle bounce motion. O’Brien et al. [11] and McGetrick et al. [12] showed high accuracy of the road roughness profile identification method by regularized least square minimization with numerical simulation. Chang et al. [13] and the author [14] also showed feasibility of the regularized least square minimization in road roughness identification through a field experiment. Those methods identify moving force of the vehicle firstly and convert the force to the road roughness profile in the second step, although there is a risk of identification error caused by numerical integration process converting the moving force to the road roughness profile. Therefore, it is desirable to identify the road roughness profile directly, not through the moving force identification.

The direct road roughness profile identification by the least square minimization is already proposed by the authors [15], however this method used a pseudo-inverse matrix to solve the least square minimization, and it may cause an identification error by the calculation of large size inverse matrix and also take much calculation time. To solve those difficulties, it is better to use a dynamic programming to solve the least square minimization, which does not require any calculation of large size inverse matrices. In this paper, the direct road roughness profile identification by least square minimization with dynamic programming is proposed, which is a combination of the advantages of the direct road roughness profile identification and dynamic programming. A field moving vehicle experiment is carried out, and the accuracy of the road roughness profile identification by dynamic regularized least square minimization (DRLS minimization) is investigated in respect of Power Spectral Density (PSD) and International Roughness Index (IRI) [16]. The accuracy of the proposed method is compared with that of Kalman filter because Kalman filter also has been studied actively as one of the road roughness profile identification methods [6, 17, 18].

2 Road Profile Identification Method

2.1 Discrete-Time Linear State-Space Model

A discrete-time linear state-space model of a vehicle model is firstly derived. The vehicle model is 2-degrees-of-freedom (2DOF) model as shown in Fig. 1. Dynamic equation of motion of the 2DOF vehicle is shown as Eq. (1).

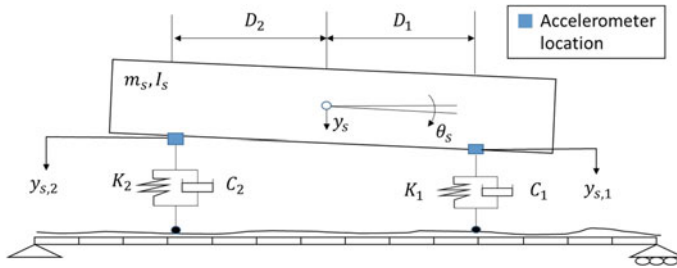


Fig. 1 Two-degrees-of-freedom half-car model

$$\mathbf{M}_v \ddot{\mathbf{y}}_v + \mathbf{C}_v \dot{\mathbf{y}}_v + \mathbf{K}_v \mathbf{y}_v = \mathbf{f}_v \tag{1}$$

where, $\mathbf{M}_v, \mathbf{C}_v$ and \mathbf{K}_v denote matrices of mass, damping, and stiffness of the vehicle, respectively. \mathbf{y}_v is a vehicle displacement vector and contains displacements in bounce and pitch. Dots above a variable means differential in time. \mathbf{f}_v is an external force vector which can be expressed as Eq. (2).

$$\mathbf{f}_v = \mathbf{K}_r \mathbf{r} + \mathbf{C}_r \dot{\mathbf{r}} \tag{2}$$

where, $\mathbf{r}(= \{r_1, r_2\}^T)$ is a road roughness profile vector which contains road roughness profiles under both front and rear axles of the vehicle. \mathbf{K}_r and \mathbf{C}_r are defined as Eqs. (3) and (4), respectively.

$$\mathbf{K}_r = \begin{bmatrix} K_1 & K_2 \\ D_1 K_1 & -D_2 K_2 \end{bmatrix} \tag{3}$$

$$\mathbf{C}_r = \begin{bmatrix} C_1 & C_2 \\ D_1 C_1 & -D_2 C_2 \end{bmatrix} \tag{4}$$

where C_i, K_i , and D_i denote a damping coefficient, a stiffness coefficient, and distance from the center of gravity of the vehicle, respectively. Subscript i ($=1, 2$) shows front and rear axles, respectively. The dynamic equation of motion of the 2DOF vehicle in Eq. (1) thus can be rewritten as discrete-time linear state-space model as Eqs. (5) and (6).

$$\mathbf{X}_{j+1} = \mathbf{M}\mathbf{X}_j + \mathbf{G}\mathbf{f}_{v,j} \tag{5}$$

$$\mathbf{X}_j = \begin{bmatrix} \mathbf{y}_{v,j} \\ \dot{\mathbf{y}}_{v,j} \end{bmatrix} \tag{6}$$

Derivation of \mathbf{M} and \mathbf{G} in Eq. (5) can be referred in [13]. Relationship between the road profile vector and its first derivative is shown as Eq. (7).

$$\dot{\mathbf{r}}_j = (\mathbf{r}_{j+1} - \mathbf{r}_j) / \Delta t \tag{7}$$

where, Δt is an interval of discrete time steps. By defining a new state vector as Eq. (8), a new discrete-time linear state-space model is obtained as Eq. (9).

$$\widehat{\mathbf{X}}_j = [\mathbf{X}_j^T \ \mathbf{r}_j^T \ \mathbf{r}_{j+1}^T]^T \tag{8}$$

$$\widehat{\mathbf{X}}_{j+1} = \begin{bmatrix} \mathbf{M} & \mathbf{G}_1 & \mathbf{G}_2 \\ 0 & 0 & \mathbf{I} \\ 0 & 0 & 0 \end{bmatrix} \widehat{\mathbf{X}}_j + \begin{bmatrix} 0 \\ 0 \\ \mathbf{I} \end{bmatrix} \mathbf{r}_{j+2} \tag{9}$$

where, \mathbf{G}_1 and \mathbf{G}_2 are defined as Eqs. (10) and (11), respectively.

$$\mathbf{G}_1 = \mathbf{G}(\mathbf{K}_r - \mathbf{C}_r / \Delta t) \tag{10}$$

$$\mathbf{G}_2 = \mathbf{G}\mathbf{C}_r / \Delta t \tag{11}$$

The advantage of the discrete-time linear state-space model defined in Eq. (9) is that this form is suitable to apply the dynamic programming in the regularized least square minimization. If a measured vehicle acceleration vector is defined as $\ddot{\mathbf{y}}_{v,j}$, relationship between measured vector and the state vector can be written as Eqs. (12) and (13).

$$\ddot{\mathbf{y}}_{v,j} = \mathbf{Q}_0 \widehat{\mathbf{X}}_j \tag{12}$$

$$\mathbf{Q}_0 = \mathbf{M}_v^{-1} [-\mathbf{K}_v \ -\mathbf{C}_v (\mathbf{K}_r - \mathbf{C}_r / \Delta t) \ \mathbf{C}_r / \Delta t] \tag{13}$$

2.2 Dynamic Regularized Least Square Minimization

The DRLS minimization is a novel approach which combines the advantages of the regularized least square minimization and the dynamic programming [19] for road roughness identification in higher accuracy. A cost function in the DRLS minimization is written as Eq. (14).

$$l = \sum_{j=1}^N \left(\ddot{\mathbf{y}}_{v,j} - \mathbf{Q}_0 \widehat{\mathbf{X}}_j \right)^T \left(\ddot{\mathbf{y}}_{v,j} - \mathbf{Q}_0 \widehat{\mathbf{X}}_j \right) + \lambda \mathbf{r}_j^T \mathbf{r}_j \quad (14)$$

where, N is a number of total time steps. In the Eq. (14), Tikhonov regularization [20] is applied. λ stands for the regularization parameter which takes a balance between the first and second terms in Eq. (14). The optimal value of λ can be obtained by L-curve method [21]. In the L-curve method, candidate λ values in a regular interval need to be preset. For each of candidate λ s, regularized least square minimization problem is solved and L2 norm of error as Eq. (15) and L2 norm of unknown parameter as Eq. (16) are obtained.

$$E_{norm} = \sqrt{\sum_{j=1}^N \left(\ddot{\mathbf{y}}_{v,j} - \mathbf{Q}_0 \widehat{\mathbf{X}}_j \right)^T \left(\ddot{\mathbf{y}}_{v,j} - \mathbf{Q}_0 \widehat{\mathbf{X}}_j \right)} \quad (15)$$

$$F_{norm} = \sqrt{\sum_{j=1}^N \mathbf{r}_j^T \mathbf{r}_j} \quad (16)$$

E_{norm} and F_{norm} corresponding to candidate λ s are plotted in log–log scale graph, where E_{norm} is placed on the horizontal axis and F_{norm} is on the vertical axis. A plotted curve line basically has a shape like a letter of “L”, and the point which has a maximum curvature is extracted as an optimal λ point [20].

2.3 Kalman Filter

Kalman filter also has been widely studied in the area of road roughness profile identification. It is observed that road roughness profile identification by Kalman filter has a reasonable accuracy, especially in case of using not only vehicle acceleration but also gyro data [18]. This study investigates the identification accuracy by DRLS minimization by comparison to the accuracy by Kalman filter. Therefore, Kalman filter in the direct road roughness identification is briefly explained in this section.

To apply Kalman filter, a discrete-time linear state-space model is used as form of Eqs. (17) and (18).

$$\mathbf{x}_{k+1} = \mathbf{A}\mathbf{x}_k + \mathbf{B}\mathbf{u}_k \quad (17)$$

$$\mathbf{y}_k = \mathbf{C}\mathbf{x}_k + \mathbf{w}_k \quad (18)$$

where, \mathbf{x}_k is a state vector, \mathbf{y}_k is a measurement vector, and subscript k is discrete time index. \mathbf{u}_k and \mathbf{w}_k are system noise and measurement noise, respectively. \mathbf{u}_k and \mathbf{w}_k follow a normal distribution as Eqs. (19) and (20).

$$\mathbf{u}_k \sim N(0, \mathbf{Q}) \quad (19)$$

$$\mathbf{w}_k \sim N(0, \mathbf{R}) \quad (20)$$

Under these conditions, Kalman filter is applied by iterative calculation of prediction step as Eqs. (21) and (22), and update step as Eqs. (23), (24), and (25).

$$\hat{\mathbf{x}}_{k+1|k} = \mathbf{A}\hat{\mathbf{x}}_{k|k} \quad (21)$$

$$\mathbf{P}_{k+1|k} = \mathbf{A}\mathbf{P}_{k|k}\mathbf{A}^T + \mathbf{B}\mathbf{Q}\mathbf{B}^T \quad (22)$$

$$\mathbf{K}_{k+1} = \mathbf{P}_{k+1|k}\mathbf{C}^T(\mathbf{R} + \mathbf{C}\mathbf{P}_{k+1|k}\mathbf{C}^T)^{-1} \quad (23)$$

$$\hat{\mathbf{x}}_{k+1|k+1} = \hat{\mathbf{x}}_{k+1|k} + \mathbf{K}_{k+1}(\mathbf{y}_{k+1} - \mathbf{C}\hat{\mathbf{x}}_{k+1|k}) \quad (24)$$

$$\mathbf{P}_{k+1|k+1} = (\mathbf{I} - \mathbf{K}_{k+1}\mathbf{C})\mathbf{P}_{k+1|k} \quad (25)$$

where, $\hat{\mathbf{x}}_{j|i}$ is a predicted state vector at time step j , which is obtained using measured data until time step i . $\mathbf{P}_{j|i}$ is the estimated covariance matrix of state vector at time step j , which is obtained using measured data until time step i . In Kalman filter, it is needed to preset values of \mathbf{Q} , \mathbf{R} , and $\mathbf{P}_{1|1}$, because those values are not calculated automatically in Kalman filter process, and such parameters are generally called as hyper parameters.

Kalman filter can estimates state vector at a specific time step based on past data. On the other hand, a method to estimate a state vector at a past time step based on measured data up to the present is generally called as smoothing. Road roughness profile identification considering measured data in all-time series is achieved by applying both of Kalman filter and Kalman smoother. Kalman smoother should be applied after Kalman filter. In Kalman smoother, Eqs. (26), (27), and (28) are applied at each time step from future to past in order.

$$\mathbf{D}_k = \mathbf{P}_{k|k}\mathbf{A}^T\mathbf{P}_{k+1|k}^{-1} \quad (26)$$

$$\hat{\mathbf{x}}_{k|N} = \hat{\mathbf{x}}_{k|k} + \mathbf{D}_k(\hat{\mathbf{x}}_{k+1|N} - \hat{\mathbf{x}}_{k+1|k}) \quad (27)$$

$$\mathbf{P}_{k|N} = \mathbf{P}_{k|k} + \mathbf{D}_k(\mathbf{P}_{k+1|N} - \mathbf{P}_{k+1|k})\mathbf{D}_k^T \quad (28)$$

Table 1 Vehicle properties

Dimension (m)	Wheel base	2.72
	Front axle—centroid	0.82
	Rear axle—centroid	1.90
Moment of inertia ($kg \cdot m^2$)	–	3954
Mass (kg)	Front axle	1391
	Rear axle	603
	Total	1994
Spring constant (N/m)	Front axle	75,749
	Rear axle	99,646
Damping coefficient ($N \cdot s/m$)	Front axle	12,535
	Rear axle	3602

At $k = N$, it is assumed that $\mathbf{P}_{N+1|N} = \mathbf{P}_{N|N}$, and $\hat{\mathbf{x}}_{N+1|N} = \hat{\mathbf{x}}_{N|N}$.

3 Field Experiment and Road Roughness Profile Identification

3.1 Experiment

A field experiment using a moving vehicle was conducted. Vehicle accelerations were measured while the vehicle is running through a 40 m span bridge in order to verify validity of the road roughness profile identification by both DRLS minimization and Kalman filter. A vehicle used in the experiment is X-trail (Nissan Motor Co., Ltd.). Properties of the vehicle are summarized in Table 1. The properties were estimated considering a free vibration test, model update experiment results by particle filter, and product information catalogue. Two accelerometers are installed on the vehicle body, and accelerations in bounce and pitch were measured. Accelerometers used in the experiment were quartz sensors (M-A550AC2x by Seiko Epson Corporation). Sampling frequency was 200 Hz, and vehicle speed was about 10 km/h. The test vehicle runs three times, and each runs are denoted as T1, T2, and T3.

3.2 Road Roughness Profile Identification

The road roughness profile identification by DRLS minimization is investigated. Regularization parameter is defined as Eq. (29), and candidate values for L-curve method are preset by changing β . For the range of β , the lower limit was set as -8, the upper limit was set as 5, and the change interval was 0.5.

$$\lambda = 10^\beta$$

One of the identified results by DRLS minimization with L-curve method is shown in Fig. 2. It is obvious that the identified road roughness profile is comparable with true road roughness profile. The true road roughness profile was obtained utilizing a measurement car equipped with laser displacement sensors.

In the road roughness profile identification by Kalman filter, three hyper parameters of $\mathbf{P}_{1|1} \in \mathbb{R}^{8 \times 8}$, $\mathbf{R} \in \mathbb{R}^{2 \times 2}$, and $\mathbf{Q} \in \mathbb{R}^{2 \times 2}$ should be predefined. The best hyper parameters in applying Kalman filter are investigated by comparing the identified and true road roughness profile. However, it is difficult to investigate a vast range of the combination of those three parameter values, and the basic values of $\mathbf{P}_{1|1}$, \mathbf{R} , and \mathbf{Q} are preset as $\tilde{\mathbf{P}}_{1|1}$, $\tilde{\mathbf{R}}$, and $\tilde{\mathbf{Q}}$ and road roughness profile is identified in three patterns as follows: Pattern 1 considers only changes in $\mathbf{P}_{1|1}$; Pattern 2 considers only changes in \mathbf{R} ; Pattern 3 considers only changes in \mathbf{Q} . Diagonal components of $\tilde{\mathbf{P}}_{1|1}$, $\tilde{\mathbf{R}}$, and $\tilde{\mathbf{Q}}$ were obtained from a moving vehicle simulation on 10 randomly generated road roughness profiles. In specific, the average values of the variances of each parameters obtained from simulation were used in those diagonal components. Diagonal components of $\tilde{\mathbf{P}}_{1|1}$, $\tilde{\mathbf{R}}$, and $\tilde{\mathbf{Q}}$ are summarized in Table 2. Patterns of the change in $\mathbf{P}_{1|1}$, \mathbf{R} , and \mathbf{Q} are shown in Table 3 in which α is used to change the hyper parameter. For the range of α , the lower limit was set as -8, the upper limit was set as 8, and the change interval was 0.5. For all patterns in Table 3, Root Mean Squared

Fig. 2 Identified road roughness profile by DRLS minimization

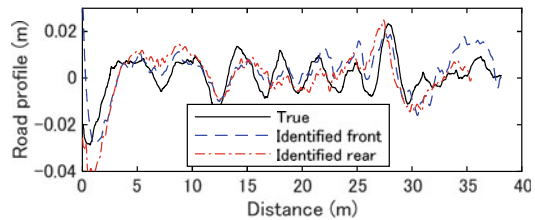


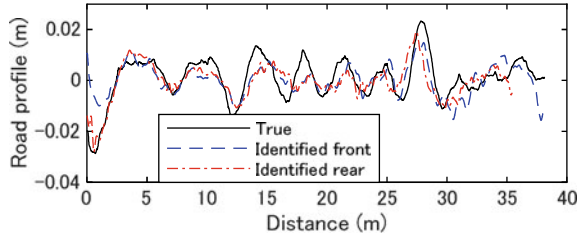
Table 2 $\tilde{\mathbf{P}}_{1|1}$, $\tilde{\mathbf{R}}$, and $\tilde{\mathbf{Q}}$
($\times 10^{-5}$)

	$\tilde{\mathbf{P}}_{1 1}$	$\tilde{\mathbf{R}}$	$\tilde{\mathbf{Q}}$
(1,1) component	3.86	77.2	4.35
(2,2) component	0.47	38.2	4.35
(3,3) component	13.69	–	–
(4,4) component	8.26	–	–
(5,5) component	4.35	–	–
(6,6) component	4.35	–	–
(7,7) component	4.35	–	–
(8,8) component	4.35	–	–
Non-diagonal component	0	0	0

Table 3 Hyper parameter patterns in Kalman filter

	Set $P_{1 1}$	Set R	Set Q
Pattern 1	$\tilde{P}_{1 1} \times 10^\alpha$	\tilde{R}	\tilde{Q}
Pattern 2	$\tilde{P}_{1 1}$	$\tilde{R} \times 10^\alpha$	\tilde{Q}
Pattern 3	$\tilde{P}_{1 1}$	\tilde{R}	$\tilde{Q} \times 10^\alpha$

Fig. 3 Identified road roughness profile by Kalman filter



Error (RMSE) shown in Eq. (30) is calculated to find the best hyper parameters.

$$RMSE = \sqrt{\frac{1}{N} \sum_{i=1}^N (r_{true,i} - r_{est,i})^2} \tag{30}$$

where $r_{true,i}$ is true road roughness profile, $r_{est,i}$ is identified road roughness profile, i is a discrete time index, and N is a total number of time steps. Among all patterns in Table 3, $\alpha = 0.5$ in Pattern 3 showed the lowest RMSE. One of the examples of identified road roughness profile when $\alpha = 0.5$ in pattern 3 is shown in Fig. 3 where it can be seen that identified road roughness profile by Kalman filter is well comparable with true one as well as that by DRLS minimization shown in Fig. 2.

3.3 Power Spectral Density and IRI

Identified results by both DRLS minimization and Kalman filter are converted to power spectral density (PSD) as shown in Fig. 4 and Fig. 5. In Fig. 4 and Fig. 5, PSD identified Kalman filter looks like having a larger identification error than DRLS minimization at spatial frequency less than 0.1 cycle/m, especially at the rear axle. In order to assess the identification accuracy numerically, Root Mean Squared Logarithm error (RMSLE) shown in Eq. (31) is adopted.

$$RMSLE = \sqrt{\frac{1}{N} \sum_{l=1}^N (\log(PSD_{true,l} + 1) - \log(PSD_{est,l} + 1))^2} \tag{31}$$

Fig. 4 PSD Identified by DRLS minimization

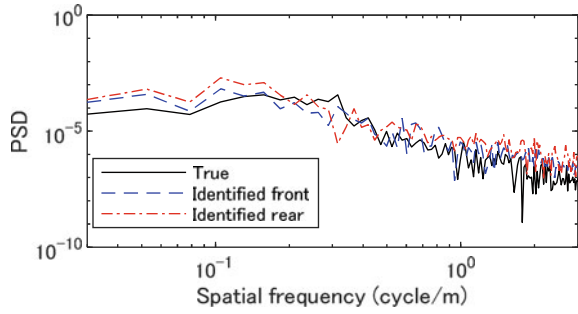
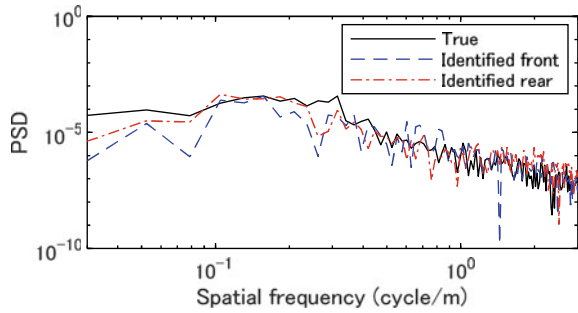


Fig. 5 PSD Identified by Kalman filter



where, $PSD_{true,i}$ and $PSD_{est,i}$ stand for true and identified PSDs, respectively. i is a discrete spatial frequency index. RMSLE of PSD identified by DRLS minimization were 3.9×10^{-6} for the front axle and 2.1×10^{-6} for the rear axle. RMSLE of PSD identified by Kalman filter were 9.6×10^{-6} for the front axle and 9.0×10^{-6} for the rear axle. Those RMSLE values were obtained by averaging results of three runs. Both in front and rear axles, DRLS minimization showed smaller RMSLE of PSD than that of the Kalman filter.

International roughness index (IRI) is an indicator of the road roughness profile that is defined by World Bank, and widely used in practice. IRI can be calculated by applying a vehicle running simulation through the target road roughness profile. In this study, IRI is calculated for the road roughness profiles identified by both DRLS minimization and Kalman filter, and the identification accuracy of IRI are investigated using an error indicator as defined in Eq. (32).

$$Error(\%) = \frac{|IRI_{true} - IRI_{est}|}{IRI_{true}} \times 100 \tag{32}$$

where IRI_{true} and IRI_{est} denote true and identified values of IRI, respectively. Identification error of IRI is summarized in Table 4, and it can be seen that DRLS minimization has higher accuracy than Kalman filter, and its average error was less than 14%.

Table 4 IRIs of identified road roughness profiles

Run	Method	Front axle	Rear axle
T1	Kalman filter: $\alpha = 0.5$, Pattern 3	18.7	23.8
	DRLS minimization	1.2	1.5
T2	Kalman filter: $\alpha = 0.5$, Pattern 3	17.7	30.5
	DRLS minimization	5.6	15.6
T3	Kalman filter: $\alpha = 0.5$, Pattern 3	24.6	31.5
	DRLS minimization	7.2	22.8
Average	Kalman filter: $\alpha = 0.5$, Pattern 3	20.3	28.6
	DRLS minimization	4.7	13.3

DRLS minimization has two advantages comparing to the Kalman filter. The one is that the accuracy in PSD and IRI is higher than Kalman filter. The other advantage is that no needs to preset the hyper parameter in the DRLS minimization, because it can automatically select the optimal hyper parameter. On the contrary, hyper parameters need to be preset in Kalman filter. It should be noted that hyperparameters affect largely to the identification accuracy, but it is difficult to obtain the optimal values of them based on the experience.

4 Conclusions

This paper proposes the road roughness profile identification method based on a new discrete-time linear state-space model, and the regularized least square minimization combined with the dynamic programming, so as to directly identify the target road roughness profile. The road roughness profile identification accuracy of the proposed method is compared to that of the Kalman filter using accelerations measured during the field experiment. Observation through this study demonstrated that the DRLS minimization resulted in a higher identification accuracy in respect of PSD and IRI comparing to the Kalman filter.

L-curve method is used in the DRLS minimization in order to obtain an optimal regularization parameter. The regularization parameter obtained by L-curve method contributed to obtain high identification accuracy. The L-curve method based DRLS minimization showed advantages in automatic selection of hyper parameters, while the Kalman filter requires to preset hyper parameter values.

References

1. Kitching KJ, Cole DJ, Cebon D (2000) Theoretical investigation into the use of controllable suspensions to minimize road damage. *Proc Inst Mech Eng Part D: J Automob Eng* 214(1):13–31
2. González A, O'Brien EJ, Li YY, Cashell K (2008) The use of vehicle acceleration measurements to estimate road roughness. *Veh Syst Dyn* 46(6):483–499
3. Hu Z, Xiang Z, Lu Q (2020) Passive tap-scan damage detection method for beam structures. *Struct Control Health Monit* 27(4):1–20
4. Kim CW, Kawatani M (2009) Challenge for a drive-by bridge inspection. *Saf Reliab Risk Struct Infrastructures Eng Syst* 758–765
5. Sitton JD, Zeinali Y, Rajan D, Story BA (2020) Frequency estimation on two-span continuous bridges using dynamic responses of passing vehicles. *J Eng Mech* 146(1)
6. Wang H, Nagayama T, Su D (2019) Estimation of dynamic tire force by measurement of vehicle body responses with numerical and experimental validation. *Mech Syst Signal Process* 123:369–385
7. Yang YB, Lin CW, Yau JD (2004) Extracting bridge frequencies from the dynamic response of a passing vehicle. *J Sound Vib* 272(3–5):471–493
8. Yang YB, Xu H, Zhang B, Xiong F, Wang ZL (2020) Measuring bridge frequencies by a test vehicle in non-moving and moving states. *Eng Struct* 203
9. Yang YB, Zhang B, Qian Y, Wu Y (2018) Contact-point response for modal identification of bridges by a moving test vehicle. *Int J Struct Stab Dyn* 18(5)
10. Yang Y, Cheng Q, Zhu Y, Wang L, Jin R (2020) Feasibility study of tractor-test vehicle technique for practical structural condition assessment of beam-like bridge deck. *Remote Sens* 12(1)
11. O'Brien EJ, McGetrick PJ, González A (2014) A drive-by inspection system via vehicle moving force identification. *Smart Struct Syst* 13(5):821–848
12. McGetrick PJ, Kim CW, Gonzalez A, O'Brien EJ (2013) Dynamic axle force and road profile identification using a moving vehicle. *Int J Arch Eng Constr* 2(1):1–16
13. Chang KC, Kim CW, Hasegawa S, Nakajima S, McGetrick PJ (2019) Estimation of bridge surface profile from moving vehicle accelerations by means of moving force identification - an experimental field study. *Int J Lifecycle Perform Eng* 3(3/4):289–309
14. Hasegawa S, Kim CW, Chang KC, Toshi N (2020) Discussion on ill-posed problem in drive-by pavement roughness identification. In: *EURODYN 2020 XI international conference on structural dynamics, 2020*
15. Hasegawa S, Kim CW, Toshi N, Chang KC (2020) Discussion on the roadway roughness profile identification methods utilizing acceleration measured on a moving vehicle. *J Appl Mech JSCE* 76(2):I_77-I_88 (in Japanese)
16. Sayers M, Gillespie T, Paterson W (1986) Guidelines for conducting and calibrating road roughness measurements. World Bank technical paper number, p 46
17. Qin Y, Langari R, Wang Z, Xiang C, Dong M (2017) Road profile estimation for semi-active suspension using an adaptive Kalman filter and an adaptive super-twisting observer. In: *Proceedings of the American control conference*, pp 973–978
18. Zhao B, Nagayama T, Xue K (2019) Road profile estimation, and its numerical and experimental validation, by smartphone measurement of the dynamic responses of an ordinary vehicle. *J Sound Vib* 457:92–117
19. González A, Rowley C, O'Brien EJ (2008) A general solution to the identification of moving vehicle forces on a bridge. *Int J Numer Meth Eng* 75(3):335–354
20. Tikhonov AN, Arsenin VY (1977) Solutions of ill-posed problems. Wiley, New York, United States
21. Hansen PC, O'Leary DP (1993) The use of the L-curve in the regularization of discrete ill-posed problems. *SIAM J Sci Comput* 14(6):1487–1503

Damage Free and Resilience for Seismic Disaster

Rheological Model and Parameter Identification of a Kinetic Sand Used as a Smart Damping Material



Jacek M. Bajkowski, Bartłomiej Dyniewicz, Czesław Bajer,
and Jerzy Bajkowski

Abstract Although being rarely categorised as “smart”, bulk materials seem to be useful for attenuating vibrations due to their nontypical dissipating properties, when subjected to underpressure. Granules in a typical particle impactor are free to move and collide. On the contrary, the proposed prototype beam, with a core filled with dilatant sand, explores the properties of the granular media in a quasi-solid phase, also called the jammed state. Using a controlled underpressure signal, properties of the sand core may be adjusted, giving a possibility of using such material as a smart damping member. An experimental study on the properties of a prototype layered beam filled with a non-Newtonian sand mixture is presented. Special beam construction allows pressurising grains by evacuating the air from inside the cover. By intensifying the compression, sand grains become jammed, resulting in increased stiffness and damping. Based on the exemplary experimental results, a custom rheological model parameter identification is performed.

Keywords Granular material · Vibration · Damping · Control · Smart material

1 Introduction

In most machine and structure design cases, vibrations are undesired and an effort is made to reduce them by introducing isolators or additional damping solutions. The

J. M. Bajkowski (✉)

Faculty of Production Engineering, Warsaw University of Technology, Warszawa, Poland
e-mail: jacek.bajkowski@pw.edu.pl

B. Dyniewicz

Polish Academy of Sciences, Institute of Fundamental Technological Research, Warszawa, Poland

C. Bajer

Institute of Fundamental Technological Research, Warszawa, Poland

J. Bajkowski

Polish Air Force University, Dęblin, Poland

most common methods are passive dampers with a constant energy dissipation coefficient. On the other hand, a significant reduction of the vibration amplitude can be achieved using active methods. However, these treatments are energy-consuming, sensitive to power shortages, and risky for generating an unstable situation in case of malfunction.

An alternative way is to replace the active force actuators with devices utilising smart materials, allowing semi-active damping control in time. When properly designed, the adaptive damping leads to faster energy dissipation than its passive equivalent. The examples of the effectiveness of the semi-active damping control strategy utilising smart materials in the case of a rotating system [1], moving load [2], and harmonic oscillation system [3] have been already proven by the authors, reducing the amplitude of vibrations up to 40% compared with the passive solutions.

The granular damping methods usually lack the semi-active possibility of adapting parameters to the dynamic excitation, because the granular medium is used passively. The bulk granules are typically placed in a container attached externally to the vibrating system [4, 5]. During movement, the grains collide and dissipate energy through non conservative interactions combining friction, deformations, exchange of momentum, and so on [6]. While being cost-effective and robust, they lack the possibility to adapt in real-time to the dynamic excitation. The device needs to be tuned beforehand, just like in [7], where the granular dissipator was filled with a selected number of granules to achieve the desired damping capacity of the alpine ski.

To achieve semi-active damping possibility a mechanical modification of the enclosure is required to compress the bulk granula material. Such containers usually utilise moving parts that allow compressing the granules like in [8, 9] to force jamming and alter the dissipating properties. In [10] a soft, airtight sleeve was filled with granules and used to cover a steel beam. A pneumatic system was used to maintain pressure on the boundaries of the cellular damping structure. Controlling the amount of dissipation in a granular medium opens the possibility of adjusting the damping capacity over time and achieving an adaptive damping system. The concept of switching the granular system properties at selected moments has been explored in [11], where granules were placed inside a rigid cylinder with a top lid compressing the granules to obtain variable stiffness. Some more of the solutions based on the periodical switching of the system parameters were compared by Winthrop et al. in [12].

2 Experimental Setup

2.1 *Beam with a Sand Core*

In our study, the damping solution is based on a non typical granular material placed in an elastic container merged between two parallel aluminium face beams. The rectangular cross-section of a single beam is 30×1 mm, length is 540 mm, and

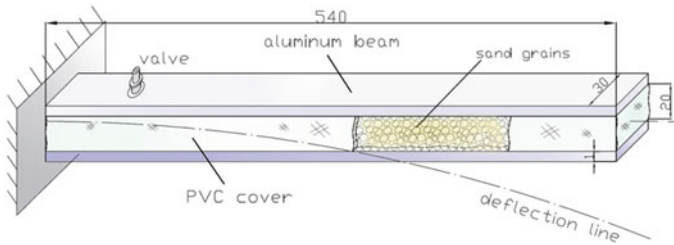


Fig. 1 Construction of a layered beam with a pressurised core made of kinetic sand (dimensions in mm)

separation of the faces is 20 mm. The sand composition consists of 96% of ultrafine sand mixed and dispersed in a 4% polydimethylsiloxane, which is a hydrophobic type of silicone that helps sand grains to agglomerate and stick together.

The sand was covered with a thin PVC envelope, which restricts the movement of grains and allows pressurising them by evacuating the air from the elastic coating. The pneumatic control allows intensifying jamming among the granules, as the static pressure influences the state of the granular material and thus its parameters. The pressure hose is connected to an electro-valve, which is connected to a vacuum pump that allows controlling the granules' compression. The scheme of the beam is presented in Fig. 1.

2.2 Experimental Setup

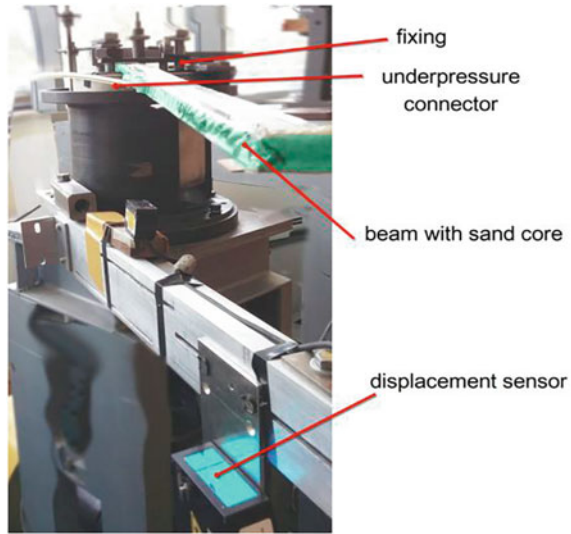
The beam was fixed in a horizontal cantilever position and initially deflected using string, looped at the beam's free end. After releasing the string, the beam was free to vibrate, while the displacement was recorded until the lateral oscillations ceased (Fig. 2). Setting various underpressure values ranging from 0 to 0.08 MPa (which is almost equal to no vacuum and 80% vacuum) results in different intensities of jamming.

The displacement's amplitude was recorded using a laser sensor. At the same time, the underpressure was monitored using a digital sensor to measure the influence of the constant pressure on the response of the cantilever. Since the first mode of vibration was considered in the experimental research, only the displacement at the beam's tip was recorded.

3 Results

This section presents some exemplary results of the beam vibrations for a one-time selection of a constant underpressure. The measurements occurred after the initial

Fig. 2 Scheme of the experimental stand



jamming. The experimental results for the initial deflection of 60 mm and zero initial velocity are depicted in Fig. 3a, while other results are compared with the simulations shown in Fig. 3b and c.

The beam with a core filled with kinetic sand is heavily overdamped, experiencing minor initial oscillations after releasing when no underpressure is applied. The deflection amplitude drops from 60 to 23 mm in 0.35 s for no underpressure because of the high energy accumulated in the deflected aluminium strips. After reaching 23 mm, the kinetic sand limits the return movement as the dissipation starts to overtake the return movement. It takes up to 20 s (not shown in Fig. 3) for the beam with 0 MPa underpressure to return to the non-deflected state.

Applying an underpressure greatly intensifies the damping. For 0.02 MPa, the beam needs around 35 s to return to non-deflected state, while for 0.04 MPa it takes almost 60 s. When the underpressure is further increased to 0.08 MPa, the beam becomes heavily overdamped, and the compressed sand core prevents it from returning to the non-deflected state. The beam remains plastically deformed at 44 mm. When the electrovalve is opened and the sleeve becomes unsealed, the beam returns to a non-deflected state. It opens the possibility to dynamically alter the total stiffness and take advantage of the parametric modification of the structure.

A proper model of the underpressure granular structure and identifying its parameters are necessary to answer the question of whether it is possible to use these structures in semi-active vibration damping as an interesting and cost-effective alternative to smart materials. The considered model must describe the system's global behavior rather than individual interactions among the grains. On the other hand, reasonable computational models for mathematical simulations require knowing the values of the stiffness and viscosity. That is why the Zener, Kelvin-Voigt, and classic Maxwell models were initially selected to model pressurised granular material, and

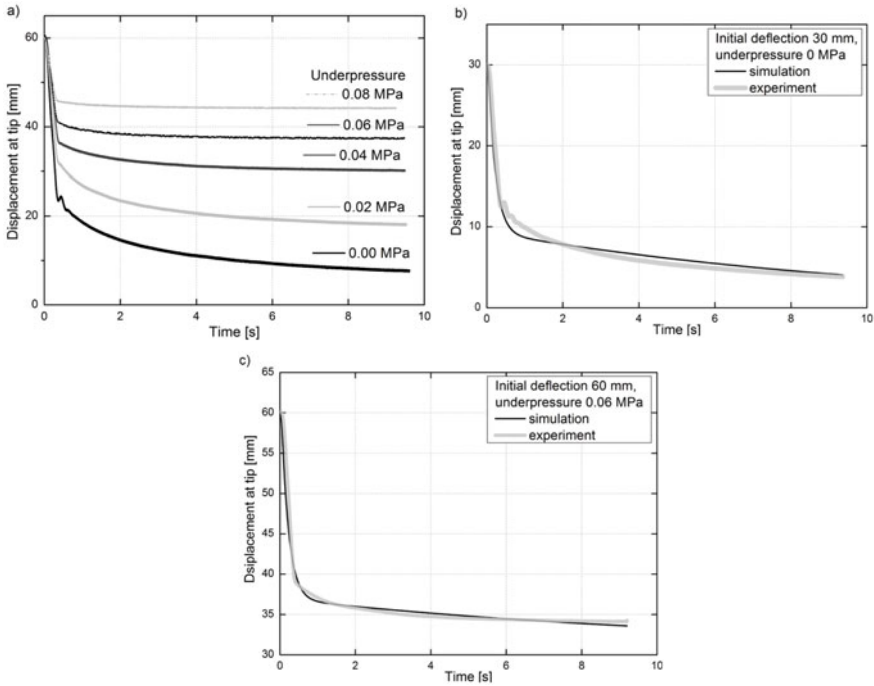


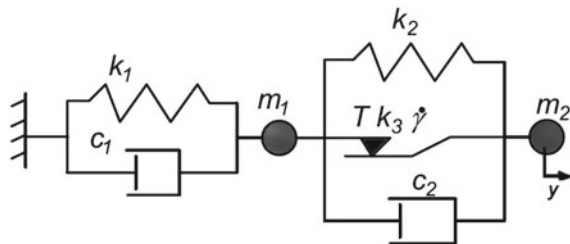
Fig. 3 a Experimental results for different underpressure and initial deflection of 60 mm, b comparison of simulation and experimental results for initial deflection of 30 mm and 0 MPa, and c comparison of simulation and experimental results for initial deflection of 60 mm and 0.06 MPa

their parameters were identified for different granular systems in [13]. In this paper, the considered model consists of nonlinear oscillators with a frictional element that activates the spring and the accompanying dashpot (Fig. 4). The total displacement combines elastic (y_e) and irreversible permanent (y_p) components

$$y = y_e + y_p \tag{1}$$

The constitutive force equation takes into account the elastic stiffness k

Fig. 4 Rheological model considered in the modelling of the system response



$$F = k(y - y_p) \tag{2}$$

The obtained motion equation is

$$\dot{y}_p = \dot{\gamma} \text{sign}(F) \tag{3}$$

with loading–unloading conditions assumed as

$$\dot{\gamma} = \begin{cases} 0 & \text{for } f < 0 \\ \dot{\gamma}_0 & \text{for } f = 0, \dot{f} = 0 \\ 0 & \text{for } f = 0, \dot{f} < 0 \end{cases} \tag{4}$$

The kinetic friction component T influences the Coulomb friction law

$$f(F, T) = |F| - T \tag{5}$$

The model parameters were identified separately, assuming displacement in time as the reference function. The minimisation problem was solved similarly to the least square method for the initial 10 s of vibrations selected as the source data. The computed and simplified values of the parameters or their functions are presented in Table 1. As one can notice from Table 1, some of the identified parameters were assumed as constants, while the others depend on the underpressure value denoted Δp . Since the phenomenological model provides several parameters to be identified and tuned, some simplifications should be worth considering to make it less computationally expensive for further optimisation problems.

The comparison of the experimental and simulation results recorded for the selected initial deflection of the beam under different underpressure values are presented in Fig. 3b and c. A fair agreement backed up by the low error was observed for a broad range of initial deflections and different underpressure values.

Table 1 An exemplary set of estimated decision variables of the rheological model for different underpressure values

Parameter	Value or function [unit]
γ	$500,000 \cdot [\text{m}^2\text{s/kg}] \Delta p [\text{Pa}] + 25,000 [\text{m/s}]$
T	$1730 [\text{m}^2] \cdot \Delta p [\text{Pa}] + 100 [\text{N}]$
m_1	3.19 [kg]
m_2	28.12 [kg]
k_1	3489.70 [N/m]
k_2	12.67 [N/m]
k_3	9.75 [N/m]
c_1	38.12 [Ns/m]
c_2	90.25 [Ns/m]

4 Conclusions

Due to its conceptual simplicity, effectiveness, and low cost, the proposed solution for controlling the mechanical properties of vacuum granular structure is an interesting alternative to classic damping systems based on composites and expensive smart materials. The shape of the low-cost, efficient granular damping elements can be easily modified, which allows tailoring it to fit into irregular spaces. Numerous applications which use of controllable stiffness and the unique characteristics of innovative materials may benefit from this alternative approach. The experimental research shows the efficiency of the kinetic sand used as filling for the damping core. The phenomenological model provided good parameter estimation, but some simplifications are worth considering. The proposed models offer the opportunity to calculate the optimal control strategy using the concept of switched jamming. Using a proper control strategy, makes it possible to detract vibrations from the resonance, affecting the properties of the system and alternating operational factors. Due to the time delay, such pneumatically controlled damping structures would be preferred for low-frequency applications.

Acknowledgements This research has been supported within the projects UMO-2017/26/E/ST8/00532 and UMO-2019/33/B/ST8/02686 funded by the Polish National Science Centre, which the authors gratefully acknowledge.

References

1. Dyniewicz B, Pregowska A, Bajer CI (2014) Adaptive control of a rotating system. *Mech Syst Signal Process* 43(1–2):90–102. <https://doi.org/10.1016/j.ymsp.2013.09.006>
2. Konowrocki R, Bajer CI (2105) Intelligent adaptive control of the vehicle-span/track system. *Mech Syst Signal Process* 58(59):1–14. <https://doi.org/10.1016/j.ymsp.2014.12.007>
3. Dyniewicz B, Bajkowski JM, Bajer CI (2015) Semi-active control of a sandwich beam partially filled with magnetorheological elastomer. *Mech Syst Signal Process* 60(61):695–707. <https://doi.org/10.1016/j.ymsp.2015.01.032>
4. Wang B, Yang M (2000) Damping of honeycomb sandwich beams. *J Mater Process Technol* 105(1–2):67–72. [https://doi.org/10.1016/S0924-0136\(00\)00564-1](https://doi.org/10.1016/S0924-0136(00)00564-1)
5. McDaniel JG, Dupont P, Salvino L (2000) A wave approach to estimating frequency-dependent damping under transient loading. *J Sound Vib* 2(231):433–449. <https://doi.org/10.1006/jsvi.1999.2723>
6. Sanchez M, Rosenthal G, Pugnaroni LA (2012) Universal response of optimal granular damping devices. *J Sound Vib* 20(331):4389–4394. <https://doi.org/10.1016/j.jsv.2012.05.001>
7. . Bajkowski JM, Dyniewicz B, Bajer CI (2021) An experimental study on granular dissipation for the vibration attenuation of skis. *Proc Inst Mech Eng Part P: J Sport Eng Technol* 235:13–20. <https://doi.org/10.1177/1754337120964015>
8. Tang N, Rongong JA, Sims ND (2018) Design of adjustable tuned mass dampers using elastomeric O-rings. *J Sound Vib* 433:334–348. <https://doi.org/10.1016/j.jsv.2018.07.025>
9. Rongong J, Tomlinson G (2005) Amplitude dependent behaviour in the application of particle dampers to vibrating structures. In: 46th AIAA/ASME structures, structural dynamics and materials conference, Austin, Texas, pp 1–9. <https://doi.org/10.2514/6.2005-2327>

10. Bajkowski JM, Zalewski R (2014) Transient response analysis of a steel beam with vacuum packed particles. *Mech Res Commun* 60:1–6. <https://doi.org/10.1016/j.mechrescom.2014.04.004>
11. Wong CX, Rongong JA (2009) Control of particle damper nonlinearity. *AIAA J* 4(74):953–960. <https://doi.org/10.2514/1.38795>
12. Winthrop MF, Baker WP, Cobb RG (2005) A variable stiffness device selection and design tool for lightly damped structures. *J Sound Vib* 4(287):667–682. <https://doi.org/10.1016/j.jsv.2004.11.022>
13. Bajkowski JM, Dyniewicz B, Bajer CI (2016) Semi-active damping strategy for beams system with pneumatically controlled granular structure. *Mech Syst Signal Process* 70–71, 387–396. <https://doi.org/10.1016/j.ymssp.2015.09.026>

Numerical Investigation on Longitudinal Forces on Bridges of Indian Railways



Swapnil Chaurasia and Di Su

Abstract The impact of increased longitudinal loads applied on bridges by modern railway vehicles is a major concern for Indian railways. The extent of load transferring to the substructures has been overestimated in the design codes which does not take the dispersion of longitudinal forces to the adjoining regions into account. Experimental studies were conducted to assess the extent of load transfer to the substructures. Field tests were complemented by numerical models for simulation of rail-bridge interaction forces. Due to the large domain size of the numerical model, methodologies have been developed by utilizing various ABAQUS features like user-subroutine, non-linear connector elements, friction elements etc. to simulate phenomena like rail-wheel interaction, fastening systems and boundary conditions. Correlation of applied load with the dispersion of forces to adjoining regions is established. Increase in the longitudinal loads has been observed to enhance the dispersion mechanism on bridges and thus mitigating the effects of increased loadings. Dispersion of loads is significant in steel girder bridges, and it should be included in the design codes for the assessment of design loads in substructures. Numerical model for investigating thermal effects of LWR over bridges has also been developed in this work. Fracture in LWR installed over bridge is simulated on the numerical model for a range of creep-resistance practically observed in railway tracks.

Keywords Longitudinal loads · Dynamic rail-wheel interaction · Finite element analysis · Experimental analysis of railway bridges · Numerical modeling

1 Introduction

With the advent of modern train sets, loads on existing infrastructures have increased drastically. Increase in the traction and braking power of locomotives has led to a much more dramatic increase in the longitudinal loads on the track structures than the vertical loads. In Indian railways, over the last 80 years, longitudinal loads have

S. Chaurasia · D. Su (✉)

Department of Civil Engineering, The University of Tokyo, Tokyo, Japan
e-mail: su@bridge.t.u-tokyo.ac.jp

© The Author(s), under exclusive license to Springer Nature Switzerland AG 2023
Z. Wu et al. (eds.), *Experimental Vibration Analysis for Civil Engineering Structures*,
Lecture Notes in Civil Engineering 224,
https://doi.org/10.1007/978-3-030-93236-7_55

665

increased by around 2.5 times [1]. There are about 131,000 railway bridges in India of which more than 70% are older than 50 years [2]. These bridges were designed for the prevailing loading standards. The impact of increased longitudinal loads on railway bridges is a major concern for Indian railways as loads of the entire span converge to the substructures and thereby rendering bridges unsafe for the modern traffic. However, the extent of load transferring to the substructures has been overestimated in the design codes. There is a need to update the design provisions with a more rational approach towards the longitudinal loading on the bridges.

To restrict the transfer of these loads on railway bridges, it is important to isolate the rails from the girder. Accordingly, traditional steel girders are designed with steel channel sleepers and “rail free fastenings”. Rail free fastenings do not have clamping force between rails and sleepers; therefore, it allows the relative movement of rails with respect to sleepers in the longitudinal direction and theoretically isolates the track from the girder. Practically longitudinal loads due to traction/braking flow from rail level to the girders due to the frictional interaction between rails and sleepers. More longitudinal load flow occurs due to corrosion and over-bolting of fastenings. Aim of this study is to understand the interactions between the different components of the bridge which drives the flow of longitudinal forces.

Schematic representation of a typical railway bridge along with the longitudinal load transfer mechanism is shown in Fig. 1. The extent of load transferred from rails to the girder is dictated by the rail-bridge interaction. All the load transferred to the girders will eventually transmit to the substructure through its bearings. Most of the longitudinal loads that are transferred to the superstructure goes to the fixed (pin) bearing. As the longitudinal load gets increased, it poses maximum problems in the substructure as loads get accumulated here.

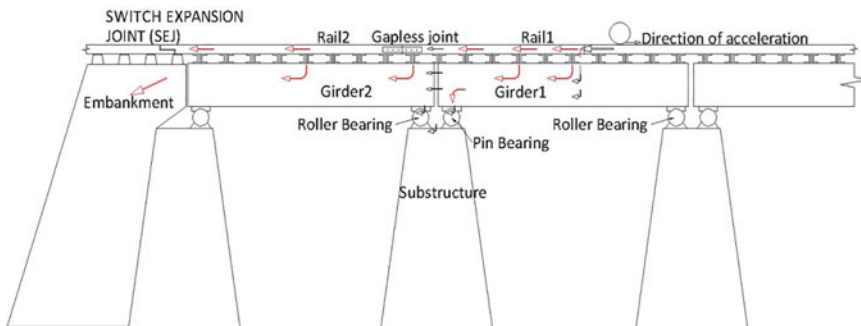


Fig. 1 Overview of a girder bridge and its interaction

2 Literature Review

The interaction between railway vehicles and track takes place in the contact zones between wheels and rails and results in surface stresses distributed over the contact patch [4]. Contact forces are the major force input for both, the vehicle, and the track [5]. Two materials contacting at rolling interfaces are influenced by geometry of the contacting interface, material attributes, and loading and boundary conditions [6]. Some traditional theories worth mentioning are Hertz model [7] for solving the normal contact problem, creep theories of Carter [8], Kalker [9, 10] (Linear theory, strip theory, Empirical theory, simplified theory, and the Exact Three-Dimensional Rolling Contact Theory) for estimating the tangential contact problem [11]. The basis of all modern analytical and computational methods is derived from the Hertz contact theory. Modern research on rail-wheel contact is done by Finite Element method as with the development of advanced algorithms, accuracy and computational efficiency of Finite Element Analysis has improved.

A 3D model of the track for the assessment of longitudinal loads is developed by [12]. Distribution and magnitude of longitudinal force in the concrete crosstie and their relationships with track design parameters were examined in the study. In this model, rail-wheel contact is simulated which restricts the size of the model due to its high computational demands. In case of simulation of rail-bridge interaction, model size and the number of interacting components is quite large, and thus it warrants simplification of rail-wheel contacting interface and other interacting parts. Analytical solutions of contact stresses between two curved solid bodies can be utilized in the FE model as an alternate to the physical simulation of the phenomena. Utilizing the contact programs like FASTSIM or CONTACT developed by Kalker were considered but the computational burden added by co-simulation of contact programs with the FE model developed in ABAQUS were still very large and thus could not be used in our model. As the focus of our research is not to simulate the local effects of contact interactions which can lead to enormously complex situations, we focus on the location and magnitude of the total force applied by the contact models.

3 Development of the Numerical Model

3.1 Load Application by User Subroutine

User subroutine is a feature in ABAQUS that allows users to customize a wide variety of ABAQUS capabilities. It is an extremely powerful and flexible tool for analysis. Codes written in FORTRAN, C or C++ can be executed during the analysis along with the model to adapt ABAQUS to their analysis requirements. ABAQUS/Standard provides users with an extensive array of user subroutines. Some popular subroutines are CREEP, DLOAD, FRIC, UMAT, USDFLD, UTRACLOAD etc.

Contact patch explained by Hertz contact theory can be coded in any programming language along with its spatial variation to simulate the load application due to the passage of a locomotive. A simplified method has been devised in which normal and tangential loads are applied by means of user-subroutines. DLOAD and UTRACLOAD are used in the model for simulating load application by generating normal pressure distribution and traction loads respectively. User subroutines DLOAD and UTRACLOAD can be used to define the variation of a distributed load as a function of position, time, element number, load integration point number etc. Both subroutines are called at each load integration point for each element-based or surface-based non-uniform distributed load definition during stress analysis. A FORTRAN program is used to generate an elliptical loading surface over the wheel. The area of this elliptical load surface is calculated by Hertz theory for the given values of rail curvatures, wheel curvature and vertical pressure. Pressure and traction load distribution is also kept elliptical as per Hertz contact theory.

ABAQUS solver sends information of all the integration points of the loaded elements to the FORTRAN compiler. From the given information of step time and coordinates, values of force (vertical pressure in case of DLOAD, traction in case of UTRACLOAD) can be defined for each integration point at every time increment. Contact patch generated by the FORTRAN code is shown in Fig. 2. Pressure contours generated on the application of user-subroutine loads are shown in Fig. 3, which shows the ellipsoidal loading.

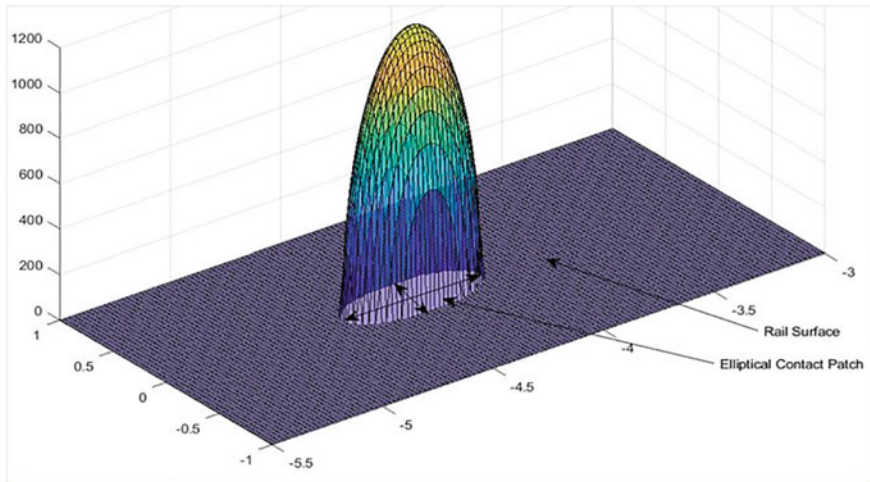
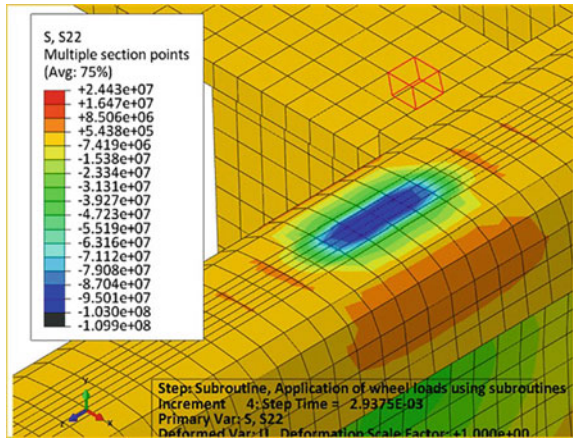


Fig. 2 Contact patch generated by FORTRAN code

Fig. 3 Pressure contours on application of loads via user-subroutines



3.2 Fastening System and Contact Interaction

Rail free fastenings theoretically isolates rails from the girder but does not allow the lifting of rails during the passage of trains. The interaction between rails and bolt clamps is relatively complex due to the gap between them. Rail will lift freely before touching the bottom of the clamp. After the contact, clamp will start exerting a resisting force on the rail foot. This resisting force will increase non-linearly with the uplift of the rail. To simulate this behavior, non-linear connector elements are used to develop a system of fastening in the model as shown in Fig. 4. The connector element used in this fastening mechanism only transmits the vertical axial loads to limit lifting of rails during the passage of a train.

For simulating the flow of longitudinal loads in a girder bridge, the most important aspect is to correctly model the rail-sleeper connection. Rubber pads installed between the different components allow some elastic movement due to the bulk modulus of the rubber-pads during the frictional load development in the rail-sleeper interface. Therefore, penalty type friction interactions are employed in the rail-sleeper

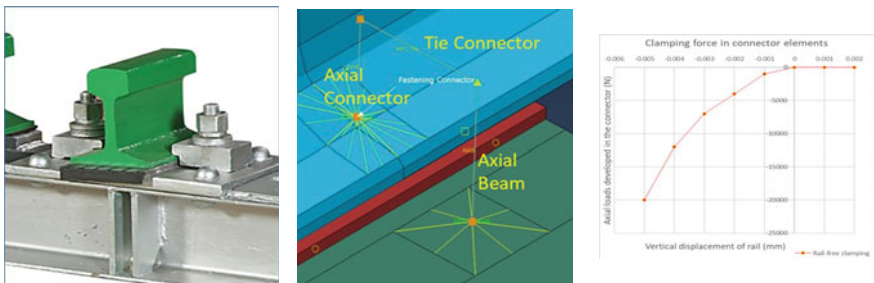


Fig. 4 Rail-free fastening. **a** picture **b** fastening system developed by connector elements. **c** Non-linear behavior of the connector

interface. Combination of rail-wheel interaction with the fastening mechanism is capable of simulating rail-free fastening system. Connection between other interfaces in the girder are modeled as tie-constraints.

3.3 Boundary Conditions

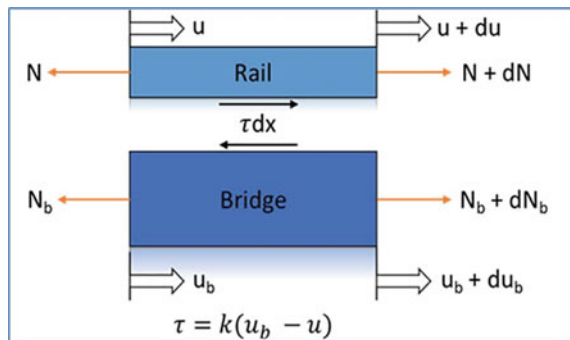
Forces which are transmitted from the rail level to the girder level depend on the relative movement of the rails with respect to the sleepers. This relative movement is dependent on many factors like fastening system, frictional coefficient, nearby track conditions, residual thermal stresses etc. When we use computer simulations to predict the response of structures subjected to dynamic loading, it is necessary to keep the size of the computer model within practical bounds [16]. Only the girder on which loading is directly applied should be modeled with the required detailing, while the rest of the system should be captured by generating some reasonable boundary situations (Fig. 5).

Boundary conditions have two important functions in the model.

1. To simulate the adjoining track conditions with representative track stiffness in the longitudinal direction.
2. To absorb the dynamic forces transmitted to the boundaries and do not reflect them back to the girder.

A system of connector elements has been developed to reproduce the influence of adjoining track on the instrumented rail section. A schematic diagram of the connector system developed is shown in Fig. 6. Elastic connectors represent the rails and friction type connectors represent rail-sleeper connection. Both connectors are place in parallel to each other. Penalty type friction formulation is used to simulate the friction type connector as there is a finite value of stick-stiffness due to rubber pads which allow some movement of rail for mobilizing full friction force.

Fig. 5 Longitudinal interaction between rail and bridge elements



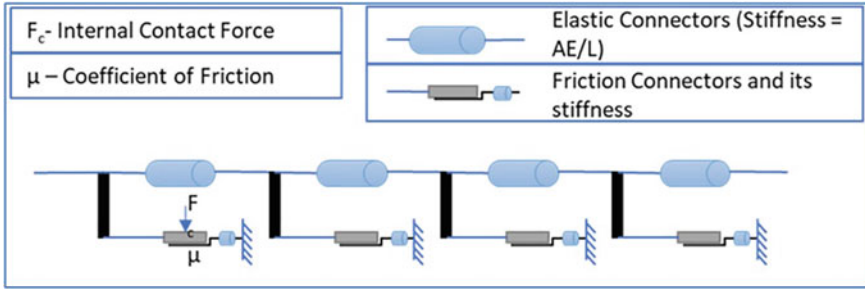


Fig. 6 Schematic diagram of connectors used to simulate boundary conditions

3.4 Verification of User-Subroutine Loading Method

To validate the user-subroutine method for simulating contact interaction, a FE model is developed in which loading is done by two different methods. In the first method, load is applied by physically modelling a wheel and its contact interaction with rail. While, in the second method, loading is done via user subroutines according to the methodology discussed in Sect. 3.4 (Fig. 7).

3.4.1 Finite Element model- Wheel Loading Case

A FE model is developed in ABAQUS/Standard code which simulated traction load application by wheel-rail interaction. A small track segment of 1.2 m length has been developed for this purpose. The FE model simulated rolling of a locomotive wheel on a railway track. This analysis is divided into two phases. First phase is to establish contact between the rail and the wheel. As rail surface is curved, the initial placement of wheel will be at a single point on the rail. To establish contact, a displacement-controlled loading is applied on the wheel as it is much more stable compared to

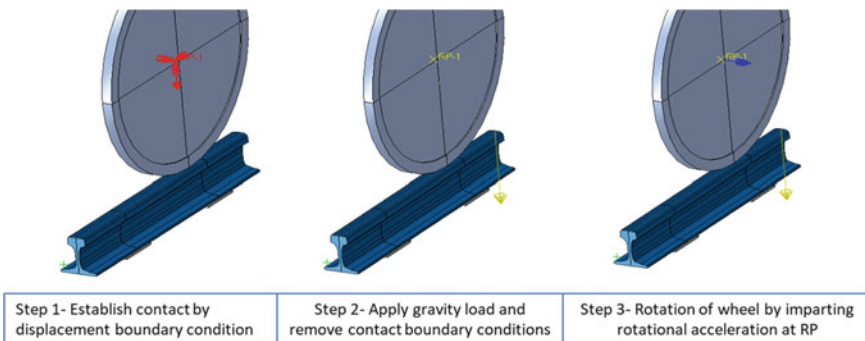


Fig. 7 Steps of Finite element analysis in Wheel loading model

force-controlled loading. A vertical displacement of 1 mm is applied on the wheel, which will push the wheel against the rail by 1 mm and will establish the contacting interface between the two bodies. The second phase is application of wheel load and its movement. This phase is performed in two steps. In the first step, a vertical load of 103.005 kN is applied on the wheel. In this step, the displacement which was imparted to the wheel in the first phase is also gradually released. In the next dynamic implicit step, a rotational acceleration is imparted to the wheel by rotating the reference node placed at the center of the wheel. A rotational acceleration of 1.0 rad/s² is applied to the wheel.

3.4.2 Finite Element model- User-Subroutine Case

In this case, wheel is not physically modeled. On the track model described in Sect. 3.4.1, loading is applied by user-subroutine method, keeping other model details same. Movement of wheel is simulated in this case by defining a contact patch of elliptical shape in the FORTRAN code. Contact ellipse size and maximum pressure is calculated from results obtained from the analysis of the wheel loading case. Pressure and traction load is applied on all the mesh elements which lie inside the contact patch.

3.4.3 Comparison of Result Obtained by Two Loading Methods

Total loads (vertical and longitudinal) applied in the two methods are kept same. Total load applied to the model is obtained by summing up all the reaction forces on the boundaries of the model. Plots of the total vertical reaction force is shown in Fig. 8. Longitudinal strain obtained at the rail-web location at the mid-point of the rail is shown in Fig. 9.

4 Experimental Study

Research Design and Standards Organization (RDSO) collaborated with CSIR-Structural Engineering Centre (CSIR-SERC) to carry out the experimental studies to study the flow and dispersion of longitudinal forces on a steel girder bridge. An existing steel plate girder bridge (bridge no. 514) was selected to carry out the experimental work. Static and dynamic tests are carried out using a test train formation. From the test data, longitudinal load flow on a steel girder bridge is investigated. All major components of the selected girder along with the adjoining girders and track are instrumented to measure their responses.

For tractive effort tests, longitudinal loads at rail level at near one end at a particular time is 18.29 tons. At the same time frame, the longitudinal force in the adjacent rail is observed as 7.47 tons. Therefore, the remaining force, which is around 10.81

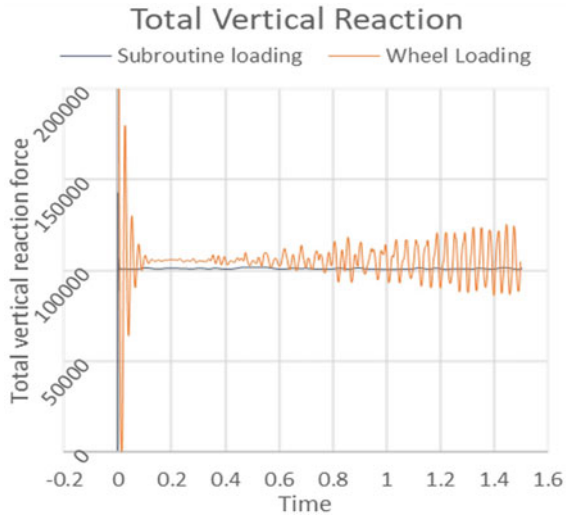


Fig. 8 Comparison of total vertical reaction for two loading methods

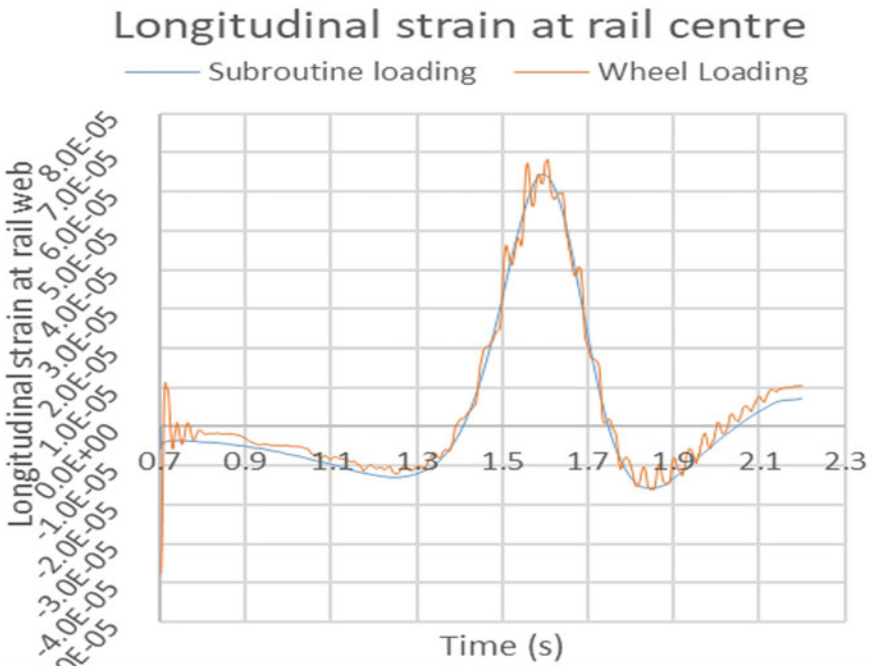


Fig. 9 Comparison of longitudinal strains at rail-web for the two loading methods

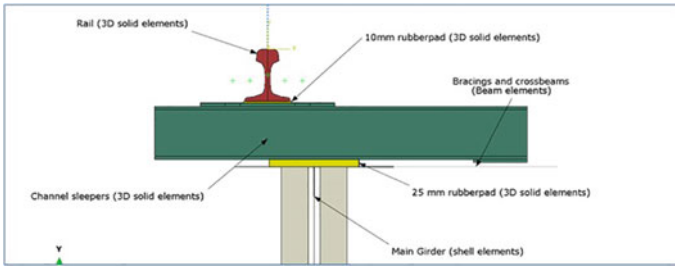


Fig. 10 Front elevation of the integrated FE model

tons must be transferred to the girder level. The percentage of longitudinal force that is dispersed to the adjoining track is calculated and given in Table 1. From the observations of the strain gauge reading at the rail levels, it is seen that around 40% of the longitudinal force generated at rail level is dispersed to the adjoining areas.

A major limitation with the field tests is that the load applied by the locomotive is not its maximum loading capacity as it depends on many factors like gradient of track, train load, surface conditions etc. Numerical models which are validated by the experimental results can be used for further investigation of the phenomena. Numerical models can also overcome the limitation of the experimental studies as applied loading can be easily modified (Fig. 10).

5 Integrated Bridge Model

5.1 FE Model Overview

FE bridge model consists of a bridge girder developed in accordance with the bridge drawing of the selected bridge. Length of the girder is 20.8 m and center to center distance between the bearings is 21.0 m. Track (rail-sleeper system) of length 21.0 m is placed over the girder. Three major components of the model are rail, steel channel sleepers and girder. 10 mm thick rubber pads are placed between the rail and sleepers. 25 mm thick rubber pads are placed between sleepers and the girder. Sleeper spacing is kept as 0.6 m. These rubber pads establish the interaction interface between the different components of the bridge. Salient features of the FE model as follows:

1. Single rail is modeled as longitudinal loads are symmetrical.
2. Bridge girder is formulated using shell elements.
3. Beam elements are used for modeling the bracings and crossbeams.
4. Railway track components are modeled as 3D solid elements.

5.2 *Boundary Conditions and Loading Procedure*

Boundary conditions are developed as explained in Sect. 3.3. A system of connector elements is developed in this study which can simulate different track conditions which are generated during the passage of a train. The developed system of connectors can simulate all three types of approach track conditions by modifying the parameters of the connector elements.

The FE analysis has 2 steps. The first step is application of gravity load over the complete structure. In the second step, loading is applied by user subroutine method described in Sect. 3.1. Locomotive load is applied on the structure as an elliptical contact patch at the rail surface. Pressure and traction distribution inside the contact patch is also elliptical. A locomotive contains 6 axles and thus 6 contact patches are first applied at the girder. For application of longitudinal loads, dynamic implicit analysis is performed in which loading is applied via user-subroutine method. A dynamic implicit analysis usually gives stable solutions with larger time increments, it is adopted as the simulation time of the analysis is longer. Loading in the model is carried out first as per the loading standard. The contact patch moves over the analysis time step at an acceleration of 1.5 m/s^2 . Maximum pressure inside the contact patch is kept as $8.01 \times 10^7 \text{ Pa}$ and maximum traction is $1.485 \times 10^7 \text{ Pa}$. The effects of the remaining part of the train are simulated in the boundaries by generating loaded track with rail-free fastenings conditions in the connector elements on one end of the girder.

5.3 *Results of Dynamic Simulation*

Numerical simulation with dynamic loading on the bridge-track model is carried out for a simulation period of 5 s. Von Mises stress contours at a particular time step is shown in Fig. 11. The time history of the stress contour is used for checking the functioning of the FORTRAN code and the movement of the load patch. Time history of the longitudinal strain at the center of the rail web is shown in Fig. 12. In the figure, field recording of longitudinal strains at rail-web is also plotted and comparisons are drawn. It is evident that the longitudinal strains produced in the rail due to the application of locomotive loads has similar trends as the field observations. The similarity of longitudinal strain data is used to establish the validity of the model.

The focus of the study is to identify the fraction of longitudinal loads that gets dispersed to the adjoining regions with respect to the fraction of load that gets transferred to the girders and thus to the substructures. Total longitudinal loads transferred to the girder are calculated from the time history data of the spring elements which act as the pin bearings of the structure. To verify the calculations of the longitudinal loads by spring elements, another model with boundary conditions imposed for simulating bearings of the bridge is analyzed and the longitudinal loads in the two models are compared. For high rigidity spring elements, the results obtained in

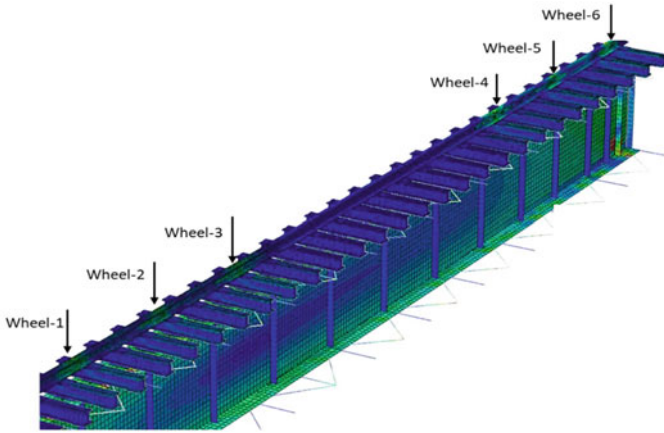
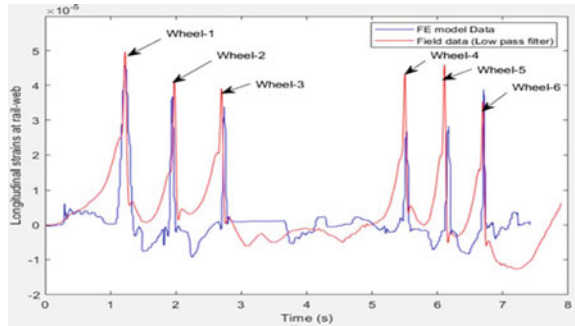


Fig. 11 Stress contours on a bridge girder after application of locomotive loads

Fig. 12 Comparison of longitudinal strains at rail web between FE model and field data



the two cases are same. Frictional resistance of the roller bearing is simulated by installing friction connector element connected to the ground at the roller ends of the girder.

Time history plots of the observed values of total longitudinal forces in the boundary connector elements and in girders are shown in Fig. 13. To calculate the percentage of loads which gets dispersed to the adjoining regions, average value of loads in the two components are compared. The general trend observed is that the dispersion of longitudinal forces increases slightly with the increase in the applied traction loads. FE model shows slightly higher dispersion of loads in comparison to the field test data. Field test data had the limitation on the application of the traction loads, which is overcome by the numerical model in which higher values of tractive forces can be applied. The variation of dispersion of loads with the increase in the traction loads is shown in Fig. 14. The increased dispersion of the longitudinal loads mitigates the adverse effects of the excessive traction forces imparted to the bridges.

Fig. 13 Longitudinal force transferred to different bridge components \hat{I}

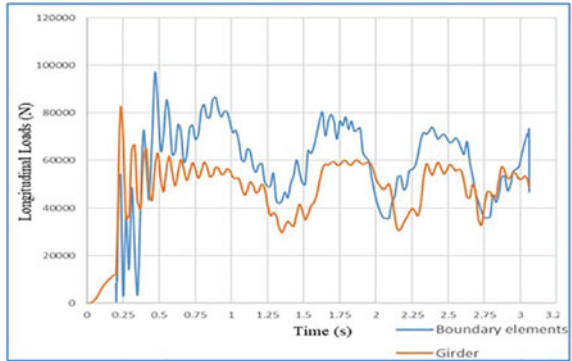
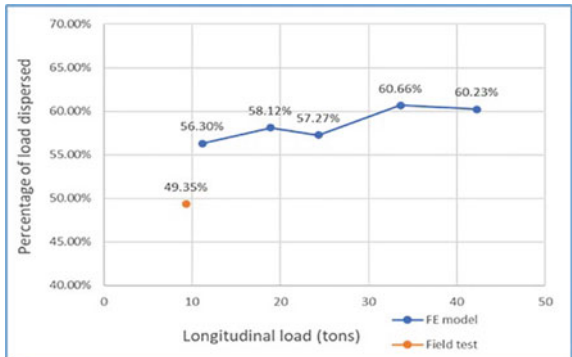


Fig. 14 Variation of load dispersion for different traction loads



6 Summary and Conclusion

6.1 Summary

FE analyses of railway track bridge system were carried out to investigate the behavior of railway bridges on the application of longitudinal loads. Dynamic implicit analysis was carried out to simulate the locomotive loads on railway bridges. User-subroutines were employed for reproducing the stresses generated at rail-wheel interface and system of connector elements with frictional properties and elastic-plastic response were developed to replicate the effects of adjoining tracks on the rail. A range of traction loads were applied over the bridge model and the magnitude of force transferred to different components of the bridge were analyzed. Correlation of applied load with the dispersion of forces to adjoining regions is established. Increase in the longitudinal loads has been observed to enhance the dispersion mechanism on bridges and thus mitigating the effects of increased loadings. Dispersion of loads is significant in steel girder bridges, and it should be included in the design codes for the assessment of design loads in substructures.

Table 1 Longitudinal load transfer to the adjoining span for different tests

Test Case	F.L. at the rail level on the main span	F.L. at the rail level on the adjacent span	Difference in rail force transferred	Percentage load transferred to adjoining span (%)
Test-4	18.29	7.47	10.81	41.90
Test-5	18.59	9.17	9.41	49.38
Test-6	15.46	6.86	8.61	44.31

6.2 Conclusion

Tractive loads ranging from 1.867 tons per wheel to 5.610 tons per wheel were applied in the numerical model. Results corresponding to the application of 1.867 tons were validated with the field test data. Dispersion of longitudinal loads to the adjoining tracks were observed in the analysis. Dispersion ranges from 56.30% for 1.867 tons load to 60.23% for 5.610 tons load. Increase in the longitudinal load keeping the vertical loads unchanged leads to more loads getting dispersed to the adjoining sections of the bridge. This observation can be attributed to the stiffness of the boundary elements owing to the longitudinal rigidity of the rails and the use of penalty type friction interaction at rail-sleeper interface.

6.3 Future Scope

Parameters considered in the study are only the different locomotive traction loads. To have a comprehensive insight into the longitudinal load distribution and its flow in a bridge, parameters like COF, clamping forces, adjoining track conditions can be integrated with different traction loads to have a broad understanding of the longitudinal load flow in different field conditions.

References

1. "Indian Railways Permanent Way Manual," (2004) p 297
2. Senthil K, Khan RA, Arvin S, Singh A (2017) "Structural behavior of railway bridges against wheel loading by finite element analysis 3:1–14.
3. Yusuke K, Mamoru F, Yuya N, Kataoka H (2014) Evaluation of the influence of installing continuous welded rail on existing (a) case A2 (a) case B1. QR RTRI 55(4):211–215
4. Piotrowski J, Chollet H (2005) Wheel-rail contact models for vehicle system dynamics including multi-point contact. Veh Syst Dyn 43(6–7):455–483. <https://doi.org/10.1080/00423110500141144>
5. Zhao X, Li Z, Dollevoet R (2007) The dynamic stress state of the wheel-rail contact the dynamic stress state of the wheel-rail contact, pp 1–8

6. Aalami MR, Anari A, Shafighfard T, Talatahari S (2013) A robust finite element analysis of the Rail-Wheel rolling contact. *Adv Mech Eng* <https://doi.org/10.1155/2013/272350>.
7. Yan W, Fischer FD (2000) Applicability of the Hertz contact theory to rail-wheel contact problems. *Arch Appl Mech* 70(4):255–268. <https://doi.org/10.1007/s004199900035>
8. Carter F (1926) On the action of a locomotive driving wheel. *Proc R Soc Lond* 112:151–157
9. Kalker J (1967) On the rolling contact of the two elastic bodies in the presence of dry friction. Delft
10. Kalker J (1973) Simplified theory of rolling contact. Delft university of Technology
11. Vo KD, Tieu AK, Zhu HT, Kosasih PB (2014) A 3D dynamic model to investigate wheel-rail contact under high and low adhesion. *Int J Mech Sci* 85:63–75. <https://doi.org/10.1016/j.ijmecs.2014.05.007>
12. Zhang Z (2015) Finite element analysis of railway track under vehicle dynamic impact and longitudinal loads. Master's thesis, pp 1–27
13. Pandit A (2014) LONG Welded Rails, no. i. Pune: Indian Railways Institute of Civil Engineering
14. Aikawa A, Sakai H, Abe K (2013) Numerical and experimental study on measuring method of rail axial stress of continuous welded rails based on use of resonant frequency. *Q. Rep. RTRI (Railw. Tech. Res. Institute)* 54(2):118–125. <https://doi.org/10.2219/rtriq.54.118>
15. RD, Organisation S (2005) Manual of instructions on long welded rails, 2nd edn., vol 8. Lucknow
16. Nielsen AH (2006) Absorbing boundary conditions for seismic analysis in ABAQUS. In: 2006 ABAQUS user's conferences

Monitoring-Based MBS-FEM Analysis Scheme for Wind-Vehicle-Bridge Interaction System and Experimental Validation



Qi Hu and Di Su

Abstract The vehicle running stability on the bridge under a strong crosswind has become a hot topic with increasing concern in recent years. The traditional analysis method of wind-vehicle-bridge system is complicated and time-consuming, which has not fully utilized a large amount of valuable in-situ monitoring data and cannot meet the requirement of timely decision. Besides, the previous analysis method has not been validated through the experiment. This study presents a combined analysis scheme integrating the FEM (Finite Element Method) and MBS (Multiple Body Simulation) to be more convenient and comprehensive to analyze the Vehicle-Bridge-Interaction (VBI) system. A new double-dummy coupling method is proposed to simulate the vehicle-bridge connection to solve the vehicles' responses accurately and efficiently. Other influence factors like tire model, wind force, and road roughness are taken into account as well. Furthermore, to consider the wind effect on the VBI system and avoid the complicated fluid–structure interaction, the in-situ monitoring data could be fully applied in this scheme. A monitoring-based approach is proposed to hybrid the monitoring data and MBS-FEM model to obtain the vehicle response. To validate the proposed analysis scheme, a vehicle passing through Chongqi Bridge under the strong wind is an experiment case study. Firstly, regarding to the limited number of measurement sensors on the bridge, the bridge monitoring response is expanded through an improved perturbed force method combined with genetic algorithm method, and the wind speed is simulated with linear filtering method. Next the expanded monitoring data is combined with MBS-FEM model to comprehensively consider the wind effect on the vehicle and bridge. Finally, the vehicle responses from the MBS-FEM model are compared with experimental data, showing the accuracy and good reliability of this method. This monitoring-based MBS-FEM method also is expected be used for stability analysis of vehicles running on bridges under the strong wind.

Q. Hu (✉)

Department of Civil Engineering, The University of Tokyo, Tokyo, Japan

e-mail: hu.qi@bridge.t.u-tokyo.ac.jp

D. Su

The University of Tokyo, Tokyo, Japan

Keywords Vehicle-bridge-interaction · FEM · MBS · Monitoring data

1 Introduction

Coupled vibration of the vehicle-bridge interaction system is one of the primary concerns in both bridge and vehicle engineering that has been long recognized. Vehicle safety and ride comfort are more easily facing a significant challenge when crosswind combined with the Vehicle-Bridge Interaction (VBI) system.

Many researchers have already contributed to this field, and Finite element method (FEM) was used for solving the wind-vehicle-bridge interaction problem to obtain the structural dynamic performance. Cai and Chen [1] presented a framework of dynamic analysis of the coupled three-dimensional vehicle-bridge system under strong winds. An overall and then partial automobile accident analysis framework is proposed. The vertical, yawing, and pitching responses of the vehicle can be obtained through the overall WVB analysis, and the vehicle's lateral and rolling response is further obtained in the local accident analysis model focused on the vehicle itself. Xu and Guo [2] proposed a relatively complete analysis model to analyze the safety and ride comfort of running vehicle under crosswind. By introducing a lateral damper model related to bridge motion parameters, consider the lateral coupling relationship between the vehicle and bridge to predict vehicle accidents. However, as Wang [3] pointed out in his review, simplified assumptions [4], including lumped masses of the vehicle, stationary aero-dynamic wind forces [5], and linear elastic assumption of the bridge material, are unavoidable, which may bring errors into the simulated results [6].

Another efficient and high-fidelity analysis method to solve this issue is to utilize the Multiple-body Simulation (MBS) method, which can be more accurate to investigate the detailed behavior of the vehicle. Several researchers have recently applied this method to carry out the train-bridge coupling analysis. He et al. [7] proposed a rigid-flexible coupling method to simulate the train-bridge vibration under the actions of wind loads. Chen et al. [8] analyzed the track integral rigidity distribution considering a variation of rail section and elastic support, bending deformation of turnout sleeper, spacer block, and sharing pad effects.

In the current WVB system, numerical simulation is widely used to obtain the responses of bridges and vehicles for subsequent analysis. Due to the extensive computation burden and complicated human manipulation, these simulation-based methods cannot meet the needs to obtain timely information [3]. Simultaneously, whether the results obtained can truly reflect the actual situation is also debatable. The in-situ monitoring data is a valuable resource for the VBI system, especially when the external force applied to the structure is not so clear. Meanwhile, the real structure response can be obtained accurately based on advanced sensor measurement technology. Only a few researchers focus on combining the real test data and the model for analysis [9]. Recently, a monitoring-based approach was proposed [3] to estimate dynamic vehicle responses. However, it is also combined with the traditional

VBI analysis method and cannot handle the problems mentioned before. Also, this method has not yet been verified by the experiment result.

Currently, the VBI system has not been studied by the MBS-FEM combined method, which integrates the FEM and MBS and fully takes advantage of two methods that obtain the accuracy response of both structure and vehicle. In this study, a new method called the double-dummy coupling method is used to connect the vehicle and bridge in the MBS-FEM system and validated by the measurement data. Besides, a monitoring-based MBS-FEM method for estimating the dynamic responses of the vehicle running on the bridge is presented. The novelty of this method is the hybrid combination of on-site monitoring data and the MBS-FEM model. The previous cumbersome and time-consuming calculation process will be simplified, and a more reasonable analysis of the vehicle response will be combined with the measured data.

2 Vehicle-Bridge System in MBS-FEM

2.1 MBS-FEM Combine Method

MBS is carried out to study the kinetic and kinematic behavior of mechanisms. In this research, the MBS software Simpack and FEM software Abaqus are used for analysis.

Figure 1 shows the vehicle-bridge coupling flowchart using the MBS-FEM method. Firstly, bridge is modelled by FEM and then output as a flexible-body substructure. After incorporating the substructure into the SIMPACK, the vehicle model couples with bridge model in the MBS. Finally, other factors like wind, road roughness, and driver behavior can be simulated in the analysis system. Comparing

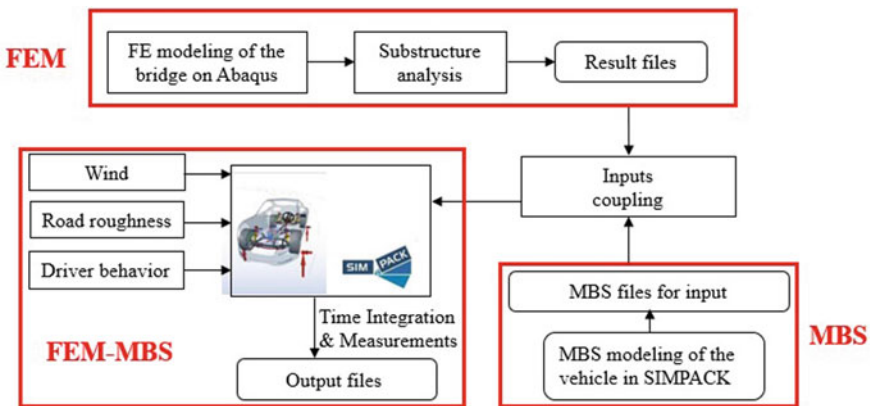


Fig. 1 Procedures of MBS-FEM method

with the FEM method, the MBS-FEM method has significant advantages, such as no need to decouple the system and easy to implement to complicated bridge models even considering the structure details.

2.2 *Bridge Model and Setting*

In Abaqus, the bridge finite element model should first be established and then set reasonable master nodes, coupling the master nodes with relevant surfaces. After that, creating boundary conditions and retaining all nodal degrees of freedom of those master nodes, finally conducting the frequency and substructure analysis. The key point is choosing reasonable master nodes, which define the interface between the FEM and MBS system. According to Guyan's law, the rational selection of the master DOF mainly follows the following principles [10]:

- (1) The total number of master DOF should be at least twice the number of modes to be studied.
- (2) Choose the master DOF to be distributed as evenly as possible.
- (3) Select all nodes with boundary conditions to be the master nodes and keep the DOF as the master DOF.
- (4) Choose the master DOF where the mass is relatively large and the rigidity is relatively small.
- (5) The DOF of the nodes where the geometry of the structure changes.
- (6) Select the DOFs of nodes parallel to or close to the centerline in the axisymmetric model as master DOFs.
- (7) In the rigid-flexible coupling model, select the DOF of joint and force element connection points as the master DOF.
- (8) If the DOF to be selected belongs to a coupled constraint set, only need to select the first DOF in the coupled set.
- (9) Select the master DOF in the vibration direction of the structure.
- (10) The master DOF selected should include all possible movements as much as possible.
- (11) Select the master DOF at the position where the force or non-zero displacement is applied.
- (12) Select the master DOF (bending, translation, torsion, stress or strain, and others) at the point where the calculation result will be obtained.
- (13) Ensure that the node position of the contact part between the super element and the ordinary element is accurate and coincident.

In the FEM model, slave nodes and master nodes are connected through certain constraints. After the master node of the structure is determined, other nodes on the same cross-sectional position can be determined as slave nodes, which can be connected with master nodes through coupling.

2.3 Vehicle Model and Double Dummy Method

In the MBS system, four basic modeling element categories (body, joint, force element, and external force) and other components (such as reference frame, marker, constraint, sensor) are assembled to form a typical model. The vehicle is a multi-DOF spatial system with complicated vibration composed of longitudinal, lateral, vertical, yaw, pitch, and roll motions. In this paper, a simple car is simulated consisting of 9 bodies (chassis, wheel carriers (4), wheels (4)), and the topological map of the vehicle is shown in Fig. 2.

One of the critical points of the VBI coupled vibration is the simulation of the coupling relationship between the vehicle and the bridge in the MBS. He et al. [7] have achieved the train-track coupling through MBS-FEM based on a single dummy method. It failed when applied to the VBI system with the problems of not well considering the vehicle tire, wind force, and road roughness factors together because the tire lateral nonlinear properties and the excitation due to the roughness cannot be well simulated. In this paper, a new double-dummy method is proposed, as shown in Fig. 3.

The rigid vehicle body and flexible bridge body are connected by the dummy body 1 based on the Curve-Curve 2D-Contact method in the Simpack. In this method, two kinds of markers called parent and child markers are generated and used in a pair. The two markers work together, and each follows a 2D contour, trying to find a position on their respective contour where a potential contact point between the two contours may occur. The joint 1 connecting the dummy body 2 and the dummy body 1 is created to include the road roughness problem. A moved marker is created on the dummy body 2 with the property of translation with vertical movement, determined by the vertical tire movement. This marker is used for representing the relative movement

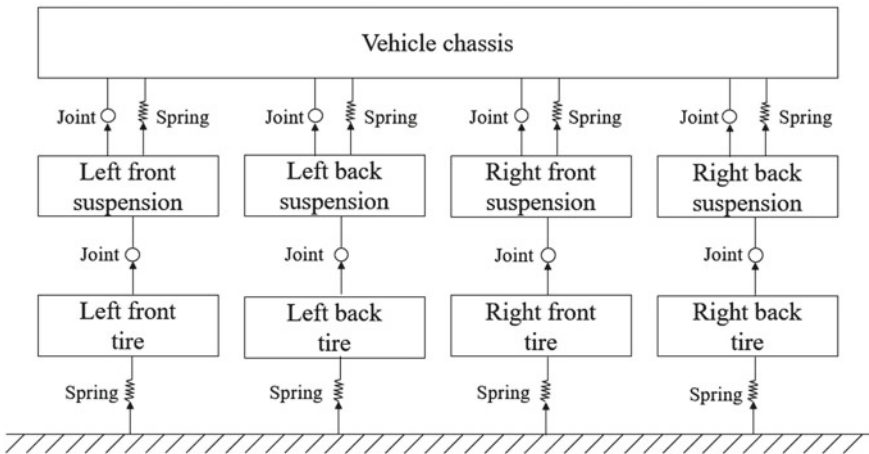


Fig. 2 Topological map of the vehicle

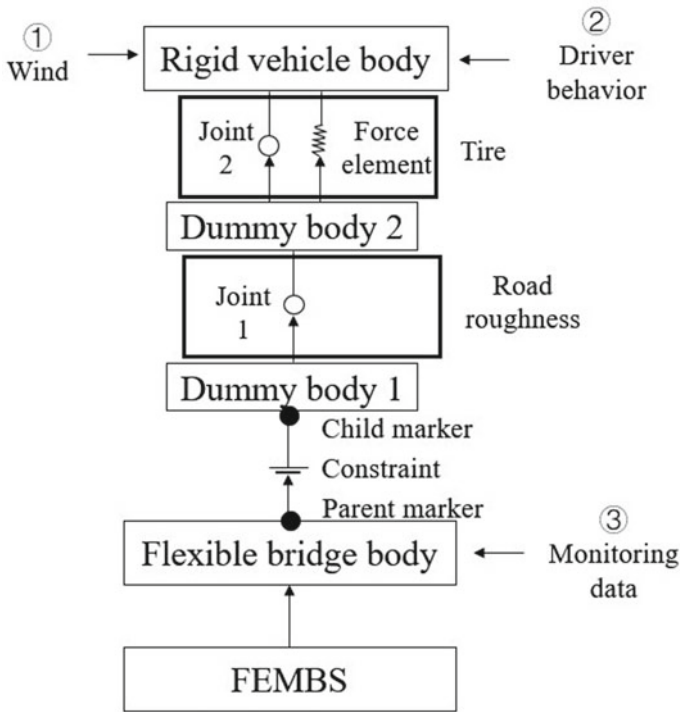


Fig. 3 Topological map of the vehicle

between the tire and bridge road surface. The vehicle tire properties can be well simulated by connecting the rigid vehicle body and dummy body 2. Different kinds of force elements between these two parts can be used for representing different tire properties. The tire’s nonlinear characteristics can be imported to the SIMPACK through specific user-defined tire files or input functions. The joint 2 between the rigid vehicle body and dummy 2 can ensure regular tire rotation.

2.4 Wind Force on the Vehicle

The wind force acting on the vehicle can be calculated using the quasi-static method, which can both consider the static and dynamic load effects. where V is the vehicle running speed, U and u are mean wind speed and turbulent wind speed on the vehicle, respectively. β is the angle between the wind and vehicle running direction.

$$F_x(t) = \frac{1}{2} \rho U_r^2 C_D(\psi) A, F_y(t) = \frac{1}{2} \rho U_r^2 C_S(\psi) A, F_z(t) = \frac{1}{2} \rho U_r^2 C_L(\psi) A,$$

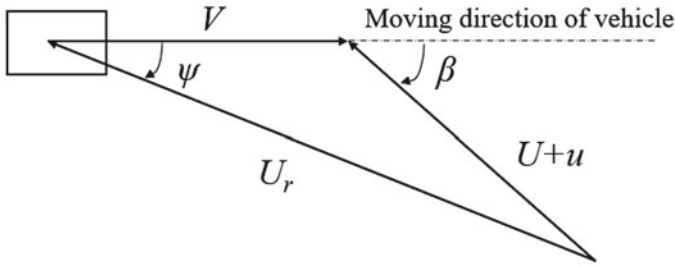


Fig. 4 Velocity diagram on the vehicle

$$M_x(t) = \frac{1}{2} \rho U_r^2 C_R(\psi) A h_v, M_y(t) = \frac{1}{2} \rho U_r^2 C_P(\psi) h_v, M_z(t) = \frac{1}{2} \rho U_r^2 C_Y(\psi) h_v \tag{1}$$

where $F_x(t)$, $F_y(t)$, $F_z(t)$, $M_x(t)$, $M_y(t)$ and $M_z(t)$ are the drag force, side force, lift force, rolling moment, pitching moment and yawing moment acting on the vehicle. $C_D(\psi)$, $C_S(\psi)$, $C_L(\psi)$, $C_R(\psi)$, $C_P(\psi)$ and $C_Y(\psi)$ are relative aerodynamic coefficients, respectively, which are functions of the angle ψ between the relative wind direction and the vehicle moving direction. A is the windward area of the vehicle and h_v is distance from the road surface to the gravity center of the vehicle. U_r is the relative wind speed to the vehicle and can be expressed as Fig. 4.

$$U_r^2(x, t) = [V + (U + u(x, t)) \cos \beta]^2 + [(U + u(x, t)) \sin \beta]^2 \tag{2}$$

3 Methodology of the Monitoring-Based Approach

3.1 Vehicle Motion Equation

The equation of motion of the vehicle model can be expressed as

$$M_v \ddot{q}_v + C_v \dot{q}_v + K_v q_v = F_c \tag{3}$$

where M_v , C_v , K_v are the mass, damping, and stiffness matrices of the vehicle separately. q_v is the vehicle absolute response and F_c is the contact force. The relative response q_{rv} can be obtained from q_v and the bridge absolute response q_b through $q_{rv} = q_v - q_b$. Substitute q_{rv} into Eq. (3) and transfer the items of q_{rv} to the left side, the undated equation is

$$M_v \ddot{q}_{rv} + C_v^* \dot{q}_{rv} + K_v^* q_{rv} = F_c^* \tag{4}$$

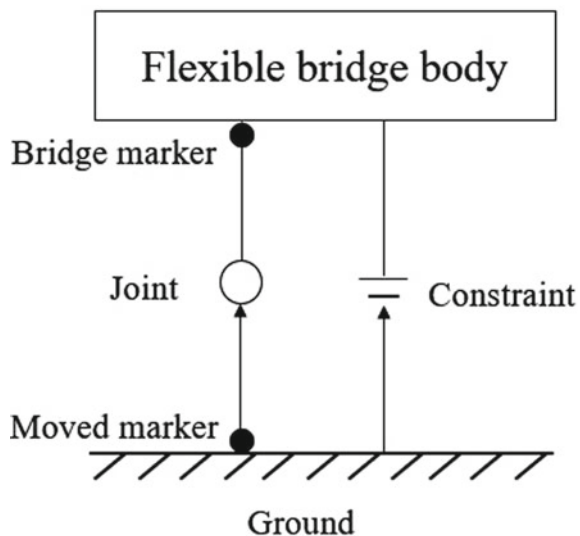
where C_v^* , K_v^* are the updated matrices and F_c^* is the function of the bridge absolute response q_b . If the real-time vibration response of the bridge is known, the q_{rv} can be obtained through solving the Eq. (4) by using numerical integration methods, and q_v can be obtained through $q_v = q_{rv} + q_b$.

3.2 Monitoring-Based Approach in MBS-FEM

In the MBS system, moved markers are established at the ground projection position of the bridge input vibration location as shown in Fig. 5, and are connected to the corresponding bridge input vibration position through a joint, which is used to simulate the bridge absolute movement q_b . The expanded bridge on-site monitoring responses are imported into simpack in the form of an input function, and then the corresponding excitations are established to obtain u-vectors to ensure that the moved markers have the movement of the expanded response.

Also, a constraint that links the bridge test point and ground is generated to ensure the deformation is precisely the same as the real test result. The number and location of bridge test points does affect the result and can be determined by the optimal sensor placement method.

Fig. 5 Details of connection part between the bridge and ground



4 Experiment Validation

Two experiments are carried out on the Tsukige Bridge and Chongqi Bridge, separately. The experiment which was conducted on the Tsukige Bridge is used for MBS-FEM method and monitoring-based method validation. The experiment result of Chongqi Bridge can be used to compare with the MBS-FEM monitoring-based method which considering the wind effect in the wind-vehicle-bridge system.

4.1 MBS-FEM Method Experimental Validation by Tsukige Bridge

The experiment [11] was conducted on the Tsukige Bridge, which located in Chiba prefecture, Japan. The bridge is a simply supported steel bridge with a length of 59 m and a width of 4.7 m. A Toyota HiAce van was chosen as the probe car to conduct the dynamic experiment. Vehicle model is shown as Fig. 6 and parameters can be found in Table 1. Bridge acceleration was obtained by wireless sensors installed on the bridge, and vehicle acceleration can be obtained through sensors installed on the front tire and rear tire. The vehicle speed in each case keeps constant, increasing from

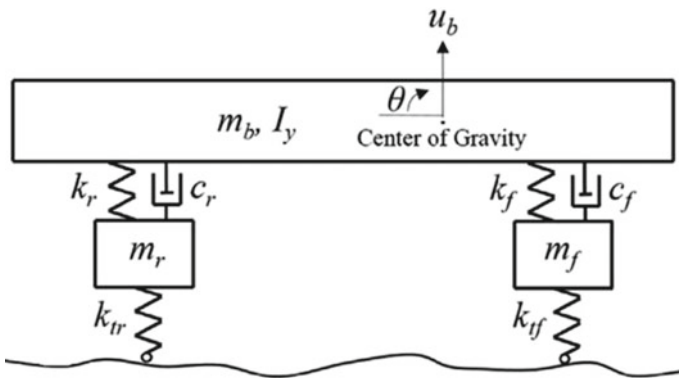


Fig. 6 Vehicle model

Table 1 Vehicle parameters [12]

Parameter	Value	Parameter	Value
m_b (kg)	1028.6	k_r (N/m)	109,890
m_f (kg)	271.2	c_f (N·s/m)	2673.8
m_r (kg)	550.2	c_r (N·s/m)	1385.3
I_y (m ²)	1676.5	k_{tf} (N/m)	1,725,000
k_f (N/m)	80,156	k_{tr} (N/m)	1,809,900



Fig. 7 Tsukige Bridge experiment

15 km/h to 55 km/h with an increase of 5 km/h. Six repeatability tests are conducted under each speed condition. The whole experiment view can be found in Fig. 7.

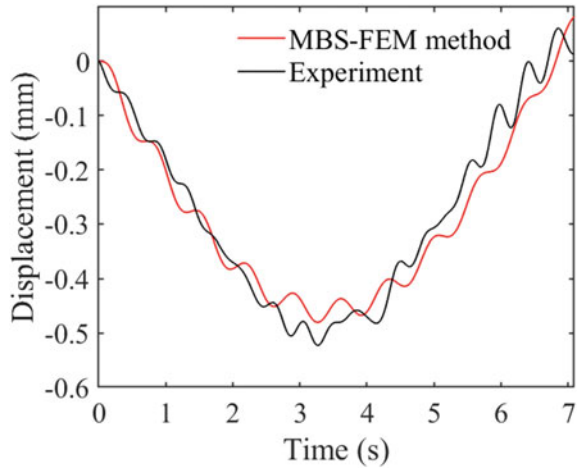
where m , k , c are mass, stiffness, and damping coefficients, respectively. Subscript b, f, r, tf, tr indicate vehicle body, front suspension, rear suspension, front tire, and rear tire.

Figure 8 shows comparisons of the vertical displacement at the midpoint of the bridge between the MBS-FEM method and field test data at the speed of 40 km/h. The quality indicator -Time Response Assurance Criterion (TRAC) [13] is a tool used to determine the degree of correlation between two time traces, which can be found in Eq. (5). The TRAC value is a positive real number with a value between 0 and 1. A value close to 1 indicates that the time history is completely consistent, while a lower value indicates errors.

$$TRAC = \frac{[(y_{test})^T y_{simu}]^2}{[(y_{test})^T y_{test}][(y_{simu})^T y_{simu}]} \quad (5)$$

where y_{test} and y_{simu} represent the real test response and simulation result separately. The TRAC value of Fig. 7 is 0.96, which shows the high accuracy of the MBS-FEM method. The result of bridge response matches well due to the more realistic Pacejka

Fig. 8 Bridge displacement results comparison of midspan



tire model is applied to the model, which not used in the previous VBI system. The tire model and road roughness in the MBS plays an essential role in the simulation.

Figure 9 shows the vehicle acceleration comparison between the real test and result from the MBS-FEM with a vehicle speed of 40 km/h. The average Root Mean Square (RMS) value error is 3.3%, which reflected the accuracy of the MBS-FEM method.

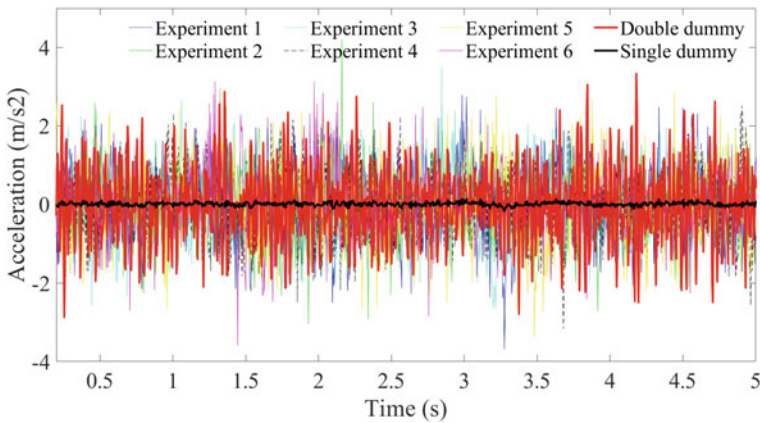


Fig. 9 Vehicle vertical acceleration comparison

4.2 MBS-FEM Monitoring-Based Method Validation by Chongqi Bridge

The wind-vehicle-bridge coupling system analysis system is verified by the Chongqi experiment test under the actual wind environment. The experiment is conducted between 2020 September 2nd and 4th, and the main bridge has a total length of 944 m and is a six-span steel continuous beam bridge (102 m + 4 × 185 m + 102 m). Typhoon Maysak formed in the Pacific Ocean at the end of August. It was upgraded to a super typhoon on September 1. After that, it gradually turned to the east-north direction and reached 140 km east of the area where Chongqi Bridge was located at noon on September 2. During the typhoon period, a truck passed at a constant speed of 60 km/h-100 km/h (at 10 km/h intervals), and each case is repeated twice, as shown in Fig. 10. 6 Mobile phones are installed as accelerometers at the position of the dashboard center, four suspensions, and the middle of the outside of the car. The MBS-FEM model can be found in Fig. 11.

Figure 12 shows the comparison between the vehicle acceleration in the experiment and the result calculated by the MBS-FEM method when the vehicle passes through the bridge at 80 km/h. The RMS error of vehicle acceleration under the two speed conditions are 4.74% and 5.61%, respectively, and the trend and value of the PSD curve show a good agreement.

Figure 13 is a summary of the RMS error values for five vehicle speed cases.

As the vehicle speed increases, the RMS error value gradually increases. When the vehicle speed is 60 km/h, the error is 2.68%, and when the vehicle speed is 120 km/h, the maximum error is 6.70%. The comparison results show that the wind-vehicle-bridge MBS-FEM model based on the monitoring-based method can realistically reflect the actual situation. Compared with the previous method, this method has proved its feasibility through experiments, and the RMS error is within an acceptable range. The complex fluid-structure coupling can be avoided through this method. Meanwhile, the effect of wind on vehicles and bridges can be well considered and simulated. The advantages of on-site measured data have been fully utilized, and more accurate vehicle responses can be obtained.

5 Conclusions

A novel monitoring-based MBS-FEM analysis scheme for vehicle-bridge interaction analysis is presented in this paper. To avoid an inconvenient and complicated computation process, the MBS-FEM method is applied to the VBI system. A new double-dummy coupling method is used to connect the vehicle and bridge parts in the MBS system and well considered the effects of the vehicle tire, wind force, and road roughness. In order to fully utilized the real test data and seeks a more efficient and accurate way to estimate the vehicle response, a monitoring-based approach in which hybrid in-situ data with the MBS-FEM model is proposed. Two experiments



Fig. 10 Truck passed through the Chongqi bridge

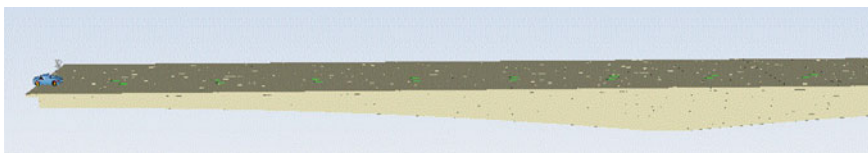


Fig. 11 Chongqi bridge MBS-FEM model

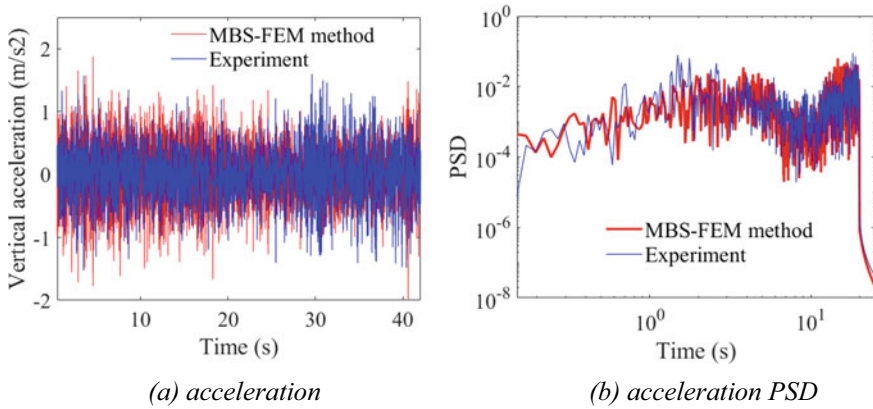
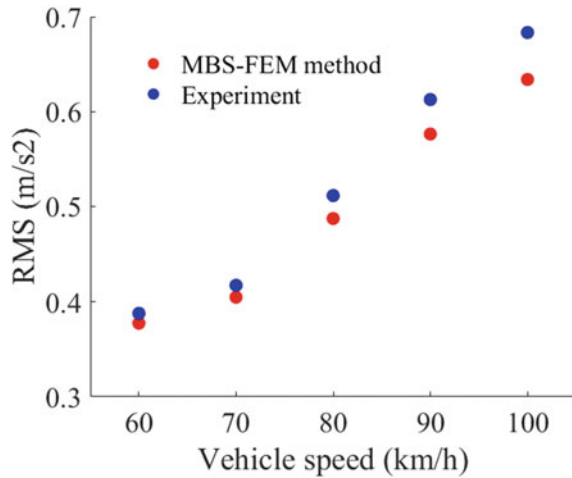


Fig. 12 Vehicle acceleration comparison-80 km/h

Fig. 13 Vehicle acceleration comparison-80 km/h



are conducted to validate the proposed methods. The comparison between the experiment and MBS-FEM results shows the good accuracy of the methods and can be used for further analysis.

Acknowledgements The first author gratefully acknowledges the CSC scholarship (No. 201806260249) for supporting this research. This work was partially supported by R&D Grant (KyoCho No.12) of Japan Bridge Association.

References

1. Cai CS, Chen SR (2004) Framework of vehicle-bridge-wind dynamic analysis. *J Wind Eng Ind Aerodyn* 92(7):579–607
2. Xu YL, Guo WH (2004) Effects of bridge motion and crosswind on ride comfort of road vehicles. *J Wind Eng Ind Aerodyn* 92(7):641–662
3. Wang H, Mao JX, Spencer BF (2019) A monitoring-based approach for evaluating dynamic responses of riding vehicle on long-span bridge under strong winds. *Eng Struct* 189:35–47
4. Guo WH, Xu YL (2001) Fully computerized approach to study cable-stayed bridge-vehicle interaction. *J Sound Vib* 248(4):745–761
5. Tao TY, Wang H, Li AQ (2016) Stationary and nonstationary analysis on the wind characteristics of a tropical storm. *Smart Struct Syst* 17(6):1067–1085
6. Han WS, Yuan YG, Xie Q et al (2017) Reliability-based truck weight regulation of small-to medium-span bridges. *J Bridg Eng* 23(1):04017109
7. He XH, Gai YB, Wu T (2017) Simulation of train-bridge interaction under wind loads: a rigid-flexible coupling approach. *DEStech Trans Eng Technol Res* 6(3):163–182
8. Chen M, Luo YY, Zhang B (2014) Dynamic characteristic analysis of irregularity under turnout by vehicle-turnout rigid-flexible coupling model. *Adv Mater Res* 591–595
9. Chen SR, Chen F, Liu JH et al (2010) Mobile mapping technology of wind velocity data along highway for traffic safety evaluation. *Transp Res Part C: Emerging Technol* 18(4):507–518
10. Cui S (2009) Research on refined simulation of vehicle-bridge coupling vibration based on multibody system dynamics and finite element method. Southwest Jiaotong University, PhD (In Chinese)
11. Wang H, Nagayama T, Zhao B et al (2017) Identification of moving vehicle parameters using bridge responses and estimated bridge pavement roughness. *Eng Struct* 153:57–70
12. Wang H, Nagayama T, Nakasuka J et al (2018) Extraction of bridge fundamental frequency from estimated vehicle excitation through a particle filter approach. *J Sound Vib* 428:44–58
13. Perter A, Pawan P (2012) Prediction of full field dynamic strain from limited sets of measured data. *Shock Vib* 19:765–785